The Influence of Duration and the Selection and Scaling of Accelerograms in Engineering Design and Assessment

A thesis submitted to the University of London

for the degree of Doctor of Philosophy

and for the Diploma of Imperial College

by

Jonathan Hancock

Department of Civil and Environmental Engineering

Imperial College

University of London

March 2006

ABSTRACT

Seismic design of structures is currently based on the amplitude of ground motions caused by earthquakes expressed in terms of the acceleration or displacement response of SDOF oscillators. The duration of ground shaking is generally not considered. A review of the technical literature shows that some studies find a link between duration and structural demand, whilst others do not. Part of the reason for this disagreement is that there are different definitions of ground-motion duration and number of cycles; most of which are poorly correlated. The seismological characteristics that influence duration and number of cycles are reviewed and a new predictive equation is derived for bracketed duration. This shows that earthquake magnitude has the primary influence on ground-motion duration and number of cycles.

Analysis of an 8-storey reinforced concrete wall frame building shows that accelerograms can be linearly scaled by factors of 10 without causing a bias (over- or under-estimation) of the response, provided they are initially selected to match the earthquake magnitude and spectral shape. **A new method of adjusting accelerograms using wavelets to match smooth elastic response spectra at multiple damping levels is developed. This enables structural response to be predicted with greater confidence and with fewer analyses than possible using accelerograms selected by seismological criteria and linearly scaled to match the response spectrum.**

An extensive study of strength and stiffness degrading masonry structures is conducted. This shows that ground-motions with longer duration, for a given level of spectral acceleration, cause greater damage. Analysis of a reinforced concrete wall frame building with spectrally matched accelerograms demonstrates that the influence of the ground-motion duration principally depends on the damage metric used; peak response measures (such as inter-storey drift) are not influenced by duration, whilst hysteretic energy and fatigue damage measures are generally positively correlated with ground-motion duration.

Acknowledgements

Firstly I must thank Dr Julian Bommer for proposing this research project. His advice and guidance throughout the project is greatly appreciated.

I would like to particularly thank Dr Norman Abrahamson, Dr Guido Magenes and Professor I.M. Idriss for their assistance and guidance on separate sections of the work conducted for this thesis.

I am grateful to Dr Paul Greening and Dr Rui Pinho for their thorough review of the thesis and valuable feedback from the PhD viva. I would also like to thank Dr Rui Pinho and Dr Stelios Antoniou for assistance with their excellent SeismoSoft applications, which were used in several of the parts of this thesis.

The kind advice of Dr John Douglas for help with the analysis of strong ground motion records is acknowledged. I would also like to acknowledge John Alarcon, Professor N. Ambraseys, Katrin Bayer, Dr Juliet Bird, Miguel Castro, Dr George Chlimintzas, George Cossenas, Dr Elghazouli, Dr Leroy Gardner, Dr Damian Grant, Alexandros Markatis, Rishmila Mendis, Dr Tiziana Rossetto, Dr Sarma, Fleur Strasser, and Dr Iain Tromans and for the many interesting discussions related to this project at Imperial College London.

I have presented several sections of this work at different conferences around the world. This has given me the opportunity to discuss and improve my ideas. I am indebted many people for lively and interesting discussions on my work including: Ana Acevedo, Edmund Booth, Dr Andrew Chanerley, Professor Allin Cornel, Helen Crowley, Dr Matthew Free, Dr Russell Green, Dr Fatemeh Jalayer, Dr Andreas Kappos, Professor Dave Potts, Professor Nigel Priestley, Professor Paul Somerville, Dr Amador Teran-Gilmore, Dr Robert Tremblay, Dr Manuel Lopez, Zygmunt Lubkowski, Dr Nicolas Luco, Dr Peter Merryman, Dr Susanne Sargeant, Nick Sartain, Dr Nilesh Shome, Ian Smith, Jennie Watson-Lamprey and Professor Yousef Bozorgnia.

This work is supported by an EPSRC doctoral training grant from Imperial College London. The funding provided by the Council is gratefully acknowledged. I would also like to thank Mrs Margaret Hancock and Dr John Douglas, for proof reading. Finally, and most importantly, I would like to express my thanks to my wife for her ongoing support and encouragement.

CONTENTS

1. INTRODUCTION 32

2. MEASURES OF SEISMIC ACTION 34
2.1 Accelerograms 34
2.1.1 Types of accelerograph 34
2.1.2 Noise and processing accelerograms 36
2.2 Overview of Strong-Motion Parameters 37
2.2.1 Measures of peak ground motion and effective peak motion 38
2.2.2 Measures of spectral response 46
2.2.3 Measures of energy 57
2.2.4 Hybrid ground-motion measures 59
2.3 Definitions of Ground-Motion Duration 60
2.3.1 Bracketed duration 60
2.3.2 Uniform duration 61
2.3.3 Significant duration 62
2.3.4 Structural duration 63
2.3.5 Classification of duration measures 63
2.4 Definitions of Number of Cycles 65
2.4.1 Peak counting definitions 66
2.4.2 Level crossing definitions 67
2.4.3 Range counting definitions 69
2.4.4 Indirect counting methods 70
2.4.5 Definitions based on structural response 71
2.4.6 Procedures for determining effective number of constant amplitude cycles 72
2.4.7 Reference level 75
2.4.8 Classification of cycle counting definitions 77
2.5 Correlations Between Duration and Number of Cycles 77
2.6 Summary 79

3. REVIEW OF THE INFLUENCE OF DURATION ON STRUCTURAL DAMAGE 81
3.1 Introduction 81
3.2 Field Evidence 83
3.3 Experimental Results 83
3.4 Studies Measuring Drift or Displacement 87
3.4.1 Studies measuring maximum drift or displacement 87
3.4.2 Studies using cumulative measures 89
3.5 Studies Using Energy Measures 92
3.6 Studies Using Spectral Response 96
3.7 Summary 105

4. THE INFLUENCE OF DURATION ON MASONRY STRUCTURES 106
4.1 Structural Model 106
4.2 Damage Measures 107
4.3 Strong-motion Accelerograms 109
4.4 Average Spectral Acceleration 111
4.5 Influence of Duration 113
4.6 Time-domain Response Spectra 120

4.7 Damage Measure Based on 3D Spectra 124
4.8 Summary and Further Work 127

5. PREDICTING DURATION AND NUMBER OF CYCLES 130
5.1 Predicting the Number of Cycles of Motion 130
5.1.1 The influence of earthquake magnitude 131
5.1.2 Source-to-site distance 134
5.1.3 Rupture directivity 137
5.1.4 Site soil classification 138
5.1.5 Ground motions with broad-banded frequency content 138
5.2 Developing Liquefaction-Based Bracketed Duration 140
5.2.1 Premise of duration definition 141
5.2.2 Liquefaction-based duration 146
5.2.3 Strong-motion database 149
5.2.4 Primary dataset 149
5.2.5 Secondary dataset 153
5.2.6 Influence of duration definition on predictions 154
5.2.7 Influence of direction of motion on duration 156
5.2.8 Comparisons with significant duration definitions 157
5.2.9 Basic correlations 158
5.2.10 Regression of data 163
5.2.11 Review of functional forms 163
5.2.12 Selection of functional form 166
5.2.13 Regression of primary dataset 167
5.2.14 Regression of secondary dataset 174
5.2.15 Influence on liquefaction assessment 178
5.3 Summary and Further Work 180

6. WAVELET ADJUSTMENT OF RECORDED GROUND MOTIONS 181
6.1 Time Domain Dynamic Analysis 181
6.2 Existing Methods of Creating Spectral Compatible Ground Motions 181
6.3 Use of Wavelets in Engineering Seismology 184
6.3.1 Simplified structural analysis 185
6.3.2 Response identification 185
6.3.3 Analysis of accelerograms 186
6.3.4 Simplified representation of the ground motion 186
6.3.5 Adjustment of accelerograms 187
6.4 Lilhanand and Tseng Matching Procedure 188
6.5 Wavelets 191
6.5.1 Wavelet used by Lilhanand and Tseng 191
6.5.2 New displacement-compatible wavelets 192
6.6 Solution Stability 195
6.6.1 Change in time of response peaks 196
6.6.2 Reduction of off-diagonal *C* matrix elements 197
6.6.3 Adding secondary peaks 199
6.6.4 Reduction of correction amplitude 200
6.6.5 New solution algorithm 202
6.7 Spectral Target For Match 202
6.7.1 Matching spectral displacements 202
6.7.2 Matching spectral accelerations 203

6.8 Criteria for Selecting Seed Records 204
6.9 Target Periods and Solution Tolerance 206
6.10 Examples of Spectral Matching 210
6.11 Summary and Further Work 221

7. EQUIVALENT SDOF SYSTEMS 223
7.1 Background 223
7.2 MDOF Systems Investigated 225
7.2.1 Structural models 225
7.2.2 Analytical modelling 227
7.2.3 Material parameters 229
7.2.4 Shear deformations 230
7.3 Measures of Damage 231
7.4 Strong-motion Data Set 231
7.5 Equivalent SDOF Systems 232
7.6 Comparison of MDOF and SDOF Response 238
7.6.1 Peak drift at the effective height of structure 238
7.6.2 Peak inter-storey drift 240
7.6.3 Displacement time-series 247
7.6.4 Global damage measures dependent on time-series 252
7.7 Summary and Further Work 259

8. SELECTION AND SCALING OF ACCELEROGRAMS 262
8.1 Design Code Provisions 262
8.2 Assessment of "True" MDOF Response 264
8.3 Ground Motions 264
8.4 Damage Measures 266
8.5 Regression Method and Functional Form 266
8.6 Predictive Equations for Damage 269
8.6.1 Peak roof drift and inter-storey drift 269
8.6.2 Local element damage measures 273
8.6.3 Spectral acceleration 285
8.7 Selecting and Scaling Accelerograms 289
8.7.1 Target Scenario 289
8.7.2 Selection based on seismological characteristics 290
8.7.3 Linearly scaled to SA at the initial period of the structure 292
8.7.4 Linearly scaled average SA 294
8.8 Mean vs. Median 295
8.9 Response from Scaled Records 296
8.9.1 Peak drift 297
8.9.2 Local element damage measures 302
8.9.3 Scale Factor bias 324
8.10 Summary and Further Work 326

9. LINEARLY SCALED vs. SPECTRAL MATCHED ACCELEROGRAMS 329
9.1 Spectral Matched Accelerograms – 5% Damping 330
9.2 Spectral Matched Accelerograms – Multiple Damping 331
9.3 Spectral Matched Records with Different Durations 332
9.4 Response from Scaled and Matched Records 335
9.4.1 Peak drift 335

9.4.2 Local element damage measures 340
9.5 Influence of Duration on Structural Response 362
9.6 Summary 365

10. CONCLUSIONS AND RECOMMENDATIONS 366
10.1 General Overview and Summary 366
10.2 Summary of Conclusions 366
10.3 Summary of recommendations for further work 372

REFERENCES 374

APPENDIX 1. ACCELEROGRAMS USED FOR RC FRAME ANALYSIS 411

APPENDIX 2. SELECTION OF NUMERICAL INTEGRATION SCHEME 419

APPENDIX 3, COEFFICIENTS OF PREDICTIVE EQUATIONS 422

LIST OF FIGURES

Figure 2.1. - Photograph of an SMA-1 optical-mechanical accelerograph. (Hudson 1979) 35

Figure 2.2. - Schematic illustration of the recording mechanism of an SMA-1 instrument. (Hudson 1979) 35

Figure 2.3. – Kinemetrics Makalu digital accelerograph (Kinemetrics, 2004) 36

Figure 2.4. - Acceleration time-history and response spectra from 1994 M_w 6.7 Northridge earthquake (*upper*) recorded at distance of 59km at 950 Briarcliff on soil, (*lower*) recorded at a distance of 9km at Chalon Road on stiff soil 38

Figure 2.5. – Standard deviations for different methods of combining horizontal ground-motion components (Douglas 2001). 41

Figure 2.6. – Difference in RMS for different duration definitions: Accelerogram from M_w 6.7 1994 Northridge Earthquake recorded 13km from the fault rupture at Los Angeles-UCLA grounds (*Upper*); Stationary signal from JONSWAP random wave simulation, 6.3m H_s, 11 seconds peak period, γ=1 (*Lower*). 44

Figure 2.7. – Illustration of construction of response spectrum. Maximum response of each SDOF system is plotted against the period of the system 48

Figure 2.8. – The concept of UHS for a location affected by local sources of moderate seismicity and distant sources of greater activity (Bommer *et al.* 2000b, after Reiter 1990) 51

Figure 2.9. – Different Hysteretic models: (a) elasto-plastic; (b) bilinear; (c) tri-linear; (d) Q-model; (e) Takeda 1; (f) Takeda 2; (g) degrading strength; (h) shear-slip1; (i) flag (Modified from Fajfar *et al.1*989) 53

Figure 2.10. – Constant displacement ductility spectrum, 5% viscous damping, elastic-perfectly plastic hysteretic system, for the 1989 M_w 6.93 Loma Prieta Earthquake recorded 71km from the fault rupture at Diamond Heights (record 00794T in the NGA database) 53

Figure 2.11. – Definition of accumulative ductility (Mahin and Lin 1983) 54

Figure 2.12. – Definition of normalized hysteretic energy ductility (Mahin and Lin 1983) 54

Figure 2.13. – Constant cyclic ductility spectrum (accumulative ductility/ hysteretic energy ductility), 5% viscous damping, elastic-perfectly plastic hysteretic system, as for Figure 2.10 55

Figure 2.14. – (*below*) Fourier Amplitude Spectra from (*upper*) harmonic and single cycle motion. Demonstrating that whilst the amplitude and period of the continuous signal is well defined by the Fourier amplitude spectra, both the period and amplitude of the single impulse are poorly defined. 56

Figure 2.15. – Build up of Arias Intensity with time (Husid plot) for the 1989 M_w 6.9 Loma Prieta Earthquake recorded 71km from the fault rupture at Diamond Heights (record 00794T in the NGA database) 58

Figure 2.16. - Definition of Bracketed Duration (Bommer and Martínez-Pereira 1999) 61

Figure 2.17. – Definition of Uniform Duration (Bommer and Martínez-Pereira 1999) 62

Figure 2.18. - Definition of Significant Duration (Bommer and Martínez-Pereira 1999) 63

Figure 2.19. - Accelerogram recorded for the 3.9Mw Coalinga earthquake recorded at 5.7km at Sulphur Baths. Box shows section of motion used for cycle counting examples. 66

Figure 2.20. - Peak counting example, with non-zero crossings excluded. 67

Figure 2.21. - Level crossing example, with non-zero crossings excluded. 68

Figure 2.22. - Range counting example using rainflow counting technique, solid lines show full cycles, dashed lines show half cycles. 68

Figure 2.23. - Rainflow counting procedure 69

Figure 2.24. - Illustration of number of equivalent cycles for an elasto-plastic system. 71

Figure 2.25. - Illustration of Miner's linear damage accumulation. Applied cyclic loading (*upper*), and number of cycles to failure represented by a S-N curve with linear axes (*lower left*) and log-log axis (*lower right*) 73

Figure 2.26. – Ratios of number of relative effective cycles, N_{PR}, predicted by Liu *et al.* (2001) to the absolute bracketed duration at 0.05g, $D_{BA}(0.05g)$, and relative bracketed duration at 20% PGA, $D_{BR}(20\%)$, predicted by Kawashima and Aizawa (1989). 78

Figure 2.27. – Correlations between the absolute number of cycles defined using the rainflow counting method converted to an effective number of cycles using an exponent of 2.0, $N_{RA}(2.0)$, vs. uniform duration (*left*) and significant duration (*right*) for the 655 accelerograms from the Abrahamson and Silva (1997) dataset 79

Figure 3.1. - Plastic rotation vs fatigue life of top-and-seat angle connection (Mander *et al. 1995*) 86

Figure 3.2. - Fatigue plots of confined concrete (Dutta and Mander 2001) 93

Figure 3.3. - Illustration of the Influence of duration on demand spectrum as used in the HAZUS loss estimation methodology, M=7, at 20km, WUS, Site Class E. Note that HAZUS defines M7 as Moderate duration. (Kircher *et al.* 1997) 100

Figure 3.4. - Illustration of the influence of different earthquake magnitudes on demand spectrum reduced by duration as used in the HAZUS loss estimation methodology, low-rise, low-design code masonry structure, CEUS 20km hypocentral distance on a rock site. 100

Figure 3.5. - Amplification factor Ω_v for equivalent input energy velocity. (Chai and Fajfar 2000). 102

Figure 3.6. - Influence of significant duration Trifunac and Brady (1975a) on inelastic design spectra for a structure with $\beta^* = 0.15$, $\mu_m=4$, peak ground acceleration of 0.4g and peak ground velocity of 0.667m/s, characteristic period $T_c= 0.85$, developed using procedure proposed by Chai *et al.* (1998). 105

Figure 4.1. - Comparison between hysteretic model used in algorithm (solid line) and hysteretic behaviour of masonry structure determined by testing (Magenes *et al.* 1996)..... 107

Figure 4.2. - Correlations between strength degradation (maxdegR), stiffness degradation (maxdegK) and total energy dissipation (Ediss) from 473 analyses on the model with natural period of vibration of 0.15 second (Penazzo 2001)..... 108

Figure 4.3. - Magnitude-distance distribution of the full strong-motion dataset used in the masonry structures study, grouped according to generic rock or soil site classification (*upper*) and for only those records with a more detailed classification scheme (*lower*). 110

Figure 4.4. - Strength degradation of structure with 0.15 second initial natural period vs. spectral acceleration at 0.15 seconds period. Solid line shows S-Form trend line..... 112

Figure 4.5. – Standard deviation from S-form trend lines for a range of F-factors. Masonry structures with initial periods of 0.1, 0.15, 0.2, 0.25, 0.3, 0.4 and 0.5 seconds. 112

Figure 4.6. - Strength degradation of structure with 0.15 second initial natural period vs. spectral acceleration averaged from 0.15 to 0.40 seconds period.... 113

Figure 4.7. – As Figure 4.6 but with data grouped according to the bracketed duration at 0.1g (*top left*), effective duration (*top right*), 5-75% significant duration (*lower left*) and significant duration over shortest 90% Arias Intensity (*lower right*) 114

Figure 4.8. – As Figure 4.6 but with the data grouped according to the uniform duration at an acceleration threshold of 0.1g (*upper*). Results plotted to 100% strength degradation, events with less than 10% strength degradation excluded and the upper limit of trend lines fitted by least squared regression (*lower*). Note that different duration intervals are used in the two figures..... 116

Figure 4.9. As Figure 4.6 but with the data grouped according to earthquake magnitude, with 3 (*upper*) and 4 (*lower*) magnitude bins..... 118

Figure 4.10. – Upper: As Figure 4.6 but with the data grouped according to the uniform duration at an acceleration threshold of 0.1g. Lower: Residuals from the trend line for different uniform duration bins; solid line indicates median, dashed lines show plus and minus one standard deviation. 119

Figure 4.11. - Response Envelope Spectrum for Event 9, NS component of an aftershock from the 1940 Imperial Valley earthquake, recorded at El Centro, 10% damping; dashed and solid lines indicate Rayleigh and Love wave arrivals respectively (Trifunac 1971a)..... 121

Figure 4.12. - 3D response spectra for 1994 Northridge (6.7M_w) earthquake, recorded at 2 km from the fault rupture at West Pico Canyon Road. Solid black lines on response spectra show stiffness degradation of masonry structures with 0.1, 0.15, 0.2, 0.25, 0.3, 0.4 and 0.5s initial period. Analysis of 0.2-0.5s structures halted when 2% drift limit exceeded..... 122

Figure 4.13. - 3D response spectra for 1992 Landers earthquake (7.3M_w), recorded 26km from the fault rupture at Fun Valley. Solid black lines on response spectra show stiffness degradation of masonry structures with 0.1, 0.15, 0.2, 0.25, 0.3, 0.4 and 0.5s initial period..... 123

Figure 4.14. - Correlation between 3D spectral intensity proposed by Şafak (1998) and the strength degradation of masonry structures with 0.15s initial period. Intensity evaluated for period ranges 0 to 5s (*left*) and 0.15 to 0.4s (*right*)..... 125

Figure 4.15. - 3D response spectra for 1994 Northridge (6.7M_w) earthquake, recorded at 87 km from the fault rupture on soft soil downstream of the Prado dam. Solid black lines on response spectra show stiffness degradation of masonry structures with 0.1, 0.15, 0.2, 0.25, 0.3, 0.4 and 0.5s initial period..... 126

Figure 4.16. - 3D response spectra for 1984 Morgan Hill (6.3M_w) earthquake, recorded at 11 km from the fault rupture on stiff soil at Gilroy 6. Solid black lines on response spectra show stiffness degradation of masonry structures with 0.1, 0.15, 0.2, 0.25, 0.3, 0.4 and 0.5s initial period. Analysis of 0.5s structure halted after 2% drift limit exceeded. 127

Figure 5.1. - Predicted median values of the number of effective cycles at 65% maximum amplitude as a function of magnitude: 1 – Haldar and Tang (1981), mean weighting; 2a – Green (2001) 60km distance; 2b Green (2001) 40km distance; 2c Green (2001) 20km distance; 2d Green (2001), 0km Distance; 3a – Liu et al. (2001) 10km distance, field-based weighting; 3b – Liu et al. (2001) 10km distance, averaged weighting; 3c – Liu et al. (2001) 10km distance, laboratory-based weighting; 4 – Arango (1996); 5 – Seed and Idriss (1971); 6a – Seed et al., (1975) using the strongest component of motion; 6b – Seed et al., (1975) using both components of motion, evaluated separately; 7 – Valera and Donovan (1977). 131

Figure 5.2. - Relationship between number of effective cycles and earthquake magnitude. All accelerograms were recorded between 5 and 20km from surface projection of the fault rupture at sites classified as rock. Exponential trend lines shown by dashed and solid lines. 134

Figure 5.3. - Predicted median values of the number of effective cycles at 65% maximum amplitude as a function of distance, according to the equations of Liu *et al.* (2001). 135

Figure 5.4.- Predicted total number of velocity cycles as a function of source-to-site distance, according to the equations of Lu *et al.* (2001)..... 135

Figure 5.5. - Relationship between number of effective cycles and source-to-site distance for 78 accelerograms from the 1994 6.7 M_w Northridge earthquake; linear trend lines shown by dashed and solid lines..... 136

Figure 5.6. - Accelerograms and response spectra from the 1994 6.7M_w Northridge earthquake, recorded at Castaic – Old Ridge Route (*upper*) and Monte Nido Fire Station (*lower*), both stations on rock approximately 20km from the fault rupture. 137

Figure 5.7. - Displacement time histories of 2.5s and 0.5s SDOF systems with 5% damping under the action of 1992 7.1 M_w Cape Mendocino (Petrolia) earthquake ground motions recorded 32km from the fault rupture at Shelter Cove 2 (stiff soil). 139

Figure 5.8. - Fourier amplitude spectra of the time histories shown in Figure 5.7. 140

Figure 5.9. - Time-series of shear stresses induced by earthquake ground motions 141

Figure 5.10. - Typical form of the relationship between cyclic shear stress and the number of cycles to cause failure – simple shear conditions 142

Figure 5.11. - Cyclic stress ratio required to reach initial liquefaction (From shaking table tests by DeAlba *et al.* 1976) 143

Figure 5.12. - Cyclic stress ratios required to cause 5% double amplitude axial strain of in-situ frozen samples (***FS***) compared with those of conventional "undisturbed" tube samples (***TS***) and samples reconstituted by pluviation through air (***PA***) and samples reconstituted by moist tamping (***MT***); effective initial consolidation pressure = 98 kPa (from Yoshimi *et al.* 1984). 144

Figure 5.13. - Comparison of the cyclic stress ratio to cause liquefaction obtained for frozen samples and tube samples tested by Yoshimi *et al.* (1984) and for reconstituted samples tested by DeAlba *et al.* (1976) 145

Figure 5.14. - Normalized cyclic stress ratio versus number of cycles to cause liquefaction 145

Figure 5.15. - Time-series of Cyclic Stress Ratio induced by earthquake ground motions 146

Figure 5.16. - Liquefaction-based bracketed duration – positive side (19.1 – 2.9 = 16.2 sec), negative side (19.8 – 2.7 = 17.1 sec) and independent of sign (19.8 – 2.7 = 17.1 sec) 148

Figure 5.17. - Magnitude-distance distribution of the primary strong-motion dataset grouped according to site classification. 150

Figure 5.18. - Magnitude-distance distribution of the primary strong-motion dataset grouped according to style of faulting. 151

Figure 5.19: Magnitude-distance distribution of the secondary strong-motion dataset grouped according to site classification. 153

Figure 5.20. - Magnitude-distance distribution of the secondary strong-motion dataset grouped according to style of faulting. 154

Figure 5.21. - Comparison of showing difference if positive or negative acceleration limits are used. 156

Figure 5.22. - Comparison showing differences between longest or shortest horizontal component. 157

Figure 5.23. - % Arias intensity between duration limits 158

Figure 5.24. - Relationship between duration and magnitude with soil type, with linear trend lines; primary dataset. 159

Figure 5.25. - Correlation between duration and magnitude with soil type for different CSR levels; primary dataset. 160

Figure 5.26. – Relationship between duration and magnitude with fault mechanism, with linear trend lines; primary dataset 160

Figure 5.27. - Correlation between duration and magnitude with fault mechanism for different CSR levels; primary dataset. 161

Figure 5.28. - Relationship between duration and distance with soil type, with logarithmic trend lines; primary dataset 161

Figure 5.29. - Correlation between duration and distance with soil type for different CSR levels; primary dataset. 162

Figure 5.30. - Relationship between duration and distance with earthquake mechanism, with logarithmic trend lines; primary dataset. 162

Figure 5.31. - Correlation between duration and distance with earthquake mechanism for different CSR levels; primary dataset. 163

Figure 5.32. - Prediction of LBBD at 25% max CSR vs. magnitude, for different site soil types, strike-slip faulting, 50km distance 168

Figure 5.33. - Prediction of LBBD at 25% max CSR vs. magnitude, for different earthquake faulting mechanisms, rock sites, 50km distance 168

Figure 5.34. - Prediction of LBBD at 25% max CSR vs. distance, for different site soil types, strike-slip faulting, magnitude M7.5. 169

Figure 5.35. - Prediction of LBBD at 25% max CSR vs. distance, for different earthquake faulting mechanisms, rock sites, magnitude M7.5. 169

Figure 5.36. - Residuals for LLBD at 25% Maximum CSR vs. magnitude, horizontal lines represent median (long dashes), one standard deviation (dot, dash) and two standard deviations (dots) 170

Figure 5.37. - Residuals for LLBD at 25% Maximum CSR vs. distance, horizontal lines represent median (long dashes), one standard deviation (dot, dash) and two standard deviations (dots) 170

Figure 5.38. - Residuals for LLBD at 25% Maximum CSR vs. soil type, horizontal lines represent median (long dashes), one standard deviation (dot, dash) and two standard deviations (dots) 171

Figure 5.39. - Residuals for LLBD at 25% Maximum CSR vs. earthquake fault mechanism, horizontal lines represent median (long dashes), one standard deviation (dot, dash) and two standard deviations (dots) 171

Figure 5.40. - Residuals for LLBD at 25% maximum CSR vs. epicentral depth, horizontal lines represent median (long dashes), one standard deviation (dot, dash) and two standard deviations (dots) 172

Figure 5.41. - Comparison of LBBD at 25% max CSR (PGA), 50km distance, reverse faulting, rock sites and relative bracketed durations predicted at 50%PGA by McGuire and Barnhard (1979), and at 20% and 30%PGA by Kawashima and Aizawa (1979). 173

Figure 5.42. - Comparison of LBBD at 25% max CSR (PGA), M7.5, reverse faulting, rock sites and relative bracketed durations predicted at 50%PGA by McGuire and Barnhard (1979), and at 20% and 30%PGA by Kawashima and Aizawa (1979). 173

Figure 5.43. - Comparison of LBBD at 25% max CSR (PGA) derived with primary dataset, secondary dataset and surface projection of fault rupture distance, secondary dataset and rupture distance, 50km distance, reverse faulting, rock sites. 174

Figure 5.44. - Comparison of LBBD at 25% max CSR (PGA), derived with primary dataset, secondary dataset and surface projection of fault rupture distance, secondary dataset and rupture distance, M7.5, reverse faulting, rock sites..... 175

Figure 5.45. – Magnitude scaling factors derived by various investigators (Youd and Idriss 2001)..... 178

Figure 5.46. – SPT Clean-sand base curve normalized to magnitude 7.5 earthquakes with data from liquefaction case histories (Youd and Idriss, 2001) 179

Figure 6.1. – Three artificially generated accelerograms designed to match, on average, the S1 soil category elastic response spectrum from the French seismic design code (after Bommer and Ruggeri 2002). 182

Figure 6.2. – Records selected based on spectral shape by Bommer and Acevedo 2004 to match, on average, EC8 type 1 spectrum with site class B anchored to PGA of 0.36g between periods of 0.1 to 0.4s..... 184

Figure 6.3. - Basic methodology of RSPMatch program..... 189

Figure 6.4. - Reverse impulse wavelet with 5% damping, 0.6 seconds period, 6 seconds duration. Acceleration time-series (*top*), velocity time-series (*middle*) and displacement time-series (*lower*). 192

Figure 6.5. - Suarez and Montejo wavelet with 5% damping, 0.6 seconds period, 6 seconds duration. Acceleration time-series (*top*), velocity time-series (*middle*) and displacement time-series (*lower*). 194

Figure 6.6. - Suarez and Montejo wavelet with polynomial correction, 5% damping, 0.6 seconds period. Acceleration time-series (*top*), velocity time-series (*middle*) and displacement time-series (*lower*). Wavelet with 6 seconds duration (*left*) and 1.2 seconds duration (*right*)..... 195

Figure 6.7. - Suarez and Montejo wavelet with sinusoidal correction, 5% damping, 0.6 seconds period, 6 seconds duration. Acceleration time-series (*top*), velocity time-series (*middle*) and displacement time-series (*lower*)..... 196

Figure 6.8. - Illustration of sources of diverging response. Note that the response amplitude remains approximately unchanged at the time of the

original peak response, but the response increases through both a phase shift and the emergence of a secondary peak. 197

Figure 6.9. – Prevention of diverging response with an additional wavelet adjustment. 199

Figure 6.10. – Prevention of diverging response with reduction of correlated wavelet targets. 200

Figure 6.11. - RSPMatch methodology including new solution algorithms. 201

Figure 6.12. - Differences between spectral displacement and that calculated from absolute spectral acceleration (SA). 203

Figure 6.13. – Match to broad range of frequencies (0.01 s to 10 seconds) for a 5% damped elastic response spectra. Elastic response spectral (*top left*), acceleration time-series (*top right*), velocity time-series (*lower left*), displacement time-series (*lower right*) 204

Figure 6.14. - Elastic response spectra from the 1940 M_w 7.0 Imperial Valley Earthquake recorded 6.1km from the fault rupture at El Centro Array #9. Response matched from 0.05 to 5s period. Matched to 5% damped spectrum (*top row*); 5 and 10% damped spectra (*second row*); 5, 10 and 20% damped spectra (*third row*); 5, 10, 20 and 30% damped spectra (*bottom row*). Pseudo spectral acceleration (*left column*) and spectral displacement (*right column*) 207

Figure 6.15. - Elastic response spectra from the 1989 M_w 6.9 Loma Prieta Earthquake recorded 71km from the fault rupture at Diamond heights. Response matched from 0.05 to 5s period. Matched to 5% damped spectrum (*top row*); 5 and 10% damped spectra (*second row*); 5, 10 and 20% damped spectra (*third row*); 5, 10, 20 and 30% damped spectra (*bottom row*). Pseudo spectral acceleration (*left column*) and spectral displacement (*right column*) 210

Figure 6.16. - Elastic response spectra from the 1940 M_w 7.0 Imperial Valley Earthquake recorded 6.1km from the fault rupture at El Centro Array #9. Original linearly scaled accelerogram (*top*), response matched from 0.05 to 1s period (*middle*) and response matched to 0.05 to 5s period (*lower*). Pseudo spectral acceleration (*left*) and spectral displacement (*right*) 214

Figure 6.17. - Acceleration (*top*), velocity (*middle*) and displacement (*lower*) time-series from the 1940 M_w 7.0 Imperial Valley Earthquake recorded 6.1km from the fault rupture at El Centro Array #9 (record 00006L in the NGA database). Adjusted series for spectral match from 0.05 to 1 second period 215

Figure 6.18. - Acceleration (*top*), velocity (*middle*) and displacement (*lower*) time-series from the 1940 M_w 7.0 Imperial Valley Earthquake recorded 6.1km from the fault rupture at El Centro Array #9 (record 00006L in the NGA database). Adjusted series for spectral match from 0.05 to 5 seconds period 216

Figure 6.19. –Arias Intensity from the 1940 M_w 7.0 Imperial Valley Earthquake recorded 6.1km from the fault rupture at El Centro Array #9 (record

00006L in the NGA database). Original linearly scaled record and the record adjusted to 1 and 5 seconds..... 217

Figure 6.20. - Elastic response spectra from the 1989 M_w 6.9 Loma Prieta Earthquake recorded 71km from the fault rupture at Diamond heights (record 00794T in the NGA database). Original accelerogram (*top*), response matched from 0.05 to 1s period (*middle*) and response matched to 0.05 to 5s period (*lower*). Pseudo spectral acceleration (*left*) and spectral displacement (*right*) 218

Figure 6.21. - Acceleration (*top*), velocity (*middle*) and displacement (*lower*) time-series from the 1989 M_w 6.9 Loma Prieta Earthquake recorded 71km from the fault rupture at Diamond heights. Adjusted series for spectral match from 0.05 to 1 second period..... 219

Figure 6.22. - Acceleration (*top*), velocity (*middle*) and displacement (*lower*) time-series from the 1989 M_w 6.9 Loma Prieta Earthquake recorded 71km from the fault rupture at Diamond heights. Adjusted series for spectral match from 0.05 to 5 seconds period. 220

Figure 6.23. –Arias Intensity from the 1989 M_w 6.9 Loma Prieta Earthquake recorded 71km from the fault rupture at Diamond heights. Original linearly scaled record and the record adjusted to 1 and 5 seconds..... 221

Figure 7.1. – Principles of representing a MDOF with a SDOF. A pushover analysis is conducted assuming a shape vector (top left) to establish the inelastic displaced shape and the backbone of the hysteretic loop (Solid line, lower left plot). Note that different hysteretic rules make different assumptions on the unloading characteristics (dashed lines, lower plots)..... 224

Figure 7.2. - Plane and sectional elevation of the buildings: 8-storey irregular frame (*left*); 12-storey regular frame; 8-storey regular frame-wall building (Mwafy, 2001)..... 226

Figure 7.3. – Adopted modelling approach for regular and irregular frame buildings (Mwafy, 2001)..... 226

Figure 7.4. - Adopted modelling approach for frame-wall buildings (Mwafy, 2001) 227

Figure 7.5. – Fibre plasticity discretization in a reinforced concrete section (López-Menjivar 2004). 228

Figure 7.6. – Location of Gauss points along the member length (López-Menjivar 2004). 228

Figure 7.7. – Illustration of different hysteretic curves (after SeismoSoft 2005b) ... 233

Figure 7.8. – Force-displacement characteristics of the different RC frames from pushover analysis. Approximated bi-linear and tri-linear backbone curves also shown. 234

Figure 7.9. – Ability of different bi-linear and tri-linear equivalent SDOF models to predict MDOF displacement at the effective height of the structure. Trend line shown by solid line; ideal 1:1 target shown by dashed line..... 239

Figure 7.10. – Transfer functions relating drift at the effective height with inter-storey drift from pushover with triangular force distribution (*left*) and uniform force distribution (*right*). Solid lines show transfer functions from pushover analysis. Data points show results from time-history analysis..... 242

Figure 7.11. – Ability of different bi-linear and Takeda equivalent SDOF models to predict MDOF inter-storey drift for critical storeys of different frame structures. Trend line shown by solid line; ideal 1:1 target shown by dashed line..... 246

Figure 7.12. – Examples of cases where the bi-linear SDOF response has a good match with the regular frame MDOF response at the effective height of the structure. MODF and SDOF response under the action of the 1987 M_W 6.5 Superstition Hills earthquake recorded 1km from the fault rupture on stiff soil at parachute test site (*upper*) and the 1994 M_W 6.7 Northridge earthquake recorded 5.3km from the fault rupture on stiff soil at Sylmar Converter Station (*lower*). All SDOF hysteretic models developed using pushover analysis with triangular lateral load distribution. 248

Figure 7.13. - Example of cases where the bi-linear SDOF response has a good match with the regular frame MDOF response by chance. MODF and SDOF response under the action of the 1999 M_W 7.1 Duzce earthquake recorded 6.5km from the fault rupture on stiff soil at Duzce. All SDOF hysteretic models developed using pushover analysis with triangular lateral load distribution. 249

Figure 7.14. – Force-displacement characteristics of Takeda, bi-linear and tri-linear hysteretic models compared to the regular frame MDOF response at the effective height of the structure under the action of the 1987 M_W 6.5 Superstition Hills earthquake recorded 1km from the fault rupture on stiff soil at Parachute Test Site. 249

Figure 7.15. – MODF and SDOF response under the action of the 1989 M_W 6.9 Loma Prieta earthquake recorded 3.8km from the fault rupture on stiff soil at LGPC. MDOF response at the effective height of the 12-storey regular frame. SDOF hysteretic curves derived using triangular pushover. 251

Figure 7.16. – Force-displacement characteristics of Takeda, bi-linear and tri-linear hysteretic models compared to the regular frame MDOF response at the effective height of the structure under the action of the 1989 M_W 6.9 Loma Prieta earthquake recorded 3.8km from the fault rupture on stiff soil at LGPC..... 251

Figure 7.17. – 3D elastic response spectra of the 1989 M_W 6.9 Loma Prieta earthquake recorded 3.8km from the fault rupture on stiff soil at LGPC. 252

Figure 7.18. - Ability of bi-linear and tri-linear equivalent SDOF models to predict regular frame MDOF response at the effective height of the structure. Trend line shown by solid line; ideal 1:1 target shown by dashed line..... 257

Figure 7.19. – Comparison of displacement time-series of regular frame MDOF and bi-linear SDOF representation based on the initial period of the structure, under the action of the 2002 M_W 7.9 Denali recorded on stiff soil 2.78km from the fault rupture at TAPS pump station #10..... 259

Figure 8.1. – Magnitude –Distance distribution of the dataset for earthquake style of faulting and site classification. 265

Figure 8.2. – Residuals of roof drift vs. Magnitude. Thin dashed lines indicate median, ±1 and 2 standard deviations of the whole dataset. Solid lines indicate median and ±1 standard deviation of the data binned in 0.2M units... 268

Figure 8.3. - Predicted median and median-plus-one-standard-deviation peak drift vs. Source-to-site distance for Magnitude M_w7.0, soft soil site and strike-slip rupture mechanism. 270

Figure 8.4. – Predicted median and median-plus-one-standard-deviation peak drift vs. Magnitude for a source-to site distance of 5km; soft soil site and strike-slip rupture mechanism. 270

Figure 8.5. - Comparison of peak roof drift predicted by the predictive equations (solid line-median; plus and minus one standard deviation-dashed) and those of the measured data binned by magnitude and distance, adjusted to strike-slip and stiff soil using the coefficients of predictive equation (diamonds median, error bars plus minus one standard deviation).... 271

Figure 8.6. – Residuals for roof drift in terms of earthquake magnitude (*top left*), source-to-site distance (*top right*), site classification (*lower right*) and rupture mechanism (*lower left*). 271

Figure 8.7. - Comparison of peak end rotation of the base of the outer ground floor column predicted by the predictive equations (solid line-median; plus and minus one standard deviation-dashed) and those of the measured data binned by magnitude and distance, adjusted to strike-slip and stiff soil using the coefficients of the predictive equation (diamonds median, error bars plus minus one standard deviation). 274

Figure 8.8. – As Figure 8.7 but for the outer end of the 1st floor beam at the edge of the structure. 274

Figure 8.9. – Residuals for peak end rotation of the base of the outer ground floor column in terms of earthquake magnitude (*top left*), source-to-site distance (*top right*), site classification (*lower right*) and rupture mechanism (*lower left*). 275

Figure 8.10. – Residuals for peak end rotation the outer end of the 1st floor beam at the edge of the structure in terms of earthquake magnitude (*top left*), source-to-site distance (*top right*), site classification (*lower right*) and rupture mechanism (*lower left*). 275

Figure 8.11. - Comparison of the absorbed hysteretic energy of the base of the outer ground floor column predicted by the predictive equations (solid line-median; plus and minus one standard deviation-dashed) and those of the measured data binned by magnitude and distance, adjusted to strike-slip and stiff soil using the coefficients of the predictive equation (diamonds median, error bars plus minus one standard deviation)..... 276

Figure 8.12. – As Figure 8.11 but for the outer end of the 1st floor beam at the edge of the structure. 277

Figure 8.13. – Residuals for absorbed hysteretic energy of the base of the outer ground floor column in terms of earthquake magnitude (*top left*), source-

to-site distance (*top right*), site classification (*lower right*) and rupture mechanism (*lower left*)..... 277

Figure 8.14. – Residuals for absorbed hysteretic energy of the outer end of the 1st floor beam at the edge of the structure in terms of earthquake magnitude (*top left*), source-to-site distance (*top right*), site classification (*lower right*) and rupture mechanism (*lower left*). 278

Figure 8.15. – Comparison of member end moment-rotation relations from triangular pushover analysis and that calculated from section analysis with different axial loads. Pushover forces decrease the axial load in the right-hand ground floor column to zero at approximately 0.08 radians rotation..... 279

Figure 8.16. - Comparison of the Park and Ang damage of the base of the outer ground floor column predicted by the predictive equations (solid line-median; plus and minus one standard deviation-dashed) and those of the measured data binned by magnitude and distance, adjusted to strike-slip and stiff soil using the coefficients of predictive equation (diamonds median, error bars plus minus one standard deviation)..... 280

Figure 8.17. – As Figure 8.16 but for the outer end of the 1st floor beam at the edge of the structure. 281

Figure 8.18. – Residuals for Park and Ang damage index of the base of the outer ground floor column in terms of earthquake magnitude (*top left*), source-to-site distance (*top right*), site classification (*lower right*) and rupture mechanism (*lower left*). 281

Figure 8.19. – Residuals for Park and Ang damage index of the outer end of the 1st floor beam at the edge of the structure in terms of earthquake magnitude (*top left*), source-to-site distance (*top right*), site classification (*lower right*) and rupture mechanism (*lower left*). 282

Figure 8.20. - Comparison of the fatigue damage of the base of the outer ground floor column predicted by the predictive equations (solid line-median; plus and minus one standard deviation-dashed) and those of the measured data binned by magnitude and distance, adjusted to strike-slip and stiff soil using the coefficients of predictive equation (diamonds median, error bars plus minus one standard deviation)..... 283

Figure 8.21. – As Figure 8.20 but for the outer end of the 1st floor beam at the edge of the structure. 284

Figure 8.22. – Residuals for fatigue damage index of the base of the outer ground floor column in terms of earthquake magnitude (*top left*), source-to-site distance (*top right*), site classification (*lower right*) and rupture mechanism (*lower left*)..... 284

Figure 8.23 – Residuals for fatigue damage index of the outer end of the 1st floor beam at the edge of the structure in terms of earthquake magnitude (*top left*), source-to-site distance (*top right*), site classification (*lower right*) and rupture mechanism (*lower left*). 285

Figure 8.24. – Pseudo spectral acceleration and spectral displacement spectra predicted by the new equations for a M_W 7.0 strike-slip earthquake at 20km R_{jb} for a site with stiff soil. 286

Figure 8.25. – Pseudo spectral acceleration and spectral displacement spectra predicted by the new equations for a M_W 5.5 strike-slip earthquake at 20km R_{jb} for a site with stiff soil. 286

Figure 8.26. – Comparison of the prediction of pseudo spectral acceleration for the 5% damped spectrum from this work with the predictive equations of other researchers 287

Figure 8.27. - Comparison of pseudo spectral acceleration for 5% damping at 0.2s period predicted by new predictive equations (smooth lines, solid line median, plus and minus one standard deviation dashed) and those of the observed data binned by magnitude and distance adjusted to strike-slip and stiff soil using the coefficients of predictive equation (diamonds median, error bars plus minus one standard deviation). 288

Figure 8.28. – As Figure 8.27 but for a pseudo spectral acceleration for 5% damping at 0.6s period. 288

Figure 8.29. – As Figure 8.27 but for a pseudo spectral acceleration for 5% damping at 1.2s period. 289

Figure 8.30. – 5% Damped response spectra for records selected on the basis of seismological characteristics 291

Figure 8.31. – 5% damped-elastic spectral response from records selected by spectral shape and magnitude, scaled to the 5% damped target spectral acceleration at the initial period of the structure. Median target spectra (l*ower*) and median-plus-one-standard-deviation (*upper*) 292

Figure 8.32. – 5% damped elastic spectral response from records linearly scaled to match to the 5% damped target spectral acceleration between 0.5 and 1.2s. Median target spectra (l*ower*) and median-plus-one-standard-deviation (*upper*) 294

Figure 8.33. – Distribution of peak roof drift of 8-storey regular wall-frame structure under the action of 100 unscaled horizontal accelerograms from earthquakes with magnitude M_w 6.5 -7.0 and R_{jb} 0 to 15.5km. 295

Figure 8.34. – Distribution of the peak elastic spectral acceleration at 0.56s period (5% damping) under the action of 100 unscaled horizontal accelerograms from earthquakes with magnitude M_w 6.5 -7.0 and R_{jb} 0 to 15.5km 296

Figure 8.35. – Peak roof drift from records selected and scaled based on seismological characteristics, SA at the initial period, SA over a range of periods. Error bars show median and ±1 standard deviation. Dashed lines show drift predicted by regression of 1656 unscaled MDOF time-history analyses. 298

Figure 8.36. – Peak inter-storey drift from records selected and scaled based on seismological characteristics, SA at the initial period, SA over a range of periods. Error bars show median and ±1 standard deviation. Dashed lines show drift predicted by regression of 1656 unscaled MDOF time-history analyses. 299

Figure 8.37. – Peak end rotation of beams at the edge of the structure from records selected and scaled based on seismological characteristics, SA at

the initial period, SA over a range of periods. Error bars show median and ±1 standard deviation. Dashed lines show drift predicted by regression of 1656 unscaled MDOF time-history analyses. 303

Figure 8.38. – Peak end rotation of the base of the columns at the edge of the structure from records selected and scaled based on seismological characteristics, SA at the initial period, SA over a range of periods. Error bars show median and ±1 standard deviation. Dashed lines show drift predicted by regression of 1656 unscaled MDOF time-history analyses. 304

Figure 8.39. – Absorbed hysteretic energy at the end of the beams at the edge of the structure from records selected and scaled based on seismological characteristics, SA at the initial period, SA over a range of periods. Error bars show median and ±1 standard deviation. Dashed lines show drift predicted by regression of 1656 unscaled MDOF time-history analyses. 308

Figure 8.40. – Absorbed hysteretic energy at the base of the columns at the edge of the structure from records selected and scaled based on seismological characteristics, SA at the initial period, SA over a range of periods. Error bars show median and ±1 standard deviation. Dashed lines show drift predicted by regression of 1656 unscaled MDOF time-history analyses. 309

Figure 8.41. – Park and Ang damage index at the end of the beams at the edge of the structure from records selected and scaled based on seismological characteristics, SA at the initial period, SA over a range of periods. Error bars show median and ±1 standard deviation. Dashed lines show drift predicted by regression of 1656 unscaled MDOF time-history analyses. 313

Figure 8.42. – Park and Ang damage index at the based of the columns at the edge of the structure from records selected and scaled based on seismological characteristics, SA at the initial period, SA over a range of periods. Error bars show median and ±1 standard deviation. Dashed lines show drift predicted by regression of 1656 unscaled MDOF time-history analyses. 314

Figure 8.43. – Fatigue damage index at the end of the beams at the edge of the structure from records selected and scaled based on seismological characteristics, SA at the initial period, SA over a range of periods. Error bars show median and ±1 standard deviation. Dashed lines show drift predicted by regression of 1656 unscaled MDOF time-history analyses. 319

Figure 8.44. – Fatigue damage index at the base of the columns at the edge of the structure from records selected and scaled based on seismological characteristics, SA at the initial period, SA over a range of periods. Error bars show median and ±1 standard deviation. Dashed lines show drift predicted by regression of 1656 unscaled MDOF time-history analyses. 320

Figure 8.45. – Scale factor vs different response measures, demonstrating that there is no consistent increase or decrease (bias) introduced with scale factor. Median level motions (*left*), median-plus-one-standard-deviation motion (*right*). Straight lines show linear trend lines fitted through the data by least squares regression. 325

Figure 9.1. – 5% damped elastic spectral response from records matched to the 5% damped target spectral acceleration using RSPMatch2005. Median

target spectrum (*lower*) and median-plus-one-standard-deviation target spectrum (*upper*) 330

Figure 9.2. – 1, 5, 10 and 20% damped elastic spectral response from records matched to the 1% and 5% damped target spectral acceleration using RSPMatch2005. Median target spectra (*lower*) and median-plus-one-standard-deviation target spectra (*upper*)..... 331

Figure 9.3. – Comparison of target spectra and median spectra from selected records with different durations which have been matched to fit the target using RSPMatch..... 332

Figure 9.4. – Comparison of 5% damped target spectrum and the spectra from selected records with different durations, which have been matched to fit the target using RSPMatch..... 333

Figure 9.5. – Correlation between different definitions of duration and numbers of effective cycles. Number of cycles measured using rainflow counting and converted to an equivalent number of cycles using exponent 2.0 (see 2.4.6). 333

Figure 9.6. – Peak roof drift from records selected on seismological characteristics and those selected and matched to the target spectra at different damping levels. Error bars show median and +/-1 standard deviation. Dashed lines show drift predicted by regression of 1656 unscaled MDOF time-history analyses. 336

Figure 9.7. – Inter-storey drift from records selected on seismological characteristics and those selected and matched to the target spectra at different damping levels. Error bars show median and +/-1 standard deviation. Dashed lines show drift predicted by regression of 1656 unscaled MDOF time-history analyses. 337

Figure 9.8. – Peak end rotation of beams at the edge of the structure from records scaled and matched using different criteria. Error bars show median and ±1 standard deviation. Dashed lines show drift predicted by regression of 1656 unscaled MDOF time-history analyses. 342

Figure 9.9. – Peak end rotation of the base of the columns at the edge of the structure from records scaled and matched using different criteria. Error bars show median and ±1 standard deviation. Dashed lines show drift predicted by regression of 1656 unscaled MDOF time-history analyses. 343

Figure 9.10. – Park and Ang damage index of beams at the edge of the structure from records scaled and matched using different criteria. Error bars show median and ±1 standard deviation. Dashed lines show drift predicted by regression of 1656 unscaled MDOF time-history analyses. 347

Figure 9.11. – Park and Ang damage index of the base of the columns at the edge of the structure from records scaled and matched using different criteria. Error bars show median and ±1 standard deviation. Dashed lines show drift predicted by regression of 1656 unscaled MDOF time-history analyses. 348

Figure 9.12. – Absorbed hysteretic energy (rad.mm) of beams at the edge of the structure from records scaled and matched using different criteria. Error

bars show median and ±1 standard deviation. Dashed lines show drift predicted by regression of 1656 unscaled MDOF time-history analyses. 352

Figure 9.13. – Absorbed hysteretic energy (rad.mm) of the base of the columns at the edge of the structure from records scaled and matched using different criteria. Error bars show median and ±1 standard deviation. Dashed lines show drift predicted by regression of 1656 unscaled MDOF time-history analyses..... 353

Figure 9.14. – Fatigue damage index of beams at the edge of the structure from records scaled and matched using different criteria. Error bars show median and ±1 standard deviation. Dashed lines show drift predicted by regression of 1656 unscaled MDOF time-history analyses. 357

Figure 9.15. – Fatigue damage index of the base of the columns at the edge of the structure from records scaled and matched using different criteria. Error bars show median and ±1 standard deviation. Dashed lines show drift predicted by regression of 1656 unscaled MDOF time-history analyses. 358

Figure 9.16. – Influence of duration on peak roof drift for accelerograms matched to the elastic spectral acceleration at multiple damping levels..... 362

Figure 9.17. – Influence of duration on peak inter-storey drift for accelerograms matched to the elastic spectral acceleration at multiple damping levels..... 363

Figure 9.18. – Influence of duration on different damage measures for the base of the outer ground floor column (*left*) and the outer end of the first floor beam (*right*). Analysis using accelerograms matched to the elastic spectral acceleration at multiple damping levels..... 364

LIST OF TABLES

Table 2.1. - Classification of definitions of strong-motion duration (Adapted from Bommer and Martínez-Pereira 2000) 64

Table 2.2. - Summary of cycle counting definitions used by different authors 76

Table 3.1. - Summary of the Relevance of Load Duration/Number of Cycles from Experimental Testing 84

Table 3.2. - Summary of the Relevance of Load Duration/Number of Cycles for Studies Measuring Extreme Drift or Displacement 88

Table 3.3. - Summary of the Relevance of Load Duration/Number of Cycles for Studies Using Cumulative Measures 91

Table 3.4. - Summary of the Relevance of Load Duration/Number of Cycles for Studies Using Energy Measures 95

Table 3.5. - Summary of the Relevance of Load Duration/Number of Cycles for Studies Using Spectral Response 97

Table 4.1. - Summary of constants describing trend lines and standard deviations of data points 115

Table 5.1. - Number of cycles based on line for frozen samples in Figure 5.16 147

Table 5.2. - Number of cycles based on line for reconstituted samples in Figure 5.16 148

Table 5.3. - Earthquakes used in final primary dataset 151

Table 5.4. - Earthquakes used in secondary dataset 155

Table 5.5. - Coefficients and standard deviations from regression of primary dataset 176

Table 5.6. - Significance level of coefficients using F-Test from regression of primary dataset 176

Table 5.7. - Coefficients and standard deviations from regression analysis using secondary dataset, 25% $_{max}$CSR 177

Table 5.8. - Significance level of coefficients using F-Test from regression using secondary dataset, 25%$_{max}$CSR 177

Table 6.1. - Typical *C* matrix for eight spectral points (two periods and four damping levels) with no subdivision 198

Table 6.2. - Typical *C* matrix for eight spectral points (two periods and four damping levels) split into four subgroups 198

Table 6.3. - RMS of difference between measured and target spectral acceleration (ΔSA_{RMS}) between 0.05 and 5 seconds period. 1940 M_w 7.0 Imperial Valley Earthquake recorded 6.1km from the fault rupture at El Centro Array #9 208

Table 6.4. - RMS of difference between measured and target spectral displacement (ΔSD_{RMS}) between 0.05 and 5 seconds period. 1940 M_w 7.0

Imperial Valley Earthquake recorded 6.1km from the fault rupture at El Centro Array #9 208

Table 6.5. - Average spectral misfit between 0.05 and 5 seconds period. 1940 M_w 7.0 Imperial Valley Earthquake recorded 6.1km from the fault rupture at El Centro Array #9. 209

Table 6.6. - RMS of difference between measured and target spectral acceleration (ΔSA_{RMS}) between 0.05 and 5 seconds period. 1989 M_w 6.9 Loma Prieta Earthquake recorded 71km from the fault rupture at Diamond heights. 209

Table 6.7. - RMS of difference between measured and target spectral displacement (ΔSD_{RMS}) between 0.05 and 5 seconds period. 1989 M_w 6.9 Loma Prieta Earthquake recorded 71km from the fault rupture at Diamond heights. 209

Table 6.8. - Average spectral misfit between 0.05 and 5 seconds period. 1989 M_w 6.9 Loma Prieta Earthquake recorded 71km from the fault rupture at Diamond heights. 209

Table 6.9. – Initial Linear Scale Factors Applied to Seed Accelerograms 212

Table 6.10. - Average spectral misfit between 0.05 and 5 seconds period. 1940 M_w 7.0 Imperial Valley Earthquake recorded 6.1km from the fault rupture at El Centro Array #9. 212

Table 6.11. - RMS of difference between measured and target spectral acceleration (ΔSA_{RMS}) between 0.05 and 5 seconds period. 1940 M_w 7.0 Imperial Valley Earthquake recorded 6.1km from the fault rupture at El Centro Array #9 212

Table 6.12. - RMS of difference between measured and target spectral displacement (ΔSD_{RMS}) between 0.05 and 5 seconds period. 1940 M_w 7.0 Imperial Valley Earthquake recorded 6.1km from the fault rupture at El Centro Array #9 213

Table 6.13. - Average spectral misfit between 0.05 and 5 seconds period. 1989 M_w 6.9 Loma Prieta Earthquake recorded 71km from the fault rupture at Diamond heights. 213

Table 6.14. - RMS of difference between measured and target spectral acceleration (ΔSA_{RMS}) between 0.05 and 5 seconds period. 1989 M_w 6.9 Loma Prieta Earthquake recorded 71km from the fault rupture at Diamond heights. 213

Table 6.15. - RMS of difference between measured and target spectral displacement (ΔSD_{RMS}) between 0.05 and 5 seconds period. 1989 M_w 6.9 Loma Prieta Earthquake recorded 71km from the fault rupture at Diamond heights. 213

Table 7.1. – Material properties used in the analysis 229

Table 7.2. - Effective height of MDOF structures 234

Table 7.3. – Properties of equivalent single degree-of-freedom systems 235

Table 7.4. – Detailed properties of bi-linear equivalent single degree-of-freedom systems 236

Table 7.5. – Detailed properties of Takeda equivalent single degree-of-freedom systems 236

Table 7.6. – Detailed properties of tri-linear equivalent single degree-of-freedom systems 237

Table 7.7. – Ability of different SDOF models to predict MDOF displacement at the effective height of the structure. Best values given in bold. 240

Table 7.8. – Mean and standard deviation of the difference between actual inter-storey drift from MDOF time-history analysis and the transfer function relating inter-storey drift and displacement at the effective height obtained from pushover analysis. Best values given in bold. 243

Table 7.9. – Gradient (Grad) and coefficient (R^2) of determination of linear trend line between SDOF predictions of inter-storey drift and drift obtained from MDOF time-history analysis for wall frame structure. Best values given in bold. 244

Table 7.10. – Gradient (Grad) and coefficient (R^2) of determination of linear trend line between SDOF predictions of inter-storey drift and drift obtained from MDOF time-history analysis for irregular frame structure. Best values given in bold. 244

Table 7.11. – Gradient (Grad) and coefficient (R^2) of determination of linear trend line between SDOF predictions of inter-storey drift and drift obtained from MDOF time-history analysis for regular frame structure. Best values given in bold. 245

Table 7.12. – Gradient (Grad) and coefficient (R^2) of determination of linear trend line between SDOF predictions of absorbed hysteretic energy, global Park and Ang damage, Global Fatigue with exponents 2.0 and 3.86 and values obtained from MDOF time-history analysis for wall frame structure. Best values given in bold. 255

Table 7.13. – Gradient (Grad) and coefficient (R^2) of determination of linear trend line between SDOF predictions of absorbed hysteretic energy, global Park and Ang damage, Global Fatigue with exponents 2.0 and 3.86 and values obtained from MDOF time-history analysis for irregular frame structure. Best values given in bold. 255

Table 7.14. – Gradient (Grad) and coefficient (R^2) of determination of linear trend line between SDOF predictions of absorbed hysteretic energy, global Park and Ang damage, Global Fatigue with exponents 2.0 and 3.86 and values obtained from MDOF time-history analysis for regular frame structure. Best values given in bold. 256

Table 8.1. – Distribution of the dataset for earthquake style of faulting and site soil classification. 265

Table 8.2. – Earthquake mechanism classification used for NGA database 266

Table 8.3. – Regression coefficients and standard deviations for inter-storey drift and roof drift 272

Table 8.4. – Number of records (each with two horizontal components) from the full NGA database within ±0.2 magnitude units of the scenario event..... 290

Table 8.5. – Records selected based on seismological characteristics..... 291

Table 8.6. – Records selected by spectral shape and magnitude..... 293

Table 8.7. – Statistics of peak roof drift predicted from suites of records selected and linearly scaled using different criteria. 300

Table 8.8. – Statistics of peak inter-storey drift at the 8th storey, predicted from suites of records selected and linearly scaled using different criteria. 300

Table 8.9. – Statistics of peak inter-storey drift at the 6th storey, predicted from suites of records selected and linearly scaled using different criteria. 301

Table 8.10. – Statistics of peak inter-storey drift at the 1st storey, predicted from suites of records selected and linearly scaled using different criteria. 301

Table 8.11. – Statistics of peak end rotation of the beam on the 8th storey at the edge of the structure, predicted from suites of records selected and linearly scaled using different criteria. 305

Table 8.12. – Statistics of peak end rotation of the beam on the 6th storey at the edge of the structure, predicted from suites of records selected and linearly scaled using different criteria. 305

Table 8.13. – Statistics of peak end rotation of the beam on the 1st storey at the edge of the structure, predicted from suites of records selected and linearly scaled using different criteria. 306

Table 8.14. – Statistics of peak end rotation of the base of the column on the 8th storey at the edge of the structure, predicted from suites of records selected and linearly scaled using different criteria. 306

Table 8.15. – Statistics of peak end rotation of the base of the column on the 6th storey at the edge of the structure, predicted from suites of records selected and linearly scaled using different criteria. 307

Table 8.16. – Statistics of peak end rotation of the base of the column on the 1st storey at the edge of the structure, predicted from suites of records selected and linearly scaled using different criteria. 307

Table 8.17. – Statistics of the absorbed hysteretic energy at the end of the beam on the 8th storey at the edge of the structure, predicted from suites of records selected and linearly scaled using different criteria. 310

Table 8.18. – Statistics of the absorbed hysteretic energy at the end of the beam on the 6th storey at the edge of the structure, predicted from suites of records selected and linearly scaled using different criteria. 310

Table 8.19. – Statistics of the absorbed hysteretic energy at the end of the beam on the 1st storey at the edge of the structure, predicted from suites of records selected and linearly scaled using different criteria. 311

Table 8.20. – Statistics of the absorbed hysteretic energy at the base of the column on the 8th storey at the edge of the structure, predicted from suites of records selected and linearly scaled using different criteria. 311

Table 8.21. – Statistics of the absorbed hysteretic energy at the base of the column on the 6th storey at the edge of the structure, predicted from suites of records selected and linearly scaled using different criteria. 312

Table 8.22. – Statistics of the absorbed hysteretic energy at the base of the column on the 1st storey at the edge of the structure, predicted from suites of records selected and linearly scaled using different criteria. 312

Table 8.23. – Statistics of Park and Ang damage index at the end of the beam on the 8th storey at the edge of the structure, predicted from suites of records selected and linearly scaled using different criteria. 315

Table 8.24. – Statistics of Park and Ang damage index at the end of the beam on the 6th storey at the edge of the structure, predicted from suites of records selected and linearly scaled using different criteria. 315

Table 8.25. – Statistics of the Park and Ang damage index at the end of the beam on the 1st storey at the edge of the structure, predicted from suites of records selected and linearly scaled using different criteria. 316

Table 8.26. – Statistics of the Park and Ang damage index at the base of the column on the 8th storey at the edge of the structure, predicted from suites of records selected and linearly scaled using different criteria. 316

Table 8.27. – Statistics of the Park and Ang damage index at the base of the column on the 6th storey at the edge of the structure, predicted from suites of records selected and linearly scaled using different criteria. 317

Table 8.28. – Statistics of the Park and Ang damage index at the base of the column on the 1st storey at the edge of the structure, predicted from suites of records selected and linearly scaled using different criteria. 317

Table 8.29. – Statistics of fatigue damage at the end of the beam on the 8th storey at the edge of the structure, predicted from suites of records selected and linearly scaled using different criteria. 321

Table 8.30. – Statistics of fatigue damage at the end of the beam on the 6th storey at the edge of the structure, predicted from suites of records selected and linearly scaled using different criteria. 321

Table 8.31. – Statistics of the fatigue damage at the end of the beam on the 1st storey at the edge of the structure, predicted from suites of records selected and linearly scaled using different criteria. 322

Table 8.32. – Statistics of the fatigue damage at the base of the column on the 8th storey at the edge of the structure, predicted from suites of records selected and linearly scaled using different criteria. 322

Table 8.33. – Statistics of the fatigue damage at the base of the column on the 6th storey at the edge of the structure, predicted from suites of records selected and linearly scaled using different criteria. 323

Table 8.34. – Statistics of the fatigue damage at the base of the column on the 1st storey at the edge of the structure, predicted from suites of records selected and linearly scaled using different criteria. 323

Table 8.35. – Statistics of the numbers of analyses required to predict the median of different damage measures to +/-10% accuracy (log) at one

standard deviation confidence, predicted from suites of records selected and linearly scaled using different criteria. 326

Table 9.1. – Accelerograms selected to have different durations 334

Table 9.2. – Statistics of roof drift predicted from suites of records selected and matched to the target spectrum using different criteria..... 338

Table 9.3. – Statistics of 8th storey drift predicted from suites of records selected and matched to the target spectrum using different criteria..... 338

Table 9.4. – Statistics of 6th storey drift predicted from suites of records selected and matched to the target spectrum using different criteria..... 339

Table 9.5. – Statistics of 1st storey drift predicted from suites of records selected and matched to the target spectrum using different criteria..... 339

Table 9.6. – Statistics of peak end rotation of the beam on the 8th storey at the edge of the structure, predicted from suites of records selected, linearly scaled and matched using different criteria..... 344

Table 9.7. – Statistics of peak end rotation of the beam on the 6th storey at the edge of the structure, predicted from suites of records selected, linearly scaled and matched using different criteria..... 344

Table 9.8. – Statistics of peak end rotation of the beam on the 1st storey at the edge of the structure, predicted from suites of records selected, linearly scaled and matched using different criteria..... 345

Table 9.9. – Statistics of peak end rotation of the base of the column on the 8th storey at the edge of the structure, predicted from suites of records selected, linearly scaled and matched using different criteria..... 345

Table 9.10. – Statistics of peak end rotation of the base of the column on the 6th storey at the edge of the structure, predicted from suites of records selected, linearly scaled and matched using different criteria..... 346

Table 9.11. – Statistics of peak end rotation of the base of the column on the 1st storey at the edge of the structure, predicted from suites of records selected, linearly scaled and matched using different criteria..... 346

Table 9.12. – Statistics of the Park and Ang damage index of the beam on the 8th storey at the edge of the structure, predicted from suites of records selected, linearly scaled and matched using different criteria..... 349

Table 9.13. – Statistics of the Park and Ang damage index of the beam on the 6th storey at the edge of the structure, predicted from suites of records selected, linearly scaled and matched using different criteria..... 349

Table 9.14. – Statistics of the Park and Ang damage index of the beam on the 1st storey at the edge of the structure, predicted from suites of records selected, linearly scaled and matched using different criteria..... 350

Table 9.15. – Statistics of the Park and Ang damage index of the base of the column on the 8th storey at the edge of the structure, predicted from suites of records selected, linearly scaled and matched using different criteria..... 350

Table 9.16. – Statistics of the Park and Ang damage index of the base of the column on the 6th storey at the edge of the structure, predicted from suites of records selected, linearly scaled and matched using different criteria..... 351

Table 9.17. – Statistics of the Park and Ang damage index of the base of the column on the 1st storey at the edge of the structure, predicted from suites of records selected, linearly scaled and matched using different criteria..... 351

Table 9.18. – Statistics of absorbed hysteretic energy (rad.mm) of the beam on the 8th storey at the edge of the structure, predicted from suites of records selected, linearly scaled and matched using different criteria..... 354

Table 9.19. – Statistics of absorbed hysteretic energy (rad.mm) of the beam on the 6th storey at the edge of the structure, predicted from suites of records selected, linearly scaled and matched using different criteria..... 354

Table 9.20. – Statistics of absorbed hysteretic energy (rad.mm) of the beam on the 1st storey at the edge of the structure, predicted from suites of records selected, linearly scaled and matched using different criteria..... 355

Table 9.21. – Statistics of absorbed hysteretic energy (rad.mm) of the base of the column on the 8th storey at the edge of the structure, predicted from suites of records selected, linearly scaled and matched using different criteria. 355

Table 9.22. – Statistics of absorbed hysteretic energy (rad.mm) of the base of the column on the 6th storey at the edge of the structure, predicted from suites of records selected, linearly scaled and matched using different criteria. 356

Table 9.23. – Statistics of absorbed hysteretic energy (rad.mm) of the base of the column on the 1st storey at the edge of the structure, predicted from suites of records selected, linearly scaled and matched using different criteria. 356

Table 9.24. – Statistics of the fatigue damage index of the beam on the 8th storey at the edge of the structure, predicted from suites of records selected, linearly scaled and matched using different criteria..... 359

Table 9.25. – Statistics of the fatigue damage index of the beam on the 6th storey at the edge of the structure, predicted from suites of records selected, linearly scaled and matched using different criteria..... 359

Table 9.26. – Statistics of the fatigue damage index of the beam on the 1st storey at the edge of the structure, predicted from suites of records selected, linearly scaled and matched using different criteria. 360

Table 9.27. – Statistics of the fatigue damage index of the base of the column on the 8th storey at the edge of the structure, predicted from suites of records selected, linearly scaled and matched using different criteria..... 360

Table 9.28. – Statistics of the fatigue damage index of the base of the column on the 6th storey at the edge of the structure, predicted from suites of records selected, linearly scaled and matched using different criteria..... 361

Table 9.29. – Statistics of the fatigue damage index of the base of the column on the 1st storey at the edge of the structure, predicted from suites of records selected, linearly scaled and matched using different criteria..... 361

Table 9.30. – Statistics of the numbers of analyses required to predict the median of different damage measures to +/-5% accuracy (log) at one standard deviation confidence, predicted from suites of records selected, linearly scaled and spectrally matched using different criteria..... 365

1. INTRODUCTION

The design and assessment of complex structures, those with non-linear response and safety critical facilities, requires time-history analysis. The ground motions used in this analysis should be representative of the seismic hazard. However, selecting accelerograms purely on the basis of seismological characteristics, such as magnitude and distance, usually results in an unacceptably wide dispersion of structural response, so that the response cannot be estimated to sufficient confidence with the number of analysis typically required by current design codes or feasible in a commercial design office. This is usually addressed by scaling accelerograms to reduce the variability of the response. However, knowledge of the characteristics of the ground motion that govern the structural response is required to know how to select and scale accelerograms. The influence of the ground-motion duration on structural response is the cause of much debate and has received little agreement in the technical literature.

This thesis addresses this problem by first reviewing the most commonly used measures of the seismic action (Chapter 2). A state-of-the-art review of the influence of duration on structural damage is conducted in Chapter 3. As the literature review finds that degrading structures are influenced by the duration of the ground motion, a detailed investigation is then conducted into the response of strength and stiffness degrading masonry structures (Chapter 4). Duration is found to be an import consideration for this type of structure, so the characteristics of the seismic hazard that control the duration and number of cycles of the ground motion is presented in Chapter 5, with a new predictive equation for estimating relative bracketed duration.

Elastic spectral acceleration – specifically the elastic response spectrum – is the most commonly used measure of the seismic action used to select and scale accelerograms. A method of adjusting accelerograms to match smooth response spectra, whilst preserving the other characteristics of the motion, is developed in Chapter 6. A promising option for future methods of selecting and scaling accelerograms is to use the response of non-linear single degree-of-freedom systems (SDOFs). A first step to make this possible presented in Chapter 7, where the ability of different non-linear SDOFs to estimate the response of three multi-degree-of-freedom (MDOF) reinforced

concrete frame structures is conducted. Chapter 8 investigates the number of analyses required to estimate a range of damage measures of an 8-storey reinforced concrete wall-frame structure to a given confidence level by linearly scaling accelerograms to match the elastic response spectrum. The potential bias, defined as over- or under-estimation of the response, caused by using small suites of scaled accelerograms is investigated by determining an estimate of the true response with regression of the response from 1656 unscaled accelerograms. Chapter 9 investigates the bias and number of records required to predict response to a given level of confidence from accelerograms linearly scaled to match the response spectrum on average and accelerograms adjusted with the new procedure to closely match the smooth response spectrum at one and at multiple damping levels. The thesis ends with Chapter 10, which summarizes the main conclusions from the research and on this basis recommends future work.

2. MEASURES OF SEISMIC ACTION

This section reviews a range of different measures of seismic action proposed in the technical literature. The section starts with a review of some of the issues associated with the data obtained from accelerograms. This is followed by an overview of some of the most commonly used strong-motion parameters, including measures of peak amplitude, spectral response, energy content, duration and number of cycles. The section ends with a summary of the use of measurements from accelerograms and the different measures of seismic action.

2.1 Accelerograms

Accelerograms are the principle source of data from which the characteristics of earthquake ground motion are obtained. This subsection provides a brief overview of how accelerograms are recorded and processed. Sources of error and the consequences of these errors on the ability to predict ground-motion characteristics are also discussed.

2.1.1 Types of accelerograph

The first accelerographs were installed in the early 1930s to record earthquakes in California. These early instruments are analogue and record the ground motions on paper or photographic film. One of the most popular analogue instruments, which are still the most commonly used, is the SMA-1 (Figure 2.1). The SMA-1 is triggered and starts recording when the vertical ground motion exceeds 0.01g. The ground motions are recorded by a weighted mirror rotating within the instrument displacement, changing the way light falls on the photographic film (Figure 2.2). The film is then processed and digitised. The digitisation process was initially completed manually on purpose built digitising machines, but more recently is conducted using automated processes and commercial scanners (Trifunac *et al.* 1999).

A second generation of digital accelerographs is gradually replacing the older analogue instruments. These operate using a force balance transducer and record digitally onto solid state or magnetic media. One such instrument is the Kinemetrics Makalu Digital Accelerograph (Figure 2.3). This instrument uses GPS to obtain

timing accuracy to ±0.5ms and can be connected to a network via radio, telephone or satellite communication links (Kinemetrics, 2004). Digital accelerographs have the advantage that they do not require the trace to be digitised and can be operated continuously so do not miss the beginning of the ground motion that is below the trigger level of the analogue instruments.

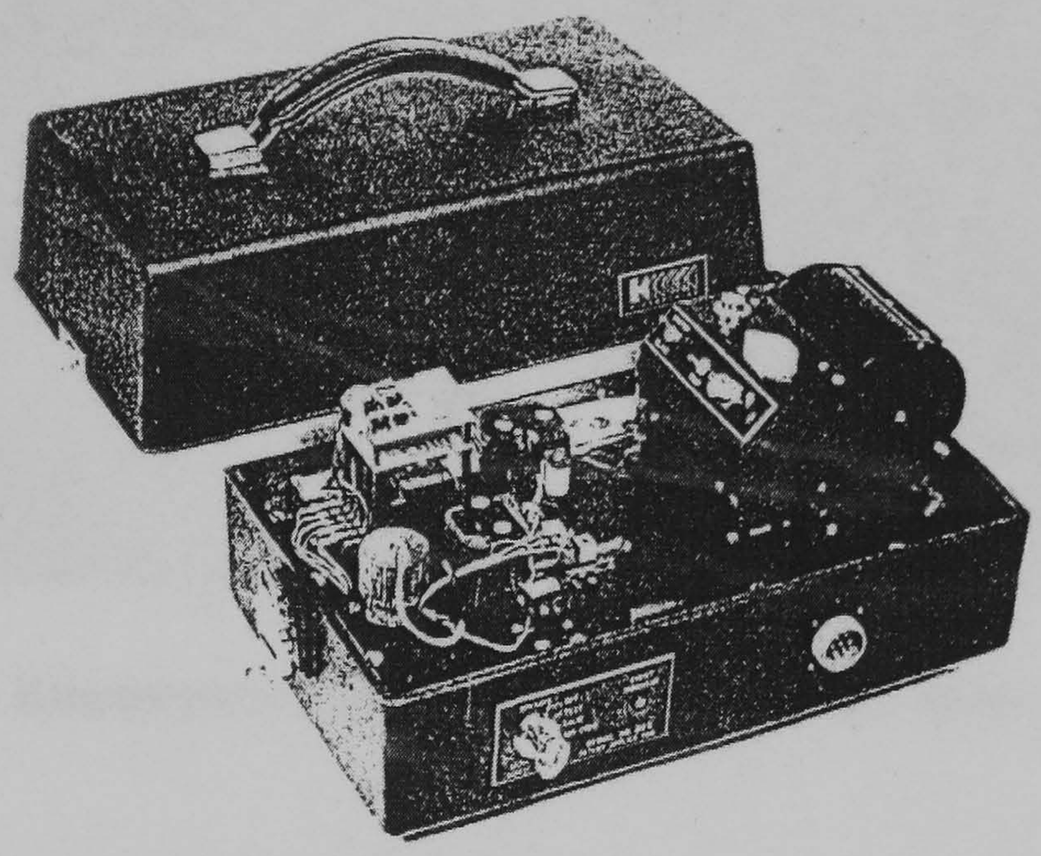


Figure 2.1. - Photograph of an SMA-1 optical-mechanical accelerograph. (Hudson 1979)

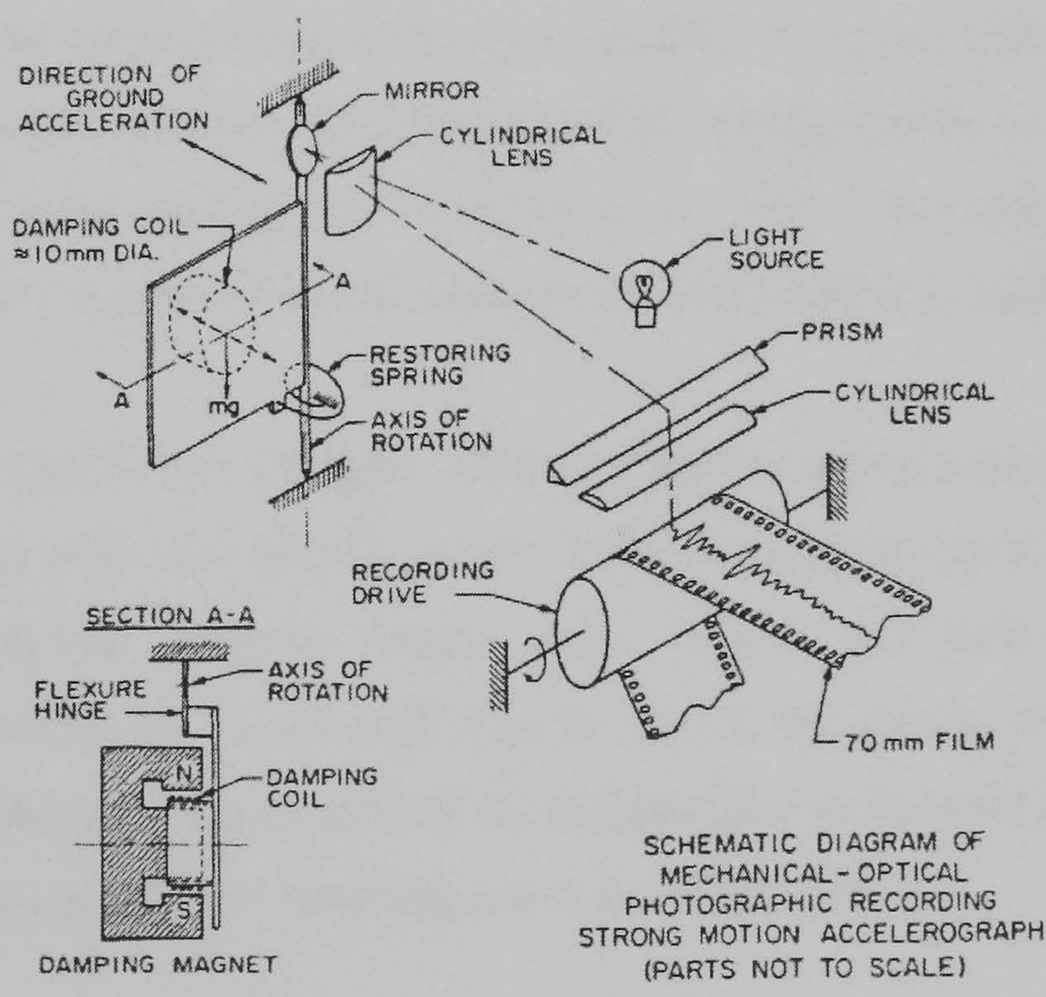


Figure 2.2. - Schematic illustration of the recording mechanism of an SMA-1 instrument. (Hudson 1979)

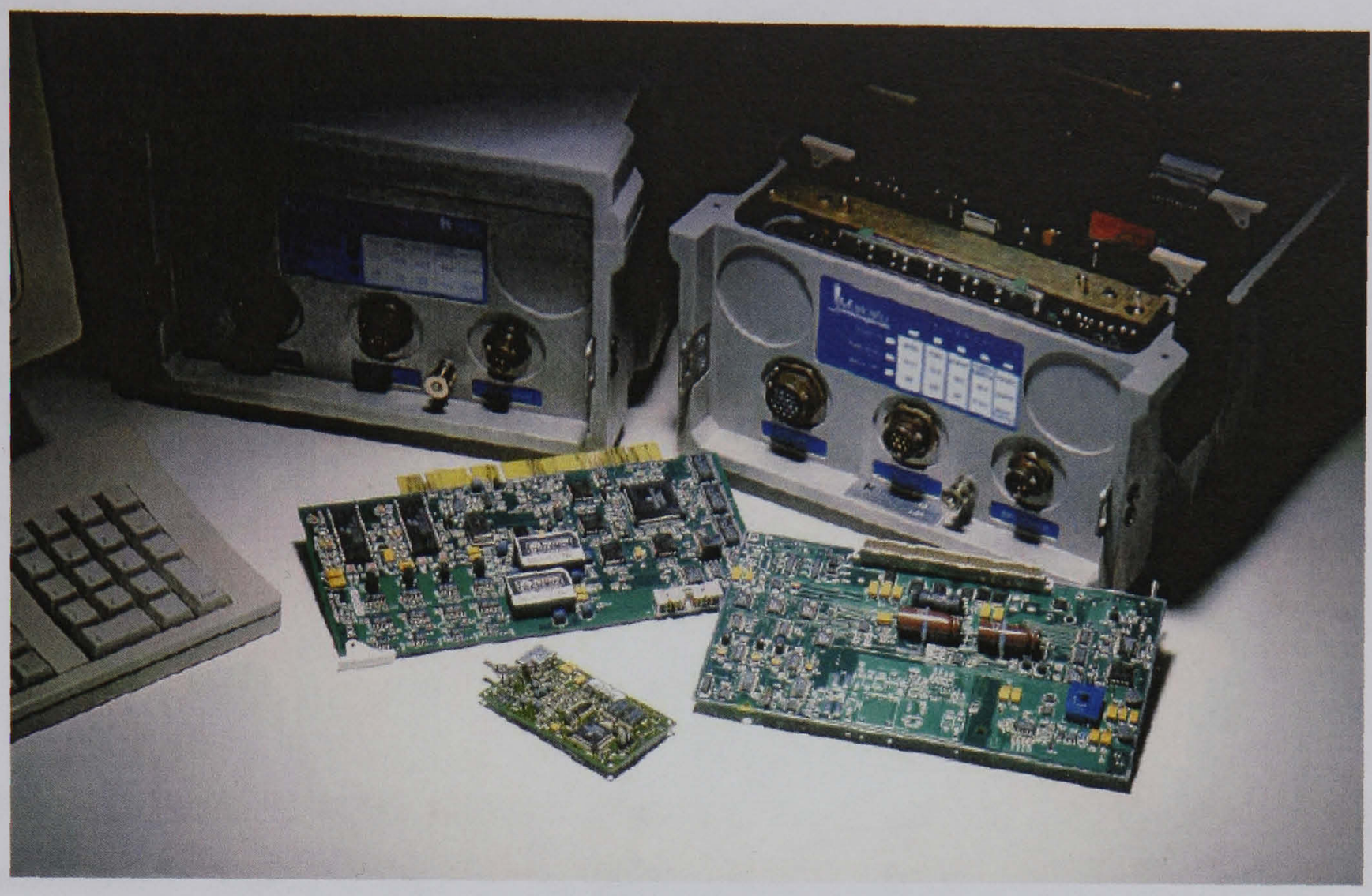


Figure 2.3. – Kinemetrics Makalu digital accelerograph (Kinemetrics, 2004)

2.1.2 Noise and processing accelerograms

As would be expected accelerograms from analogue instruments have the greatest potential for errors. Most of the error potential originates in the digitisation process. Spurious peaks can be created when a record is digitised if the recording is of poor quality. Of considerable concern is that each axis of the strong-motion record may not be digitised with the same starting time (Trifunac *et al.* 1999). This makes it difficult to determine the relative phases of the vertical, lateral and transverse motions.

Boore and Bommer (2005) and Douglas (2003a) point out that accelerograms from digital accelerographs may also contain errors. If the instrument has a digitiser that does not have sufficient dynamic range, weak records can have a step-like appearance, as the resolution is not sufficient to record the details of the motion. Digital records can also have a slow-drift in the baseline due to material fatigue of the sensor; problems also occur if the sampling rate is low (Chiu 1997).

Most accelerograms are digitally processed before they are used. There is a wide range of processing techniques available (see Boore and Bommer 2005), which include:

- High-pass filtering to remove high-frequency noise
- Low-pass filtering to remove low-frequency noise
- Base-line correction to recover more physically plausible velocities and displacements
- Period-dependent correction to adjust for known instrument response characteristics

Errors induced from filtering are magnified by integration, so although accurate acceleration measurements can be obtained from accelerograms, special attention to the filter characteristics needs to be given to obtain accurate displacement time histories (Bommer and Elnashai 1999). Permanent ground deformations also present challenges for recordings near to the fault. Significant errors in the estimation of the ground displacement and velocity can result if zero net ground displacement is incorrectly assumed (Tromans, 2004).

2.2 Overview of Strong-Motion Parameters

There are many different parameters proposed in the literature to measure the characteristics of the ground shaking. These parameters are reviewed and classified in this section under the sub-headings of:

- Measures of peak ground motion
- Measures of spectral response
- Measures of energy
- Hybrid ground-motion measures
- Definitions of ground-motion duration
- Definitions of the number of cycles

2.2.1 Measures of peak ground motion and effective peak motion

Peak ground acceleration (PGA)

Peak ground acceleration is undoubtedly the most widely used parameter for characterising strong motion. This is probably because it is easily applied to structural and analysis. Newton's law states that force equals mass times acceleration, so the approximate maximum equivalent lateral force applied to very stiff short-period structure is equal to PGA multiplied by the mass of the structure. The invention of the strong-motion accelerograph has also made peak ground acceleration one of the most reliably measured parameters. However, the use of PGA has many limitations; in particular PGA is generally poorly correlated with damage and most of the other variables it is used to predict, it also has little geophysical significance.

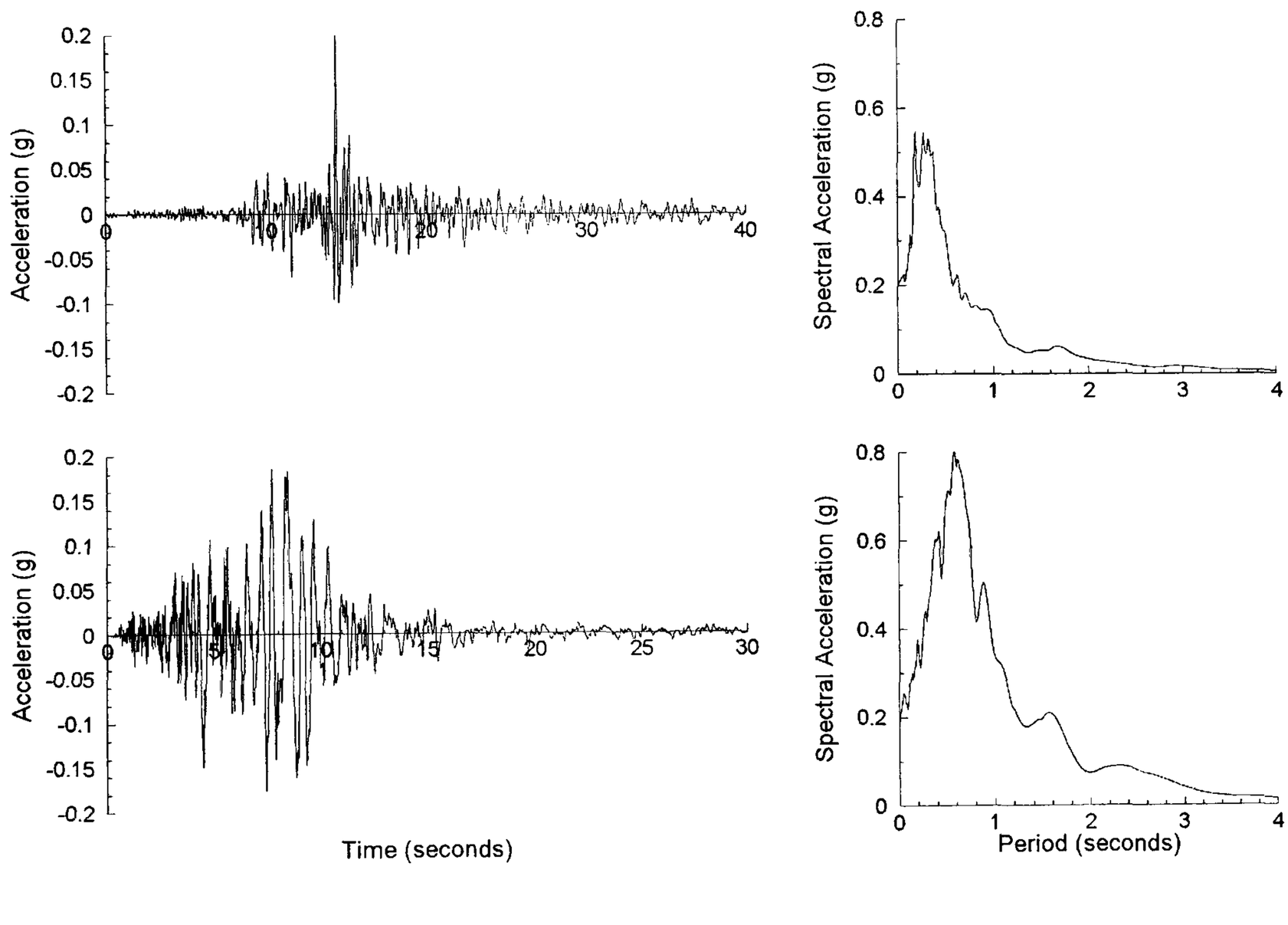


Figure 2.4. - Acceleration time-history and response spectra from 1994 M_w 6.7 Northridge earthquake (*upper*) recorded at distance of 59km at 950 Briarcliff on soil, (*lower*) recorded at a distance of 9km at Chalon Road on stiff soil.

Two horizontal accelerograms recorded at different sites from the 1994 M_w 6.7 Northridge earthquake illustrate the difficulties (Figure 2.4). The upper ground motion has about 10% larger PGA, but was recorded 55km further from the fault

rupture. Closer inspection of the records shows that the lower record, which has lower PGA, is more likely to be damaging as it has longer duration (87% longer bracketed duration at 0.05g), larger secondary peaks, and greater spectral acceleration at medium and long periods. The peak acceleration in the upper record appears to be caused by several in-phase waves creating an isolated high-frequency peak.

Most strong-motion instruments record translational accelerations in three orthogonal planes, two horizontal and one vertical. Campbell (1985) and Douglas (2003b) state that there are seven different ways to combine the two horizontal components $a_1(t)$ and $a_2(t)$:

1. Arithmetic mean: $a_M = \dfrac{\left[\max|a_1(t)| + \max|a_2(t)|\right]}{2}$
2. Both: $a_{B1} = \max|a_1(t)|$ and $a_{B2} = \max|a_2(t)|$
3. Geometric mean: $a_G = \sqrt{\max|a_1(t)|.\max|a_2(t)|}$
4. Largest component: $a_L = \max\left[\max|a_1(t)|, \max|a_2(t)|\right]$
5. Random: $a_{B1} = \max|a_1(t)|$ or $a_{B2} = \max|a_2(t)|$ chosen randomly
6. Resultant: $a_r = \max\left[\max|a_1(t)\cos\theta + a_2(t)\sin\theta|_{fort}\right]_{for\theta}$ correct calculation of this combination requires that the axes of the two horizontal components are exactly perpendicular and the timing of the components is perfectly synchronised. This may not be true, especially for digitised accelerograms from analogue instruments.
7. Vectorial addition: $a_v = \sqrt{\max|a_1(t)|^2_{fort} + \max|a_2(t)|^2_{fort}}$. This assumes that the maximum ground amplitudes occur simultaneously on the two horizontal components; this is a conservative assumption.

The above definitions use the accelerograms recordings directly and do not attempt to rotate the horizontal axis. Somerville *et al.* (1997) shows that motions from forward directivity can be strongly polarized in the fault-normal component, so many recent studies rotate the horizontal axies of the recording to be fault normal and fault parallel. Boore *et al.* (2006) show that different orientations of the horizontal axies

can cause geometric mean of the spectral acceleration to be different by factors of up to about two. To overcome this inconsistency Boore *et al.* (2006) provide two new definitions that are independent of the orientation of the instrument axis. The first is RMRotD, which is evaluated by calculating the geometric mean of the spectral acceleration at the period of interest for all non-redundant axis rotation angles (0 to 89 degrees in steps of 1 degree) the 50th percentile spectral acceleration is then taken as RMRotD. Unfortunately, the rotation angle used to evaluate GMRotD varies with period so to overcome these Boore *et al.* (2006) propose a second parameter GMRotI, which is independent of period. GMRotI is defined as the geometric mean calculated at a rotation angle with the lowest penalty function over the range of useable periods for the record (where the longest period is controlled by the processing required to remove the long period noise). The penalty function is defined by:

$$penalty(\theta) = \sum_{i=j}^{k} [GM(\theta, T_i) / GMRotD(T_i) - 1]^2 \qquad (2.1)$$

where, the range of usable periods extends from T_j to T_k, $GM(\theta,T_i)$ is the geometric mean of the response spectra for period T_i computed for rotation angle θ, and $GMRotD(T_i)$ is the 50th percentile value of the geometric mean over all non-redundant angles.

Douglas (2003b) shows that ground-motion prediction equations are usually derived for the log of the ground-motion characteristic, so the geometric mean is transformed to $\log a_G = \dfrac{\log \max|a_1(t)| + \log \max|a_2(t)|}{2}$. This means that the regression coefficients derived using the geometric mean gives exactly the same regression coefficients as those derived using both ground-motion components. However, the standard deviation of the equation derived using the geometric mean will be different. The differences the in standard deviation from different methods of combining the horizontal components are illustrated by Douglas (2001) using 180 near-field records (Figure 2.5).

The peak vertical acceleration is commonly assumed to be two thirds the peak horizontal acceleration (e.g. Newmark and Hall 1982). However, several authors (e.g. Campbell 1985; Abrahamson and Litehiser 1989) have shown that this ratio is generally greater for ground motions near to the fault rupture of large earthquakes. Bozorgnia and Campbell (2004) and Ambraseys and Douglas (2003a) show that the vertical component of motion is of higher frequency and decays more rapidly than the horizontal component. The peak in vertical acceleration is usually associated with the P-wave arrivals, and hence usually occurs earlier than the peak horizontal acceleration, which is usually caused by S-waves. This can result in larger vertical peak ground acceleration than horizontal PGA for near-field measurements of large earthquakes. Mohammadioun (1997) uses results from Port Island Down hole array under the action of the 1995 Kobe earthquake to show that non-linear site effects can also increase the ratio between peak vertical and horizontal ground motion. The soil layer, in this case, reduced the amplitude of the horizontal shear waves, but increased the amplitude of the vertical accelerations.

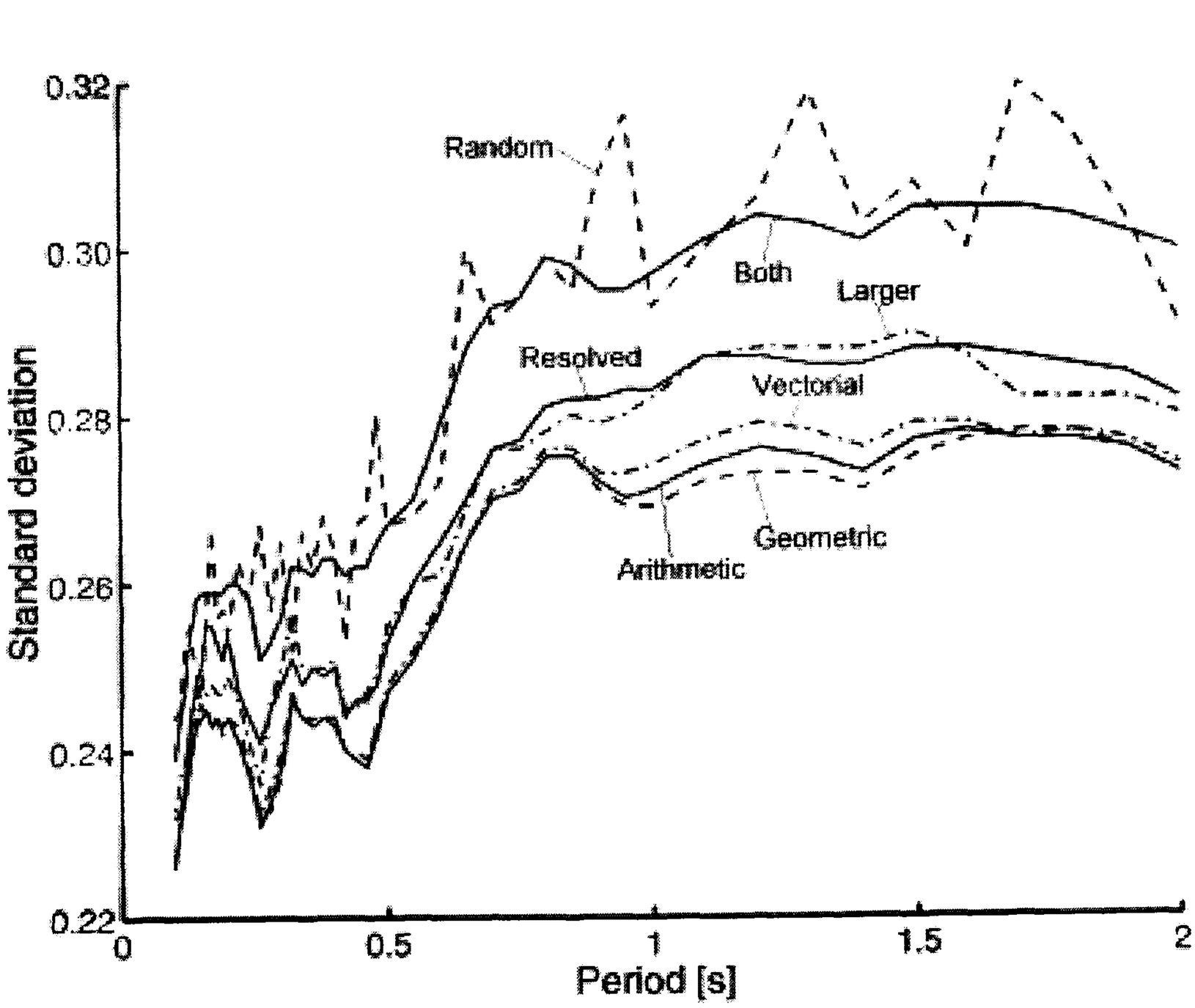


Figure 2.5. – Standard deviations for different methods of combining horizontal ground-motion components (Douglas 2001).

Effective peak acceleration (EPA)

As peak ground acceleration is poorly correlated with damage and other predictor variables, several researchers have suggested methods to evaluate effective peak ground acceleration. Many different techniques have been proposed to achieve this aim, although these can be split into four generic categories:

- Definitions based on secondary acceleration peaks (e.g. Mortgat 1979; Bolt and Abrahamson 1982; Gupta 1994; Schwarz 1998)
- Definitions based on the amplitude of structural response, typically elastic SDOF systems (e.g. ATC 1978; Ohsaki *et al.* 1980; Naeim *et al.* 1994; Paciello *et al.* 2000; Sabetta and Bommer 2002)
- Definitions combining the above, based on the number of cycles of structural response (e.g. Zahrah and Hall 1984; Kawashima and Aizawa 1986; Schwarz 1996; Basu and Gupta 1998)
- Definitions based on energy, such as Sarma and Yang (1987) who define EPA as the acceleration level which contains 95% of the energy in the accelerogram.

One of the most widely used definitions of EPA is the average spectral acceleration between a given period range, which can also be divided by a factor of 2.5 so that it resembles PGA (e.g. ATC 1978; Paciello *et al.* 2000; Sabetta and Bommer 2002). Sabetta and Bommer (2002) suggest that this definition of EPA gives similar results as PGA, whilst Paciello *et al.* (2000) find that EPA increases more rapidly with magnitude and attenuates more slowly with distance than PGA. Differences in these conclusions may be a result of differences in the strong ground-motion datasets used. The work of Paciello *et al.* (2000) includes recordings from earthquakes in Italy and Greece, whilst Sabetta and Bommer (2002) only consider Italian earthquakes.

ATC (1978) and Naeim *et al.* (1994) point out that the spectral acceleration, and hence EPA defined using this measure, does not provide any indication of the duration of the ground motion. To account for this the EPA values given by ATC (1978) have been corrected using expert judgement so that areas with short duration ground motions have decreased EPA. Naeim *et al.* (1994) overcome this shortcoming

by using spectra of hysteretic energy dissipated by elastoplastic SDOF oscillators rather than EPA.

RMS Acceleration

The root mean square, RMS_A, of a given ground acceleration $a(t)$ is:

$$RMS_A = \sqrt{\frac{\int_1^2 a^2(t)}{t_2 - t_1}} \tag{2.2}$$

where the t_1 and t_2 is the start and end of the duration D over which the RMS is evaluated. One of the properties of the RMS acceleration is that it is the square root of the mean rate of increase of the Arias intensity over the duration, D. RMS is one of a family of functions called spectral moments, which were originally developed to measure the number and amplitude of extreme peaks in stationary random signals, such as random noise in electrical systems and the heights of sea waves during a storm (e.g. Rice 1945; Cartwright Longuet-Higgins 1956). The use of RMS for non-stationary functions, such as earthquake ground motion presents additional challenges as the RMS varies considerably for different duration definitions (Figure 2.6). The RMS can be thought of as a measure of the average amplitude in a stationary signal; however, as earthquake ground motions are dominated by the build-up and decay of the motion, shorter duration definitions produce higher RMS levels (Pauschke and Krishnamurty 1984). Indeed the differences are up to a factor of 4 for the different definitions shown in Figure 2.6, while the RMS of the stationary signal, in this case a JONSWAP 3 hour random wave simulation, which is used by offshore engineers to represent the waves in the North Sea induced by storm (see Barltrop and Adams 1991), is essentially the same for all duration definitions. The difference in the RMS for the stationary signal for the Vanmarcke and Lai (1980) definition is because this definition fixes RMS to equal the peak of the motion divided by 2.74, which is plainly not appropriate in this case.

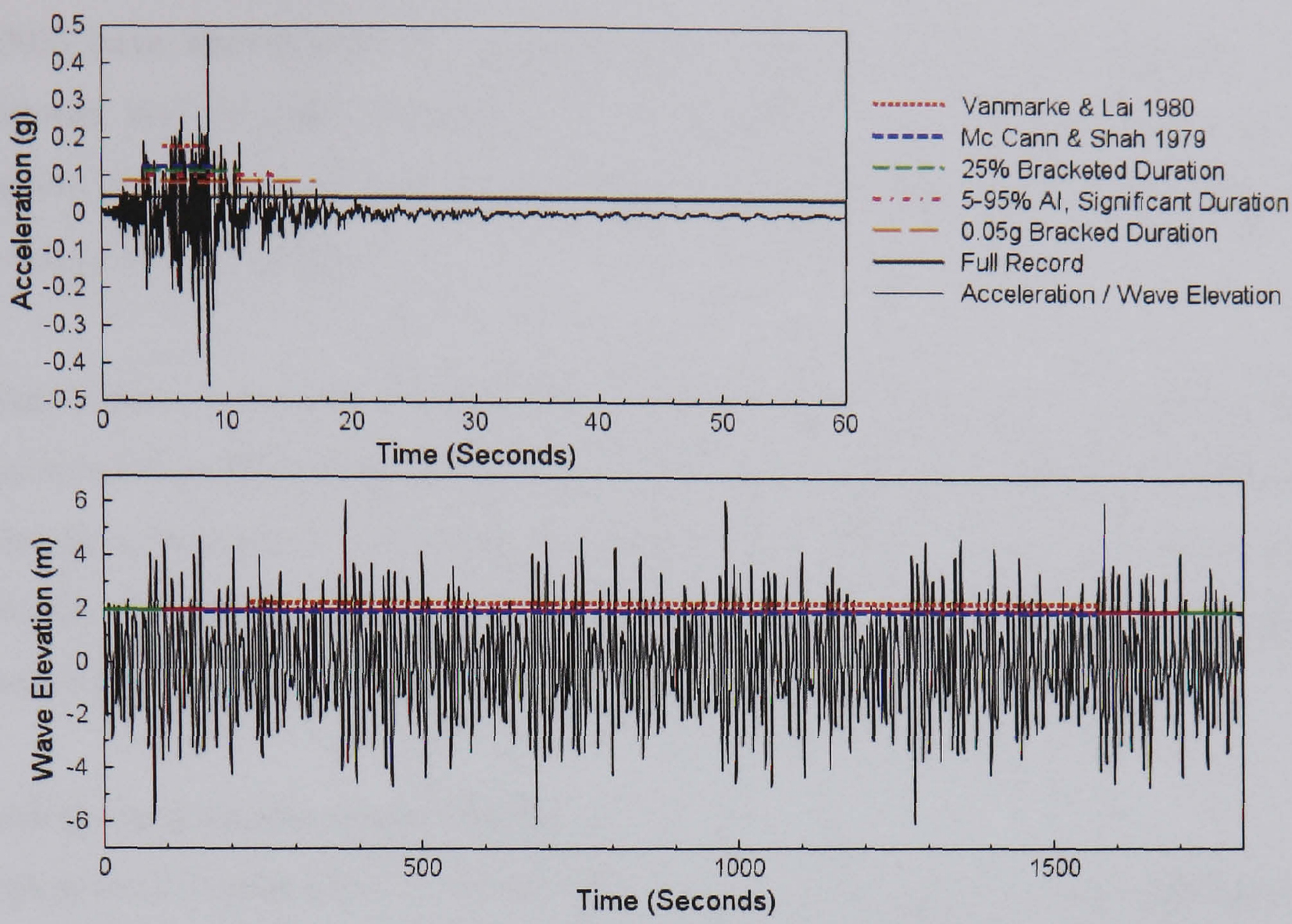


Figure 2.6. – Difference in RMS for different duration definitions: Accelerogram from M_w 6.7 1994 Northridge Earthquake recorded 13km from the fault rupture at Los Angeles-UCLA grounds (*Upper*); Stationary signal from JONSWAP random wave simulation, 6.3m H_s, 11 seconds peak period, γ=1 (*Lower*).

Attenuation relations for RMS acceleration have been developed by several authors, however, there is no agreement that RMS is a good parameter to use. Hanks and McGuire (1981), Kavazanjian *et al.* (1985) and Huh *et al.* (2000) imply that the use of RMS provides better predictions than PGA, whilst the study of McCann and Boore (1983) find that RMS does not reduce the variability.

Peak ground velocity (PGV)

The peak ground velocity is the maximum velocity obtained from the ground velocity time-series, which is found by integrating properly filtered and corrected accelerograms. The integration of the accelerogram increases the sensitivity of the PGV to the filtering and correction processes. It is widely acknowledged that the amplitude of the response spectrum at intermediate periods can be related to PGV and hence is one of the parameters used to derive the smooth design response spectra (e.g. Newmark and Hall 1982, 1969). However, recent studies by Bommer and Alarcon

(2005) have shown that the relationship between PGV and SA is far from exact. Bommer and Alarcon (2005) also show that PGV has a better correlation with spectral acceleration at 0.5s period, rather than spectral acceleration at 1.0s period, which as usually assumed.

Other authors have found that PGV is a better measure of damage to medium-period structures than PGA (e.g. Matsumura 1992; Akkar and Ozen 2005). As the ground velocity is related to the energy demand of the ground motion, the peak ground velocity can also be related to the maximum kinetic energy demand of the ground motion (Uang and Bertero 1988, 1990; Fajfar and Fischinger 1990a)

Peak ground displacement (PGD)

Peak ground displacement is taken from the ground displacement time-series which is obtained by double integration of the acceleration time-series. As the integration process magnifies errors the ground displacement time-series is more sensitive to filtering techniques than ground acceleration or velocity time-series. An additional issue is that, without other data such as Global Positioning System (GPS) measurements, it is impossible to determine if there is any permanent ground deformation recorded by analogue accelerographs as they do not record the start of the ground motion. This has led to the common practice of adjusting the base-line of accelerograms to ensure a zero initial and final displacement. Whilst this is usually acceptable, any accelerogram that records permanent ground deformation will be adjusted to remove this feature, and in doing so the actual ground displacement will be incorrectly modified rendering it impossible to accurately determine the PGD.

Paradoxically, it is widely recognised that structural displacements are a more accurate measure of damage than accelerations or velocities (e.g. Miranda and Ruiz-Garcia 2002; Priestley and Kowalsky 2000). This is logical as damage is caused by excessive material strains, either from monotonic or cyclic loading, which are in turn produced by excessive structural displacements. Peak ground displacements control structural displacements at long periods, which has led several researchers to develop predictive equations for PGD using carefully filtered and adjusted accelerograms (e.g. Bommer *et al.* 2000a; Tromans and Bommer 2002)

2.2.2 Measures of spectral response

It has long been recognised that the period of the ground motions influences their destructiveness. Robert Mallet (1810-1881) was one of the first to suggest that blocks of different height to diameter ratios could be used to measure the damage potential of earthquakes. Later, Kyoji Suyehiro (1977-1932), the first director of the Earthquake Research Institute at Tokyo University, proposed that simple pendulums with different periods of vibration would give a useful indication of the nature and severity of the ground shaking (Housner 1965). One of the most well known examples of the fact that different period ground motions damage different types of structures is the damage observed from the 1985 Mexico Earthquake. In this earthquake deep, soft lakebed deposits under Mexico City amplified the ground motions of the distant (360km) large magnitude (M_s 8.1) earthquake at 2.0 seconds period. This caused significant damage to moderately tall buildings with ten to eighteen storeys as the natural period of these structures was very similar to the dominant period of the ground motion (Esteva 1988).

Elastic response spectra

Elastic response spectra were first obtained by Biot (1941) using a mechanical analogue. The widespread availability of the digital computer enabled spectra to be calculated efficiently numerically (e.g. Nigam and Jennings 1969). Today there are many computer programs that have been written to calculate response spectra; several of these are free to download from the Internet (e.g. SeismoSoft 2005a; Hachem 2004).

All elastic response parameters are derived from the solution of the equations of motion for a viscously damped elastic SDOF system:

$$ma + cv + ku = -ma_g \tag{2.3}$$

where m is the mass, a is the absolute acceleration of the mass, c is the viscous damping, v is the relative velocity between the mass and the ground, k is the elastic stiffness, u is the relative displacement between the mass and the ground and a_g is the acceleration of the ground. It is generally more convenient to express the

characteristics of the system in terms of its natural period, T_0, or natural frequency, ω_0, and damping ratio, β:

$$T_0 = \frac{1}{2\pi}\sqrt{\frac{m}{k}} \tag{2.4}$$

$$\omega_0 = \sqrt{\frac{k}{m}} = \frac{2\pi}{T_0} \tag{2.5}$$

$$\beta = \frac{c}{2m\omega_0} \tag{2.6}$$

Substituting these into equation (2.3) yields:

$$a + \beta 2\omega_0 v + \omega_0^2 u = -a_g \tag{2.7}$$

Equation (2.7) can be solved to find the relative displacement u(t) under the action of an arbitrary ground acceleration time-series by integration or by solving Duhamel's convolution integral. Duhamel's integral describes the response in terms of the input ground-motion amplitude and the time of the motion. The response at any given time is found by multiplying the ground-motion amplitude at each instant by a harmonic transfer function and a weighting function that decreases the influence of the ground motion on the response amplitude with time:

$$u(t) = -\frac{1}{\omega_d}\int a_g(\tau) e^{-\beta\omega_0(t-\tau)} \sin[\omega_d(t-\tau)]d\tau \tag{2.8}$$

where ω_d is the damped circular frequency $\omega_d = \omega_o\sqrt{1-\beta^2}$ and τ is the time of the ground acceleration. The relative velocity is found by differentiating equation (2.8) and the absolute acceleration found using equation (2.7).

Response spectra of spectral acceleration, SA, spectral velocity, SV, and spectral displacement, SD, are constructed by plotting the maximum response quantity

required for many SDOF systems with a range of spectral periods or frequencies (Figure 2.7).

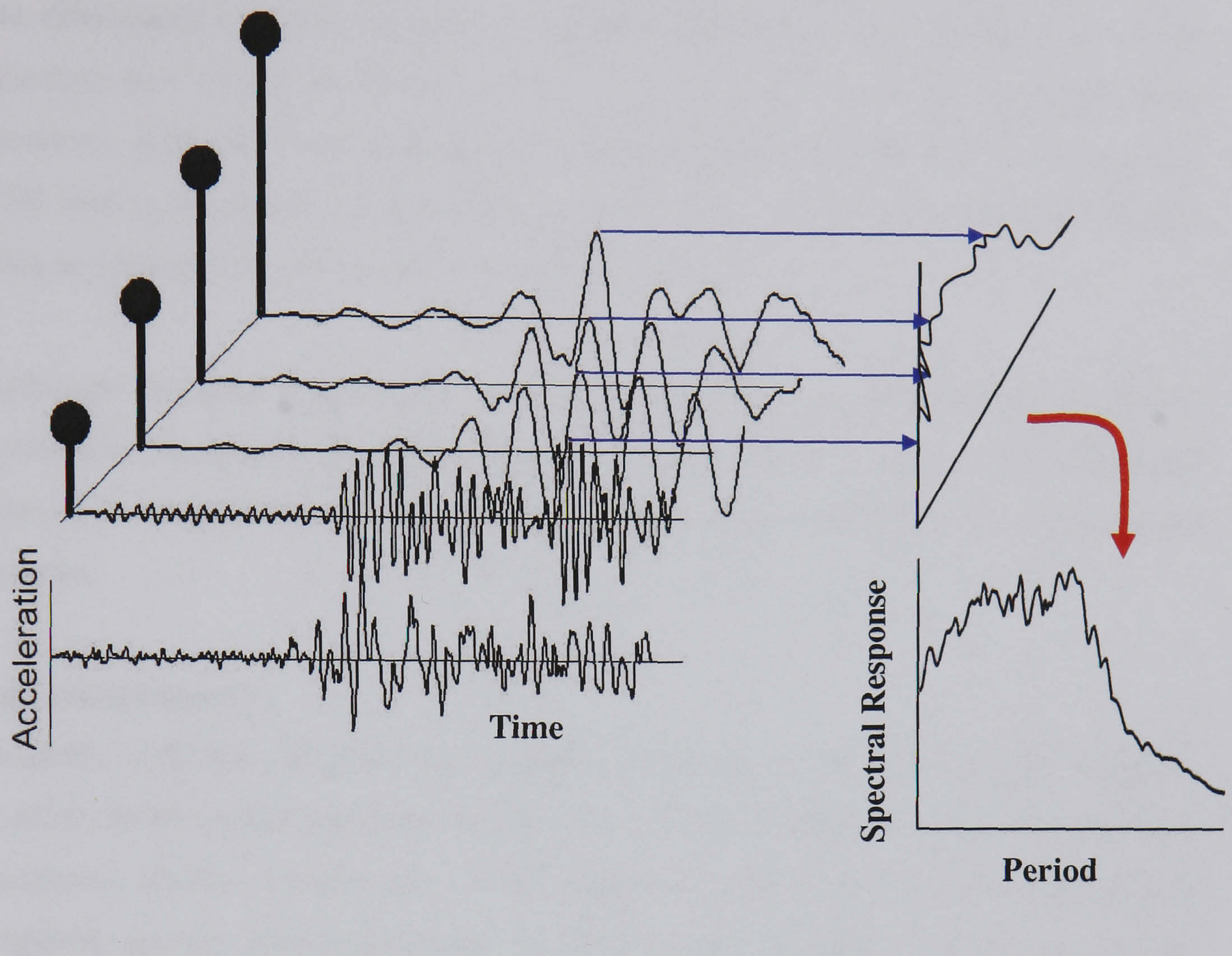


Figure 2.7. – Illustration of construction of response spectrum. Maximum response of each SDOF system is plotted against the period of the system

Approximate relationships exist between spectral acceleration, velocity and displacement. As these relationships are not exact the resulting values are called the pseudo spectral acceleration (PSA) and pseudo spectral velocity (PSV) respectively:

$$PSA = \left(\frac{2\pi}{T}\right)^2 SD \tag{2.9}$$

$$PSV = \left(\frac{2\pi}{T}\right) SD \tag{2.10}$$

As a result of the exact relationship between SD, PSV and PSA these spectral parameters can be plotted on triple log axis to form a tripartite plot. A discussion of the differences between the pseudo and actual definitions is available from many standard text books on dynamics (e.g. Chopra 1980) so is not repeated here. However, it is noted that at damping levels less than about 20% of critical PSA and PSV tend to SA and SV, respectively, except at very short and long periods. In fact, PSA and SA are exactly equal when damping is zero.

Although the peak acceleration correlates with the peak displacement in SDOF systems Weitzmann *et al.* (2006) show that in many cases the acceleration time-series does not correlate with the displacement time-series for multiple degree-of-freedom systems.

Spectrum intensity

Benioff (1934) was one of the first authors to propose that the area under the response spectra can be used as a measure of the destructiveness. However, the concept is more frequently attributed to Housner (1952) who proposed that the area under the velocity response spectra should be used, opposed to the displacement spectra as was proposed by Benioff (1934). The limits of the integration required to calculate the area under the velocity response spectra remains a matter of debate: Housner (1952) originally proposed that 0.1 to 2.5s is appropriate, but other authors suggest the limits should be based on the properties of the structure under investigation (e.g. Martinez-Rueda 1998). The spectrum intensity concept has more recently been extended into the time domain by Şafak (1998) who has proposed that the volume under a 3D response spectra, with number of cycles on the third axis, as an alternative measure of damage.

Smoothed response spectra

Individual accelerograms produce a jagged response spectrum but it is desirable to have a smooth spectrum for the specification of ground motions. This ensures that the design loading varies smoothly for structures with different periods and recognises that the response spectrum of the actual earthquake that will shake the structure is not known at the design stage. The procedure used by Newmark and Hall (1969) to construct smooth design spectra recognises that PGA controls the short-

period motions, the PGV the intermediate-period motions and the PGD the long-period motions. This observation leads to the creation of a response spectrum with straight line sections in each of the period ranges which are anchored to PGA, PGV and PGD for the short-, medium- and long-period motions respectively. Many design codes use this concept but avoid using the PGA, PGV and PGD explicitly, instead anchoring the whole spectral shape to the PGA. Unfortunately, the spectral shape is strongly governed by earthquake magnitude, a parameter which is not given in any current seismic design code. This means that spectral accelerations at periods other than PGA will not necessarily provide an acceleration level consistent with the expected hazard (McGuire 1977; Bommer *et al.* 2000b). This issue is partly addressed in Eurocode 8 (CEN 2004) by utilizing two types of response spectra, one with motions predominantly in the short-period range for countries with hazards dominated by small magnitude earthquakes and another with more long-period motions for countries with larger magnitude earthquakes. The International Building Code 2000 (IBC 2000) overcomes the issue by defining the spectra in terms of two spectral ordinates, which are given on two separate seismic hazard maps.

If a probabilistic seismic hazard assessment[1] (PSHA) is used to derive the response spectra it is likely to be presented in the format of a uniform hazard spectrum (UHS). The UHS shows the spectral amplitudes with the equal probability of exceedance. This is useful if the seismic hazard is dominated by a single source, but can produce a spectrum which is strongly influenced by two or more hazards, for example a combination of small local events and large distant events (Figure 2.8). As the ground motions from each of these events will have very different characteristics, and the probability of the two events occurring at the same time is negligible, it is better to treat each event as a separate design scenario. This can be conducted explicitly by disaggregating the hazard to determine the scenario (e.g. McGuire 1995; Bazzurro and Cornell 1999)

[1] Description of the mechanics of conducting PSHA can be found in Reiter (1990), and a discussion on the relative merits of PSHA and deterministic hazard assessment is given by Bommer (2002).

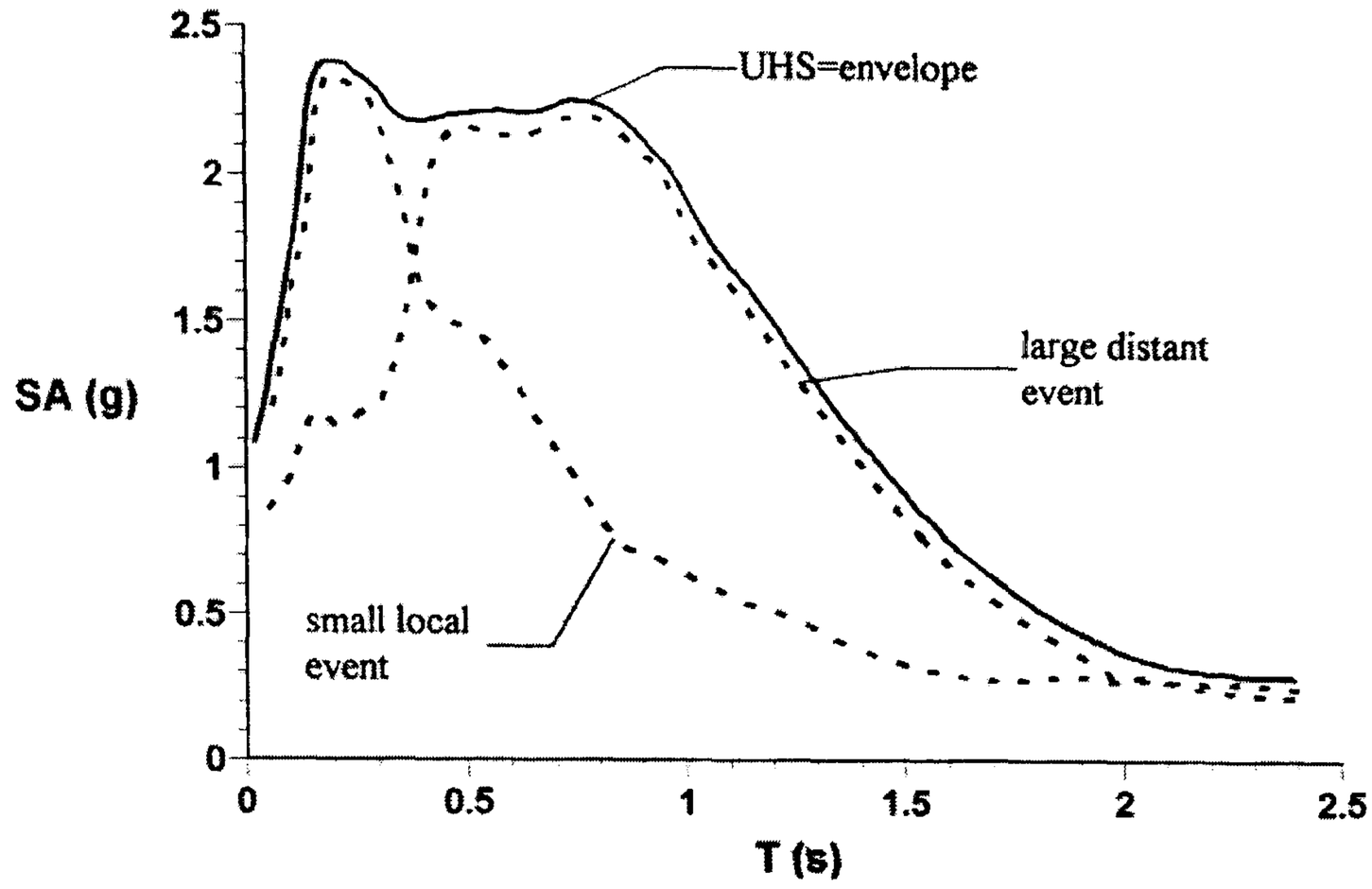


Figure 2.8. – The concept of UHS for a location affected by local sources of moderate seismicity and distant sources of greater activity (Bommer *et al.* 2000b, after Reiter 1990)

The ideal shape for a smoothed response spectrum is still a mater of considerable debate and must be a function of the underlying seismic hazard. More recent advances specify spectra of pseudo spectral acceleration that also provide good matches to the spectral displacement (Bommer *et al.* 2000a). This is particularly useful for displacement based design approaches (e.g. Priestley and Kowalsky 2000). Displacement based design also requires spectral displacements at damping levels greater than 5% of critical. This is usually conducted by applying adjustment factors to the 5% damped spectra such as the formula proposed by Bommer *et al.* (2000), which was subsequently adopted by Eurocode 8 (CEN 2004):

$$\eta = \sqrt{\frac{10}{5+\xi}} \tag{2.11}$$

where, η is the linear scale factor between the 5% damped response spectrum and the required spectrum at ξ% damping. Recent research has shown that the difference between the damping levels is dependent on the duration of the ground motion and so is dependent on the earthquake magnitude (Bommer and Mendis 2005; Mendis and Bommer 2006).

Inelastic response spectra

Inelastic response spectra are constructed in a similar manner to elastic response spectra, with the exception that the responses of inelastic SDOFs are used. There is a wide range of different non-linear hysteretic properties that can be used, some of which are shown in Figure 2.9. The simplest, and the most widely used, is the elastic-perfectly plastic (Figure 2.9 a). This hysteretic model has an initial stiffness K_0, a yield force F_y. and a yield at displacement of u_y. The maximum displacement of a yielding system u_{max} is frequently expressed in terms of displacement ductility, μ, which is the ratio of the maximum displacement divided by the yield displacement:

$$\mu = \frac{u_{\max}}{u_y} \tag{2.12}$$

The displacement ductility can be used to plot constant displacement ductility spectra. These are constructed by iteratively adjusting the yield strength of each SDOF system until it has the target displacement ductility. The absolute acceleration of the mass is then plotted as a function of period (Figure 2.10). This concept of ductility assumes that damage is only proportional to the peak displacement and ignores the amplitude and number of the smaller cycles. However, other ductility definitions are available that do not make this assumption. The accumulative displacement ductility assumes that damage is proportional to the sum of the inelastic displacements (Figure 2.11). The normalized hysteretic energy ductility assumes that damage is proportional to the normalized hysteretic energy (Figure 2.12). If an elastic-perfectly plastic model is used the accumulative displacement ductility and normalized hysteretic energy ductility spectra are identical. Cumulative ductility factors offer a lower reduction from the elastic spectrum than the displacement ductility spectra (Figure 2.13). The previous definitions of cumulative ductility are taken from Mahin and Lin (1983) and assume that damage is proportional to a linear sum of inelastic displacements. However, this is not always the case as low-cycle fatigue damage is approximately proportional to the inelastic amplitude squared. Other spectra which do not make this assumption are discussed in Section 3.6.

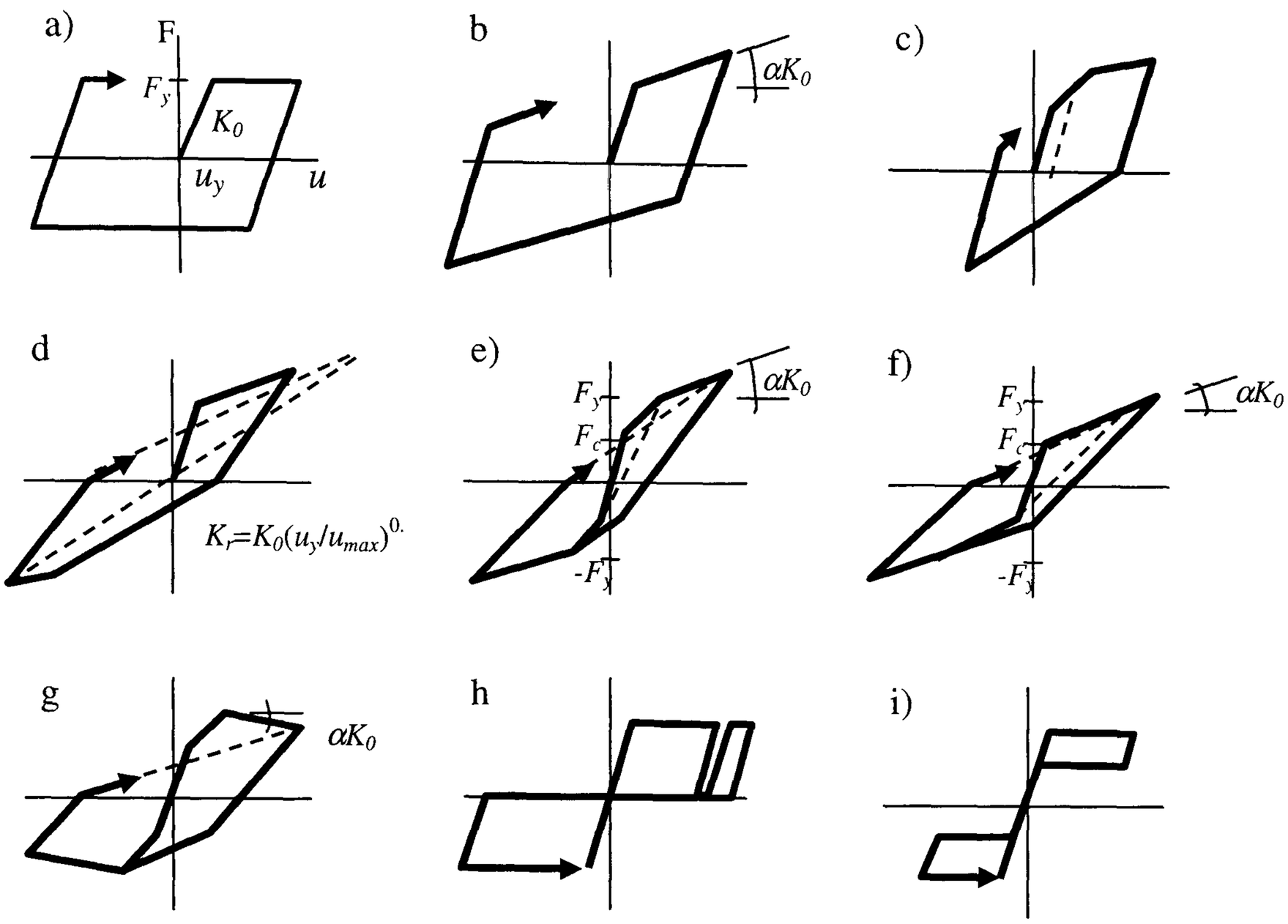


Figure 2.9. – Different Hysteretic models: (a) elasto-plastic; (b) bilinear; (c) tri-linear; (d) Q-model; (e) Takeda 1; (f) Takeda 2; (g) degrading strength; (h) shear-slip1; (i) flag (Modified from Fajfar *et al.1989*)

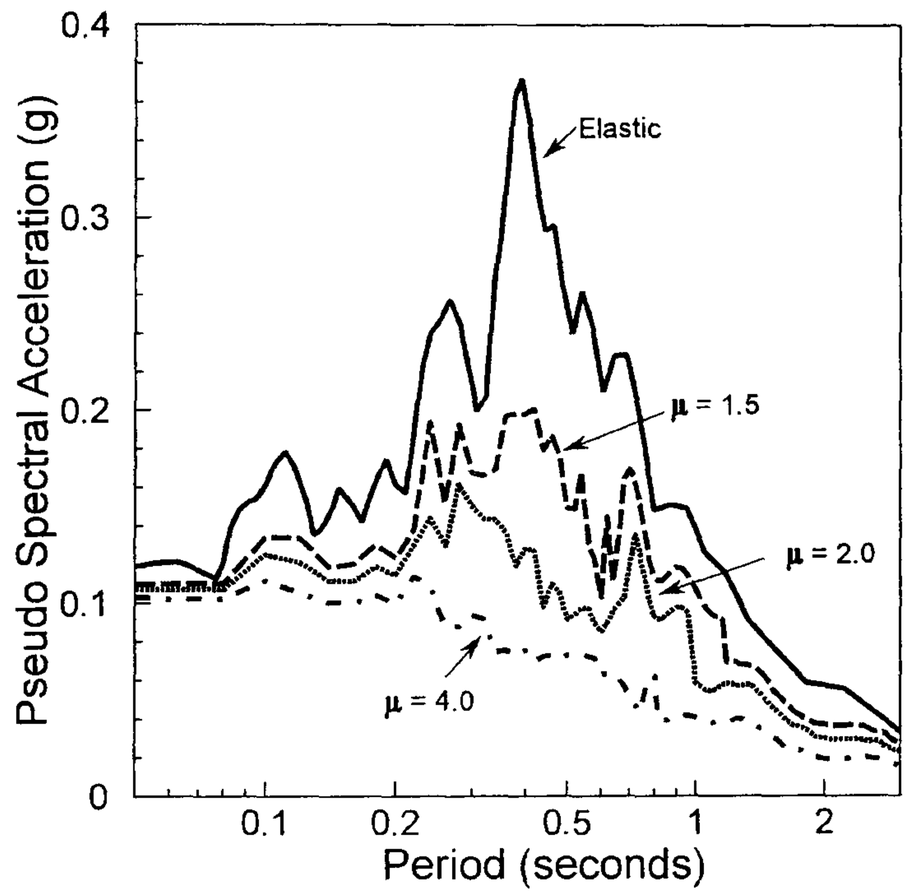
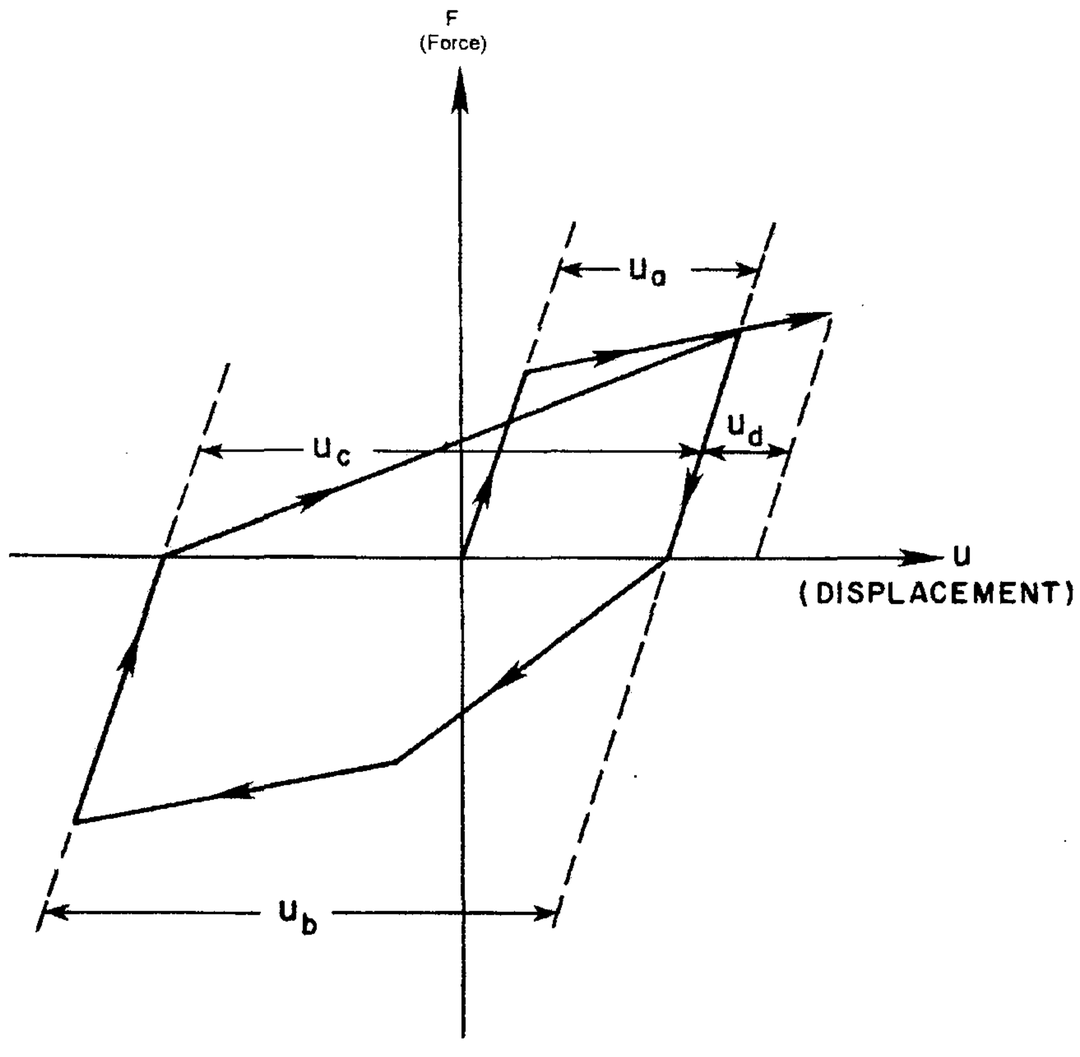


Figure 2.10. – Constant displacement ductility spectrum, 5% viscous damping, elastic-perfectly plastic hysteretic system, for the 1989 M_w 6.93 Loma Prieta Earthquake recorded 71km from the fault rupture at Diamond Heights (record 00794T in the NGA database)

Constant ductility spectra are widely used but have a number of conceptual problems: firstly, the yield force at each period is adjusted independently of the others so

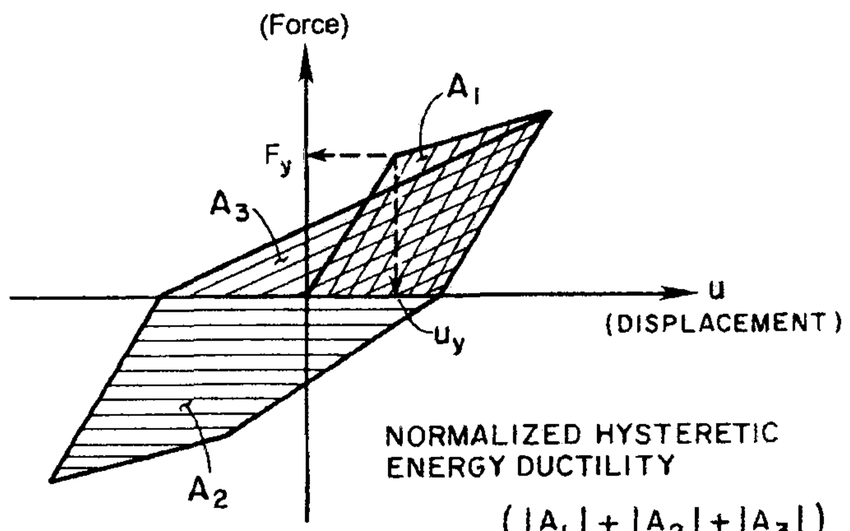
considers a different "structure" at each period; secondly, if weak ground motions are analysed the "structures" represented by the response spectrum will have unrealistically low strength to ensure the required ductility level.



$$\text{ACCUMULATIVE DUCTILITY} = \Sigma\,(u_{pl})_i / u_y + 1$$

$$= \frac{(|u_a| + |u_b| + |u_c| + |u_d|)}{u_y} + 1$$

Figure 2.11. – Definition of accumulative ductility (Mahin and Lin 1983)



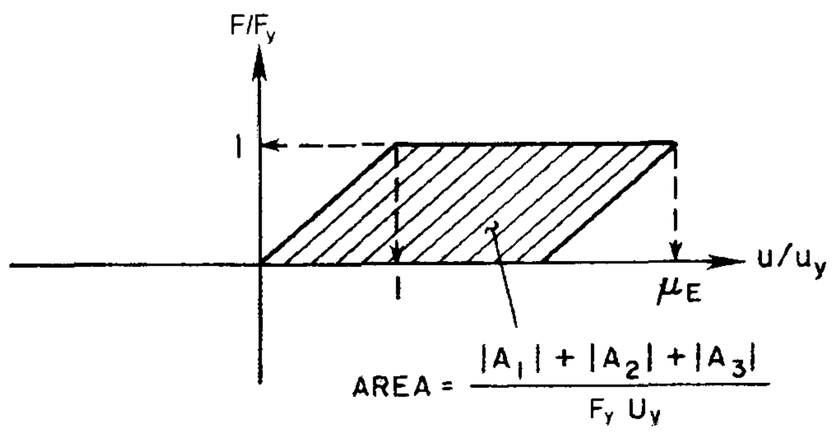


Figure 2.12. – Definition of normalized hysteretic energy ductility (Mahin and Lin 1983)

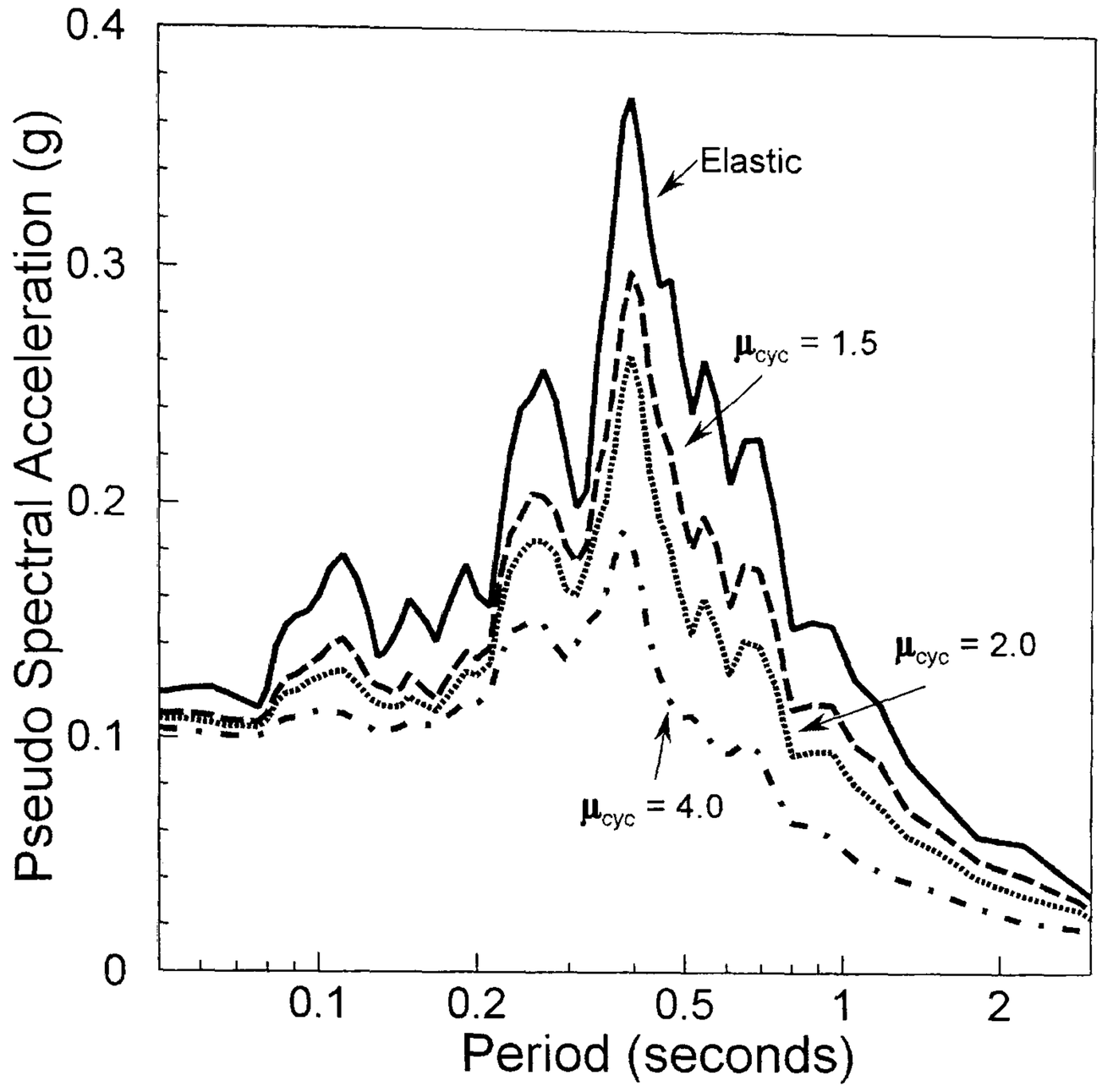


Figure 2.13. – Constant cyclic ductility spectrum (accumulative ductility/ hysteretic energy ductility), 5% viscous damping, elastic-perfectly plastic hysteretic system, as for Figure 2.10

Fourier amplitude spectra

The Fourier transform decomposes a function into a spectrum of harmonic, sinusoidal components that if summed would make up the original function. Any harmonic signal is completely described if the amplitude and phase of the harmonic is known. Indeed, there are two types of Fourier spectra: Fourier amplitude spectra, which contain information on the amplitude of the harmonics, and Fourier phase spectra, which contain information on the phase. As it is the amplitude of the motions that are usually of most interest, only Fourier Amplitude Spectra will be presented here; the reader is directed to Paz (1997) for more extensive treatment of the subject.

Fourier amplitude spectra are excellent for the investigation of functions that have a stationary, or near stationary, frequency content but have a few problems when used to analyse non-stationary signals such as earthquake ground motions. This is best demonstrated with an example: consider an idealised ground motion made up of two signals, a 0.1g continuous sine wave with a period of 0.5s and a 0.7g single cycle pulse with a period of 1.0s (Figure 2.14). The Fourier amplitude spectra show a well defined peak at 0.5s period, with

amplitude of 0.092g, accurately picking up the continuous harmonic component of the motion. However, the single cycle motion is only present in one tenth of the record, so has a Fourier amplitude of approximately one tenth of the amplitude of the impulse. In addition, the single-cycle motion is poorly defined in the frequency domain (Figure 2.14).

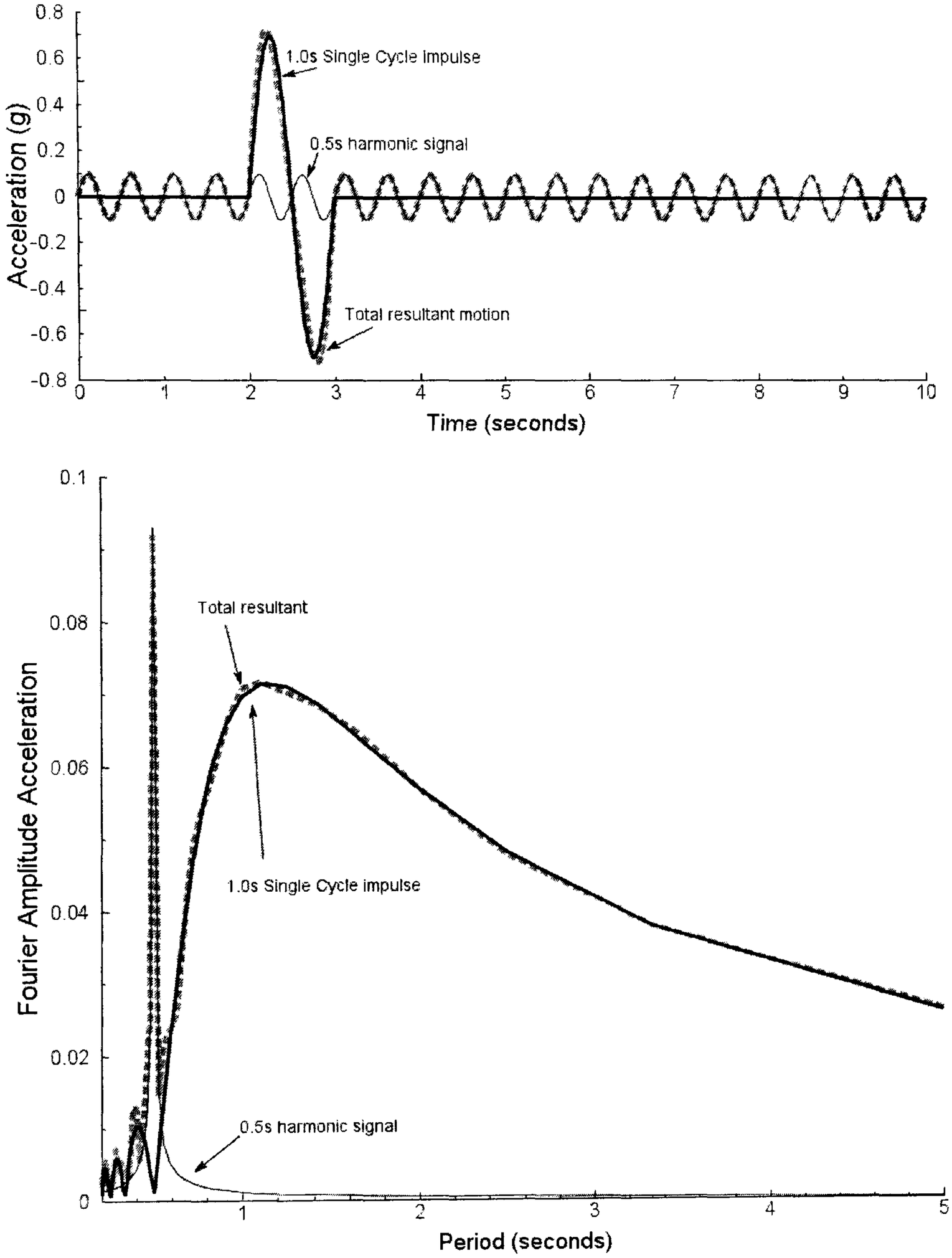


Figure 2.14. – (*below*) Fourier Amplitude Spectra from (*upper*) harmonic and single cycle motion. Demonstrating that whilst the amplitude and period of the continuous signal is well defined by the Fourier amplitude spectra, both the period and amplitude of the single impulse are poorly defined.

Despite these shortcomings Fourier amplitude spectra are widely used in seismology to model ground motions. This is commonly achieved by assuming that the Fourier amplitude spectrum of a particular ground motion $FA(\omega)$ can be expressed as the combination of factors; Lam *et al.* (2000) review several seismological models, including Boore (1983), that use a source spectrum $S(w)$, a geometric attenuation function $G(r)$, anelastic attenuation function A(w) and a function describing the attenuation in the upper crust P(w):

$$FA(\omega) = S(\omega).G(r).A_n(\omega).P(\omega) \tag{2.13}$$

The source spectra and attenuation functions used to make up the resultant spectra can be estimated using empirical or semi-empirical relationships (e.g. Brune 1970; Hanks 1979; Hanks and McGuire 1981). Once the Fourier amplitude spectrum has been estimated a synthetic ground motion can be produced by the summation of a number of harmonics (sinusoids) with random phases (e.g. Boore 1983). Time domain characteristics, such as the build-up and decay of the motion, are usually achieved using empirical window functions.

2.2.3 Measures of energy

Many measures of energy have been proposed over the years, but the most widely used parameter is the Arias intensity (*AI*) (Arias 1970):

$$AI = \frac{\pi}{2g}\int_0^{D_T} a_g^2(t)dt \tag{2.14}$$

where g is the acceleration due to gravity, a_g is the ground acceleration and D_T is the total duration of the record. This intensity measure can be plotted as a function of time to form the Husid plot (Husid 1969) (Figure 2.15). Bommer *et al.* (1997) show that ground motions with similar energy levels are more damaging if they have shorter duration. This is logical as the amplitude of ground motions is larger if the energy is released over a shorter period of time. The rate of energy release can be measured by the gradient of the Husid plot. However, as the gradient changes throughout the duration of the ground motion (Theofanopoulos and Drakopoulos 1986) different results will be achieved depending on where the gradient is measured.

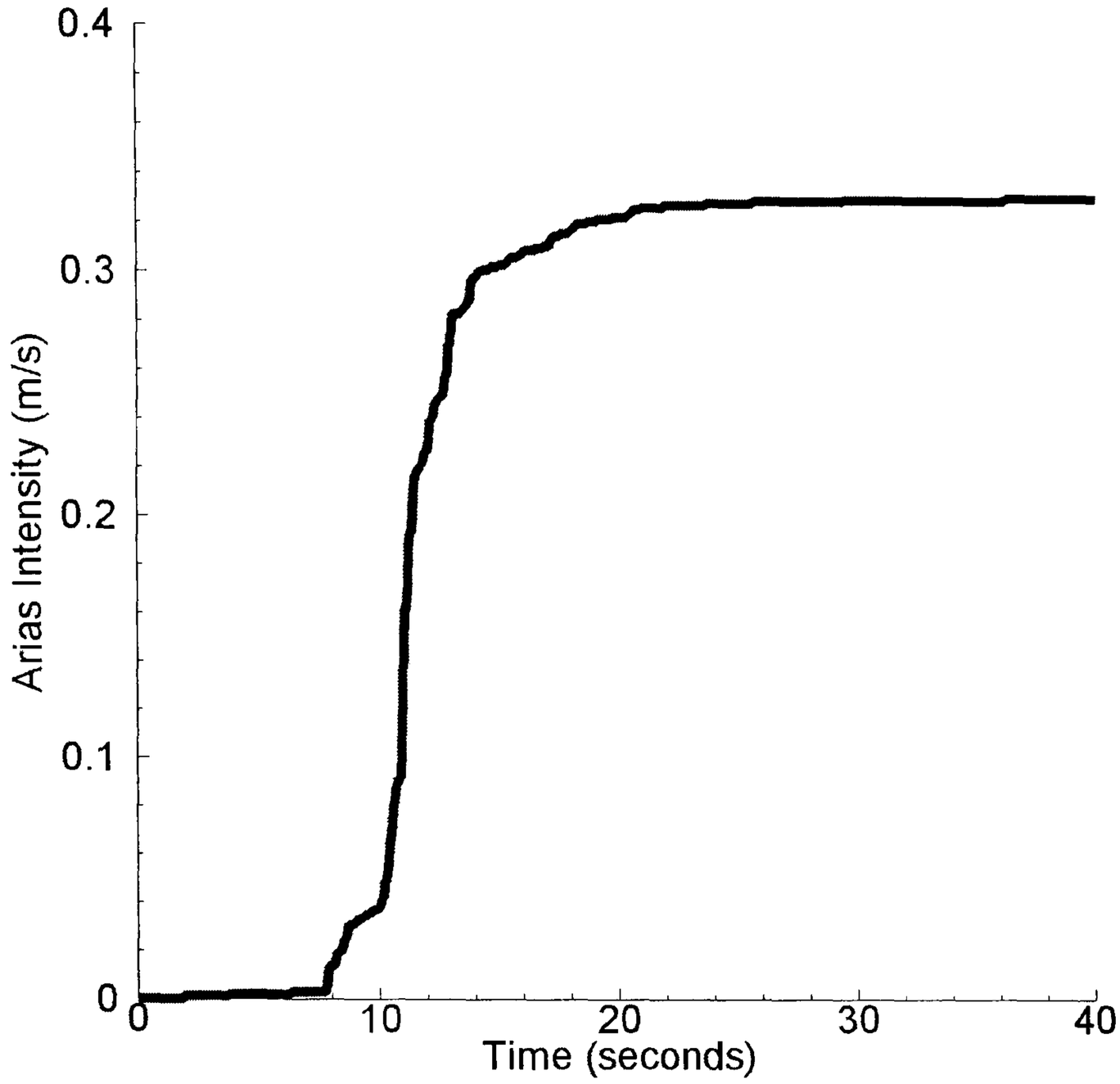


Figure 2.15. – Build up of Arias Intensity with time (Husid plot) for the 1989 M_w 6.9 Loma Prieta Earthquake recorded 71km from the fault rupture at Diamond Heights (record 00794T in the NGA database)

Sarma (1971) shows that the energy density, E, at a recording station can be calculated from:

$$E = \frac{1}{4} S\rho \int_0^{D_T} \dot{x}(t)^2 \, dt \tag{2.15}$$

where S is the wave propagation velocity in the material carrying the wave, ρ is the mass density of the material, D_T is the total duration of the ground motion and $\dot{x}(t)$ is the particle velocity. Assuming that ρ is constant and that the energy at a point comes mainly from the contribution of S-waves (so have the same velocity), the normalised energy density can be simplified as:

$$E' = \int_0^{D_T} \dot{x}(t)^2 \, dt \tag{2.16}$$

Araya and Saragoni (1980) and Saragoni (1985, 1990) proposed that the destructiveness of an earthquake is proportional to the energy contained in each pulse of motion. They use parameter, P_D, to measure the potential for damage as follows:

$$P_D = \frac{AI}{\nu_0^2} \tag{2.17}$$

where AI is Arias Intensity and ν_0 is the intensity of zero crossings per second. Unfortunately the P_D parameter was designed using stationary stochastic simulations and does not always behave as intended with recorded accelerograms. This is because the predominant period and the frequency of zero crossings vary with time (Joannon *et al.1977*) so P_D is dependent on the start and end times of the record. Anderson and Bertero (1988) avoid the issue of the zero crossings by using just the area under the acceleration pulse; they call this parameter the incremental velocity.

2.2.4 Hybrid ground-motion measures

There are many different parameters that have been proposed in the technical literature using combinations of the above parameters. For example Cosenza and Manfredi (1998) define a damage index using the Arias intensity, but make the measure dimensionless by dividing the integral of the squared acceleration by PGA and PGV

$$Iz = \frac{\int_0^{Dt} a(t)^2\, dt}{PGA.PGV} \tag{2.18}$$

Damage measures combining measures of ground-motion amplitude with the duration are also proposed by Aptikaev (1982) and Park *et al.* (1984, 1985). Aptikaev correlates damage measured in terms of the Modified Mercelli Intensity with the damage parameter:

$$I_{ap} = PGA * D_{UR,0.5PGA}^{0.5} \tag{2.19}$$

where $D_{UR,0.5PGA}$ is the uniform duration measured at an acceleration level of 0.5*PGA (see following section). Park *et al.* (1984, 1985) use a combination of the RMS acceleration (RMS_A) and an undefined measure of the strong-motion duration D to define the damage parameter I_{pa} which they show has a good correlation with the Park and Ang damage index (Park and Ang 1985):

$$I_{pa} = RMS_A^{1.5} D^{0.5} \tag{2.20}$$

2.3 Definitions of Ground-Motion Duration

This section briefly summarises the work of Bommer and Martínez-Pereira (1999, 2000) who conduct extensive reviews of the different definitions of strong-motion duration. Bommer and Martínez-Pereira find that there is no consistent measure of strong ground-motion duration with over 30 different definitions in the technical literature.

Duration definitions can be divided into four groups:

- Bracketed Duration
- Uniform Duration
- Significant Duration
- Structural Duration

Each of these definitions is described in the following sections.

2.3.1 Bracketed duration

Bracketed duration (D_B) measures are defined as the total time elapsed between the first and last excursions of a specified acceleration level, a_0 as illustrated in Figure 2.16. The advantage of this definition is that it is conceptually simple. The disadvantage is that it considers only the first and last excursions of the specified threshold and ignores the characteristics of the strong shaking phase. This can result in long durations being estimated for earthquakes with small sub-events occurring after the main shock. The duration can be unstable if low thresholds of acceleration are employed and, for some accelerograms, a change of the threshold, from say 0.03 g

to 0.02 g, can result in an increase of the bracketed duration by 20 seconds or more (Pagratis 1995).

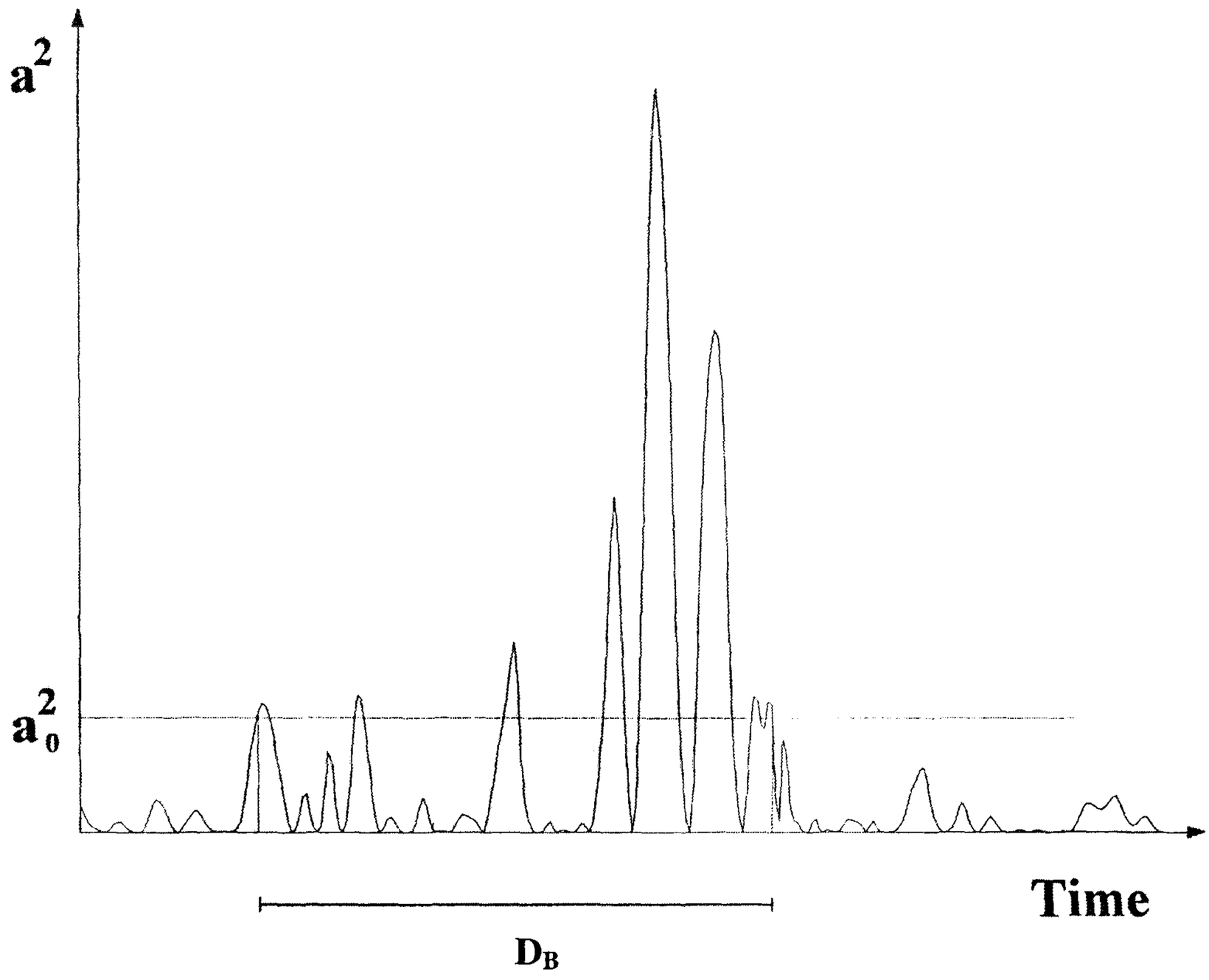


Figure 2.16. - Definition of Bracketed Duration (Bommer and Martínez-Pereira 1999)

2.3.2 Uniform duration

Uniform durations (D_U) are also defined by a threshold level of acceleration, a_0, but rather than as the interval between the first and last excursions that exceed this level, the duration is defined as the sum of the time intervals during which the acceleration is greater than the threshold. The concept of uniform duration is illustrated in Figure 2.17. This definition is less sensitive to the threshold level than the bracketed duration, but it has the disadvantage that it does not define a continuous time window of strong shaking.

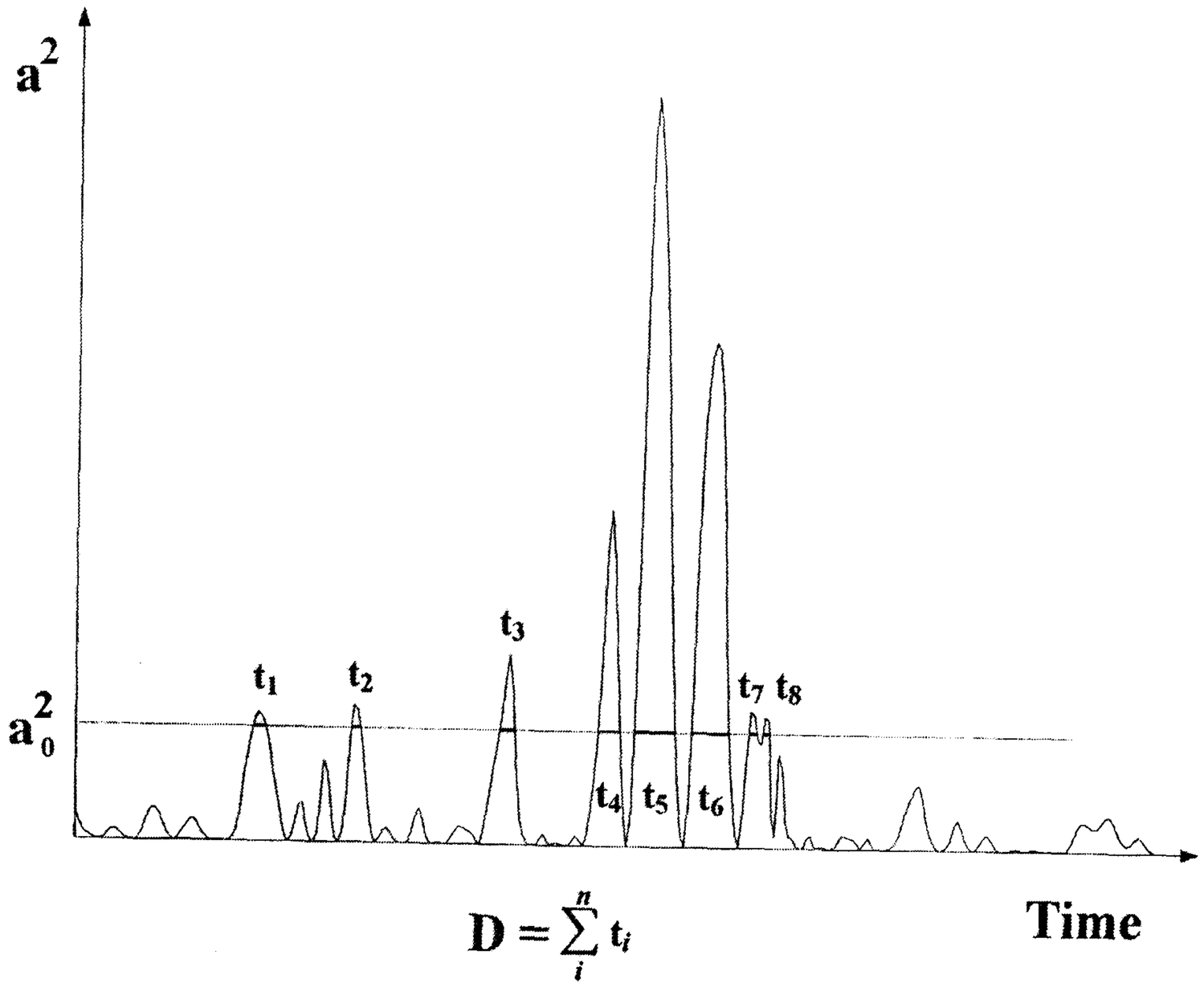


Figure 2.17. – Definition of Uniform Duration (Bommer and Martínez-Pereira 1999)

2.3.3 Significant duration

Significant duration measures are based on the accumulation of energy in the accelerogram represented by the integral of the square of the ground acceleration, velocity or displacement. If the integral of the ground velocity is used, then the quantity is directly related to the energy density (Sarma 1971), whereas if the integral of the ground acceleration is employed then the quantity is related to the Arias intensity, AI (Arias 1970). The significant duration is defined as the interval over which some proportion of the total integral is accumulated. This is illustrated for arbitrary limits on a plot of the build-up of Arias intensity, known as a Husid plot (Husid 1969), in Figure 2.18. Significant duration measures have the advantage that they consider the characteristics of the entire accelerogram and define a continuous time window in which the motion may be considered as strong.

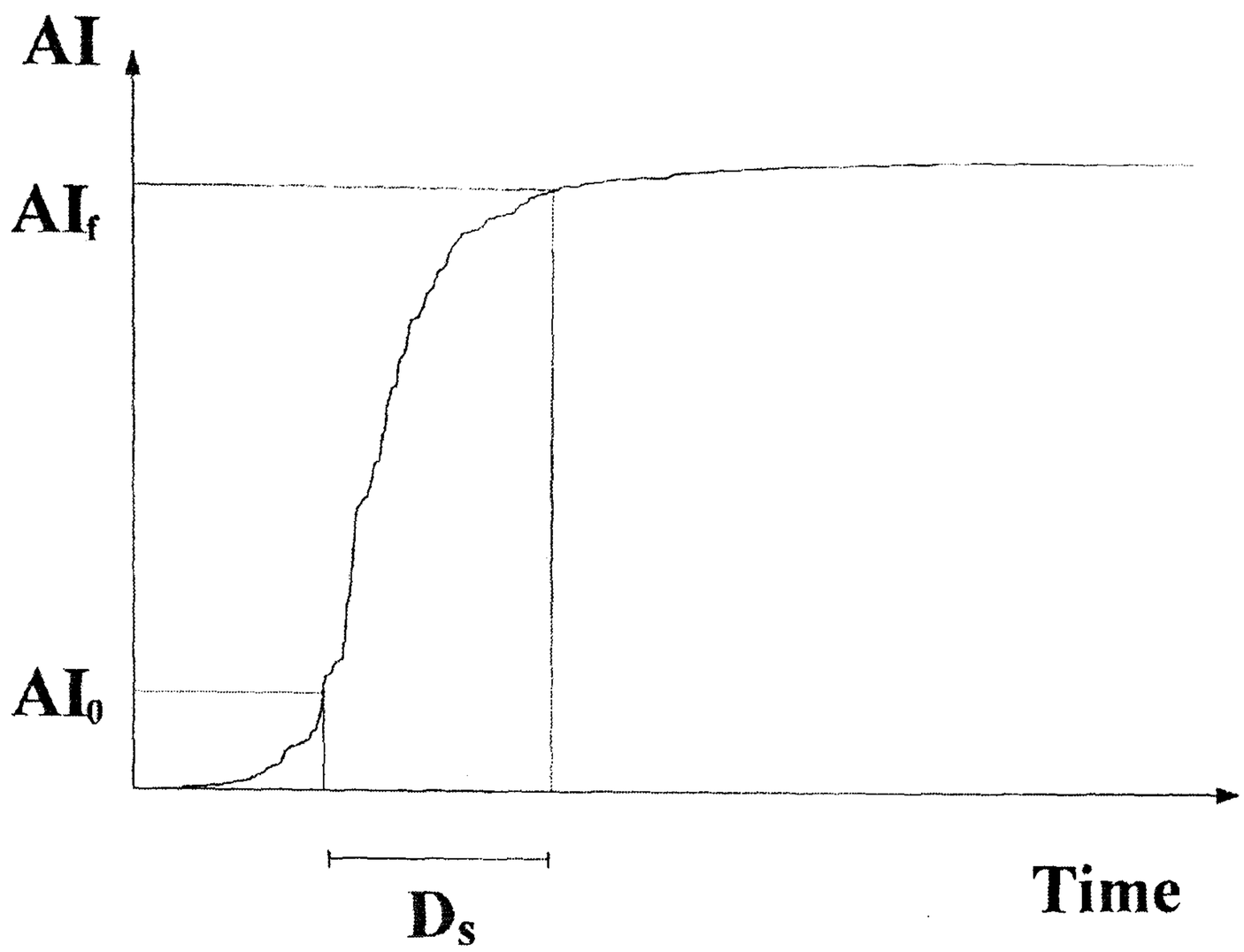


Figure 2.18. - Definition of Significant Duration (Bommer and Martínez-Pereira 1999)

2.3.4 Structural duration

Some definitions of strong-motion duration are based on the characteristics of the response motion of a specified structure subjected to the ground motion. These definitions are considered as a fourth generic group, although they can usually also be classified into the same three groups described above, since in effect they are applications of the bracketed, uniform or significant duration to the response time-history.

2.3.5 Classification of duration measures

All definitions of duration require a threshold level at which the ground motions are considered to be strong, and the duration measured. Depending on the duration measure employed this level can be defined as a fixed absolute value for all records, or can be a relative measure which is expressed as a fraction of the peak motion or the Arias Intensity of each record. This difference in definition is critical as it changes the behaviour of duration with site-to-source distance.

Table 2.1. - Classification of definitions of strong-motion duration (Adapted from Bommer and Martínez-Pereira 2000)

Definition	Bracketed Rel.	Bracketed Abs	Uniform Rel.	Uniform Abs	Significan Rel.	Significan Abs	Structural Rel.	Structural Abs
Rosenblueth and Bustamente (1962)							○	
Housner (1965)		●						
Ambraseys and Sarma (1967)		●						
Lynch (1967)								●
Husid (1969)					●			
Kobayashi (1971)		●						
Page *et al.* (1972)		●						
Donovan (1972)					●			
Bolt (1973)		○		○				
Housner (1975)					●			
Trifunac and Brady (1975a)					●			
O'Brien *et al.* (1978)	●							
Hisada and Ando (1976)	●							
Aptikaev (1977)	●							
Trifunac and Westermo (1977)			○		○			
Saragoni (1977)					●			
McGuire and Barnhard (1979)	●	●			●			
McCann and Shah (1979)					●			
Perez (1980)								○
Takizawa and Jennings (1980)					●			
Vanmarcke and Lai (1980)					●			
Zahrah and Hall (1984)								○
Zhou and Xie (1984)					●			
Shahabi and Mostaghel (1984)					●			
Theofanopoulos and Drakopoulos (1986)					●			
Elghadamsi *et al.* (1988)					●			
Xie and Zhang (1988)								○
Mohraz and Peng (1989)					○			
Theofanopoulos and Watabe (1989)					●			
Kawashima and Aizawa (1989)	●	●						
Ellis *et al.* (1990)					●			
Sarma and Casey (1990)			●					
Papazachos *et al.* (1992)		●						
Bommer and Martínez-Pereira (1996)					●	●		
Somerville *et al.* (1997)					●			
Wenbo and Kezhong (1997)	●							
Şafak (1998)							○	
Bommer and Martínez-Pereira (1999)						●		
Reinoso *et al.* (2000)					●			

● frequency-independent duration ○ frequency-dependent duration

The duration of ground motion measured using an absolute threshold will decrease with distance as the amplitude of motions decrease. However, measures using relative thresholds increase with distance due to dispersion of the different seismic phases (waves), which travel at different speeds.

Some authors pass ground motions through narrow-band filters before calculating the duration to determine the duration at a particular frequency. The disadvantage of this is the additional complexity and the requirement to select suitable frequencies for the filters. However, this technique does enable the duration of different seismic waves to be detected and may be useful for assessing the different damage potential to structures with different natural periods of vibration. The most recent list of duration definitions proposed by different authors is presented in Table 2.1.

2.4 Definitions of Number of Cycles

Many different approaches to identify and measure the number of cycles of accelerograms have been proposed by different researchers (Hancock and Bommer 2005). These definitions are reviewed and evaluated in this section.

The following three sub-sections describe the main generic techniques used for direct cycle counting. These are loosely based on categories used for classifying cycle counting definitions developed for fatigue testing (ASTM 1985; Dowling 1972). Statistical techniques proposed by some authors for estimating the number of cycles indirectly, and definitions based on structural response are discussed in the fourth and fifth sub-sections respectively. Cycle counting definitions are illustrated using a 1-second section of an accelerogram recorded in the $3.9M_w$ 1985 Coalinga earthquake (Figure 2.19).

To allow comparison of different cycle counting definitions, the irregular cycle amplitudes produced by each cycle counting definition are converted into a single number of effective cycles using an absolute measure (N_A), as used by Malhotra (2002) to measure the damage potential of a ground motion:

$$N_A = \sum_{i=1}^{2n} u_i^2 \tag{2.21}$$

where, u_i is the acceleration amplitude of the i^{th} half cycle and n is the number of cycles.

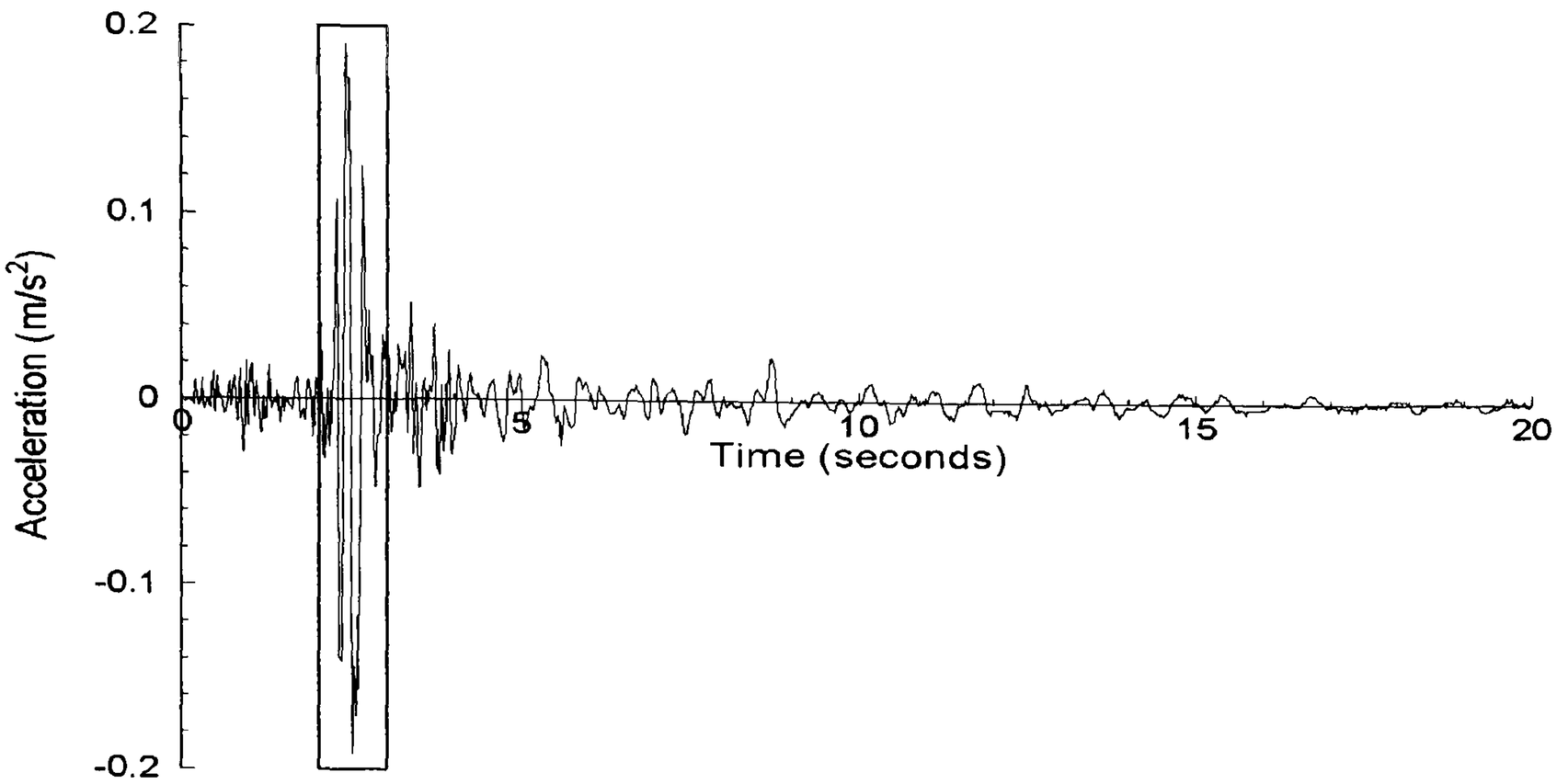


Figure 2.19. - Accelerogram recorded for the 3.9Mw Coalinga earthquake recorded at 5.7km at Sulphur Baths. Box shows section of motion used for cycle counting examples.

Before proceeding further, it is important to note the difference between cycle counting definitions and definitions of ground-motion duration. Although the number of cycles of ground motion provides an indication of duration, most cycle counting techniques are used because they also contain a measure of the amplitude of the motion. It is also important to note that cycle counting definitions used for fatigue analysis typically measure cycle *ranges* (the distance between peak and trough), whilst those used in earthquake engineering almost exclusively count *amplitudes* (the distance between peak and the zero mean).

2.4.1 Peak counting definitions

Peak counting definitions are the most common definition used in earthquake engineering. They are used in a wide range of applications including damage estimation parameters and liquefaction potential. A cycle counting definition is classified as peak counting if it explicitly counts the number of peaks. There are

several different variations of peak counting, the two main differences between definitions being:

- Cut-off level: to prevent many small peaks dominating the results some definitions do not count peaks below a low-amplitude cut off.
- Zero-crossing counting: some definitions only count the largest peaks between zero crossings, others count all peaks.

Figure 2.20 shows an example of a peak counting definition with no low amplitude cut off and where only zero crossing peaks are counted. The number of absolute effective cycles N_A evaluated using this definition is 0.127; if non-zero crossing peaks are included the parameter increases by 25% to 0.160.

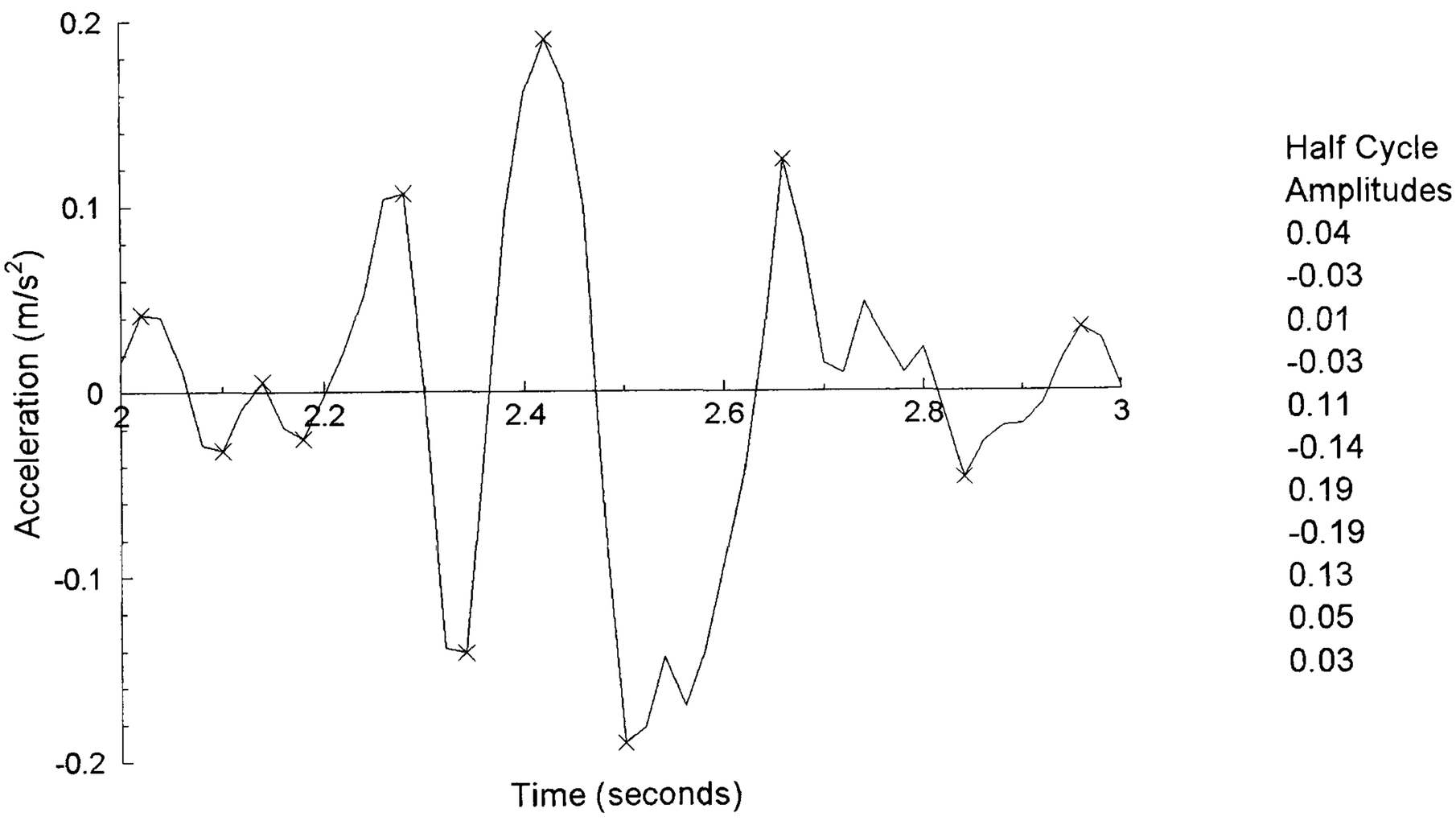


Figure 2.20. - Peak counting example, with non-zero crossings excluded.

2.4.2 Level crossing definitions

Level crossing definitions are not normally used to measure amplitudes of motion but are commonly used to measure the period or frequency of the motion. The most common measure is the zero-mean crossing period (e.g. Vanmarcke and Lai 1980), but Sarma and Srbulov (1998) propose that other levels can be used. They define the frequency as half the number of excursions above a set level, divided by the duration

spent above the level, using the uniform duration as proposed by Sarma and Casey (1990). It is the convention in cycle counting (ASTM 1985) to count only level crossings with positive gradient on the positive axis and crossings with a negative gradient on the negative axis (Figure 2.21).

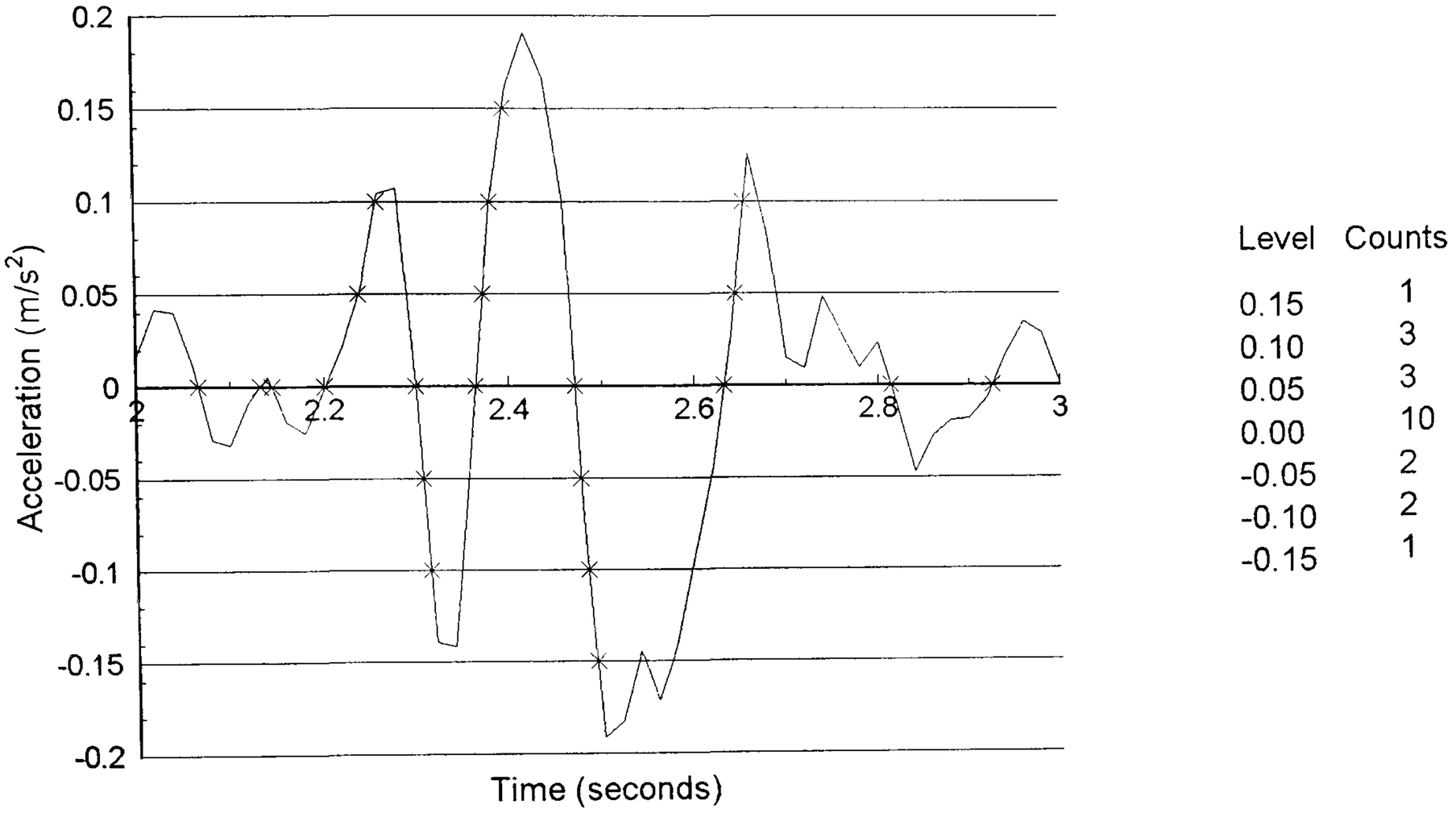


Figure 2.21. - Level crossing example, with non-zero crossings excluded.

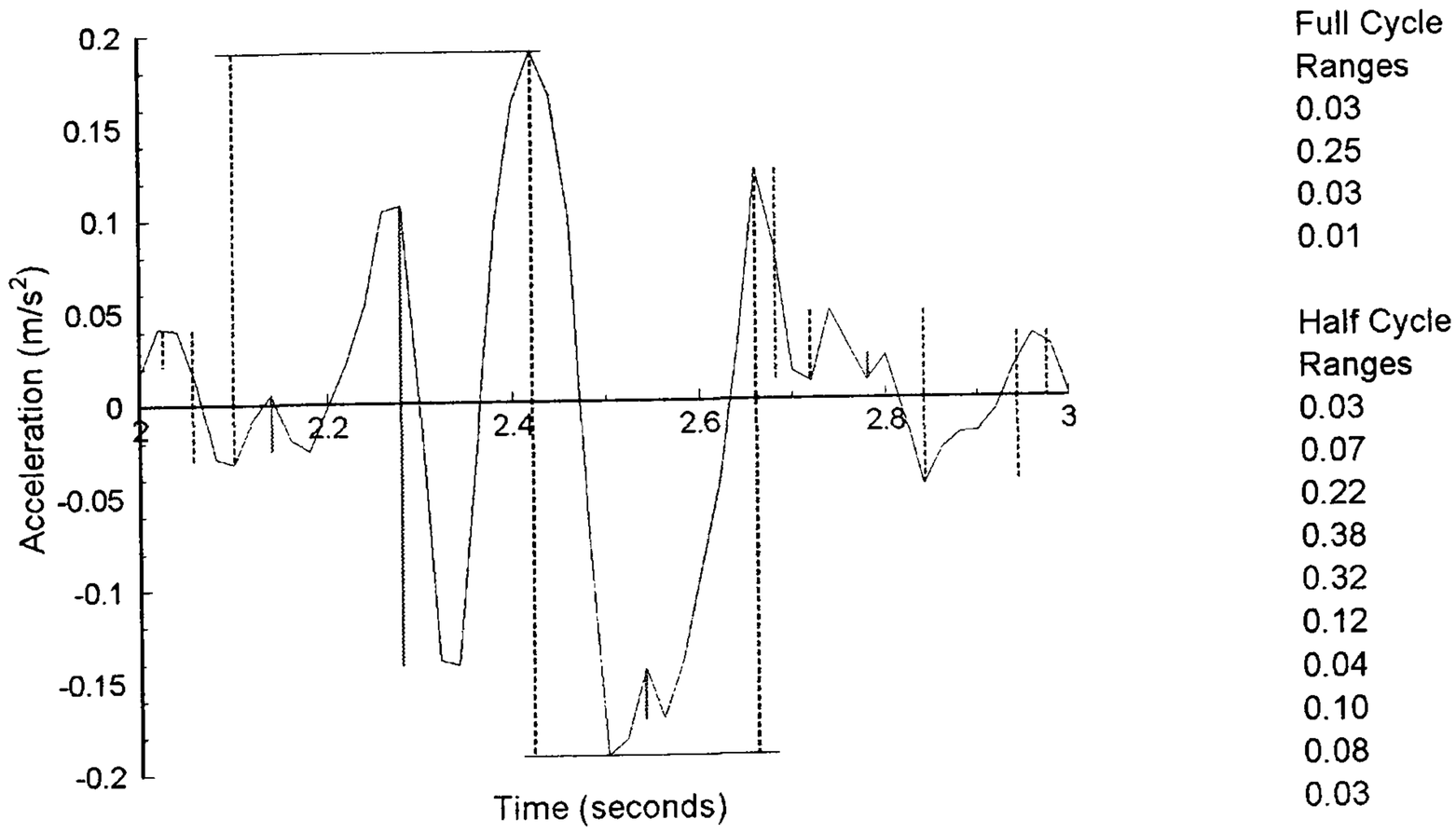


Figure 2.22. - Range counting example using rainflow counting technique, solid lines show full cycles, dashed lines show half cycles.

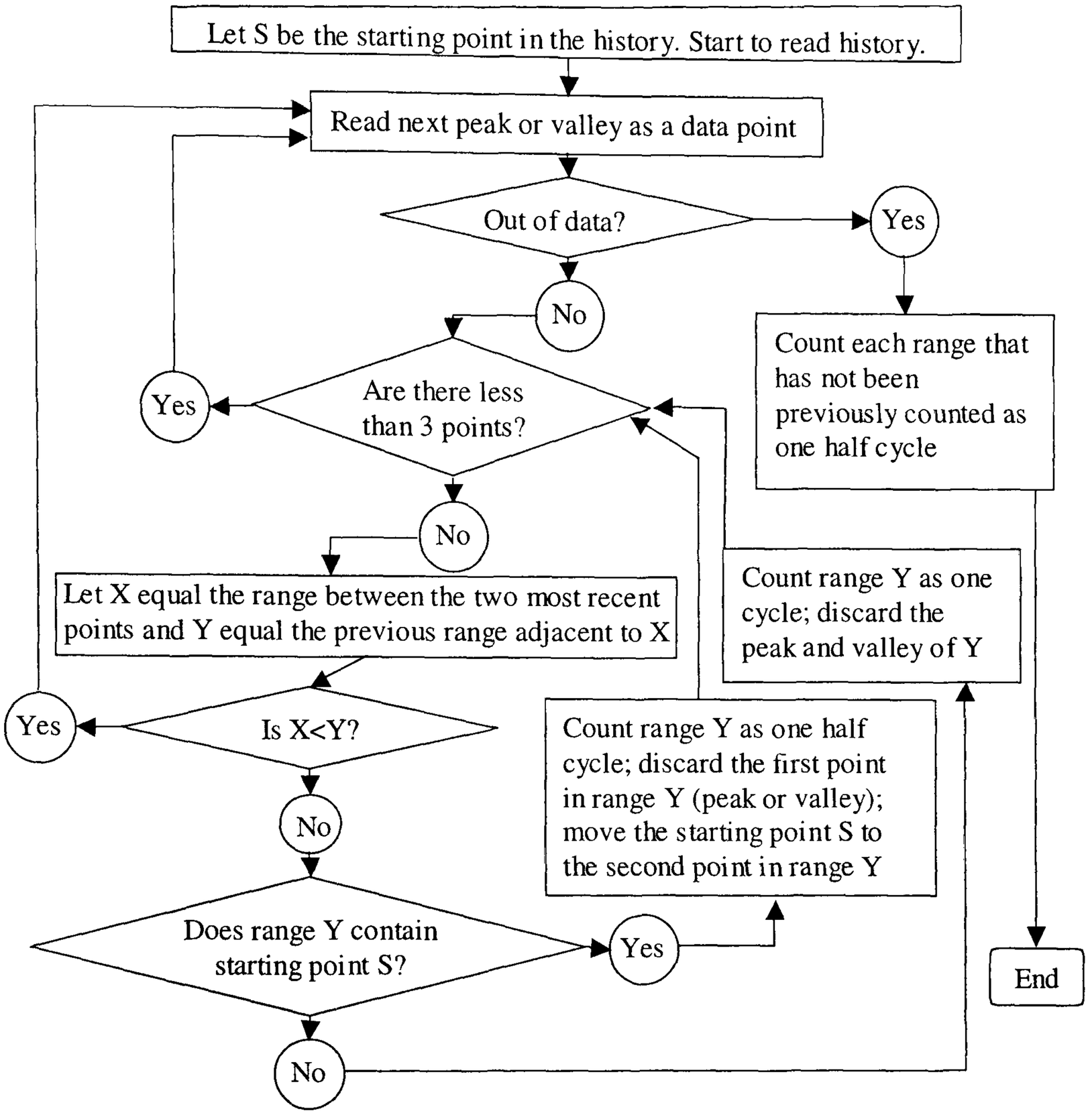


Figure 2.23. - Rainflow counting procedure

2.4.3 Range counting definitions

Range counting definitions are most commonly used for the analysis of fatigue. In earthquake engineering this is related to problems such as the assessment of low-cycle fatigue, typically in the joints of steel framed buildings (e.g. Calado *et al.* 1998; Calado *et al.* 2002; Mander *et al.* 1995; Taucer *et al.* 2000; Tremblay and Bouatay 2002). These principles have also been extended for use with reinforced concrete structures (e.g. Dutta and Mander 2001). The most popular range counting method is the rainflow range counting method as it counts both high- and low-frequency cycles in broad-banded signals. This procedure is used to count the number of cycles in the time-series as shown in Figure 2.22. The rainflow counting method, as described by ASTM (1985), is explained in Figure 2.23. It is not possible to determine peak

amplitudes from cycle ranges for motions with irregular amplitude; however, for the purpose of this thesis cycle ranges are converted to peaks assuming two half-cycle ranges equal one peak and one full cycle can be taken as two half cycles of half the amplitude. This gives the absolute number of effective cycles (N_A) calculated using rainflow counting as 0.18, a factor of 1.4 greater than that predicted by zero crossing peak counting definitions.

2.4.4 Indirect counting methods

Indirect counting methods are those that do not count the number of cycles directly from a time-series, but use statistical techniques to approximate the number of cycles. The most common are definitions based on random vibration theory, which use spectral moments to determine the predominant frequency and hence the number of extreme peaks per unit time (e.g. Boore 1983). Most of these definitions assume that the peaks are not strongly correlated and are part of a stationary process. The method given by Boore (1983) to determine the number of extreme responses, N, in time interval T is:

$$N = 2\tilde{f}T \tag{2.22}$$

where $\tilde{f}$ is the predominant frequency, given by:

$$\tilde{f} = \frac{1}{2\pi}(m_4 / m_2)^{1/2} \tag{2.23}$$

m_2 and m_4 are the second and fourth spectral moments respectively, given by:

$$m_2 = \frac{1}{\pi}\int_0^\infty \omega^2 |A(\omega)|^2 d\omega \tag{2.24}$$

$$m_4 = \frac{1}{\pi}\int_0^\infty \omega^4 |A(\omega)|^2 d\omega \tag{2.25}$$

where ω is the circular frequency and $A(\omega)$ is the acceleration spectrum. Amini and Trifunac (1981); Gupta (1991, 1994) and Gupta and Trifunac (1998a, 1998b, 2000) point out that real accelerograms are non-stationary and use order statistics to derive the effective peak acceleration of a stationary accelerogram. Elghadamsi *et al.* (1988)

overcome this issue by modelling strong ground-motion with a stationary component plus a non-stationary envelope function.

2.4.5 Definitions based on structural response

Several authors measure a parameter related to structural response and use this to determine a number of effective cycles of motion. This is usually based on the approach suggested by Zahrah and Hall (1984) who determine the equivalent number of yield cycles n_{eq} by dividing the total hysteretic energy (E_H) by the equivalent energy that would be absorbed had the structure been loaded monotonically to the same maximum displacement. This definition of the number of equivalent cycles can be defined using an elasto-plastic model and used as a comparative index to assess the severity of ground motion:

$$n_{eq} = \frac{E_H}{F_y.\left(x_{\max} - x_y\right)} \tag{2.26}$$

where F_y is the yielding force, x_{max} is the maximum displacement and x_y is the yield displacement. The physical concept of this parameter is illustrated in Figure 2.24. Manfredi *et al.* (2003) find that the number of equivalent cycles defined in this way increases with distance from the fault rupture although the peak demand decreases.

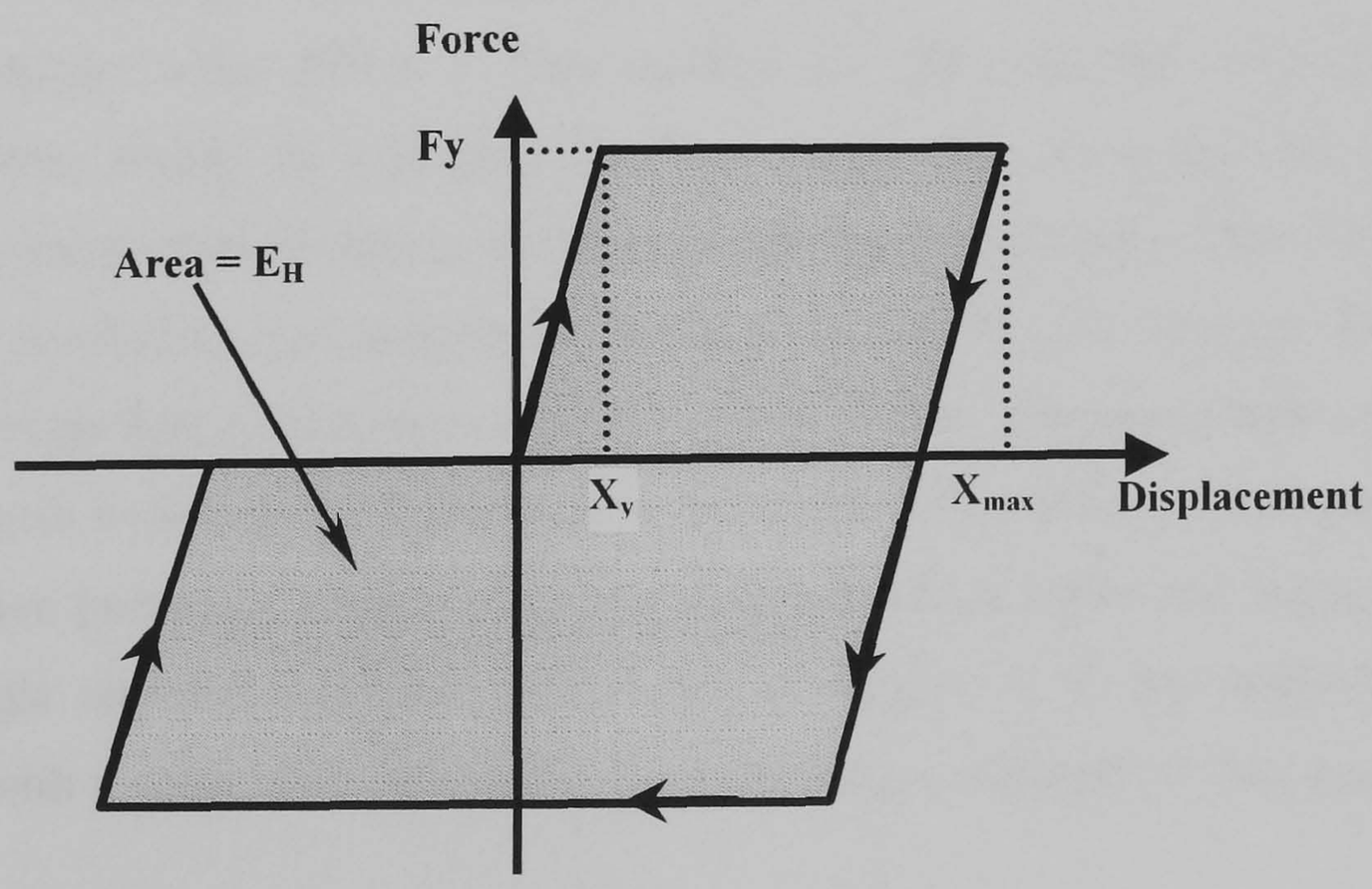


Figure 2.24. - Illustration of number of equivalent cycles for an elasto-plastic system.

2.4.6 Procedures for determining effective number of constant amplitude cycles

Although measures of ground-motion duration provide an indication of the number of cycles of motion, cycle counting techniques are usually used because they also convey a measure of the amplitude of the motion. Whilst this feature provides additional and important information, it also presents some extra challenges. Most applications require the number of equivalent cycles of constant amplitude. However, this information is not obtained directly from most cycle counting definitions as they produce tallies of the cycles with different amplitudes within a time-history. For this tally of irregular cycle amplitudes to be converted to a single number representing the effective number of cycles of constant amplitude an assumption has to be made regarding the relative importance of different cycles. The transformation to constant-amplitude cycles is usually conducted assuming linear damage accumulation, which was first proposed by Miner (1945) for the calculation of fatigue damage, *FD*, in aluminium:

$$FD = \sum \frac{n_i(S_i)}{N_i(S_i)} \tag{2.27}$$

where n_i is the number of load cycles applied at stress range S_i, and N_i is the number of cycles required to cause failure at stress range S_i. The key to the method is that failure occurs when $FD = 1$. This method has been adapted to several different applications simply by replacing the stress range with other measures of damage, such as strain range for low-cycle fatigue assessment and cyclic stress ratio (which is directly proportional to ground acceleration) in liquefaction analysis. The principle can be illustrated graphically, consider a time-history containing four cycles with a range (peak-to-trough) of 1 followed by one cycle with a range of 2 (Figure 2.25). For illustrative purposes, a failure line is prescribed which states that failure will occur with eight uniform-amplitude cycles with a range of 1 or two uniform-amplitude cycles with a range of 2. Therefore, the total fatigue damage for this loading regime is:

$$FD = \frac{4}{8} + \frac{1}{2} = \frac{1}{2} + \frac{1}{2} = 1 \tag{2.28}$$

Half of the fatigue life is used by the first four cycles and the remaining half used by the final cycle, implying that the component is expected to fail at the end of the loading.

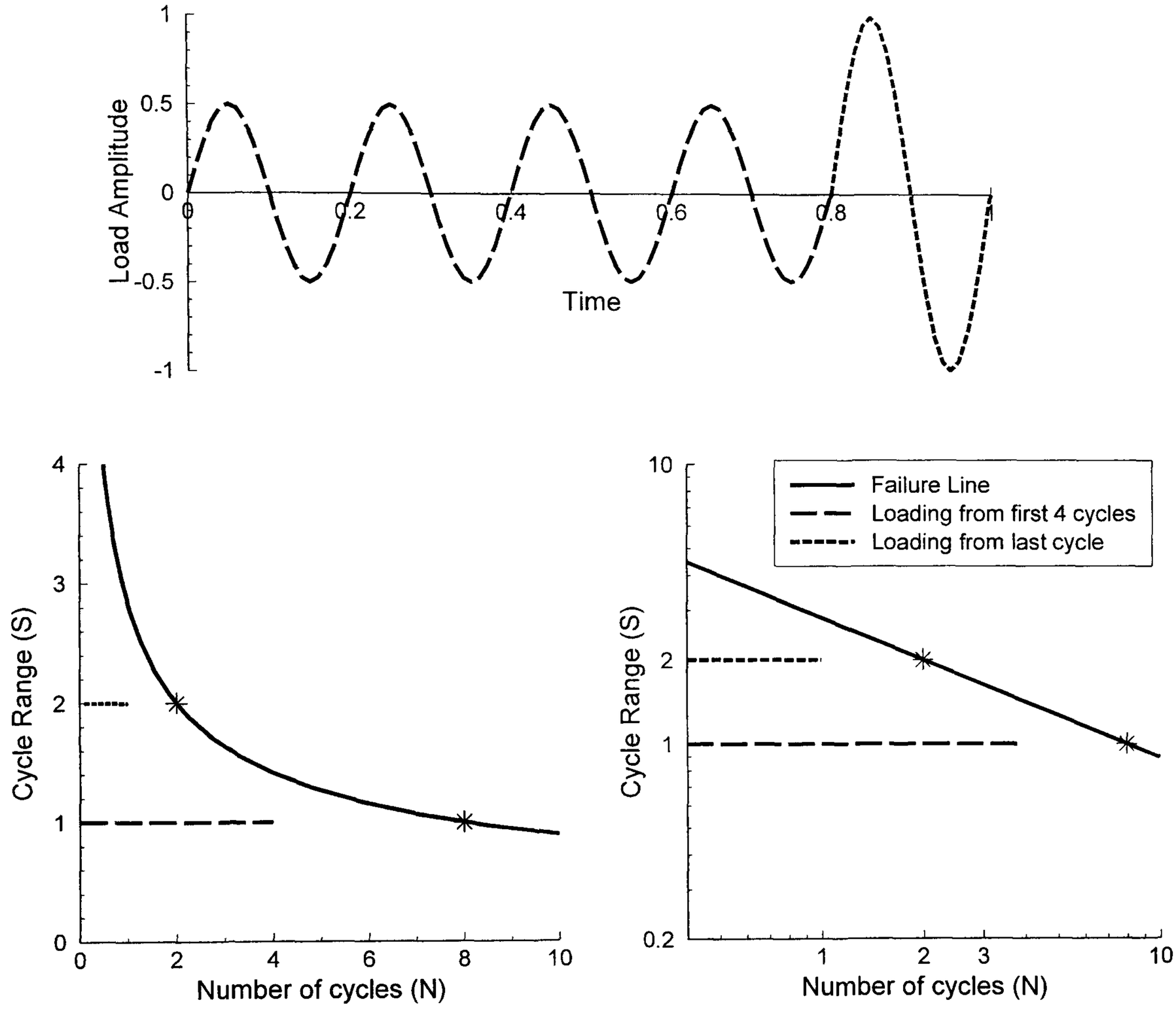


Figure 2.25. - Illustration of Miner's linear damage accumulation. Applied cyclic loading (*upper*), and number of cycles to failure represented by a S-N curve with linear axes (*lower left*) and log-log axis (*lower right*)

A common practice is to assume that the damage caused by each cycle is proportional to its amplitude raised to a power, which expressed in terms of the range is:

$$S = \left(\frac{N}{a}\right)^{-\frac{1}{k}} \tag{2.29}$$

where a and k are constants dependent on the material properties and, if used in a structural application, the geometry of the component under investigation. Constants a and k represent a linear scale factor and the gradient of a straight line on the S-N curve when plotted on log-log axes (e.g. Figure 2.25). Although the constant a may vary considerably for different applications and is dependent on the units used, the constant k is more stable and, as shown below, is of greater importance.

The procedure illustrated above can be generalised for any excitation. Consider a time-history with n_1 cycles with a range S_1 followed by groups of n_i cycles each with a range S_i. The damage caused by these irregular amplitude cycles is:

$$FD = \frac{n_1(S_1)}{aS_1^{-k}} + \sum \frac{n_i(S_i)}{aS_i^{-k}} \tag{2.30}$$

The number of uniform amplitude equivalent cycles N_{eq} at range S_{ref}, which cause the same damage as the irregular amplitude cycles is:

$$\frac{N_{eq}(S_{ref})}{aS_{ref}^{-k}} = \frac{n_1(S_1)}{aS_1^{-k}} + \sum \frac{n_i(S_i)}{aS_i^{-k}} \tag{2.31}$$

which simplifies to:

$$N_{eq}(S_{ref}) = S_{ref}^{-k}\left(\frac{n_1(S_1)}{S_1^{-k}} + \sum \frac{n_i(S_i)}{S_i^{-k}}\right) \tag{2.32}$$

Eq. (2.32) shows that coefficient a cancels out, and it is coefficient k that is of prime importance as it determines the relative damage caused by different amplitude cycles. The reference range S_{ref} is also different depending on the cycle counting definition: for relative counting measures S_{ref} is expressed as a fraction of the maximum cycle amplitude in the time-history, whereas absolute counting definitions use a fixed reference amplitude for all time histories.

Miner's damage accumulation theory assumes that the sequence of the loading cycles and the direction of the load (positive or negative) have no influence on the ensuing damage. Whilst this is a reasonable assumption for many applications, more complex damage measures have been proposed which do not make these assumptions (Chung *et al.* 1988, 1989; Green and Lee, 2005). However, increasing the complexity of the damage measure increases the difficulty in reliably calibrating the measure with experimental test results. This has led to the relatively simple models, such as that explained above, being the most widely used.

2.4.7 Reference level

Different cycle counting definitions express the number of equivalent cycles at different reference amplitudes: for example, liquefaction studies frequently use the number of equivalent cycles at 65% maximum amplitude (Seed *et al.* 1975). This is not a significant problem as conversion between different reference amplitudes can be made if the relative damage assumed to be caused by each cycle amplitude is known (Lee and Chan 1972):

$$N_{new} = N_{ref}\left(\frac{Nf_{new}}{Nf_{ref}}\right) \tag{2.33}$$

where N_{new} is the number of cycles at the new reference amplitude, N_{ref} is the number of cycles at the original reference amplitude, Nf_{new} is the number of cycles to cause failure at the new reference amplitude and Nf_{ref} is the number of cycles to cause failure at the original reference amplitude. However, it is not possible to make such a conversion from a cycle counting definition based on relative amplitudes to another based on absolute amplitudes.

Table 2.2. - Summary of cycle counting definitions used by different authors

Generic Category	Level Crossing		Peak Count		Range Count		Indirect/ Structural Method
	Rel.	Abs	Rel	Abs	Rel	Abs	
Ambraseys & Sarma (1967)				o			
Lee & Chan (1972)			+				
Seed *et al.* (1975)			+				
Trifunac & Westermo (1976)							+
Annaki & Lee (1977)			+				
Joannon *et al.* (1977)							+
Mortgat (1979)				+			
Vanmarcke & Lai (1980)	o						
Araya & Saragoni (1980)	o						
Amini & Trifunac (1981)							+ Δ
Bolt & Abrahamson (1982)				●			
Boore (1983)							+
Zahrah & Hall (1984)							Δ
Pauschke (1985)			o				
Saragoni (1985)	o						
ASTM (1985)		● o		● o		●	
Kawashima & Aizawa (1986)			+	+			
Sarma & Yang (1987)			o				
Jeong & Iwan (1988)				o			o
Joyner & Boore (1988)							+
Siddharthan and Norris (1990)						●	
Saragoni (1990)	o						
Gupta (1991)							+
Gupta (1994)							+
Manzocchi *et al.* (1994)				o			
Mander *et al.* (1995)						+	
Gupta & Trifunac (1996)							+
Şafak (1998)				●			
Basu & Gupta (1998)							+Δ
Calado *et al.* (1998)						●	
Lu *et al.* (1998)					●		
Sarma & Srbulov (1998)		+					
Gupta & Trifunac (1998a)							+
Gupta & Trifunac (1998b)	● o						● o
Schwarz (1998)			+				
Bursi & Caldara (2000)						●	
Perera *et al.* (2000)						●	
Taucer *et al.* (2000)						+	
Liu *et al.* (2001)			●				
Manfredi (2001)							Δ
Stewart *et al.* (2001)			●				
Calado *et al.* (2002)						●	
Erberik & Sucuoglu (2002)			o	o			
Tremblay & Bouatay (2002)						●	
Malhotra (2002)			+	+			Δ
Manfredi *et al.* (2002, 2003)							Δ
Osinov (2003)				+			
Teran-Gilmore *et al.* (2003)						●	
Kunnath & Chai (2004)							Δ
Green *et al.* (2004)							Δ
Green & Teri (2005)							
Green & Lee (2005)							Δ

●=including zero crossing peaks, o=excluding zero crossing peaks,
+= zero crossing counting method not specified, Δ=Structural method

2.4.8 Classification of cycle counting definitions

One of the most important distinctions amongst different definitions is if they are calculated using the absolute amplitude of the cycles or using levels relative to the cycle with the largest amplitude. The damage parameter given in Eq.(2.22) is typical of an absolute measure when S_{ref} is expressed as a fraction of the maximum cycle amplitude and the definition of number of effective cycles given in Eq.(2.33) is typical of a relative measure. Most definitions of the effective number of cycles used in earthquake engineering employ relative amplitude measures.

To illustrate the range of definitions employed in the technical literature a summary of different cycle counting definitions proposed by different authors is presented in Table 2.2. Beyond the broad generic categories, the main differences amongst the definitions are whether they use relative or absolute amplitudes and whether or not they count non-zero crossing peaks.

2.5 Correlations Between Duration and Number of Cycles

An extensive investigation into the correlation between different duration and number of effective cycles has been conducted by the author and co-workers. Due to space limitations the full results are not presented here and the interested reader is directed to Bommer *et al.* (2006) for a more in-depth discussion of the topic.

The differences between the number of effective cycles and different duration measures can be illustrated by comparing the ratios of the equation derived by Liu *et al.* (2001) to predict the relative number of effective cycles, N_{PR}, and the equations derived by Kawashima and Aizawa (1989) to predict relative, $D_{BR}(20\%)$, and absolute, $D_{BA}(0.05g)$, bracketed durations (Figure 2.26). The ratio of the two relative definitions shows a stable relationship between magnitude and distance. However, the ratio is consistently greater for sites with rock site classification, presumably due to the longer-period content of the motion at soil sites. The ratio of the relative and absolute measures shows essentially no dependence with site class but a strong dependence on magnitude and distance. The ratio increases rapidly with distance due to the increase of the number of cycles measured using a relative threshold and the rapid decay of the bracketed duration measured against an absolute acceleration

threshold. Both the ratio and the distance-dependence of the ratio decrease with increasing earthquake magnitude. All of these observations point to the influence of the frequency content of the motion, since motions with longer periods will have fewer cycles of motion for a given duration: the long-period content of the ground motion is greater for larger magnitude earthquakes and for softer sites, and due to the more rapid attenuation of high-frequency motion the long-period content also increases with distance.

Although the comparison from the ratios of the predictive equations, which estimate the median number of cycles and duration, produce physically meaning full trends they do not prove if it is possible to estimate the number of effective cycles from a measure of the ground-motion duration. To achieve this objective the number of effective cycles and duration of the ground-motion is calculated using a range of different definitions for the 655 accelerograms of the Abrahamson and Silva (1997) dataset. This shows that in general it is not possible to reliably predict the number of effective cycles of ground-motion from most definitions of strong ground-motion duration. However, there is one exception to this as the uniform duration, measured at a threshold of 0.1g, has a moderate correlation with the absolute numbers of cycles, $N_{RA}(2.0)$ (Figure 2.27).

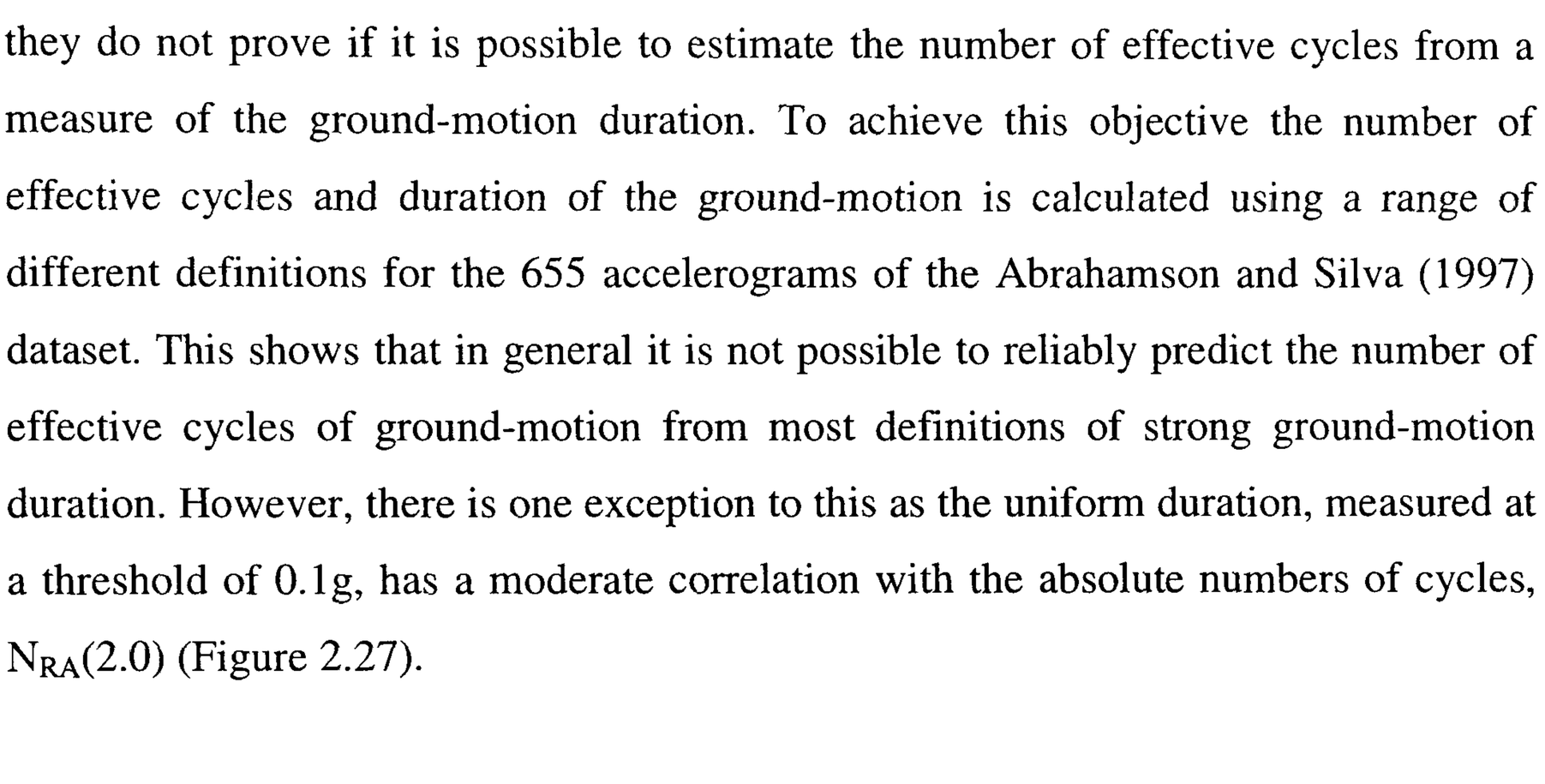


Figure 2.26. – Ratios of number of relative effective cycles, N_{PR}, predicted by Liu *et al.* (2001) to the absolute bracketed duration at 0.05g, $D_{BA}(0.05g)$, and relative bracketed duration at 20% PGA, $D_{BR}(20\%)$, predicted by Kawashima and Aizawa (1989).

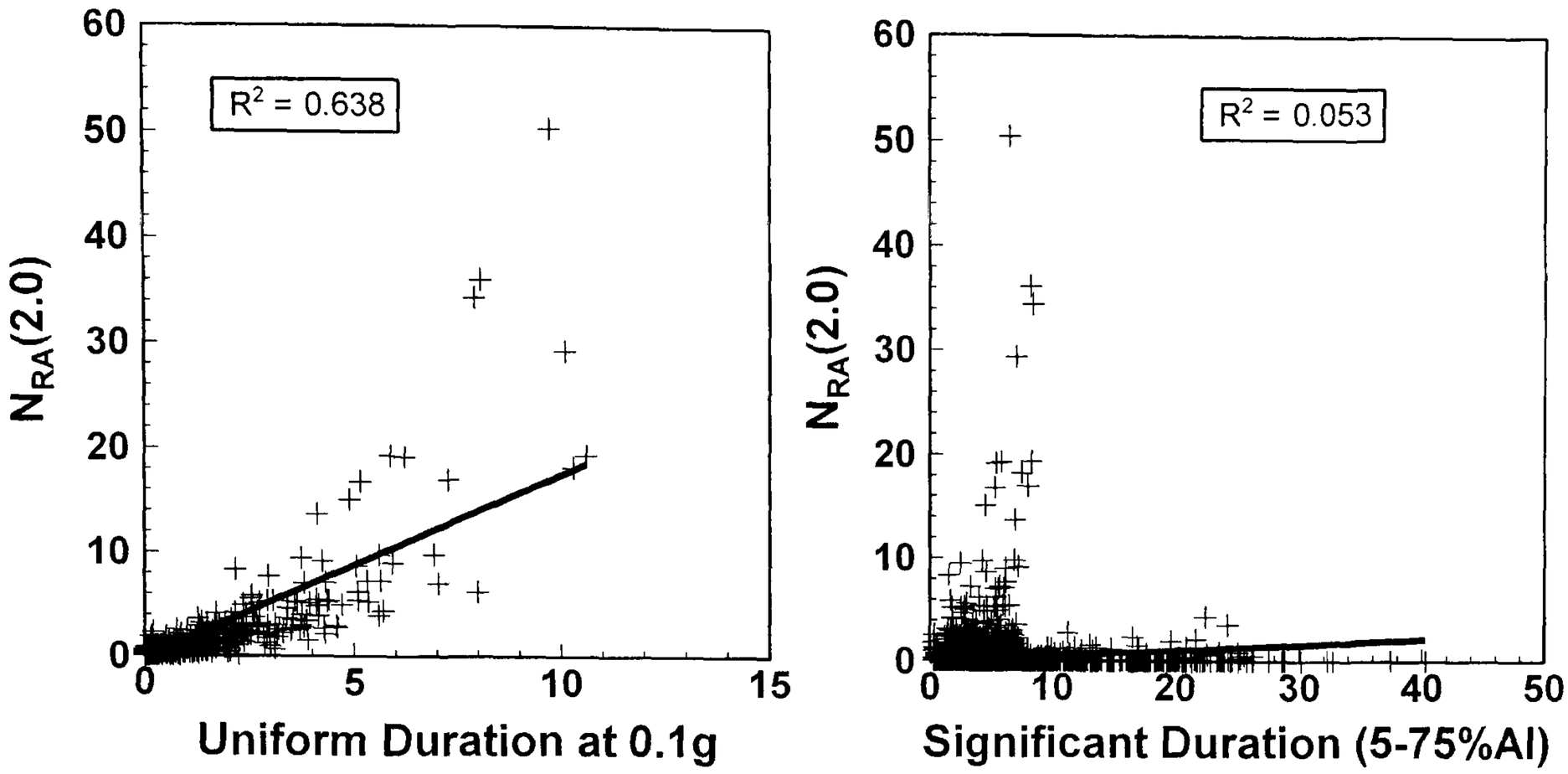


Figure 2.27. – Correlations between the absolute number of cycles defined using the rainflow counting method converted to an effective number of cycles using an exponent of 2.0, $N_{RA}(2.0)$, vs. uniform duration (*left*) and significant duration (*right*) for the 655 accelerograms from the Abrahamson and Silva (1997) dataset.

2.6 Summary

Accelerograms provide the principle source of information on the characteristics of earthquake ground motions. Although digital instruments are being slowly introduced, the majority of strong-motion accelerograms in use were recorded on analogue instruments. Inaccuracies in the processes used to digitise the accelerograms from these instruments makes it difficult to accurately determine the relative start time of the three axes and also to accurately measure the ground displacement time-series.

The elastic response spectrum is one of the more reliable measures of the peak amplitude of the ground motion as it is sensitive to the frequency content of the ground motion. As the response spectrum uses the peak response it does not encounter the difficulties with the non-stationary character of the motion which are associated with the Fourier amplitude spectra.

There are many different definitions of ground-motion duration and number of effective cycles in the technical literature. One of the most important differences between the definitions is if they are measured relative to an absolute or relative threshold. In general definitions of the strong-motion duration cannot be used to

estimate the number of effective cycles, although a fair correlation does exist between the uniform duration at 0.1g and absolute measures of the number of effective cycles of the ground motion.

3. REVIEW OF THE INFLUENCE OF DURATION ON STRUCTURAL DAMAGE

There are several hundred papers in the literature that link structural damage to parameters related either directly or indirectly to the duration of strong ground motion. The conclusions of these studies differ widely with regard to the influence of strong-motion duration on structural demand, ranging from null to significant. This chapter provides a summary and critical review of the literature on this subject, classifying the studies in terms of the structural models employed, the definition of duration used, other strong-motion parameters considered and the measure of structural damage. A considerably abridged description of this work is provided in Hancock and Bommer (2006a).

3.1 Introduction

The specification of earthquake actions in current seismic design codes is predominantly independent of strong-motion duration. However, duration is explicitly taken into account in the HAZUS methodology for earthquake loss estimation (FEMA 1999, 2003; Kircher *et al.* 1997; Whitman *et al.* 1997). In HAZUS large magnitude earthquakes have an increased demand spectrum because the longer duration of these events is expected to cause greater strength and stiffness degradation.

There are also many studies reporting correlations between structural damage and parameters related either directly or indirectly to strong ground-motion duration. For example Fajfar and co-workers (e.g. Chai and Fajfar 2000) suggest that longer duration ground motion should increase inelastic design base shear, while Shome *et al.* (1998) find that provided ground motions are scaled to the same elastic spectral acceleration, the ground-motion duration does not have a significant influence on maximum inelastic displacements. The latter study supports the policy in current codes to neglect duration, whereas the conclusions of the former study would suggest that duration should be incorporated into the specification of seismic design loads. This is clearly an issue on which the jury is still out, but the situation can be clarified by identifying common features amongst studies either supporting or denying an appreciable influence of duration on inelastic demand.

Structures fail under seismic loading because of the combination of extreme displacement with repeated number of loading cycles. This can be illustrated by considering the ways in which a steel moment resisting frame can fail:

1. Extreme storey displacement can lead to the formation of plastic hinges, buckling of critical elements and structural collapse. (e.g. Anastasiadis *et al.* 2000)
2. Repeated cyclic loading causes the initiation of a fracture, typically in the joints of the frame, which grow with each load cycle causing member failure and potentially structural collapse (e.g. Taucer *et al.* 2000; Tremblay *et al.* 1996; Chai *et al.* 1995; De Matteis *et al.* 2000).
3. Interaction of the above, for example cyclic loading and fatigue of welds in built up column sections, followed by a storey displacement capable of buckling the weakened columns, causing structural collapse (e.g. Osteraas and Krawinkler 1989; Bruneau *et al.* 1996).

This example also highlights the importance of the damage metric used. If maximum storey displacement is measured then failure mode 1 will be adequately considered but failure modes 2 and 3 will not be properly represented. Measures of cumulative damage or energy have been proposed by many authors to enable all potential failure modes to be considered.

At least part of the reason that studies have differing conclusions on the importance of strong ground-motion duration is the use of different structural models and damage indices. Obviously, structures exhibiting degradation of strength and/or stiffness under cyclic loading will be more sensitive to the number of cycles of motion and hence the duration of shaking. In addition to this there is no consistent measure of strong ground-motion duration with over 30 different definitions in the technical literature (Bommer and Martínez-Pereira 1999, 2000). Cumulative damage and energy functions are dependent on the amplitude of the ground motion as well as the duration, so the specific influence of duration cannot be easily decoupled.

The following two subsections review inferences made regarding the influence of duration on damage from field studies of earthquakes and from experimental

investigations. Subsections 3.4 to 3.6 review studies based on theoretical models of structural response grouped on the basis of the damage metric employed. The chapter ends with conclusions regarding what appears to be well established with respect to the influence of duration and what remains to be resolved by further studies.

3.2 Field Evidence

Several authors note differences between the damage caused by longer duration subduction events than crustal earthquakes. Bommer *et al.* (1997) and Iyama and Kuwamura (1999) observe greater damage from the rapid release of energy of shorter crustal events. However, Tremblay (1998) suggests that the greater numbers of strong cycles from subduction events are more damaging. These observations are compatible as the greater number of cycles observed by Tremblay lead to an increased energy input and hence greater damage, while the studies of Bommer *et al.* and Iyama and Kuwamura compare events with equal total energy.

Failure of the joints of steel moment resisting frames has been observed after the Northridge and Kobe earthquakes (e.g. Tremblay *et al.* 1995, 1996). Some of the failures are from the fracture of joints with poorly detailed partial penetration welds; these may have failed after a single loading pulse, so failure could be independent of the earthquake duration. However better detailed joints with full penetration welds also failed. The cracks in these joints usually originate in the weld or heat affected zone then propagate into the flanges and web of the joint. This failure mechanism is associated with low-cycle fatigue where cracks propagate under repeated loading cycles, and hence the duration of the loading is of critical importance. More conclusive evidence of this failure type has been found through experimental testing, which is detailed in the next section.

3.3 Experimental Results

Table 3.1 contains a summary of papers reporting the results of experimental testing. Each of the studies is given a rating that indicates whether duration or the number of load cycles was found to be of importance. A study with an importance rating of 10 would imply that duration or the number of cycles was found to be of critical

significance, while a rating of 0 shows that duration was found to have no significance. The rating scheme is of course subjective, however it enables general conclusions to be drawn on the relative importance of duration in each study and provides an indication of the factors that influence the importance of duration.

Table 3.1. - Summary of the Relevance of Load Duration/Number of Cycles from Experimental Testing

Study	Structural Model	Duration Related Measure	Other Input Parameters	Importance Rating*
Calado *et al.* [1998 & 2002]	Steel Frame	Num. of stress cycles	Cycle amplitude	9
Dutta & Mander [2001]	R.C. Columns	Num. of disp. cycles	Plastic Curvature	9
Matteis *et al.* [2000]	Steel Frame	Num. of disp cycles	Cycle amplitude	9
Castiglioni *et al.* [2000]	Steel Frame	Num. of stress cycles	Cycle amplitude	9
El-Bahy *et al.* [1999a & b]	R.C. Columns	Num. of disp. cycles	Lateral drift	9
Plumier *et al.* [1998]	Steel frame	Num. of Eq. stress cycles	Cycle amplitude	9
Bernuzzi *et al.* [1997]	Steel joints	Cyclic disp. and energy	Plastic rotation	9
Manfredi & Pecce [1997]	R.C. beams	Num. of disp. cycles	Cycle amplitude	9
Mander & Dutta [1996 & 1997]	R.C. Columns	Num. of disp. cycles	Plastic Curvature	9
Ballio & Castiglioni [1995]	Steel beams	Num. of disp. cycles	Cycle amplitude	9
Mander *et al.* [1994a & 1995]	Steel joints	Cyclic disp. and energy	Plastic rotation	9
Mander *et al.* [1994b]	Steel Reinforcing bars	Num. of disp. cycles	Cycle amplitude	9
Yamada [1992]	Various Steel and R.C. beams	Num. cycles to failure	Cycle amplitude	9
Yamada *et al.* [1988a]	Various Steel and R.C. beams	Num. cycles to failure	Cycle amplitude	9
Yamada *et al.* [1977]	Braced Steel Frames	Num. cycles to failure	Cycle amplitude	9
Krawinkler [1987]	Steel joints	Num. cycles to failure	Plastic strain range	9
Krawinkler & Zohrei [1983]	Steel joints	Num. cycles to failure	Plastic strain range	9
Yamada [1969]	Various Steel and R.C. beams	Num. cycles to failure	Cycle amplitude	9
Calado [2003]	Steel cantilever	Num. displacement cycles	Cycle amplitude	8
Schreiber *et al.* [2002]	R.C. beams	Acc. hyst enrg	Cycle amplitude	8
Chai *et al.* [1995]	Steel cantilever	Acc. hyst enrg	Max drift	7
Park *et al.* [1987]	Steel and R.C.	Acc. hyst enrg	Max deformation	6
Park & Ang [1985]	R.C. members	Acc. hyst enrg	Max deformation	6
Park *et al.* [1985]	R.C. buildings	Acc. hyst enrg	Max deformation	6
Sorace [1998]	Steel frame	Acc. hyst enrg	Max deformation	6
Taucer *et al.* [2000]	Steel Frame	Num. disp. cycles	Cycle amplitude	6
Hsu & Liang [2003]	R.C. columns	Num. cycles	Applied load	6
Matsumoto *et al.* [2000]	Steel Joints	Cumulative deformation	Cycle amplitude	5

*10 implies duration/number of cycles are of critical significance, 5 represents marginal or unproved significance, 0 shows that duration was found to have no significance. Disp = displacement, hyst. = hysteretic, enrg. = energy, Eq. = equivalent.

A considerable amount of experimental testing has been conducted following the failure of the joints of many steel frame buildings during the Northridge and Kobe earthquakes (e.g. Mander *et al.* 1994a, 1995; Chai *et al.* 1995; Plumier *et al.* 1998; Abed *et al.* 1998; Calado *et al.* 1998, 2002; Matteis *et al.* 2000; Taucer *et al.* 2000; Matsumoto *et al. 2000*; Castiglioni *et al.* 2000). Although the test set-up, specimen configuration and post-test analysis of each study are different, the principle findings of Mander *et al.* (1994a, 1995) are typical and are supported by the results of the other authors. Mander and co-workers conducted tests on top-and-seat angle connections under constant and variable amplitude cyclic loading. Mander *et al.* (1995) found that failure could be predicted using a linear damage accumulation model, similar to that proposed by Miner (1945) for high cycle fatigue of metals. The importance of the number of loading cycles, and hence ground-motion duration, in the prediction of failure is also evident. For example, if an earthquake causes one plastic joint rotation cycle of 1.5 degrees (2.62×10^{-2} radians) only 10% of the damage required to cause failure would have been caused, but if the event is of longer duration and causes 10 cycles at this amplitude the joint is likely to fail.

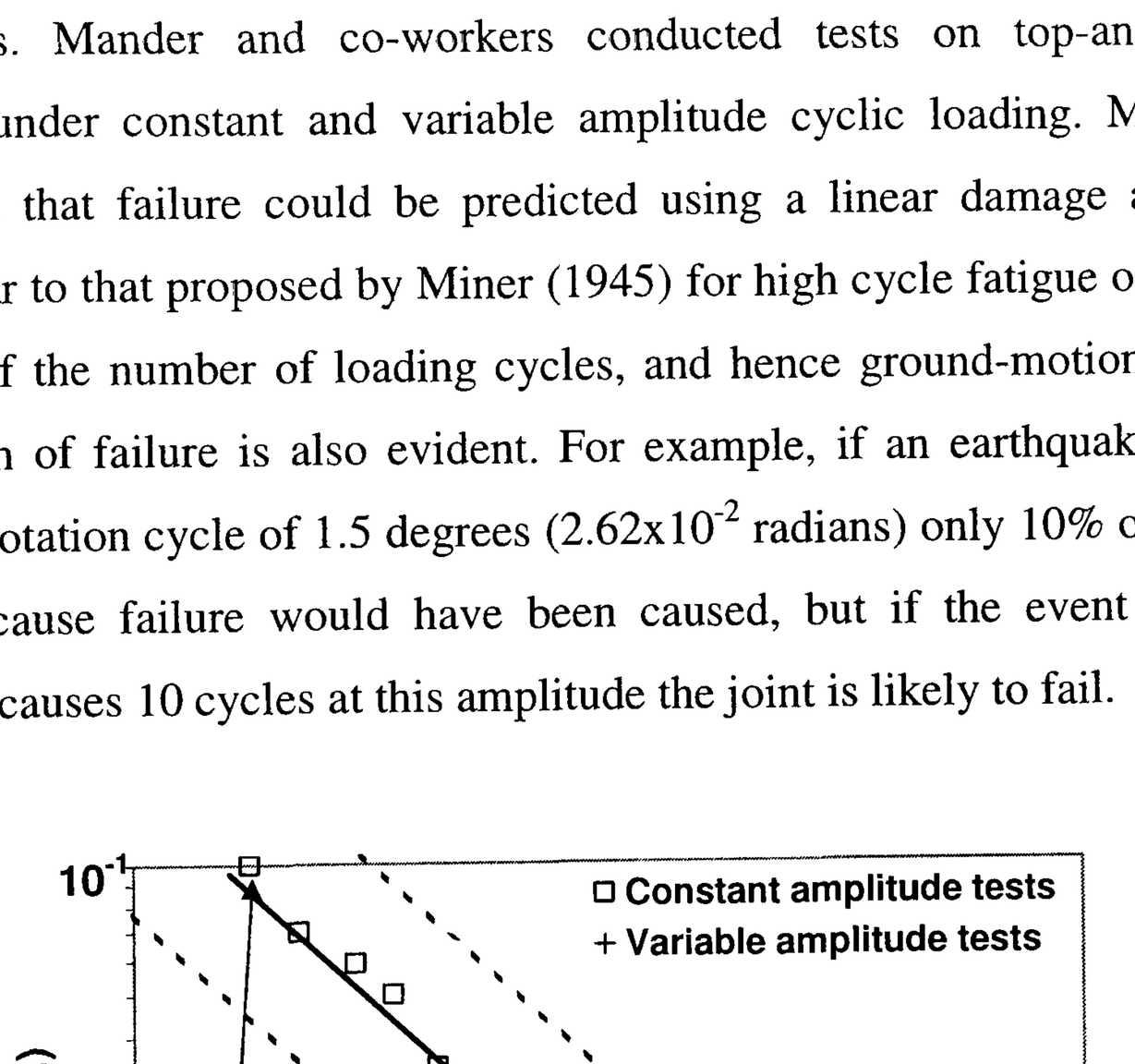


Figure 3.1. - Plastic rotation vs fatigue life of top-and-seat angle connection (Mander *et al. 1995*)

Linear cumulative damage models, like the one described above, are only one of several methods used to predict damage to structures. Another widely used model, which has also been derived from the results of experimental testing, is that proposed by Park and Ang (1985) and Park *et al.* (1985, 1987, 1988). This model has been applied to steel elements, but was originally designed to estimate the damage of reinforced concrete beams and columns. The damage of individual elements is estimated from the combination of both the maximum deformation and accumulated hysteretic energy, which is dependent on the ground-motion duration:

$$D_{pa} = \frac{\delta_M}{\delta_u} + \frac{\beta}{Q_y \delta_u} \int de \tag{3.1}$$

where D_{pa} is the damage index equalling 1 at collapse and 0 in the undamaged state, δ_M the maximum response deformation, δ_u the ultimate deformation capacity under static loading, Q_y the calculated yield strength, $\int de$ the accumulated incremental absorbed hysteretic energy (excluding potential energy). The β coefficient is a measure of the importance of the duration-dependent hysteretic energy term to damage. Structural elements with ductile or strength degrading characteristics have higher β factors, implying that the ground motion duration has greater importance. Chai *et al.* (1995) have shown that the Park and Ang damage index is also applicable to steel structures and also proposed that the damage index should be modified $\left(D^*_{pa}\right)$ so that the absorbed energy to monotonic failure $\left(\int dem\right)$ is not double counted in the damage measure:

$$D^*_{pa} = \frac{\delta_M}{\delta_u} + \frac{\beta^*}{Q_y \delta_u}\left(\int de - \int dem\right) \tag{3.2}$$

The main aim of this proposal is to provide a better definition of β, which is now designated β^*. One of the main issues with the Park and Ang damage model is the selection of the β coefficient. Park *et al.* (1987) suggest values of 0.05 for reinforced

concrete and 0.025 for steel, whilst Cosenza and Manfredi (1998) give values ranging from -0.3 to 1.2 with a median value of 0.15. Median β factors of 0.147 and 0.032 were found by Sorace (1998) to have the best fit for test results of braced and unbraced steel frames respectively. This suggests that the β factor, and hence the influence of strong-motion duration, is dependent on the type of structural system; elements in more redundant systems are less sensitive to extreme displacement, more sensitive to accumulated hysteretic energy and hence more sensitive to the duration of strong ground-motion. Obtaining an appropriate value of the β factor is critical: Cosenza and Manfredi (2000) suggest that the index is equivalent to energy methods with $\beta = 0.6$ to 0.8, while values of 0.05 to 0.1 mean that energy dissipation has little influence on the results.

3.4 Studies Measuring Drift or Displacement

Many studies measure parameters related to the drift or displacement. These can be subdivided into two subsets, those that use only the maximum response peak, and those that use cumulative measures.

3.4.1 Studies measuring maximum drift or displacement

Studies measuring maximum drift or displacement generally find that there is no correlation with the strong ground-motion duration (e.g. Bazzurro and Cornell 1992, 1994a, b; Rahnama and Manuel 1996; Shome *et al. 1998*). The exception to this is for studies using strength or stiffness-degrading models (e.g. Gupta *et al.,* 2001; Eibl *et al.* 1996). Table 3.2 summarises the results of studies measuring maximum response. The results of each study using maximum drift or displacement are given a rating that indicates whether duration or the number of load cycles was found to be of importance.

The studies of Bazzurro and Cornell (1992, 1994a, b) consider heavily braced steel jacket offshore platforms. Although these structures are constructed of bracing elements with degrading characteristics, they have a globally increasing post-yield stiffness at the displacement levels considered. These studies suggest that any recorded ground motion, of any duration, can be used provided it is scaled to the

target elastic spectral acceleration. This study does not check accumulated fatigue damage, which is undisputedly related to the number of load cycles and often a critical design case for this type of structure (e.g. Barltrop and Adams 1991). Tremblay (2003) conducted a study of multi-storey braced steel frames, using typical levels of bracing, and found that the selection and scaling of ground motions is important. Records containing strong pulses of motion are particularly destructive for the lower floors of the building, and those with long duration give greater probability of failure because of excessive storey drift, which accumulates in one direction due to the influence of gravity loads.

Table 3.2. - Summary of the Relevance of Load Duration/Number of Cycles for Studies Measuring Extreme Drift or Displacement

Study	Structural Model	Duration Related Measure	Other Input Parameters	Importance Rating*
Jennings & Husid [1968]	Elasto-Plastic inc. G.	Dur of sim strg motion	Syn. accelerograms	8
Eibl et al. [1996]	Degrading masonry	Bracketed duration	Accel. time-series	8
Mahin [1980]	Bi-linear softng. SDOF	Inc aftershocks	Syn. accelerograms	8
Aschheim & Black [1999]	Bi-linear softng. SDOF	Inc foreshocks	-	8
Tremblay [2003]	Braced Steel Frame	Different ground motions	Spectral acceleration	7
Gupta et al. [2001]	Stren and stiff deg.	Inc aftershocks	Accel. time-series	6
Bonelli, P. [1998a & b]	Bi-linear R.C. model	-	Long duration pulse	3
Iervolino *et al.* [2005]	12 Non-linear SDOF	Significant dur. (5-95%)	Accel. time-series	0
Cosenza *et al.* [2004]	Inelastic SDOF	Significant dur. (5-95%)	SA	0
Aschheim & Black [1999]	Bi-linear hardng SDOF	Inc foreshocks	-	0
Shome et al. [1998]	Moment resist. Frame	Equk mag	Spectral acceleration	0
Cornell [1997]	Non-linear SDOF	Equk mag	Accel. time-series	0
Rahnama & Manuel [1996]	Elasto-plastic	Significant dur. (5-95%)	Sim. and rec. grnd-mtn	0
Bazzurro & Cornell [1992]	Inelastic model	Equk mag	Spectral acceleration	0
Araya & Saragoni[1980]	Elasto-plastic	Dur of sim strg motion	Long duration pulse	0
Saragoni[1985]	Elasto-plastic	Dur of sim strg motion	Long duration pulse	0
Bertero et al. [1978]	Elasto-plastic	-	Long duration pulse	0

*10 implies duration/number of cycles are of critical significance, 5 represents marginal or unproved significance, 0 shows that duration was found to have no significance: Note that rating applies only to results from each study measuring extreme drift or displacement. Sim = simulated, syn = synthetic, inc. G. = includes gravity

The de-stabilising action of gravity loads at increased displacements of unbraced structures represented by elastoplastic SDOF systems with different post-yield stiffness is modelled by Mahin (1980) and Jennings and Husid (1968). These

researchers find that aftershocks and longer duration ground motion significantly increase ductility demand and likely failure. Aschheim and Black (1999) also find that structures with negative post-yield stiffness are susceptible to aftershocks. However, these researchers suggest that only models with positive post-yield stiffness are representative of properly designed structures and the maximum drift of these types of structures is not sensitive to the duration of the ground motion.

It is widely reported that the maximum storey displacements are related to the duration of individual acceleration pulses, rather than total duration of strong shaking (Bertero *et al.* 1978; Naeim 1995; Bonelli 1998a, 1998b; Araya and Saragoni 1980; Saragoni 1985). Acceleration pulses with long duration can be caused by a range of different phenomena including fling, forward directivity and constructive interference of reflected waves. Fling is only observed at sites close to the fault rupture and is caused by a displacement pulse created by the permanent deformation along the fault. Forward-directivity is also a near-field effect and is the result of the propagation of the fault rupture towards the site, which causes constructive interference of the seismic radiation leading to concentrated pulse or pulses of motion. The dominant period, or duration, of these pulses increases with earthquake magnitude (Trifunac and Novikova 1995; Somerville *et al.* 1997; Somerville, 2000; Bommer *et al.*, 2001). Pulses can also be caused at greater distances by the constructive interference of surface waves reflected from horizontal sediment layers, although these typically have lower energy content than the near-field pulses (e.g. Yamada *et al.* 1988b).

3.4.2 Studies using cumulative measures

Cumulative damage functions using variations of Miner's linear damage accumulation (Miner 1945) are commonly used for the assessment of low-cycle fatigue problems. Section 2.4.6 describes this type of damage model and section 3.3 also shows that experimental test results confirm the applicability of the model. This section reviews theoretical studies using cumulative damage models. Each study is summarized in Table 3.3, together with a rating indicating whether duration or the number of load cycles was found to be of importance.

Chung *et al.* (1988, 1989) develop one of the most comprehensive cumulative damage functions (D_e). This enables the incorporation of differences in loading direction and stiffness degradation in the structure:

$$D_e = \sum_i \left(\alpha_i^+ \frac{n_i^+}{N_i^+} + \alpha_i^- \frac{n_i^-}{N_i^-} \right) \tag{3.3}$$

where i is the indication of displacement or curvature level, N_i is the number of cycles to cause failure at curvature level i, n_i is the number of cycles actually applied at curvature level i, α_i is the damage modifier used to capture the loading history effect, and + and – are indicators of loading sense. The load history level is captured by α_i which is defined, for positive loading, as:

$$\alpha_i^+ = \frac{\sum_{j=1}^{n_i^+} k_{ij}^+}{n_i^+ \bar{k}_i^+} \cdot \frac{\phi_i^+ + \phi_{i-1}^+}{2\phi_i^+} \tag{3.4}$$

where k_{ij}^+ is the stiffness $\left(\frac{M_{ij}^+}{\phi_i^+} \right)$ during the j^{th} cycle up to load level i, $\bar{k}_i^+$ is the average stiffness during N_i cycles up to load level i.

The factor $\frac{\phi_i^+ + \phi_{i-1}^+}{2\phi_i^+}$ is used to normalise damage increments in the case of changing load amplitudes. M_{ij} and ϕ_i are the moment and curvature reached after j cycles of loading respectively. The damage modifier for negative loading a_i^- is essentially the same as the modifier for positive loading a_i^+, except negative moments and curvatures are used. The main issue with this damage measure is its complexity, which requires the user to know the moment and curvature time histories and the number of cycles to failure for each load level. In addition the damage measure is formulated assuming the absorbed hysteretic energy of the section is a better indicator of damage than the number and amplitude of the material strains, an assumption that has not been rigorously confirmed by experimental evidence.

Cosenza *et al.* (1990, 1993) review the use of damage functions using linear cumulative damage and energy measures. They measure the inelastic response of an

elastoplastic model to recorded ground motions and find that the scatter in the damage predictions from different types of cumulative damage model is lower than those of different types of energy model, including the damage parameter proposed by Park and Ang (1985).

Table 3.3. - Summary of the Relevance of Load Duration/Number of Cycles for Studies Using Cumulative Measures

Study	Structural Model	Duration Related Measure	Other Input Parameters	Importance Rating*
Tang & Yao [1972]	Elasto-plastic	Acc. plastic strain	Stochastic grd-mtn.	9
Stephens & Yao [1986]	R.C. Frame	Num. of cycles	Plastic Strain	8
Jeong & Iwan [1988]	Softening SDOF	Num. of cycles	Gaussian process	8
Chung *et al.* [1989 & 1988]	Stren. and stiff. deg RC	Num. B.M. cycles	-	8
Cosenza & Manfredi [1997]	Elasto-plastic	AI, Num. plastic cycles	Cycle amplitude	8
Heredia-Zavoni *et al.* [2000]	Bi-linear	Num. inelastic cycles	Disp. amplitude	8
Malhotra [2002]	Elastic SDOF	Num. of cycles	PGA,PGV, PGD	8
Kunnath & Chai [2004]	Inelastic SDOF	Num. of cycles	PGA, PGV	8
Chai [2005]	Inelastic SDOF	Num. of cycles	PGA, PGV	8
Cosenza *et al.* [1990]	Elasto-plastic	Cumulative disp.	Dissipated energy	7
Manzocchi *et al.* [1994]	Hysteretic SDOF	Num. of cycles	Load amplitude	7
Cosenza *et al.* [2004]	Inelastic SDOF	Equivalent Num cycles	SA	7
Basu & Gupta [1998]	Bi-linear SDOF	Num. of cycles	PGA	6
Calado *et al.*[1995 & 1998]	Steel Frame	Num. of cycles	Effective stress range	6
Perera *et al.* [2000]	Elasto-plastic	Num. of cycles	Joint rotation	6
Cornell [1997]	Non-linear SDOF	Equk mag	Rec. ground motions	0

*10 implies duration/number of cycles are of critical significance, 5 represents marginal or unproved significance, 0 shows that duration was found to have no significance B.M. = bending moment, stren. = strength, stiff = stiffness, disp. = displacement, AI = Arias intensity (Arias 1970).

Tang and Yao (1972) and Jeong and Iwan (1988) model non-stationary earthquake action by adding an envelope function to a stationary stochastic process. They use a low-cycle fatigue damage accumulation function to assess the accumulated damage. Tang and Yao show that greater damage is caused for long-duration ground motions. Jeong and Iwan use different structural constants to model the different behaviour of concrete structures compared to steel and their results indicate that reinforced concrete structures are more sensitive to earthquake duration than steel structures.

Calado *et al.* (1995) and Castiglioni and Calado (1996) use cumulative damage functions to define the behaviour factors for steel frames. Although their test results show that different duration ground motions produce different behaviour factors, the limited data, which only uses ground motions with 15 and 25 seconds total duration, does not enable this difference to be explored.

Heredia-Zavoni *et al.* (2000) use a cumulative damage function with Bayesian analysis to predict expected damage levels after earthquake ground motion. The authors suggest that this method can aid decision-making on the maintenance of structures as the expected cost of maintenance can be determined for different thresholds of planned damage repair. The amplitude and duration of the ground motion is of critical importance to the method as it controls the number and amplitude of the displacement cycles of the structure, which is used to determine the damage level.

Kunnath and Chai (2004) and Chai (2005) combine low-cycle fatigue and spectral energy concepts to derive inelastic demand spectra which depend on the duration of the ground motion. A more comprehensive description of the techniques used by Chai and co-workers to derive demand spectra by balancing the input ground motion energy with the energy dissipated by the structure is given in Section 3.6.

3.5 Studies Using Energy Measures

Housner (1956) was one of the first authors to suggest that structures should be designed so that they have sufficient energy absorbing capability to be able to resist the energy demands exerted by the ground motion. Housner (1965) also suggested that two ground motions with the same spectral intensity might have markedly different damage effects if the duration of one is much greater than the other. Many studies have used energy principles since Housner's original proposal; some of these are summarized in (Table 3.4). The results of each study are given a rating that indicates if duration or the number of load cycles were found to be of importance.

Uang and Bertero (1988, 1990) conduct an extensive investigation into the energy demand of structures under the action of earthquakes. They show that the energy demands from the ground motion are dissipated by the structure in the form of kinetic, damping, recoverable elastic strain and irrecoverable hysteretic energy. The relationship between input energy and equivalent velocity is related to the duration of the strong ground-motion by:

$$\frac{V_i^{\max}(\mu=5,\xi=5\%)}{v_{g(\max)}} = 1.0 + 0.12 * D_{SR,5-95} \tag{3.5}$$

where v_g is the ground velocity, $V_i^{\max}$ is the maximum equivalent velocity for ductility ratio μ and viscous damping ratio ξ and $D_{SR,5-95}$ is the duration between 5 and 95% Arias intensity levels as proposed by Trifunac and Brady (1975). This conclusion is supported by the findings of Shome *et al.* (1998) and Rahnama and Manuel, (1996) who show that input energy demand and hysteretic energy are correlated with ground-motion duration.

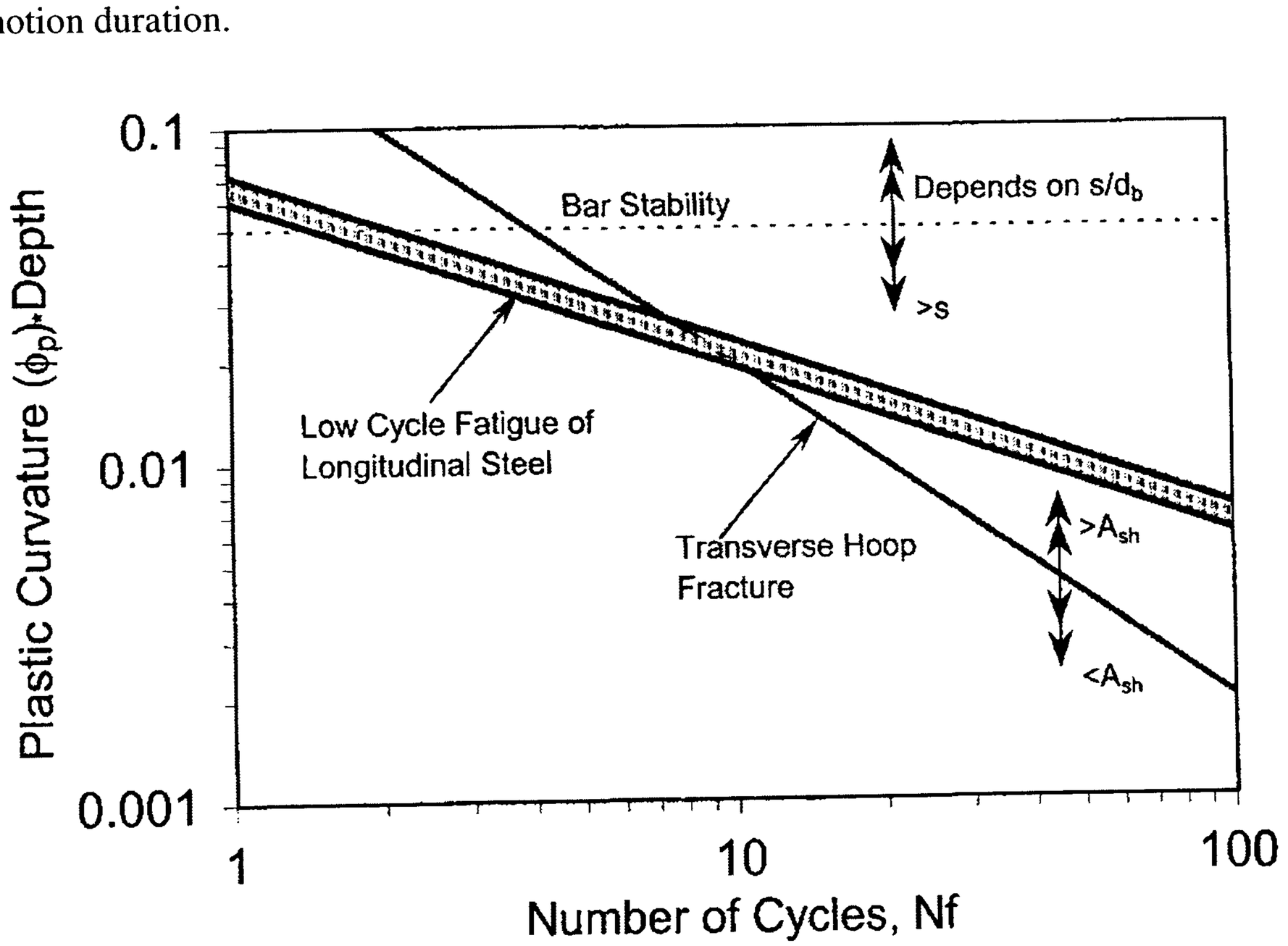


Figure 3.2. - Fatigue plots of confined concrete (Dutta and Mander 2001).

Mander and Dutta (1996, 1997) and Dutta and Mander (2001) propose an energy-based design methodology for reinforced concrete columns. The principle of the methodology is to provide enough reinforcement such that the section has greater energy absorption capacity than the external work applied to it by the cyclic loads. The volume of hoop or lateral reinforcement is detailed such that failure always occurs from low-cycle fatigue of the longitudinal reinforcement (Figure 3.2).

One of the issues debated at the 1997 NCEER workshop on the national representation of seismic ground motion for new and existing highway facilities was "should energy or duration be used in a design procedure" (Friedland *et al.* 1997). At the conference Cornell (1997) presented results suggesting that many structural demand parameters including displacement ductility have little dependence on the duration of the ground motion. Cornell did find a link between duration and the absorbed hysteretic energy, which at the same conference Krawinkler (1997) argued should be used to describe seismic demands. However, Krawinkler (1997) was not able to find a definition of duration that consistently had a good correlation with hysteretic energy for structures with different periods or strengths. The conference participants concluded that although some measure of energy of the ground motions is important to the response of a bridge, at the time of the conference there was not an accepted design procedure available that accounted for energy (Friedland *et al.* 1997).

Rodriguez (1994) also investigates the number of effective cycles of the ground motion and uses this with the roof drift to create a measure of damage capacity I_d:

$$I_d = n_{eq}\left(\frac{D_{rm}}{D_{rd}}\right)^2 \tag{3.6}$$

where n_{eq} is the number of equivalent cycles, D_{rm} is the maximum measured roof drift and D_{rd} is the maximum allowable roof displacement. This mix of energy and maximum displacement is similar to the damage parameter proposed by Park and Ang, which is discussed in section 3.3.

Table 3.4. - Summary of the Relevance of Load Duration/Number of Cycles for Studies Using Energy Measures

Study	Structural Model	Duration Related Measure	Other Input Parameters	Rating*
Mander & Dutta [1996 & 1997]	R.C. Columns	Energy applied	Plastic Curvature	9
Dutta & Mander [2001]	R.C. Columns	Energy applied	Plastic Curvature	9
Iervolino *et al.* [2005]	12 Non-linear SDOF	Significant dur. (5-95%)	Accel. time-series	8
Meskouris [1983]	ElPlast.	Significant dur. (5-95%)	Spectral acceleration	8
Manfredi [2001]	ElPlast.	No. cycles	PGA, PGV, SA	8
Uang & Bertero [1988]	ElPlast. SDOF	Significant dur. (5-95%)	Equiv. velocity amp. fctr	8
Cornell [1997]	Non-linear SDOF	Equk mag	Accel. time-series	8
Uang & Bertero [1990]	ElPlast. SDOF	Significant dur. (5-95%)	Equiv. velocity amp. fctr	8
Shome *et al.* [1998]	Moment resist. Frame	Earthquake magnitude	Spectral acceleration	8
Reinoso *et al.* [2000]	ElPlast.	Significant dur.(2.5-97.5%)	Dominant soil period	8
Rahnama & Manuel [1996]	ElPlast.	Significant dur. (5-95%)	Sim. and rec. grnd-mtn.	8
Penazzo [2001]	Stren. and stiff. deg	Several dur. definitions	SA	8
Xie & Zhang [1988]	Stren. and stiff. deg	Bracketed dur.	Grnd accel.	8
Manfredi *et al.* [2003]	ElPlast.	Number of cycles	PGA, PGV, AI	8
Zahrah & Hall [1984]	ElPlast.	No. equiv. cycles	Energy absorbed	7
Naeim *et al.* [1994]	ElPlast.	Bracketed (0.05g)	PGA and PGV.	7
Rodriguez [1994]	ElPast and stiff. deg	No. equiv. cycles	Roof drift	7
Cosenza *et al.* [1990]	ElPlast.	Disp. energy	Max. disp.	7
Sucuoglu & Nurtug [1995]	ElPlast.	Significant dur (5-95%)	Energy disp.	7
Erberik & Sucuoglu [2002]	Exp. Mod, R.C.	Half cycle number	Energy disp.	7
Mork [1994]	Stren. and stiff. deg R.C.	Motion duration (UnKwn)	PGA	7
Fajfar *et al.* [1990]	Stren. and stiff. deg	Significant dur. (5-95%)	PGA, PGV and PGD	7
Chai & Fajfar [2000]	ElPlast.	Significant dur. (5-95%)	PGA and PGV	7
Fajfar & Vidic [1994]	Bi-linear and stiff. deg	AI	PGA and PGV	7
Vidic *et al.* [1994]	Bi-linear and stiff. deg	AI	PGA and PGV	7
Fajfar *et al.* [1989];	Bi-linear	Significant dur. (5-95%)	PGA and PGV	7
Fajfar & Fischinger [1990a,b]	Bi-linear	Significant dur. (5-95%)	PGA and PGV	7
Chai *et al.* [1998]	Bi-linear SDOF	Significant dur. (5-95%)	PGA and PGV	7
Park *et al.* [1988]	Stren and stiff. deg R.C.	Acc. hysteretic energy	Max. deformation	6
Krawinkler [1997]	Bi-linear SDOF	Undefined duration	Accel. time-series	5
Elenas [2000]	Stren and stiff. deg R.C.	Significant dur. (5-95%)	PGA, SA, AI	2
Elenas & Meskouris [2001]	Stren and stiff. deg R.C.	Significant dur. (5-95%)	PGA, SA, AI	2

*10 implies duration/number of cycles are of critical significance, 5 represents marginal or unproved significance, 0 shows that duration was found to have no significance. UnKwn= Exact definition unknown, fctr=factor, disp=dissipated, ElPlast. = Elasto-plastic.

Elenas (2000) and Elenas and Meskouris (2001) investigate correlations between a range of structural damage indicators and ground-motion parameters. They find that ground-motion duration measures are less well correlated to damage than amplitude measures, such as spectral acceleration. It is worth noting that a direct correlation between damage and duration would not be expected, as the duration does not measure the amplitude of the motion, which is of critical importance to the damage level.

3.6 Studies Using Spectral Response

Duration-dependent response spectra are normally constructed to determine *inelastic* response by applying duration-dependent reduction factors to either idealised elastic response spectra of the Newmark and Hall type (Newmark and Hall 1987), or elastic spectra calculated from a specific accelerogram. Other studies, however, have developed *elastic* response spectra that show the amplitudes of vibration sustained for a given number of cycles (e.g. Perez 1980; Amini and Trifunac 1981; Kawashima and Aizawa 1986; Gupta 1991; Gupta 1994; Schwarz 1998; Malhotra, 2002). Table 3.5 summarises different studies presenting duration-dependent response spectra. A rating is also given to each study indicating the criticality of ground-motion duration or number of load cycles.

Peng *et al.* (1988, 1989) propose a stochastic procedure for the analysis of inelastic SDOF systems. They use the power spectral density of recorded accelerograms and extreme value theory to obtain the distribution of inelastic drift, with total drift being the algebraic summation of previous individual drift displacements. The assumptions made in the development of the stochastic procedure are such that only the duration, which controls the number of drifts, has pronounced effect on the inelastic de-amplification. However, studies by other authors (e.g. Bazzurro and Cornell 1992; Rahnama and Manuel 1996; Shome *et al.* 1998), using recorded ground motions, find that the inelastic de-amplification is not well correlated to the ground-motion duration. This suggests the stochastic simulation used in this study may not be a good representation of actual ground motions.

Many authors have proposed damage parameters based on the duration or number of cycles of spectral response, although this is not without contention. Saragoni (1990) investigates the surprisingly low levels of damage caused by the 7.8 magnitude Chilean earthquake of 1985 and concludes that observed damage has better correlation with the damage potential parameter P_D, detailed in Equation (2.16) than elastic spectral accelerations.

Table 3.5. - Summary of the Relevance of Load Duration/Number of Cycles for Studies Using Spectral Response

Study	Structural Model	Duration Related Measure	Other Input Parameters	Importance Rating*
Kunnath & Chai [2004]	Stiffness deg	Significant dur. (5-95%)	Cyclic Ductility	9
Peng *et al.* [1989]	Elastic SDOF	Dur. stochastic process	RMS acceleration	9
Peng *et al.* [1988]	Elasto-plastic	No. of yield crossings	inelastic drift	9
Vidic & Fajfar [1995]	Stiffness deg	Significant dur. (5-95%)	Disp. Ductility	8
Kircher *et al.* [1997]	Inelastic SDOF	Eq. mag	SA	8
Yayong & Minxian [1990]	Bi-linear	Significant dur (5-95%)	PGV	8
Tremblay [1998]	Bi-linear hrdng	Significant dur. (5-95%)	SA	8
Malhotra [2002]	Elastic SDOF	No. cycles	PGA,PGV, PGD	8
Amini & Trifunac [1981]	Elastic SDOF	No. cycles	SA	7
Gupta [1991]	Elastic SDOF	No. cycles	SA	7
Kawashima & Aizawa [1986]	Elastic SDOF	No. cycles	SA	7
Perez [1980]	Elastic SDOF	No. cycles	SA	7
Schwarz, J. [1998]	Elastic SDOF	No. cycles	SA	7
Şafak [1998]	Elastic SDOF	No. cycles	SA	7
Tiwari & Gupta [2000]	Elasto-plastic	Significant dur(shrt 90%)	PGA	6

*10 implies duration/number of cycles are of critical significance, 5 represents marginal or unproved significance, 0 shows that duration was found to have no significance. Significant dur(shrt 90%) = significant duration as proposed by Trifunac and Westermo (1976).

Yayong and Minxian (1990) construct elastic and inelastic response spectra for a number of parameters including earthquake magnitude, source-to-site distance and site conditions. They calculate accumulated damage functions from modified Clough and bilinear structural models (Clough and Penzien 1975). From this they show that peak ground velocity and significant duration between 5 and 95% Arias intensity levels strongly influence accumulated damage, and conclude that this should be included in the development of response spectra.

Hu *et al.* (1985) present a method to evaluate the joint probability density of a ground-motion vector (A) containing two parameters, the ground-motion duration and spectral acceleration:

$$P(A) = P[a > A] = \int_M \int_R P[a > A|M,R] f(M,R) dM dR \tag{3.7}$$

where $P(A)$ is the joint probability exceedance of the vector of parameters A, $P[a > A|M,R]$ is the joint probability of ground motion a exceeding a given vector "A" under given condition of earthquake M and transmitting path R, and f(M,R) is the probability density function of simultaneous occurrence of M and R. Methods for calculating the seismic hazard in terms of two parameters using vectors is described in more detail by Bazzurro and Cornell (2002).

Şafak (1998) proposes an intensity parameter that measures the volume under a 3D velocity response spectrum which has the number of cycles on the third axis. Unfortunately the method is not described in detail, leaving open the specification of spectral period limits and the cycle counting method. Some authors suggest a limit to the total number of cycles counted can be used (Koliopoulos and Margaris 2001). Alternatively a low-amplitude cut-off should be applied to prevent residual vibration dominating response (Mortgat 1979).

Reinoso *et al.* (2000) develop response spectra for number of cycles. They suggest that ground-motion duration could be an important consideration for the design of reinforced concrete structures, particularly for buildings on sites with soft soils. They propose that a modulated harmonic function can be used to create a synthetic accelerogram to model ground motions on soft soil sites. The method was verified for the unique case of Mexico City where the deep deposits of soft soil create the formation of long duration, quasi-sinusoidal ground motions:

$$A_s(t) = A_{\max} . \sin\left[\frac{2\pi t}{S_p}\right] . \sin\left[\frac{2\pi t}{T_s}\right] \tag{3.8}$$

where $A_s(t)$ is the ground acceleration, A_{max} is the peak acceleration, S_p is the dominant soil period, and T_s is the strong-motion duration, which must be longer than S_p.

Duration is explicitly taken into account in the HAZUS methodology for earthquake loss estimation (FEMA 1999, 2003; Kircher *et al.* 1997; Whitman *et al.* 1997). In HAZUS the demand spectrum is reduced by a factor related to the level of effective damping. This is made of two components, elastic damping and a hysteretic damping. Hysteretic damping is calculated in terms of an equivalent viscous damping multiplied by a κ factor that simulates degradation of the hysteretic loop with longer earthquake duration. The influence of different κ values on the reduced demand spectrum is illustrated in Figure 3.3. HAZUS only distinguishes short, moderate and long duration shaking, with significant variation in the values of κ between the categories. These duration categories are defined only on the basis of the earthquake magnitude. For unreinforced masonry buildings designed to seismic codes, the values of κ are 0.5, 0.3 and 0.1 for short, moderate and long duration respectively. The influence of duration on the demand spectrum in the HAZUS methodology is not easily demonstrated as hysteretic damping is linked to the size and shape of the 5% damped demand spectrum, which is related to earthquake magnitude, which in turn is used as the indicator of earthquake duration. For example a low-rise masonry structure on a rock site in Central Eastern United States (CEUS) at 20 km hypocentral distance will have the 5% damping demand spectrum reduced by a factor of approximately 1.2 for M_w 7.5 events, 1.43 for M_w 7.0 events, 1.12 for M_w 6 events and no reduction for events less than M_w 5.0 as the demand does not exceed the elastic capacity of the building (Figure 3.4).

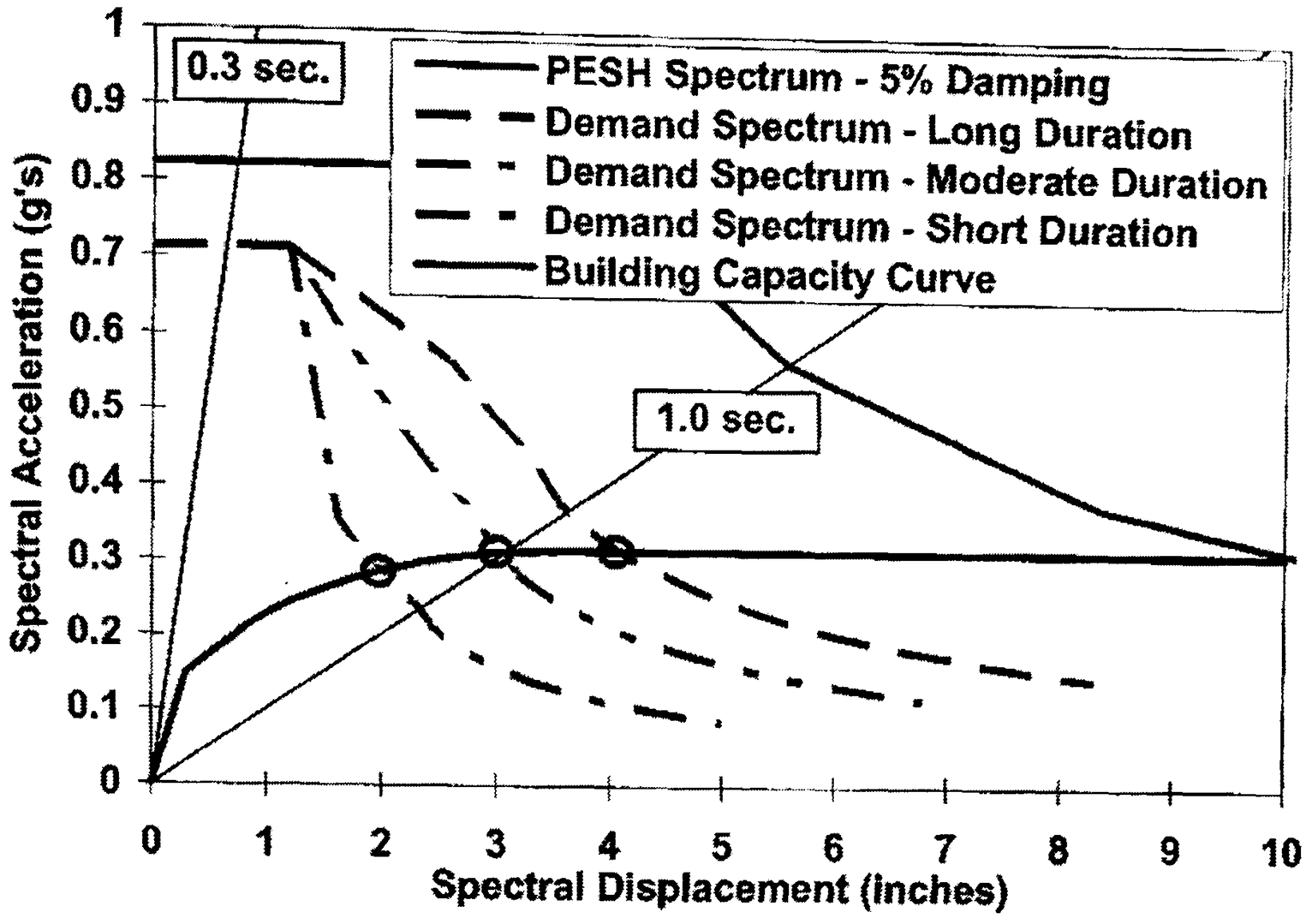


Figure 3.3. - Illustration of the Influence of duration on demand spectrum as used in the HAZUS loss estimation methodology, M=7, at 20km, WUS, Site Class E. Note that HAZUS defines M7 as Moderate duration. (Kircher *et al.* 1997)

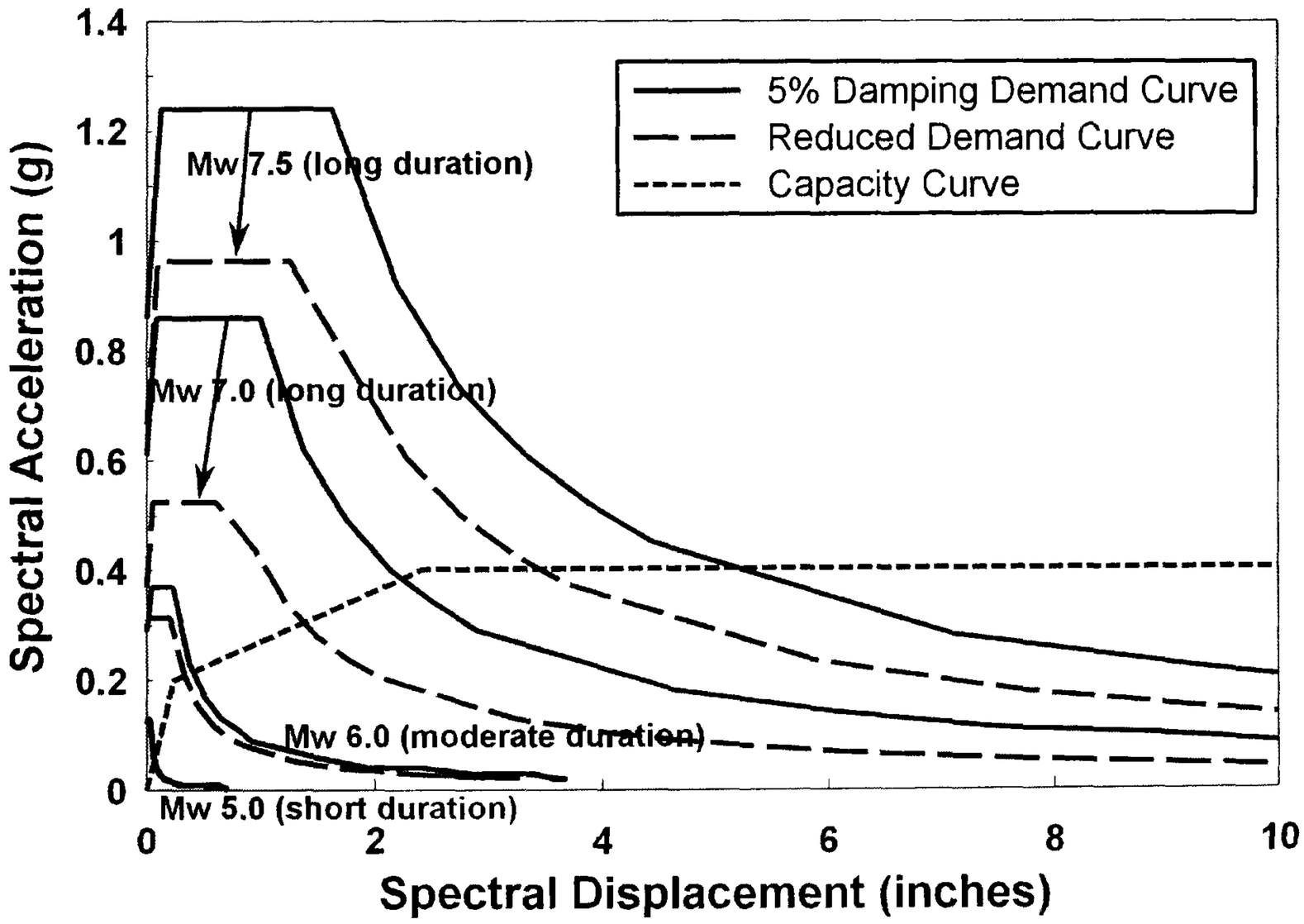


Figure 3.4. - Illustration of the influence of different earthquake magnitudes on demand spectrum reduced by duration as used in the HAZUS loss estimation methodology, low-rise, low-design code masonry structure, CEUS 20km hypocentral distance on a rock site.

Fajfar *et al.* (1989, 1990), Fajfar *et al.* (1990), Fajfar and Fischinger (1990a, 1990b) and Fajfar (1992) show that response parameters of medium-period structures correlate well with seismic demand index I_v which is related to peak ground velocity (*PGV*) and the duration between 5 and 95% Arias intensity levels proposed by Trifunac and Brady (1975a) $D_{SR(5\text{-}95\%)}$:

$$I_v = PGV.D_{SR(5-95\%)} \tag{3.9}$$

Fajfar and co-workers also used this parameter with low-cycle fatigue concepts to construct inelastic design spectra, where monotonic ductility is reduced for ground motions with numerous inelastic cycles. Fajfar and Vidic (1994) and Vidic *et al.* (1994) further refine their method proposing that a non-dimensional parameter γ can be used to estimate the reduction of deformation capacity of structures due to repeated inelastic cycles. This parameter depends mainly on the ground-motion characteristics but also includes the influence of some structural parameters. The authors propose the following formula to estimate γ:

$$\gamma = z_T z_\mu z_g \tag{3.10}$$

where z_T, z_μ and z_g are functions of the natural period, ductility and ground motion respectively. Initially the authors define the z_g parameter using a ratio of the Arias intensity to PGA and PGV. However, as the Arias intensity is often not available, Vidic and Fajfar (1995) propose that z_g can be approximated as:

$$z_g = 0.6\left(\frac{PGA}{PGV}\right)^{0.3} D_{SR(5-95\%)} \tag{3.11}$$

More recently Chai *et al.* (1998) has provided a more complete formulation of the inelastic design spectrum by using a period-dependent factor Ω_v which relates the input seismic energy $\left(\frac{E_I}{m}\right)$, to PGV:

$$\frac{E_I}{m} = \frac{1}{2}(\Omega_v PGV)^2 \tag{3.12}$$

Initially the Ω_v factor is determined empirically but later Chai and Fajfar (2000) derive the factor explicitly and fit a bi-linear function, given below and shown in Figure 3.5.

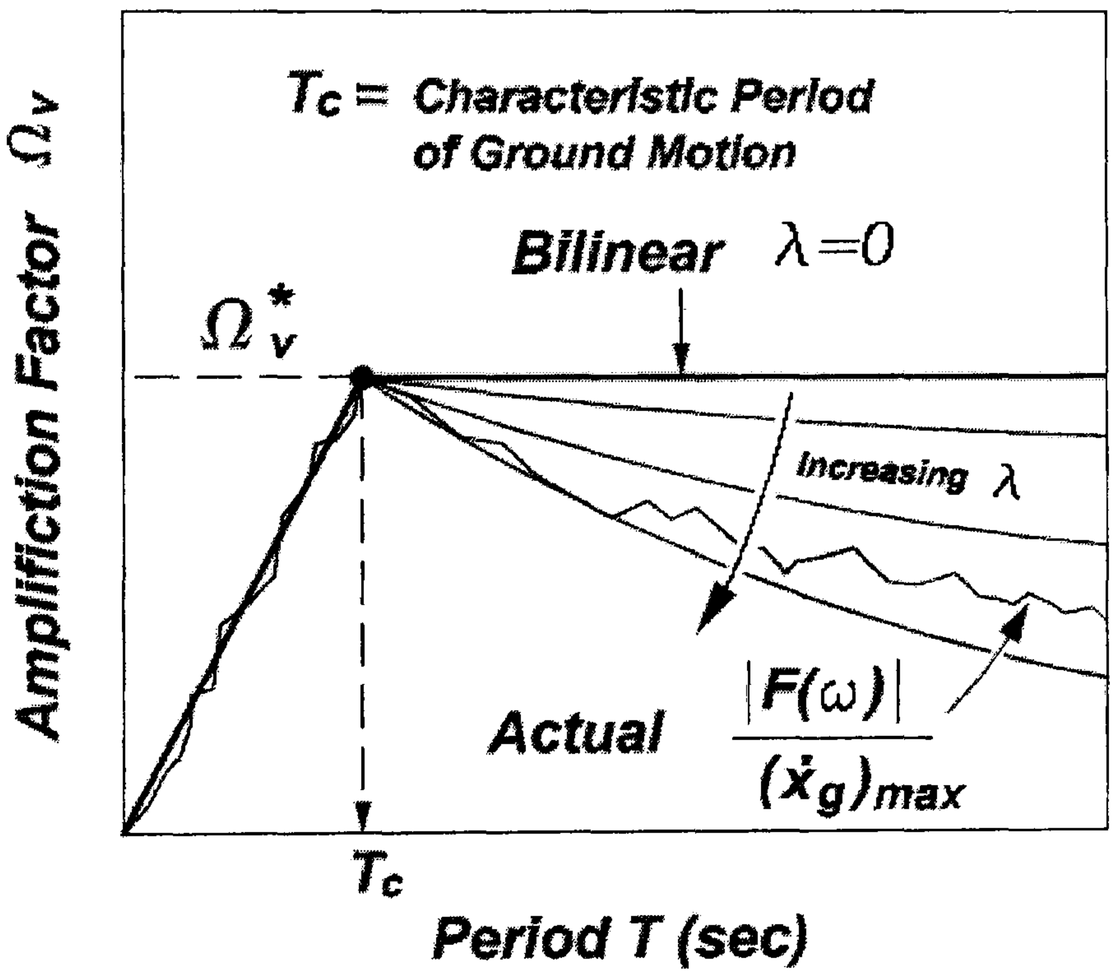


Figure 3.5. - Amplification factor Ω_v for equivalent input energy velocity. (Chai and Fajfar 2000).

$$\Omega_v = \begin{cases} \Omega_v^* \left[\frac{T}{T_c}\right] & \text{if } 0 \le T \le T_c \\ \Omega_v^* \left[\frac{T}{T_c}\right]^{-\lambda} & \text{if } T_c \le T \le \infty \end{cases} \tag{3.13}$$

$$\Omega_v^* = \frac{PGA}{Z.PGV}\sqrt{D_{SR(5-95\%)}T_c}\sqrt{\frac{\lambda+\frac{1}{2}}{2\lambda+2}} \quad \text{where } \lambda \geq 0 \tag{3.14}$$

where T_c is the characteristic period of the ground motion, λ is a parameter used to define the spectral shape for periods greater than the characteristic period (given by Equation 14 in Chai *et al.* 1998) and Z is the peak factor representing the ratio between peak ground acceleration and RMS of the ground acceleration, which is estimated from:

$$Z = \sqrt{\frac{PGA^2 D_{SR(5-95\%)}}{\int_0^{t_0} a_g(t)^2\,dt}} \tag{3.15}$$

The inelastic design spectrum is constructed by using an iterative procedure to find the cyclic displacement ductility μ_c and hence the ductility-related force reduction factor R_μ. This is done by finding the hysteretic cyclic plastic strain energy capacity $\left[\frac{E_h}{m}\right]$, which balances the input energy $\left(\frac{E_I}{m}\right)$ (equation 3.12), multiplied by an empirically derived factor α that represents the fraction of total input energy that is dissipated by member yielding and is given by:

$$\frac{E_h}{m} = \alpha\frac{E_I}{m} \tag{3.16}$$

$$\alpha = 1.13\frac{(\mu_c - 1)^{0.82}}{\mu_c} \tag{3.17}$$

The hysteretic energy is described by:

$$\frac{E_h}{m} = \left[\frac{\Omega_v PGA.T}{2\pi R_\mu}\right]^2\left[\mu_m\left(\frac{1}{\beta^*}+1\right)-\frac{1}{\beta^*}\mu_c - 1\right] \tag{3.18}$$

$$\mu_m = \left(\frac{\beta^*}{1+\beta^*}\right)\left(1+\frac{1}{\beta^*}\mu_c+\lambda\right) \tag{3.19}$$

where β* is a modified version of the β parameter proposed by Park and Ang (1985) (see Chai *et al. 1995*), and μ_m is the monotonic displacement ductility.

The influence of duration on the inelastic spectrum using this method is illustrated in Figure 3.6 for a structure with a strength deterioration $\beta^* = 0.15$ and monotonic displacement ductility μ_m=4 and for a peak ground acceleration of 0.4g and peak ground velocity of 0.667m/s.

Tan and Chao (1992) calculate the evolutionary power spectra (EPS) of seismic accelerograms. These are 3D plots of spectral power versus ground-motion duration and frequency. They determine expected EPS using a shape function anchored to PGA. A synthetic accelerogram is calculated from the EPS. Finally an elastic design response spectrum is determined from the synthetic accelerogram.

Naeim *et al.* (1994) create hysteretic and input energy spectra from 120 accelerograms from earthquakes over magnitude 5.5. They find that duration, measured by the 0.05g bracketed duration, is very significant for the damage potential (measured in terms of the input energy) of some of the records analyzed, although they note that the 0.05g limit may not be accurate for engineering purposes due to the occurrence of multiple events in accelerograms.

Tiwari and Gupta (2000) calculate inelastic strength reduction factors based on both ductility and a damage measure based on that proposed by Park and Ang (1985) for a range of spectral ordinates. They use an elasto-plastic model with 956 recorded ground motions and find that significant duration, defined as the shortest continuous duration with 90% of Arias intensity, influences the reduction factors. However, they find that the influence is generally small, period dependent, and may be ignored for high-frequency motion, for example in the design of stiff structures on rock sites.

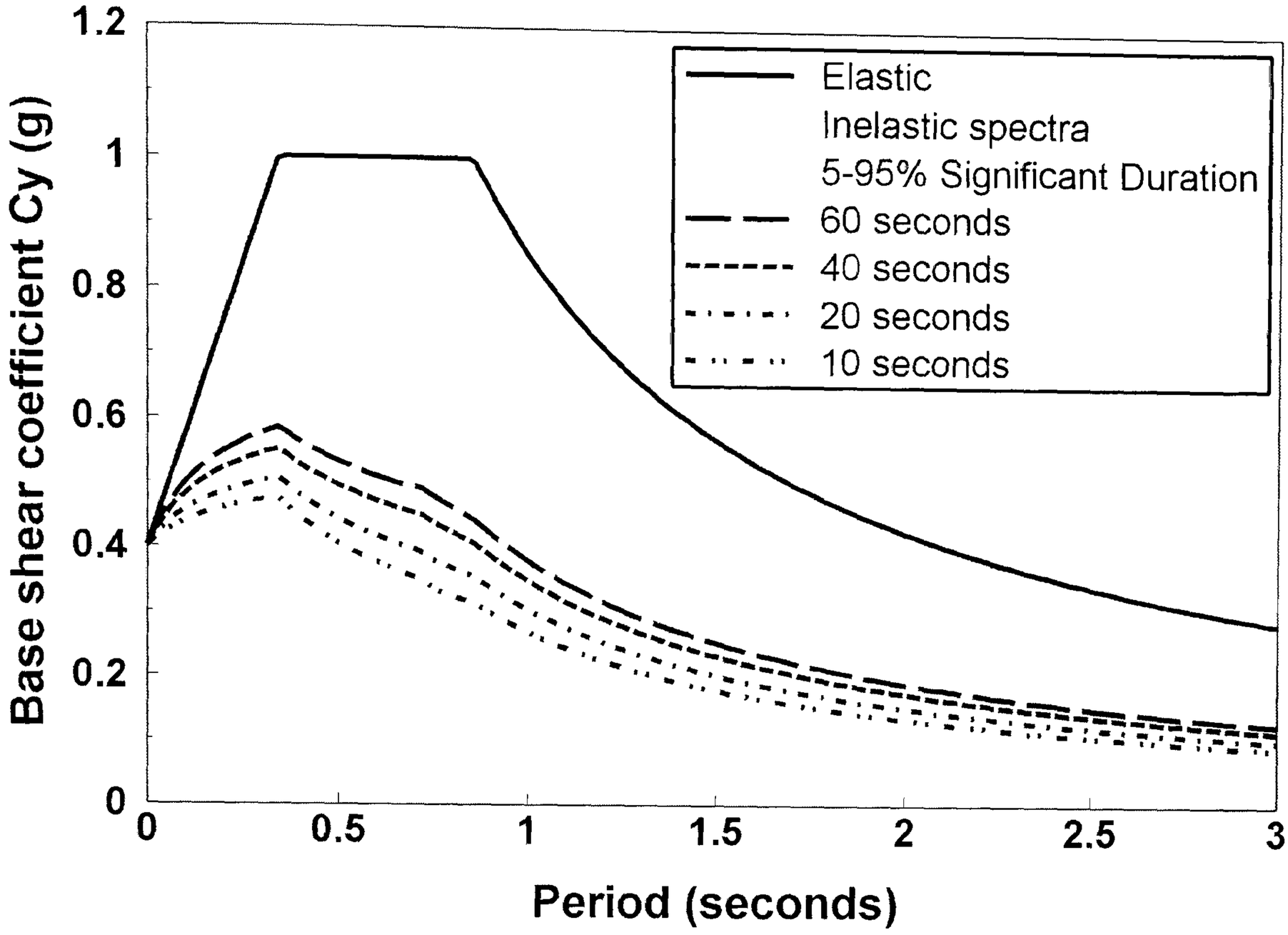


Figure 3.6. - Influence of significant duration Trifunac and Brady (1975a) on inelastic design spectra for a structure with $\beta^* = 0.15$, $\mu_m=4$, peak ground acceleration of 0.4g and peak ground velocity of 0.667m/s, characteristic period $T_c= 0.85$, developed using procedure proposed by Chai *et al.* (1998).

3.7 Summary

There are several hundred papers in the literature that make conflicting conclusions on the influence of ground-motion duration on structural damage. This study demonstrates that the primary reason for the different conclusions is the different definition of structural damage used. Studies employing damage metrics based on peak response generally do not find a link between duration and damage, whereas studies using damage metrics based on absorbed energy or cumulative fatigue generally find a positive link between duration and damage. Experimental studies of the low-cycle behaviour of a wide range of components including both steel and reinforced concrete members indicate that cumulative damage measures have the potential to provide a more accurate estimate of the likelihood of failure. However, cumulative damage measures are by definition more complex than those using maximum response and so are more difficult to calibrate and reliably estimate.

4. THE INFLUENCE OF DURATION ON MASONRY STRUCTURES

This chapter presents the results of a detailed investigation into the influence of the duration and other characteristics of the ground motion on the damage to low-to-medium rise masonry buildings.

4.1 Structural Model

The analysis uses seven single-degree-of-freedom models with natural periods chosen to represent the typical ranges of low- to medium-rise masonry buildings encountered in Europe. The models have initial periods of vibration of 0.1, 0.15, 0.2, 0.25, 0.3, 0.4, and 0.5 seconds. The yield strength of each model is inferred from the base shear coefficient (lateral force resistance per unit weight), which in all cases is fixed at 0.25, chosen as a representative average value for masonry structures, based on available experimental information. Single-degree-of-freedom models are considered adequate for this study since for the type of buildings of interest the most common global failure mechanism is that of a shear-dominated failure of the ground floor (soft storey).

The hysteretic model for the masonry structures is that developed over several years at the University of Pavia and calibrated against experimental tests on unreinforced and lightly reinforced masonry structural components (Calvi and Macchi 1990; Magenes and Baietta 1998; Penazzo 2001). The model consists of a multilinear approximation of the cyclic response, and its main feature is the dependence of strength and stiffness degradation on dissipated hysteretic energy. The numerical values of the parameters used in the analytical relationships describing strength and stiffness degradation are influenced by the dominating failure mode. Shear-dominated failure mechanisms exhibit remarkable strength degradation, as shown in Figure 4.1, where the hysteretic curve obtained with the algorithm is compared with the results of a cyclic test on a masonry wall. Stiffness and strength degradation are clearly separate effects, strength degradation being the more dangerous as it can lead to collapse; stiffness degradation causes the natural period of the structure to increase and may lead to large displacements. However, in masonry structures strength and stiffness degradation are intrinsically linked and this is reflected in the model by the fact that

they both essentially depend, although in different ways, on the energy dissipated by hysteresis. All the analyses carried out in this work make use of a shear-dominated cyclic response, since this is the prevailing failure mechanism in masonry. A linear viscous damping ratio of 5% of critical is assumed in all analyses to simulate energy dissipation before yielding occurs.

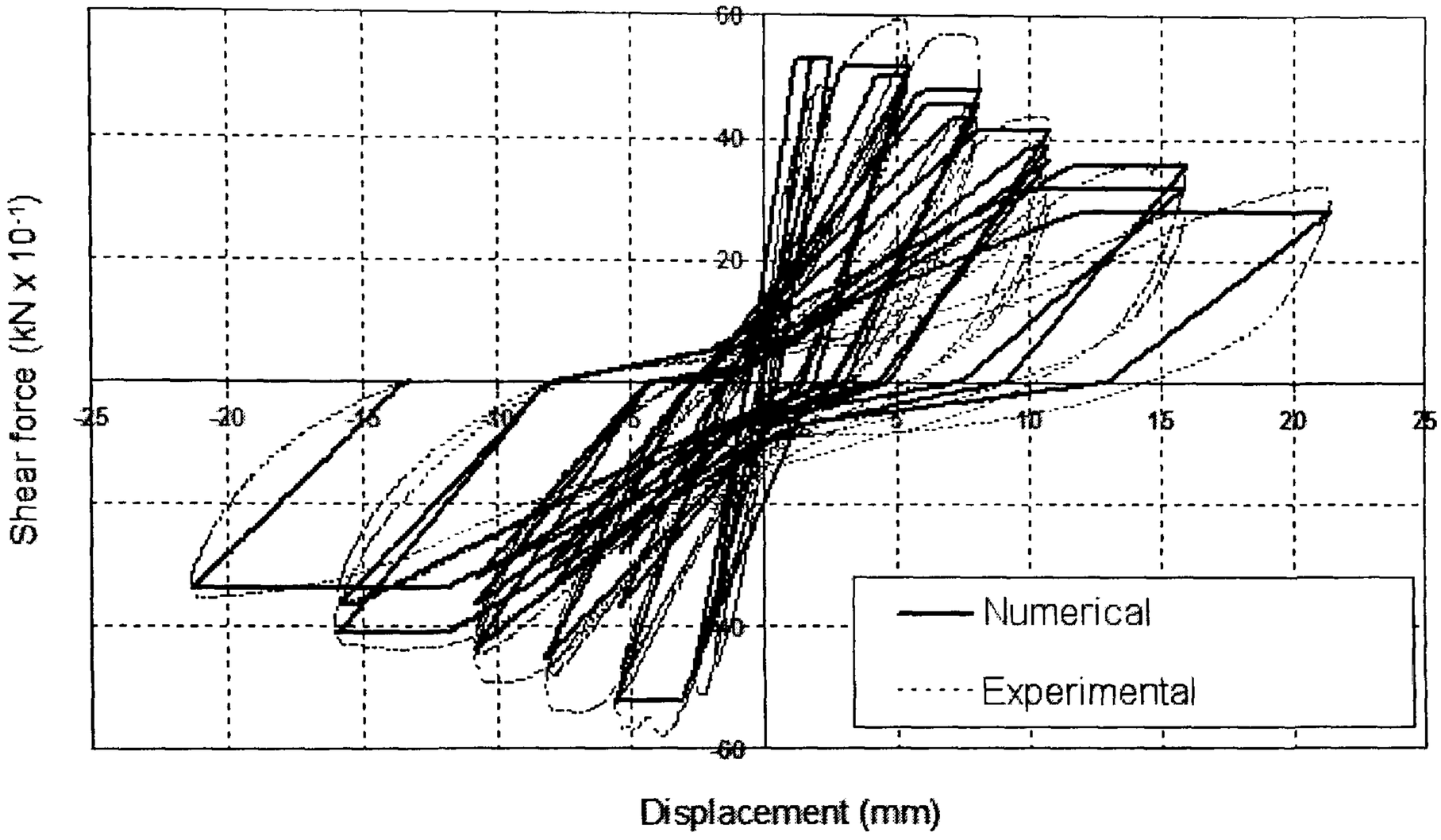


Figure 4.1. - Comparison between hysteretic model used in algorithm (solid line) and hysteretic behaviour of masonry structure determined by testing (Magenes *et al.* 1996)

4.2 Damage Measures

The choice of the demand metric in a study of this nature is critical as it may influence the interpretation of results. For this study, several structural response parameters were calculated in order to quantify the inelastic demand imposed by the ground motions. The response parameters included the global drift, displacement and ductility demand, stiffness degradation, energy dissipation and strength degradation. A common criterion to define the attainment of the ultimate limit state from experiments is to associate it with a specified level of strength degradation of the structure. Laboratory tests (Magenes et al. 1995; Magenes and Calvi 1997) have shown that a strength degradation of 30% (a threshold often associated with

"ultimate" conditions) is reached, in the case of masonry walls failing in shear, at drift levels of less than 1%. As many of the ground motions cause degradation in excess of these limits, it was decided to consider only results from analyses with strength degradation up to 50% or a drift up to 2%, so that a suitably representative sample of damaging events was obtained. Since the ultimate limit is reached, the analytical model can only be calibrated with experimental results up to 30% strength degradation, because results become less reliable and have less physical meaning beyond this point. The number of analyses in which the structure reached the 50% strength degradation limit was found to decrease with increasing natural period, with about 30% of the 473 runs reaching the limit for 0.1 s period structures, 15% for those with a period of 0.2 s and just 7% for 0.3 s.

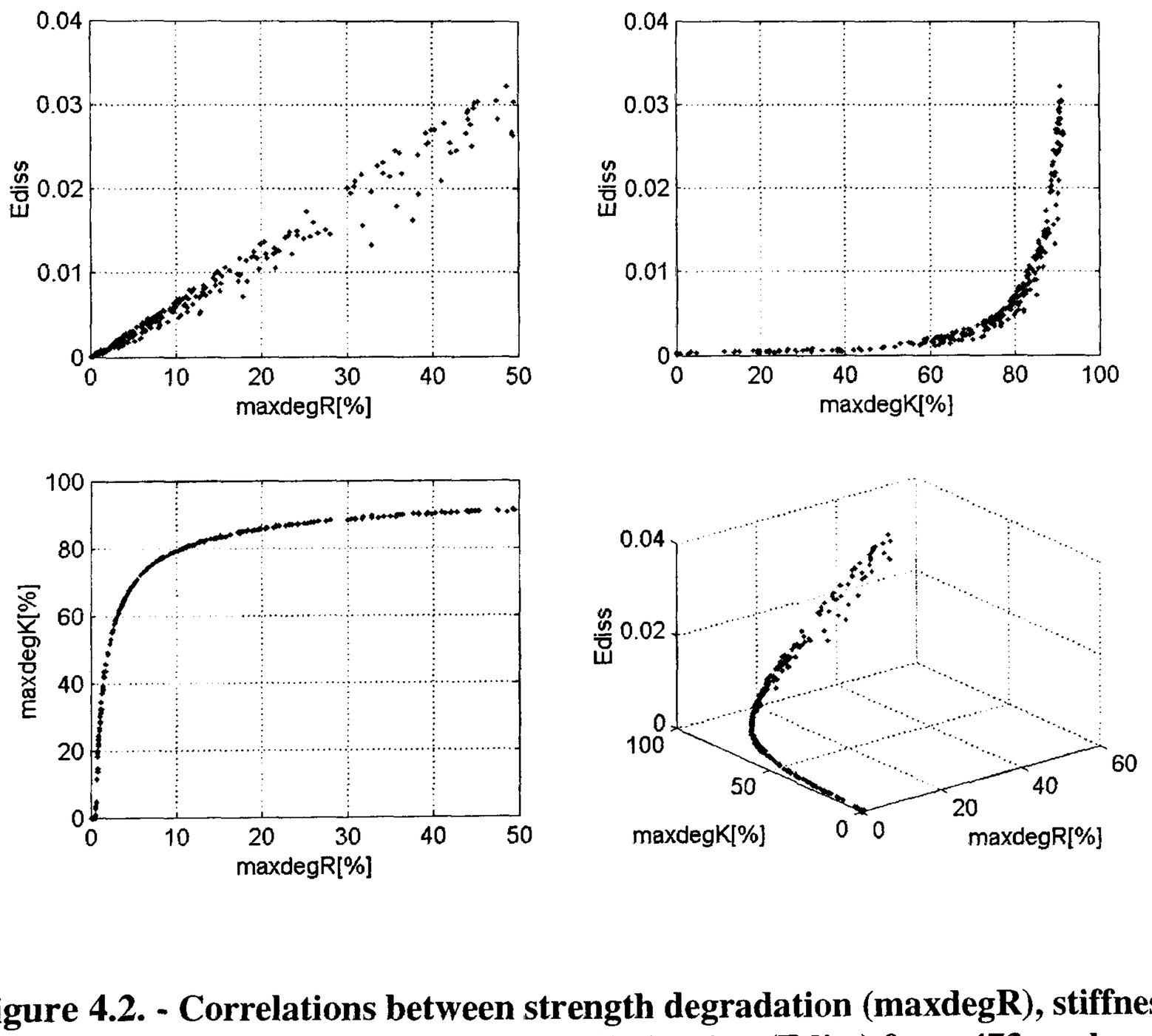


Figure 4.2. - Correlations between strength degradation (maxdegR), stiffness degradation (maxdegK) and total energy dissipation (Ediss) from 473 analyses on the model with natural period of vibration of 0.15 second (Penazzo 2001).

The critical issue for this study was the selection of a meaningful measure of inelastic demand. Since strength degradation is strongly correlated with structural damage, it was adopted here as the reference parameter to describe inelastic demand. The

hysteretic rule used herein establishes a strong correlation of strength degradation with other measures of inelastic demand, particularly stiffness degradation and hysteretic energy dissipation, as shown in Figure 4.2.

4.3 Strong-motion Accelerograms

This study uses the database of 473 strong-motion accelerograms compiled by Penazzo (2001). The records have been selected to represent a wide range of intensities from relatively weak motions to very strong shaking. Weak records that would not damage even vulnerable masonry structures are excluded: the criterion used for this exclusion was a minimum horizontal PGA of 0.15g. Records were selected without respect to geographical origin and regardless of whether the earthquakes were of crustal origin or associated with subduction zones, but only those records for which there are reliable estimates of magnitude and source-to-site distance are included. The sites are classified according to the widely used three category system based on 30m shear-wave velocities (Boore *et al.* 1993; Ambraseys *et al.* 1996) wherever possible, otherwise simply as 'rock' or 'soil'. The distributions of the selected records in magnitude-distance space, grouped by site classification, are shown in Figure 4.3: 44% of the records are classified by the three category system, 53% are classified simply as 'rock' or 'soil', and 3% of the records are from sites of unknown classification.

All of the records are obtained from source-to-site distances of less than 150 km, and 85% of the records are obtained within 50 km of the source. Figure 4.3 also shows that less than 13% of records are from earthquakes of magnitude less than 5 and that over 80% of the records were generated by events of magnitude greater than 5.5. Ten records from small magnitude events, recorded at very short distances and therefore having not insignificant peak amplitudes, are included precisely because such events would not be expected to cause appreciable damage.

The database contains a total of 473 accelerograms, with certain earthquakes, such as the 1987 Whittier Narrows and 1994 Northridge events, contributing large numbers of records (63 and 78 respectively). Strike-slip, normal and reverse events are all represented and comprise 24%, 18%, and 48% of the records respectively, with 10%

of records coming from earthquakes of unknown mechanism. Each of the seven structural models is subjected to each of the strong-motion records, resulting in a total of 3,311 non-linear analyses.

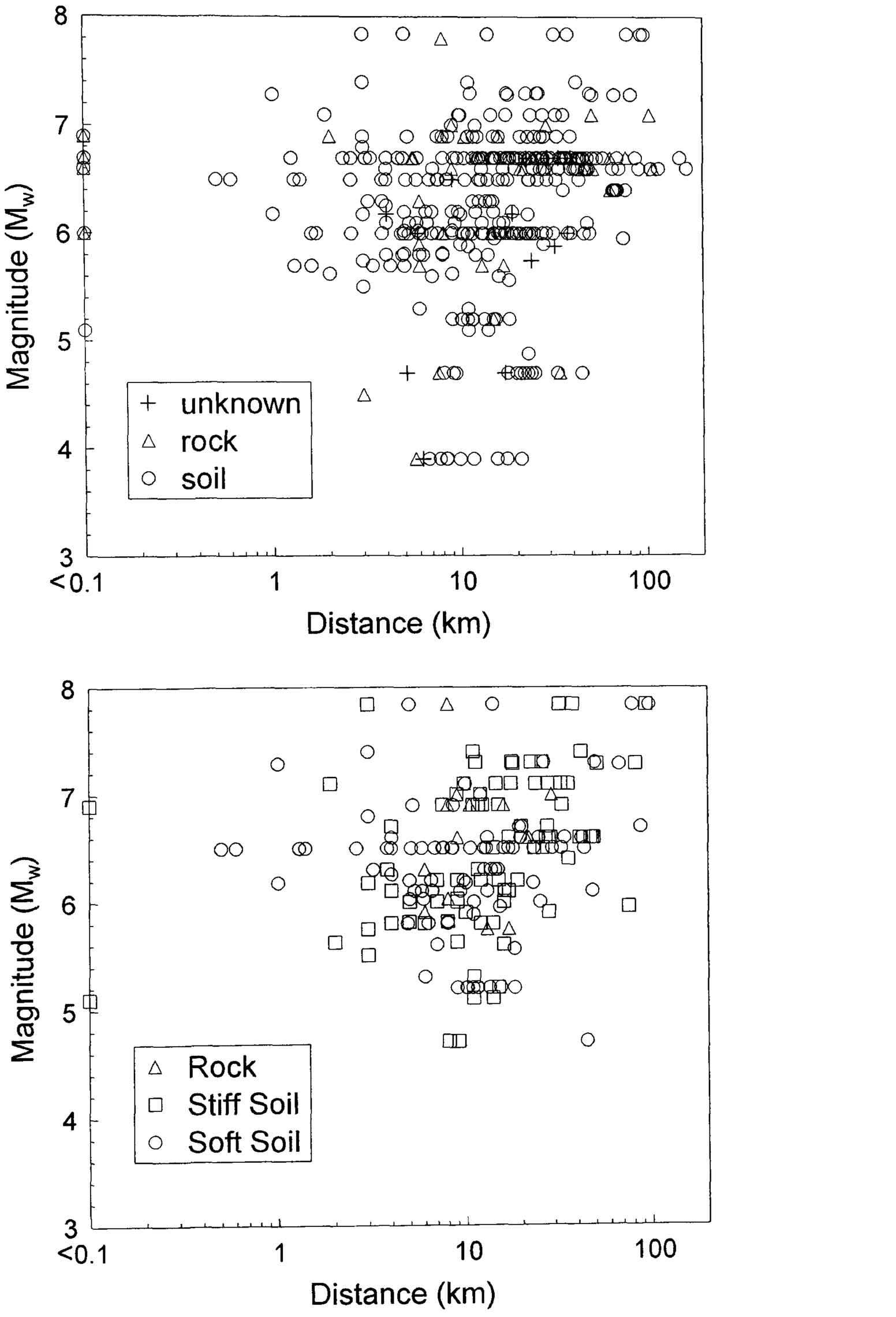


Figure 4.3. - Magnitude-distance distribution of the full strong-motion dataset used in the masonry structures study, grouped according to generic rock or soil site classification (*upper*) and for only those records with a more detailed classification scheme (*lower*).

4.4 Average Spectral Acceleration

Masonry structures exhibit significant degradation of stiffness with only small strength degradation (Figure 4.2). For example, 10% strength degradation results in nearly 80% stiffness reduction. This increases the effective natural period by a factor of about three, making the response at longer periods more important. This phenomenon also explains the poorer correlation between spectral acceleration at the initial period of the structure and the strength degradation at higher levels of structural damage (Figure 4.4). In this study an S-form trend line is used to show the general relationship between spectral acceleration and strength degradation. The S-form of the trend line is designed to take a physically meaningful form, starting at 0.1g spectral acceleration and extending up to a maximum 100% strength degradation. Only the lower half of the trend line appears on the figures if only results up to 50% strength degradation are used. The equations describing the S-form trend line are:

$$StrenDeg. = 100, \qquad \text{for } Sa.K \geq \pi \tag{4.1}$$

$$StrenDeg. = 0, \qquad \text{for } Sa. < 0.1 \tag{4.2}$$

$$StrenDeg. = 50 + \left[1 + \sin\left((Sa - 0.1).K - \frac{\pi}{2}\right)\right] \qquad \text{for } Sa.K < \pi \quad \text{and } Sa. \geq 0.1 \tag{4.3}$$

where Sa represents the spectral acceleration, K is a constant fitted by least squares regression and *StrengDeg.* represents the strength degradation.

To investigate the effect of increasing effective period with each damaging cycle, an average elastic spectral acceleration is taken from the initial uncracked natural period of the structure T_0, to a period $F\ T_0$, where F is a factor to be defined. The improvement in the goodness of the fit is quantified by calculating the standard deviation of the residuals (calculated strength degradation minus degradation predicted by trend line). By plotting the standard deviations for a range of values for F it is found that the spectral acceleration averaged between T_0 and a period approximately 3 times T_0 is optimal (Figure 4.5). A detailed investigation of averaged

spectral acceleration and the strength degradation of the structure with 0.15 s initial period found that the clearest trend, with fewest outlying points, was achieved with acceleration averaged between 0.15 s and 0.4s, implying F=2.7 (Figure 4.6).

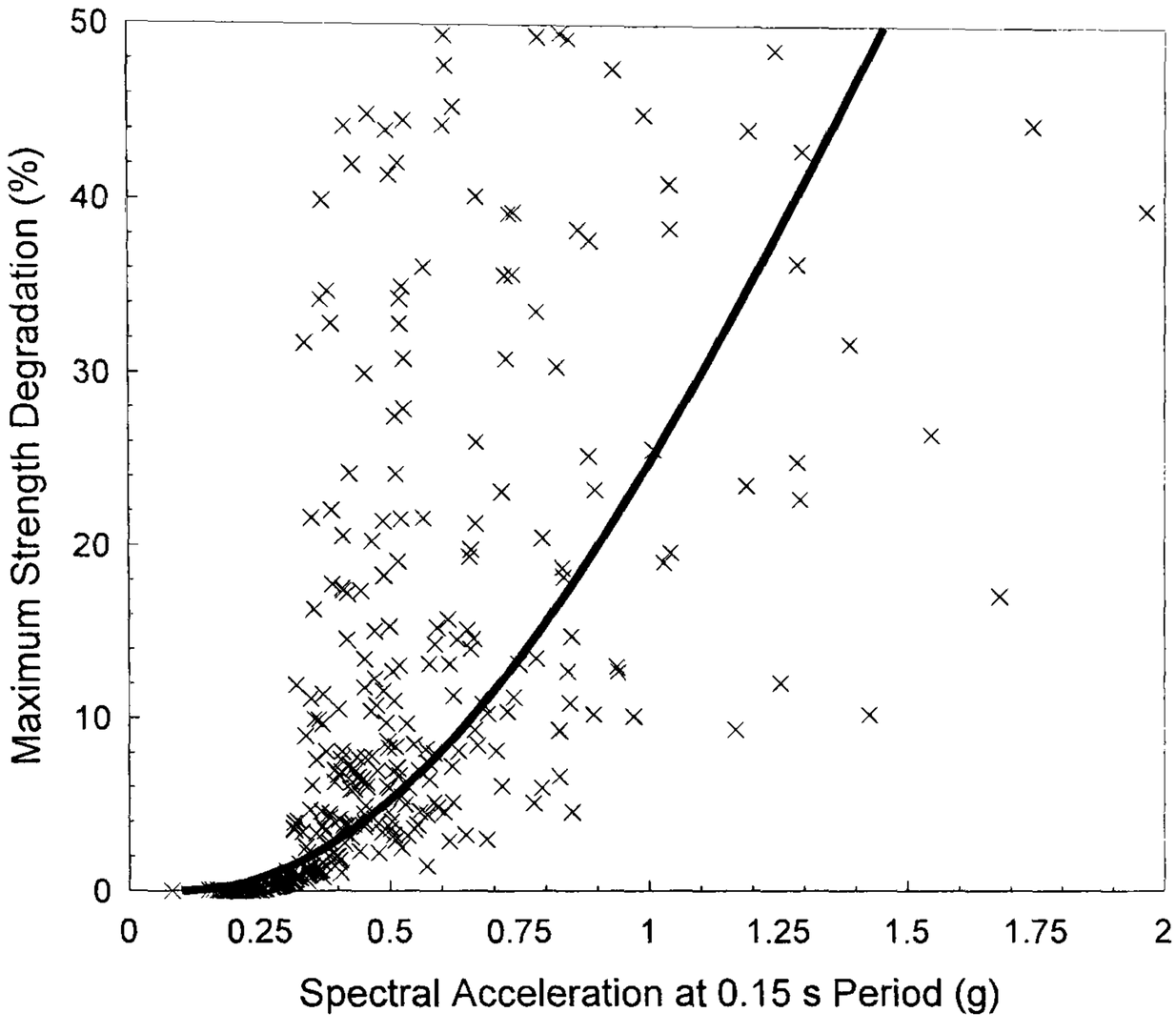


Figure 4.4. - Strength degradation of structure with 0.15 second initial natural period vs. spectral acceleration at 0.15 seconds period. Solid line shows S-Form trend line.

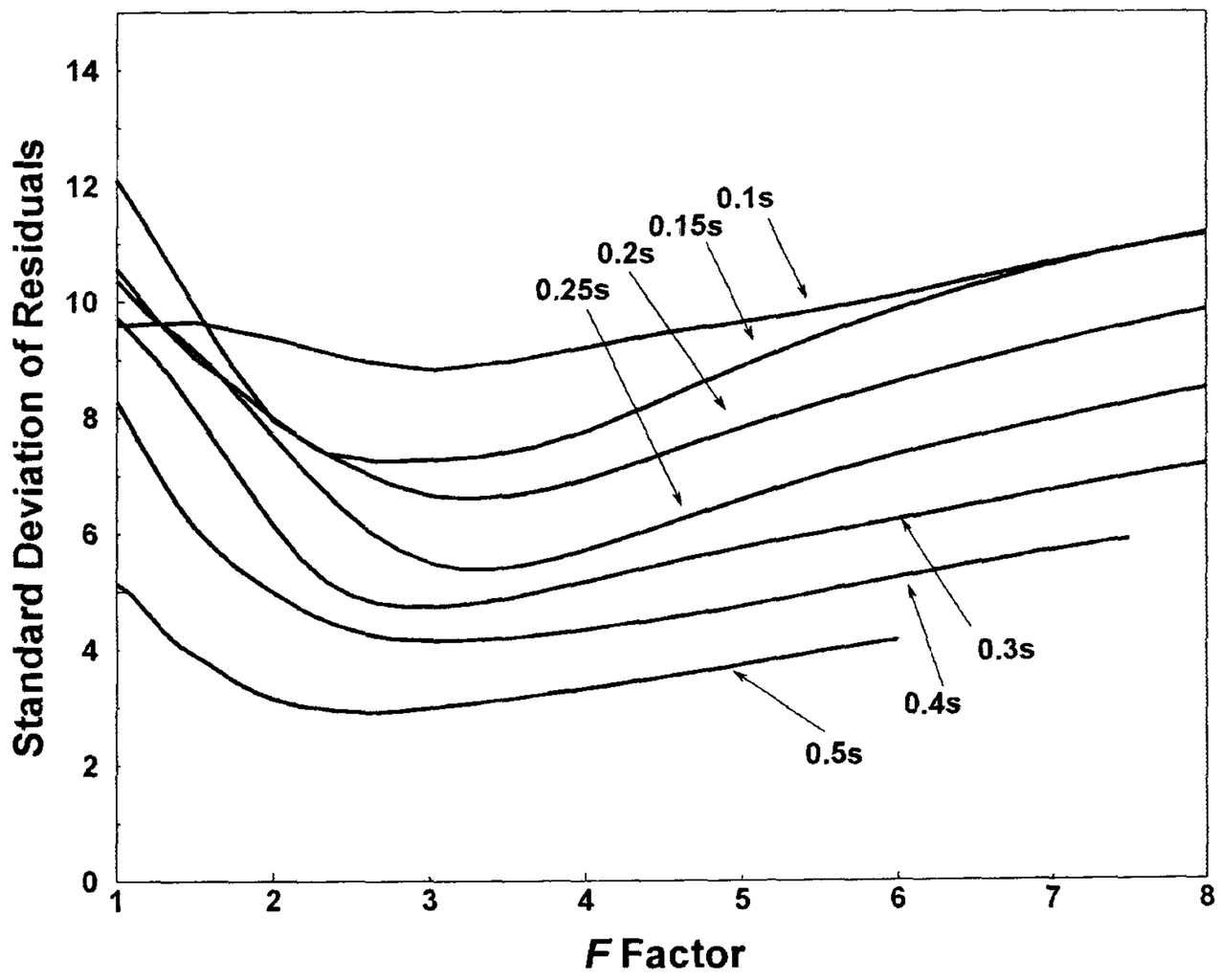


Figure 4.5. – Standard deviation from S-form trend lines for a range of F-factors. Masonry structures with initial periods of 0.1, 0.15, 0.2, 0.25, 0.3, 0.4 and 0.5 seconds.

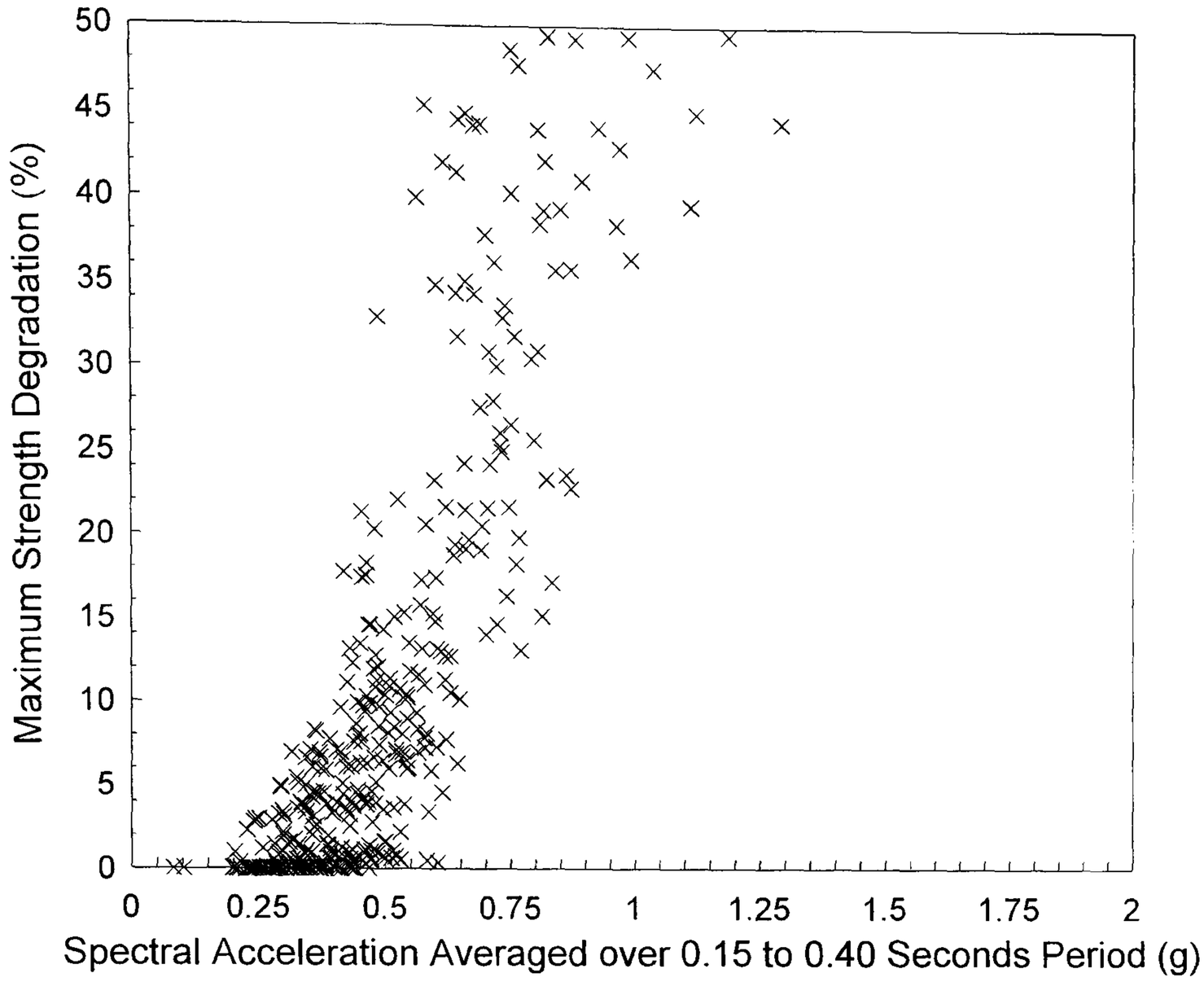


Figure 4.6. - Strength degradation of structure with 0.15 second initial natural period vs. spectral acceleration averaged from 0.15 to 0.40 seconds period.

4.5 Influence of Duration

The averaged elastic spectral acceleration discussed previously gives one of the better correlations with strength degradation. However, significant scatter still remains in the correlation (Figure 4.6); for example, for an average *Sa* of 0.75g, the resulting damage may differ by a factor of 3 or more. The hypothesis that a more accurate estimate of strength reduction can be achieved by considering both spectral accelerations and a measure of duration is investigated by examining the duration of the ground motions with similar spectral accelerations. The results from the structure with 0.15s initial natural period are used for this purpose.

The influence of the duration on the damage is illustrated by using different symbols for different levels of duration on plots of average spectral accelerations versus strength degradation (Figures 4.7 to 4.9). To enable comparisons with the HAZUS methodology, correlations are also made between earthquake magnitude and strength degradation (Figure 4.9). If there is a good correlation between strength degradation

and duration, data points with similar duration should group together defining distinct bands on the plots. S-form trend lines are fitted to the plots to show the general trends in the data.

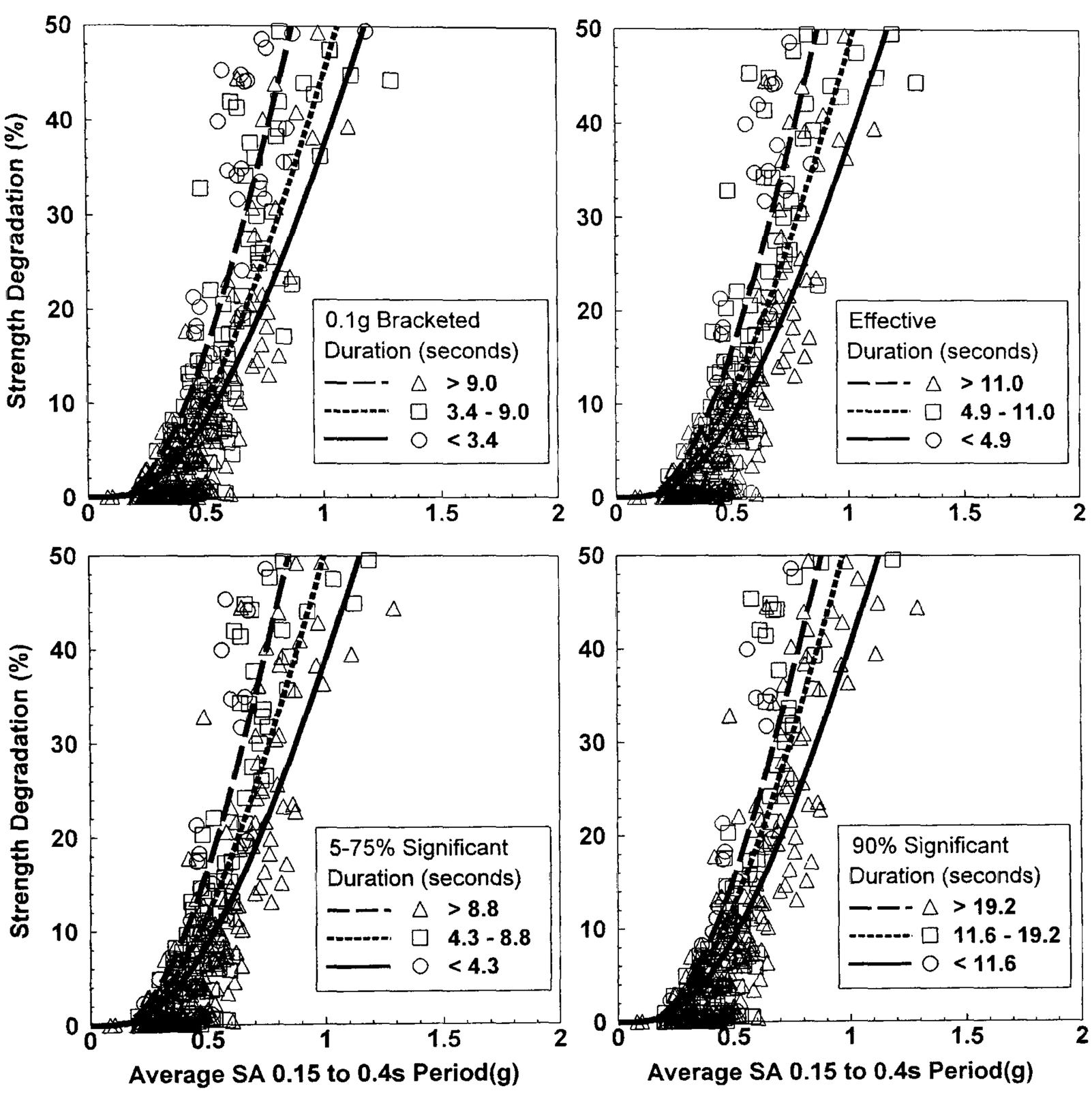


Figure 4.7. – As Figure 4.6 but with data grouped according to the bracketed duration at 0.1g (*top left*), effective duration (*top right*), 5-75% significant duration (*lower left*) and significant duration over shortest 90% Arias Intensity (*lower right*)

The trend line constant K and standard deviation are given in Table 4.1 for all duration measures investigated. The trend lines show that, as would be expected, the events with longer duration or greater magnitude generally cause greater strength degradation than smaller, shorter events for the same level of spectral acceleration. However, the correlation is relatively weak with significant overlap between events with different durations, making the differences between the curves small in

comparison to the scatter of the observations around the mean values (Figures 4.7 and 4.8)

Table 4.1. - Summary of constants describing trend lines and standard deviations of data points.

Duration Measure		**S-Form Trend line**	
		Constant "K"	**Standard Deviation[1]**
Effective duration	0 - 4.9 seconds	1.47	5.0
	4.9 - 11.0 seconds	1.70	8.2
	+ 11.0 seconds	2.04	8.8
	Weighted Average[2]		6.4
Uniform duration	0 – 1.0 seconds	1.26	4.2
at 0.1g	1.0 – 2.0 seconds	1.67	9.8
	+ 2.0 seconds	1.77	14.6
	Weighted Average[2]		5.8
Bracketed duration	0 - 3.4 seconds	1.45	4.8
at 0.1 g	3.4 - 9.0 seconds	1.62	7.6
	+9.0 seconds	2.02	9.9
	Weighted Average[2]		6.2
Relative bracketed duration	0 - 5.2 seconds	1.49	5.6
at 25% PGA	5.2 - 11.3 seconds	1.62	7.7
	+11.3 seconds	2.02	7.9
	Weighted Average[2]		6.4
Significant duration	0 - 4.3 seconds	1.50	5.7
at 5-75% Arias intensity	4.3 - 8.8 seconds	1.75	7.5
	+ 8.8 seconds	2.10	8.0
	Weighted Average[2]		6.5
Significant duration	0-11 seconds	1.54	6.8
at 5-95% Arias intensity	11-20 seconds	1.75	6.7
	+20 seconds	2.04	7.2
	Weighted Average[2]		6.8
Significant duration	0-11.6 seconds	1.53	6.1
Shortest duration over which	11.6 - 19.2 seconds	1.80	7.9
90% Arias intensity accumulates	+19.2 seconds	2.01	6.8
(Trifunac and Westermo 1982)	Weighted Average[2]		6.7
Earthquake magnitude M_w	0 - 5.5	1.47	4.8
	5.5 - 7.5	1.64	7.5
	+ 7.5	2.09	7.0
	Weighted Average[2]		7.0

Notes: [1]Standard deviation of residuals (observed minus predicted strength degradation).

[2]Weighted average based on number of records in each duration bin.

The uniform duration is the duration measure that is best correlated with strength degradation for results selected for having similar spectral accelerations (Table 4.1 and Figure 4.8). This is to be expected, as this measure is the best indication of the amount of time accelerations exceed a cracking level. The results from the significant duration measures are similar, including the hybrid uniform-significant duration measure originally proposed by Trifunac and Westermo (1976, 1982) which differentiates between the bursts of incoming wave energy by measuring the shortest duration over which 90% of Arias intensity accumulates (Table 4.1).

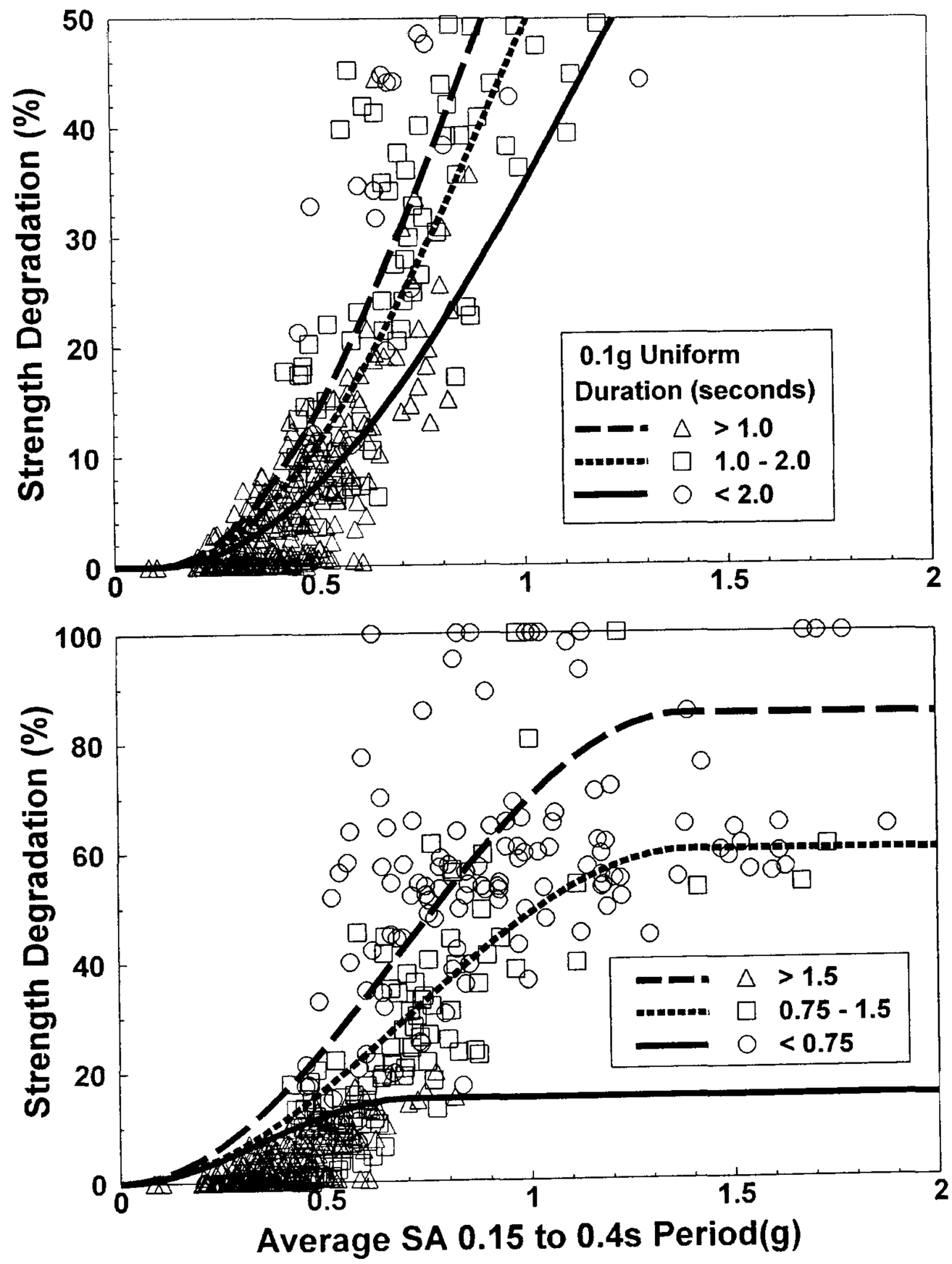


Figure 4.8. – As Figure 4.6 but with the data grouped according to the uniform duration at an acceleration threshold of 0.1g (*upper*). Results plotted to 100% strength degradation, events with less than 10% strength degradation excluded and the upper limit of trend lines fitted by least squared regression (*lower*). Note that different duration intervals are used in the two figures.

The records with 0.1g uniform duration less than 0.75 second cause a maximum strength degradation of 20%, which should be reflected in the curve fitted to the data. This is investigated by fitting S-form trend lines with free upper bounds to the whole data set. To reduce the influence of results corresponding to very low levels of damage, all values of strength degradation of 10% or less are removed. This shows that the upper limit of the 0.75-second motion tends to about 16% strength degradation and longer durations tend to about 60-80% strength degradation (Figure 4.8). However, firm conclusions cannot be drawn from this result as data points above 30% strength degradation have little physical meaning, and removing data for less than 10% strength degradation leaves relatively little reliable data.

The data points plotted for similar earthquake magnitude are also divided into the three bins proposed in the HAZUS methodology (FEMA 1999, 2003), which defines short ($M_w < 5.5$), moderate ($5.5 < M_w < 7.5$) and long duration ($M_w > 7.5$) ground motions respectively. Subdividing the data in this way gives seven long duration records, 293 moderate and 71 of short duration (Figure 4.9). As with the duration definitions, the larger magnitude events generally produce greater damage. To further explore this effect, the coarse magnitude subdivisions used in HAZUS are further subdivided to have more magnitude bins (Figure 4.9). This shows that the general trend continues with larger magnitude events generally causing increased strength degradation. Part of the remaining scatter may be explained by the fact that earthquake magnitude is not a direct measure of ground-motion duration, since duration also depends on the direction of rupture and furthermore sites situated on deep basins filled with soft soil may experience longer duration ground motions than sites founded on rock because of amplified surface waves (e.g. Trifunac and Novikova 1995).

The addition of strong-motion duration as a second explanatory variable, together with spectral acceleration, does not significantly reduce the scatter of the damage measures around the trend lines, as is confirmed by the residual plot in Figure 4.10. However, there are clear differences between the mean residuals for different classes of duration, suggesting that there is a physical influence of this parameter and that damage estimations would be refined by including duration in any predictive model. The situation is analogous to that of including additional variables, beyond magnitude

and distance, in ground-motion prediction relationships. The reduction of the aleatory variability by adding site classification (see, for example, Fig. 21 of Ambraseys *et al.* 1996) or style-of-faulting (see Fig. 9 of Bommer *et al.* 2003) is small, but this does not mean that these variables, which have been demonstrated to exert an influence on the predicted parameter and whose influence can be physically explained, should not be included in the predictive models. The addition of these explanatory variables is entirely consistent with the objective of transforming aleatory (random) variability into epistemic uncertainty.

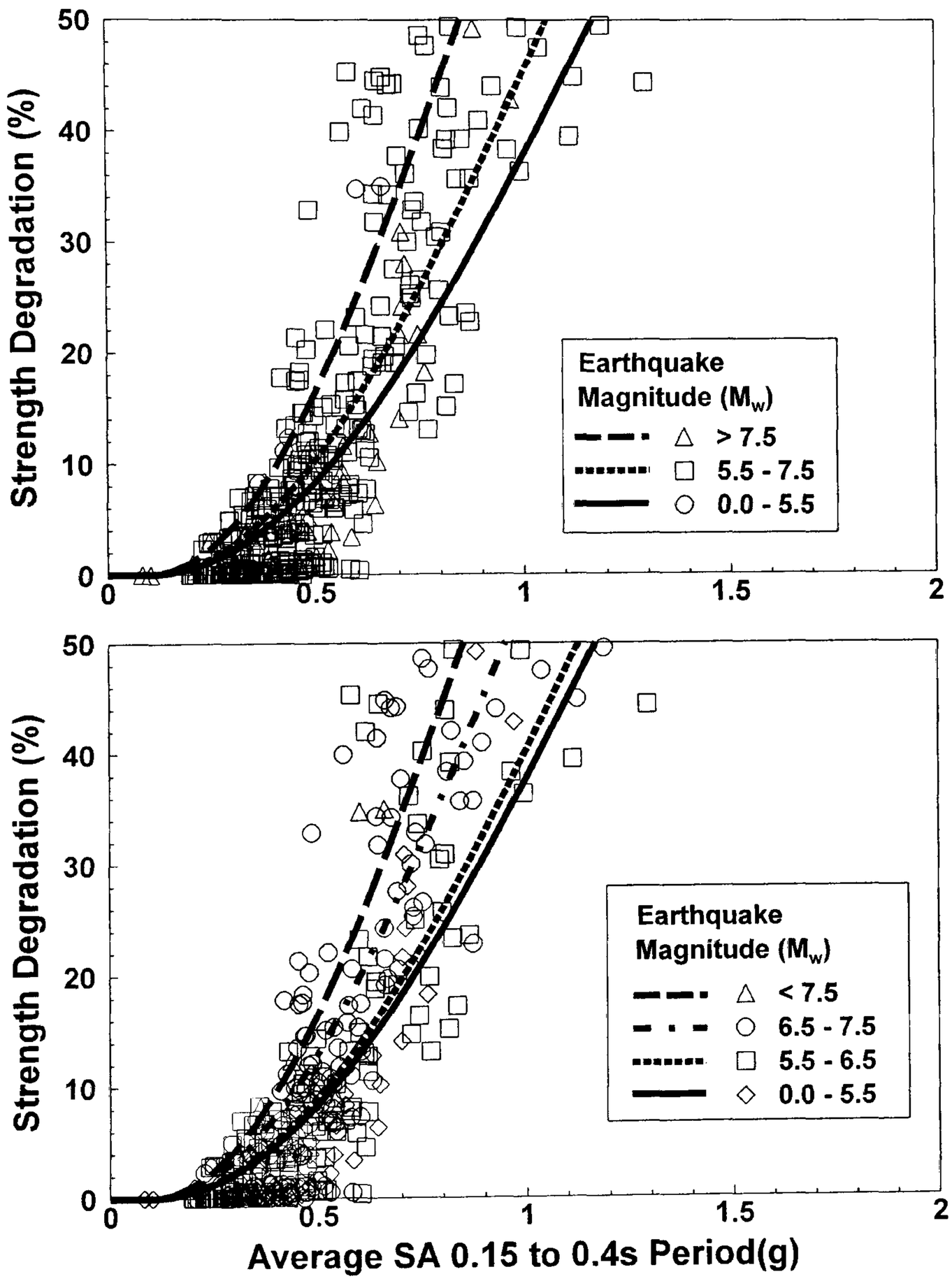


Figure 4.9. As Figure 4.6 but with the data grouped according to earthquake magnitude, with 3 (*upper*) and 4 (*lower*) magnitude bins

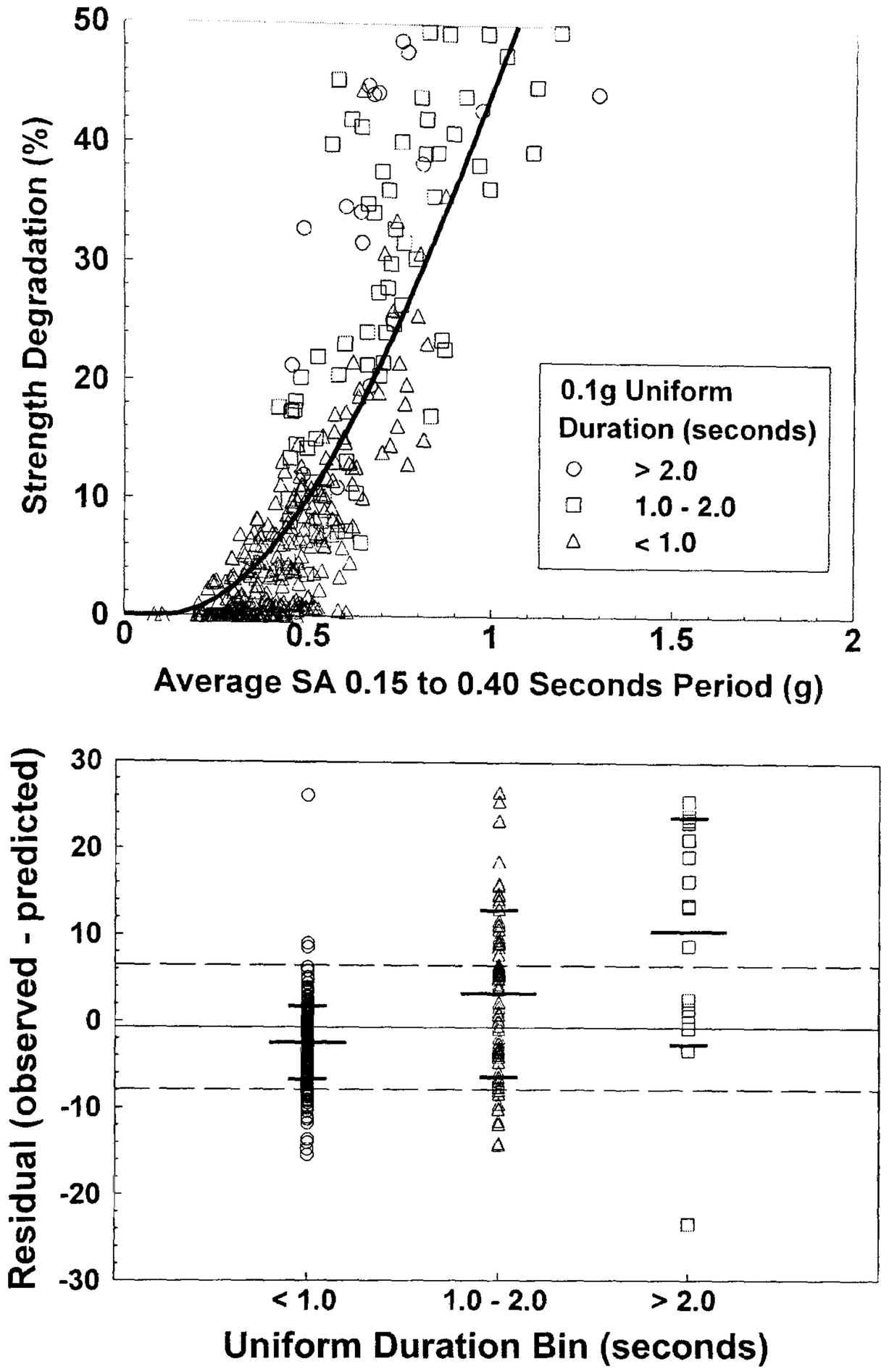


Figure 4.10. – Upper: As Figure 4.6 but with the data grouped according to the uniform duration at an acceleration threshold of 0.1g. Lower: Residuals from the trend line for different uniform duration bins; solid line indicates median, dashed lines show plus and minus one standard deviation.

The scatter illustrated in Figure 4.10 indicates that other factors also have an important role in determining the damage potential of an earthquake. To identify which parameters also have an influence on the strength degradation the records identified as outliers, with measured strength degradations that are either grossly under-or over-predicted by the correlations are examined. Ground motions containing strong pulses of velocity were found to cause more damage than others with similar duration and spectral acceleration. One such accelerogram was that of the 1994

Northridge (M_w 6.7) earthquake, recorded at 2 km from the fault rupture at West Pico Canyon Road. This record had only moderate spectral accelerations and duration, when compared with other records, but caused 100% strength degradation to the 0.1 and 0.15 second period structures and over 50% strength degradation to most of the other structures analysed. The destructive potential of high-energy pulses of motion near to the source of earthquakes is well known (e.g. Naeim 1995). These pulses are due to propagation of the fault rupture towards the site, resulting in constructive interference of the seismic radiation leading to concentrated pulses of motion, the dominant period of which increases with earthquake magnitude (Somerville *et al.* 1997; Somerville 2000; Bommer *et al.* 2001; Mavroeidis and Papageorgiou 2003).

4.6 Time-domain Response Spectra

In order to understand the influence of time-domain characteristics of the ground-motions on the response of masonry structures it is useful to plot a time-domain response spectrum of the ground motion. This contains all of the information present on a conventional response spectrum but is plotted in three-dimensions with time as the third axis. This technique has been used by several authors and is closely related to the "multiple filter technique" or "moving window analysis", which shows the frequency content of the ground motions with time. Trifunac (1971a) used three dimensional response spectra to aid the identification of the arrival of different seismic waves in the near-field for records with closely spaced arrivals and low signal-to-noise ratio. Trifunac shows that peaks in the 3D spectrum generated from strong-motion recordings of the 1940 Imperial Valley earthquake are caused initially by body waves, then by Rayleigh and Love phases reflected from different crustal layers (Figure 4.11).

Iyama and Kuwamura (1999) conduct time-frequency analysis using wavelets of the 1995 Hyogoken-Nanbu (Kobe) earthquake. They find that recordings near the source of the earthquake rapidly release energy over all frequencies, where as recordings at greater distances have longer-period motions that appear after the short-period motions. Part of this may be explained by the findings of Yokoyama (1996) who uses the results of wave propagation analysis to show that sedimentary surface waves developed in the Osaka plain under the action of the Kobe earthquake. The surface

waves travel in the thick upper sediments at velocities approximately half that of the shear waves in the underlying soil. This created long-period waves that lasted approximately 10 to 20s after the arrival of the direct seismic phases.

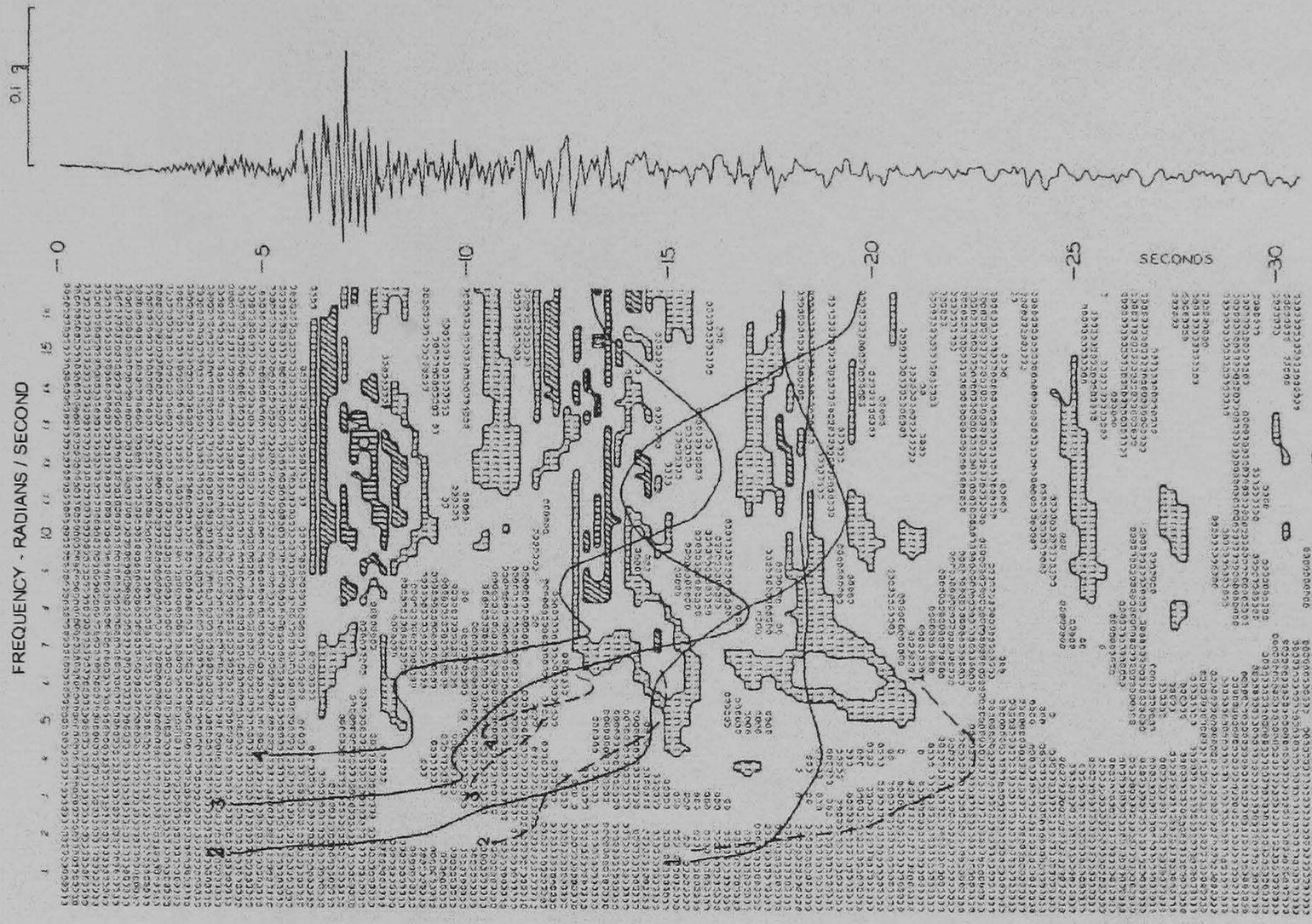


Figure 4.11. - Response Envelope Spectrum for Event 9, NS component of an aftershock from the 1940 Imperial Valley earthquake, recorded at El Centro, 10% damping; dashed and solid lines indicate Rayleigh and Love wave arrivals respectively (Trifunac 1971a)

Figure 4.12 shows the time domain response spectra of a ground motion with a high-energy pulse, which was identified in the last section as being particularly damaging. This type of ground motion is particularly damaging as the high spectral acceleration continues into the longer period range, causing continued loading as the structure degrades.

Figure 4.13 shows the frequency content of the ground motion from 1992 Landers earthquake, recorded 26km from the fault rupture at Fun Valley. The 3D response spectrum reveals the arrival of two, essentially separate, seismic phases that are not easily isolated on the original accelerogram. The first strong arrivals occur 8 to 10 seconds after the start of the record and have a predominant period of 0.3s. The

second arrivals start about 28 seconds from the start of the record and have a predominant period of 0.7s.

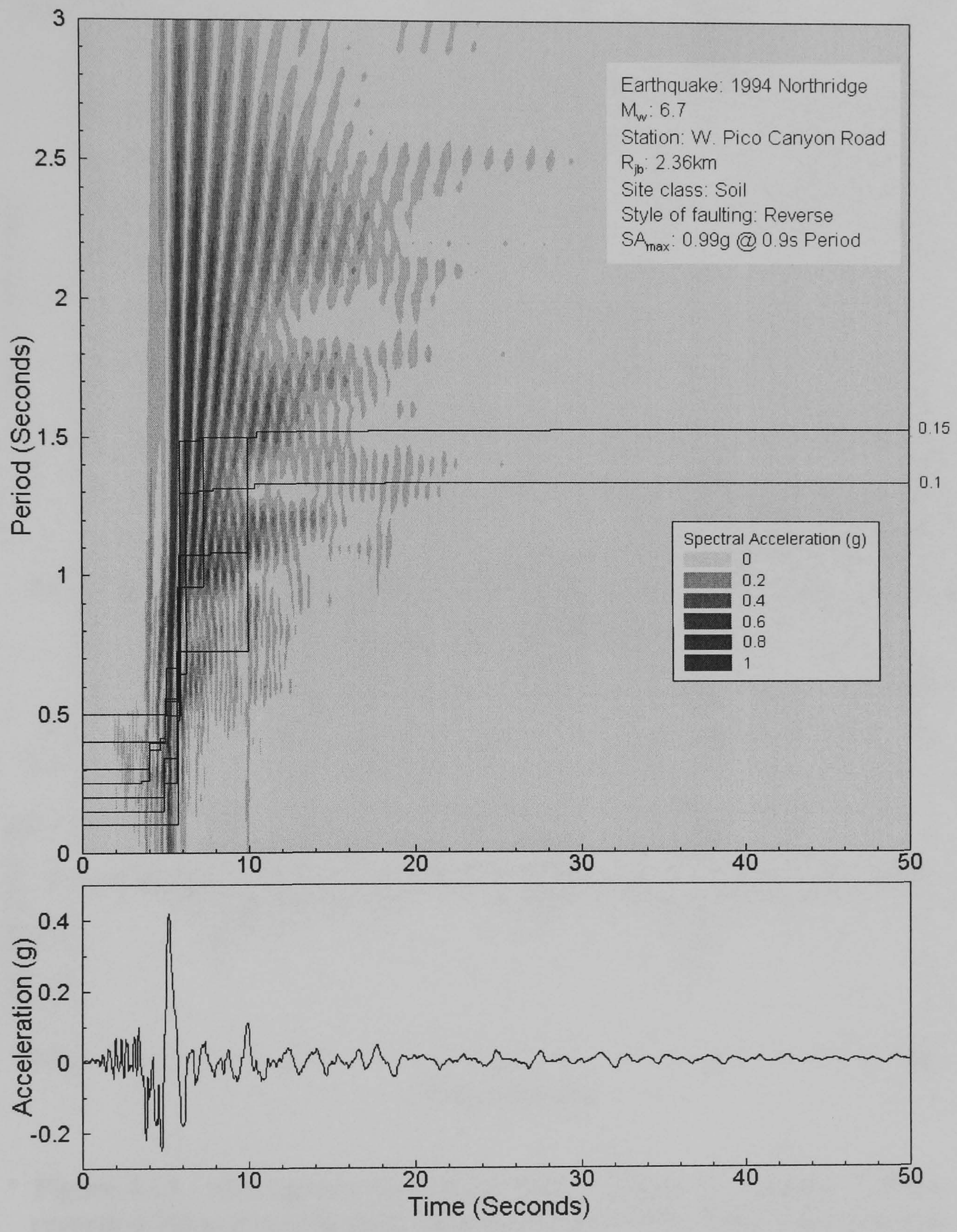


Figure 4.12. - 3D response spectra for 1994 Northridge ($6.7M_w$) earthquake, recorded at 2 km from the fault rupture at West Pico Canyon Road. Solid black lines on response spectra show stiffness degradation of masonry structures with 0.1, 0.15, 0.2, 0.25, 0.3, 0.4 and 0.5s initial period. Analysis of 0.2-0.5s structures halted when 2% drift limit exceeded.

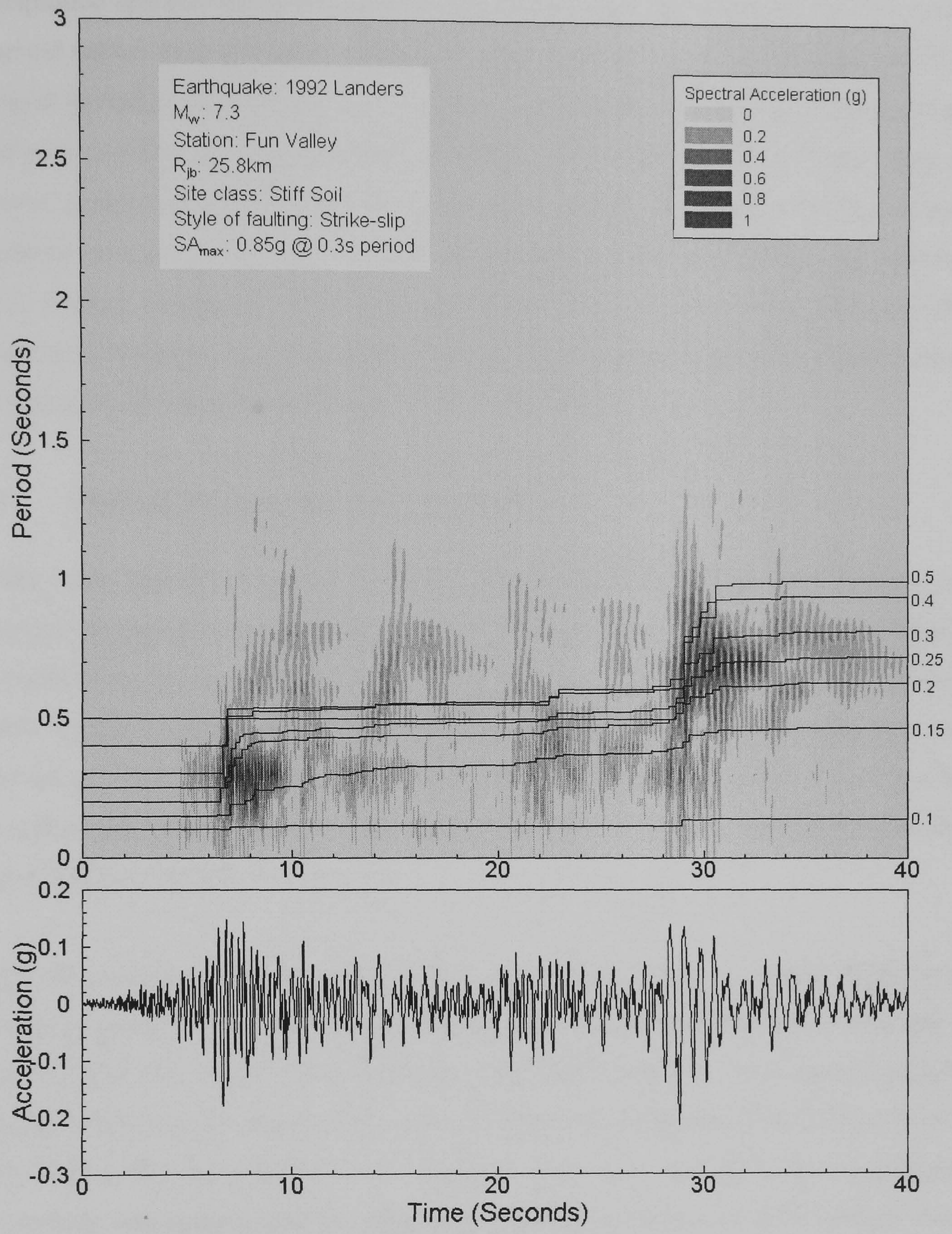


Figure 4.13. - 3D response spectra for 1992 Landers earthquake ($7.3M_w$), recorded 26km from the fault rupture at Fun Valley. Solid black lines on response spectra show stiffness degradation of masonry structures with 0.1, 0.15, 0.2, 0.25, 0.3, 0.4 and 0.5s initial period.

The influence of the different seismic phases on the response of masonry structures with different periods is shown on Figure 4.13 by solid black lines that track the increase in period as the stiffness degrades. As the ground motion contains only low-

amplitude spectral acceleration at 0.1s period, the masonry structure with this initial period suffers little damage or stiffness degradation. However, the structure with 0.2s initial period is damaged by the first wave train, which lengthens the period of the structure making it more susceptible to damage from the second wave train. Had the wave groups arrived in the opposite order, which would not be expected for recorded ground motions, the damage to the shorter-period structures would be less, although the spectral amplitude of the ground motion would be the same. This provides anecdotal evidence as to the importance of using ground motions with realistic phase content for the analysis of stiffness degrading structures.

4.7 Damage Measure Based on 3D Spectra

The correlation between the damage to the masonry structures with 0.15s initial period and the 3D spectral intensity proposed by Şafak (1998) is investigated. The 3D spectral intensity is calculated using the largest 20 cycles as proposed by Koliopoulos and Margaris (2001) with cycles counted using peak counting excluding non-zero crossings. The parameter is evaluated using both spectral velocity and spectral acceleration, but only the results using spectral acceleration are reported here as they give consistently better correlations.

The 3D intensity is evaluated between 0 to 5s period limits, the same period range used by Şafak (1998) and for a period range from the initial period of the structure T_0 to 2.7 times this period. The 3D intensity evaluated between 0 and 5s period is poorly correlated to strength degradation, with a correlation coefficient of 0.47 (Figure 4.14). Evaluating the 3D intensity over a period range from 0.15 to 0.40s significantly improves correlations and the correlation coefficient increase to 0.81 (Figure 4.14). However, the scatter is still significant and ground motions with essentially the same 3D spectral intensity create damage ranging from null to exceedance of the ultimate limit state (Figure 4.14).

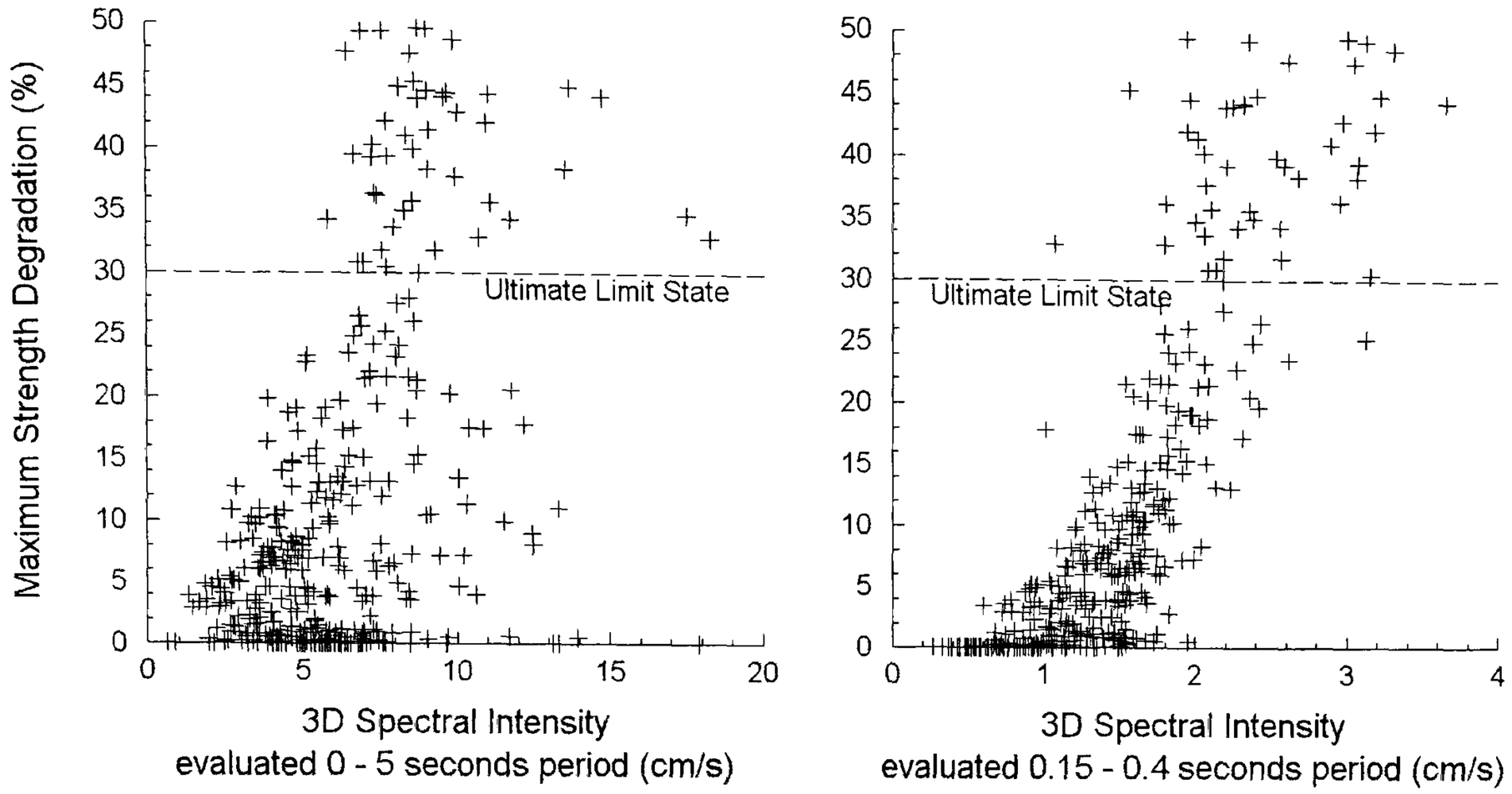


Figure 4.14. - Correlation between 3D spectral intensity proposed by Şafak (1998) and the strength degradation of masonry structures with 0.15s initial period. Intensity evaluated for period ranges 0 to 5s (*left*) and 0.15 to 0.4s (*right*).

To investigate scatter in the damage estimates from the 3D spectral intensity, time domain response spectra are plotted for two ground motions with similar 3D intensity but different damage levels. The first ground motion is from the $6.7M_w$ 1994 Northridge earthquake recorded 87km from the fault rupture on soft soil downstream of the Prado dam (Figure 4.15). This ground motion has a 3D spectral intensity, evaluated between 0.15 and 0.4s period, of 1.95 cm/s and causes a strength degradation of less than 1% in the masonry model with natural period of 0.15s. The 3D response spectrum shows that although this ground motion contains many cycles of motion these are only of damaging amplitude for a narrow period range between about 0.2 and 0.5s. The spectral acceleration at 0.15s is not sufficient to damage the structure.

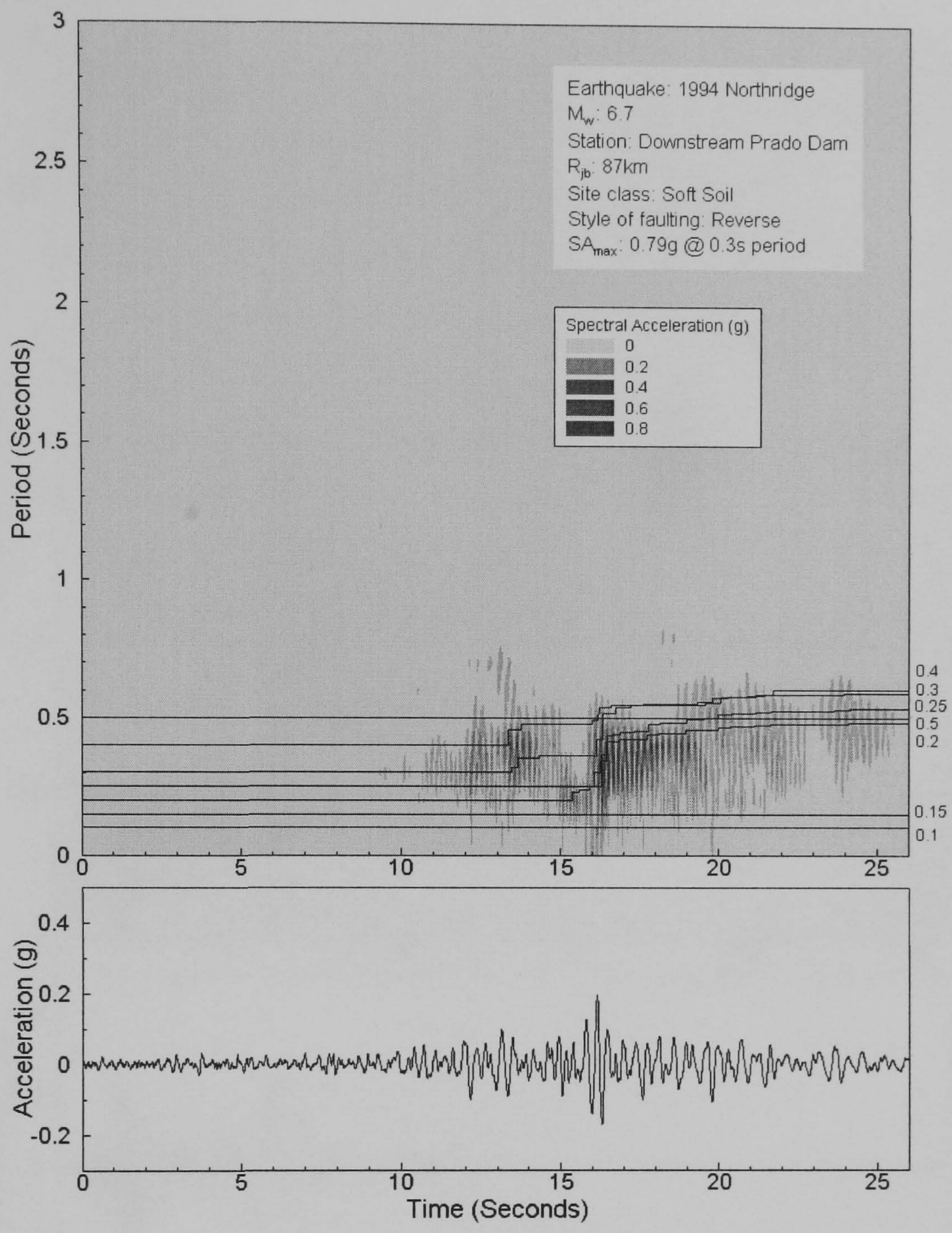


Figure 4.15. - 3D response spectra for 1994 Northridge (6.7M_w) earthquake, recorded at 87 km from the fault rupture on soft soil downstream of the Prado dam. Solid black lines on response spectra show stiffness degradation of masonry structures with 0.1, 0.15, 0.2, 0.25, 0.3, 0.4 and 0.5s initial period.

The second ground motion is from the 6.3M_w 1984 Morgan Hill earthquake recorded at 11km from the fault rupture on stiff soil at Gilroy 6 (Figure 4.16). This ground motion causes 49% strength degradation and has a 3D spectral intensity, evaluated between 0.15 and 0.4s period, of 1.94 cm/s. The 3D response spectrum shows that this ground motion is particularly damaging because the high-frequency arrivals are followed by strong accelerations with longer period, which continue to damage the more flexible weakened structure.

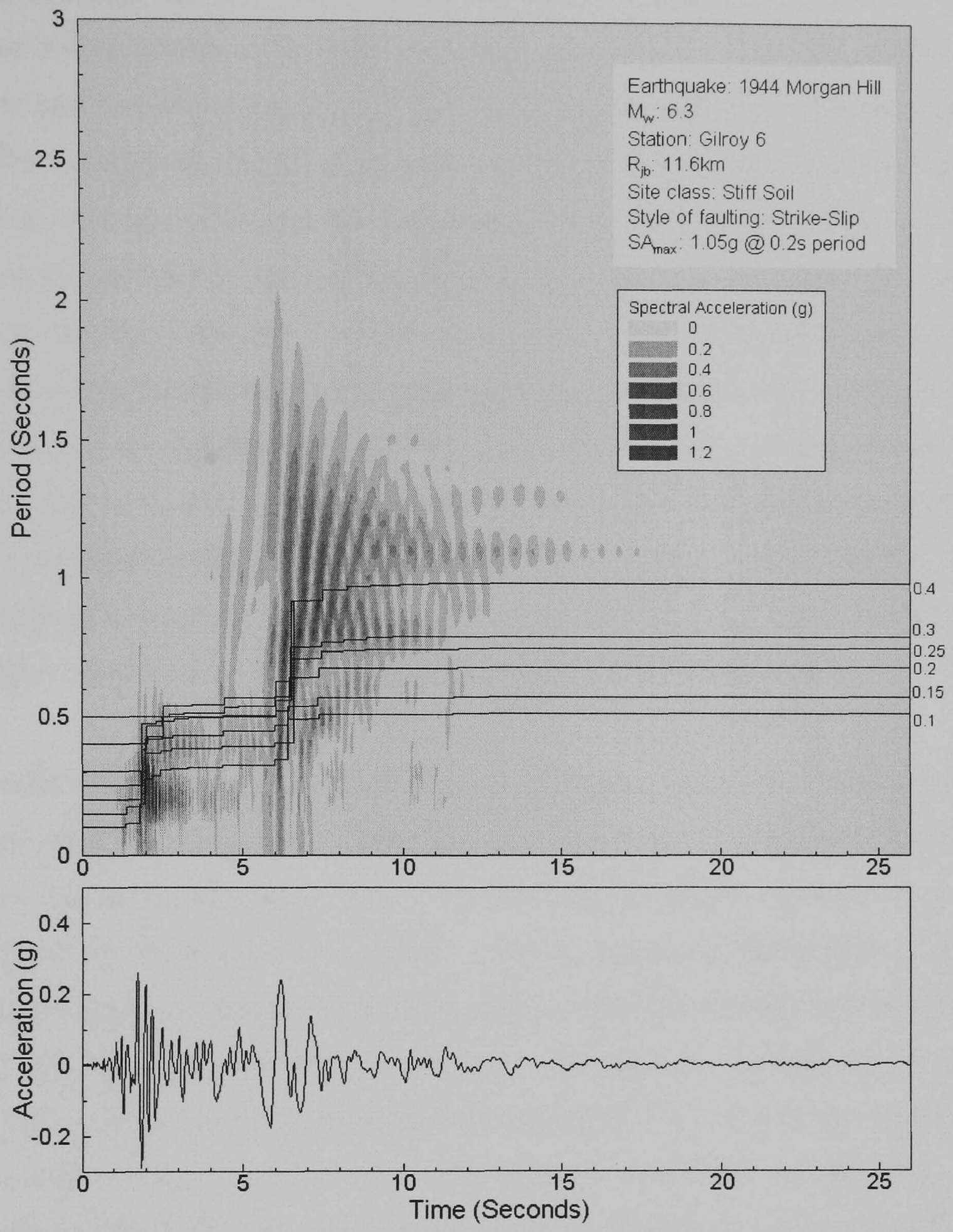


Figure 4.16. - 3D response spectra for 1984 Morgan Hill ($6.3M_w$) earthquake, recorded at 11 km from the fault rupture on stiff soil at Gilroy 6. Solid black lines on response spectra show stiffness degradation of masonry structures with 0.1, 0.15, 0.2, 0.25, 0.3, 0.4 and 0.5s initial period. Analysis of 0.5s structure halted after 2% drift limit exceeded.

4.8 Summary and Further Work

The analyses presented in this chapter have shown that for ground motions with comparable ordinates of spectral acceleration, those with longer duration cause greater damage, as measured by strength degradation, in masonry structures. This is simply empirical verification of expected structural behaviour, which suggests that

the methodology used in HAZUS for reducing demand on the basis of shorter duration is conceptually valid. The results also demonstrate the degree of influence of duration and how this influence compares with the underlying uncertainty associated with the correlations between ground-motion parameters and structural damage. Verification of the actual duration-dependent spectral adjustments made in HAZUS is not directly possible because of the different damage measures employed. HAZUS correlates damage with peak drift and accounts for effects of accumulated damage by using empirical factors, whilst this study implicitly accounts for accumulated damage by measuring the strength degradation of the structure. It would be an interesting further study to model a selection of masonry structures under the action of different ground motions using both the hysteretic model used in this chapter and the simplified procedure used in the HAZUS methodology. This would enable a more quantitive assessment of the empirical adjustment factors to be made.

This work demonstrates that the correlation between damage of masonry structures and the spectral acceleration of the ground motion can be improved by using an average spectral acceleration from the initial period of the structure to a period approximately three times this period. This is logical as the period of masonry structures increases with the decrease in stiffness caused by progressive damage. The results also show that duration is positively correlated to damage for events with similar spectral acceleration although there is significant scatter in the residuals. The range of the scatter indicates that other factors also have an important role in determining the damage potential of an earthquake. Some of the records with higher than predicted strength degradation are from events with pulse-like near-source ground motions.

The uniform duration – defined as the sum of time intervals for which the acceleration is above a specified threshold – provides a better insight into the damage potential of the ground motion, for a given average spectral acceleration, than the other duration measures. The standard deviation of other definitions of duration, such as effective, significant and bracketed durations, are comparable to one another. Since this study is based on structures with strongly degrading characteristics of strength and stiffness, features not expected in new construction, no conclusions can be drawn regarding the value of incorporating the influence of duration into force-based

seismic design. The findings do indicate, however, that the seismic assessment of existing masonry buildings would be improved by taking account of the expected duration of earthquake ground motion.

Plotting the response spectrum in three dimensions with time as a third axis can be used to show the influence of time-domain ground-motion characteristics on damage. By overlaying the effective period of the masonry structures, calculated using the degraded stiffness of the structure, on the 3D response spectra is particularly useful. This shows that the structures are initially damaged by high-frequency ground motions and then further damaged by motions at longer period. This demonstrates that it is important to have ground-motions with realistic phases for the analysis of a stiffness degrading structures, a condition not generally met by synthetically generated ground-motions.

5. PREDICTING DURATION AND NUMBER OF CYCLES

This chapter investigates the parameters that influence ground-motion duration and number of cycles. This is achieved by reviewing predictive equations derived by different authors and by examining the number of cycles in suites of recorded accelerograms. In the second section of the chapter a new predictive equation is derived for relative bracketed duration, which was proposed by Professor I. M. Idriss (UC Davis) as a simple measure that could be used for the assessment of the liquefaction potential of soils.

5.1 Predicting the Number of Cycles of Motion

This section describes the parameters that influence the number of cycles of ground motion. The existing equations in the literature for predicting the number of ground-motion cycles are reviewed and the number of effective cycles counted directly from a small suite of accelerograms is investigated. To enable easy visualization of results the number of cycles of motion that are counted directly from accelerograms are expressed in terms of the definition of the number of effective cycles (N_{cy}) used by Malhotra (2002):

$$N_{cy} = \frac{C}{2} \cdot \sum_{i=1}^{2tn} \left(\frac{u_i}{u_{\max}} \right)^c \qquad (5.1)$$

where u_i is the amplitude of the i^{th} half cycle, u_{max} is the amplitude of the largest half cycle, and tn is the total number of cycles. C and c are application-dependent damage coefficients: C is a linear scale factor and c determines the relative importance of different amplitude cycles. Krawinkler (1987) suggests that a c value from 1.5 to 2.0 is appropriate for determining the fatigue failure of welded steel components. Jeong and Iwan (1988) used c=2 to represent the fatigue damage of wide flange steel columns and c=6 for rectangular reinforced concrete columns. Malhotra (2002) proposed c=2 as a reasonable value. Values of c=2 and C=1 are adopted for this study.

5.1.1 The influence of earthquake magnitude

Earthquake magnitude is universally acknowledged as the parameter that exerts the greatest influence on the number of cycles of motion. The greater number of ground-motion cycles from larger magnitude earthquakes has led to the magnitude scaling factor used in liquefaction assessment (Youd and Idriss 2001; Arango 1996). However, Figure 5.1 shows that there is no conclusive agreement on the expected number of cycles for any given earthquake magnitude.

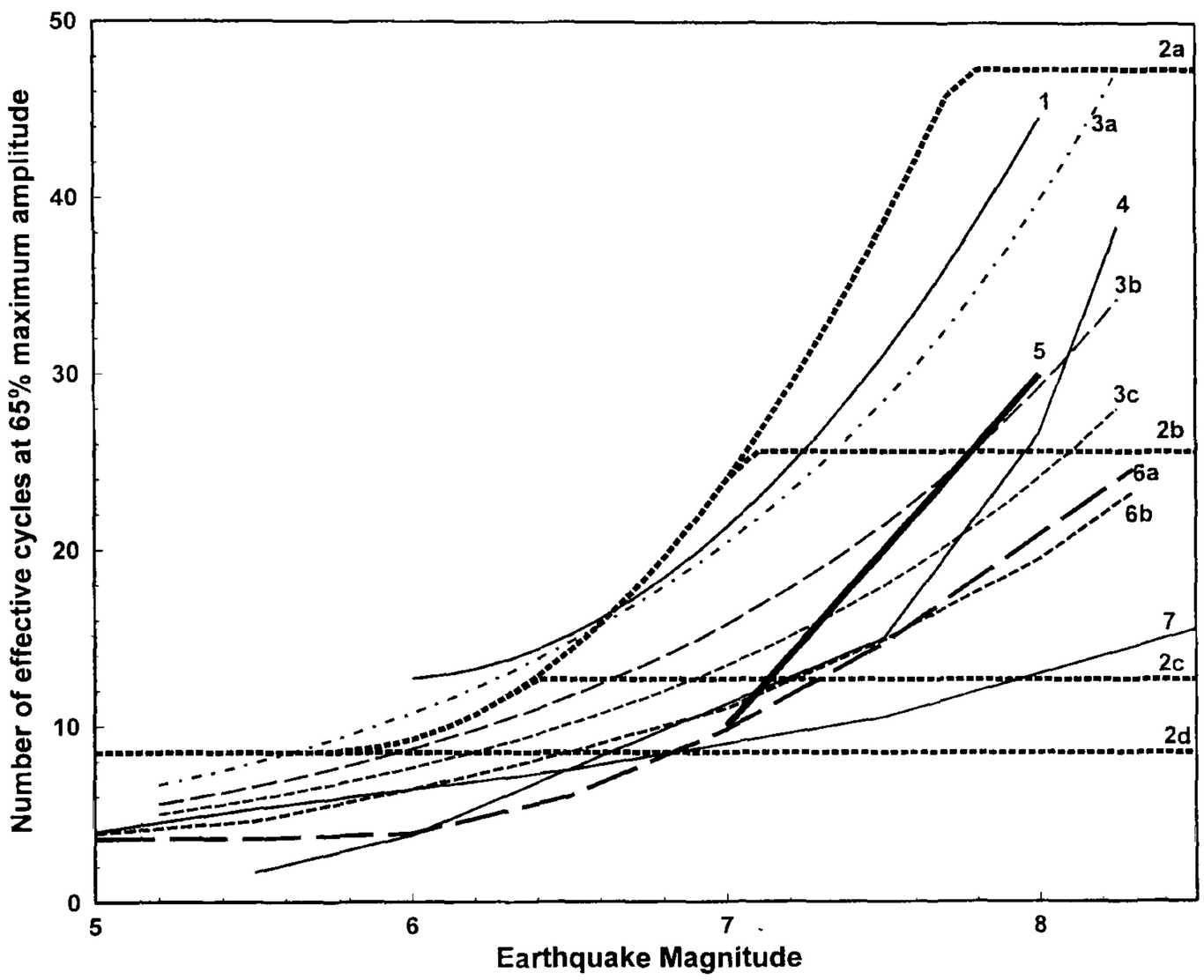


Figure 5.1. - Predicted median values of the number of effective cycles at 65% maximum amplitude as a function of magnitude: 1 – Haldar and Tang (1981), mean weighting; 2a – Green (2001) 60km distance; 2b Green (2001) 40km distance; 2c Green (2001) 20km distance; 2d Green (2001), 0km Distance; 3a – Liu et al. (2001) 10km distance, field-based weighting; 3b – Liu et al. (2001) 10km distance, averaged weighting; 3c – Liu et al. (2001) 10km distance, laboratory-based weighting; 4 – Arango (1996); 5 – Seed and Idriss (1971); 6a – Seed et al., (1975) using the strongest component of motion; 6b – Seed et al., (1975) using both components of motion, evaluated separately; 7 – Valera and Donovan (1977).

All of these studies were conducted for the assessment of liquefaction potential and use relative cycle counting definitions that count the number of effective acceleration cycles at a reference amplitude equal to 65% of the maximum peak amplitude (PGA).

The more recent studies employ moment magnitude, whilst the magnitude scale used for earlier studies is not known and may be one source for the differences amongst the predictions. Other predictive parameters such as the source-to-site distance and site classification are only used in some of the studies, which is another potential source of difference. These issues, in addition to the use of different functional forms, are a common source of disagreement amongst predictive equations for any ground-motion parameter. Differences amongst these studies could additionally be caused by the following factors related to the definition of the number of cycles:

- Different cycle counting definitions used: most studies count peaks but do not define how non-zero crossing peaks are handled. The study by Liu *et al.* (2001) is unusual as it uses the vector sum of the horizontal components and counts both peaks and troughs of the motion.
- Different amplitude-importance relationships are used to convert the numbers of irregular amplitude cycles into a number of equivalent cycles of constant amplitude.

There appears to be considerable difference in the functional forms used by different researchers. Exact differences are difficult to establish, as many studies do not state the functional form used but simply give numbers of effective cycles expected for different magnitudes. Haldar and Tang (1981) conduct extensive regression analyses for the number of effective cycles at different reference levels using a second order polynomial functional form:

$$N_{eqx} = \beta + \gamma M + \delta M^2 \tag{5.2}$$

where N_{eqx} is the number of effective cycles at a particular reference level, M is the earthquake magnitude, β, γ and δ are coefficients determined by regression. The functional form used by Liu *et al.* (2001) is the most complex and includes magnitude, source-to-site distance and site classification:

$$\ln\left(N_{PR(65\%)}\right)=\ln\left[\frac{\left(\frac{\exp\left(C_1+C_2\left(M_W-C_3\right)\right)}{10^{1.5M_W+16.05}}\right)}{4.9\cdot10^6\cdot C_4}+S\cdot C_5+R_{jb}\cdot C_6\right] \tag{5.3}$$

where C_1, C_2, C_3, C_4, C_5 and C_6 are coefficients determined by regression, M_W is the moment magnitude, R_{jb} is the shortest distance to the surface projection of the fault, S is a dummy variable that takes the value of 0 for rock sites and 1 for sites classified as soil, $N_{PR(65\%)}$ is the number of equivalent cycles counted at a reference level of 65% PGA counting both acceleration peaks and troughs.

The influence of magnitude on the number of effective cycles is also investigated in the present study using 28 strong-motion accelerograms from crustal earthquakes, with magnitudes ranging from $3.9M_w$ to $7.8M_w$. All accelerograms were recorded at sites classified as rock, at distances between 5 and 20km from the surface projection of the fault rupture. The accelerograms have been selected from the dataset used by Bommer *et al.* (2004).

The number of effective acceleration cycles (Eqn. 5.1) is calculated for each record using rainflow range counting, peak counting including and excluding non-zero crossings (Figure 5.2). As would be expected larger magnitude earthquakes generally produce ground motions with greater numbers of effective cycles. Different functional forms of trend lines were tried and, although the scatter in the results is significant, an exponential magnitude dependence gives the greatest coefficient of determination, R^2 (Figure 5.2). Part of the scatter may be caused by rupture directivity; one of the accelerograms with an exceptionally large number of cycles is that of the 1994 $6.7M_w$ Northridge earthquake recorded at Monte Nido Fire Station. This record has backward directivity and is discussed in the following section.

Small magnitude earthquakes rupture over a small area and produce high-frequency ground motions, which are typically narrow-banded because of a lack of long-period motion. These ground-motions contain few non-zero crossing peaks, so both peak counting definitions converge for small magnitude events (Figure 5.2). For the records used in this example, the rainflow counting definition gives consistently

higher numbers of effective cycles than peak counting definitions. However, this is not always the case but depends on the amplitude of the non-zero crossing peaks and troughs in the time-history.

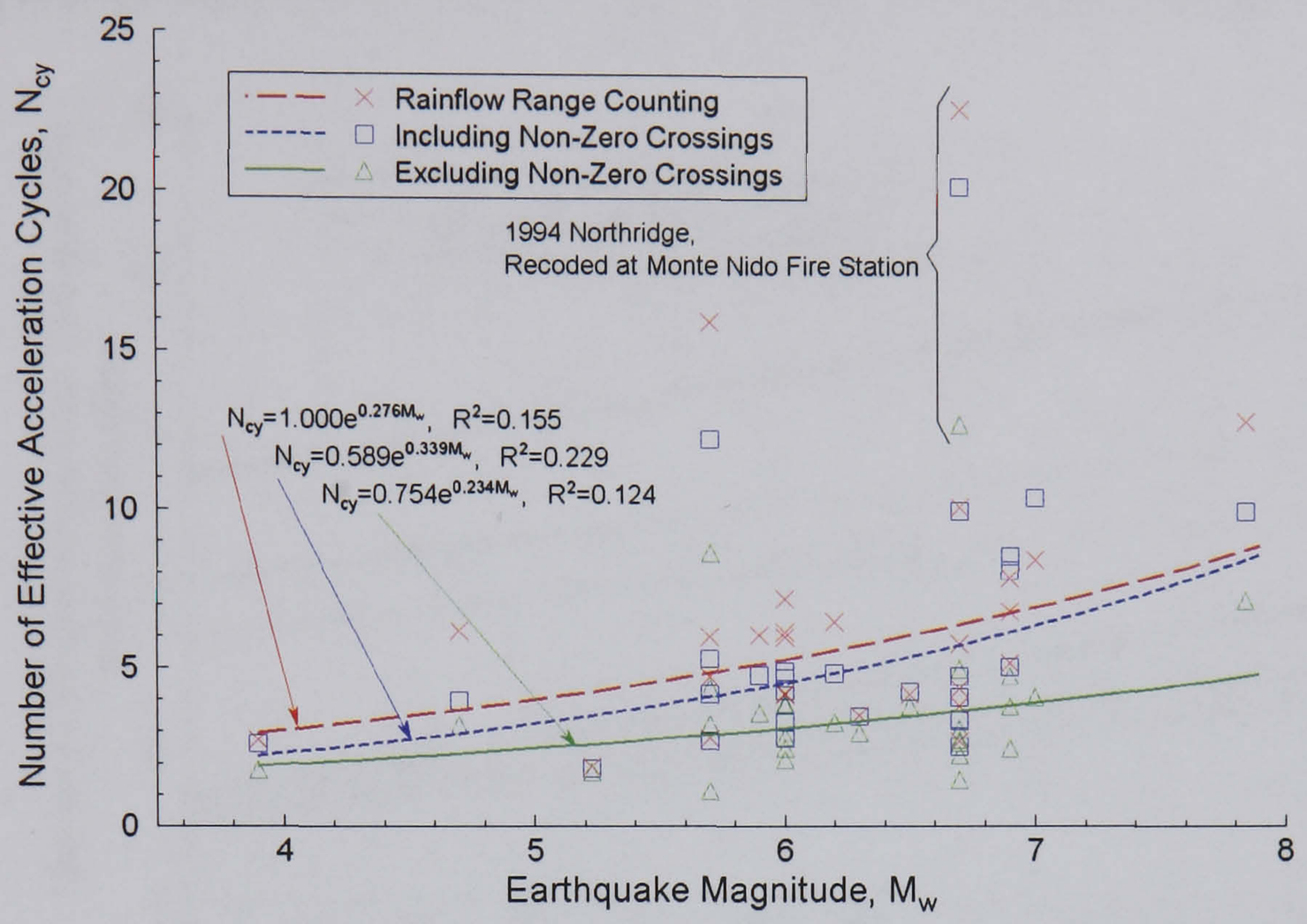


Figure 5.2. - Relationship between number of effective cycles and earthquake magnitude. All accelerograms were recorded between 5 and 20km from surface projection of the fault rupture at sites classified as rock. Exponential trend lines shown by dashed and solid lines.

5.1.2 Source-to-site distance

Only three of the studies reviewed (see section 2.4.8 for a full listing) develop predictive relations for the number of cycles of motion using the source-to-site distance as a predictive parameter. These are Lu *et al.* (1998), who derived predictive relations of the total number of ground velocity cycles for use in the fatigue assessment of pipelines, and Green (2001) and Liu *et al.* (2001) who determine predictive equations for the number of effective acceleration cycles for use in liquefaction analysis. All of these studies use relative cycle counting definitions that normalise the cycles to the maximum amplitude, which results in the number of cycles increasing with distance due to scattering, different travel paths and wave velocities (Figures 5.3 and 5.4). Manfredi *et al.* (2002, 2003) also find that the number of equivalent cycles, defined using a structural measure based on the

accumulated hysteretic energy normalised to the maximum response displacement, increases with distance by a factor of about 1.3 up to a distance comparable with the length of the rupture and a further factor of about 1.1 over greater distances.

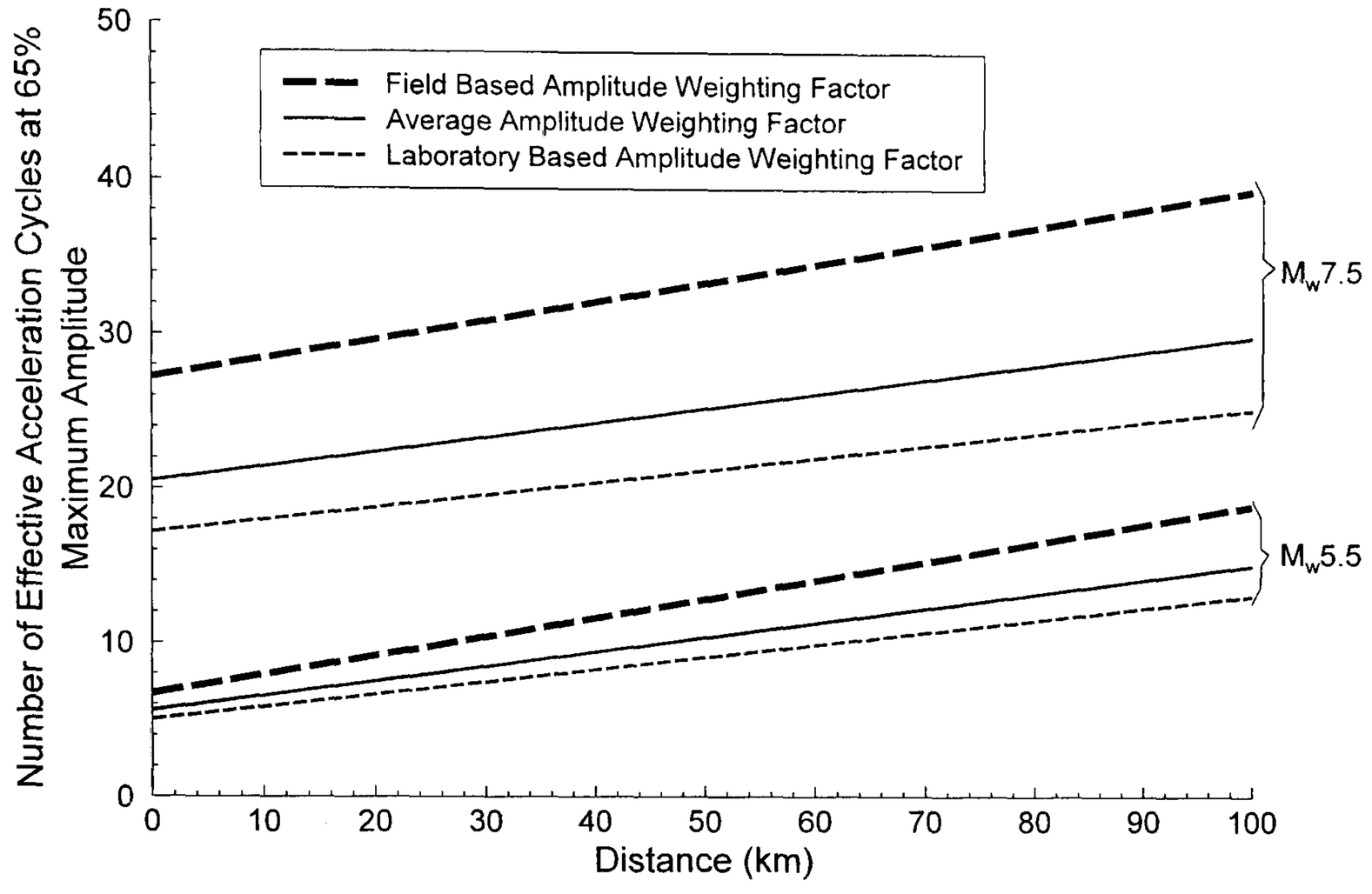


Figure 5.3. - Predicted median values of the number of effective cycles at 65% maximum amplitude as a function of distance, according to the equations of Liu *et al.* (2001).

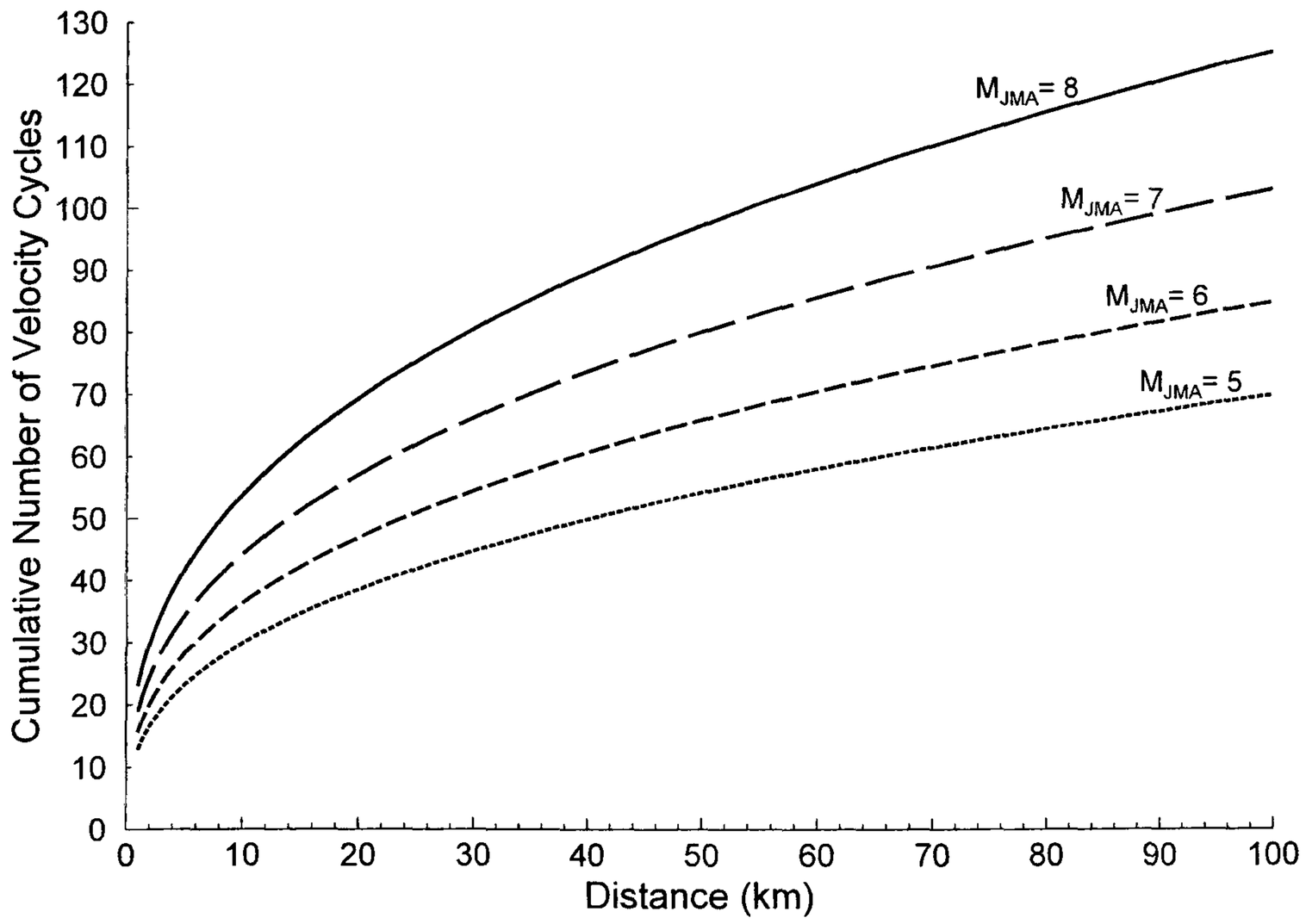


Figure 5.4.- Predicted total number of velocity cycles as a function of source-to-site distance, according to the equations of Lu *et al.* (2001).

All of the aforementioned studies employ relative definitions of the number of cycles, and find that the number of effective cycles increases with distance. However, definitions based on absolute measures, where the same absolute reference level is employed for all ground motions, would be expected to result in a decrease in the number of cycles with increasing distance.

The number of effective acceleration cycles (Eqn. 5.1) in 78 accelerograms from the 1994 6.7 M_w Northridge earthquake is calculated to investigate the influence of site-to-source distance (Figure 5.5). Distances are defined as the closest distance from the surface projection of the fault rupture to the site (R_{jb}), as proposed by Joyner and Boore (1981). The rainflow range counting, non-zero crossing and zero crossing peak counting methods are used. Trend lines indicate that the number of effective cycles increases with distance. However, the increase is small, approximately one cycle in 30km, and the scatter in the data leads the coefficients of determination, R^2, to be less than 0.04 for all forms of trend line.

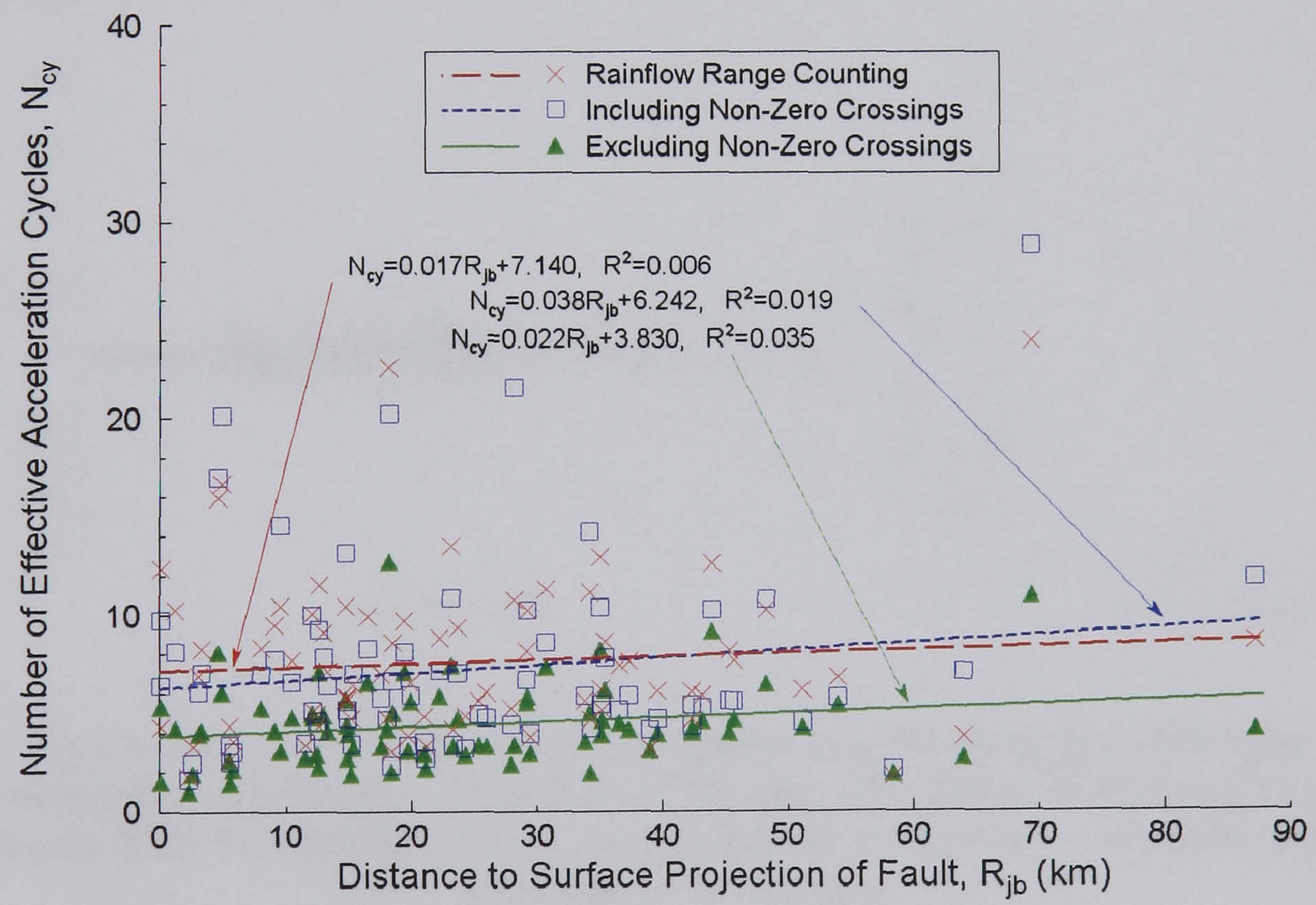


Figure 5.5. - Relationship between number of effective cycles and source-to-site distance for 78 accelerograms from the 1994 6.7 M_w Northridge earthquake; linear trend lines shown by dashed and solid lines.

The scatter in the prediction is investigated further by plotting two of the accelerograms recorded on rock at approximately 20km from the fault rupture that have different numbers of cycles (Figure 5.5). The difference appears to be caused by rupture directivity (e.g. Somerville *et al.* 1997). The accelerogram recorded at Castic (Old Ridge Route) is located in the forward directivity region, causing fewer acceleration peaks with longer period and larger amplitude. The accelerogram recorded at Monte Nido Fire Station is from the backward directivity region, which results in a greater number of acceleration peaks, although these have lower amplitude (Figure 5.6).

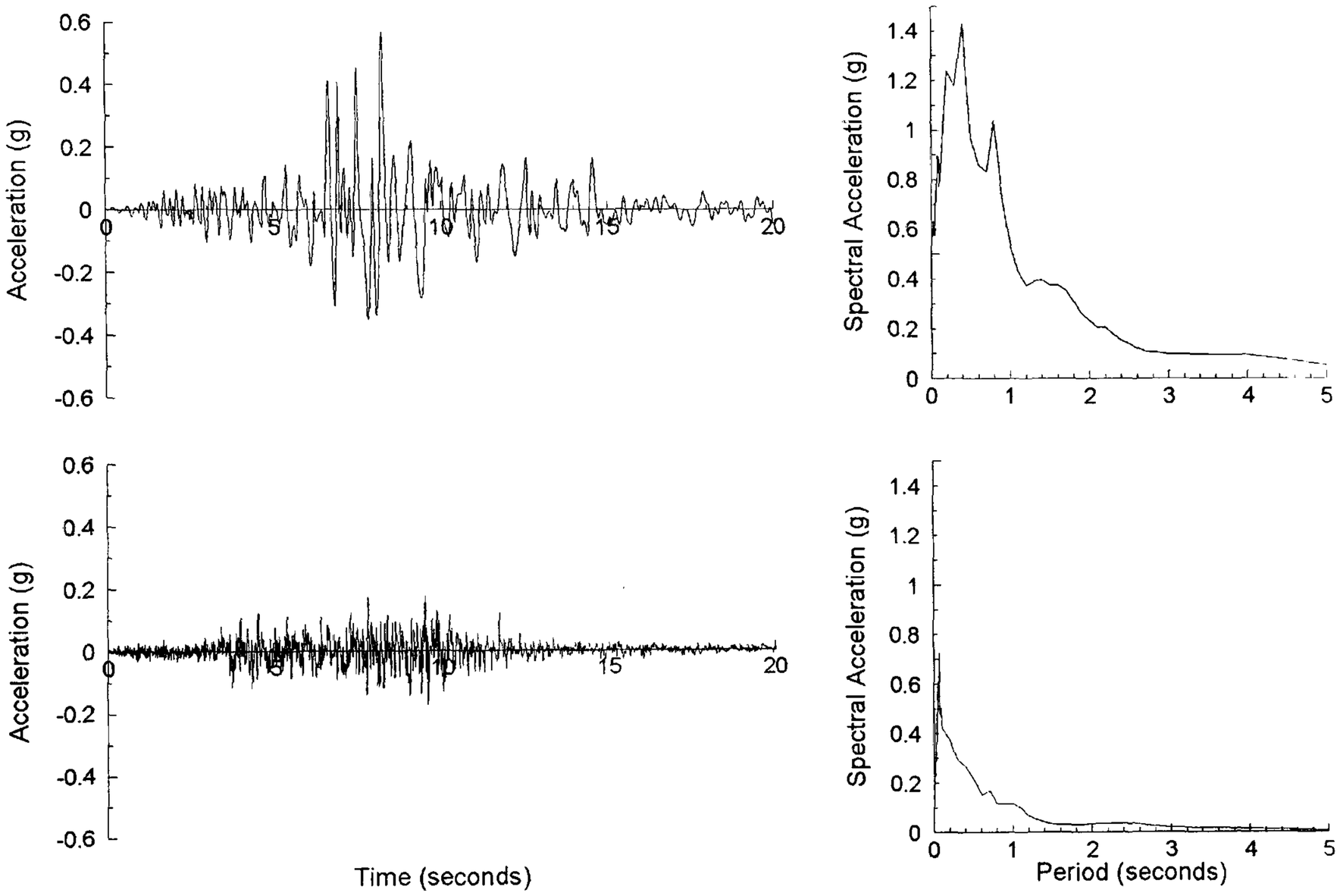


Figure 5.6. - Accelerograms and response spectra from the 1994 6.7M_w Northridge earthquake, recorded at Castaic – Old Ridge Route (*upper*) and Monte Nido Fire Station (*lower*), both stations on rock approximately 20km from the fault rupture.

5.1.3 Rupture directivity

The duration of strong-ground motions is influenced by the rupture duration, which is shorter for earthquakes with bi-lateral rupture than for those with uni-lateral rupture (Bommer and Martínez-Pereira, 1999). However, it is the direction in which the

rupture propagates that is of importance to the number of cycles of ground motion. If the rupture propagates towards the site, waves generated on different parts of the fault rupture can arrive together leading to constructive interference resulting in a few large amplitude cycles of ground motion. If the rupture propagates away from the site then the ground motions would be expected to contain many cycles of lower amplitude as the seismic waves arrive out of phase (Liu *et al.* 2001; Somerville *et al. 199*7).

5.1.4 Site soil classification

The regression analysis conducted by Liu *et al.* (2001) shows that motions at sites classified as soil have up to about 10% more cycles of motion than at those classified as rock, a small difference also suggested by a number of studies reporting recordings from downhole arrays and site responses analyse (Youd and Idriss 2001; Seed and Idriss 1967; Mohammadioun 1997). These show that the soil can change the amplitude of the motions, but the number of cycles remains approximately the same with only the high-frequency cycles filtered out by increased soil damping. An exception to this is sites located in sedimentary basins: body waves are converted to surface waves at basin edges, which then propagate across the basin (Joyner 2000). Soil damping reduces the number of high frequency cycles in the motion leaving the large amplitude, longer period basin waves to dominate the motion. The filtering of high-frequency waves at such sites would be expected to reduce the number of effective cycles measured by a relative counting definition, whilst the larger amplitude surface waves increase absolute measures of effective cycles.

5.1.5 Ground motions with broad-banded frequency content

Non-zero crossings in any time-history, including ground and structural motions, occur when the signal has broad-banded frequency content. As discussed in Chapter 2, the presence of non-zero crossings is particularly important as it causes differences in the number of cycles estimated by different cycle counting definitions.

Several researchers have developed response spectra including the number of cycles of motion (e.g. Şafak 1998; Malhotra 2002; Kawashima and Aizawa 1986). These spectra show the amplitude of the secondary peaks of motion as well as the maximum

peak traditionally displayed on a response spectra. As response spectra are produced from the motion of elastic single degree-of-freedom (SDOF) systems, some authors have suggested that the motion will be narrow banded, containing only zero crossing peaks. However, examination of the actual motion shows that only the response of SDOF systems with periods lower than the dominant period of the ground motion are narrow banded. This is illustrated in Figure 5.7, which shows the displacement time-histories of 2.5s and 0.5s SDOF systems with 5% damping under the action of ground motions recorded 32km from the fault rupture at Shelter Cove 2 from the 1992 7.1M_w Cape Mendocino (Petrolia) earthquake. The motion of the 0.5s SDOF system has few non-zero crossing peaks, while the 2.5s SDOF system has many. The Fourier transform of the motions (Figure 5.8) shows that the motion of the 2.5s SDOF system retains the broad-banded frequency content of the ground motion whist 0.5s SDOF system effectively filters out the broad-banded content of the ground motion.

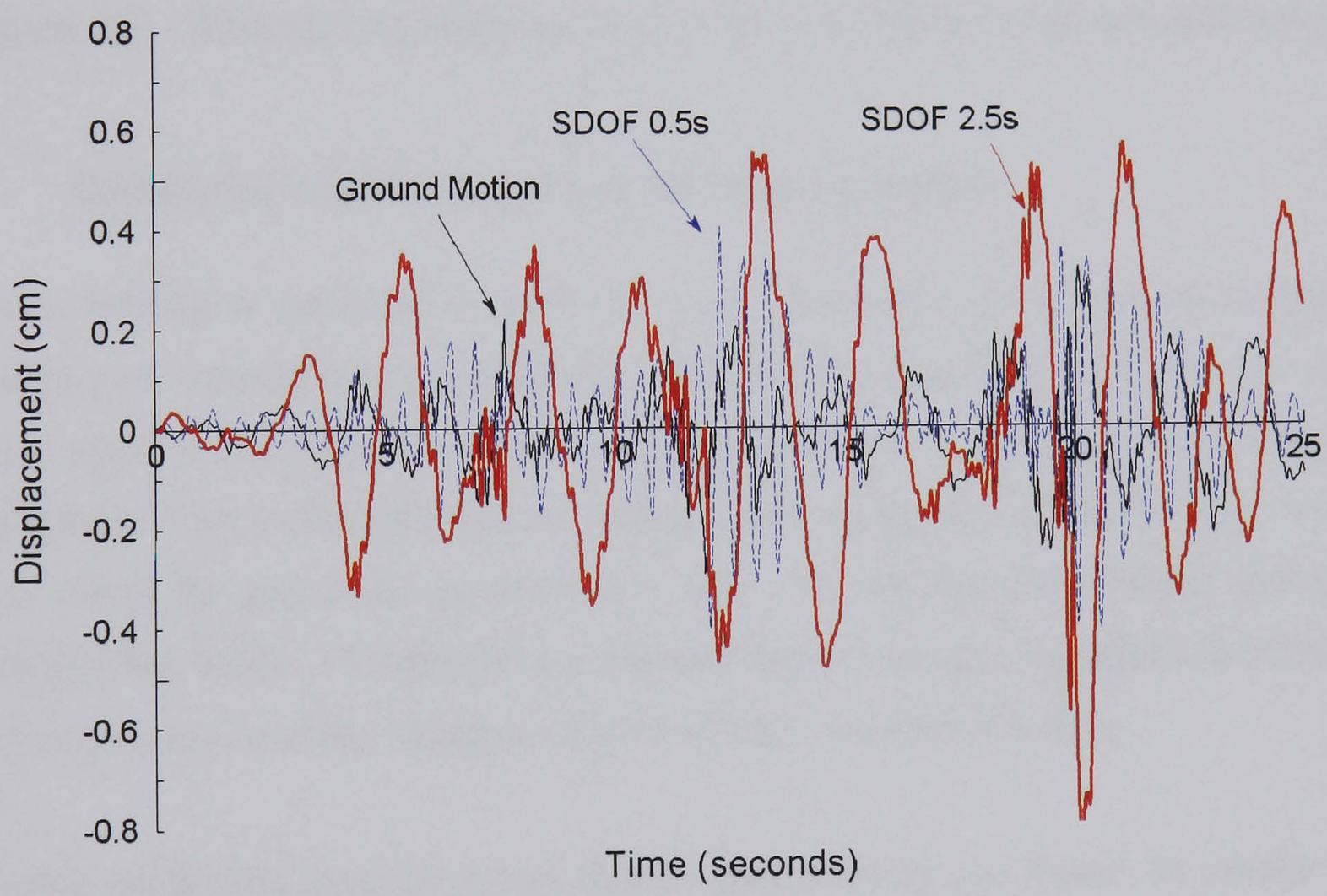


Figure 5.7. - Displacement time histories of 2.5s and 0.5s SDOF systems with 5% damping under the action of 1992 7.1 M_w Cape Mendocino (Petrolia) earthquake ground motions recorded 32km from the fault rupture at Shelter Cove 2 (stiff soil).

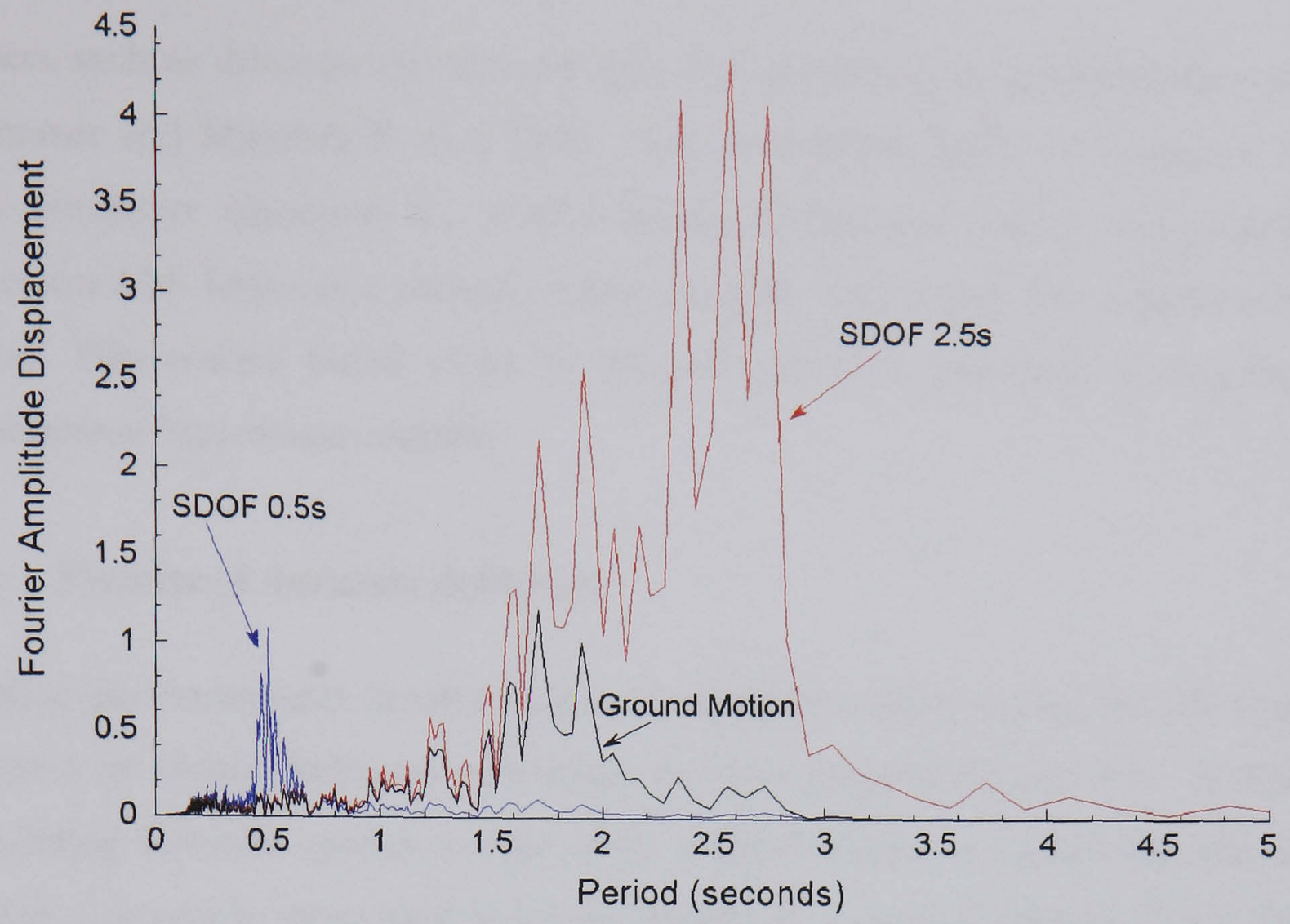


Figure 5.8. - Fourier amplitude spectra of the time histories shown in Figure 5.7.

5.2 Developing Liquefaction-Based Bracketed Duration

Cyclic loading of saturated or partially saturated granular soil during an earthquake causes pore water pressure to increase. The pressure rises with each stress or strain cycle until a condition is reached when pressure is generated faster than it is dissipated. With sufficiently severe loading conditions some soil types reach a critical state where the pore water pressure is so high that the effective stress is reduced to critically low levels. This results in a dramatic loss of strength, liquefaction of the soil and constitutes a serious hazard to any overlying structures or slopes.

Current techniques used to assess liquefaction potential are based on results from laboratory testing of soils under uniform cycles of loading and on observations of soils in the field after actual earthquakes (Scott 1994; Youd and Idriss, 2001). At present ground-motion duration and number of cycles are taken into account by a magnitude scaling factor. This assumes that ground-motion duration, and number of loading cycles, is purely related to earthquake magnitude. Whilst earthquake magnitude must be of fundamental importance it is widely recognised that other

factors such as distance and site soil type also contribute to ground-motion duration (Bommer and Martinez-Pereira 1999; Youd and Idriss, 2001). This section derives new predictive equations for relative bracketed duration, which was proposed by Professor I.M. Idriss as a parameter that could be used to develop a duration scaling factor. This scaling factor could be used instead of a magnitude scaling factor in liquefaction hazard assessments.

5.2.1 Premise of duration definition

Typical laboratory tests involve uniform amplitude loading cycles, but the variations of stress (or strain) during an earthquake are quite irregular (Figure 5.9). Methods for converting irregular cycles to equivalent uniform cycles are available and involve similar concepts to those used in fatigue studies of structures (Lee and Chan 1972) so this work is also applicable to structures with near zero period. The cyclic stress versus number of equivalent cycles, such as those shown in Figure 5.10 and Figure 5.11, provides the means to convert the irregular stress time-series into a number of uniform stress cycles.

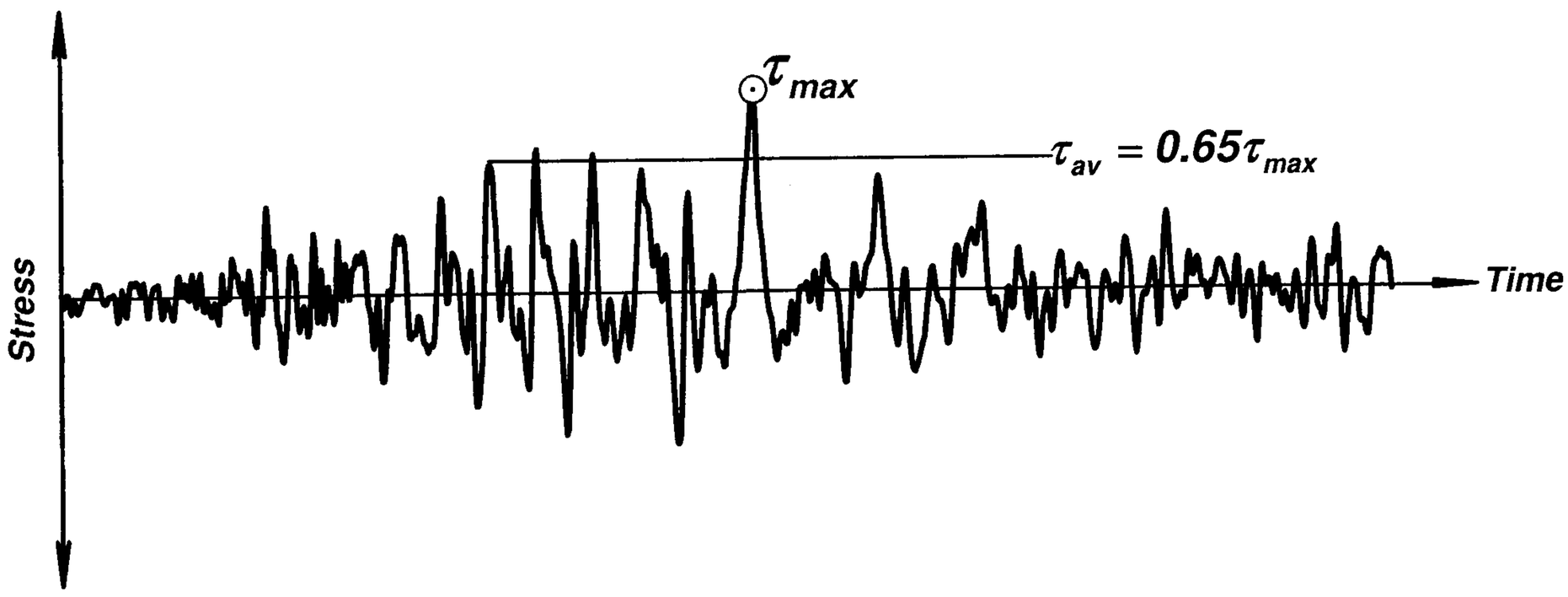


Figure 5.9. - Time-series of shear stresses induced by earthquake ground motions

The information in Figure 5.10, for example, indicates that 10 uniform cycles at a stress level of about 16 kN/m^2 would cause liquefaction in the specimen. It also indicates that at a stress level of about 12 kN/m^2, 40 cycles are required to cause

liquefaction in the specimen. Thus, if an irregular stress time-series consists of two cycles, one cycle with a peak stress of 16 kN/m^2 and the other cycle having a peak stress of 12 kN/m^2, the irregular time-series can be converted to an equivalent uniform stress time-series having 1.25 (i.e., 1 + 10/40) cycles with a peak stress of 16 kN/m^2, or 5 (i.e., 1 + 40/10) cycles with a peak stress of 12 kN/m^2.

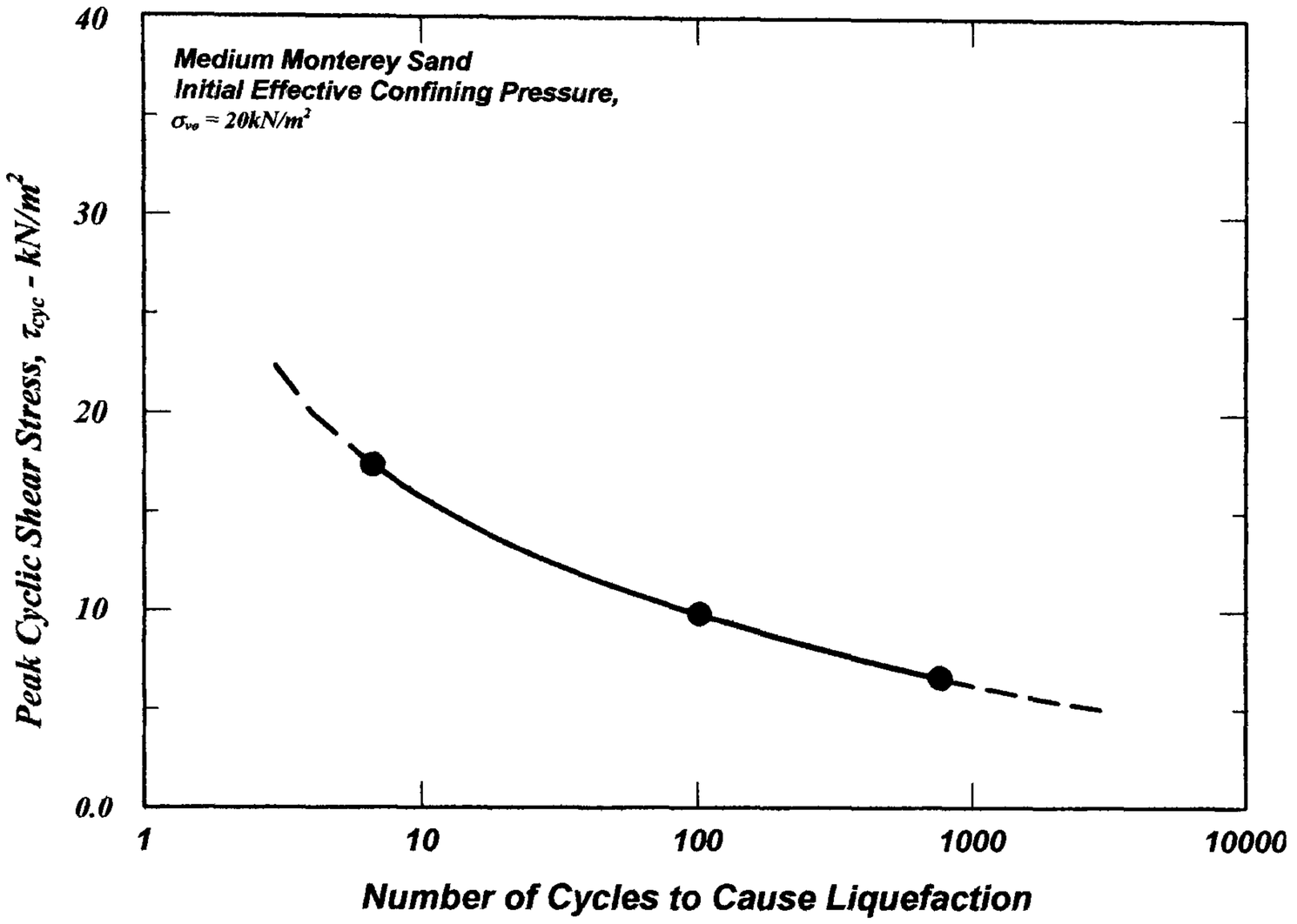


Figure 5.10. - Typical form of the relationship between cyclic shear stress and the number of cycles to cause failure – simple shear conditions

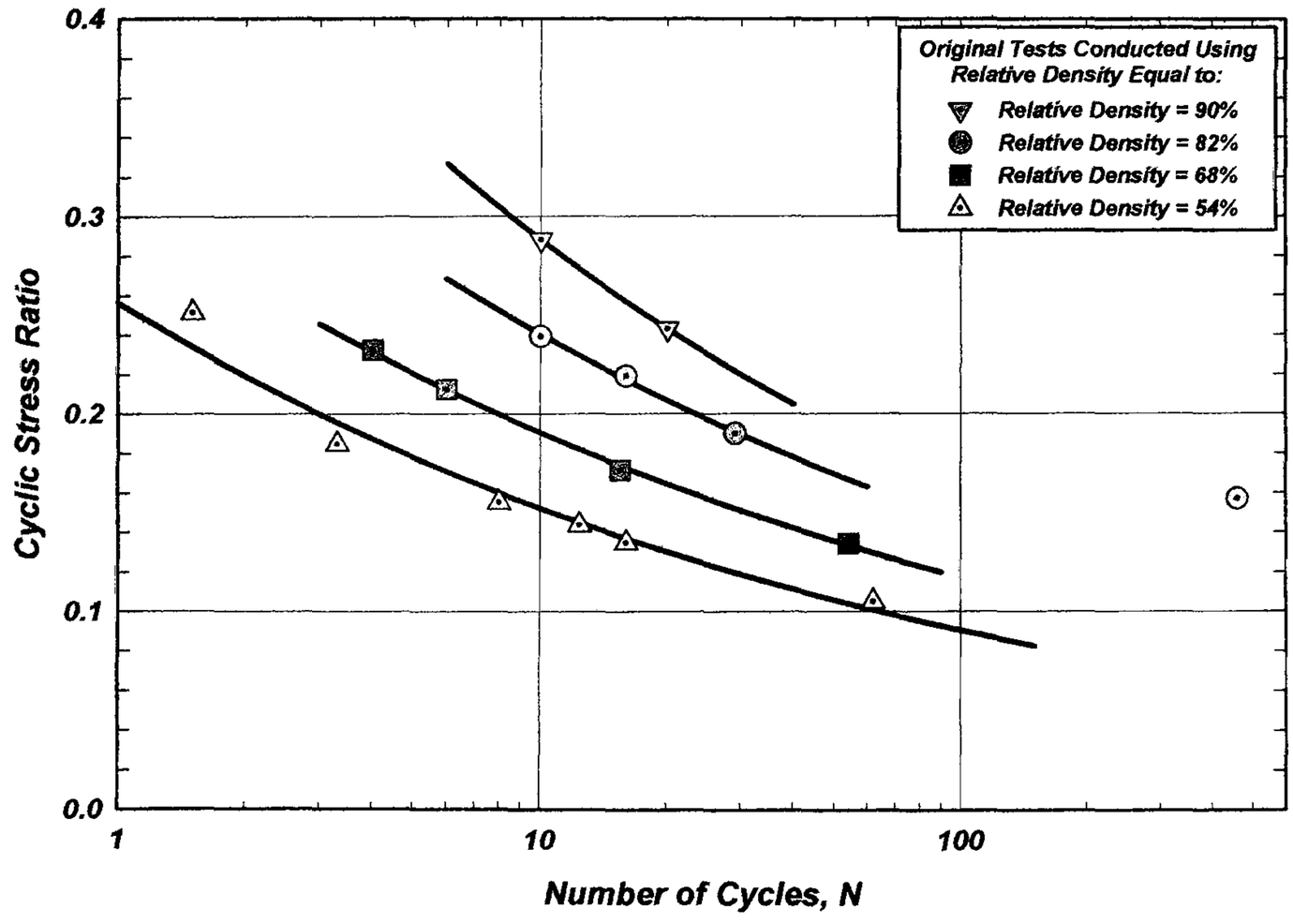


Figure 5.11. - Cyclic stress ratio required to reach initial liquefaction (From shaking table tests by DeAlba *et al.* 1976)

This process can be carried out for any given irregular time-series so that it can be represented by an equivalent number of stress cycles each having the same peak stress. Obviously, such a conversion process depends on the relationship relating cyclic stress required to cause liquefaction and number of cycles. The curve representing cyclic stress required to cause liquefaction versus number of cycles can usually be drawn as a straight line on a log-log plot. Thus, the number of equivalent uniform cycles determined for any given irregular stress time-series depends on the slope of this line. Therefore, the number of cycles would depend on the sample obtained in the field (frozen or conventional tube samples) or the method used to reconstitute remoulded samples. Examples of test results, expressed in terms of cyclic stress ratio, CSR, are shown in Figure 5.11 for reconstituted samples (DeAlba *et al. 1976*), and in Figure 5.12 for both intact and reconstituted samples (Yoshimi *et al. 1984*).

The tests by DeAlba *et al.* (1976) were conducted on samples reconstituted to relative densities of 54, 68, 82 and 90%. The data points shown in Figure 5.11 were normalized to a relative density of 68% at 10 cycles and are presented in Figure 5.13. Also shown in Figure 5.12 are the test results published by Yoshimi *et al.* (1984) for the frozen samples and for the tube samples. The best fit straight line (on a log-log plot) for each data set is also shown in Figure 5.13.

The line for the frozen samples has a much steeper slope than the line for the tube samples. The slope of the line for the reconstituted samples, however, has essentially an identical slope to that for the tube samples.

The lines in Figure 5.13 are reproduced in Figure 5.14 after normalising each line to CSR.

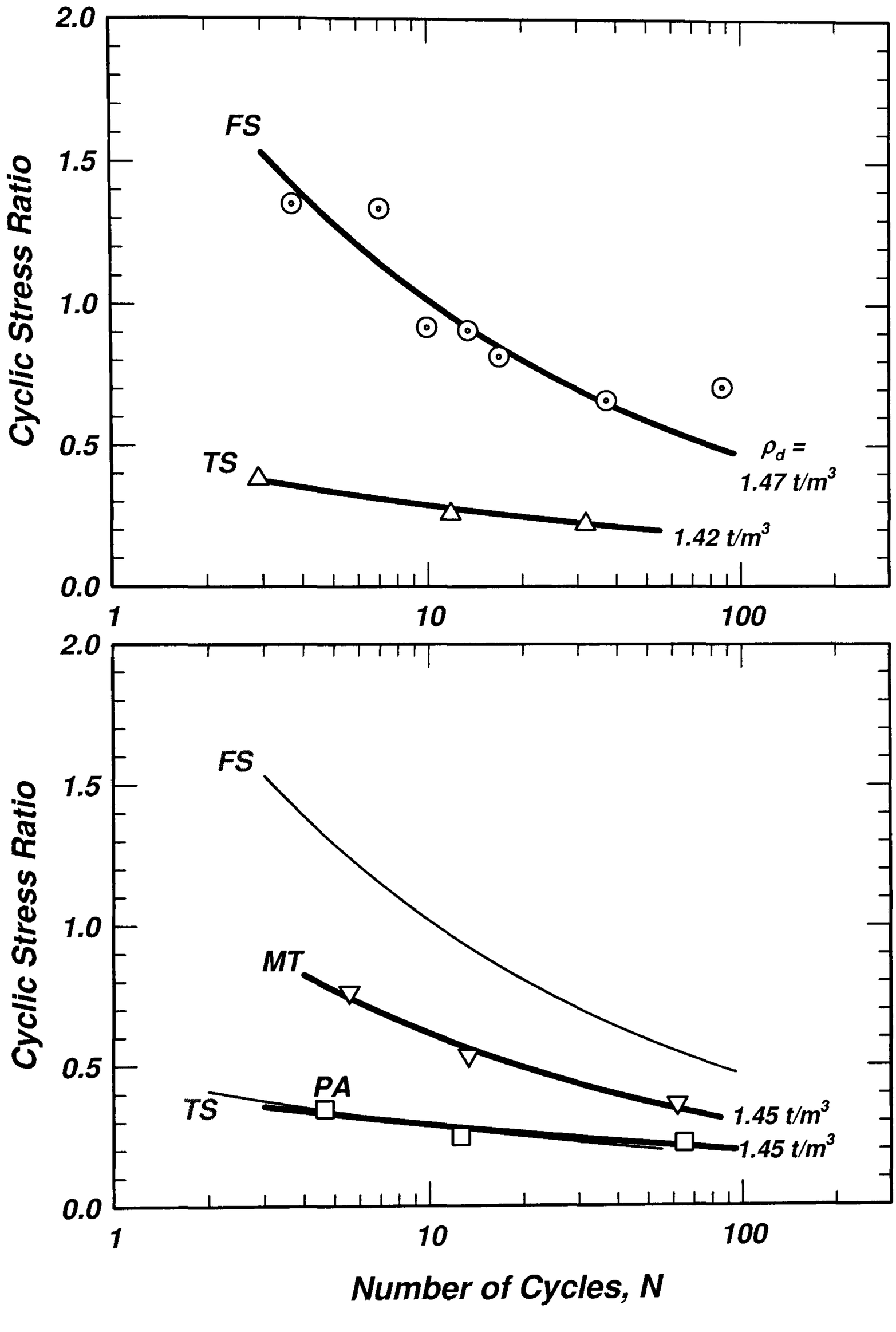


Figure 5.12. - Cyclic stress ratios required to cause 5% double amplitude axial strain of in-situ frozen samples (*FS*) compared with those of conventional "undisturbed" tube samples (*TS*) and samples reconstituted by pluviation through air (*PA*) and samples reconstituted by moist tamping (*MT*); effective initial consolidation pressure = 98 kPa (from Yoshimi *et al.* 1984).

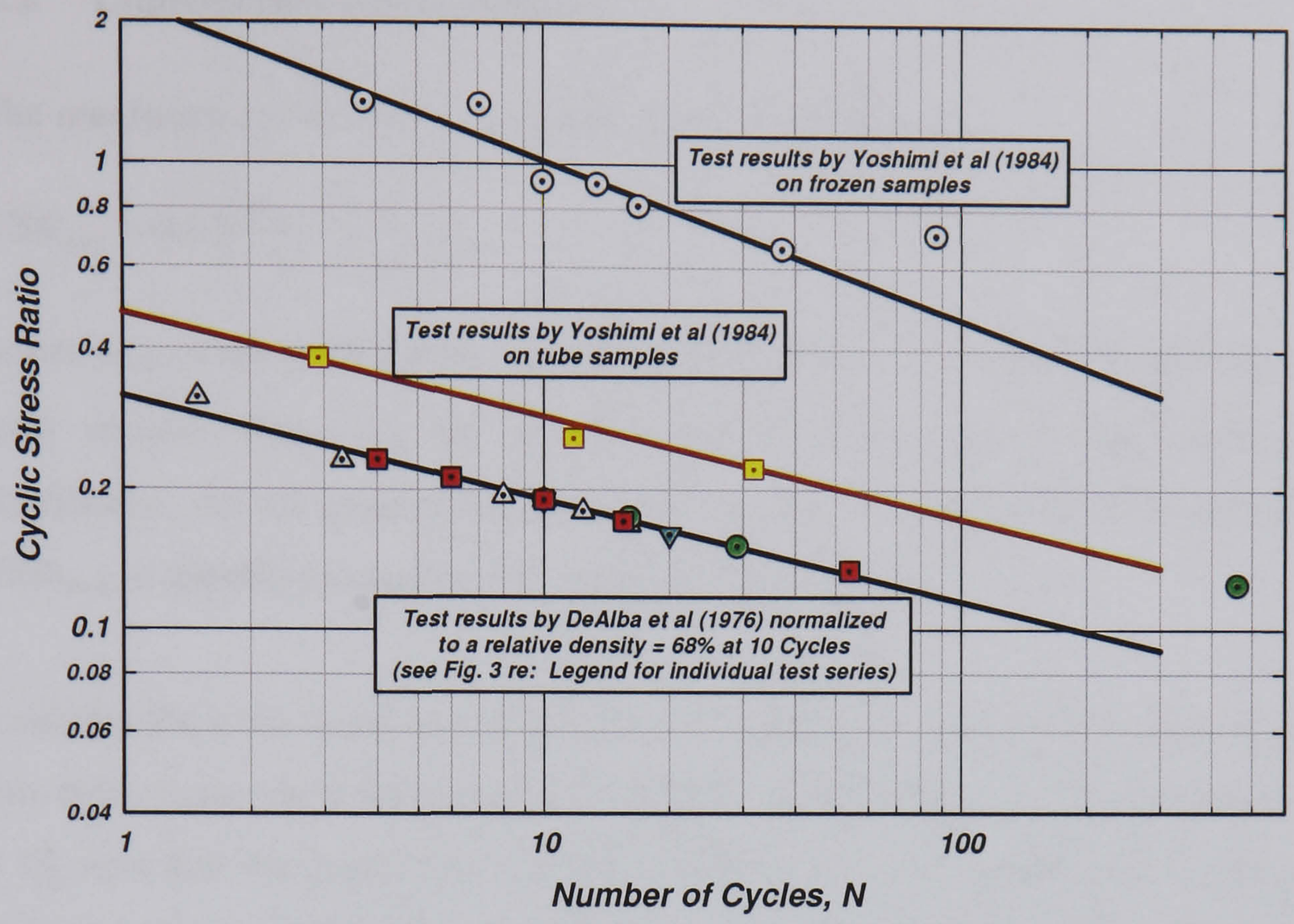


Figure 5.13. - Comparison of the cyclic stress ratio to cause liquefaction obtained for frozen samples and tube samples tested by Yoshimi *et al.* (1984) and for reconstituted samples tested by DeAlba *et al.* (1976)

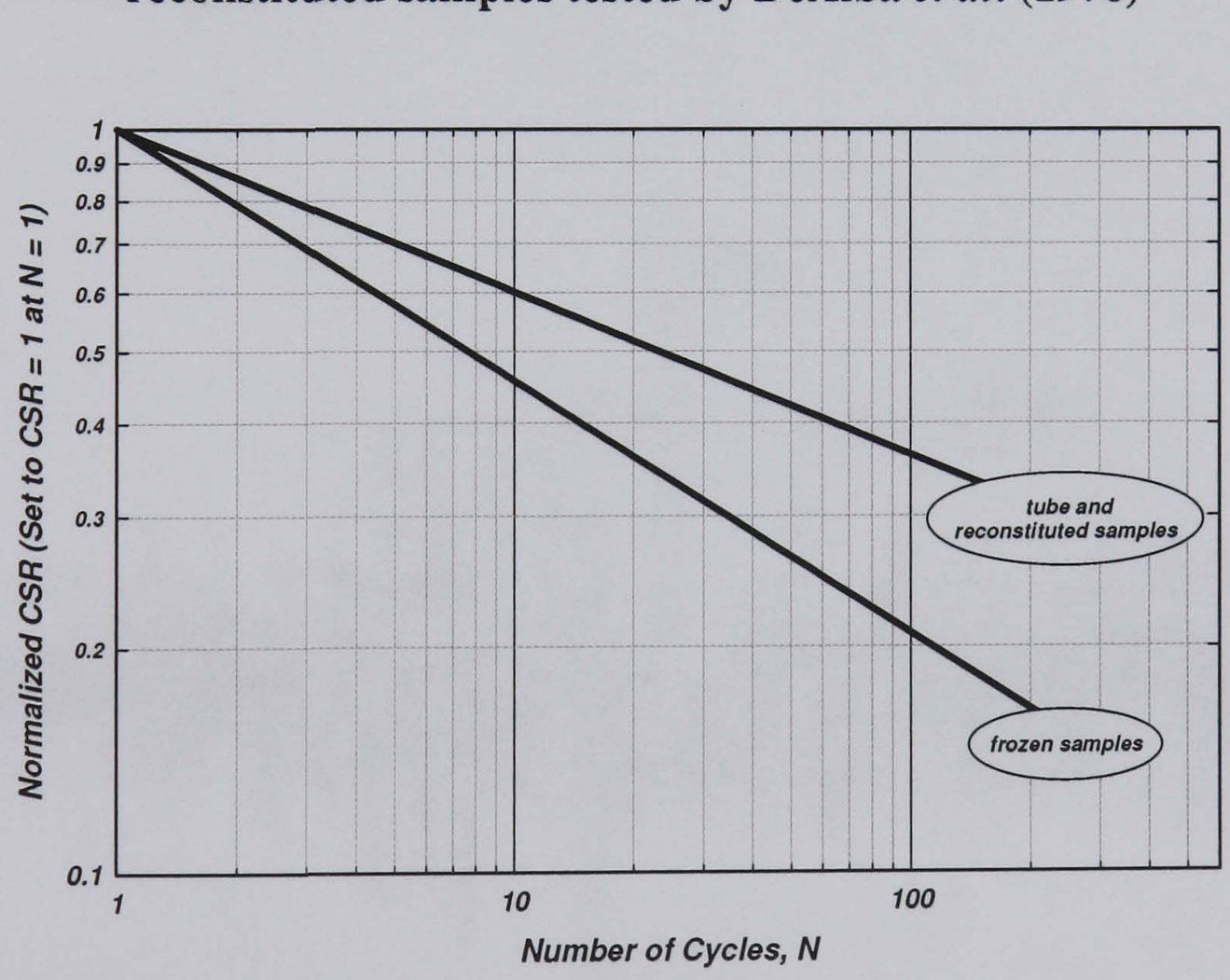


Figure 5.14. - Normalized cyclic stress ratio versus number of cycles to cause liquefaction

5.2.2 Liquefaction-based duration

The maximum cyclic shear stress ratio CSR_{max} is defined as:

$$CSR_{max} = 0.65\left(\frac{a_{max}}{g}\right).\left(\frac{\sigma_v}{\sigma_v'}\right).r_d \qquad (5.4)$$

where a_{max} is the peak ground acceleration, g is the acceleration of gravity, σ_v is the total vertical stress, σ'_v the effective vertical stress, and r_d the stress reduction coefficient. As all ground motions used in this work are recorded at the surface CSR_{max} is directly proportional to peak ground acceleration.

Consider the time-series of cyclic stress ratio shown in Figure 5.15. The ordinates of this time-series were normalised to produce a peak $CSR_{max} = 1$ as shown in Figure 5.15; note that this peak occurs on the "positive" side. The peak value on the negative side, however, is only equal to $0.75CSR_{max}$. This is typical of all recordings in which one peak is equal to the maximum and the other peak ranges from about 0.65 to as much as 0.9 of the maximum.

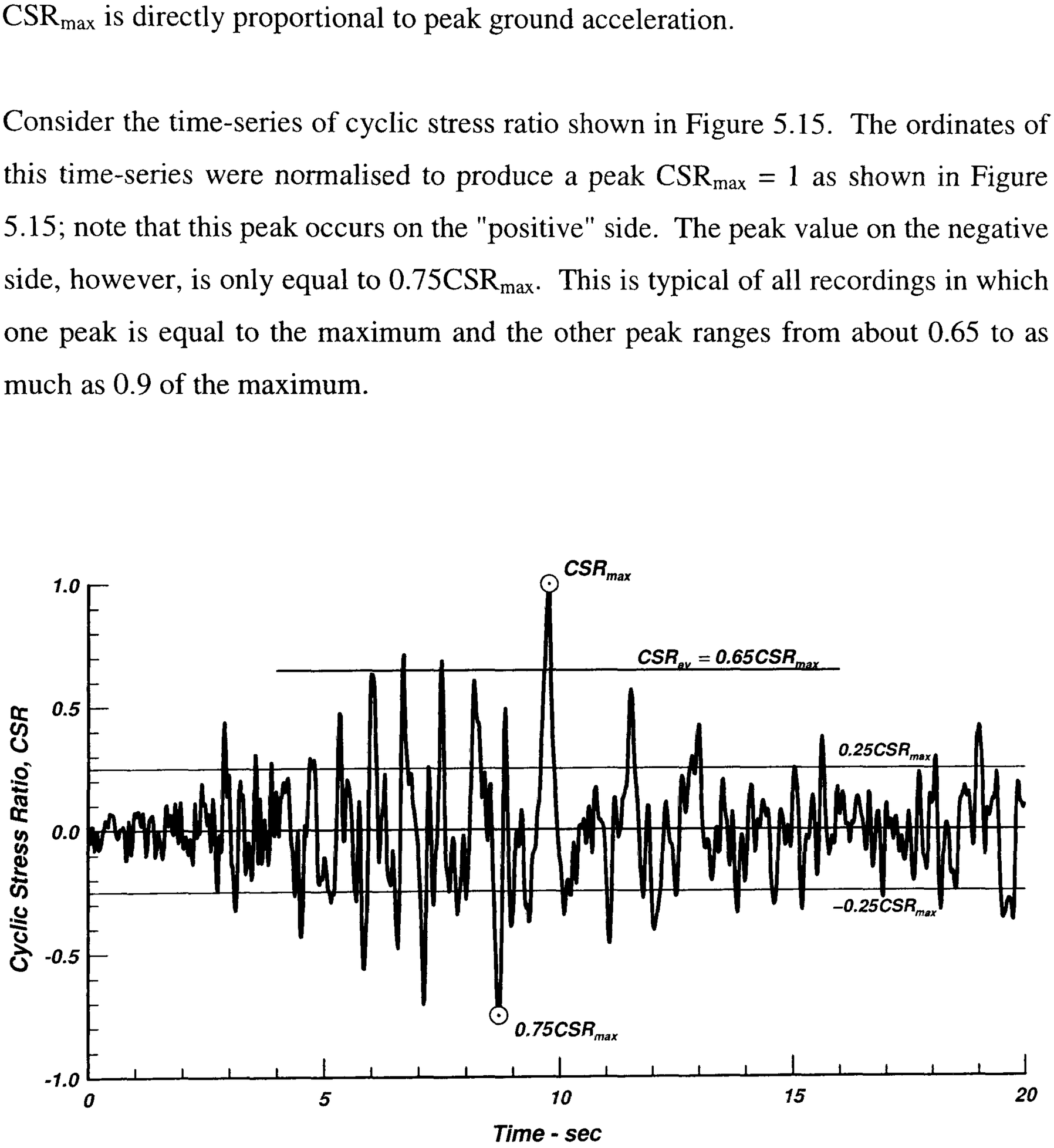


Figure 5.15. - Time-series of Cyclic Stress Ratio induced by earthquake ground motions

The equivalent number of cycles for this time-series is summarized in Table 5.1 and Figure 5.2 for frozen and reconstituted samples respectively. It can be seen that the use of $0.25CSR_{max}$ as the limiting value would result in ignoring a minor part of the contribution to the equivalent number of cycles representing the time-series at an equivalent uniform cyclic stress ratio of $0.65(CSR_{max})$. It can also be seen that the equivalent number of cycles predicted by tests of reconstituted samples is twice that predicted from tests of frozen samples at CSR_{max}. This difference adds further uncertainty to techniques that use equivalent number of cycles (e.g. Liu *et al.*, 2001) and so a duration measure is used in this chapter.

Table 5.1. - Number of cycles based on line for frozen samples in Figure 5.16

CSR	Num Cycles	Equivalent Num Cycles
CSR_{max}	1	3.55/1.00 = 3.55
$0.65CSR_{max}$	3.55	3.55/3.55 = 1.00
$0.60CSR_{max}$	4.49	3.55/4.49 = 0.79
$0.55CSR_{max}$	5.80	3.55/5.80 = 0.61
$0.50CSR_{max}$	7.68	3.55/7.68 = 0.46
$0.45CSR_{max}$	10.47	3.55/10.47 = 0.34
$0.40CSR_{max}$	14.81	3.55/14.81 = 0.24
$0.35CSR_{max}$	21.93	3.55/21.93 = 0.16
$0.30CSR_{max}$	34.51	3.55/34.51 = 0.10
$0.25CSR_{max}$	59.00	3.55/59.00 = 0.06
$0.20CSR_{max}$	113.74	3.55/113.74 = 0.03

If the bracketed duration is defined as the time between the first time $0.25(CSR_{max})$ is reached and the last time it is reached again towards the end of shaking, the following values are obtained for Figure 5.16:

Positive side of the time-series: 19.1 – 2.9 = 16.2 sec.

Negative side of the time-series: 19.8 – 2.7 = 17.1 sec.

Absolute first to last: 19.8 – 2.7 = 17.1 sec

Other ratios of CSR_{max} are also investigated and the results presented later in the chapter.

Relative measures of duration, such as the one proposed here, are only of use in combination with a measure of the amplitude of the shaking, such as CSR. This is because even the weakest records, which would never cause liquefaction, can be of long duration.

Table 5.2. - Number of cycles based on line for reconstituted samples in Figure 5.16

CSR	Num Cycles	Equivalent Num Cycles
CSR_{max}	1.00	7.06/1.00 = 7.06
$0.65CSR_{max}$	7.06	7.06/7.06 = 1.00
$0.60CSR_{max}$	10.16	7.06/10.16 = 0.70
$0.55CSR_{max}$	15.08	7.06/15.08 = 0.47
$0.50CSR_{max}$	23.24	7.06/23.24 = 0.30
$0.45CSR_{max}$	37.49	7.06/37.49 = 0.19
$0.40CSR_{max}$	63.98	7.06/63.98 = 0.11
$0.35CSR_{max}$	117.27	7.06/117.27 = 0.06
$0.30CSR_{max}$	236.07	7.06/236.07 = 0.03
$0.25CSR_{max}$	540.00	7.06/540.00 = 0.01
$0.20CSR_{max}$	1486.66	7.06/1,486.66 = 0.005

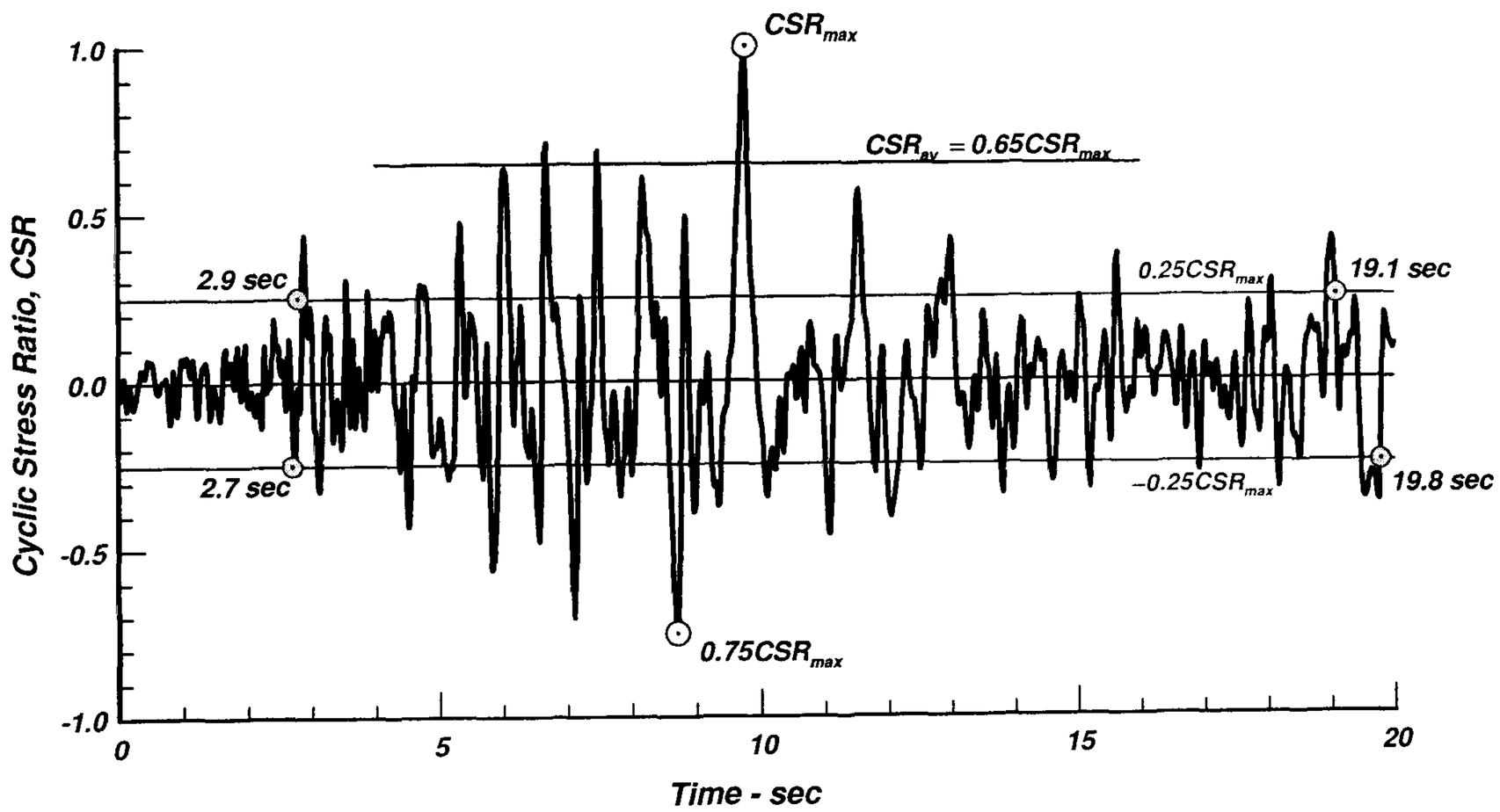


Figure 5.16. - Liquefaction-based bracketed duration – positive side (19.1 – 2.9 = 16.2 sec), negative side (19.8 – 2.7 = 17.1 sec) and independent of sign (19.8 – 2.7 = 17.1 sec)

5.2.3 Strong-motion database

An extensive strong-motion database is gathered to explore correlations between the duration of ground shaking and earthquake magnitude, distance, site conditions and style of faulting. The database consists of two components: the majority of the analysis is conducted using the primary dataset; this contains all records meeting primary acceptance criteria, detailed below in section 5.2.4. A secondary dataset is used in the second part of the regression analysis to investigate the influence of different distance metrics on duration predictions. This dataset is a subset of the primary dataset and consists of all records for which the rupture distance is known.

5.2.4 Primary dataset

A database of 1102 strong-motion accelerograms is compiled for this study. Of these, 853 records are from the global but predominantly Californian database of Abrahamson and Silva (1997), with an additional 249 records from the European database of Tromans and Bommer (2002). Only the horizontal components of each record are used and records with only one horizontal component available are discarded. Each component is treated as an independent record.

Moment magnitude (M_w) is used in this study as a consistent measure of earthquake magnitude (Kanamori 1977; Hanks and Kanamori 1979). Where the M_w is not given in the original dataset, it is obtained from the Harvard CMT catalogue (Harvard Seismology, 2003). Less than 1% of the final dataset are from earthquakes of magnitude less than 5 and approximately 95% of the records were generated by events of magnitude greater than 5.5.

The closest distance from the surface projection of the fault plane to the site (R_{jb}) is used. Where this distance metric is not given in the original dataset, it has been obtained from the Imperial College strong-motion database. Records without reliable and consistent estimates of source-to-site distance have been excluded. Records at distances in excess of 200km have been discarded as ground motions at these sites are not strong enough to be of engineering significance. Over 70% of the records in the final dataset are obtained within 50 km of the source.

Recording sites are classified as rock, stiff soil and soft soil according to the widely used three category system (Boore and Joyner 1993; Ambraseys *et al.* 1996). Where this classification is not given in the original dataset it has been obtained from the Imperial College strong-motion database. Records without consistent estimates of soil type have been excluded.

Earthquake style of faulting (rupture mechanism) is widely reported as affecting ground motions (e.g. Bommer *et al.*, 2003) and is also investigated in this study. The earthquake style-of-faulting classification system used by Abrahamson and Silva (1997) has been used for all records. This groups events into strike-slip, normal, reverse, reverse-oblique and normal oblique categories.

The final reduced dataset contains 749 records from 81 different earthquakes and aftershocks, with certain earthquakes, such as the 1989 Loma Prieta and 1994 Northridge events, contributing large numbers of records: 55 and 132 respectively (Table 5.3). Less than 3% of the dataset is from earthquakes recorded at a single station.

The distributions of the selected records in magnitude-distance space, grouped by site classification and style of faulting are shown in Figures 5.17 and 5.18 respectively.

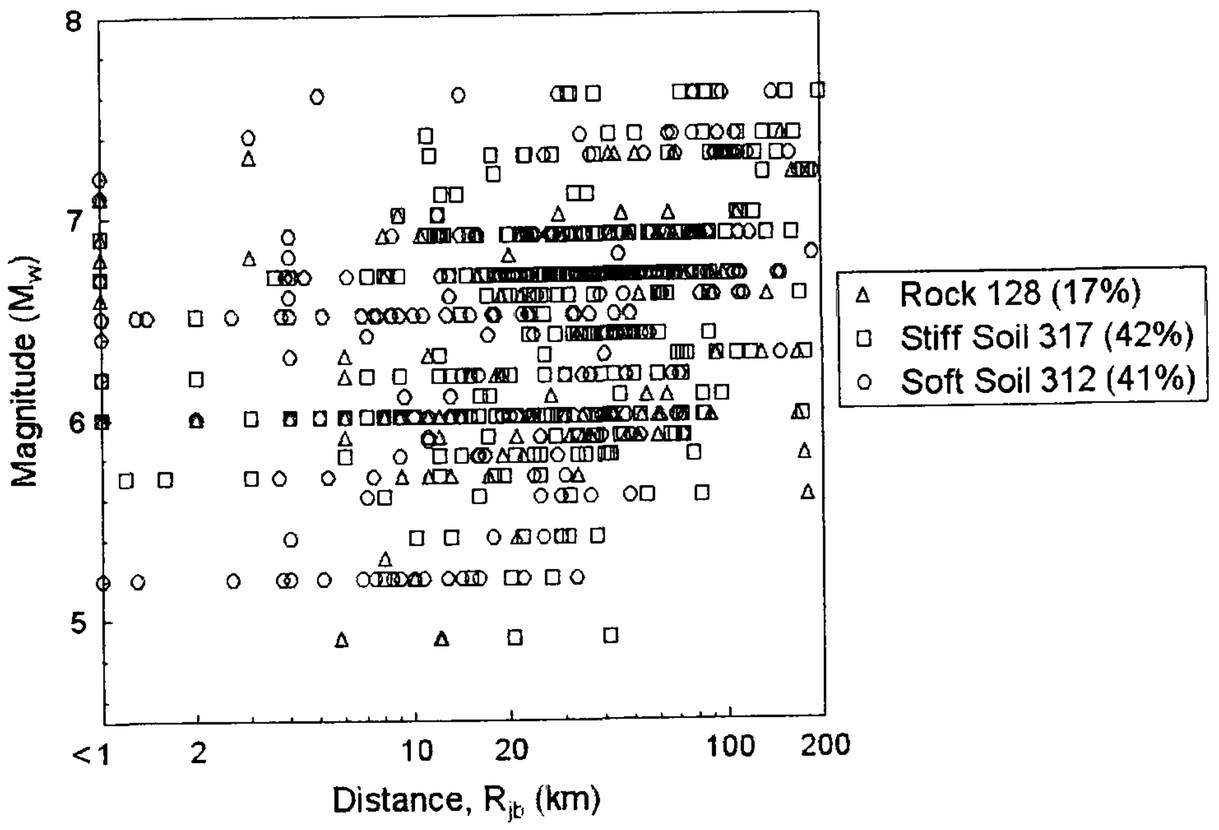


Figure 5.17. - Magnitude-distance distribution of the primary strong-motion dataset grouped according to site classification.

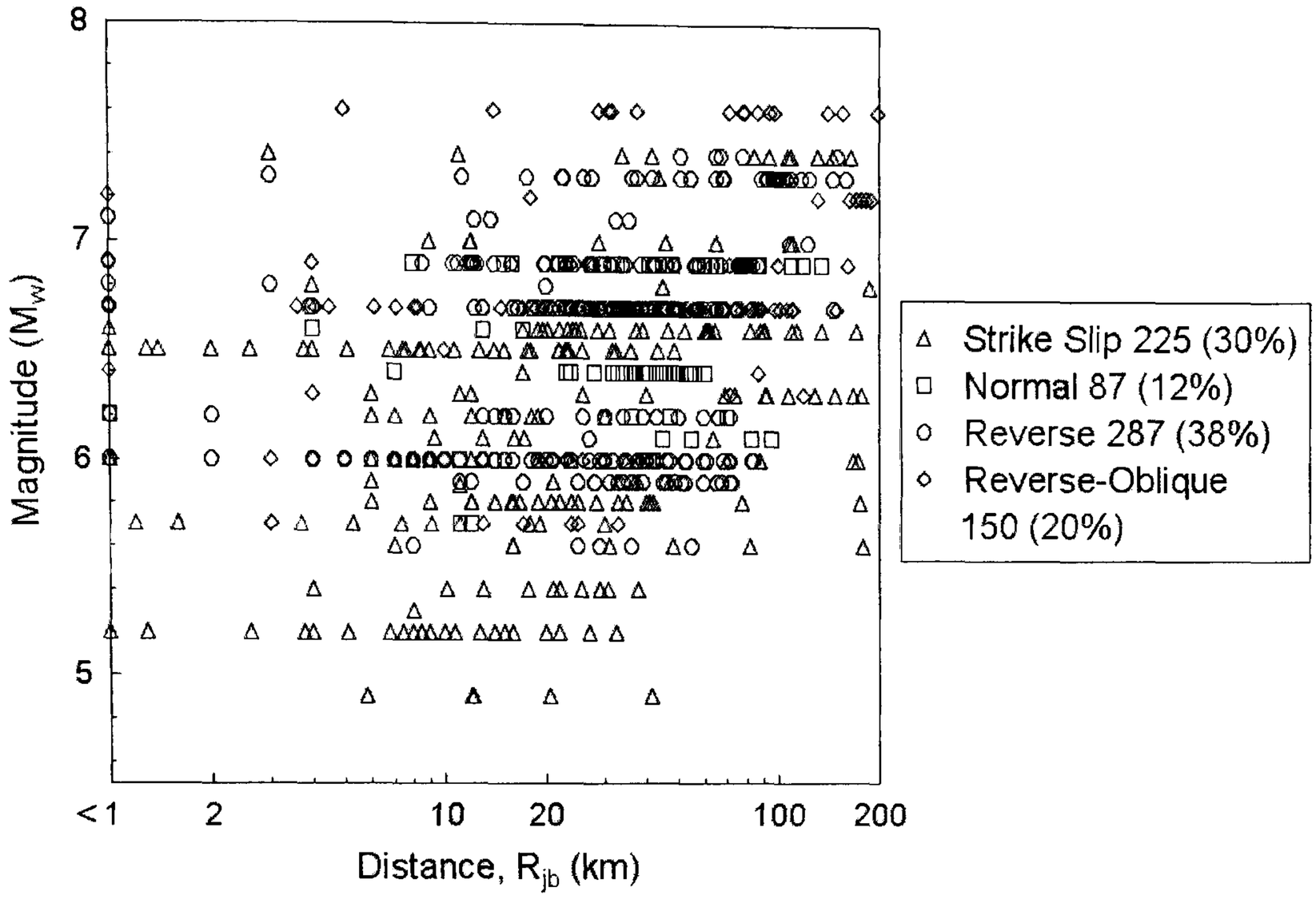


Figure 5.18. - Magnitude-distance distribution of the primary strong-motion dataset grouped according to style of faulting.

Table 5.3. - Earthquakes used in final primary dataset

Earthquake	Mechanism	Year	Mth	Day	Hr	Min	M_w	Number of records used
Oroville	Normal	1975	8	1	20	20	6	1
Thessaloniki	Normal	1978	6	20	20	3	6.4	1
Valnerina	Normal	1979	9	19	21	35	5.9	7
Campano Lucano	Normal	1980	11	23	18	34	6.9	19
Alkion	Normal	1981	2	24	20	53	6.6	2
Alkion	Normal	1981	2	25	2	35	6.4	1
Lazio Abruzzo	Normal	1984	5	7	17	49	5.9	15
Kalamata	Normal	1986	9	13	17	24	6	2
Izmir	Normal	1992	11	6	19	8	6	2
Gulf of Corinth	Normal	1992	11	18	21	19	5.9	2
Patras	Normal	1993	7	14	12	31	5.6	5
Aegion	Normal	1995	6	15	0	16	6.5	1
Dinar, TR	Normal	1995	10	1	15	57	6.4	2
Umbria, IT	Normal	1997	9	26	0	33	5.7	6
Umbria, IT	Normal	1997	9	26	9	40	6	10
Athens, GR	Normal	1999	9	7	11	56	6	12
San Francisco	Reverse	1957	3	22	19	44	5.3	1
San Fernando	Reverse	1971	2	9	14	0	6.6	30
Point Mugu	Reverse	1973	2	21	14	45	5.8	1
Ionian	Reverse	1973	11	4	15	52	5.9	1
Friuli	Reverse	1976	5	6	20	0	6.3	13
Gazli, USSR	Reverse	1976	5	17	20	0	6.8	1
Friuli	Reverse	1976	9	11	16	31	5.2	3
Friuli	Reverse	1976	9	11	16	35	5.6	5
Friuli	Reverse	1976	9	11	16	31	5.2	2
Friuli	Reverse	1976	9	11	16	35	5.6	2
Friuli	Reverse	1976	9	15	9	21	6	14

Table 5.3 - (continued): Earthquakes used in final primary dataset

Earthquake	Mechanism	Year	Mth	Day	Hr	Min	M_w	Number of records used
Tabas	Reverse	1978	9	16	15	35	7.4	7
Montenegro	Reverse	1979	4	15	6	19	7	10
Montenegro	Reverse	1979	4	15	14	43	5.8	4
Montenegro	Reverse	1979	5	24	17	23	6.2	8
Ionian	Reverse	1983	1	17	12	41	6.9	1
Whittier Narrows	Reverse	1987	10	1	14	42	6	35
Killini	Reverse	1988	10	16	12	34	5.9	2
Spitak	Reverse	1988	12	7	7	41	6.7	1
Spitak	Reverse	1988	12	7	7	45	6	1
Dzhava-Racha Mainshock	Reverse	1991	4	29	9	12	7	2
Dzhava-Racha Aftershock	Reverse	1991	6	15	0	59	6.2	5
Cape Mendocino	Reverse	1992	4	25	18	6	7.1	6
Northridge	Reverse	1994	1	17	12	31	6.7	132
Kern County	Reverse-oblique	1952	7	21	11	53	7.4	4
Lytle Creek	Reverse-oblique	1970	9	12	14	30	5.4	4
Santa Barbara	Reverse-oblique	1978	8	13	3	15	6	2
Mammoth Lakes	Reverse-oblique	1980	5	25	16	34	6.3	2
Mammoth Lakes	Reverse-oblique	1980	5	27	14	51	6	2
Coalinga	Reverse-oblique	1983	5	2	23	42	6.4	46
Nahanni, Canada	Reverse-oblique	1985	12	23	19	12	6.8	3
Golbasi	Reverse-oblique	1986	5	5	3	35	6.1	1
Golbasi	Reverse-oblique	1986	6	6	10	39	5.9	1
N. Palm Springs	Reverse-oblique	1986	7	8	9	20	6	25
Loma Prieta	Reverse-oblique	1989	10	18	0	5	6.9	55
Manjil	Reverse-oblique	1990	6	20	21	0	7.4	5
Helena, Montana	Strike-slip	1935	10	31	18	38	6.2	1
Imperial Valley	Strike-slip	1940	5	19	4	37	7	1
Parkfield	Strike-slip	1966	6	28	4	26	6.1	5
Borrego Mtn	Strike-slip	1968	4	9	2	30	6.8	2
Hollister	Strike-slip	1974	11	28	23	1	5.2	3
Friuli	Strike-slip	1976	9	15	3	15	5.8	10
Caldiran	Strike-slip	1976	11	24	12	22	7.3	1
Coyote Lake	Strike-slip	1979	8	6	17	5	5.7	10
Imperial Valley	Strike-slip	1979	10	15	23	16	6.5	33
Imperial Valley	Strike-slip	1979	10	15	23	19	5.2	16
Azores	Strike-slip	1980	1	1	16	42	6.9	1
Livermore	Strike-slip	1980	1	24	19	0	5.8	6
Livermore	Strike-slip	1980	1	27	2	33	5.4	7
Anza (Horse Cany)	Strike-slip	1980	2	25	10	47	4.9	5
Mammoth Lakes	Strike-slip	1980	5	25	16	49	5.7	2
Mammoth Lakes	Strike-slip	1980	5	25	19	44	6	3
Mammoth Lakes	Strike-slip	1980	5	25	20	35	5.7	3
Ionian	Strike-slip	1983	3	23	23	51	6.2	1
Biga	Strike-slip	1983	7	5	12	1	6.1	4
Kars	Strike-slip	1983	10	30	4	12	6.6	1
Morgan Hill	Strike-slip	1984	4	24	21	15	6.2	24
Chenoua	Strike-slip	1989	10	29	19	9	6	1
Erzincan	Strike-slip	1992	3	13	17	18	6.7	3
Erzincan	Strike-slip	1992	3	15	16	16	5.9	2
Landers	Strike-slip	1992	6	28	11	58	7.3	38
Kobe	Strike-slip	1995	1	16	20	46	6.9	14
Adana, TR	Strike-slip	1998	6	27	13	55	6.3	3
Kocaeli, TR	Strike-slip	1999	8	17	0	1	7.6	16
Duzce, TR	Strike-slip	1999	11	12	16	57	7.2	8

5.2.5 Secondary dataset

A secondary dataset is used in the second part of the regression analysis to investigate the influence of different distance metrics on duration predictions. This dataset is a subset of the primary dataset and consists of all records for which the rupture distance is known.

This dataset consists of 523 records from 34 different earthquakes and aftershocks. The distributions of records in magnitude-distance space, grouped by site classification and style of faulting are shown in Figure 5.19 and Figure 5.20 respectively. It is important to note that rupture distances are not available for European records and in fact over 95% of the records in the secondary dataset are recorded in Western North America (Table 5.4). The removal of the European records also removes all but one of the earthquakes with normal style of faulting (Figure 5.20).

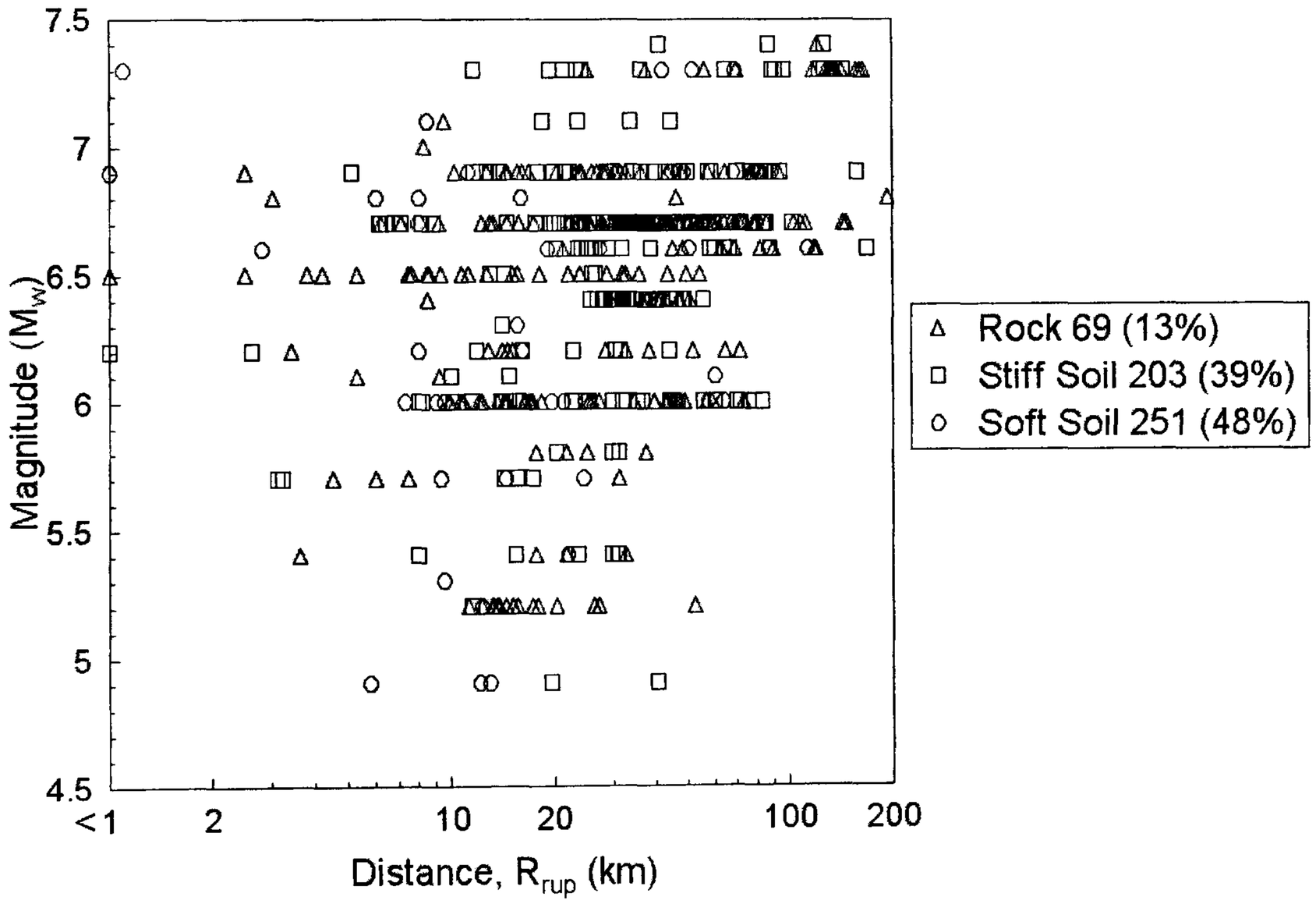


Figure 5.19: Magnitude-distance distribution of the secondary strong-motion dataset grouped according to site classification.

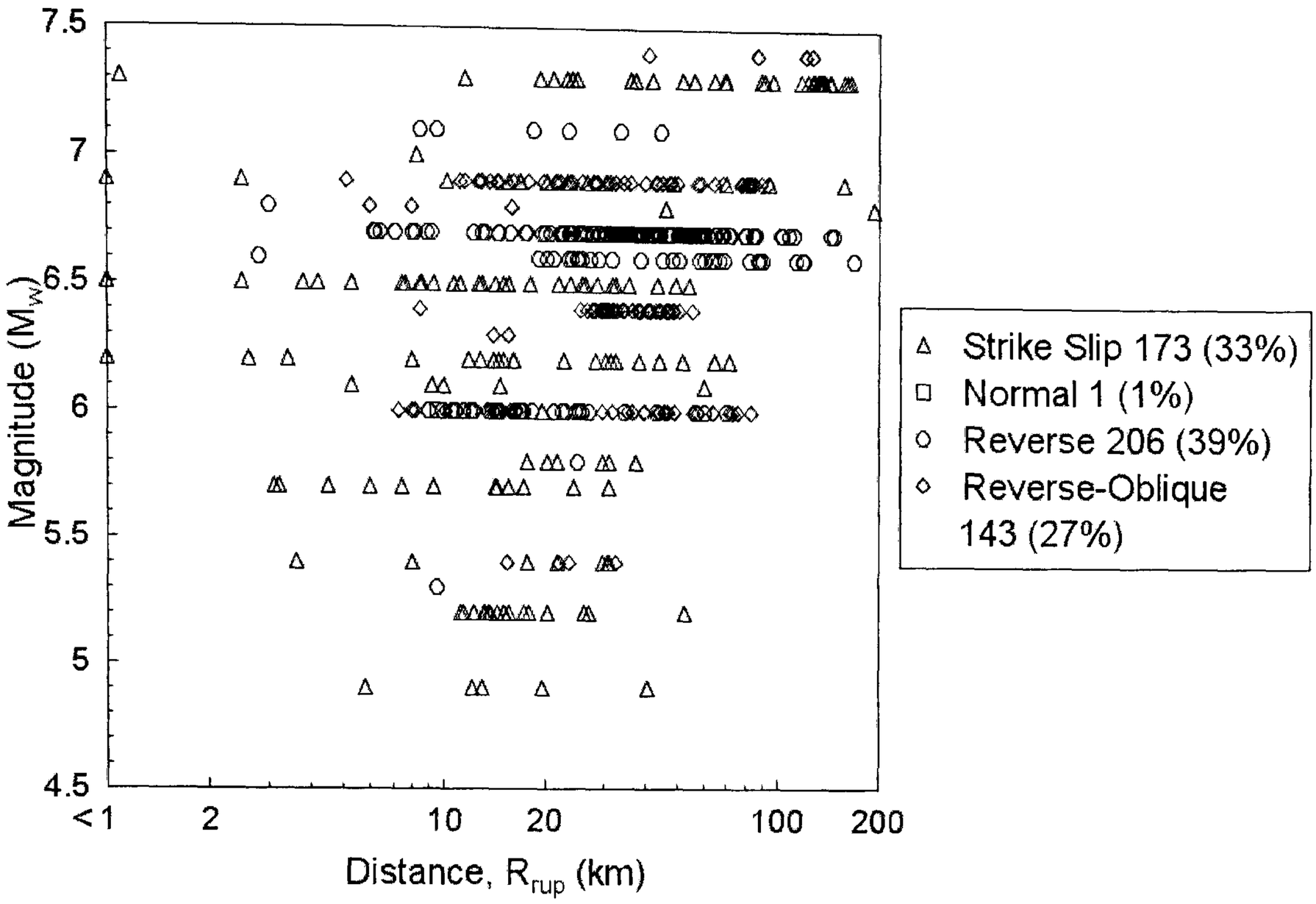


Figure 5.20. - Magnitude-distance distribution of the secondary strong-motion dataset grouped according to style of faulting.

5.2.6 Influence of duration definition on predictions

As noted in Section 5.2.2, it is possible to define duration based on the first and last times that acceleration crosses either the positive, negative or absolute first to last acceleration limits. Some records have longer duration on the positive and others on the negative side. To investigate the possible extremes, the bracketed duration is calculated for both positive and negative limits, and these are then sorted into longer and shorter durations. Figure 5.21 shows that the median duration of all records varies by about 0 to 2 seconds (typically 30% at 0.25CSR) depending on whether the longer or shorter sign convention is used. If duration is defined as the time between absolute first to last acceleration limits, it will produce results effectively the same as the longer duration sign convention (Figure 5.21).

As there is no physical meaning to positive or negative sign conventions, bracketed duration is defined in this study as the time between the first and last excursion across either the positive or negative CSR level. This has the influence of increasing the mean duration levels by up to about 30% for durations measured at 0.25(CSR_{max}),

compared to other possible sign conventions. However, this is not expected to be an issue as a consistent definition is used throughout.

Table 5.4. - Earthquakes used in secondary dataset

Earthquake	Mechanism	Year	Mth	Day	Hr	Min	Mag (Mw)	Number of records used
Helena, Montana	Strike-slip	1935	10	31	18	38	6.2	1
Imperial Valley	Strike-slip	1940	5	19	4	37	7	1
Parkfield	Strike-slip	1966	6	28	4	26	6.1	5
Borrego Mtn	Strike-slip	1968	4	9	2	30	6.8	2
Hollister	Strike-slip	1974	11	28	23	1	5.2	3
Coyote Lake	Strike-slip	1979	8	6	17	5	5.7	10
Imperial Valley	Strike-slip	1979	10	15	23	16	6.5	33
Imperial Valley	Strike-slip	1979	10	15	23	19	5.2	16
Livermore	Strike-slip	1980	1	24	19	0	5.8	6
Livermore	Strike-slip	1980	1	27	2	33	5.4	7
Anza (Horse Cany)	Strike-slip	1980	2	25	10	47	4.9	5
Mammoth Lakes	Strike-slip	1980	5	25	16	49	5.7	2
Mammoth Lakes	Strike-slip	1980	5	25	19	44	6	3
Mammoth Lakes	Strike-slip	1980	5	25	20	35	5.7	3
Morgan Hill	Strike-slip	1984	4	24	21	15	6.2	24
Landers	Strike-slip	1992	6	28	11	58	7.3	38
Kobe	Strike-slip	1995	1	16	20	46	6.9	14
Oroville	Normal	1975	8	1	20	20	6	1
San Francisco	Reverse	1957	3	22	19	44	5.3	1
San Fernando	Reverse	1971	2	9	14	0	6.6	30
Point Mugu	Reverse	1973	2	21	14	45	5.8	1
Gazli, USSR	Reverse	1976	5	17	20	0	6.8	1
Whittier Narrows	Reverse	1987	10	1	14	42	6	35
Cape Mendocino	Reverse	1992	4	25	18	6	7.1	6
Northridge	Reverse	1994	1	17	12	31	6.7	132
Kern County	Reverse-oblique	1952	7	21	11	53	7.4	4
Lytle Creek	Reverse-oblique	1970	9	12	14	30	5.4	4
Santa Barbara	Reverse-oblique	1978	8	13	3	15	6	2
Mammoth Lakes	Reverse-oblique	1980	5	25	16	34	6.3	2
Mammoth Lakes	Reverse-oblique	1980	5	27	14	51	6	2
Coalinga	Reverse-oblique	1983	5	2	23	42	6.4	46
Nahanni, Canada	Reverse-oblique	1985	12	23	19	12	6.8	3
N. Palm Springs	Reverse-oblique	1986	7	8	9	20	6	25
Loma Prieta	Reverse-oblique	1989	10	18	0	5	6.9	55

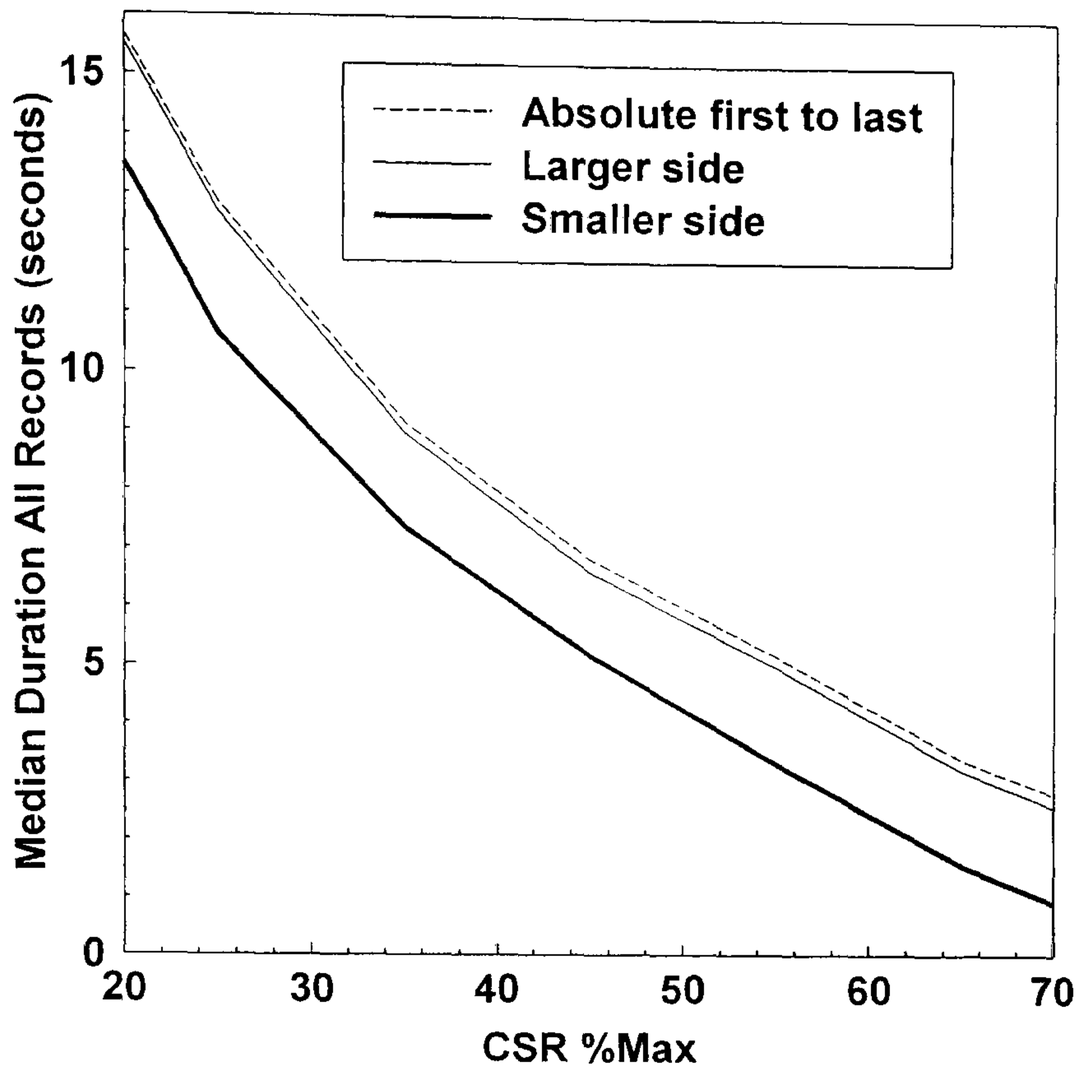


Figure 5.21. - Comparison of showing difference if positive or negative acceleration limits are used.

5.2.7 Influence of direction of motion on duration

To investigate the differences between the duration of the horizontal components of each record, records are sorted into bins of longer and shorter duration. The median duration for the shortest duration bin is typically 2-3 seconds shorter than that of the longer duration bin irrespective of CSR level (Figure 5.22). As both components are considered in the analysis, any median duration estimation has a variability of approximately ±1.5 seconds purely due to axis direction. Durations measured at higher CSR levels are more sensitive to this effect with differences of a factor of 2 in the mean duration due to direction at $0.65(CSR_{max})$ level, compared with a factor of 1.3 at the $0.25(CSR_{max})$ level.

Many of the records used are digitised recordings from analogue instruments. For these records it is generally not known if the digitisation process for both components started at exactly the same time (Trifunac *et al.* 1999). For this reason it was decided not to try to combine horizontal components to obtain durations of the resultant component of motion.

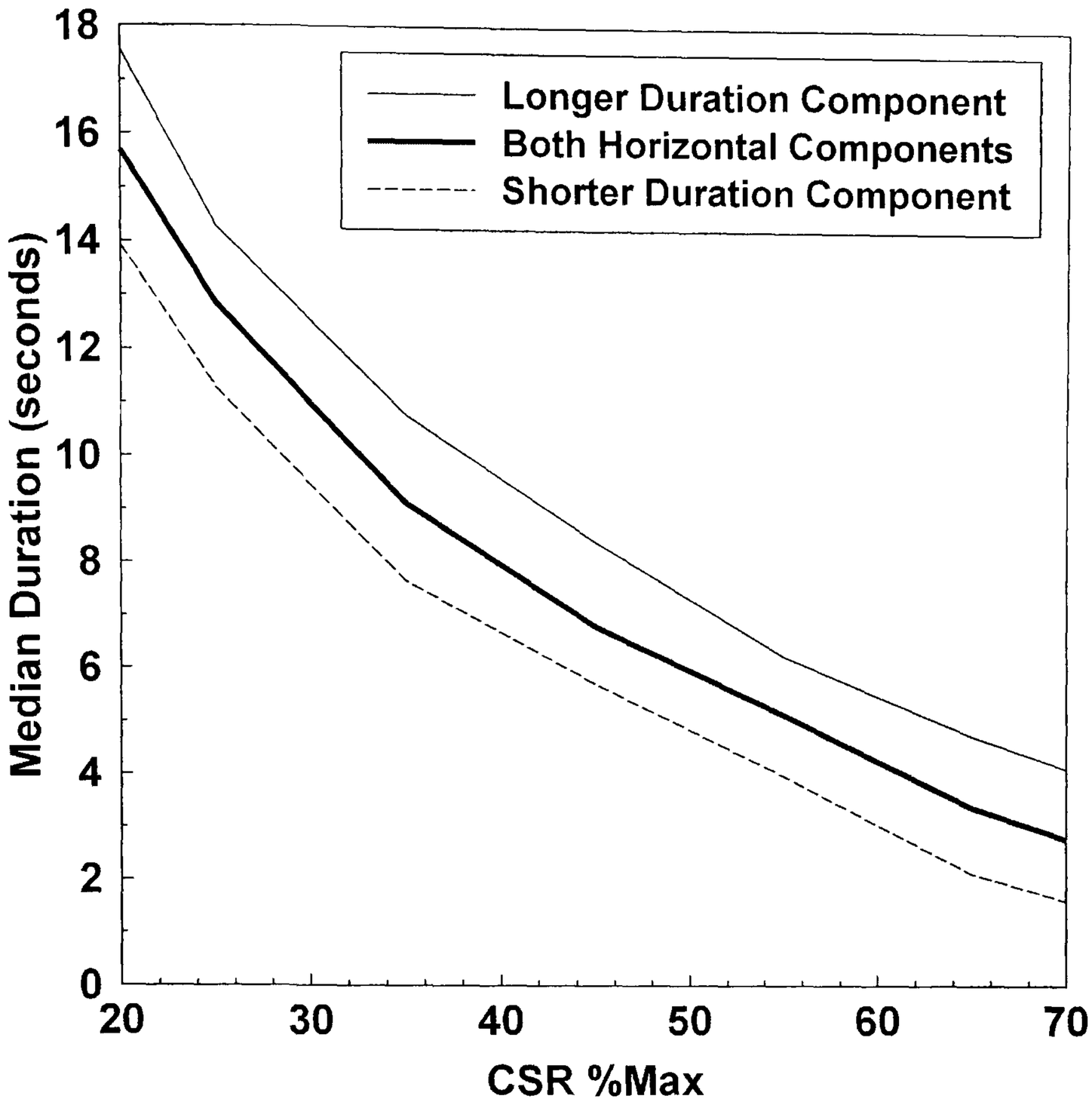


Figure 5.22. - Comparison showing differences between longest or shortest horizontal component.

5.2.8 Comparisons with significant duration definitions

Other popular relative duration definitions, such as the significant duration (Husid 1965; Dobry *et al.* 1978; Trifunac and Brady 1975a; Bommer and Martinez-Pereira 1999), are based on Arias intensity. Arias intensity is effectively a measure of the total energy in the ground motion and has also been identified as a good indicator of the capacity of ground shaking to trigger landslides (Harp and Wilson 1995). In order to explore the general relationship between bracketed duration and Arias intensity, the percentage of the total Arias intensity accumulated between the duration limits is measured. Figure 5.23 shows the median, the median plus and minus one standard deviation, maximum and minimum percentage of the total Arias intensity accumulated between the limits of each CSR level. As would be expected lower CSR levels have longer duration and accumulate larger percentages of Arias intensity. The percentage of Arias intensity is also less variable at lower CSR limits.

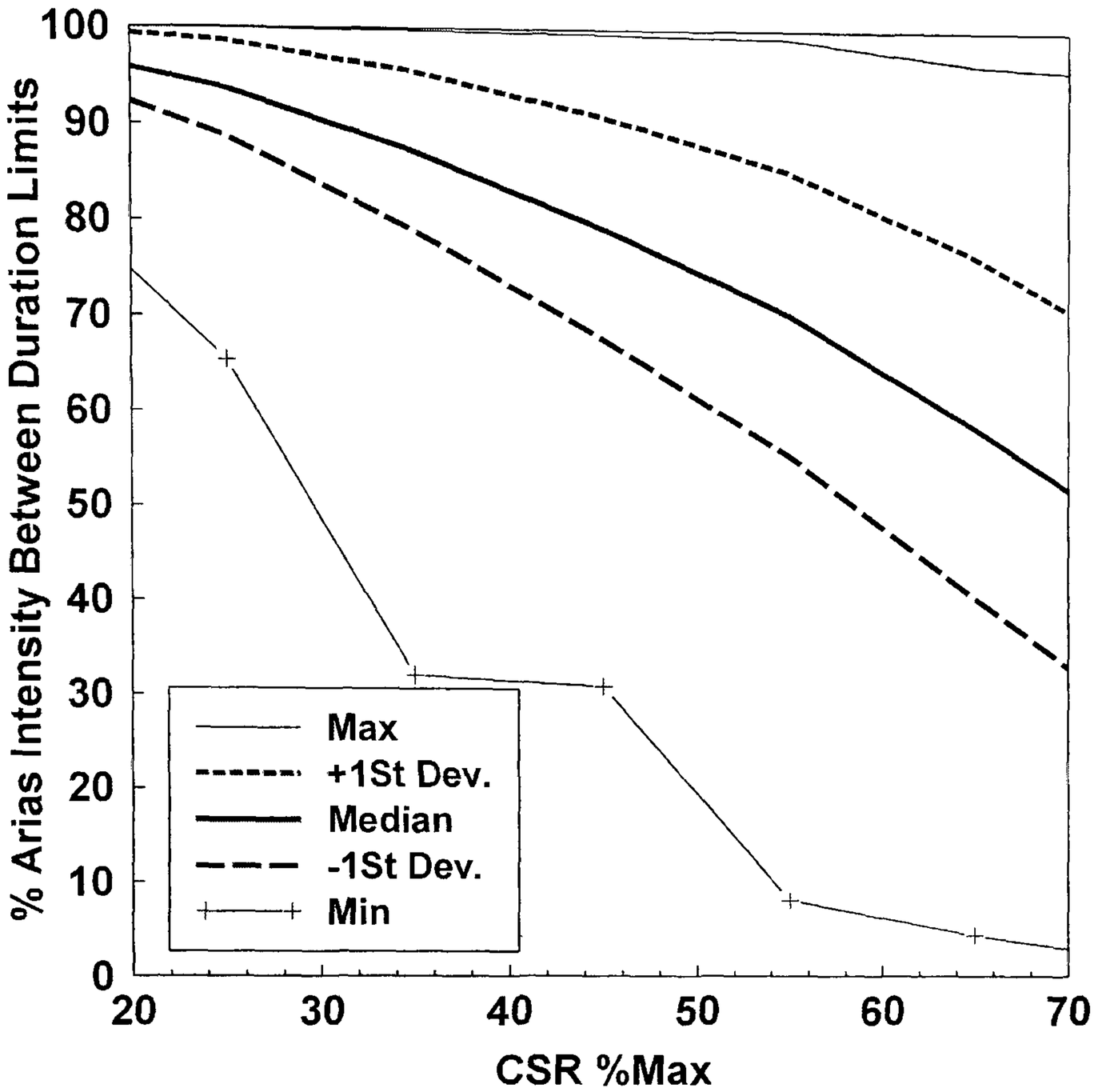


Figure 5.23. - % Arias intensity between duration limits

5.2.9 Basic correlations

Basic correlations are made between relative bracketed duration and magnitude, distance, soil type and fault mechanism. These correlations show the general trends in the data without the need to adopt a fixed functional form.

As would be expected a positive correlation is found between duration and earthquake magnitude (Figures 5.24 to 5.27). Only small differences are apparent in the correlations between magnitude and duration for sites with different soil types, which is consistent with earlier findings (e.g. Bommer and Martinez-Pereira 1999). It is found that records from normal and strike-slip events generally have longer durations than those from earthquakes with reverse faulting. This effect could be caused by the larger peak accelerations associated with earthquakes with reverse

faulting (e.g. Campbell 1997), which would cause greater maximum CSR and shorter relative bracketed duration.

A positive correlation is also found between duration and distance (Figures 5.28 to 5.31). Site soil classification appears to influence the correlation between duration and distance. Softer soil sites, on average, have longer duration and stronger correlation with distance than rock sites. This may be expected as soil sites can amplify longer period, and longer duration, ground motions that become progressively more dominant at larger distances because of wave scattering and the near-field attenuation of high-frequency waves (Dobry *et al.* 1978; Reinoso *et al.* 2000).

The best correlations are found for bracketed duration definitions using about 25% maximum CSR, confirming this level as a good choice for the duration definition. Lower cut-off levels than 25% measure small accelerations, which have little engineering significance and are more randomly distributed. Higher cut-off levels are less effective as an increasing number of records have effectively zero duration as only a single acceleration peak is measured.

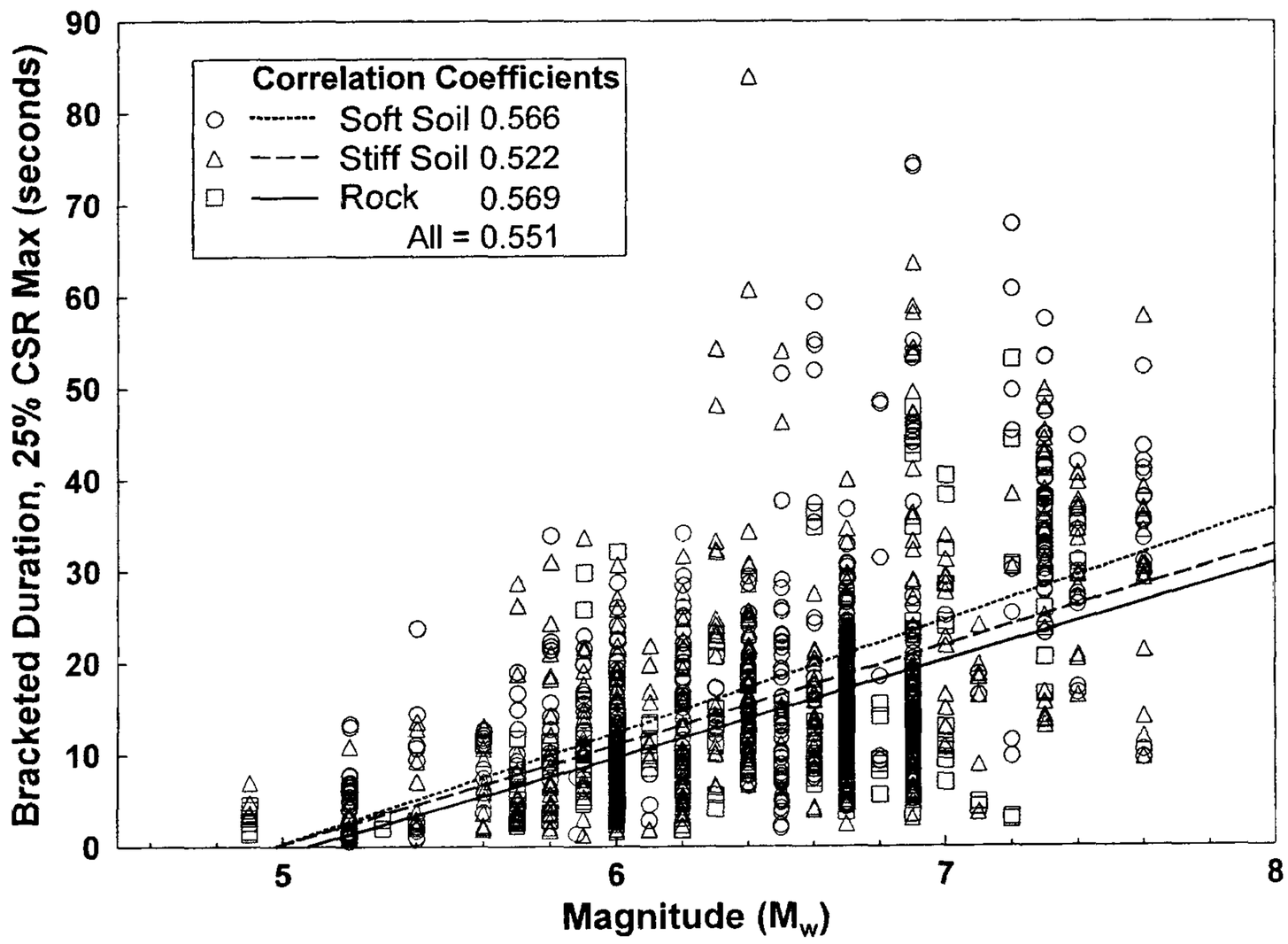


Figure 5.24. - Relationship between duration and magnitude with soil type, with linear trend lines; primary dataset.

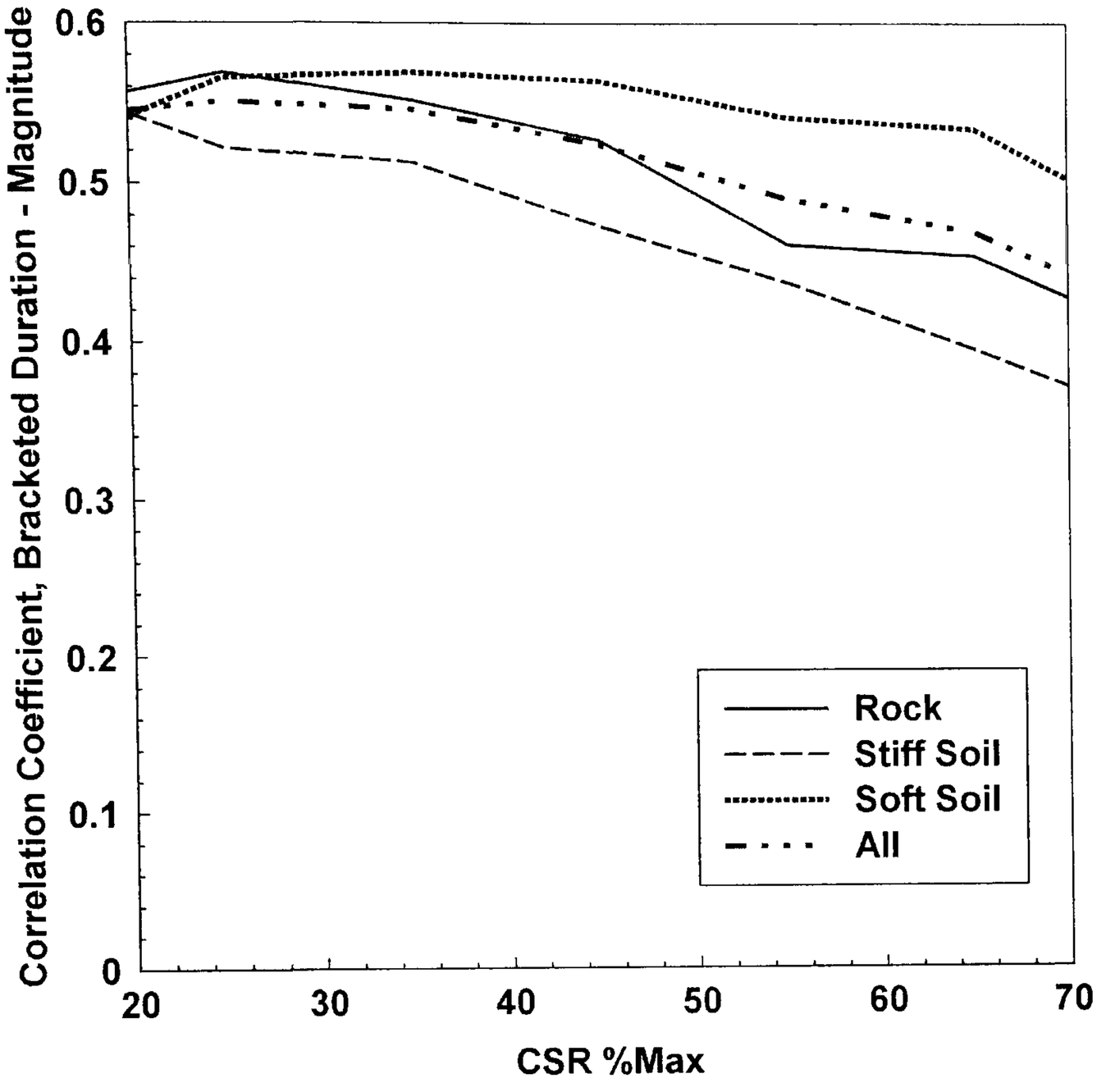


Figure 5.25. - Correlation between duration and magnitude with soil type for different CSR levels; primary dataset.

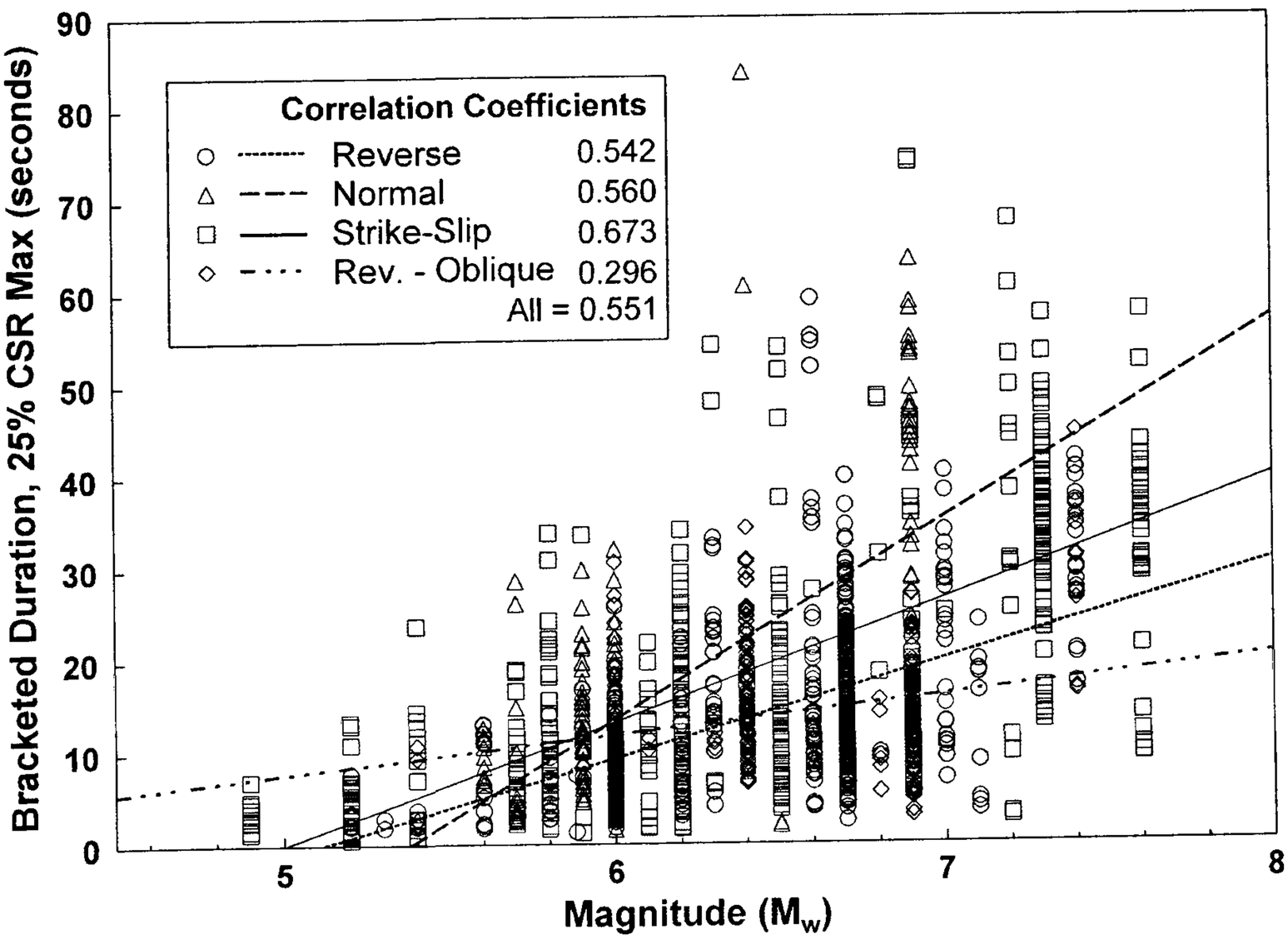


Figure 5.26. – Relationship between duration and magnitude with fault mechanism, with linear trend lines; primary dataset.

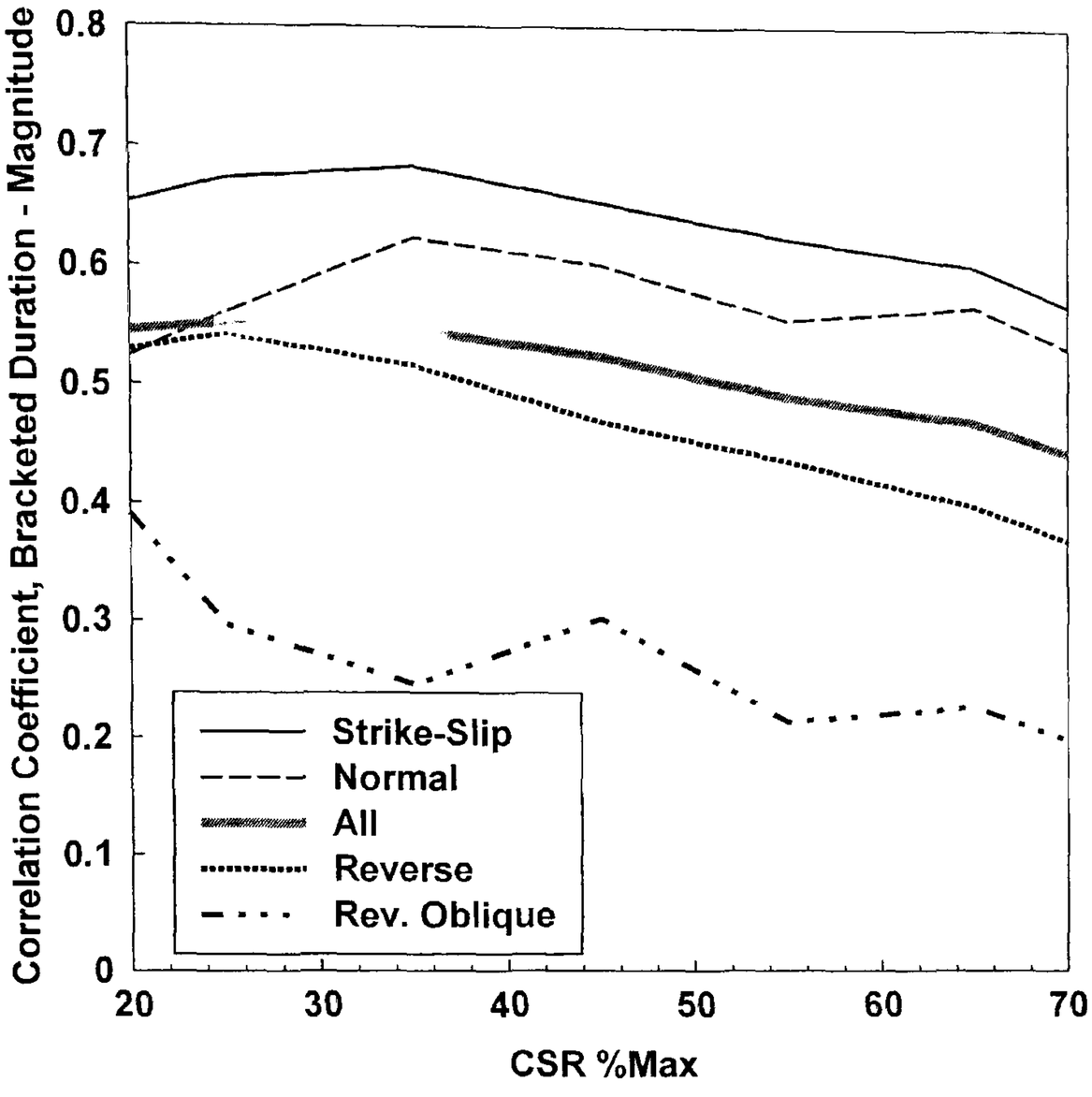


Figure 5.27. - Correlation between duration and magnitude with fault mechanism for different CSR levels; primary dataset.

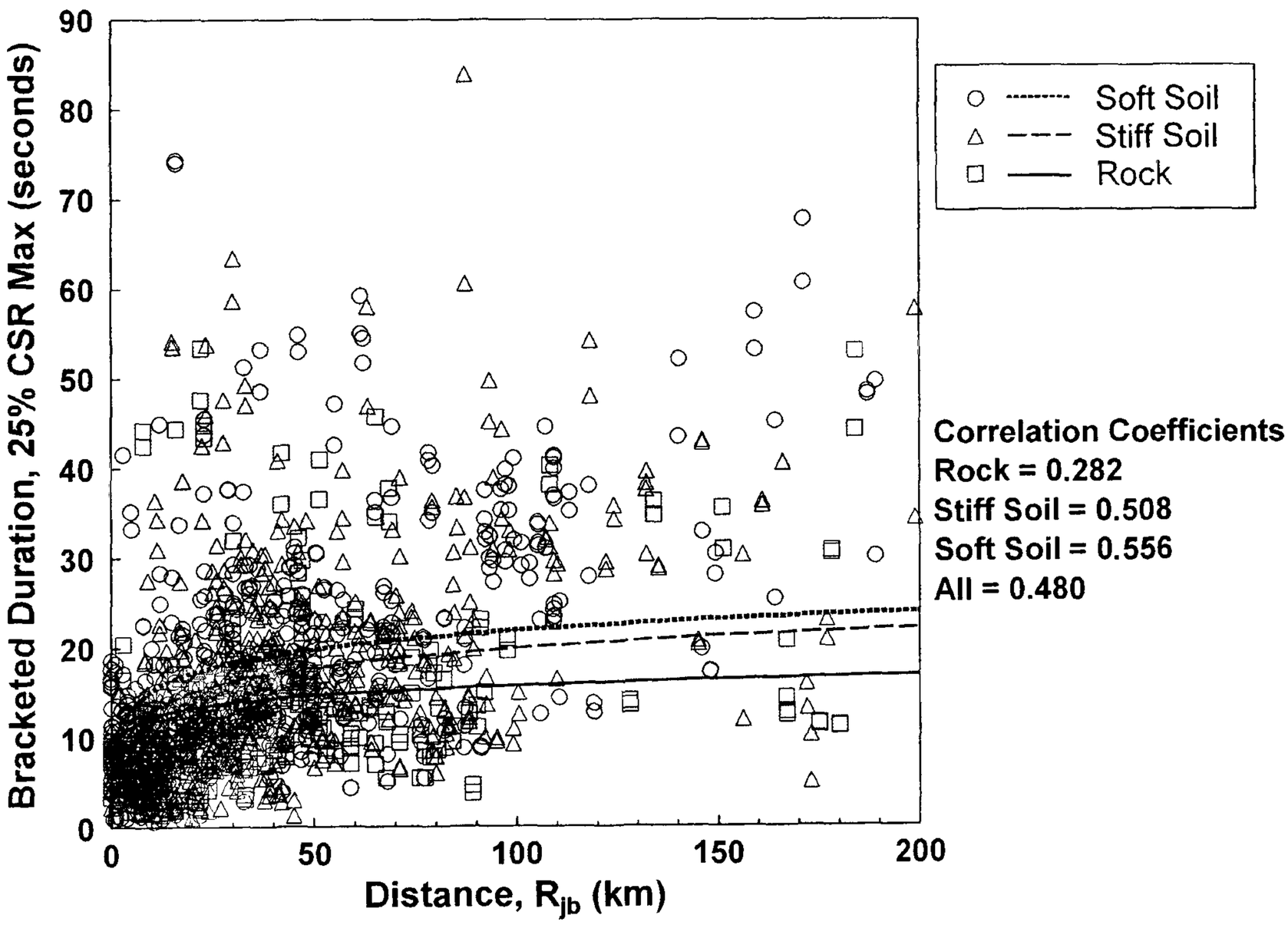


Figure 5.28. - Relationship between duration and distance with soil type, with logarithmic trend lines; primary dataset.

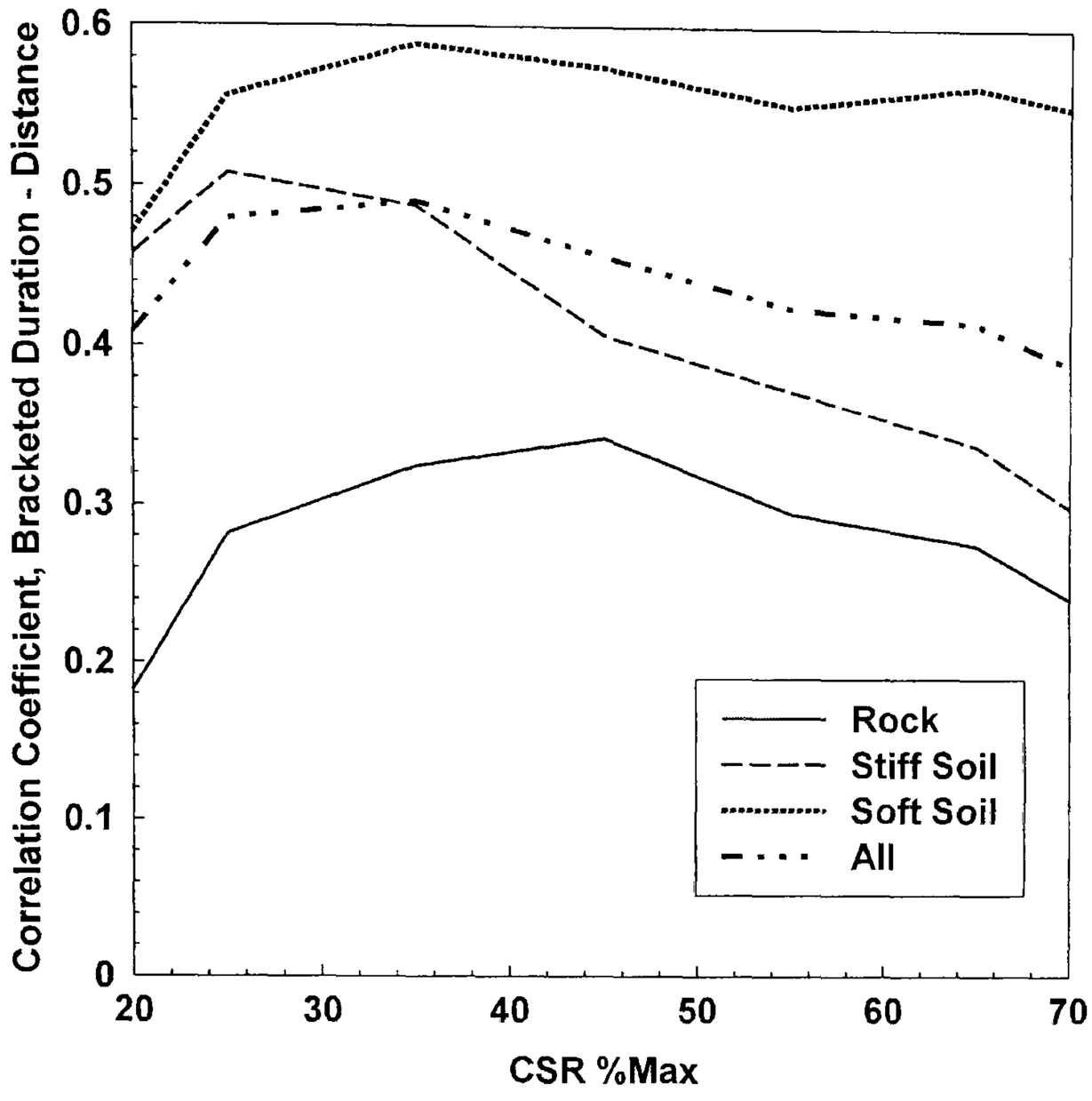


Figure 5.29. - Correlation between duration and distance with soil type for different CSR levels; primary dataset.

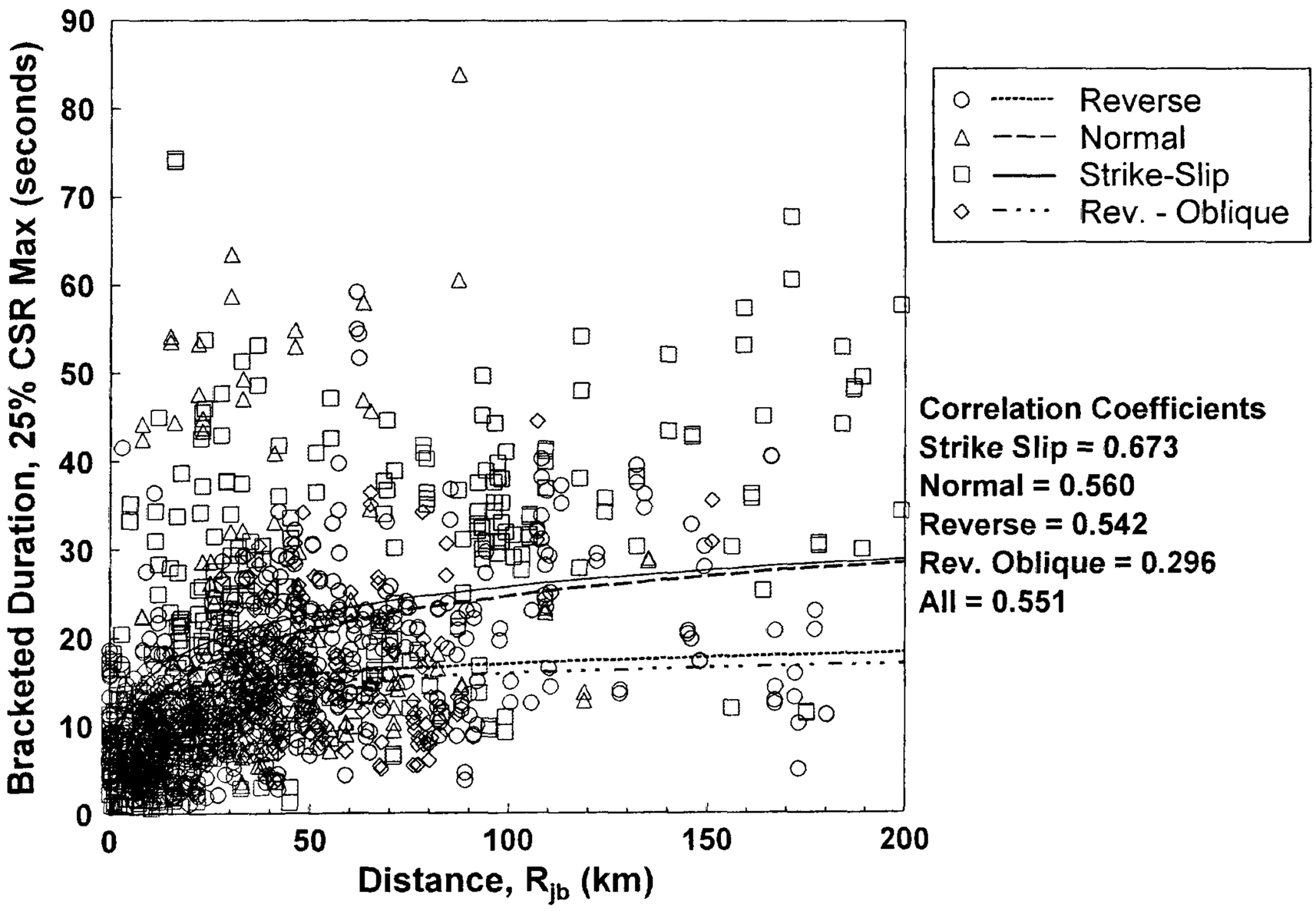


Figure 5.30. - Relationship between duration and distance with earthquake mechanism, with logarithmic trend lines; primary dataset.

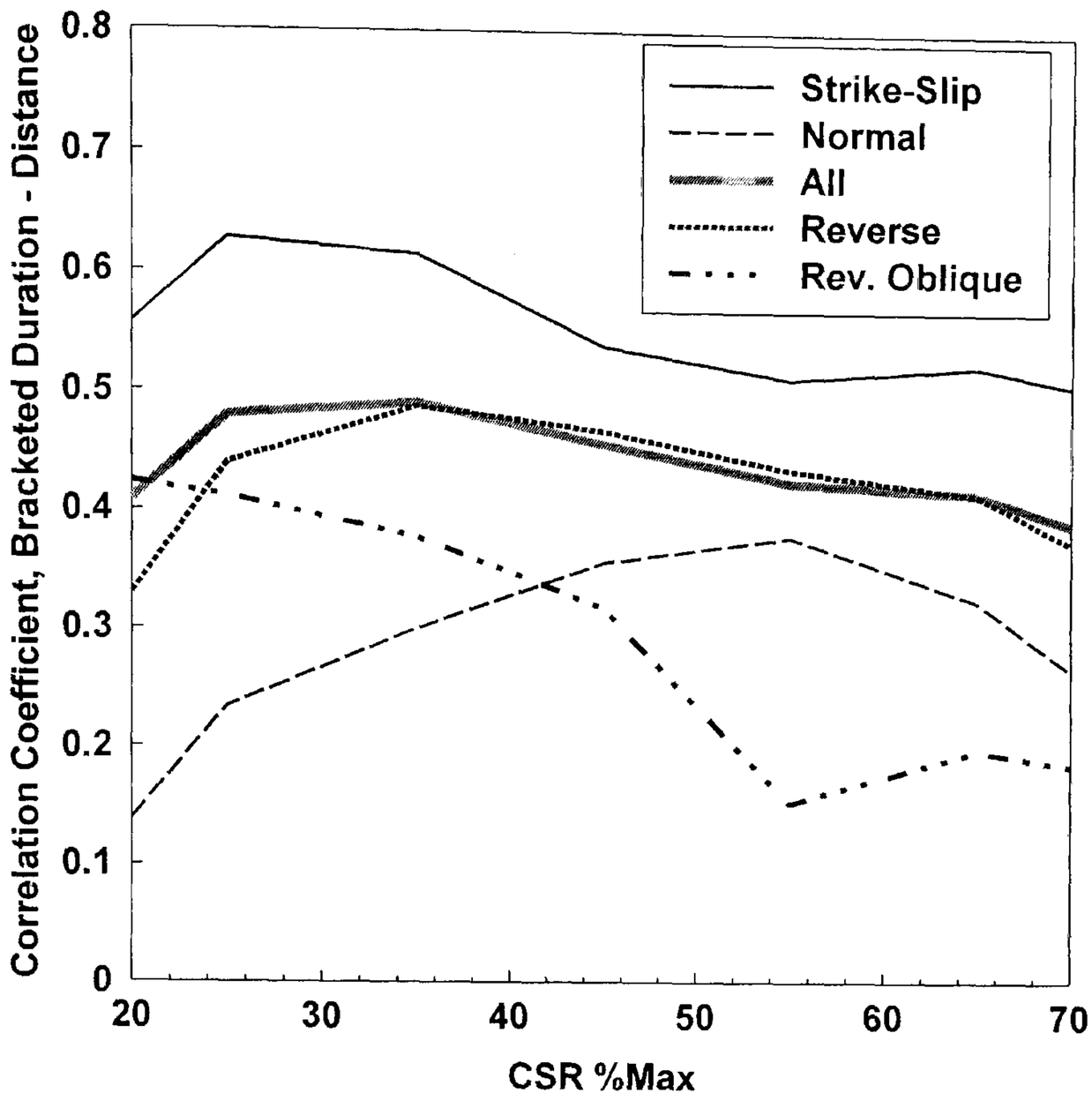


Figure 5.31. - Correlation between duration and distance with earthquake mechanism for different CSR levels; primary dataset.

5.2.10 Regression of data

It was shown in the previous sections that a bracketed duration measured at the 25% maximum CSR level is the most suitable for the assessment of liquefaction potential and is the best correlated with predictive variables. This section describes the results of regression analysis used to develop predictive equations for the relative bracketed duration at 25% maximum CSR. A single stage maximum likelihood regression analysis (Joyner and Boore 1993) is used to avoid issues caused by the cross-correlation of the influence of magnitude and distance. Predictive variables including earthquake magnitude, source-to-site distance, site classification and earthquake fault rupture mechanism are used.

5.2.11 Review of functional forms

Some of the first relations for the prediction of strong-motion duration are given by Esteva and Rosenblueth (1964) and Housner (1965). Esteva and Rosenblueth describe

an "equivalent" ground motion with uniform intensity per unit time with duration s, which they model with:

$$s = a\exp^{bM} + cr \tag{5.5}$$

where s is the duration in seconds, M is earthquake magnitude (undefined scale), r is the source to station distance in km, a, b and c are coefficients found by regression analysis. Housner proposed that the upper bound for the duration D, of undefined definition, could be predicted by:

$$D = 11.2M - 53 \text{ for } M \geq 5 \tag{5.6}$$

where D is the duration in seconds and M is the earthquake magnitude. Donovan (1972) proposed a similar functional form as Housner for predicting the duration of the strong phase of shaking:

$$D = 11(M - 5) + 4 \text{ for } M \geq 5 \tag{5.7}$$

Trifunac and Brady (1975a) use a more advanced functional form including site classification to find correlation with the duration between 5% and 95% of the build up of the integral of either the square of acceleration, $\int_0^{D_{SR}} a^2 dt$, velocity, $\int_0^{D_{SR}} v^2 dt$ or displacement, $\int_0^{D_{SR}} d^2 dt$:

$$\log\left[\int_0^{D_{SR}} \begin{pmatrix} a^2 \\ v^2 \\ d^2 \end{pmatrix} dt\right] = as + bM + c\log R_{epi} + d \pm \sigma \tag{5.8}$$

where a^2 is ground acceleration squared, v is ground velocity, d is ground displacement, D_{SR} is the significant duration, s stands for site classification taking values of 0, 1 or 2, M is earthquake magnitude, R_{epi} is epicentral distance, s is the standard deviation and a, b, and c are coefficients fitted by regression.

Dobry *et al.* (1978), point out that the scatter in the Trifunac and Brady predictions is great and large enough to mask the effect of variables other than magnitude. Dobry *et al.* (1978) propose that duration is dominated by the source duration and use the following functional form to predict the significant duration:

$$\log D_{SR} = aM + b \tag{5.9}$$

where D_{SR} is the significant duration in seconds, M is the earthquake magnitude, a and b are coefficients fitted by regression.

Westermo (1980) assumes that the total duration is the sum of the components from source, path and site effects. This is then represented with the following functional form to predict a frequency dependant significant duration, $D_{SR}(\omega)$:

$$D_{SR}(\omega) = a(\omega_c) + b(\omega_c)M + c(\omega_c)\Delta + d(\omega_c)h \tag{5.10}$$

where ω_c is the centre frequency of the frequency band at which the duration is measured. M is the published magnitude, Δ is the epicentral distance, h is the vertical distance from the source to the local basement rock, a, b, c and d are coefficients fitted by regression.

Novikova and Trifunac (1995) present an extensive report on frequency-dependant significant duration using several different regression models. Their models are based on the concept presented by Westermo (1980) that total duration is the sum of the components from the source, path and site effects. Some of the models consider that the distance term has two branches, one for near-field and another at greater distances to allow for strong reflections off the Mohorovičić discontinuity. An investigation of source directivity effects for recordings of the 1992 Landers earthquake is also presented.

Different functional forms to predict bracketed duration have been proposed by many previous authors (McGuire and Barnhard 1979; Kawashima and Aizawa 1989; Papazachos *et al.* 1992). The most common general form used is:

$$\ln(D) = C_1 + C_2 M + C_3 \ln\left(\sqrt{R^2 + C_4^2}\right) + C_5 S \pm \sigma_{\log(dur)} P \qquad (5.11)$$

where D is the duration in seconds, M is the earthquake magnitude, R is the source-to-site distance, S is a dummy variable that most authors set equal to zero for rock sites and one for soil sites; C_1, C_2, C_3, C_4 and C_5 are coefficients fitted by regression and P equals 0 for median durations and 1 for 84-percentile levels, considering lognormal distribution of the residuals with standard deviation $\sigma_{\ln(dur)}$. Some authors omit some of the coefficients, or fix C_4 to a specified value. Other coefficients are also used by specific authors to account for factors such as the duration cut-off level (Papazachos *et al. 1992*) and the difference between vertical and horizontal components (McGuire and Barnard 1978).

5.2.12 Selection of functional form

For this study additional coefficients are incorporated to enable the investigation of the influence of three styles-of-faulting and three soil classifications. The resulting functional form:

$$\ln(D_{BR25\%}) = C_1 + C_2 M_W + C_3 \ln\left(\sqrt{R_{jb}^2 + C_4^2}\right) + C_5 F_1 + C_6 F_2 + C_7 S_1 + C_8 S_2 \pm \sigma_{\log(dur)} P \qquad (5.12)$$

where $D_{BR25\%}$ is the liquefaction-based bracketed duration at 25% maximum CSR (seconds), M_W is the moment magnitude, R_{jb} is the closest distance from the surface projection of the fault rupture (Joyner and Boore 1981); S_1 and S_2 are dummy variables for site classification that have a default value of zero, S_1 equals one for soft soil sites and S_2 equals one for stiff soil sites; F_1 and F_2 are dummy variables for style-of-faulting that have a default of zero; F_1 equals one for normal and F_2 equals one for reverse events; to reduce the number of coefficients required to describe the

style-of-faulting reverse-oblique events are included as reverse faults. C_1, C_2, C_3, C_4, C_5, C_6, and C_7 are coefficients fitted by regression.

5.2.13 Regression of primary dataset

Regression coefficients for the primary dataset are given in Table 5.5. All of the coefficients are statistically significant using an F-test in excess of the 95% confidence limits except C_5, C_7 and C_8, which are only significant to 62%, 45% and 55% confidence limits respectively for 25%CSR (Table 5.6). C_5 has low significance because the small number of records (9%) with normal faulting in the dataset reduces the reliability of this coefficient. The soil coefficients determined produce results that agree with findings of other authors that ground-motion duration is longer on soft soils; however, correlation coefficients show that this conclusion cannot be confirmed by this regression analysis to a significantly high level of confidence.

As would be expected the equation predicts longer durations for larger earthquake magnitudes (Figures 5.32 and 5.33). As was observed in the initial correlations, durations for sites with soft soil classification and earthquakes with normal faulting have longer durations than sites on rock and earthquakes with reverse faulting.

The relationship between duration and distance is presented in Figures 5.34 and 5.35 for different site soil types and faulting mechanisms respectively. The findings of the initial correlations are confirmed by the regression as duration increases with distance.

The residuals from the regression analysis plotted against magnitude, distance, soil type, faulting style and focal depth are shown in Figure 5.36 to Figure 5.40. All of the residuals are approximately normally distributed with zero mean and have no clear trends, as is required for a satisfactory regression analysis. There is considerable scatter in the predictions with the median duration increased or decreased by a factor of 1.7 and 3 to obtain durations at one and two standard deviations respectively. These levels of uncertainty are generally lower than those presented for similar duration measures by other authors. For example McGuire and Barnhard (1979) investigate a bracketed duration at 50% PGA and find factors of 2.7 and 7.2

respectively between the median and one and two standard deviations for their dataset.

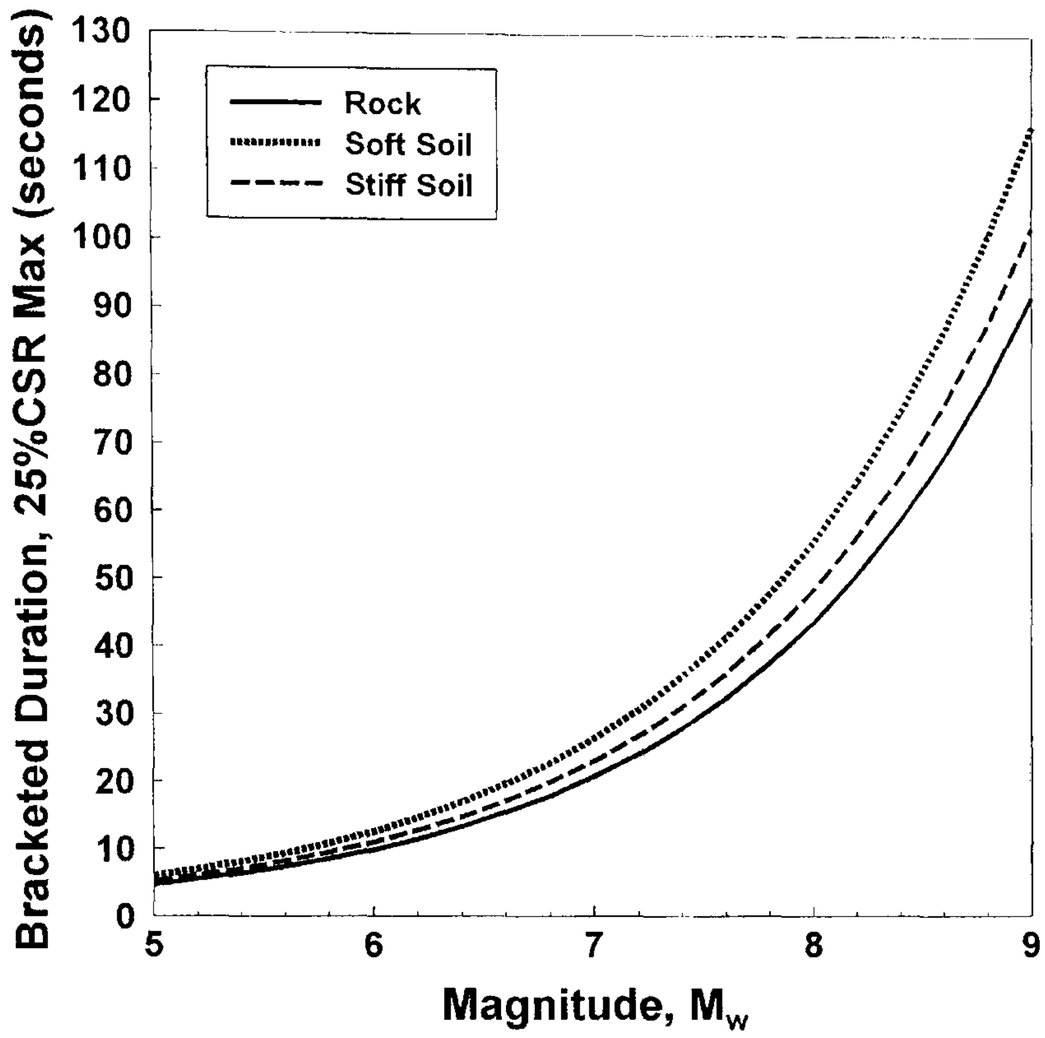


Figure 5.32. - Prediction of LBBD at 25% max CSR vs. magnitude, for different site soil types, strike-slip faulting, 50km distance.

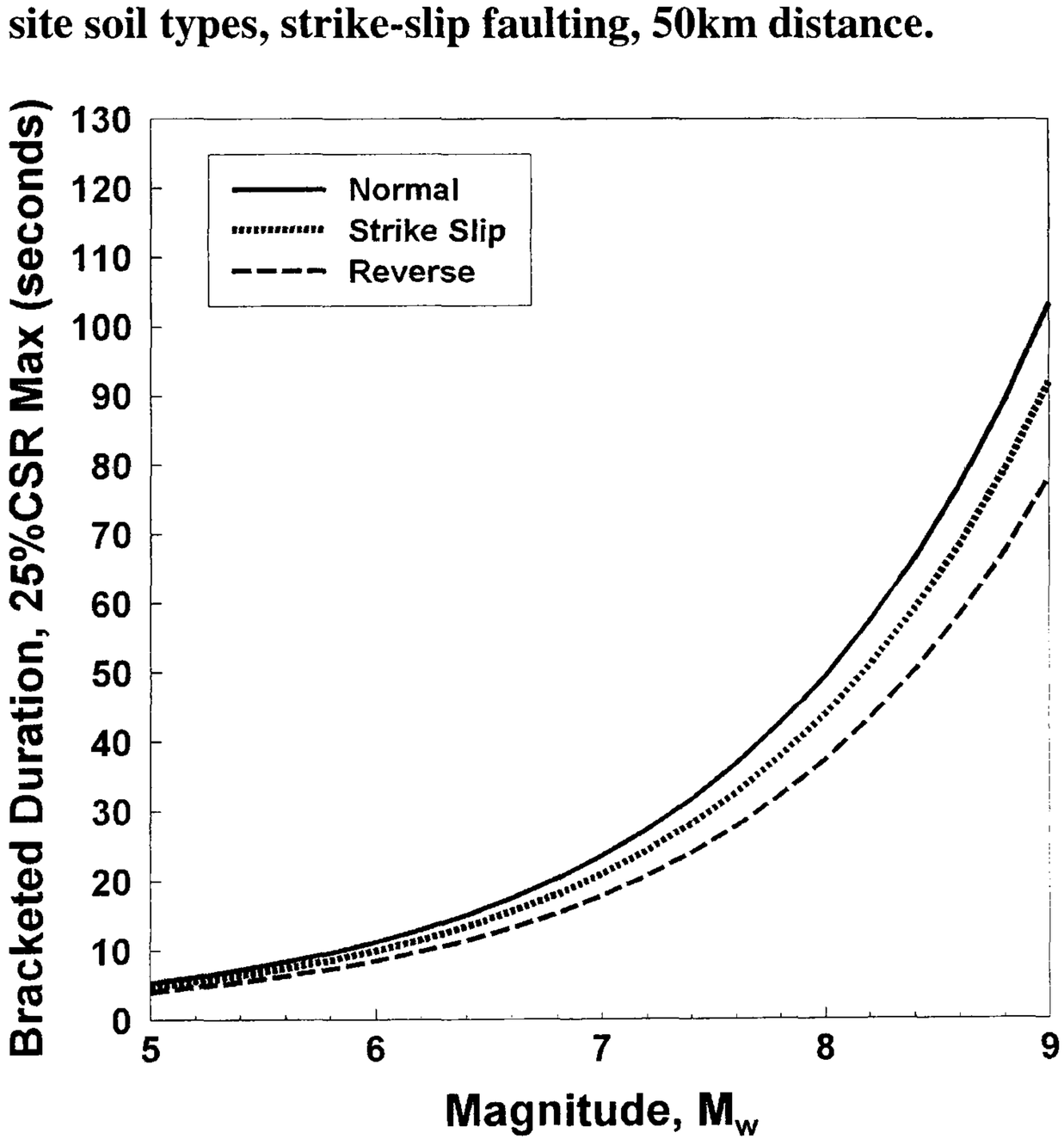


Figure 5.33. - Prediction of LBBD at 25% max CSR vs. magnitude, for different earthquake faulting mechanisms, rock sites, 50km distance.

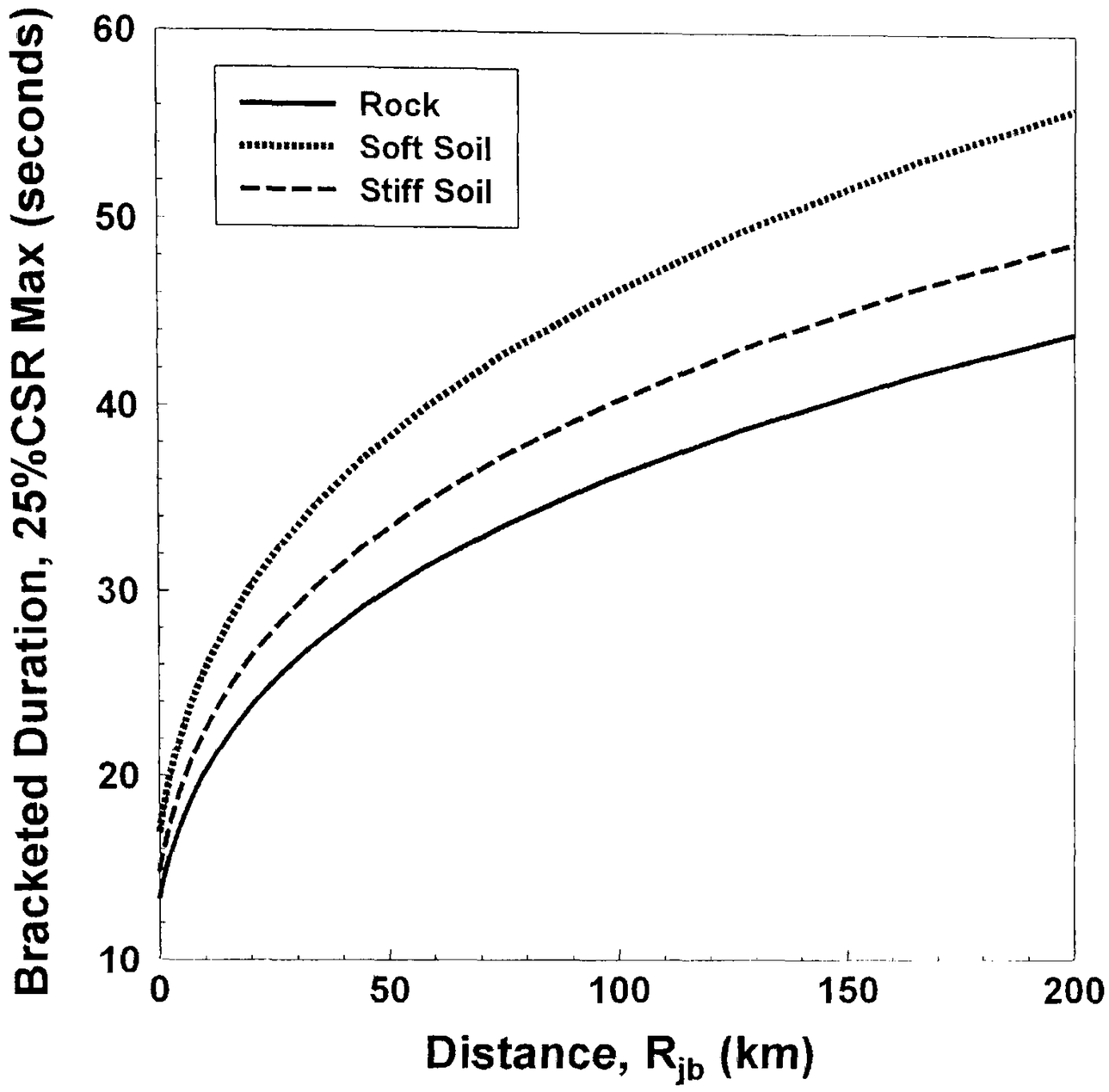


Figure 5.34. - Prediction of LBBD at 25% max CSR vs. distance, for different site soil types, strike-slip faulting, magnitude M7.5.

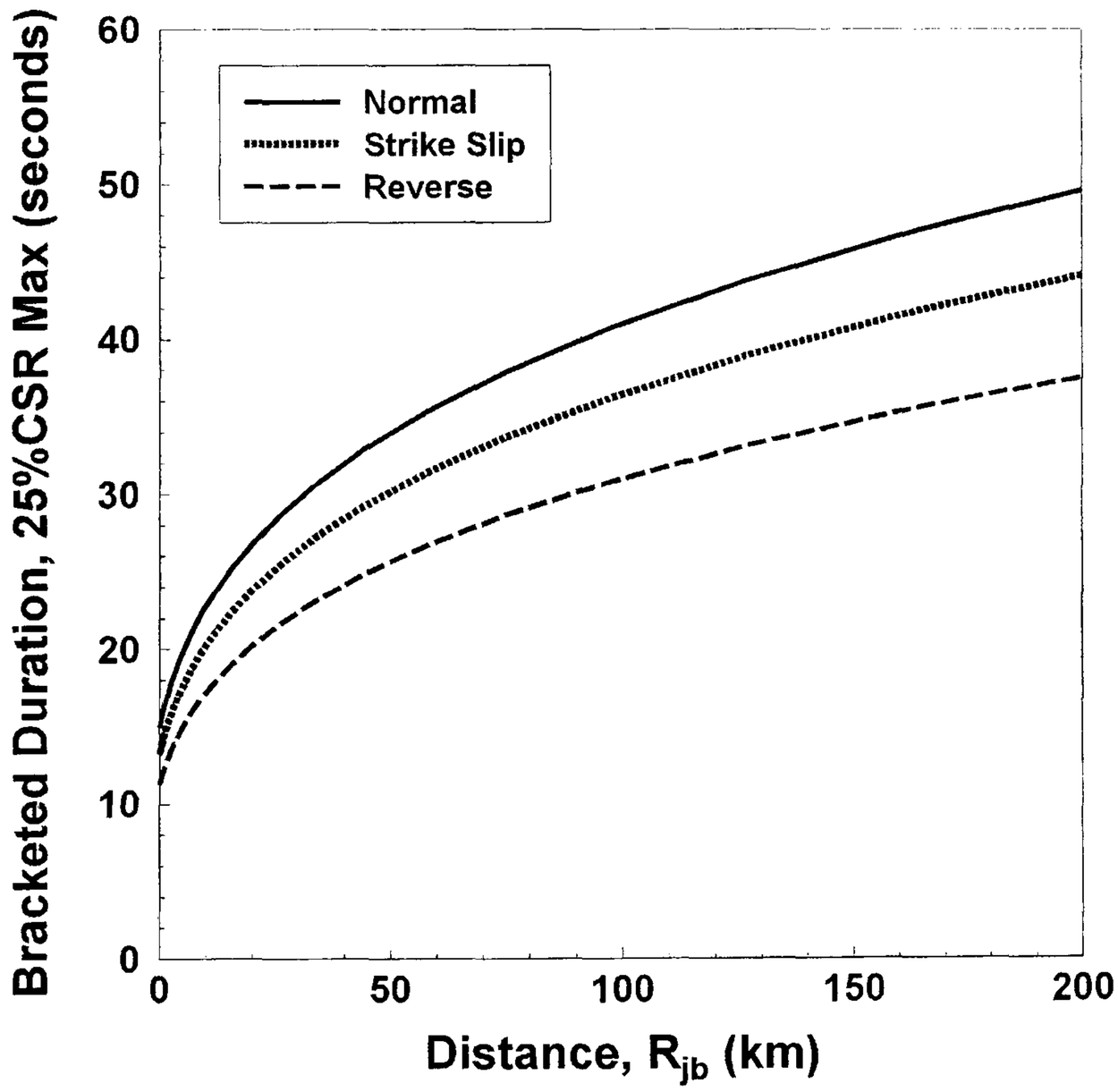


Figure 5.35. - Prediction of LBBD at 25% max CSR vs. distance, for different earthquake faulting mechanisms, rock sites, magnitude M7.5.

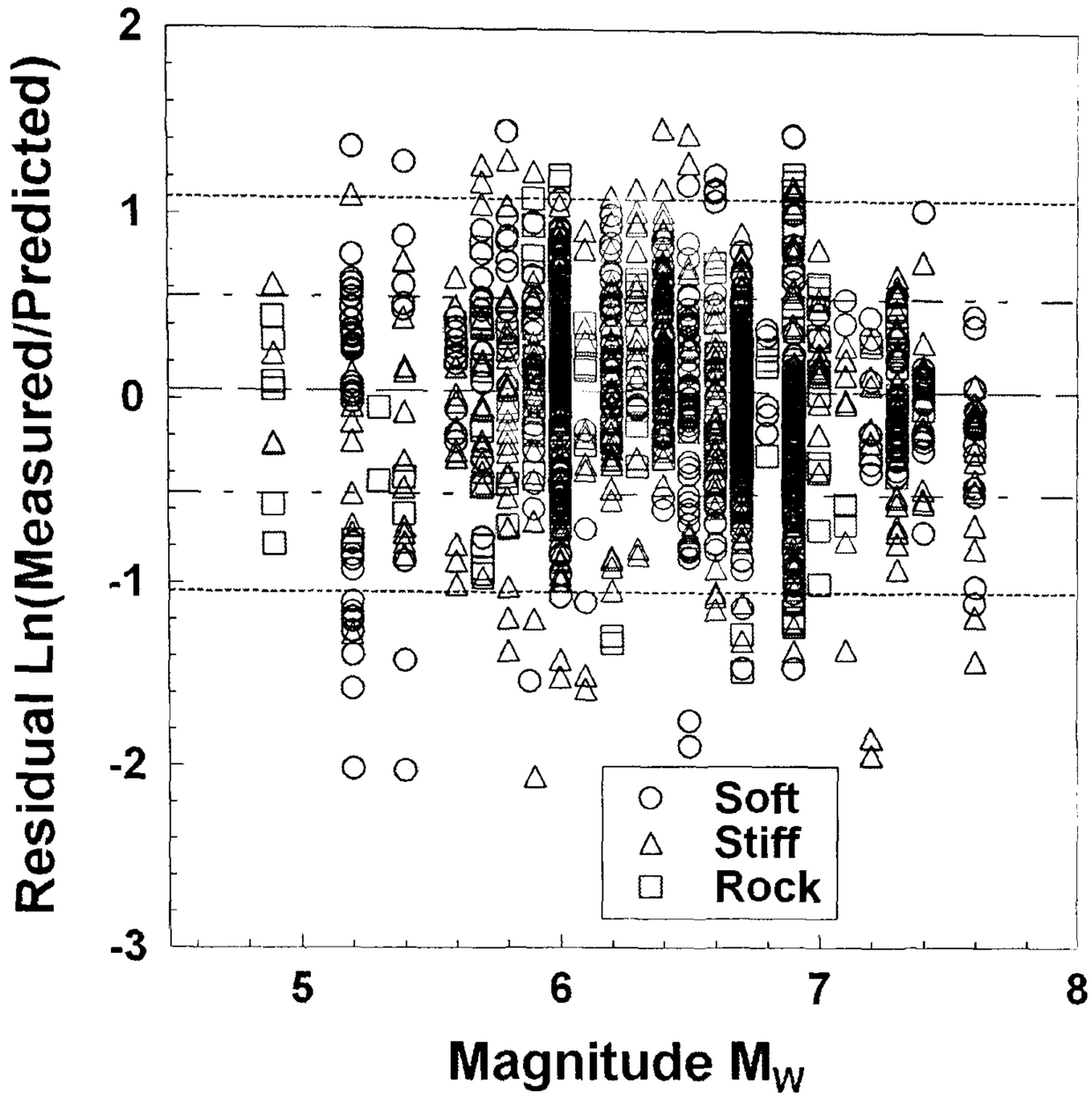


Figure 5.36. - Residuals for LLBD at 25% Maximum CSR vs. magnitude, horizontal lines represent median (long dashes), one standard deviation (dot, dash) and two standard deviations (dots).

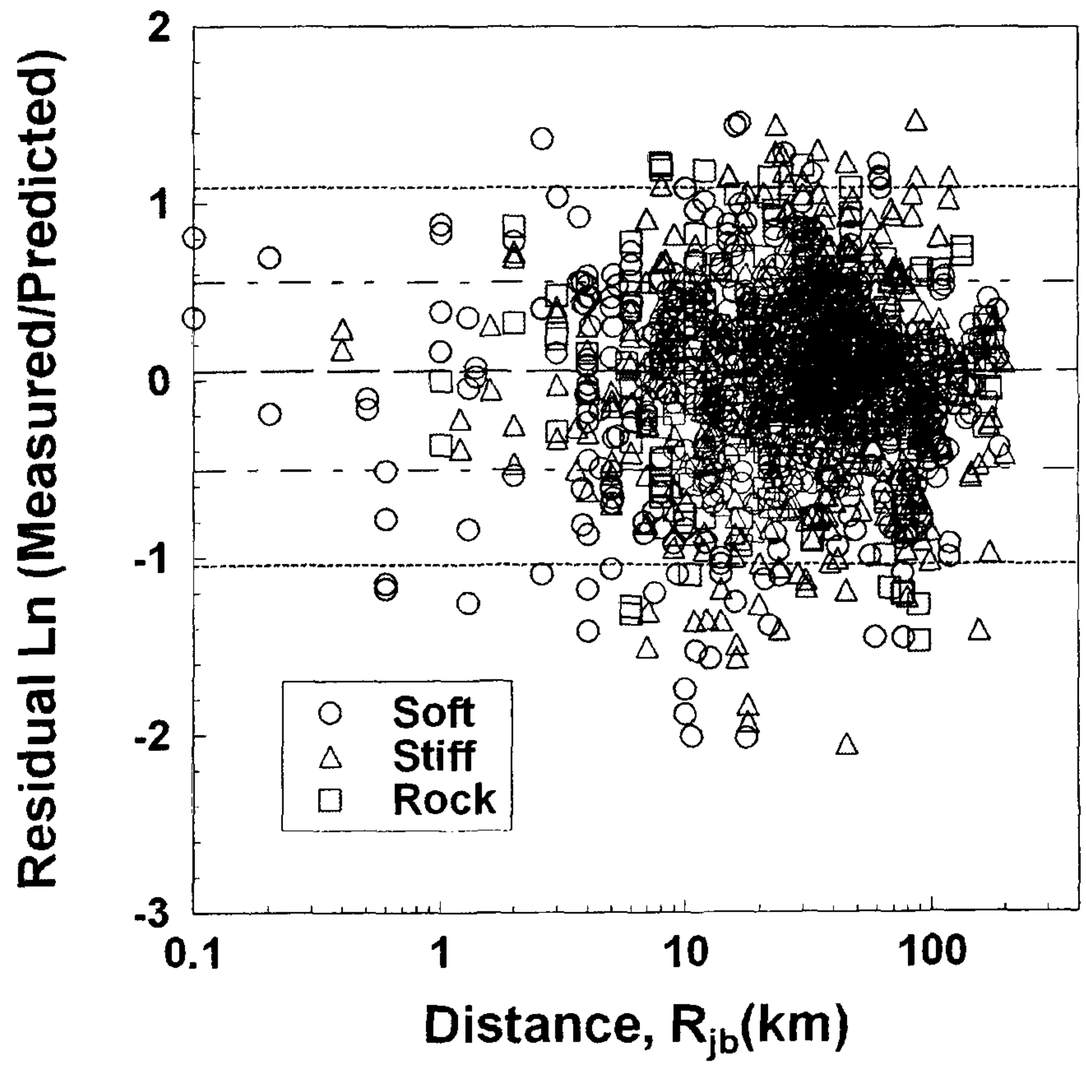


Figure 5.37. - Residuals for LLBD at 25% Maximum CSR vs. distance, horizontal lines represent median (long dashes), one standard deviation (dot, dash) and two standard deviations (dots).

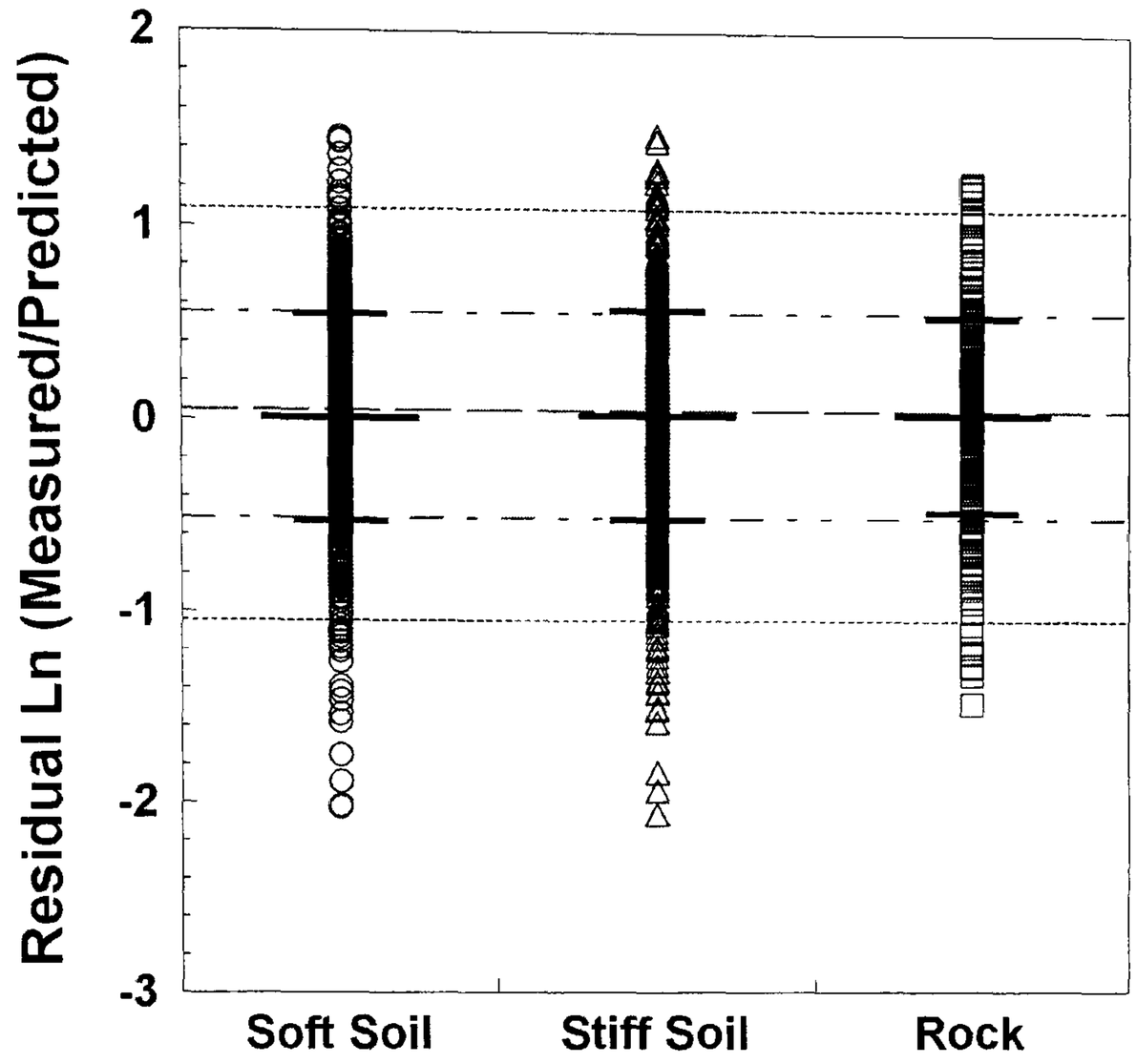


Figure 5.38. - Residuals for LLBD at 25% Maximum CSR vs. soil type, horizontal lines represent median (long dashes), one standard deviation (dot, dash) and two standard deviations (dots).

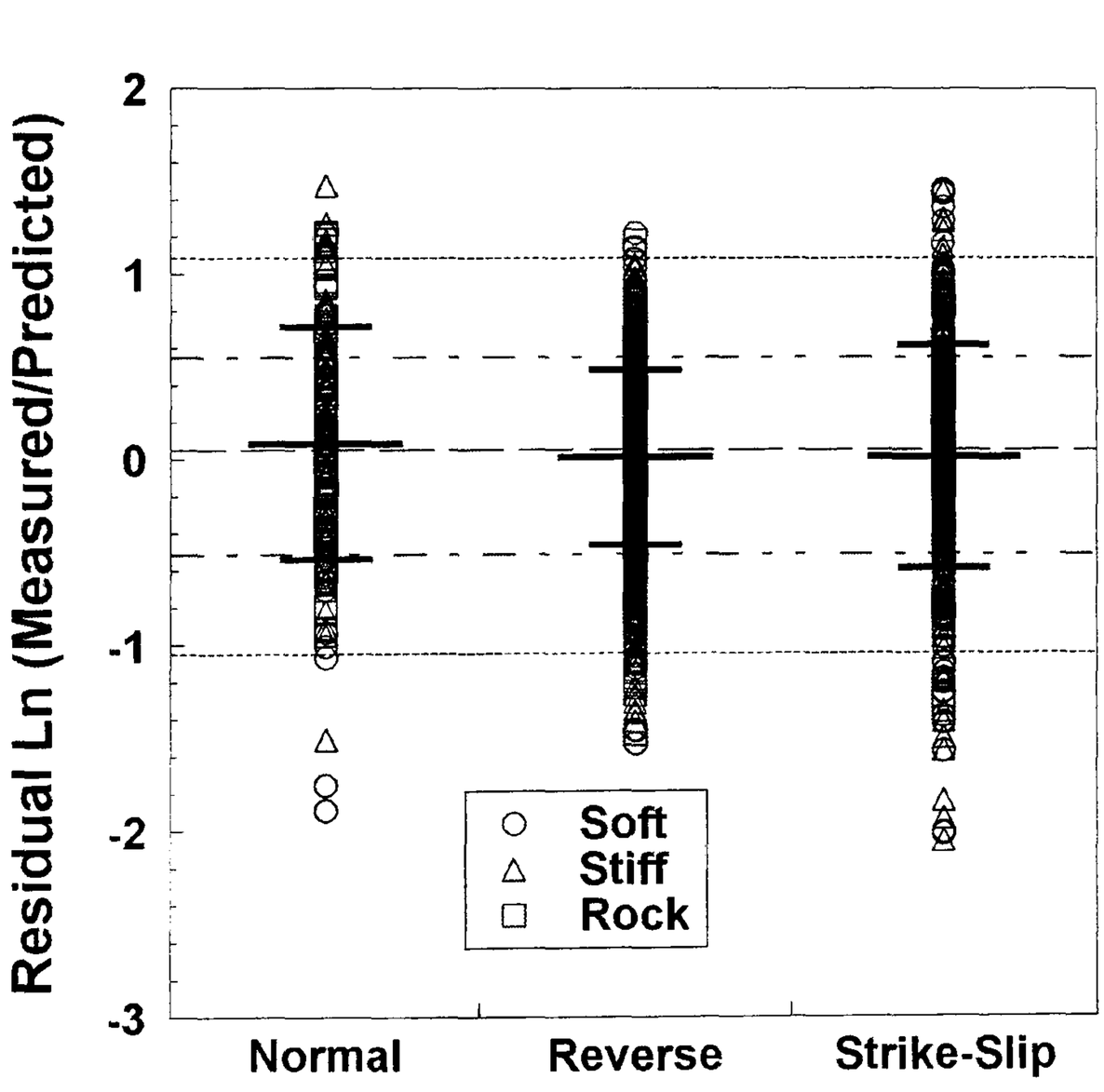


Figure 5.39. - Residuals for LLBD at 25% Maximum CSR vs. earthquake fault mechanism, horizontal lines represent median (long dashes), one standard deviation (dot, dash) and two standard deviations (dots).

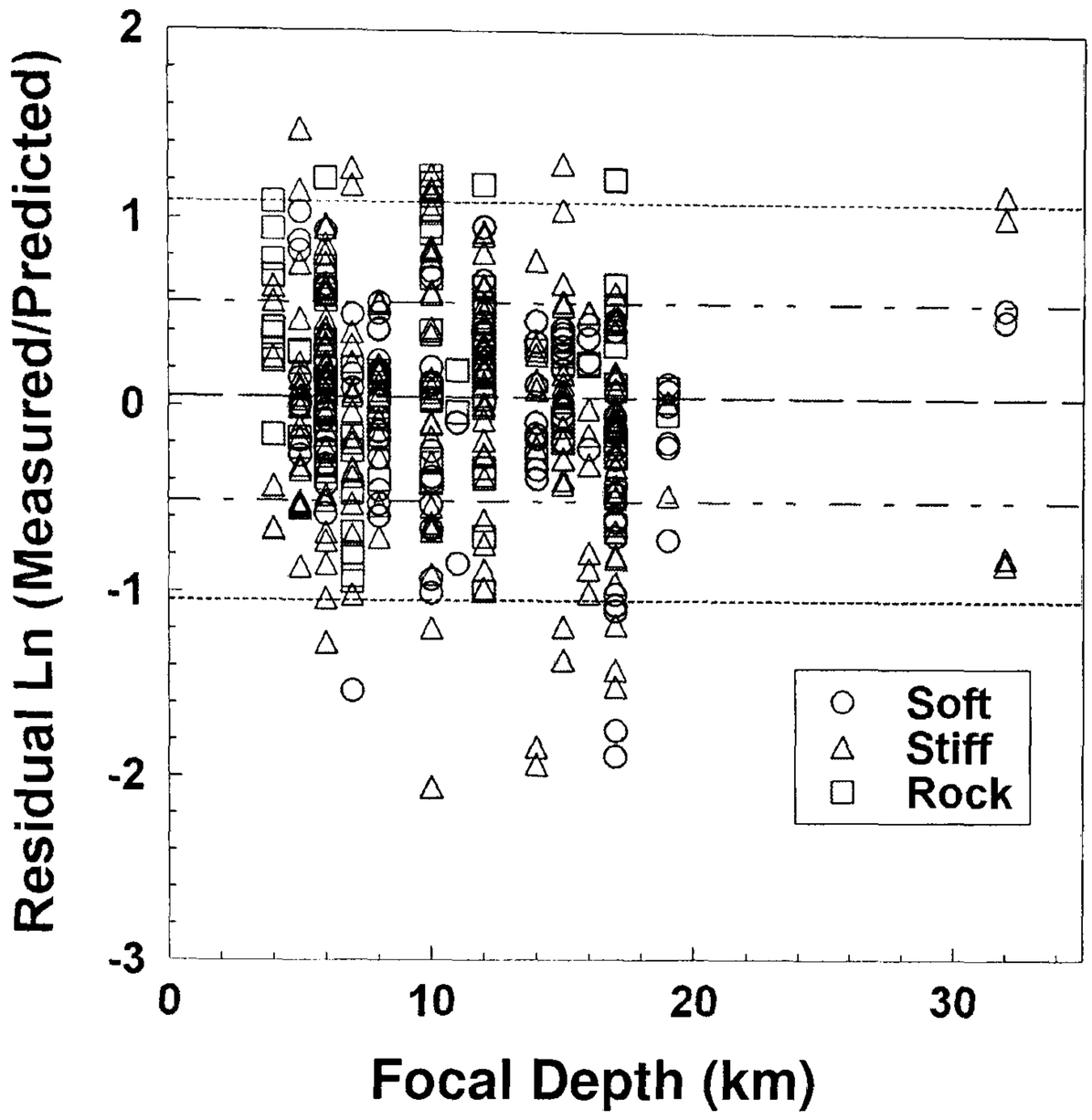


Figure 5.40. - Residuals for LLBD at 25% maximum CSR vs. focal depth, horizontal lines represent median (long dashes), one standard deviation (dot, dash) and two standard deviations (dots).

A comparison is made between predictions of the new equation and that of relationships for other relative bracketed durations developed by McGuire and Barnhard (1979) and Kawashima and Aizawa (1989). Although a direct comparison is not strictly possible because the durations are measured at different acceleration levels and the magnitude metrics of the earlier studies are not known, it appears that the new equation generally predicts equal or longer durations than the equations of the other authors, with differences up to about 40%. The general trends in the predictions are similar with durations increasing for both magnitude and distance (Figures 5.41 and 5.42).

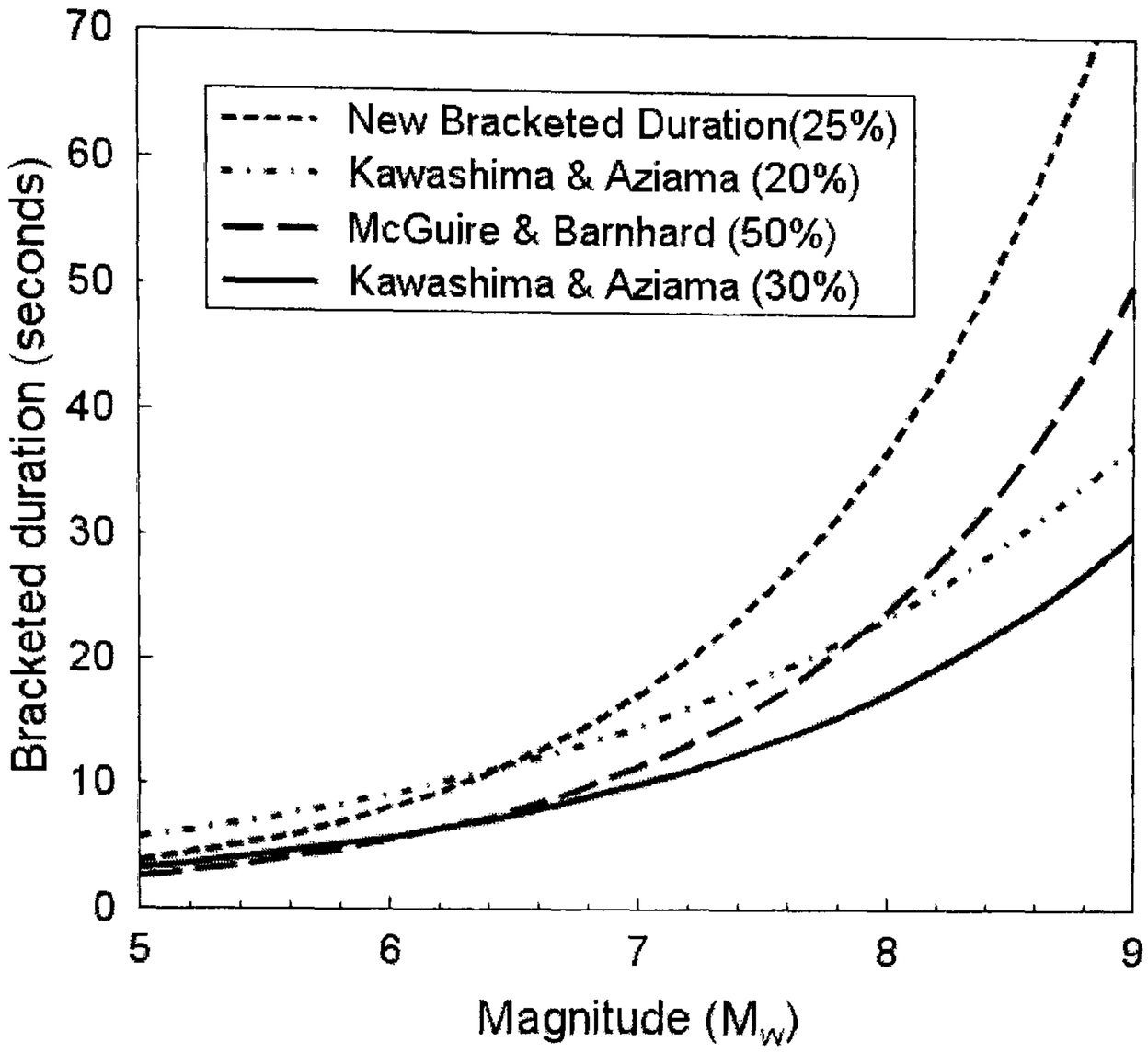


Figure 5.41. - Comparison of LBBD at 25% max CSR (PGA), 50km distance, reverse faulting, rock sites and relative bracketed durations predicted at 50%PGA by McGuire and Barnhard (1979), and at 20% and 30%PGA by Kawashima and Aizawa (1979).

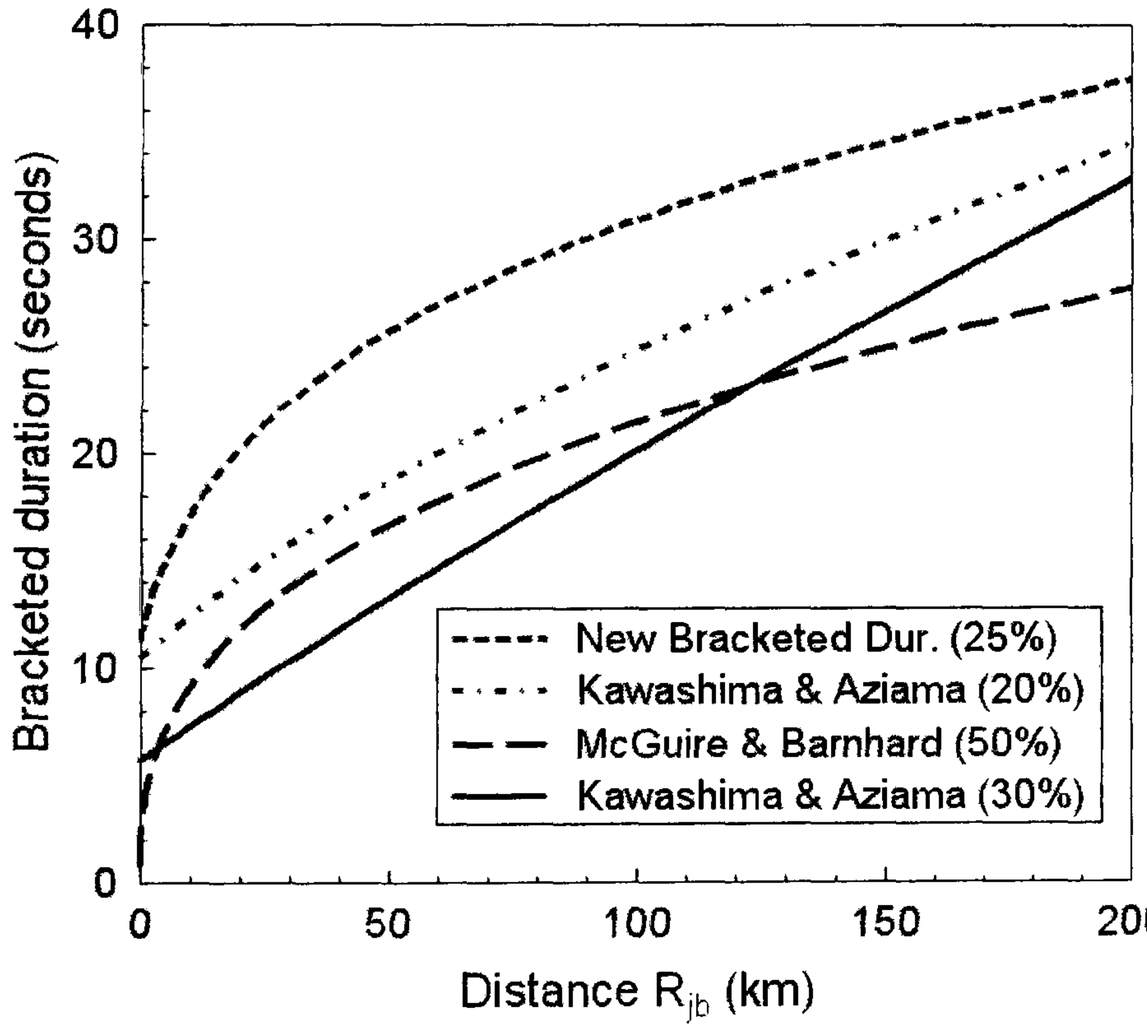


Figure 5.42. - Comparison of LBBD at 25% max CSR (PGA), M7.5, reverse faulting, rock sites and relative bracketed durations predicted at 50%PGA by McGuire and Barnhard (1979), and at 20% and 30%PGA by Kawashima and Aizawa (1979).

5.2.14 Regression of secondary dataset

A sensitivity study is conducted to determine the influence of the distance metric used on the regression analysis. All of the records in the primary database for which both the distance to the surface projection of the fault rupture and the rupture distance are known are collated to form a secondary data set (as described in section 3.1.2). Regression analysis is then conducted for both distance measures on this smaller dataset. Regression coefficients and significance of the coefficients are given in Tables 5.5 and 5.6 respectively.

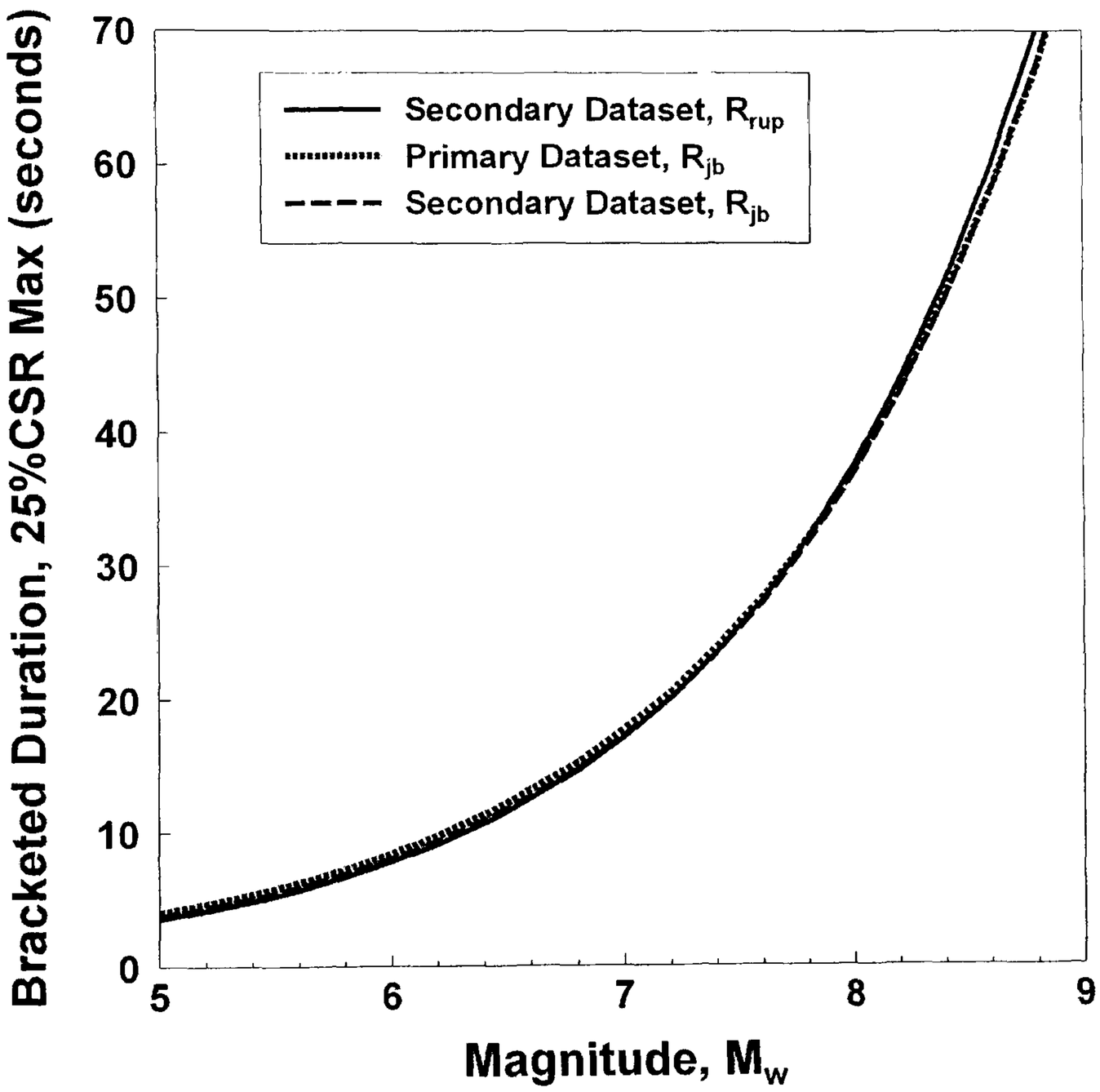


Figure 5.43. - Comparison of LBBD at 25% max CSR (PGA) derived with primary dataset, secondary dataset and surface projection of fault rupture distance, secondary dataset and rupture distance, 50km distance, reverse faulting, rock sites.

Differences between the coefficients are generally within 10%, with the exception of coefficient C_4, which is half in the equation using rupture distance. This effectively compensates for the fact that the distance to surface projection of the fault rupture is

by definition smaller than or equal to rupture distance. Comparison of the predictions made by the equations also demonstrates that the equations are effectively the same (Figures 5.43 and 5.44). As the rupture distance is not known for the European records, the secondary dataset consists of primarily US records. This is interesting as removing the European records, consisting of nearly 30% of the primary database has virtually no effect on the predictive equations. This indicates that ground-motion duration does not show significant differences between seismically active regions in the US and Europe.

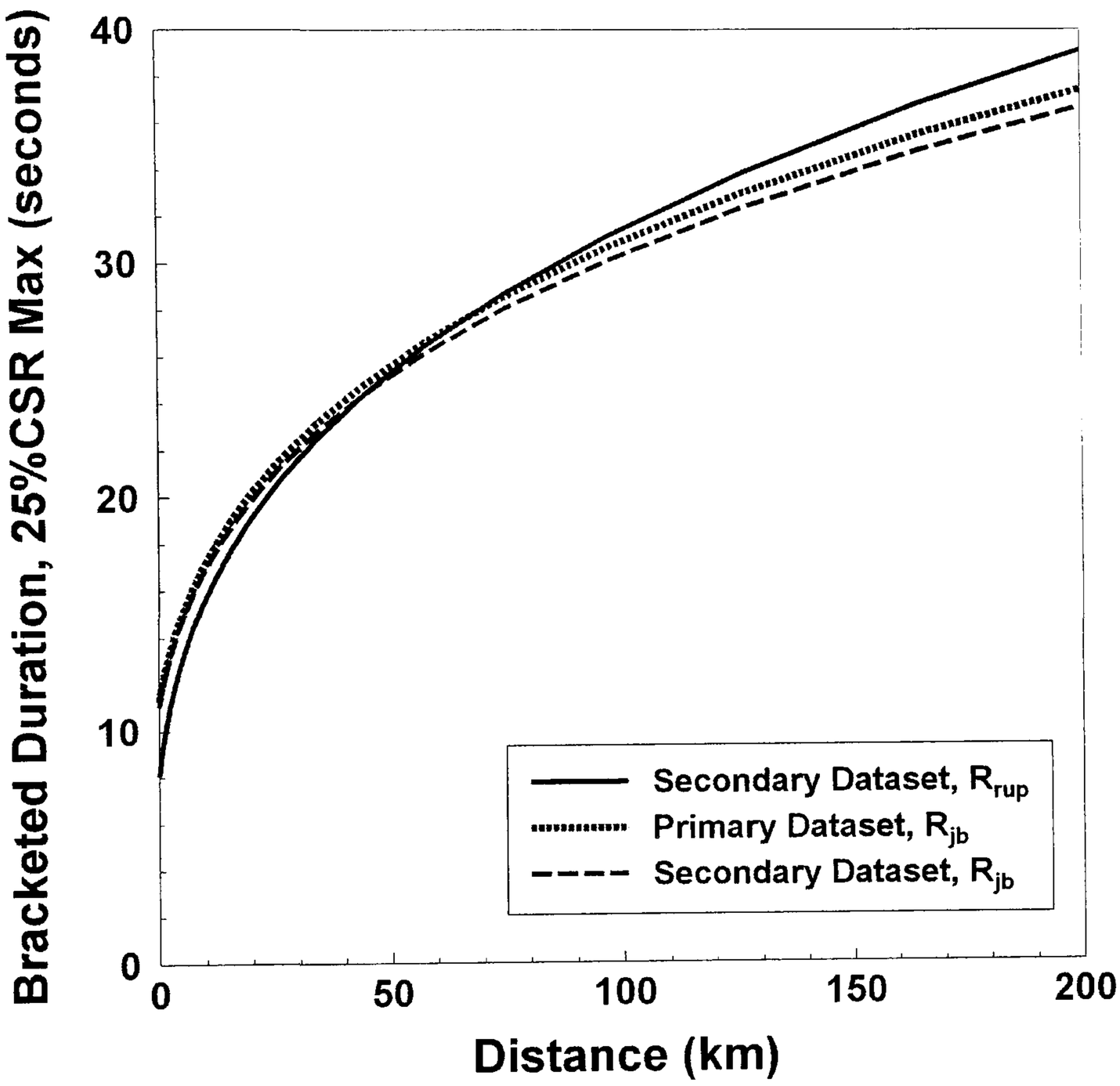


Figure 5.44. - Comparison of LBBD at 25% max CSR (PGA), derived with primary dataset, secondary dataset and surface projection of fault rupture distance, secondary dataset and rupture distance, M7.5, reverse faulting, rock sites.

Table 5.5. - Coefficients and standard deviations from regression of primary dataset

$\%_{max}$CSR	C_1	C_2	C_3	C_4	C_5	C_6	C_7	C_8	σ_r	σ_e	σ_{total}
20	-2.729	0.700	0.256	2.226	0.096	-0.149	0.217	0.101	0.458	0.208	0.503
25	-3.283	0.742	0.282	2.900	0.118	-0.163	0.241	0.106	0.496	0.233	0.548
30	-3.562	0.747	0.300	3.171	0.114	-0.166	0.259	0.131	0.539	0.251	0.595
35	-3.960	0.779	0.296	3.356	0.147	-0.166	0.287	0.152	0.592	0.267	0.649
40	-4.126	0.764	0.313	3.895	0.158	-0.155	0.307	0.175	0.637	0.301	0.704

Note

σ_r is the site-to-site component of the standard deviation

σ_e is the earthquake-to-earthquake component of the standard deviation

Table 5.6. - Significance level of coefficients using F-Test1 from regression of primary dataset

$\%_{max}$CSR	C_1	C_2	C_3	C_4	C_5	C_6	C_7	C_8
20	>99	>99	>99	>99	46	>99	17	57
25	>99	>99	>99	>99	62	>99	45	55
30	>99	>99	>99	>99	50	>99	68	76
35	>99	>99	>99	>99	48	98	83	81
40	>99	>99	>99	>99	28	94	73	84

Table 5.7. - Coefficients and standard deviations from regression analysis using secondary dataset, 25% $_{max}$CSR

Distance Metric	C_1	C_2	C_3	C_4	C_5	C_6	C_7	C_8	σ_r	σ_e	σ_{total}
Surface proj. of fault	-3.375	0.759	0.280	2.771	-0.511	-0.198	0.301	0.165	0.476	0.206	0.518
Rupture	-3.641	0.782	0.319	1.425	-0.512	-0.253	0.272	0.148	0.470	0.231	0.524

Table 5.8. - Significance level of coefficients using F-Test from regression using secondary dataset, 25%$_{max}$CSR

Distance Metric	C_1	C_2	C_3	C_4	C_5	C_6	C_7	C_8
Surface proj. of fault	>99	>99	>99	>99	10	100	95	0
Rupture	>99	>99	>99	96	12	100	100	26

5.2.15 Influence on liquefaction assessment

The duration prediction equations derived above could be used to develop a duration scaling factor, which could be used instead of the magnitude scaling factor currently employed in the assessment of liquefaction potential of soils (Figure 5.45). The cyclic resistance ratio (*CRR*) of soils is currently defined as the soil's resistance to liquefaction under the action of a magnitude 7.5 earthquake. The magnitude scaling factor (*MSF*) is used to adjust the *CRR* for earthquakes with magnitudes other than 7.5 so that the factor of safety against liquefaction (FoS) is defined as:

$$FoS = \frac{CRR(M7.5)}{CSR} * MSF \tag{5.13}$$

where CSR is the cyclic stress ratio (Eqn 5.3)

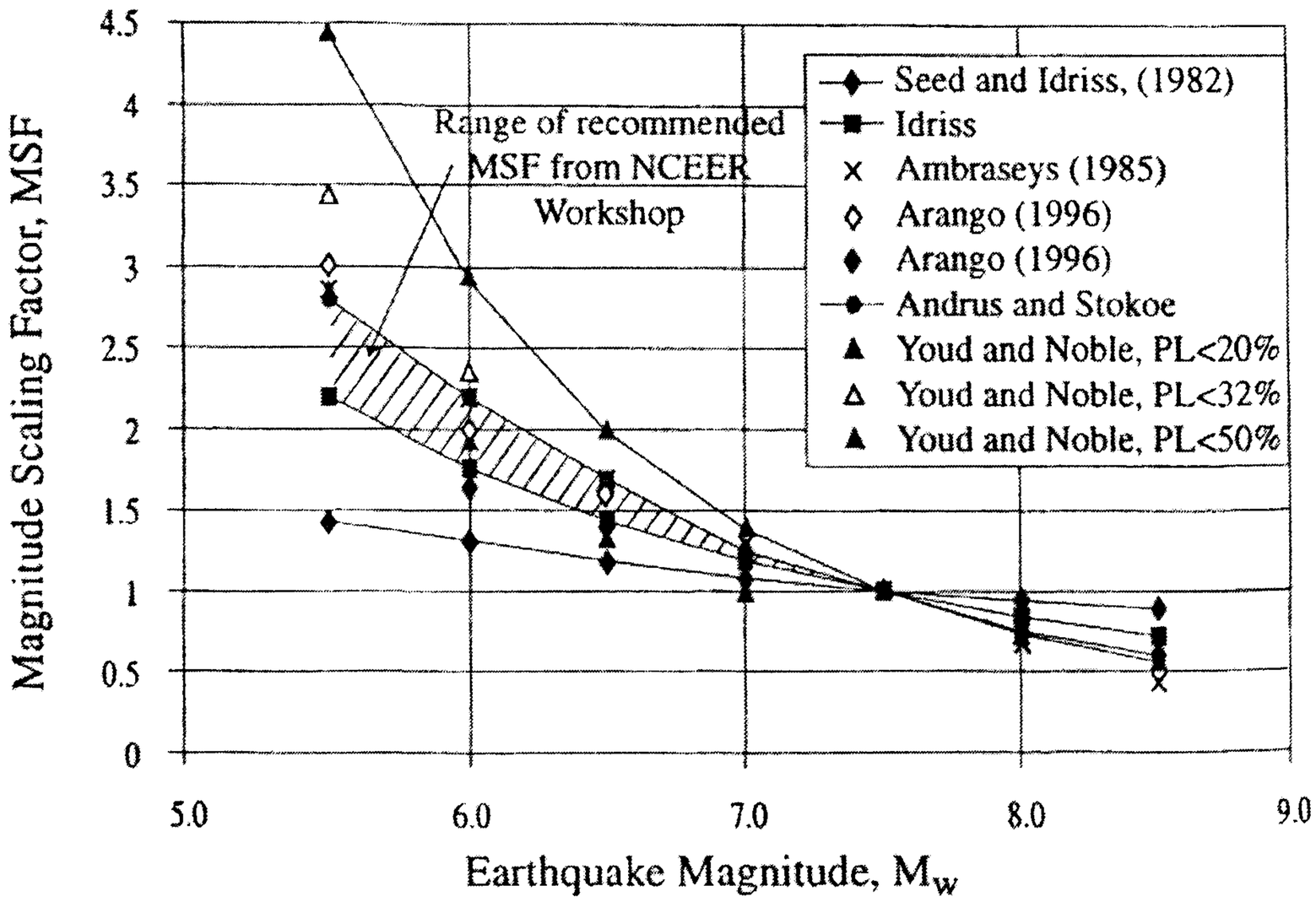


Figure 5.45. – Magnitude scaling factors derived by various investigators (Youd and Idriss 2001)

A duration scaling factor would recognise that factors other than magnitude, particularly source-to-site distance, also influence the duration and number of cycles of the ground-motion. As there is not a direct link between ground-motion duration

and liquefaction potential, duration scaling factors would need to be calibrated against empirical data. This could be achieved by estimating the ground-motion duration and *CSR* at sites that are known to have liquefied or not to have liquefied during earthquakes. The duration scaling factors could be developed so that there is a good separation between the sites which have liquefied and those that have not when *CRR* is normalized to a single ground-motion duration, in the same way that is currently conducted for earthquake magnitude (Figure 5.46).

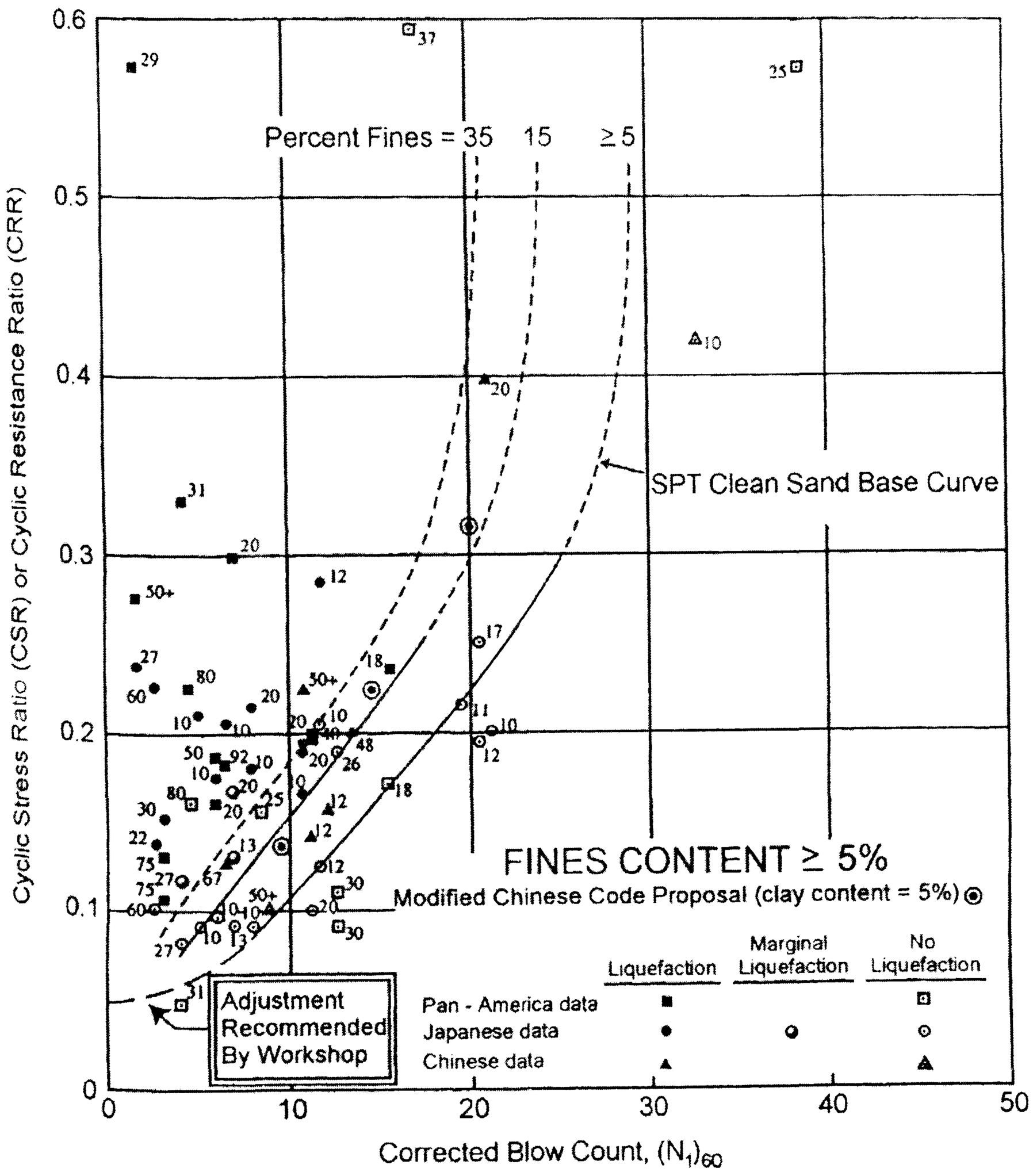


Figure 5.46. – SPT Clean-sand base curve normalized to magnitude 7.5 earthquakes with data from liquefaction case histories (Youd and Idriss, 2001)

5.3 Summary and Further Work

Different parameters that influence the duration and number of cycles of ground-motion have been investigated. The earthquake magnitude is universally acknowledged as the parameter that has the greatest influence on the number of cycles and ground-motion duration. More recent studies also include the source-to-site distance as a predictive parameter; the influence of this parameter depends on the definition as duration and number of cycles measured with relative definitions increase with distance, while those with absolute definitions decrease. Some studies indicate that rupture directivity also plays an important role in the duration and number of cycles in the near-field. However, further studies are required to determine the quantitive influence that this has on the number of ground-motion cycles. Several authors report that sites with soft soil classification have longer duration and greater number of cycles, but, the influence is usually small; for example, Liu *et al.* (2001) report an increase of approximately 10% in the number of ground-motion cycles for sites classified as soil compared to those classified as rock.

New predictive equations for relative bracketed duration have been derived from a combined dataset of 749 recorded ground motions. The equations are derived for a range of cut-off levels and the duration measured at the 25% level is recommended as this captures the majority of the ground motion of importance for liquefaction potential and has good correlation with the predictive parameters. The new equation uses consistently defined parameters (magnitude, distance, site class and style-of-faulting) which results in a lower standard deviation than predictive equations derived by earlier authors. The relative bracketed duration is simple in concept and the new predictive equations could be used for developing duration scale factors for use in liquefaction assessment. However, this would require further work to derive duration scale factors using empirical observations of liquefied and non-liquefied sites from the field.

A further study would be useful to produce predictive equations for a much wider range of definitions of duration and number of cycles. The new predictions could also address the important issue of cross-correlation between the duration and amplitude of the ground motion.

6. WAVELET ADJUSTMENT OF RECORDED GROUND MOTIONS

To reduce the number of analyses required to obtain stable estimates of the response of non-linear or safety critical structures it is desirable to reduce the variability in the input ground motion. This can be achieved by using records that have a close fit to the elastic design response spectrum. This chapter presents the work conducted to create a new version of the program RSPMatch that uses wavelets to adjust recorded ground motions so that they match target displacement spectra. The original version of RSPMatch was written by Abrahamson (1992) using the methodology proposed by Lilhanand and Tseng (1987, 1988). RSPMatch is already a useful tool and has been widely used for both academic research and on important engineering projects. The enhancements made to the program in this work improve the program by ensuring that baseline correction is not required after the wavelet adjustment and also prevent the program from diverging if multiple damping levels are matched at closely spaced periods. The advantages of using wavelets to adjust accelerograms are also highlighted. An abridged describtion of this work is provided in Hancock *et al* (2006).

6.1 Time Domain Dynamic Analysis

Seismic design of structures is invariably based on representation of the earthquake actions in the form of a response spectrum. However, in many situations including the design of critical facilities, highly irregular buildings and base-isolated structures, the simulation of structural response using a scaled elastic response spectrum is not considered appropriate to verify the earthquake resistance. In such cases dynamic non-linear analysis of the structure is required and the earthquake ground motions need to be defined in the form of acceleration time-series, which will generally be required to be compatible with the elastic response spectra representing the design seismic actions at the site.

6.2 Existing Methods of Creating Spectral Compatible Ground Motions

Bommer and Acevedo (2004) show that there are several methods of obtaining accelerograms for use in engineering design and assessment. Broadly speaking these

can be divided into two categories; those that directly use recorded ground motions and those that generate the motion artificially.

Methods that generate ground motions artificially have a considerable range in complexity. Some models include detailed modelling of the rupture propagation, path and site effects (e.g. Trifunac 1971b), whilst others are more straight-forward, simply filtering a random signal so that its Fourier or response spectrum matches a target spectrum (e.g. Scanlan and Sachs 1974; Levy and Wilkinson 1976; Iyengar and Rao 1979; Preumont 1984; Gupta and Joshi 1993; Shrikhande and Gupta 1996; Boore, 2003). The detailed seismological models produce synthetic ground motions with unique spectra that are unlikely to match a target spectrum, so will not be discussed further in this chapter. The main issue with artificially generated spectrum compatible ground motions is that they generally have poor constraint in the time domain. This can lead to large numbers of cycles, excessive energy content, and potentially unrealistic relative phases of the different frequency motions (Figure 6.1).

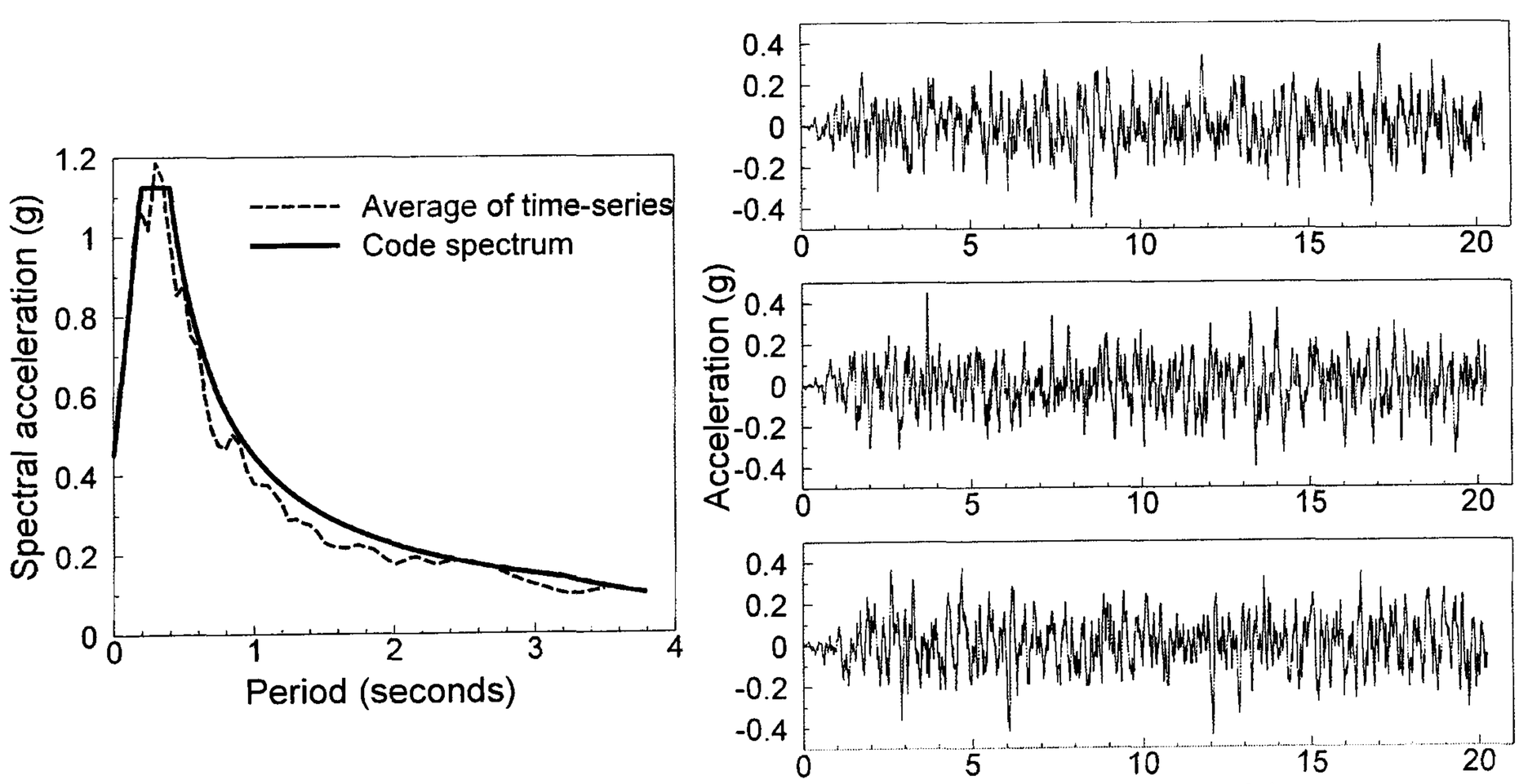


Figure 6.1. – Three artificially generated accelerograms designed to match, on average, the S1 soil category elastic response spectrum from the French seismic design code (after Bommer and Ruggeri 2002).

Methods that use recorded ground motions directly face the problem that there is no guarantee that a record with the required characteristics will be available. For example, even though there is now several global databanks, each containing several thousand records, it is still unusual to find even a single record that matches the target response spectrum to the required tolerance and even less likely to find one that also matches the desired magnitude and distance combination. The probability of finding appropriate records further decreases if several accelerograms are required. For this reason it is necessary to either make adjustments to individual accelerograms so that they have a better match to the target spectrum or to use a larger suite of accelerograms that on average match the target spectrum.

Using the average of many linearly scaled recorded records has the disadvantage that full analysis needs to be conducted with many records, which can be computationally expensive. In addition the scatter in the individual responses is not insignificant, as can be seen in Figure 6.2, which shows the records selected by Bommer and Acevedo (2004) to match, on average, the EC8 type 1 spectrum. The scatter in the individual responses can be even greater if records are selected based on seismological criteria (magnitude and distance) or if records are selected purely to match the average response without attempting to minimize the deviation of the individual responses, as is the case with the method proposed by Naeim *et al.* (2004). Using the average response from a full analysis conducted with multiple records that have been selected and scaled to match a target spectrum on average can only be strictly valid if the response of the structure is linearly proportional to the response of the elastic SDOF systems used to construct the response spectrum.

To reduce the dispersion of individual ground motions some researchers propose methods that adjust the spectra response of individual recorded accelerograms by adjusting the Fourier amplitude spectra (e.g. Rizzo *et al.* 1975, Gasparini and Vanmarcke 1976). This is useful as it generates accelerograms that are based on real ground motions but have a close match to the target spectrum. Unfortunately, adjusting the Fourier spectrum corrupts the velocity and displacement time-series and can result in motions with unrealistically high-energy content (Naeim and Lew 1995).

Wavelet adjustment of recorded accelerograms has the same advantages as the Fourier adjustment methods but leads to a more focused correction in the time domain, so introduces less energy into the ground motion. The wavelet adjustment techniques developed in this research have the additional advantage that they do not cause a drift in the velocity or displacement time-series.

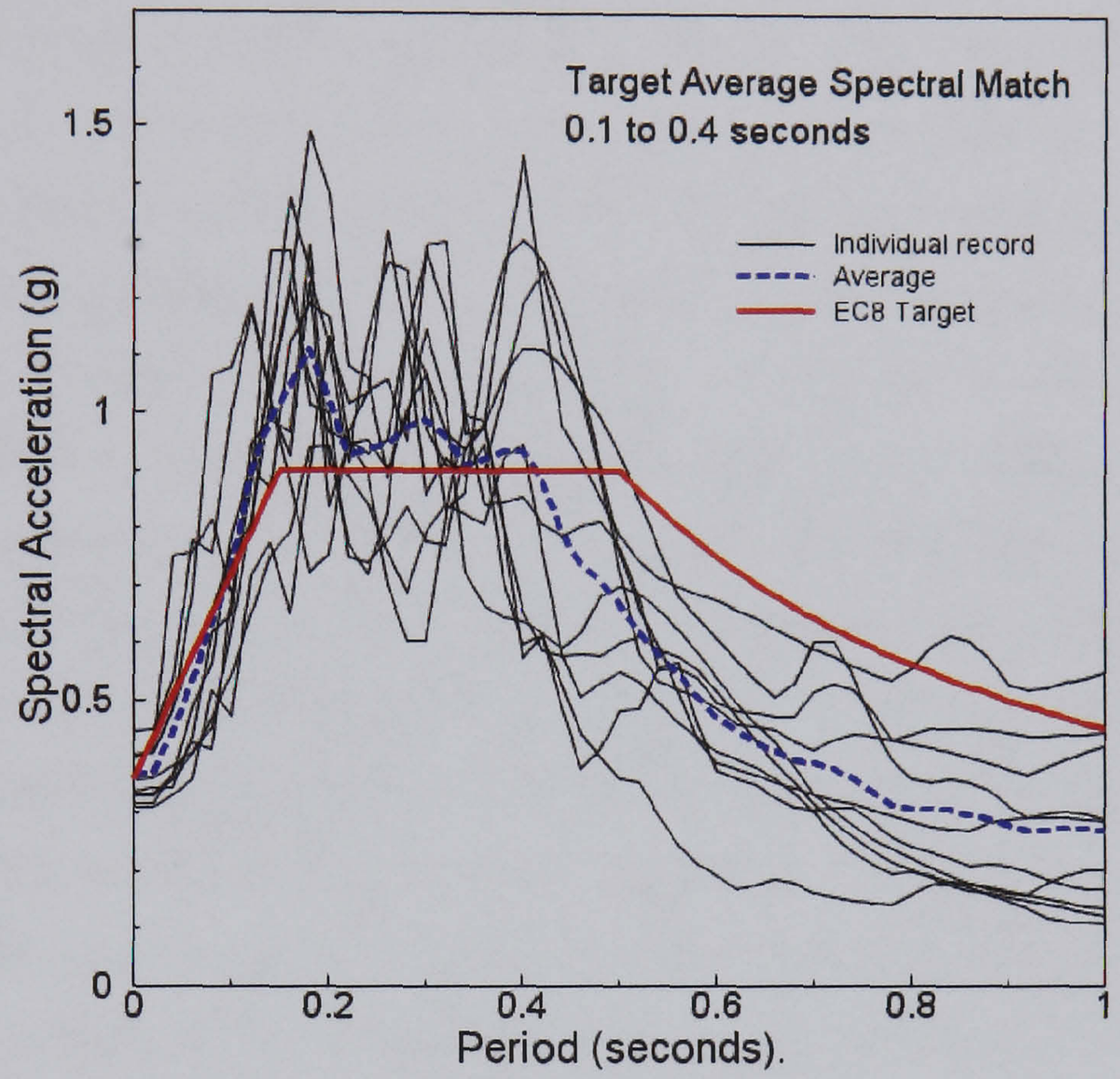


Figure 6.2. – Records selected based on spectral shape by Bommer and Acevedo (2004) to match, on average, EC8 type 1 spectrum with site class B anchored to PGA of 0.36g between periods of 0.1 to 0.4s

6.3 Use of Wavelets in Engineering Seismology

A wavelet is a function that is localized in the time and frequency domain. Most applications that use wavelets, though not RSPMatch, use the continuous wavelet transform (CWT). The CWT decomposes a signal in terms of transformations (translations and frequency changes) of the parent wavelet (Todorovska, 2004). The transformations are described in terms of basis functions that describe the signal in terms of its frequency content and the time at which the signal occurs. The ability to express signals in both frequency and time domain is particularly useful for the analysis of non-stationary signals such as earthquake ground motions, or the response

of structures under the action of earthquake ground motions. This section describes the different uses of wavelets, and the CWT in engineering seismology.

6.3.1 Simplified structural analysis

Gupta and co-workers have developed wavelet-based analysis methods to estimate the response of a range of simple structural systems from SDOF rigid sliding blocks to two dimensional seven storey linear elastic frames (Basu and Gupta 1997; Basu and Gupta 1999; Basu and Gupta 2000a; Basu and Gupta 2000b). However, as the exact analysis of these simple structures can be rapidly undertaken using time-domain methods there is no clear advantage of using the approximate wavelet methods to solve these problems. More recently Salajegheh and Heidari (2005) have used wavelets to decompose ground motions into a signal with fewer data points before conducting time-domain analysis. As the decomposed ground motions contain fewer data points the analysis speed is about one tenth of that required to analyse the original record and the maximum error is less than 8%. Unfortunately Salajegheh and Heidari (2005) only use the method to analyse relatively simple structures with run times of the order of 15 seconds, it would be particularly interesting to see if the method can be applied to the analysis of more complex structures with longer analysis run times where the time saving is of greater benefit.

6.3.2 Response identification

Kitada (1998) uses wavelets to identify the hysteretic response and damping coefficients of nonlinear structural dynamic systems. The method is verified with the results from a small scale model of a five storey building; the same procedure could be used for monitoring and damage assessment in a real structure. Kijewski-Correa and Kareem (2004) use wavelets to show the evolution of frequency content with time for ground motions in the 1985 Mexico City earthquake. They then use a similar approach to analyse the response of the thirteen storey Sherman Oaks building under the action of the 1994 Northridge earthquake, showing that wavelet analysis can identify the softening of the structure as the strong shaking progressively causes damage. Haigh *et al.* (2002) show that wavelet analysis techniques are a useful tool in the identification of resonance, attenuation due to inter-particle sliding and the

estimation of shear-wave velocities in investigating the performance of liquefiable slopes in centrifuge model testing.

6.3.3 Analysis of accelerograms

Several researchers use wavelets to filter or analyse accelerograms. Galiana-Merino *et al.* (2003) show that wavelet filters can be used to filter accelerograms and achieve a higher signal to noise ratios than traditional filters. Teymur *et al.* (2003) use wavelets to analyse the ground motions from the 1999 Kocaeli earthquake. The ability of wavelet analysis to distinguish the different arrival times of different ground motions shows that two distinct rupture events occurred in this earthquake.

Ji *et al.* (2002) use wavelets as part of a procedure to conduct fault inversion. In this procedure the amplitude of wavelet coefficients are used to quantify the error between the estimated ground motions from the finite fault model and those from the actual recordings. The optimum fault model is determined by minimizing this error function. The use of wavelet coefficients, which provide information in both time and frequency domain, enables the simultaneous and efficient inversion of the slip amplitude, slip direction, rise time and rupture velocity.

6.3.4 Simplified representation of the ground motion

As a wavelet is concentrated in time and frequency it can provide a useful approximation of a more complex ground motion for use in parametric studies. The Ricker wavelet has been utilized by several researchers to represent a simplified ground motion for use in wave propagation analyses to investigate the potential topographic amplification of ground motions near canyons (Takemiya and Fujiwara 1994; Assimaki and Gazetas 2004; Gazetas *et al.* 2002).

Mavroeidis and Papageorgiou (2003) investigate the ability of several different types of wavelet to represent the velocity pulses that characterise several near fault ground motions. They find that the Gabor wavelet has the best ability to match this type of ground motion and also derive predictive equations that can be used to estimate the period and amplitude of the wavelet for a given earthquake magnitude and source-to-site distance. Iyama and Kuwamura (1999) use Daubechies wavelets to analyse the

rate and amount of energy release from the 1995 Hyogoken-Nanbu (Kobe) earthquake for different source-to-site distances. They then propose that artificial accelerograms can be constructed from the inverse wavelet transform such that the dominant period, total energy and rate of energy release agrees with estimates of these parameters derived from observations of the Kobe earthquake. Unfortunately, it is not possible to achieve reliable estimates of the required parameters because of the considerable scatter in the observations. The resulting artificial ground motions produced with this method are not realistic because they do not contain any high-frequency motion at the end of the record and have a poor match to the required energy distribution within the record.

6.3.5 Adjustment of accelerograms

There are several different methods of using wavelets to adjust accelerograms to that they have a closer match to a target response spectrum. The method proposed by Lilhanand and Tseng (1987, 1988) is based on the work of Kaul (1978) and uses wavelets but uses the response of elastic SDOF systems rather than the CWT. This enables accelerograms to be made spectrum compatible with smaller adjustments than the other methodologies described in this section. The Lilhanand and Tseng (1987, 1988) methodology is used by RSPMatch and described in greater detail in the following sections of this chapter.

Mukherjee and Gupta (2002a and 2002b) and Suarez and Montejo (2003, 2005) use wavelets to de-compose the original acceleration time-series into a number of time-series with energy in non-overlapping frequency bands. An iterative procedure is used to scale each time-history so that when they are added together they produce a spectrum compatible ground motion. Although the approximate duration of the original accelerogram is retained using this type of adjustment procedure the adjusted accelerograms have visibly different amplitude and frequency content than the original accelerogram.

6.4 Lilhanand and Tseng Matching Procedure

The Lilhanand and Tseng (1987, 1988) method generally works well; however, there are two main problems with the procedure. Firstly the wavelet used corrupts the velocity and displacement time-series of the accelerograms, so a baseline correction is required after the wavelet adjustment which can partially undo the spectral match; secondly, the method is not always stable and diverges if closely spaced periods and multiple damping levels are attempted to be matched. The techniques developed in this research to avoid these issues are detailed in later sections of this chapter; this section details the fundamental mechanics of the method.

The Lilhanand and Tseng methodology utilises wavelet functions but is not based on conventional wavelet theory as described by Walker (1999) and employed in engineering seismology by many authors including Mukherjee and Gupta (2002a and 2000b), Suarez and Montejo (2003, 2005) and Salajegheh and Heidari (2005). The principle difference is that the methodology uses the response of elastic single-degree-of-freedom (SDOF) systems, rather than wavelet transforms, to analyse the acceleration time-series. This approach is advantageous as it only adjusts the part of the ground motion causing the peak in response, leading to a more focused adjustment, and it does not need to be assumed that the amplitude of the wavelet coefficients is directly related to the amplitude of the spectral response. In addition, as spectral response can be calculated for any arbitrary motion using numerical integration, the adjustment "wavelet" function is not limited to those for which there is a wavelet transform so any functional form may be used.

A flow chart showing the original procedure as employed in RSPMatch is given in Figure 6.3. The principle to the methodology is as follows:

1. Calculate the response of an elastic SDOF system under the action of the acceleration time-series for each period and damping level to be matched.
2. Compare the peak of each SDOF response with the target amplitude and determine the mismatch.
3. Add wavelets to the acceleration time-series with the appropriate amplitudes and phasing so that the peak of each response matches the target amplitude. One wavelet is used to match one SDOF response.

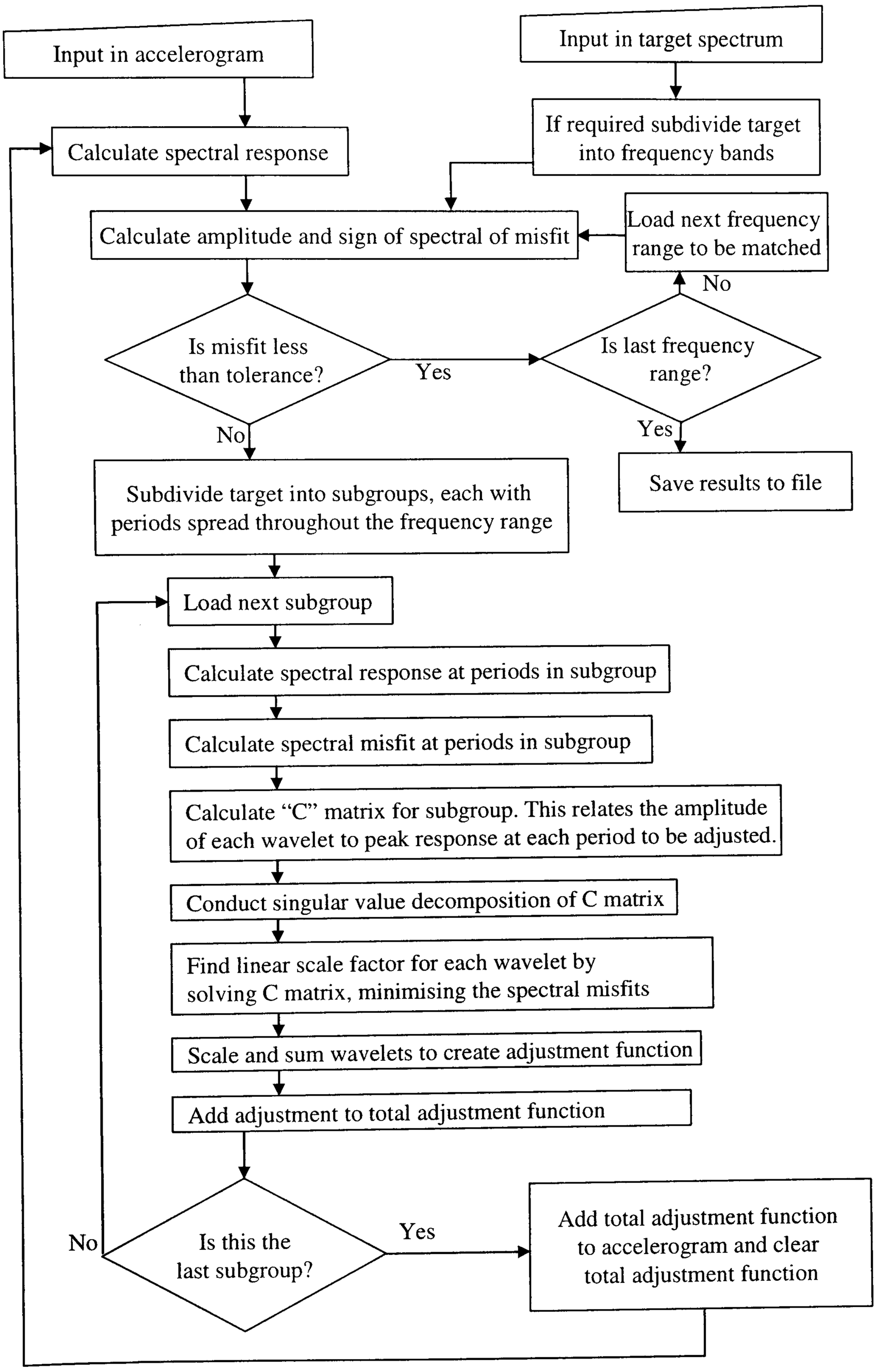


Figure 6.3. - Basic methodology of RSPMatch program

Each wavelet is applied to the time-series so that the time of maximum SDOF response under the action of the wavelet is the same as the time of the peak response to be adjusted from the unadjusted acceleration time-series. A fundamental assumption of the method is that the time of the peak response does not change as a result of adding the wavelet adjustment. This assumption is not always valid and is the reason for diverging solutions as will be discussed in more detail later.

The amplitude of each wavelet used in the adjustment is determined by the solution of a set of simultaneous equations that account for the cross correlation of each wavelet with each response to be matched. This can be expressed in matrix form;

$$C.b = \delta R \tag{6.1}$$

where, C is a square matrix with elements that describe the amplitude of each SDOF response, at the time that the response needs to be adjusted, under the action of each wavelet. b is a vector of linear scale factors for each wavelet used in the adjustment. δR is a vector of the required adjustment, the difference between the peak SDOF response of the unadjusted time-series and the required amplitude specified by the target spectra response for each period and damping level to be matched.

The wavelet scale factors in the b vector are found using amplitude of the required adjustment and the inverse of the correlation matrix C:

$$b = C^{-1}.\delta R \tag{6.2}$$

The amplitude of the wavelet adjustment function at time (t) is determined from the sum of the amplitude of each wavelet at that time, $f_i(t)$, multiplied by its scale factor b_i.

$$Adjustment(t) = \sum_{i=1}^{i=N_w} b_i.f_i(t) \tag{6.3}$$

where N_w is the total number of wavelets. The adjusted acceleration time-series is the sum of the original time-series and the adjustment function.

Unfortunately the correlation matrix C can be singular and of a size that took considerable time to solve when the method was first proposed. These problems were overcome by spitting the problem into smaller subgroups and conducting singular value decomposition on the C matrix.

6.5 Wavelets

One of the key features to the adjustment method is the function used for the wavelet adjustment. A wavelet is a harmonic or repeating function that has been modulated by a window function so that it is concentrated over a finite duration. Wavelets are particularly useful in measuring the frequency content of a non-stationary signal and are used in a wide range of applications from speech recognition to digital image compression (Walker 1999). Wavelets have many different functional forms. However, in the interest of brevity, only those used in the RSPMatch program will be described in this section.

6.5.1 Wavelet used by Lilhanand and Tseng

The original wavelet used by Lilhanand and Tseng (1987, 1988) is a reverse impulse function:

$$a_{wl}(t) = \frac{-\omega}{\sqrt{1-\beta^2}} \exp(-\omega\beta(tj-t))\left[(2\beta^2-1)\sin(\omega_d(tj-t)) - 2\beta\sqrt{1-\beta^2}\cos(\omega_d(tj-t))\right] \quad (6.4)$$

where,

$a_{wl}(t)$ is the amplitude of the wavelet at time t

tj is the duration of the wavelet

ω is the circular frequency of the correction

β is the damping level (proportion of critical)

ω_d is the damped circular frequency $\omega_d = \omega\sqrt{1-\beta^2}$

Although this wavelet is very efficient in adjusting the response, is has the disadvantage that it corrupts the velocity and displacement time-history because the wavelet does not end with zero velocity or displacement (Figure 6.4).

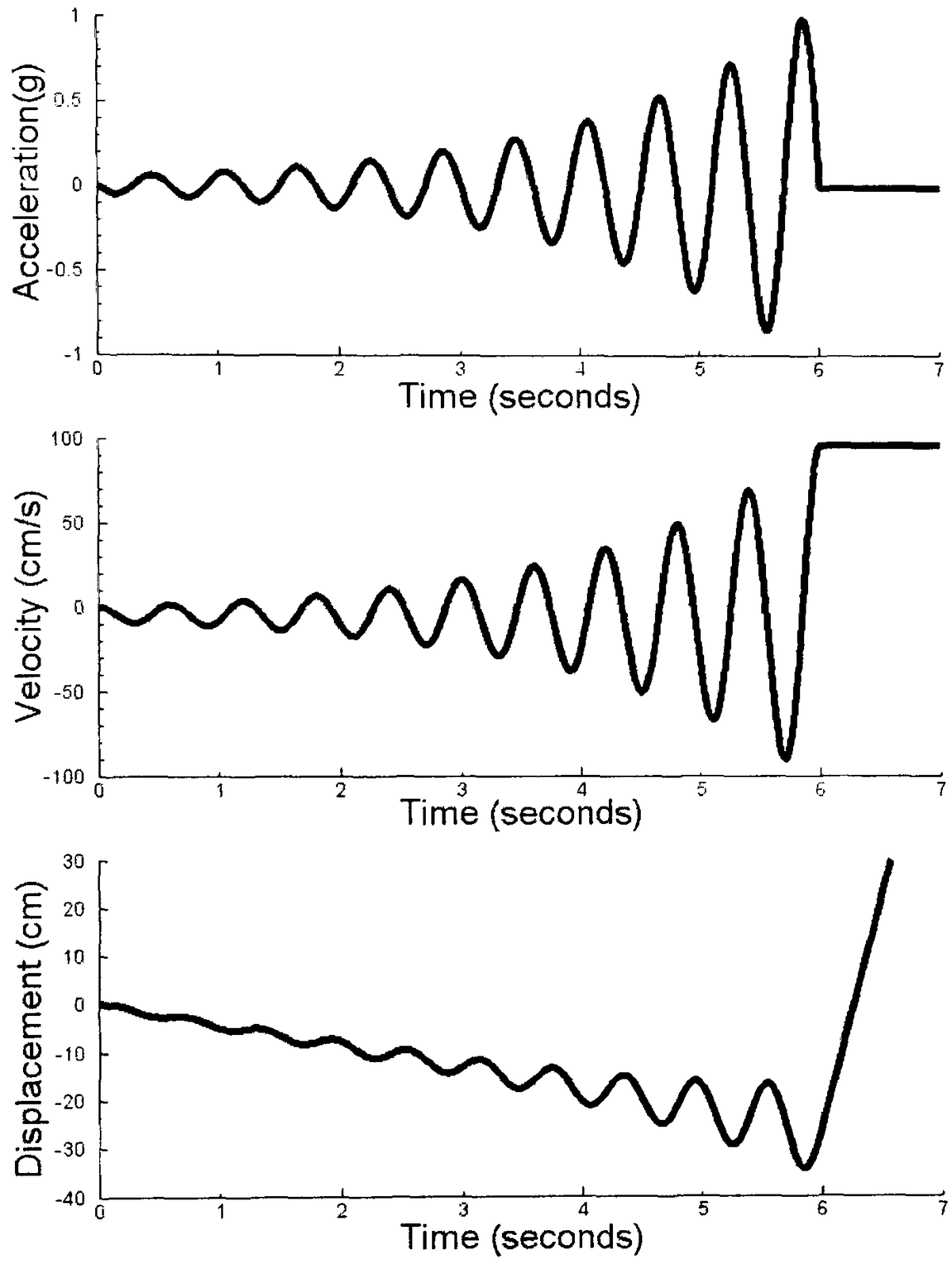


Figure 6.4. - Reverse impulse wavelet with 5% damping, 0.6 seconds period, 6 seconds duration. Acceleration time-series (*top*), velocity time-series (*middle*) and displacement time-series (*lower*).

6.5.2 New displacement-compatible wavelets

Two new wavelets have been developed that have a zero final velocity and displacement. Accelerograms adjusted with these wavelets have the same final velocity and displacement before and after the adjustment. Both of the wavelets are based on the wavelet used by Suarez and Montejo (2003, 2005), which has a zero

final velocity but non-zero final displacement (Figure 6.5). The equation describing the Suarez and Montejo wavelet is:

$$a_{ws}(t) = e^{-\beta\omega|t|}\sin(\omega t) \tag{6.5}$$

where,

$a_{ws}(t)$ is the amplitude of the Suarez and Montejo wavelet at time t

ω is the circular frequency of the correction

β is the damping level

The error in the final displacement from the Suarez and Montejo is given by the following formulae, which is obtained by double integration of the wavelet and applying the appropriate initial conditions:

$$DispError = 2\left[\frac{-2\beta - e^{\beta t_0\omega}\left(-2\beta + t_0\omega + \beta^2 t_0\omega\right)\cos(t_0\omega) + e^{\beta t_0\omega}\left(1-\beta^2+\beta t_0\omega\right)\sin(t_0\omega)}{\left(1+\beta^2\right)^2\omega^2}\right] \tag{6.6}$$

where t_0 is the start time of the wavelet; note that as the wavelet is symmetrical about the Y axis t_0 is a negative number and equal to half the wavelet duration.

The new wavelets implemented in RSPMatch are made up of two functions, the Suarez and Montejo wavelet and a function to ensure the displacement time-series has a zero final value. The first wavelet has a correction applied with a polynomial function of the form:

$$PolyCor(t) = P_1(t-t_0) + P_2(t-t_0)^2 + P_3(t-t_0)^3 \tag{6.7}$$

where,

PolyCor(t) is the amplitude of the correction at time t

P_1 is a correction coefficient equal to $2.t_0.P_3^2$

P_2 is a correction coefficient equal to $3.t_0.P_3$

P_3 is a correction coefficient equal to $\frac{15}{4}\frac{DispError}{t_0^5}$

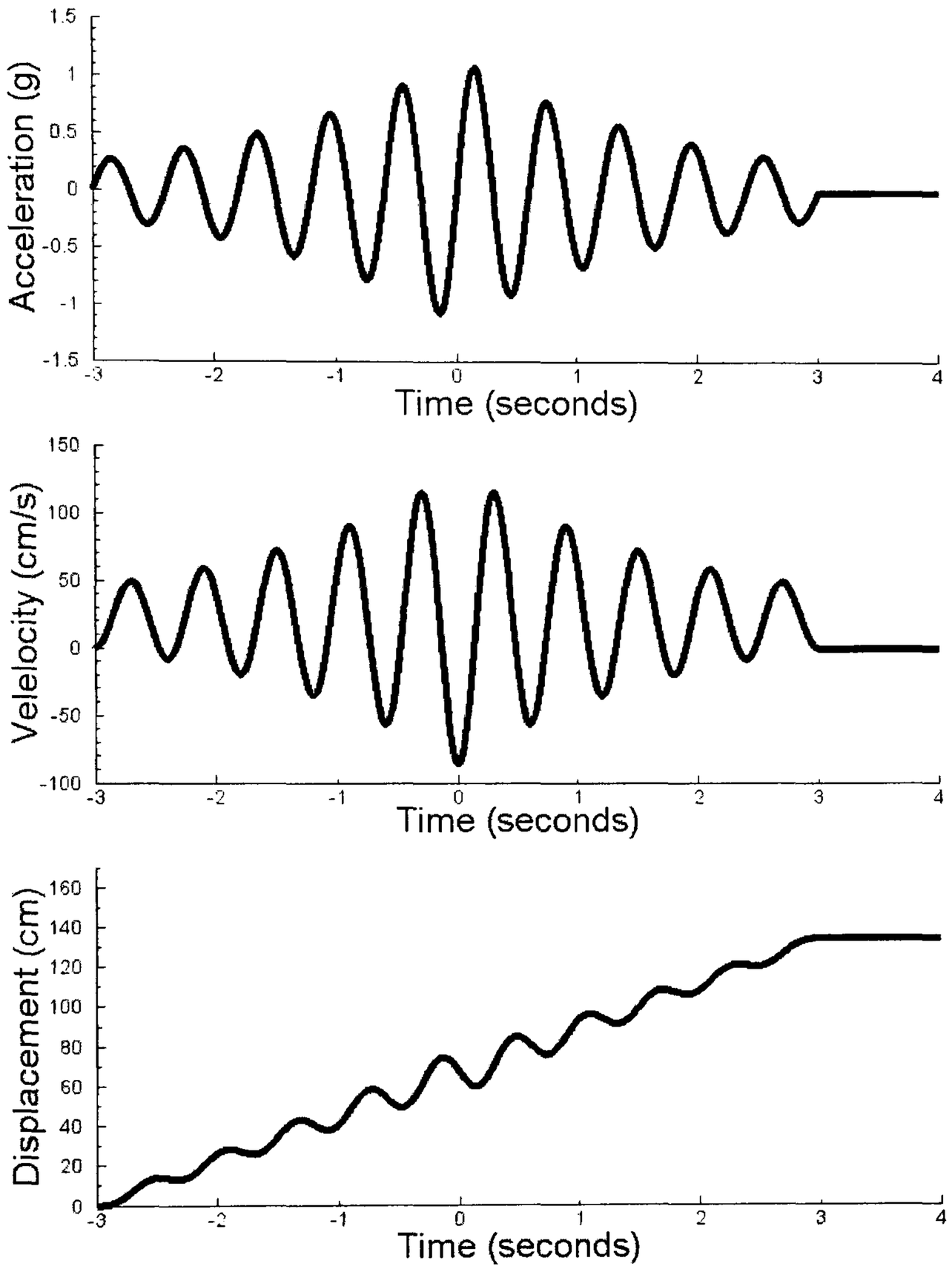


Figure 6.5. - Suarez and Montejo wavelet with 5% damping, 0.6 seconds period, 6 seconds duration. Acceleration time-series (*top*), velocity time-series (*middle*) and displacement time-series (*lower*).

The polynomial corrected wavelet is very useful for correcting wavelets with a few cycles, but starts to distort the displacement time-series for wavelets with many numbers of cycles (Figure 6.6). To overcome this problem another wavelet is proposed that uses a sinusoidal half cycle at the start and end of the wavelet to correct the displacement time-series (Figure 6.7). The amplitude of the sinusoidal correction is given by:

$$SinAmplitude = \frac{-DispError.\omega}{\left[P - \left(\frac{\sin(P.\omega)}{\omega}\right) + 4t_0\right]} \tag{6.8}$$

where P is the duration of the sinusoidal correction, equal to $\frac{2\pi}{\omega}$.

In order to ensure that the wavelet has zero final velocity and displacement only wavelets with whole numbers of cycles are used.

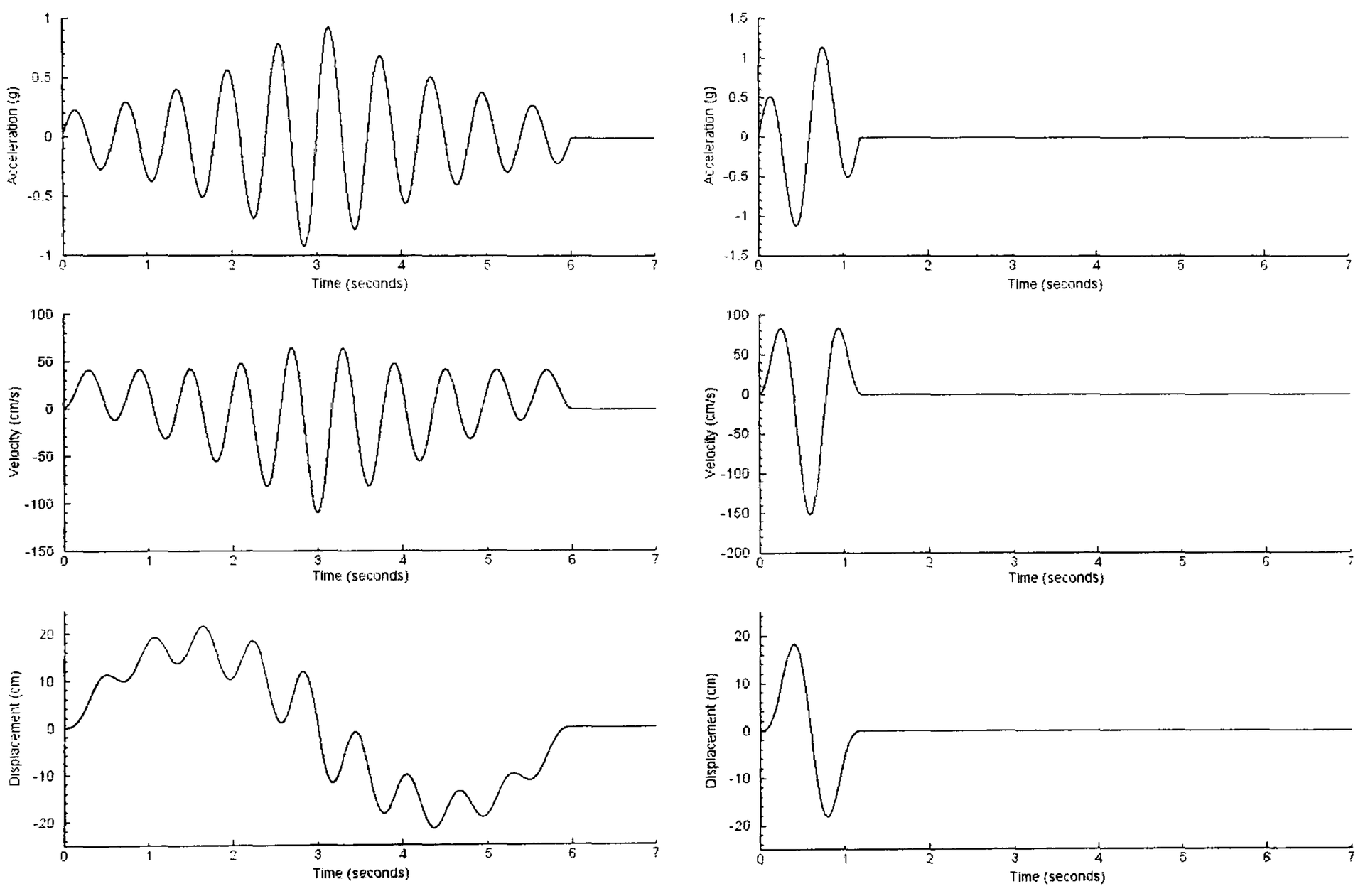


Figure 6.6. - Suarez and Montejo wavelet with polynomial correction, 5% damping, 0.6 seconds period. Acceleration time-series (*top*), velocity time-series (*middle*) and displacement time-series (*lower*). Wavelet with 6 seconds duration (*left*) and 1.2 seconds duration (*right*).

6.6 Solution Stability

This section details the work conducted to improve the solution stability of the Lilhanand and Tseng methodology. Solution instability is caused because the time of peak response changes after the adjustment function is applied.

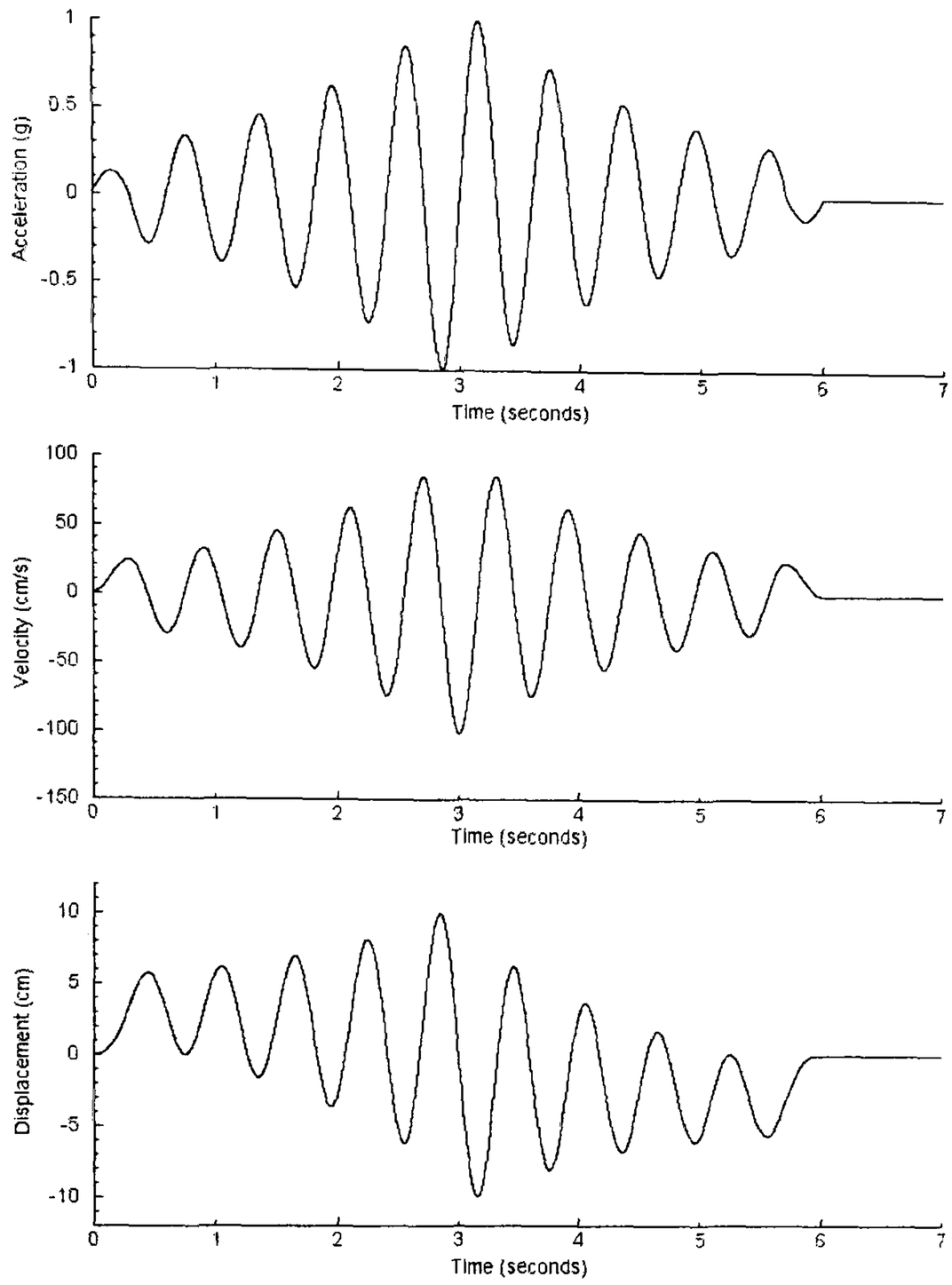


Figure 6.7. - Suarez and Montejo wavelet with sinusoidal correction, 5% damping, 0.6 seconds period, 6 seconds duration. Acceleration time-series (*top*), velocity time-series (*middle*) and displacement time-series (*lower*).

6.6.1 Change in time of response peaks

The fundamental assumption underlying the matrix solution method is that the time of the peak response is the same before and after each adjustment is applied. Unfortunately this is assumption is not always valid, particularly if closely spaced spectral points and multiple damping levels are to be matched. Movement in the time of a response peak is caused from either:

- A phase change in the response peak
- A new "secondary" peak becoming critical

Both of these sources of divergence are illustrated in Figure 6.8 and are caused by the cross-correlation of different wavelet corrections. Put simply the wavelet added to

correct one period and damping level can also affect the response of SDOF systems at different periods and damping levels.

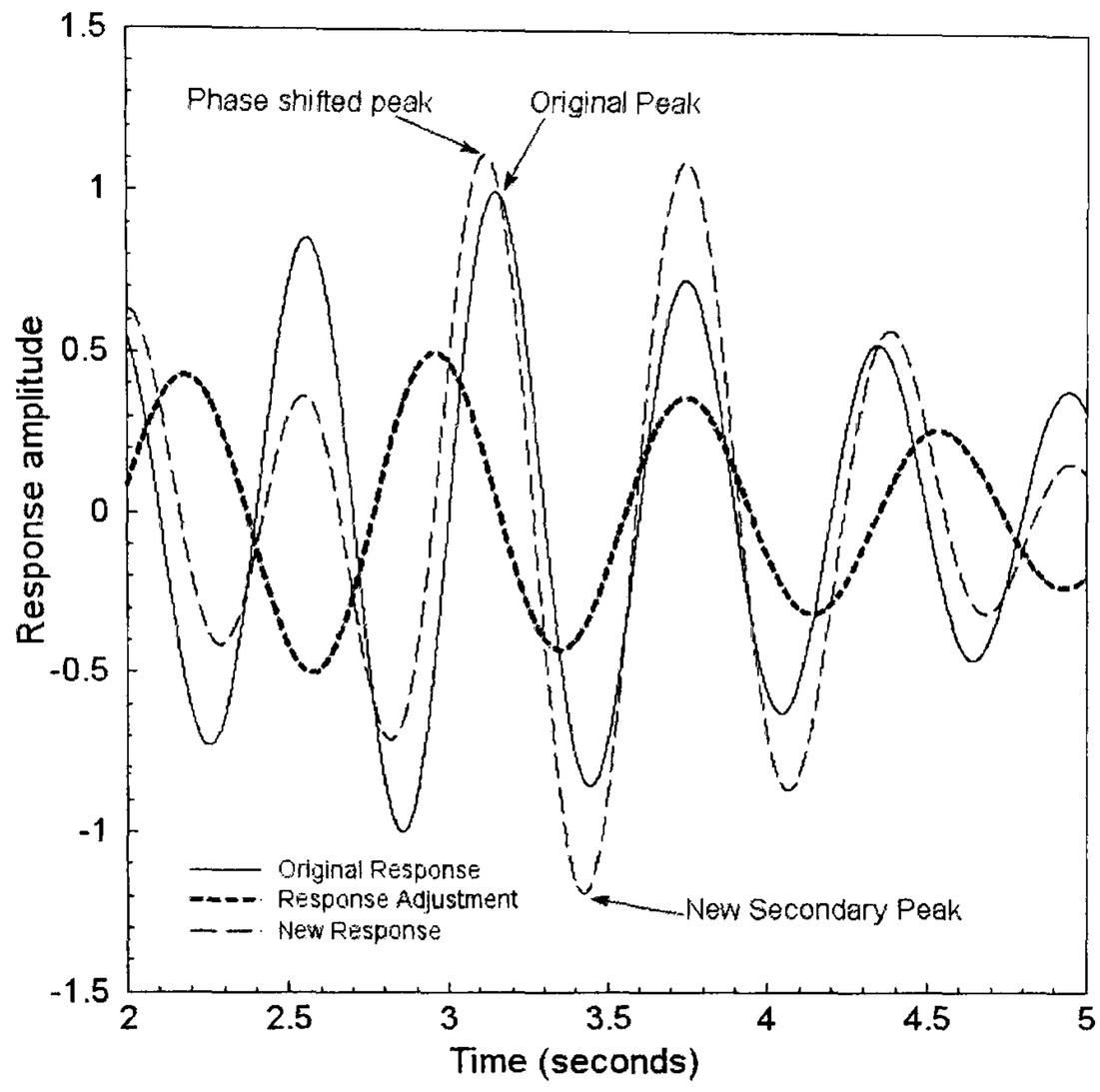


Figure 6.8. - Illustration of sources of diverging response. Note that the response amplitude remains approximately unchanged at the time of the original peak response, but the response increases through both a phase shift and the emergence of a secondary peak.

6.6.2 Reduction of off-diagonal *C* matrix elements

Subdividing the *C* matrix into smaller sub-matrices increases solution speed and also has the advantage that it reduces the cross-correlation of the wavelets. This is because the subdivision essentially sets some of the off-diagonal terms to zero, as illustrated in Tables 6.1 and 6.2. This is beneficial as it increases numerical stability, but is at the expense of the accuracy of the solution because the cross-correlation of some wavelets is not taken into account. An alternative method of improving stability is to use the full *C* matrix but reduce the off-diagonal terms by a constant factor. From conducting trials with different off-diagonal reduction factors it is found that a reduction factor of about 0.7 is very effective in reducing divergence from phase changes in the spectral peaks.

Table 6.1. - Typical *C* matrix for eight spectral points (two periods and four damping levels) with no subdivision

Damping	Damping Period	5% 0.25s	5% 0.32s	10% 0.25s	10% 0.32s	20% 0.25s	20% 0.32s	30% 0.25s	30% 0.32s
5%	0.25s	5.306	2.157	3.677	2.572	2.678	1.831	2.081	1.579
5%	0.32s	1.426	5.307	1.857	3.700	1.407	2.560	1.116	1.665
10%	0.25s	3.630	2.058	2.913	2.205	2.203	1.333	1.754	1.071
10%	0.32s	1.247	3.614	1.503	2.912	1.176	1.672	0.954	1.057
20%	0.25s	2.136	1.553	2.035	1.586	1.621	0.717	1.333	0.495
20%	0.32s	1.353	2.213	0.867	1.090	0.521	1.621	0.319	1.319
30%	0.25s	1.543	1.111	1.597	1.167	1.311	0.381	1.100	0.217
30%	0.32s	1.272	1.606	0.773	0.835	0.477	1.291	0.298	1.100

Table 6.2. - Typical *C* matrix for eight spectral points (two periods and four damping levels) split into four subgroups

Damping	Damping Period	5% 0.25s	5% 0.32s	10% 0.25s	10% 0.32s	20% 0.25s	20% 0.32s	30% 0.25s	30% 0.32s
5%	0.25s	5.306^{1}	0	0	2.572^{1}	0	0	0	0
5%	0.32s	0	5.307^{4}	0	0	0	0	1.116^{4}	0
10%	0.25s	0	0	2.913^{2}	0	0	1.333^{2}	0	0
10%	0.32s	1.247^{1}	0	0	2.912^{1}	0	0	0	0
20%	0.25s	0	0	0	0	1.621^{3}	0	0	0.495^{3}
20%	0.32s	0	0	0.867^{2}	0	0	1.621^{2}	0	0
30%	0.25s	0	1.111^{4}	0	0	0	0	1.100^{4}	0
30%	0.32s	0	0	0	0	0.477^{3}	0	0	1.100^{3}

Numbers with superscript 1 are in subgroup 1
Numbers with superscript 2 are in subgroup 2
Numbers with superscript 3 are in subgroup 3
Numbers with superscript 4 are in subgroup 4

6.6.3 Adding secondary peaks

Reducing the off-diagonal terms of the *C* matrix reduces phase shifts in the response; however, it does not reduce the occurrence of secondary peaks. To prevent this source of divergence a new wavelet can be added at the period, damping level and time of the new secondary peak. The adjustment function is recalculated using the secondary wavelet to prevent secondary peaks causing divergence. An example of the application of this method is shown in Figure 6.9.

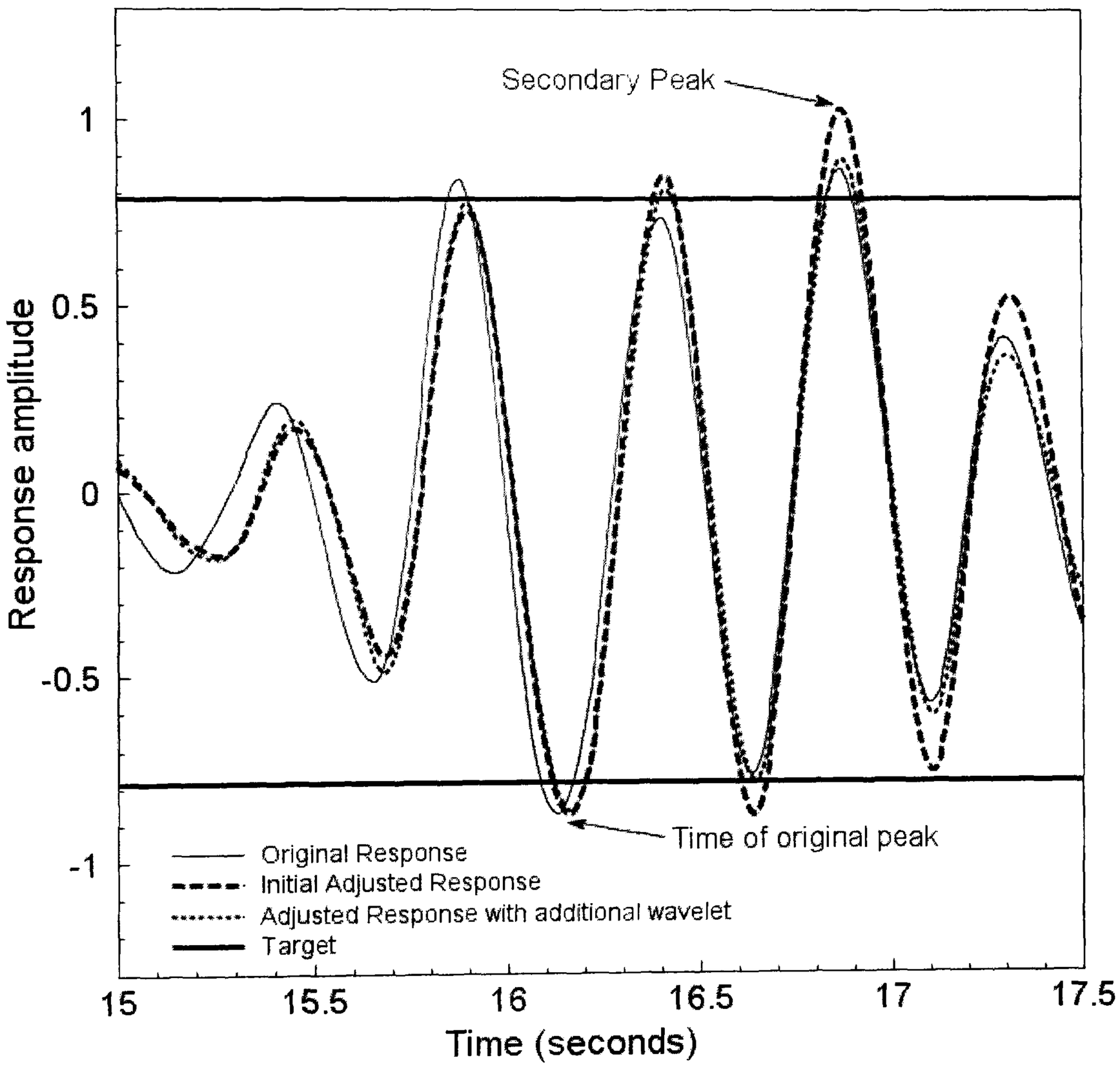


Figure 6.9. – Prevention of diverging response with an additional wavelet adjustment.

6.6.4 Reduction of correction amplitude

Unfortunately the solution can still diverge even with the addition of secondary peaks. This occurs when the cross-correlation of the responses causes a phase change of the response peak (Figure 6.10). This can be overcome by increasing the importance of the diverging response in the solution. This is achieved by reducing the amplitude of the adjustment correction, δR, for all the points to be matched except the point causing divergence. Although artificially reducing the amplitude of the adjustment function increases the numerical stability it also requires a greater number of iterations to obtain the required spectral match.

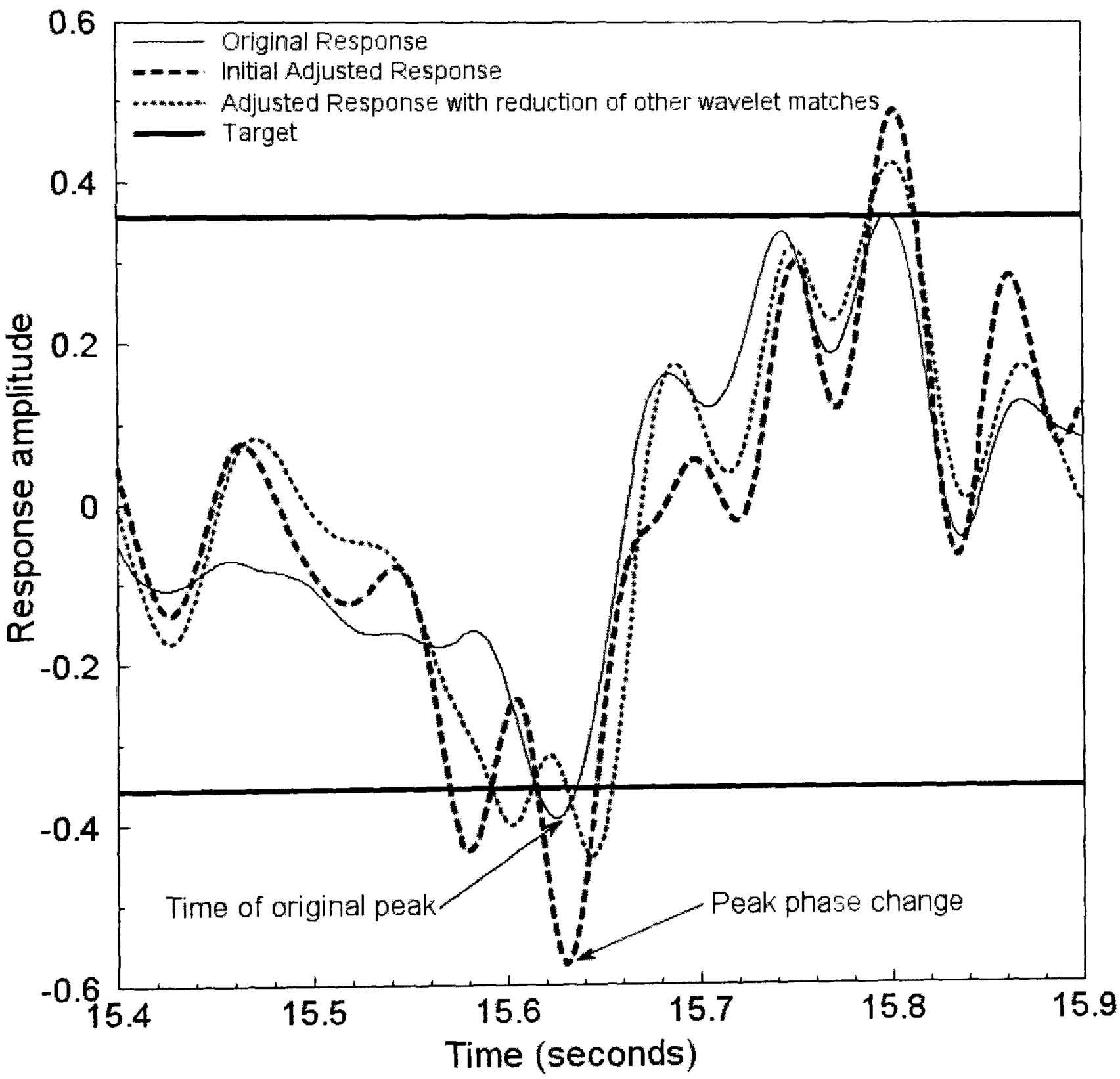


Figure 6.10. – Prevention of diverging response with reduction of correlated wavelet targets.

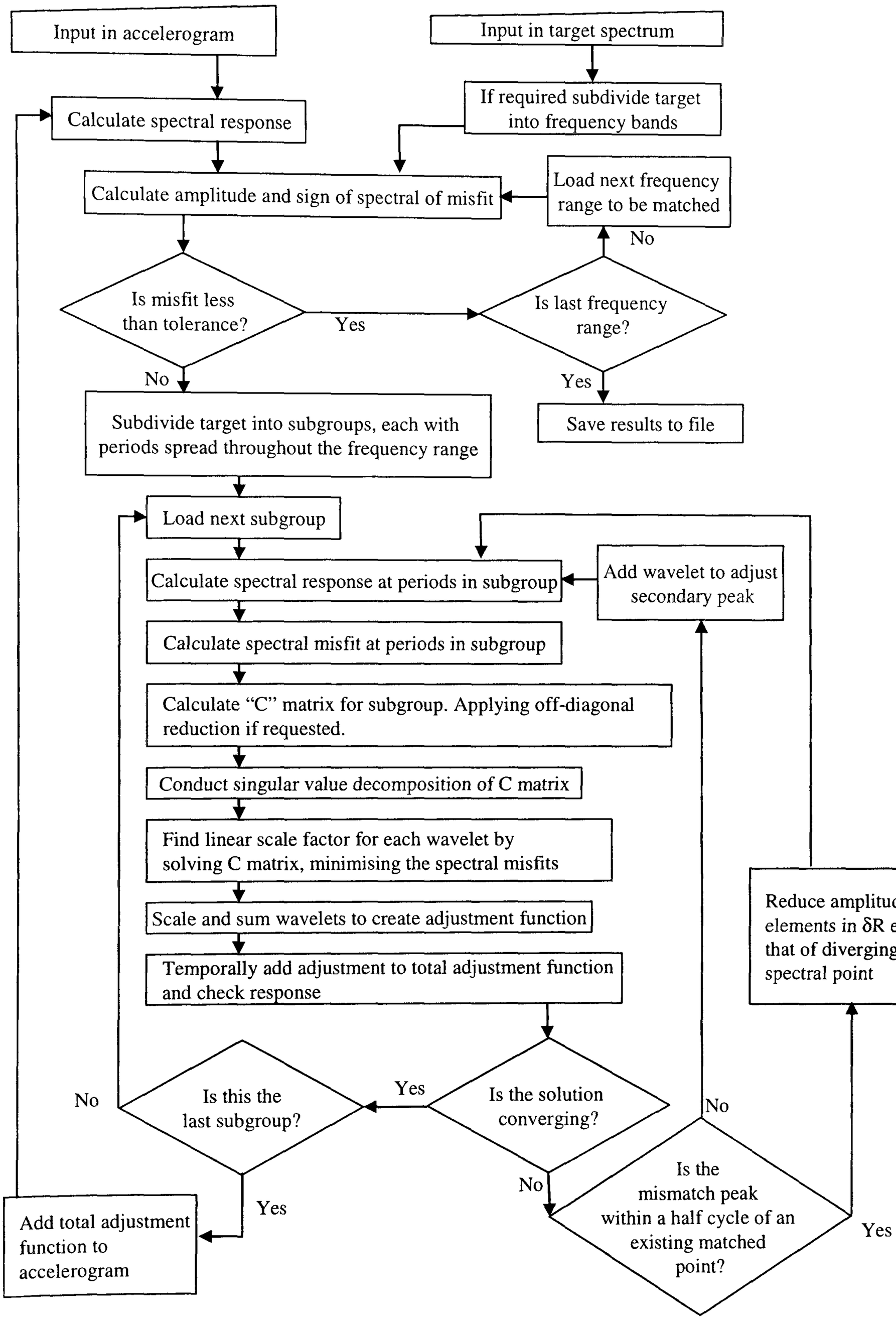


Figure 6.11. - RSPMatch methodology including new solution algorithms.

6.6.5 New solution algorithm

A flow chart detailing the new solution algorithm is shown in Figure 6.11. Although the new algorithm prevents the solution from diverging it does not guarantee that the solution will converge to within the requested tolerance. For cases with multiple damping levels and closely spaced spectral points it may be necessary to accept a more relaxed tolerance criteria than for cases where only a single damping level is to be matched. This is investigated in more detail in the following sections.

6.7 Spectral Target For Match

6.7.1 Matching spectral displacements

Spectral displacements are required for very long-period structures, tunnels, base isolated structures and for direct displacement-based design. This direct displacement design requires elastic spectral displacements for periods up to about 5 seconds and damping levels from 5% of critical up to about 30% in most cases. As spectral displacements are directly related to the pseudo spectral acceleration, not the absolute spectral acceleration, pseudo spectral accelerations should be used when matching spectral displacements. Pseudo spectral acceleration (PSA) can be calculated directly from the spectral displacement:

$$PSA = SD\left(\frac{2\pi}{T}\right)^2 \tag{6.9}$$

where SD is the spectral displacement and T is the period in seconds.

The difference between the pseudo and absolute spectral accelerations only becomes significant for damping levels over about 20% (Figure 6.12). If spectral displacements are to be matched there is little point in matching periods less than 0.05 seconds (20 Hz) as the spectral displacement tends to zero. Matching high-frequency motions also has the penalty of requiring the input accelerogram to be specified at a sufficiently small time step so that the high-frequency wavelets can be added.

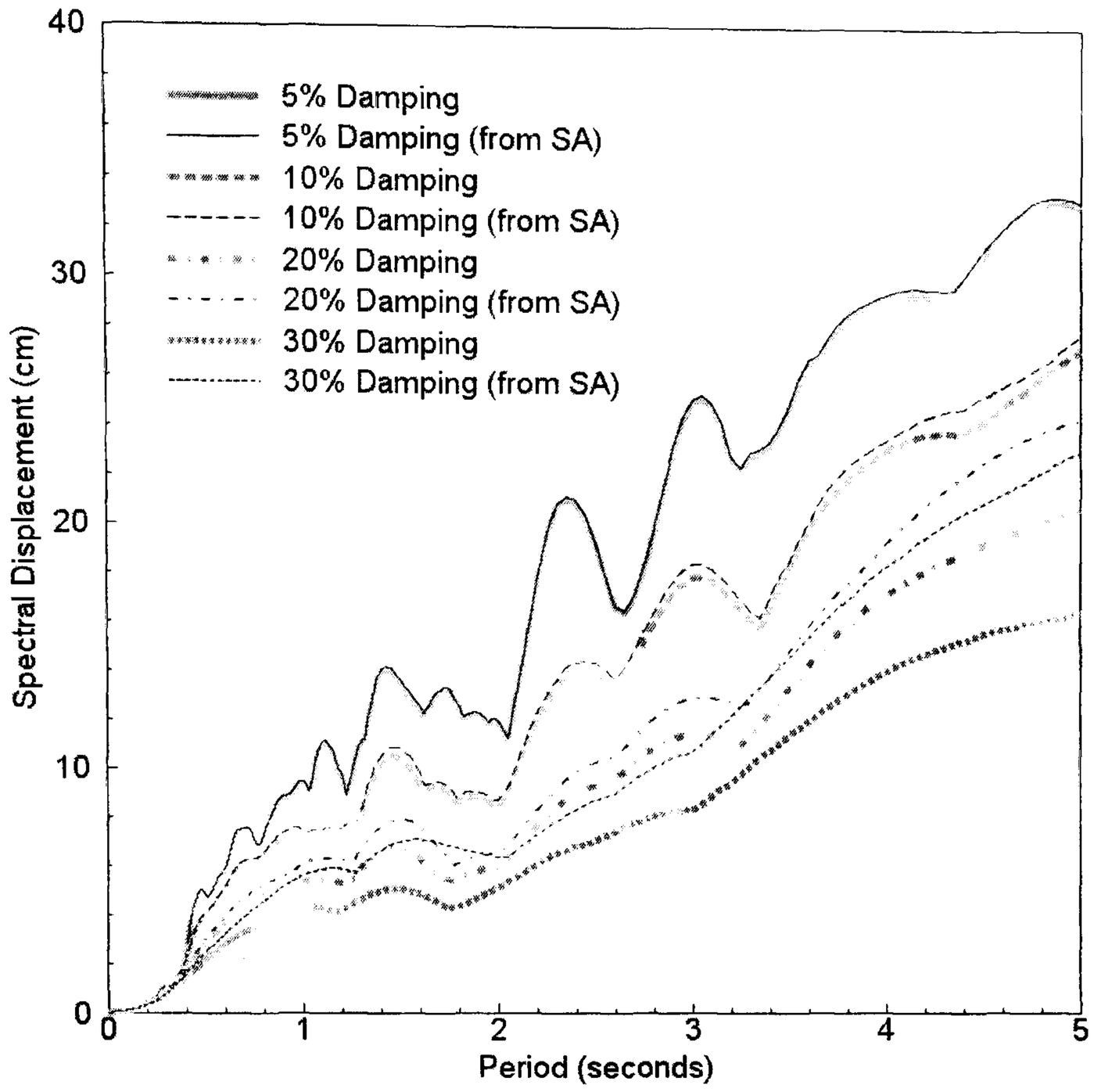


Figure 6.12. - Differences between spectral displacement and that calculated from absolute spectral acceleration (SA).

6.7.2 Matching spectral accelerations

If spectral accelerations are to be matched higher frequencies of up to 50 Hz (0.02 seconds period) may be of interest, particularly if ground motions are required for the design or assessment of mechanical or electrical equipment. In these cases lower damping levels than that required for displacement-based design are also likely to be of interest. The main motivation for this work is to develop spectra with matched spectral displacements, but the program developed in the research can also be used to match high-frequency motions (Figure 6.13). As it is not possible to create a wavelet with a zero period it is more difficult to match the peak ground acceleration than high-frequency spectral accelerations. Simply adjusting the peak acceleration without using a wavelet does not work as this can cause a drift in the velocity and displacement time-series. An option has been added to the new version of the program so that the PGA can be matched using a wavelet with high-frequency and very short duration.

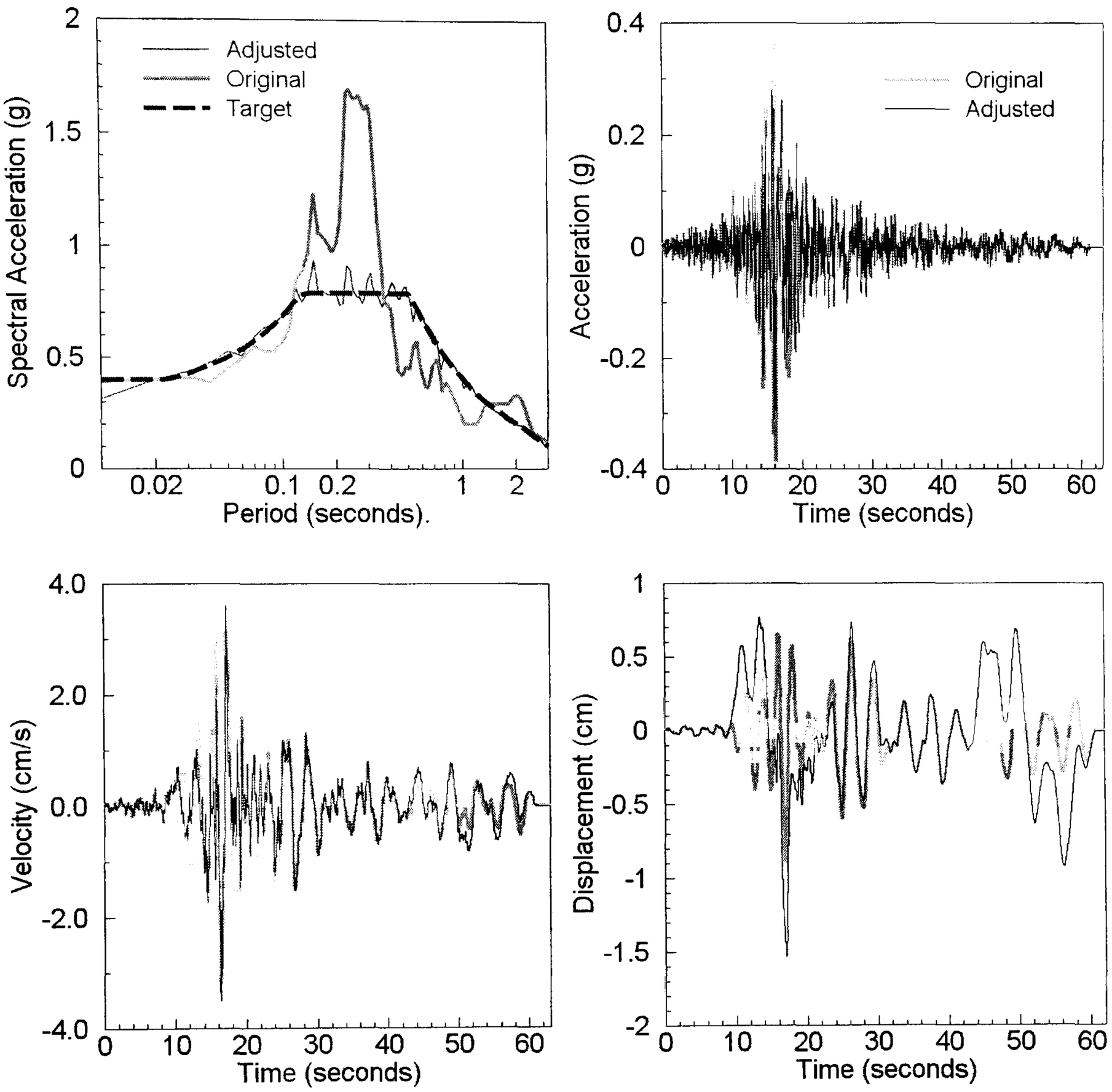


Figure 6.13. – Match to broad range of frequencies (0.01 s to 10 seconds) for a 5% damped elastic response spectra. Elastic response spectral (*top left*), acceleration time-series (*top right*), velocity time-series (*lower left*), displacement time-series (*lower right*).

6.8 Criteria for Selecting Seed Records

Careful selection of the seed accelerogram is important to minimise significant changes to the record. It is particularly important to have a reasonable initial spectral match at long periods to minimise changes to the displacement time-series. A useful strategy is to selected records using the RMS of the difference of the normalized

spectral acceleration (ΔSAn_{RMS}), which is based on the equation used by Ambraseys *et al.* (2004):

$$\Delta SAn_{RMS} = \sqrt{\frac{1}{N_p}\sum_{i=1}^{N_p}\left(\frac{PSA_0(T_i)}{PGA_0} - \frac{PSA_s(T_i)}{PGA_s}\right)^2} \tag{6.10}$$

where N_p is the number of periods at which the spectral shape is specified, $PSA_0(Ti)$ is the pseudo spectral acceleration from the record at period T_i, $PSA(T_i)$ is the target pseudo spectral acceleration at the same period; PGA_0 and PGA_s are the peak ground acceleration of the accelerogram and the zero-period anchor point of the target spectrum. As the RMS spectral acceleration only matches spectral shape and the amplitude, the seed accelerograms should be linearly scaled so that the amplitude of the spectral accelerations has a good match with the target before wavelet adjustment is made. This can be conducted manually or by minimizing the RMS of the difference between the spectral acceleration (ΔSA_{RMS}) or spectral displacement (ΔSD_{RMS}):

$$\Delta SA_{RMS} = \sqrt{\frac{1}{N_p}\sum_{i=1}^{N_p}\left[PSA_o(T_i) - PSA_s(T_i)\right]^2} \tag{6.11}$$

$$\Delta SD_{RMS} = \sqrt{\frac{1}{N_p}\sum_{i=1}^{N_p}\left[SD_o(T_i) - SD_s(T_i)\right]^2} \tag{6.12}$$

where $SD_0(Ti)$ is the spectral displacement from the record at period Ti and $SD_s(Ti)$ is the target spectral displacement at the same period.

To ensure that a realistic match to the target scenario duration and energy distribution it is recommended that the seed accelerograms have a similar magnitude as the target scenario.

6.9 Target Periods and Solution Tolerance

If the target spectral points are specified with a wide period spacing and one or two damping levels the solution is able to converge rapidly, but the spectral acceleration between the points is unlikely to match the target spectrum. The basic Lilhanand and Tseng solution does not converge if closely spaced spectral points and multiple damping levels are matched in the same matrix solution. However, as algorithms have been added to the program to prevent divergence, closely spaced spectral points can now be specified. Examples given in the following section are matched to a target with 40 points per $\log_{10}$ unit of period. To enable the true extent of any spectral misfit to be seen, the matched spectra should be plotted with a greater density of points than the points specified for matching.

When specifying the target periods and solution tolerance a balance has to be achieved between matching the target spectra and minimising the adjustment to the original ground motion. A comparison between original and adjusted acceleration, velocity and displacement time-series should always be conducted to ensure that the original characteristics of the record have been preserves. A comparison of the build up of the Arias Intensity (Husid plot) should also be conducted to ensure that excessive additional amounts of energy have not been introduced into the record by the wavelets. Progressively conducting wavelet adjustment in sweeps from the high-frequency (short periods) to low-frequency (long periods) helps to minimise the corruption to the original ground motion. For the results presented in the following section the first adjustment is applied from 0.05 to 1.0 seconds period (20 to 1.0Hz) then the second from 0.05 to 5 seconds (20 to 0.2Hz).

As was previously alluded to, it may be necessary to accept a more relaxed tolerance criteria for cases with multiple damping levels and closely spaced spectral points than for cases where only a single damping level is to be matched. To illustrate this point to two acceleration time-series, which are described in more detail in the next section, are fitted to one, two, three and four damping levels (Figures 6.14 and 6.15).

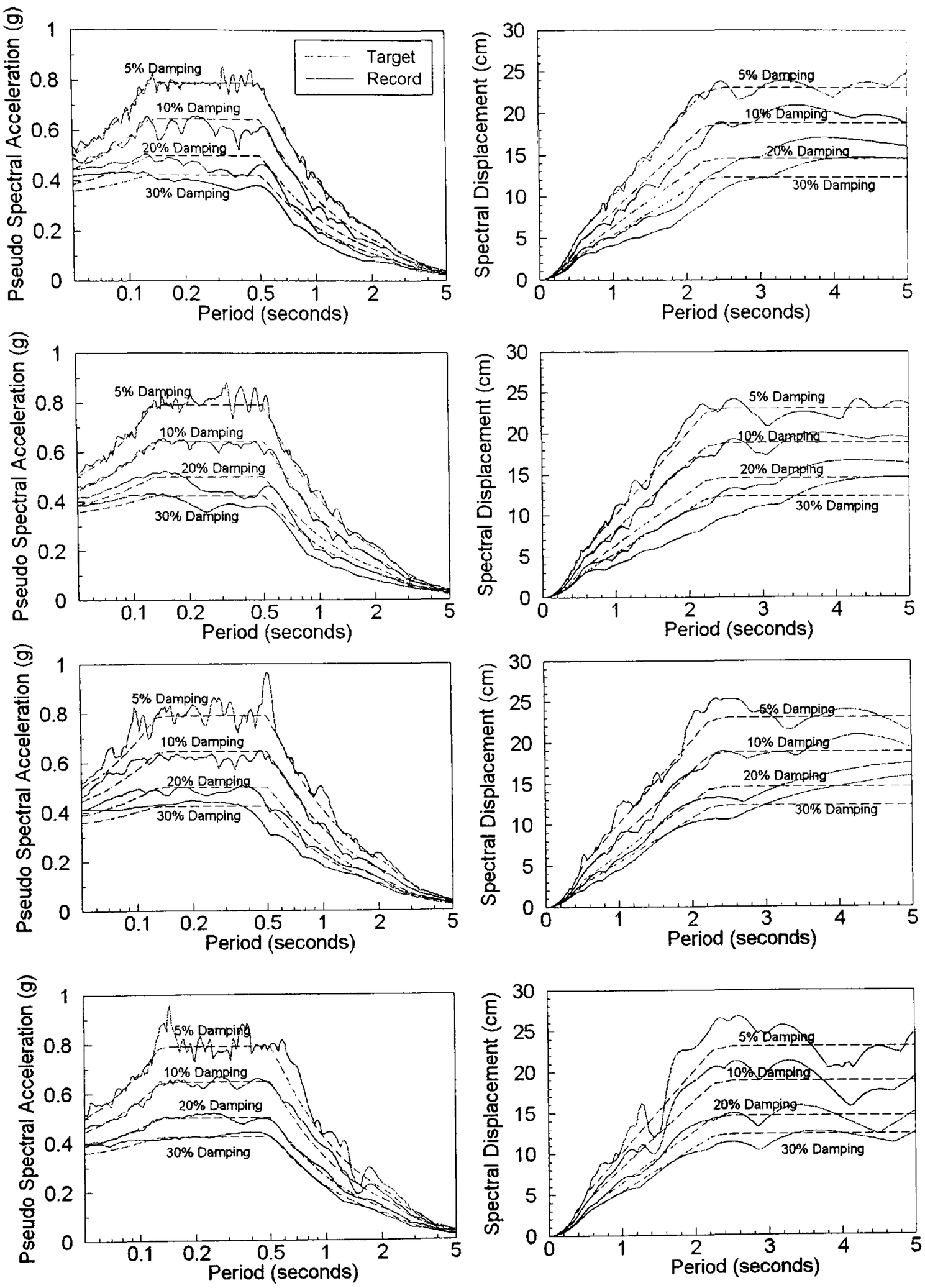


Figure 6.14. - Elastic response spectra from the 1940 M_w 7.0 Imperial Valley Earthquake recorded 6.1km from the fault rupture at El Centro Array #9. Response matched from 0.05 to 5s period. Matched to 5% damped spectrum (*top row*); 5 and 10% damped spectra (*second row*); 5, 10 and 20% damped spectra (*third row*); 5, 10, 20 and 30% damped spectra (*bottom row*). Pseudo spectral acceleration (*left column*) and spectral displacement (*right column*)

The goodness of fit between the adjusted and target spectral acceleration and spectral displacement is measured using the RMS of the difference of the spectral acceleration (ΔSA_{RMS}, Eqn. 6.11) and the RMS of the difference of the spectral displacement

(ΔSD_{RMS}, Eqn. 6.12) respectively. The average misfit over the whole period range is measured using the average of the spectral misfit:

$$AverageMisfit = \frac{1}{N_p}\sum_{i=1}^{N_p}\left|\frac{PSA_o(T_i) - PSA_s(T_i)}{PSA_s(T_i)}\right| * 100 \qquad (6.13)$$

Note that precisely the same average misfit is calculated if the PSA terms in equation 6.13 are replaced with SD.

Tables 6.3 to 6.8 show that matching to multiple damping levels consistently improves the match to the higher damping levels, but at the expense of the lower damping levels. The requirement to allow a more relaxed convergence criterion is particularly evident as a single damping level is matched to an average misfit of 1 to 2 percent, whilst two damping levels are matched to about 3 percent; three and four damping levels are matched with an average misfit of 4 to 5 percent.

Table 6.3. - RMS of difference between measured and target spectral acceleration (ΔSA_{RMS}) between 0.05 and 5 seconds period. 1940 M_w 7.0 Imperial Valley Earthquake recorded 6.1km from the fault rupture at El Centro Array #9.

	ΔSA_{RMS} of damping level:				
Damping level matched	5%	10%	20%	30%	All
Matched 5%	0.016	0.032	0.041	0.040	0.034
Matched 5 and 10%	0.027	0.016	0.044	0.041	0.034
Matched 5, 10 and 20%	0.049	0.022	0.031	0.043	0.037
Matched 5, 10, 20 and 30%	0.057	0.025	0.011	0.010	0.032

Table 6.4. - RMS of difference between measured and target spectral displacement (ΔSD_{RMS}) between 0.05 and 5 seconds period. 1940 M_w 7.0 Imperial Valley Earthquake recorded 6.1km from the fault rupture at El Centro Array #9.

	ΔSD_{RMS} of damping level:				
Damping level matched	5%	10%	20%	30%	All
Matched 5%	0.324	0.724	1.159	1.244	0.938
Matched 5 and 10%	0.533	0.380	0.979	1.217	0.847
Matched 5, 10 and 20%	0.794	0.453	0.662	0.829	0.700
Matched 5, 10, 20 and 30%	1.394	0.944	0.411	0.323	0.881

Table 6.5. - Average spectral misfit between 0.05 and 5 seconds period. 1940 M_w 7.0 Imperial Valley Earthquake recorded 6.1km from the fault rupture at El Centro Array #9.

	Average misfit of damping level:				
Damping level matched	5%	10%	20%	30%	All
Matched 5%	2.2	5.8	11.7	15.1	8.7
Matched 5 and 10%	3.8	2.9	11.5	15.0	8.3
Matched 5, 10 and 20%	5.9	3.9	7.3	11.8	7.2
Matched 5, 10, 20 and 30%	8.9	6.0	3.3	2.9	5.3

Table 6.6. - RMS of difference between measured and target spectral acceleration (ΔSA_{RMS}) between 0.05 and 5 seconds period. 1989 M_w 6.9 Loma Prieta Earthquake recorded 71km from the fault rupture at Diamond heights.

	ΔSA_{RMS} of damping level:				
Damping level matched	5%	10%	20%	30%	All
Matched 5%	0.010	0.039	0.048	0.050	0.040
Matched 5 and 10%	0.016	0.009	0.019	0.026	0.019
Matched 5, 10 and 20%	0.029	0.015	0.009	0.013	0.018
Matched 5, 10, 20 and 30%	0.041	0.018	0.009	0.008	0.023

Table 6.7. - RMS of difference between measured and target spectral displacement (ΔSD_{RMS}) between 0.05 and 5 seconds period. 1989 M_w 6.9 Loma Prieta Earthquake recorded 71km from the fault rupture at Diamond heights.

	ΔSD_{RMS} of damping level:				
Damping level matched	5%	10%	20%	30%	All
Matched 5%	0.239	0.445	0.732	0.834	0.610
Matched 5 and 10%	0.688	0.537	0.885	1.194	0.862
Matched 5, 10 and 20%	0.627	0.373	0.208	0.335	0.415
Matched 5, 10, 20 and 30%	0.704	0.423	0.293	0.245	0.453

Table 6.8. - Average spectral misfit between 0.05 and 5 seconds period. 1989 M_w 6.9 Loma Prieta Earthquake recorded 71km from the fault rupture at Diamond heights.

	Average misfit of damping level:				
Damping level matched	5%	10%	20%	30%	All
Matched 5%	1.0	6.1	10.6	12.3	7.5
Matched 5 and 10%	2.8	2.3	6.3	9.2	5.2
Matched 5, 10 and 20%	4.7	2.8	2.1	3.6	3.3
Matched 5, 10, 20 and 30%	5.0	3.2	2.5	2.5	3.3

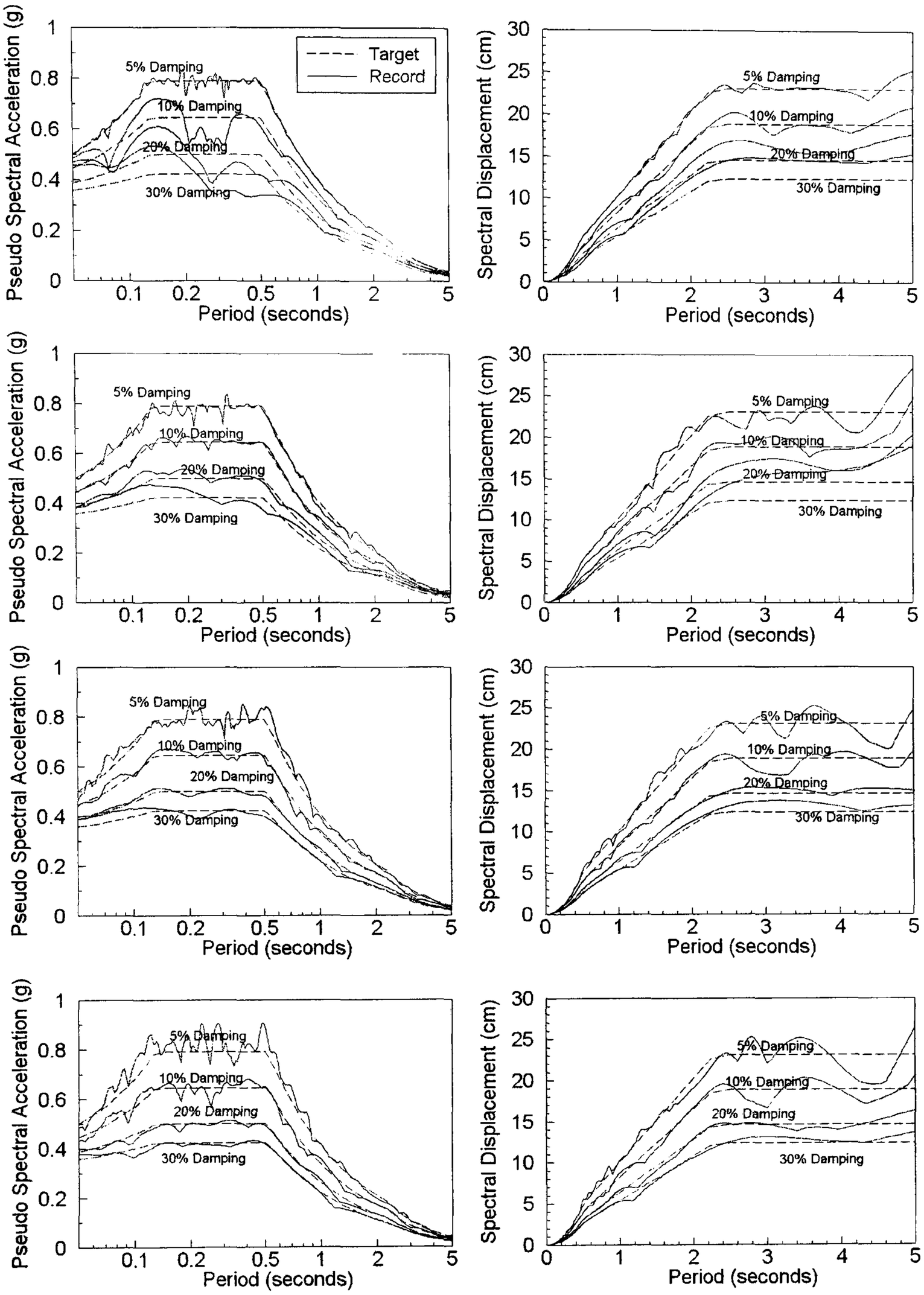


Figure 6.15. - Elastic response spectra from the 1989 M_w 6.9 Loma Prieta Earthquake recorded 71km from the fault rupture at Diamond heights. Response matched from 0.05 to 5s period. Matched to 5% damped spectrum (*top row*); 5 and 10% damped spectra (*second row*); 5, 10 and 20% damped spectra (*third row*); 5, 10, 20 and 30% damped spectra (*bottom row*). Pseudo spectral acceleration (*left column*) and spectral displacement (*right column*)

6.10 Examples of Spectral Matching

This section illustrates the new matching procedure by creating two accelerograms for the scenario of a stiff soil site 10km from an M_s 7 earthquake. Both of the records

are adjusted to match target displacement spectra at 5, 10, 20 and 30% damping levels. The median 5% damping target spectra is generated according to the method proposed by Bommer *et al.* (2000a) using the peak ground motions proposed by Tromans and Bommer (2002). Ground motions matched to spectra at other design levels can be created by linearly scaling the motions fitted to the median level. It is noted in passing that most ground-motion prediction equations, including that of Tromans and Bommer (2002), are derived from ground-motion recordings from analogue instruments and may not be capable of accurately measuring peak ground displacements (Boore and Bommer 2005). For this reason long-period spectral amplitudes should be treated with caution. The target spectra for damping levels other than 5% are obtained using the formulae proposed by Bommer *et al.* (2000a), which was subsequently adopted by Eurocode 8 (CEN 2004):

$$\eta = \sqrt{\frac{10}{5+\beta}} \tag{6.14}$$

where, η is the linear scale factor between the 5% damped response spectrum and the required spectrum at β damping. Recent research has shown that the difference between the damping levels is strictly dependent on the duration of the ground motion so is dependent on the earthquake duration (Bommer and Mendis 2004). The approximation given by Equation (6.14) is widely used and will be employed in this study.

The seed accelerograms are selected from the 3547 records of the NGA dataset. Initial selection is conducted based on the normalized RMS spectral acceleration (Eqn. 6.10) and earthquake magnitude. The records selected are the 1940 M_w 7.0 Imperial Valley Earthquake recorded 6.1km from the fault rupture at El Centro Array #9 (record 00006L in the NGA database) and the 1989 M_w 6.9 Loma Prieta Earthquake recorded 71km from the fault rupture at Diamond Heights (record 00794T in the NGA database). The accelerograms are initially linearly scaled so that, by visual inspection, the difference between the record and target PSA and SD is minimized. The linear scale factors used are given in Table 6.9.

Table 6.9. – Initial Linear Scale Factors Applied to Seed Accelerograms

Accelerogram	Scale Factor
1940 M_w 7.0 Imperial Valley – El Centro Array #9	1.2
1989 M_w 6.9 Loma Prieta – Diamond Heights	3.2

Figures 6.12 to 6.15 show the results of wavelet adjustment applied to the acceleration time-series from the 1940 Imperial Valley Earthquake. Figures 6.16 to 6.19 show results of wavelet adjustment applied to the acceleration time-series from the 1989 Loma Prieta Earthquake. Neither accelerograms have an exact fit but the adjustment procedure has approximately halved the average spectral misfit, RMS difference in spectral displacement and RMS difference in spectral acceleration (Tables 6.10 to 6.15). Examination of the acceleration, velocity and displacement time-series before and after the wavelet adjustment shows that the characteristics of the original records have been retained (Figures 6.17, 6.18., 6.20 and 6.21). Checks of the build up of Arias intensity also demonstrate that the energy distribution within the record is similar to the original ground motion and that the total energy content has been changed by less than 10% by the wavelet adjustment (Figures 6.19 and 6.23).

Table 6.10. - Average spectral misfit between 0.05 and 5 seconds period. 1940 M_w 7.0 Imperial Valley Earthquake recorded 6.1km from the fault rupture at El Centro Array #9.

Period range matched	Average misfit of damping level:				
	5%	10%	20%	30%	All
Original record	18.4	11.6	8.3	7.7	11.5
0.05 to 1.0 second	8.0	5.7	5.0	3.0	5.4
0.05 to 5.0 seconds	8.9	6.0	3.3	2.9	5.3

Table 6.11. - RMS of difference between measured and target spectral acceleration (ΔSA_{RMS}) between 0.05 and 5 seconds period. 1940 M_w 7.0 Imperial Valley Earthquake recorded 6.1km from the fault rupture at El Centro Array #9.

Period range matched	ΔSA_{RMS} of damping level:				
	5%	10%	20%	30%	All
Original record	0.116	0.062	0.043	0.030	0.071
0.05 to 1.0 second	0.037	0.021	0.015	0.009	0.023
0.05 to 5.0 seconds	0.057	0.025	0.011	0.010	0.032

Table 6.12. - RMS of difference between measured and target spectral displacement (ΔSD_{RMS}) between 0.05 and 5 seconds period. 1940 M_w 7.0 Imperial Valley Earthquake recorded 6.1km from the fault rupture at El Centro Array #9.

Period range matched	ΔSD_{RMS} of damping level:				
	5%	10%	20%	30%	All
Original record	2.354	1.150	0.609	0.452	1.364
0.05 to 1.0 second	2.393	1.567	0.826	0.408	1.502
0.05 to 5.0 seconds	1.394	0.944	0.411	0.323	0.881

Table 6.13. - Average spectral misfit between 0.05 and 5 seconds period. 1989 M_w 6.9 Loma Prieta Earthquake recorded 71km from the fault rupture at Diamond heights.

Period range matched	Average misfit of damping level:				
	5%	10%	20%	30%	All
Original record	14.8	12.7	8.7	6.6	10.7
0.05 to 1.0 second	9.4	7.7	7.4	6.5	7.8
0.05 to 5.0 seconds	5.3	3.3	2.6	2.5	3.4

Table 6.14. - RMS of difference between measured and target spectral acceleration (ΔSA_{RMS}) between 0.05 and 5 seconds period. 1989 M_w 6.9 Loma Prieta Earthquake recorded 71km from the fault rupture at Diamond heights.

Period range matched	ΔSA_{RMS} of damping level:				
	5%	10%	20%	30%	All
Original record	0.134	0.082	0.036	0.022	0.081
0.05 to 1.0 second	0.053	0.034	0.027	0.020	0.036
0.05 to 5.0 seconds	0.041	0.018	0.009	0.008	0.023

Table 6.15. - RMS of difference between measured and target spectral displacement (ΔSD_{RMS}) between 0.05 and 5 seconds period. 1989 M_w 6.9 Loma Prieta Earthquake recorded 71km from the fault rupture at Diamond heights.

Period range matched	ΔSD_{RMS} of damping level:				
	5%	10%	20%	30%	All
Original record	1.511	1.040	0.623	0.543	1.006
0.05 to 1.0 second	1.598	1.313	0.839	0.613	1.157
0.05 to 5.0 seconds	0.704	0.423	0.293	0.245	0.453

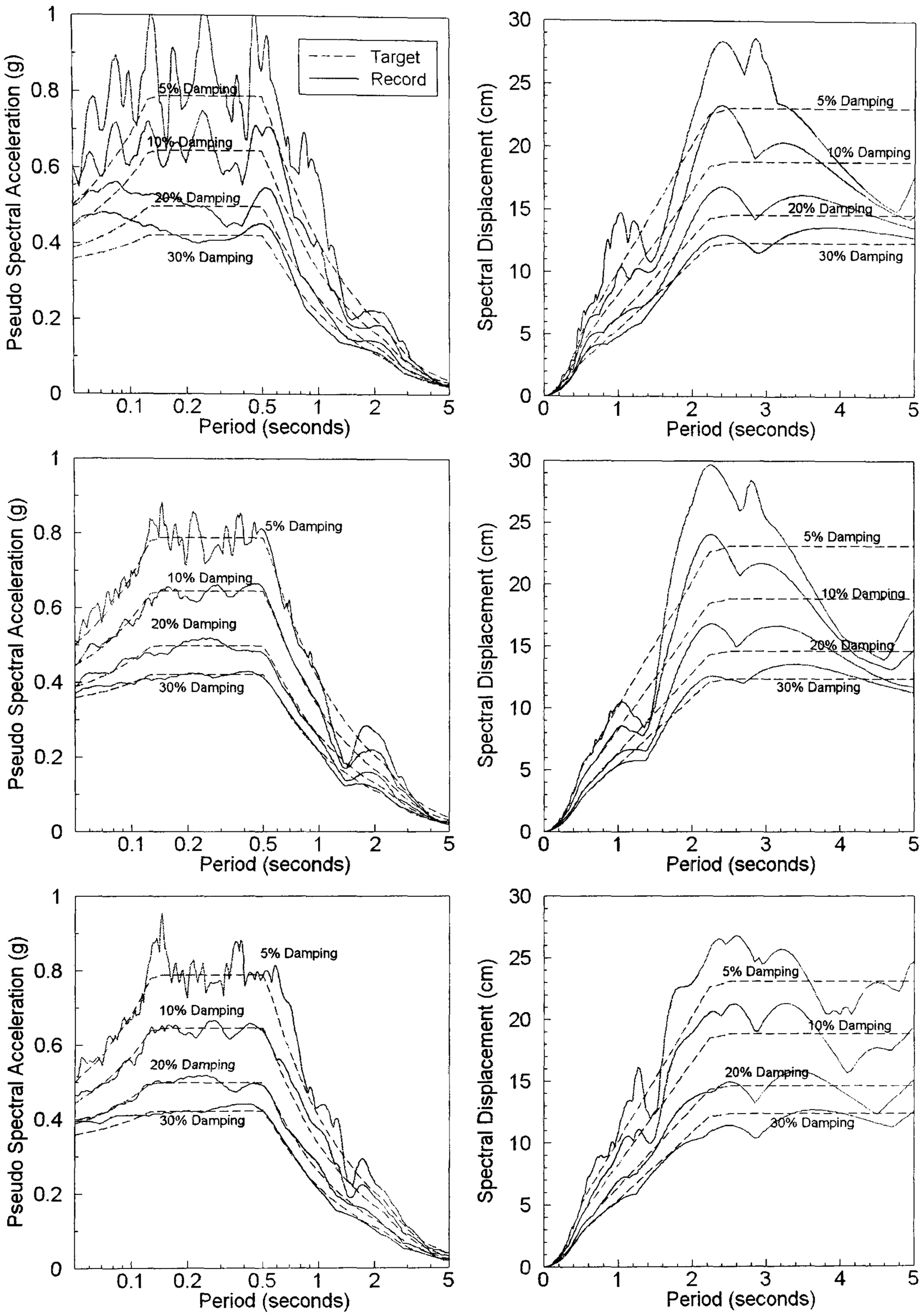


Figure 6.16. - Elastic response spectra from the 1940 M_w 7.0 Imperial Valley Earthquake recorded 6.1km from the fault rupture at El Centro Array #9. Original linearly scaled accelerogram (*top*), response matched from 0.05 to 1s period (*middle*) and response matched to 0.05 to 5s period (*lower*). Pseudo spectral acceleration (*left*) and spectral displacement (*right*)

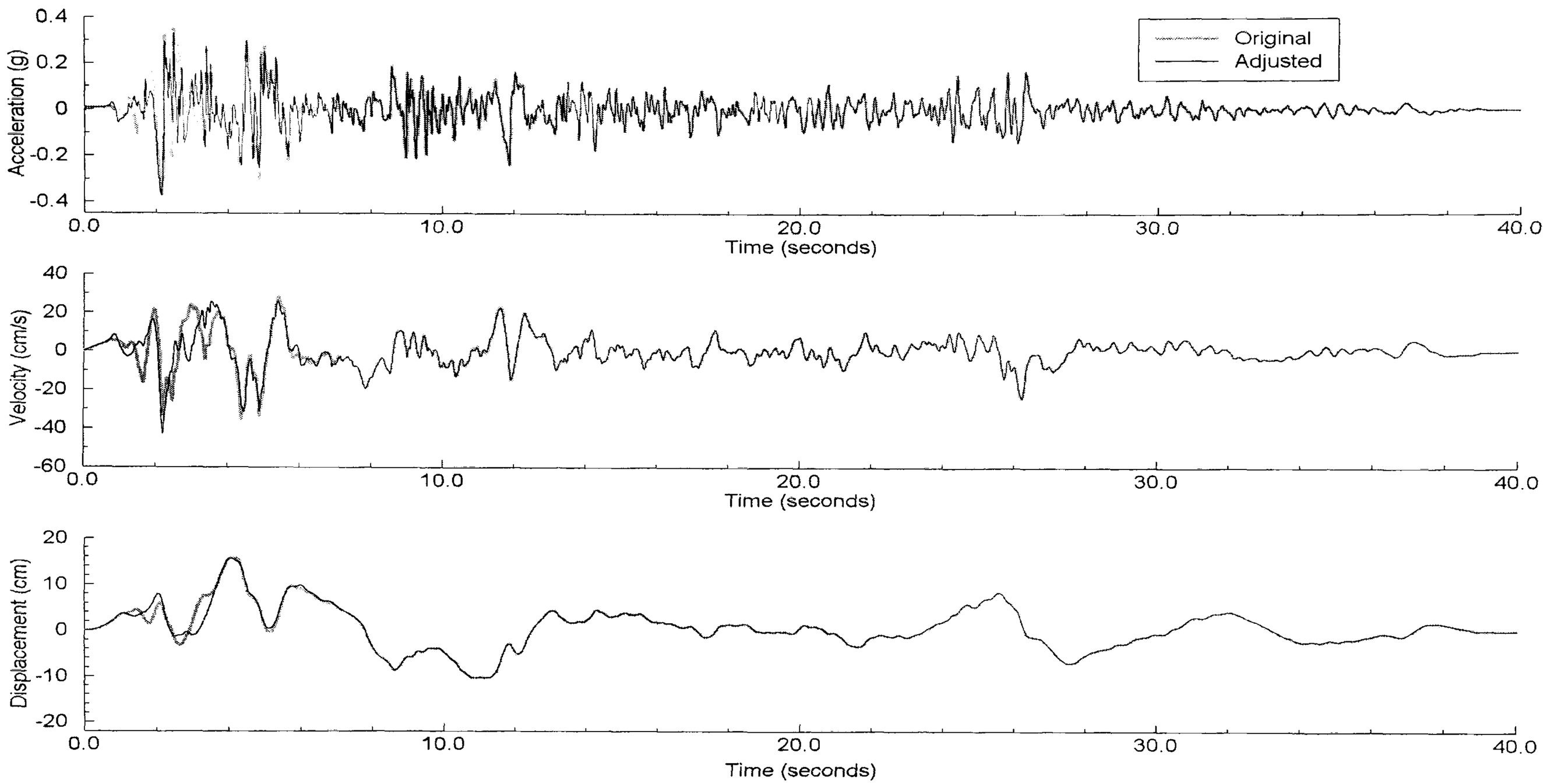


Figure 6.17. - Acceleration (*top*), velocity (*middle*) and displacement (*lower*) time-series from the 1940 M_w 7.0 Imperial Valley Earthquake recorded 6.1km from the fault rupture at El Centro Array #9 (record 00006L in the NGA database). Adjusted series for spectral match from 0.05 to 1 second period.

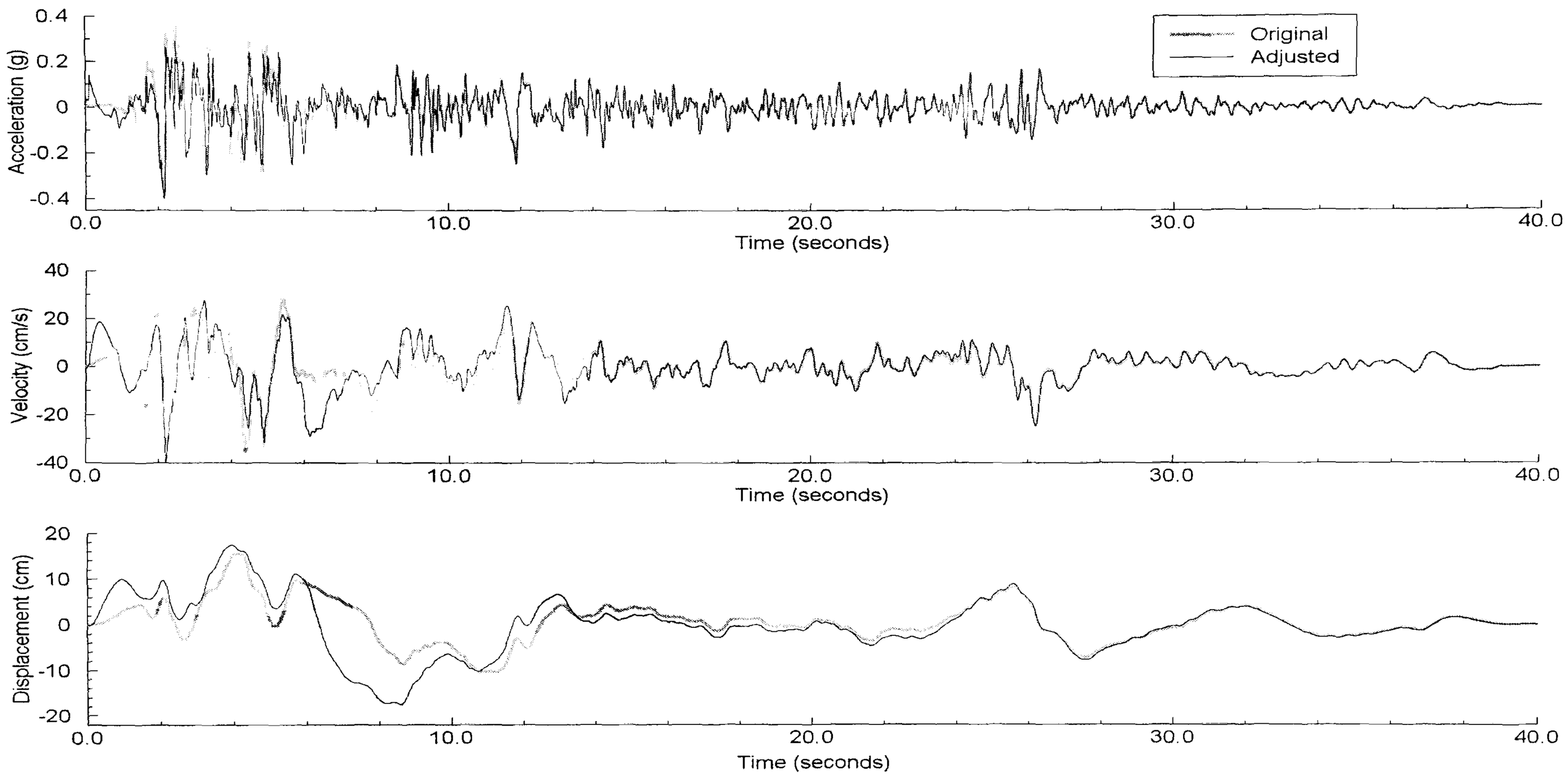


Figure 6.18. - Acceleration (*top*), velocity (*middle*) and displacement (*lower*) time-series from the 1940 M_w 7.0 Imperial Valley Earthquake recorded 6.1km from the fault rupture at El Centro Array #9 (record 00006L in the NGA database). Adjusted series for spectral match from 0.05 to 5 seconds period.

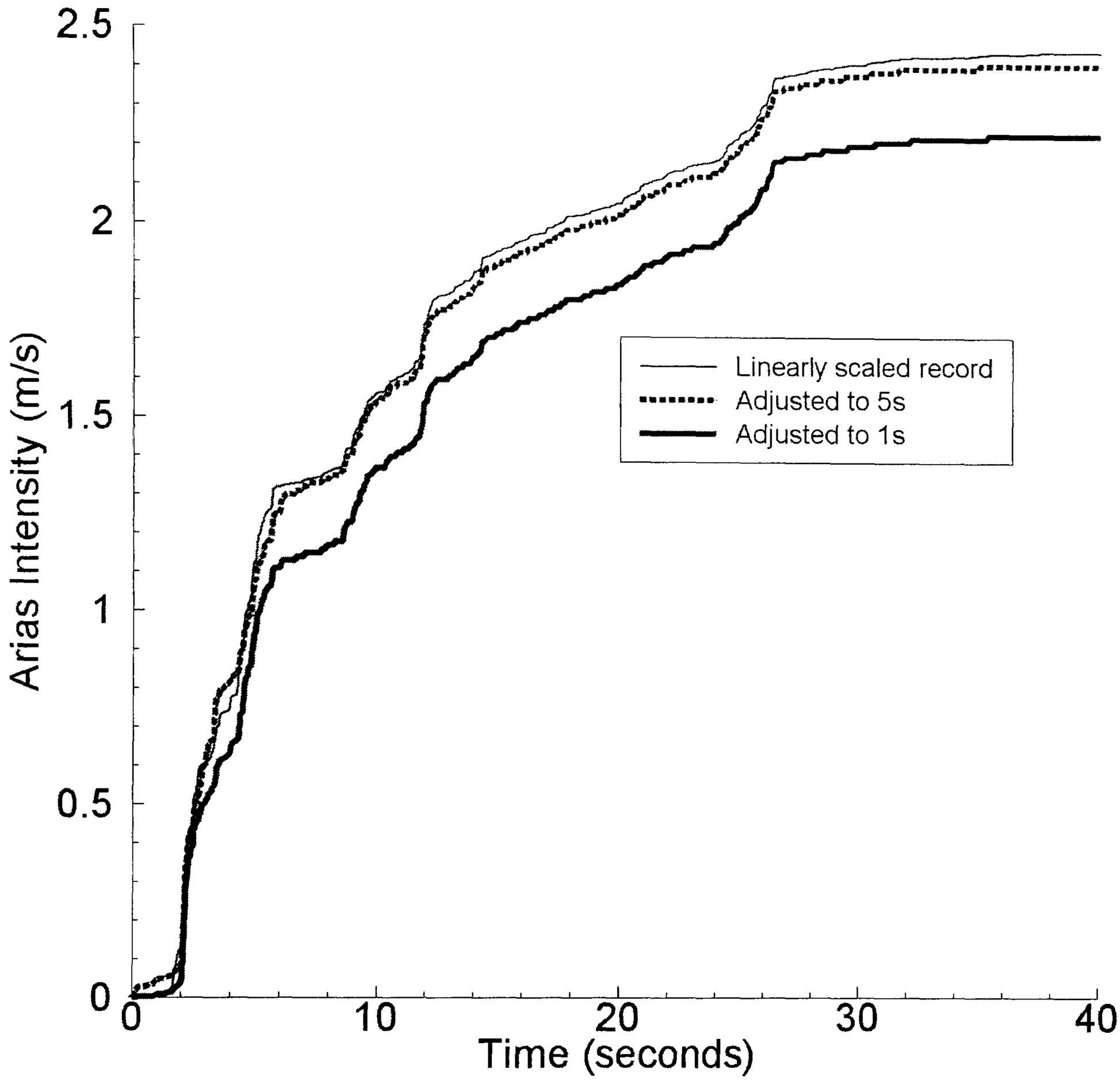


Figure 6.19. –Arias Intensity from the 1940 M_w 7.0 Imperial Valley Earthquake recorded 6.1km from the fault rupture at El Centro Array #9 (record 00006L in the NGA database). Original linearly scaled record and the record adjusted to 1 and 5 seconds.

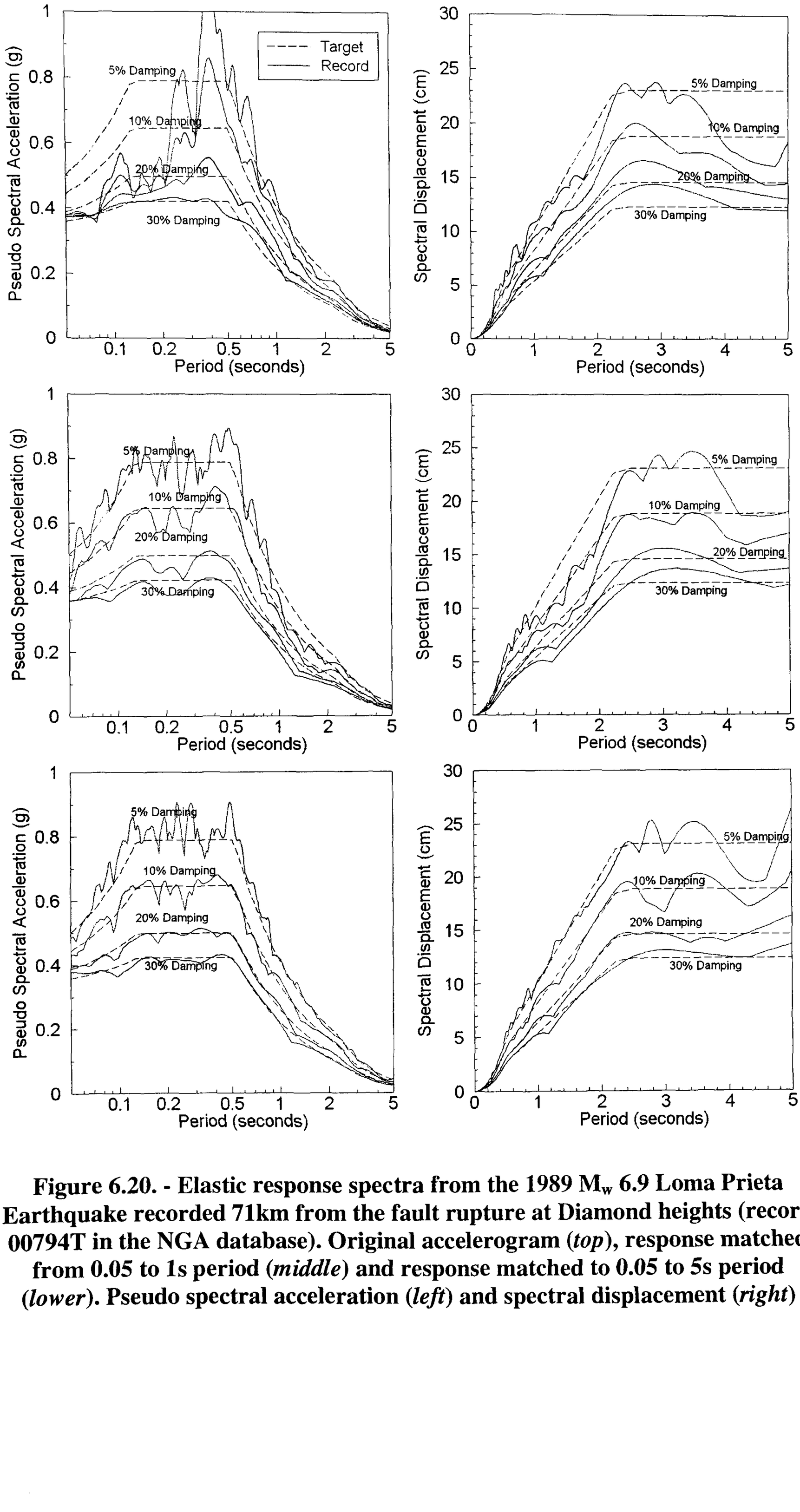


Figure 6.20. - Elastic response spectra from the 1989 M_w 6.9 Loma Prieta Earthquake recorded 71km from the fault rupture at Diamond heights (record 00794T in the NGA database). Original accelerogram (*top*), response matched from 0.05 to 1s period (*middle*) and response matched to 0.05 to 5s period (*lower*). Pseudo spectral acceleration (*left*) and spectral displacement (*right*)

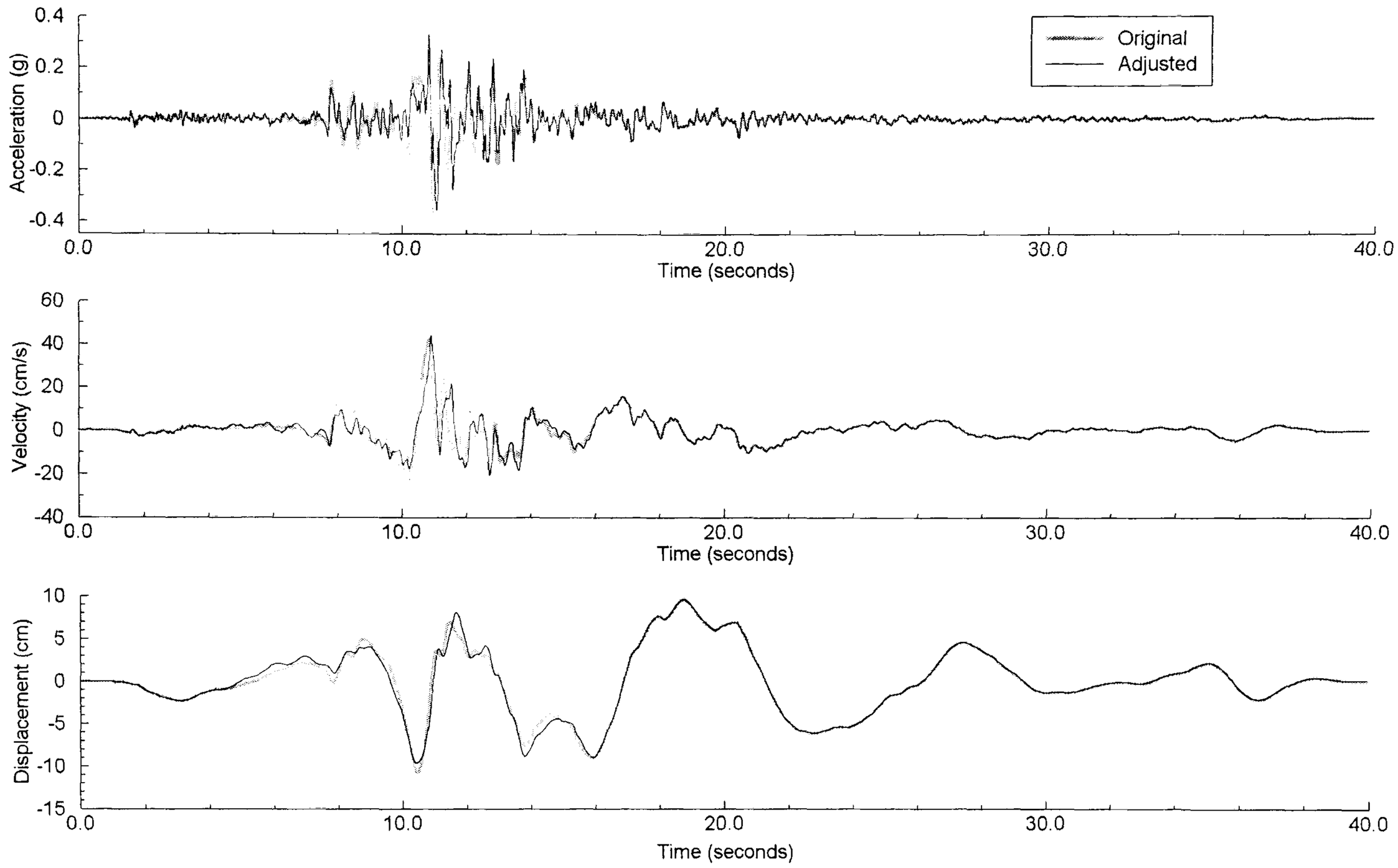


Figure 6.21. - Acceleration (*top*), velocity (*middle*) and displacement (*lower*) time-series from the 1989 M_w 6.9 Loma Prieta Earthquake recorded 71km from the fault rupture at Diamond heights. Adjusted series for spectral match from 0.05 to 1 second period.

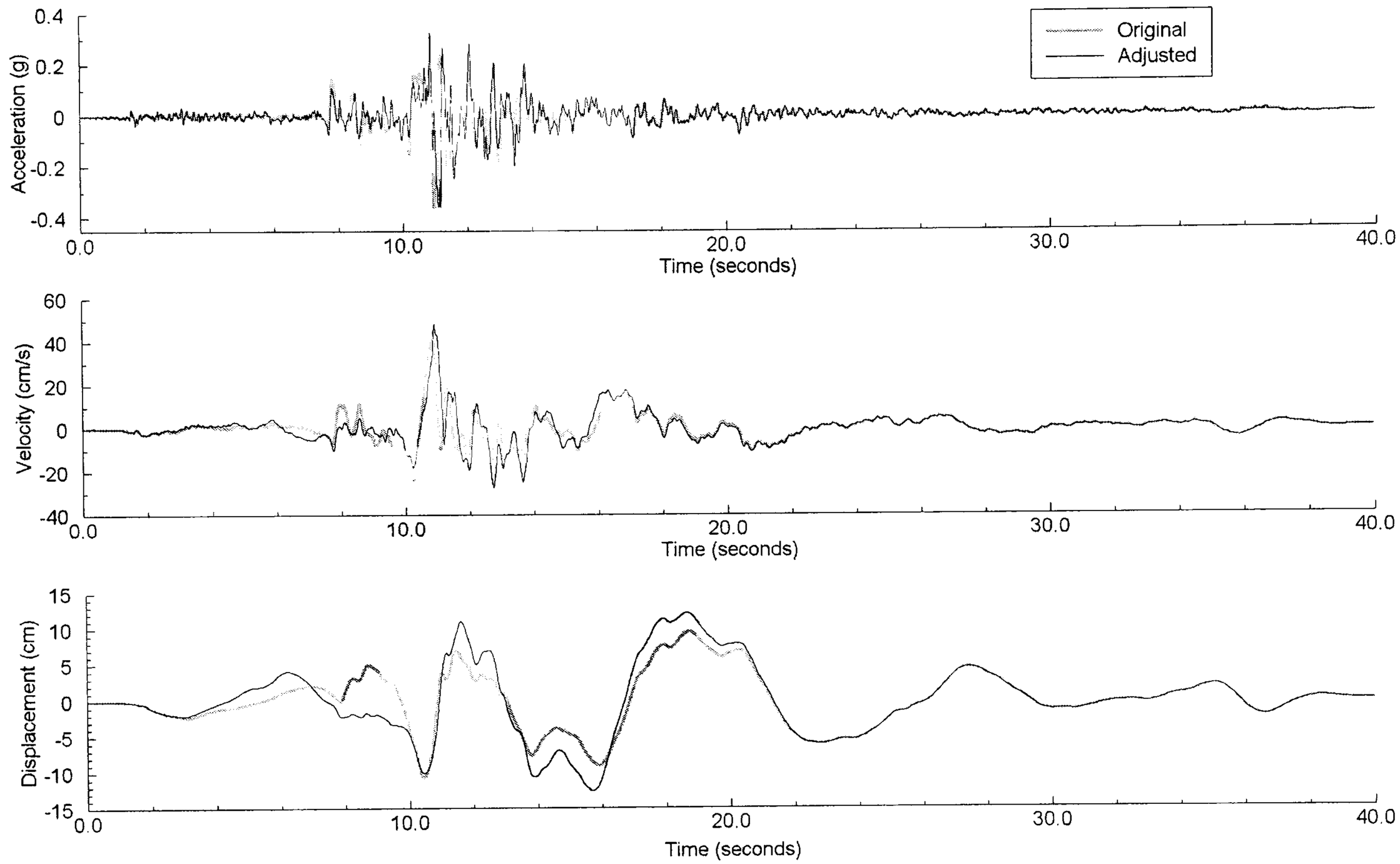


Figure 6.22. - Acceleration (*top*), velocity (*middle*) and displacement (*lower*) time-series from the 1989 M_w 6.9 Loma Prieta Earthquake recorded 71km from the fault rupture at Diamond heights. Adjusted series for spectral match from 0.05 to 5 seconds period.

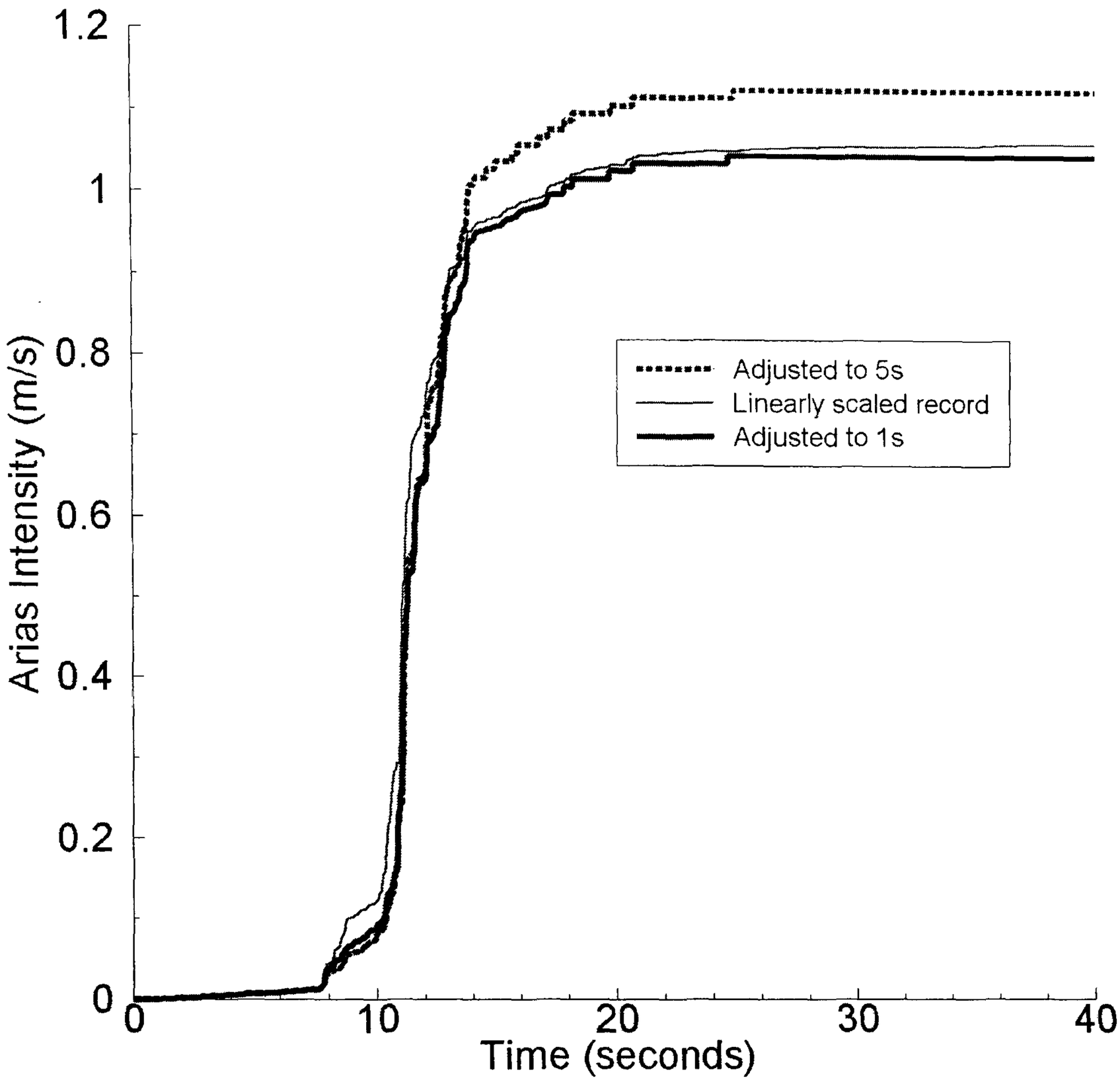


Figure 6.23. –Arias Intensity from the 1989 M_w 6.9 Loma Prieta Earthquake recorded 71km from the fault rupture at Diamond heights. Original linearly scaled record and the record adjusted to 1 and 5 seconds.

6.11 Summary and Further Work

A stable method is presented for the wavelet adjustment of recorded ground motions. This method enables records to be adjusted so that they match the target response spectra at multiple damping levels with closer period spacing than previously possible. New wavelets have been developed that have zero final velocity and displacement, ensuring that records do not require a baseline correction after wavelet adjustment. The procedure can be applied with either absolute spectral acceleration or with pseudo-spectral accelerations if spectral displacements need to be matched.

The work described in this chapter has significantly improved RSPMatch. However, further improvements to the program can still be made, these include:

1. Automatic baseline checking
2. Windows Interface
3. Checks for holes in the Fourier Amplitude Spectrum

The new adjustment procedure can introduce a slight drift in the displacement time-series, even when displacement compatible wavelets are used. This is purely due to the accumulation of rounding errors, which are more likely to occur with shorter period (high-frequency) wavelets and less well refined output acceleration time-series. It would be beneficial to add a routine to the program to check for drifts in displacement and either issue a warning or apply an automatic correction.

The current version of RSPMatch is written in Fortran and uses text files for input and output of data. This is an out-dated method of programming and the program could be considerably more user friendly if the program was Windows based. There are plans to enter into co-operation with the authors of SeismoSignal to produce a windows based version of the program.

Several users of the old version of RSPMatch have noted that the program creates artificial holes in the Fourier amplitude spectra. Preliminary checks of the new version of the program suggest that the new version does not have this issue, possibly because of the closer spaced points on the target spectrum. However, this issue needs to be explored in greater detail to conclusively verify that this is the case.

Another outstanding issue is to determine the amount of modification to the adjusted accelerogram that is acceptable for different applications. If an accelerogram is very different from the target spectrum the RSPMatch may make considerable adjustment to the original time-series. Further studies are required to determine suitable measures and limits of the adjustment.

7. EQUIVALENT SDOF SYSTEMS

A promising option for future methods of selecting and scaling accelerograms is to use the response of non-linear single degree of freedom (SDOF) systems. This study addresses one of the first steps in this process – to determine if it is possible to accurately represent Multiple Degree of Freedom (MDOF) structures with an equivalent Single Degree of Freedom (SDOF) system. The study uses three reinforced concrete frame structures and different types of response parameter including peak drift, peak inter-storey drift, global absorbed hysteretic energy, global fatigue damage and global Park and Ang damage index.

The ability to represent a MDOF system with a SDOF one is particularly attractive because of the considerable saving in analysis run time and post-processing. For example, it takes a 2.7GHz Pentium 4 PC on average two hours to analyse a regular twelve-storey reinforced concrete structure with a 2D fibre element model under the action of one accelerogram; whereas it takes the same computer approximately one minute to analyse the equivalent non-linear SDOF, two orders of magnitude less time. In addition, the results file from a single MDOF analysis requires approximately 1.1Gb storage space, while the output from the SDOF analysis is of the order of 1Mb.

7.1 Background

Many studies attempt to use an equivalent linear SDOF system to model non-linear structural response either by the use of empirical adjustment factors (e.g. Fajfar, 2000; Chopra and Goel 1999a; Chopra and Goel 1999b) or by using the secant stiffness and an increased "effective damping" (e.g. Freeman 1998; Priestley and Kowalsky, 2000). Only inelastic SDOF systems are used in this work to avoid the additional uncertainty associated with the linearization process, which may provide relatively small mean errors for the peak response under the action of a set of ground motions, but can have significant errors for individual earthquake ground motions (e.g. Miranda and Ruiz-Garcia 2002).

Several researchers have investigated the ability of different SDOF models to represent MDOF structures (e.g. Seneviratna and Krawinkler 1997; Nassar and

Krawinkler 1995; Santa-Ana and Miranda 2000). This chapter follows this work but for three specific structures, which enables a more in-depth investigation of the ability of SDOF systems to estimate different types of damage in a MDOF structure, from inter-storey drift to accumulated fatigue damage.

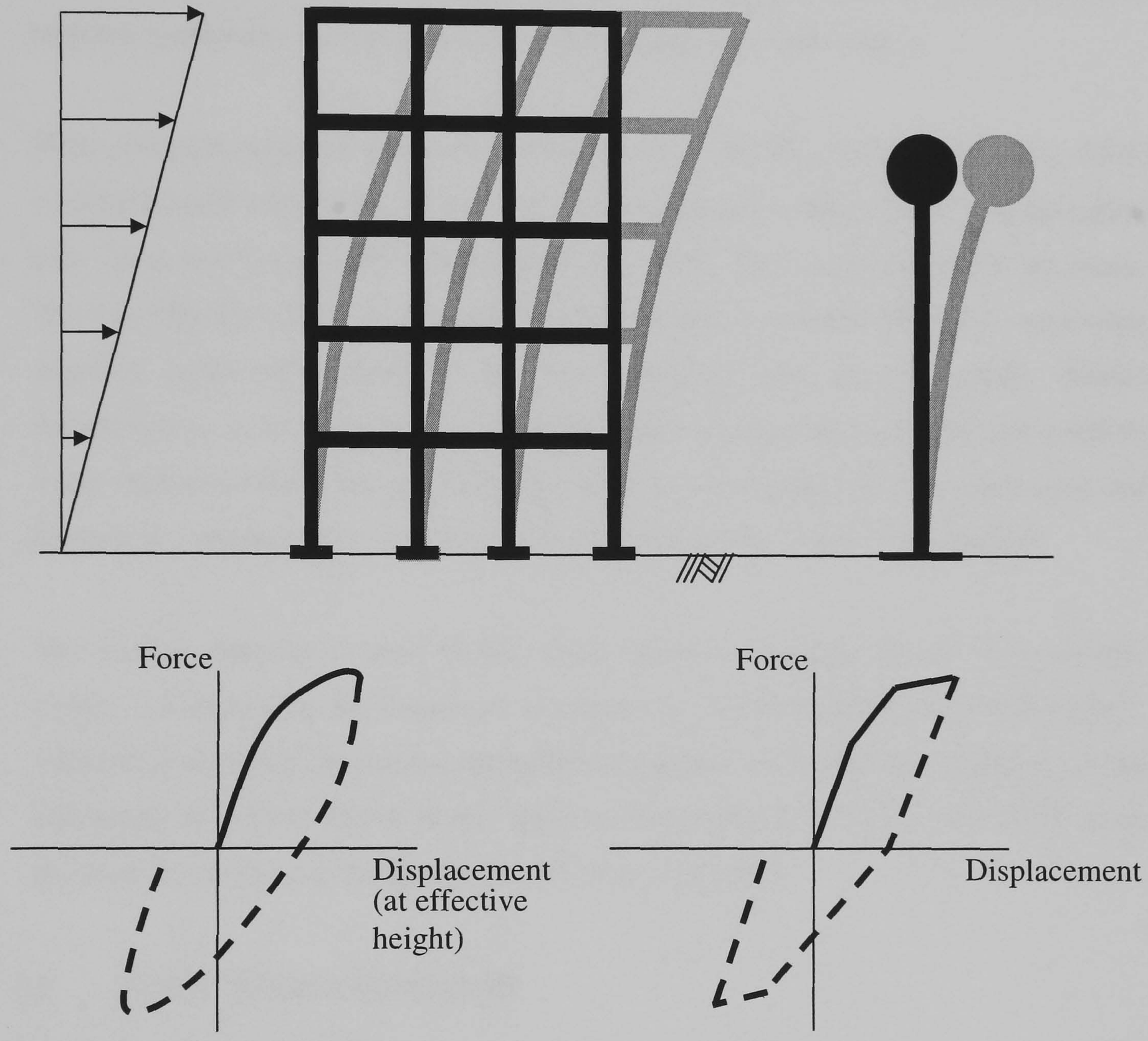


Figure 7.1. – Principles of representing a MDOF with a SDOF. A pushover analysis is conducted assuming a shape vector (top left) to establish the inelastic displaced shape and the backbone of the hysteretic loop (Solid line, lower left plot). Note that different hysteretic rules make different assumptions on the unloading characteristics (dashed lines, lower plots).

To represent a MDOF system with a SDOF system it is usual to make the assumption that the MDOF oscillates about a single dominant mode shape. Structures analysed under the action of strong earthquake ground-motions may be designed to exhibit significant non-linear deformations. For this reason the mode shape for the MDOF

needs to capture the non-linear behaviour of the materials. One of the simplest ways to determine a non-linear mode shape is to use a non-linear pushover analysis. The SDOF properties can then be chosen so that the backbone of the SDOF system maps directly to the pushover curve (Figure 7.1). A pushover analysis also enables transfer functions to be developed that relate the SDOF displacement to any desired MDOF response parameter such as inter-storey drift or member deformation.

More complex adaptive pushover techniques (e.g. Mwafy, 2001; Rovithakis, 2001; Antoniou and Pinho, 2004), or methods that use pseudo inelastic modal superposition (e.g. Chou and Uang, 2002; Chopra and Goel 2002, 2003) are not used in this study. Work by Mwafy (2001) has shown that there is only a small advantage in employing adaptive pushover techniques for the structures used in this study. Modal superposition is, by definition, not strictly valid for non-linear systems and methods using such procedures are not straightforward to implement, not yet widely used and constitute a separate area of research which is outside the scope of this project.

No viscous damping is used in this study because damping caused by hysteretic energy is included by the non-linear deformation of both MDOF and SDOF models. Additional damping from non-structural components or from energy radiation at the foundation is not considered in this study as this could not be simply modelled using the analysis program at the time this work was conducted.

7.2 MDOF Systems Investigated

7.2.1 Structural models

Three structural models of low- and medium-rise RC buildings designed to EC8 (CEN 2004) are used in this work. These have been developed by previous researchers at Imperial College and the ROSE European School for Advanced Studies in Reduction of Seismic Risk (Mwafy 2001; Rovithakis 2001; Antoniou and Pinho 2004; López-Menjivar 2004). The first is an 8-storey irregular frame structure; the second a 12-storey regular frame, and the third an 8-storey regular frame-wall structure (Figures 7.2 to 7.4). All structures have a design PGA of 0.15g and medium ductility classification. The regular frame was designed with a behaviour factor of

3.75; the irregular frame a behaviour factor of 3.0 and the wall frame a behaviour factor of 2.625. Design of the buildings was undertaken by Professor Fardis at the University of Patras (Fardis 1994). The structures were initially modelled by Mwafy (2001) as two concentric plane frames and subsequently converted into an equivalent single plane frames by Rovithakis (2001).

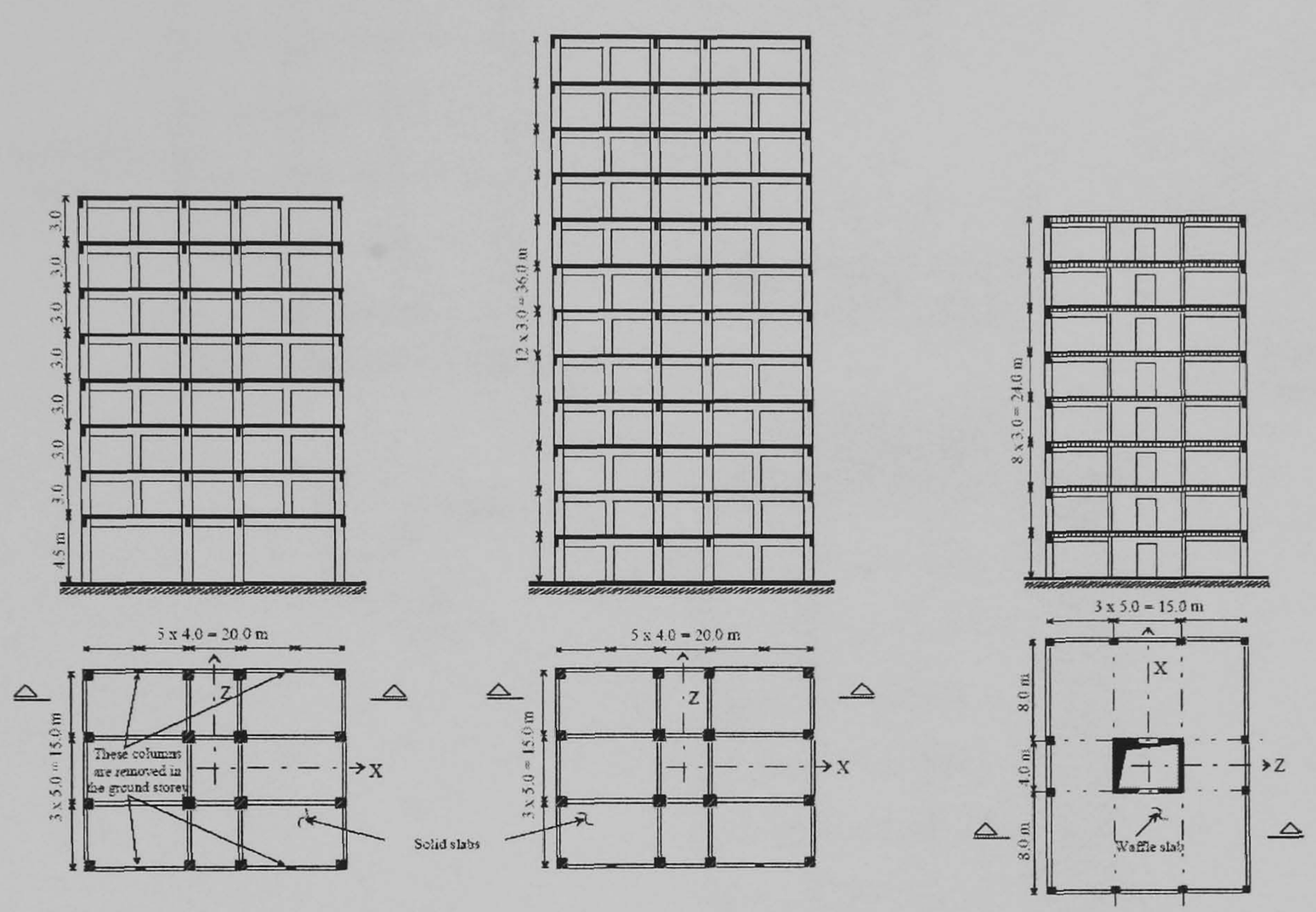


Figure 7.2. - Plane and sectional elevation of the buildings: 8-storey irregular frame (*left*); 12-storey regular frame; 8-storey regular frame-wall building (Mwafy, 2001)

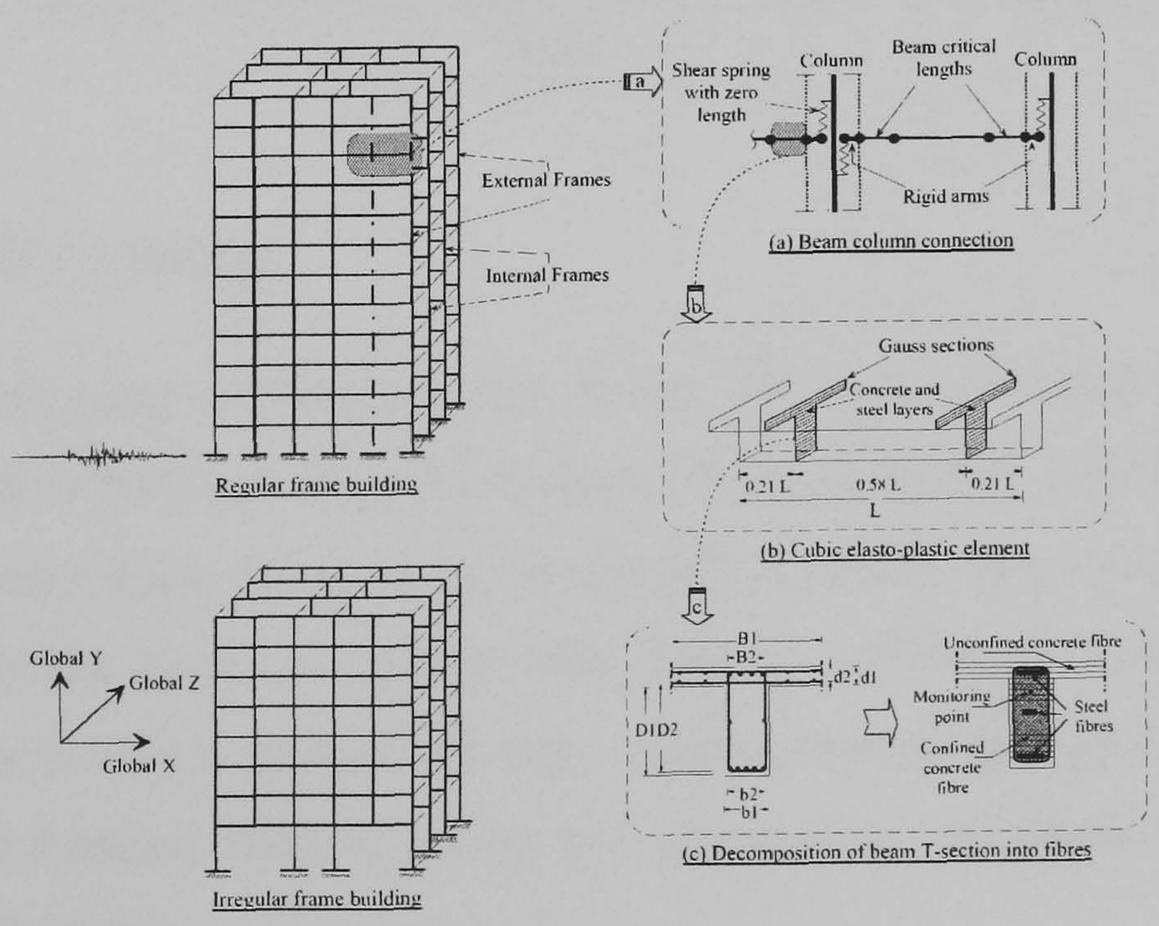


Figure 7.3. – Adopted modelling approach for regular and irregular frame buildings (Mwafy, 2001)

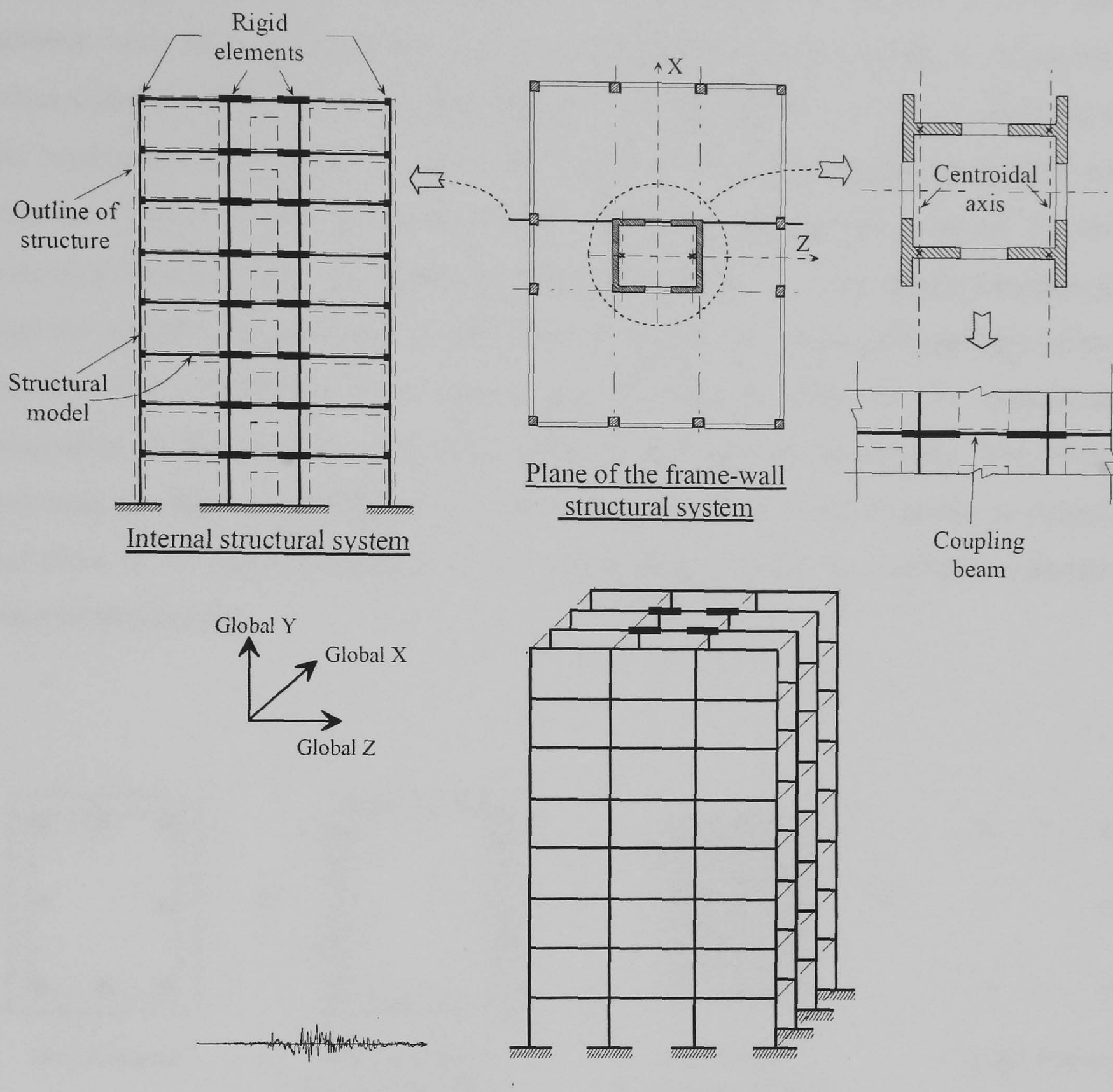


Figure 7.4. - Adopted modelling approach for frame-wall buildings (Mwafy, 2001)

7.2.2 Analytical modelling

The finite element program SeismoStruct version 3.9.7 build 85 (SeismoSoft 2005b) is used to run all of the analysis in this section. Multiple file pre- and post-processing has been automated using the program SeismoMDA, which was written specifically for this work by the author in collaboration with the authors of SeismoStruct. The analysis package is able to predict the large displacement behaviour of space frames under static and dynamic loading, taking into account both geometric non-linearities and material inelasticity.

Structural members are modelled using distributed-plasticity fibre elements which use member cross-section properties and material constitutive behaviour to explicitly define element hysteretic behaviour (Figure 7.5). The interaction of the axial force and transverse deformation is modelled using a cubic formulation suggested by Izzuddin (2001), where the strain states within the element are defined by the generalised axial strain and curvature along the element. A cubic shape function is used to calculate the transverse displacement as a function of the end rotations of the element. Two integration Gauss points per element are used for the numerical integration of the governing equations of the cubic formulation (Figure 7.6). Each structural element is modelled with typically three to four finite elements to ensure that there is sufficient refinement in the plastic hinge region to accurately estimate material inelasticity.

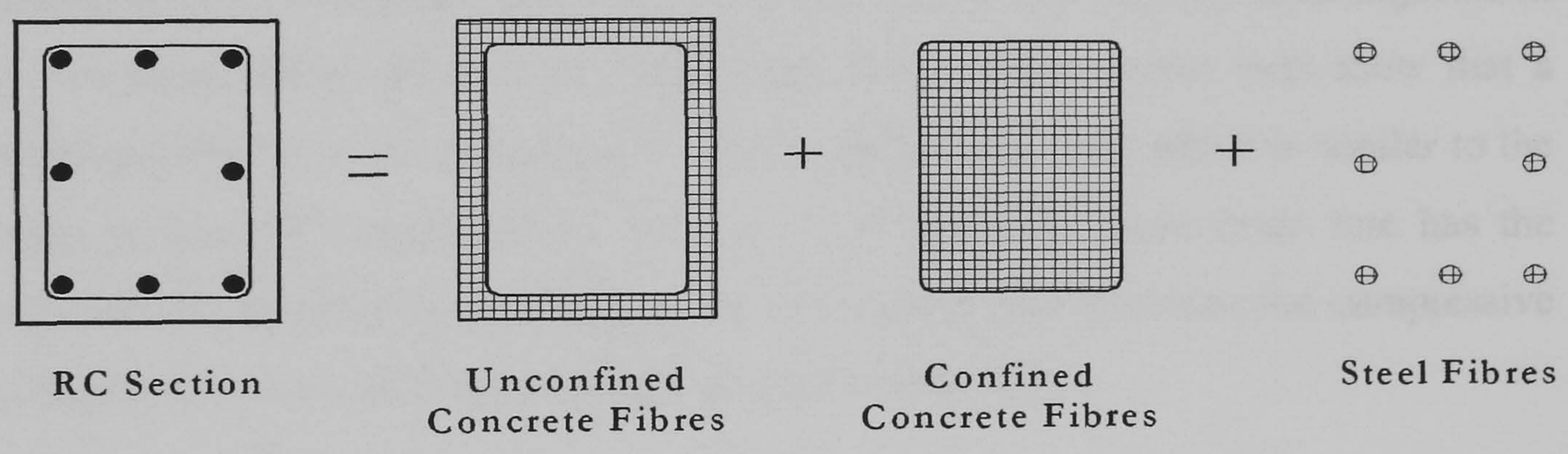


Figure 7.5. – Fibre plasticity discretization in a reinforced concrete section (López-Menjivar 2004).

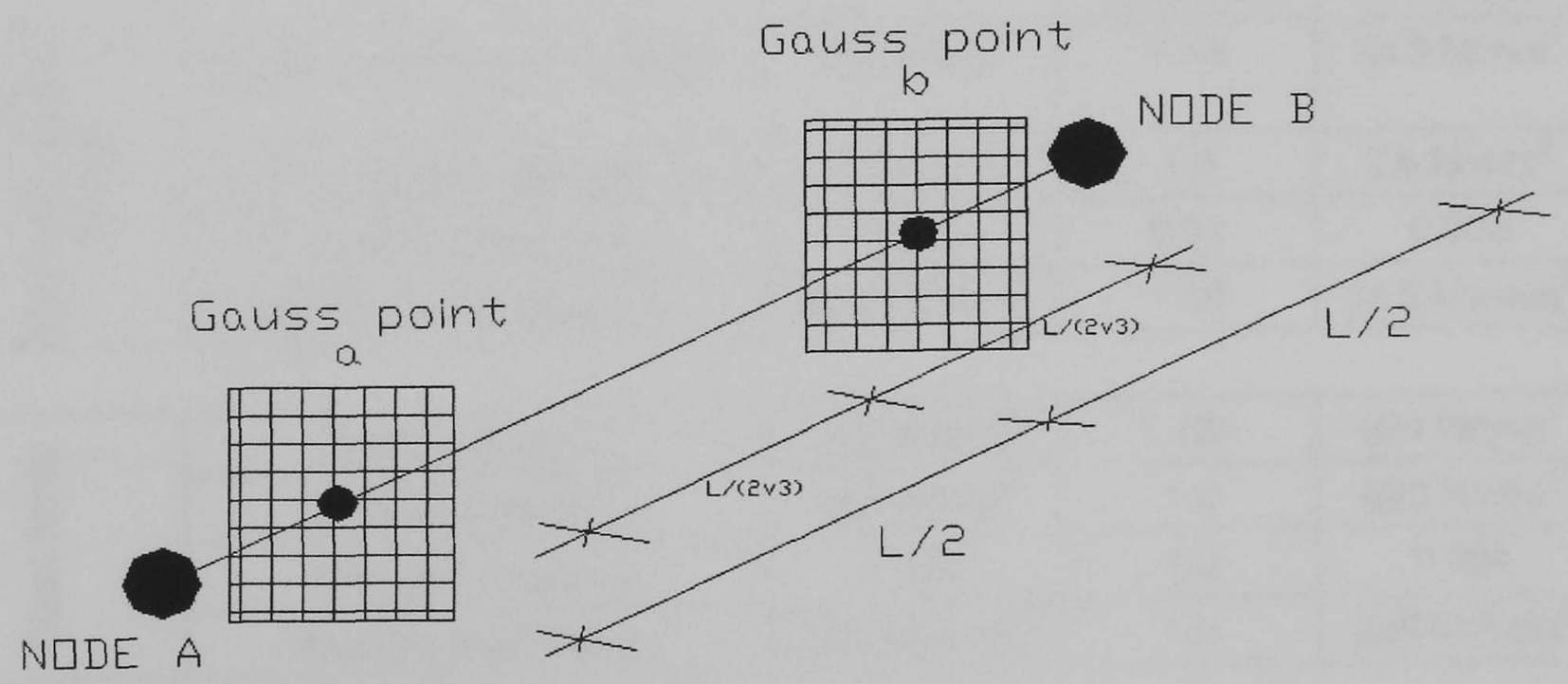


Figure 7.6. – Location of Gauss points along the member length (López-Menjivar 2004).

Shear strains and warping of the cross-section are not explicitly modelled; however, a non-linear spring is used at the end of the beams to model the shear deformations. No viscous damping is considered in the analysis as energy dissipation through hysteresis is already implicitly included within the non-linear fibre model of the elements. Non-hysteretic damping is assumed to be negligible for the purposes of this research. A brief study is conducted for this work to determine the most appropriate numerical integration scheme (Appendix 2). This demonstrates that the Hilber-Hughes-Taylor (Hilber *et al.* 1977) algorithm is required to provide numerical stability.

7.2.3 Material parameters

Mean values of material strengths are utilised in the analysis rather than the characteristic values used in design; this enables a more realistic estimation of the structural response to be obtained. The influence of the rapid strain rates experienced during seismic loading has also been accounted for by applying dynamic adjustment factors proposed by Scott *et al.* (1982) and Jones (1989). Initial tests show that a strain rate of 0.01 s^{-1} is appropriate for the models considered, which is similar to the value of 0.0167s^{-1} suggested by Scott *et al.* (1982). The rapid strain rate has the influence of reducing the crushing strain of concrete and increases the compressive strength of concrete and yield strength of steel (Table 7.1).

Table 7.1. – Material properties used in the analysis

	Material Parameter	Mean Value	Dynamic Adjustment	Value used in Analysis
Concrete grade C25/30	Mean compressive strength, f_{cm}	33 N/mm^2	1.16	38.3 N/mm^2
	Mean tensile strength, f_{ct}	2.6N/mm^2	1.0	2.6 N/mm^2
	Crushing strain, ε_c	0.0022	0.91	0.002
	Modulus of elasticity, E_c	30.5 kN/mm^2	1.09	33.3 kN/mm^2
Steel S500	Yield strength, f_y	585 N/mm^2	1.181	691 N/mm^2
	Ultimate strength, f_u	680 N/mm^2	1.0	680 N/mm^2
	Ultimate strain, ε_{su}	0.094	1.0	0.094
	Young's modulus, E_s	200 kN/mm^2	1.0	200 kN/mm^2

The concrete constitutive behaviour is modelled using the non-linear constant confinement concrete model proposed by Mander *et al.* (1989), modified by

Martinez-Rueda and Elnashai (1997) to improve numerical stability under large displacements. The concrete confinement factors are taken from those used by previous researchers (Mwafy 2001; Rovithakis 2001; Antoniou and Pinho 2004; López-Menjivar 2004).

The steel constitutive behaviour is modelled using the Menegotto-Pinto steel model (Menegotto and Pinto 1973), which was modified by Filippou *et al.* (1983) and Fragiadakis *et al.* (2004). The default parameters used to define the constitutive rule as suggested in the SeismoStruct program (SeismoSoft 2005b) are used where the values are not defined in Table 7.1.

7.2.4 Shear deformations

Bi-linear springs are used at the end of the beam to approximate the joint shear deformation. The properties of the springs are calculated based on the work of Jenkins (2004) and Park and Paulay (1975). The initial stiffness is given by product of the elastic shear modulus (G), shear web area (A_v) and half the beam length. The shear area of the web is taken as the full web area for "T" sections and the sectional area of rectangular sections divided by 1.2 to allow for the non-uniform distribution of shear stresses (Park and Paulay 1975). The elastic shear modulus is given in terms of the Poisson ratio, v:

$$G = \frac{E_c}{2(1+v)} \tag{7.1}$$

Poisson's ratio is taken as 0.17 as suggested by Jenkins (2004). The elastic modulus of concrete (E_c) is given by the equation used by Rossetto (2002):

$$E_c = 4700\sqrt{f_c} \tag{7.2}$$

where f_c is the concrete compressive strength.

The "yield" force of the shear spring is set to the product of the shear area of the web and the concrete shear strength, which is taken as the tensile strength of the concrete.

The post-yield hardening of the spring is set to 0.3, which approximates the additional shear resistance of the cracked section provided by the strut mechanism from the reinforcement. The force deformation characteristics of the spring are approximate as the true shear force-deformation characteristics are dependent on the loading time-history, axial load level and the interaction between bending and shear at the member ends. However, the simplified bi-linear model is considered to be an adequate representation for this work considering the modelling options currently available in SeismoStruct.

7.3 Measures of Damage

Chapter 3 shows that there is a wide range of damage measures proposed in the literature. These can be divided into four main categories

1. Measures of maximum response (force or displacement)
2. Cyclic fatigue measures
3. Energy measures
4. Measures using a combination of the above

Whilst it is not possible to use all the proposed damage measures at least one from each generic category is used. The damage measures employed are:

- Peak building drift (max response)
- Peak inter-storey drift (max response)
- Global displacement fatigue (cyclic fatigue)
- Absorbed hysteretic energy (energy measure)
- Global Park and Ang Damage Index (combination measure)

The more complex measures are described in greater detail later in this chapter.

7.4 Strong-motion Data Set

The strong-motion data set used for this study is taken from the NGA strong-motion database version 3.2, kindly supplied by Norman Abrahamson in November 2004. The full NGA data set consists of over 3500 records from 173 earthquakes. Records are selected for this study to capture the pertinent features of the database subset with 136 records. This is achieved by selecting records to fulfil three criteria:

1. Records with a similar magnitude – distance distribution as the full dataset
2. Records with unusual characteristics (e.g. accelerograms with velocity or displacement pulses; those recorded on V. Soft soil sites; accelerograms with particularly long or short duration etc.) to highlight the influence of the variability of the ground motion.
3. Records with high spectral accelerations between 0.6 and 1.2s period, which are likely to induce significant non-linear response

Further details of the record selection process and of the selected records are given in Appendix A1. The records used in this study have not been scaled.

7.5 Equivalent SDOF Systems

The inelastic SDOF systems used in this study are modelled using lump masses and link elements in SeismoStruct version 3.9.7 build 85 (SeismoSoft 2005b). SDOF model creation and multiple file processing have been automated using the program SeismoMDA, written specifically for this work by the author.

The following inelastic SDOF hysteretic rules are investigated in this study (Figure 7.7):

- Bi-linear
- Modified Takeda (bi-linear)
- Tri-linear (peak orientating)

The modified Takeda hysteresis loop described in Otani (1974); uses the unloading rules proposed by Emori and Schonobrich (1978). This is a bi-linear simplification of the original tri-linear model proposed by Takeda *et al.* 1970. The unloading stiffness from the post yielding curve in outer hysteresis loop (K_{rout}) is defined by:

$$K_{rout} = K_0 \left(\frac{D_y}{D_m} \right)^{\beta o} \tag{7.3}$$

where K_0 is the initial stiffness, D_y is the yield displacement, D_m is the previous maximum displacement, βo is the outer loop stiffness degradation factor. The inner loop stiffness degradation factor (K_{rin}) is defined using the inner loop stiffness degradation factor (β_t) as:

$$K_{rin} = \beta_1 * K_0 \left(\frac{D_y}{D_m} \right)^{\beta o} = \beta_1 * K_{rout} \tag{7.4}$$

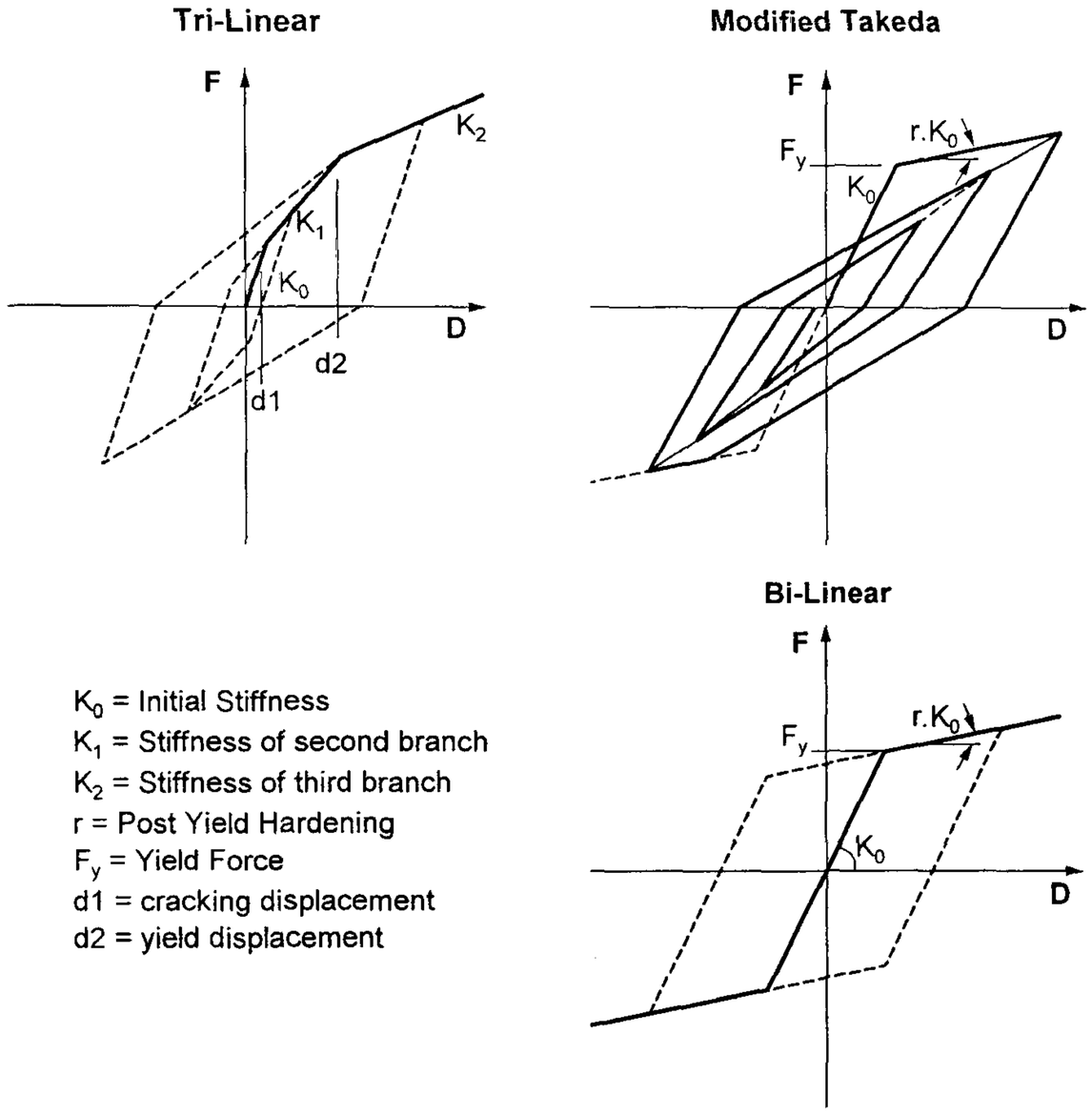


Figure 7.7. – Illustration of different hysteretic curves (after SeismoSoft 2005b)

Each hysteretic rule is mapped to three different backbone curves (force-displacement relationships) for each structure. The back bone curves are developed using non-linear pushover analyses with two lateral force distributions; a uniform force profile and a triangular force profile. The third set of backbone curves are created by setting the initial stiffness to ensure that the initial period of the SDOF system is the same as the initial (elastic) period of the first mode of the MDOF structure; the yield strength and post-yield period of these curves are set to match the SDOF developed using the triangular pushover. The pushover and SDOF force-displacement curves are given in Figure 7.8. The effective heights of the MDOF structures are given in Table 7.2 and the properties of the SDOF systems are given in Tables 7.3 to 7.6.

Table 7.2. - Effective height of MDOF structures

Structure	Effective height using triangular pushover (m)	Effective height using uniform pushover (m)
Wall-frame	16.950	13.650
Irregular-frame	17.900	14.720
Regular-frame	24.750	19.300

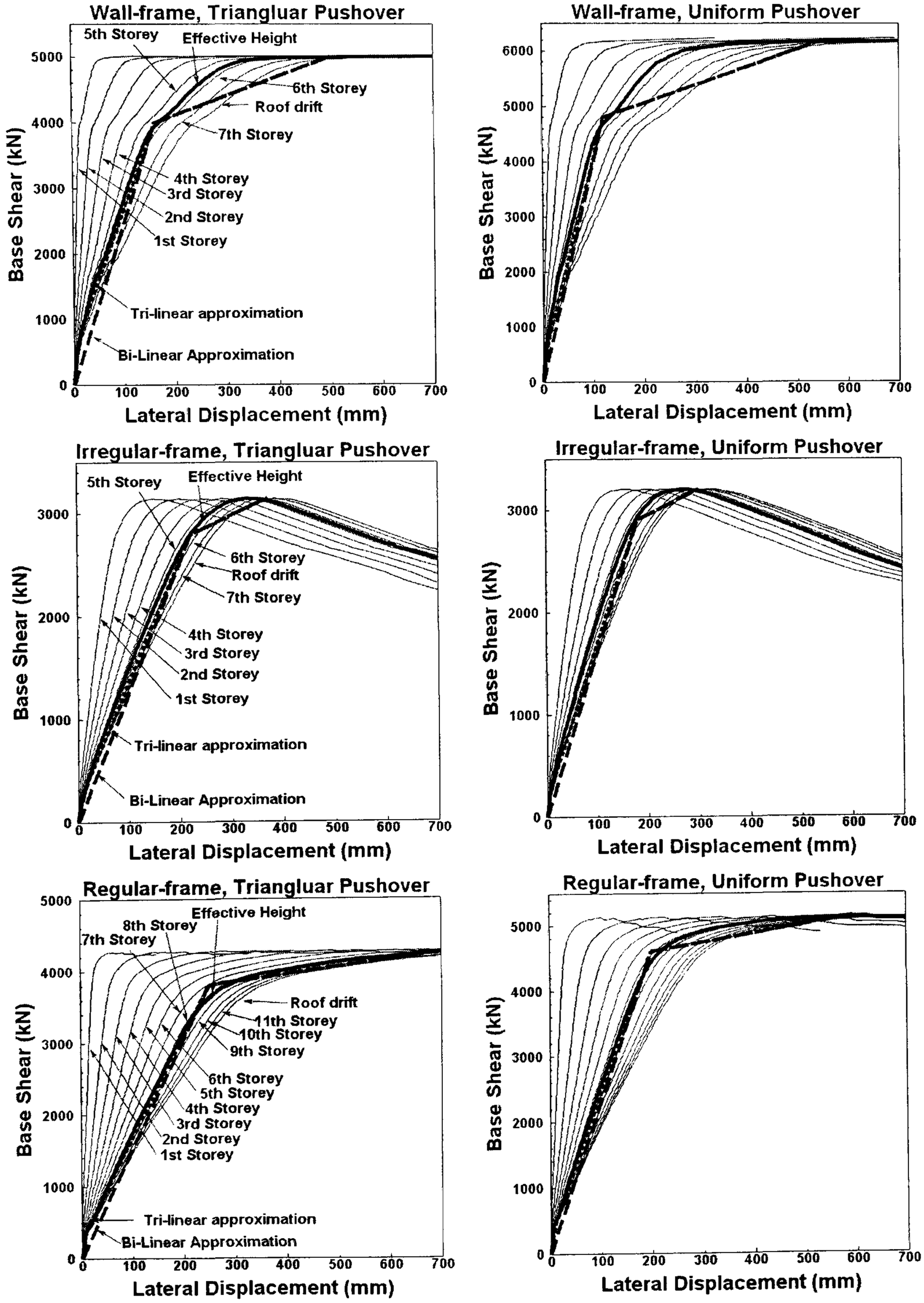


Figure 7.8. – Force-displacement characteristics of the different RC frames from pushover analysis. Approximated bi-linear and tri-linear backbone curves also shown.

Table 7.3. – Properties of equivalent single degree-of-freedom systems

Bi-linear (and backbone of Takeda)					
Initial period based on	Structure	Initial Period	Post-yield Period	Yield Displacement (mm)[1]	Base shear (g)[1]
Initial Stiffness	Wall-frame	0.554	2.703	57.1	0.749
Effective stiffness, from triangular pushover	Wall-frame	0.927	2.703	160.0	0.749
Effective stiffness, from uniform pushover	Wall-frame	0.733	2.570	120.0	0.899
Initial Stiffness	Irregular-frame	0.661	2.604	77.3	0.712
Effective stiffness, from triangular pushover	Irregular-frame	1.115	2.604	220.0	0.712
Effective stiffness, from uniform pushover	Irregular-frame	0.991	2.516	180.0	0.738
Initial Stiffness	Regular-frame	0.773	5.247	82.6	0.556
Effective stiffness, from triangular pushover	Regular-frame	1.346	5.247	250.0	0.556
Effective stiffness, from uniform pushover	Regular-frame	1.094	4.474	200.0	0.672
Tri-linear					
Initial period based on	Structure	Initial Period	Cracked Period	Cracking Disp. (mm)[2]	Base shear (g)[2]
Effective stiffness, from triangular pushover	Wall-frame	0.561	0.993	11.0	0.140
Effective stiffness, from uniform pushover	Wall-frame	0.561	0.761	11.0	0.140
Effective stiffness, from triangular pushover	Irregular-frame	0.661	1.150	6.9	0.064
Effective stiffness, from uniform pushover	Irregular-frame	0.661	1.017	6.9	0.064
Effective stiffness, from triangular pushover	Regular-frame	0.775	1.396	8.5	0.057
Effective stiffness, from uniform pushover	Regular-frame	0.773	1.125	10.2	0.069

[1]At global yield

[2]At initial cracking, global yield same as bi-linear.

Table 7.4. – Detailed properties of bi-linear equivalent single degree-of-freedom systems

Initial period based on	Structure	Mass(T)	Initial Stiffness(N/mm)	Yield force(N)	Post-yield Hardening (%)
Initial Stiffness	Wall-frame	545	70040	4000000	0.042
Effective stiffness, from triangular pushover	Wall-frame	545	25000	4000000	0.12
Effective stiffness, from uniform pushover	Wall-frame	545	40000	4800000	0.08
Initial Stiffness	Irregular-frame	401	36215	2800000	0.064
Effective stiffness, from triangular pushover	Irregular-frame	401	12727	2800000	0.18
Effective stiffness, from uniform pushover	Irregular-frame	401	16111	2900000	0.16
Initial Stiffness	Regular-frame	697	46022	3800000	0.022
Effective stiffness, from triangular pushover	Regular-frame	697	15200	3800000	0.07
Effective stiffness, from uniform pushover	Regular-frame	697	23000	4600000	0.06

Table 7.5. – Detailed properties of Takeda equivalent single degree-of-freedom systems

Initial period based on	Structure	Mass(T)	Yield force(N)	Initial Stiffness(N/mm)	Post Yield Hardening(%)	Outer Loop deg factor	Inner Loop deg factor
Initial Stiffness	Wall-frame	545	4000000	70040	0.042	0.4	0.9
Effective stiffness, from triangular pushover	Wall-frame	545	4000000	25000	0.12	0.4	0.9
Effective stiffness, from uniform pushover	Wall-frame	545	4800000	40000	0.08	0.4	0.9
Initial Stiffness	Irregular-frame	401	2800000	36215	0.064	0.4	0.9
Effective stiffness, from triangular pushover	Irregular-frame	401	2800000	12727	0.18	0.4	0.9
Effective stiffness, from uniform pushover	Irregular-frame	401	2900000	16111	0.16	0.4	0.9
Initial Stiffness	Regular-frame	697	3800000	46022	0.022	0.4	0.9
Effective stiffness, from triangular pushover	Regular-frame	697	3800000	15200	0.07	0.4	0.9
Effective stiffness, from uniform pushover	Regular-frame	697	4600000	23000	0.06	0.4	0.9

Table 7.6. – Detailed properties of tri-linear equivalent single degree-of-freedom systems

Initial period based on	Structure	Mass(T)	Initial Stiffness (N/mm)	Displacement d1 (mm)	Stiffness of 2nd branch (N/mm)	Displacement d2 (mm)	Stiffness of 3rd branch (N/mm)
Effective stiffness, from triangular pushover	Wall-frame	545	68182	11.0	21812	160	2941
Effective stiffness, from uniform pushover	Wall-frame	545	68182	11.0	37156	120	3256
Effective stiffness, from triangular pushover	Irregular-frame	401	36232	6.9	11966	220	2333
Effective stiffness, from uniform pushover	Irregular-frame	401	36232	6.9	15309	180	2500
Effective stiffness, from triangular pushover	Regular-frame	697	45882	8.5	14120	250	1000
Effective stiffness, from uniform pushover	Regular-frame	697	46078	10.2	21760	200	1375

7.6 Comparison of MDOF and SDOF Response

7.6.1 Peak drift at the effective height of structure

The peak drift at the effective height of the MDOF structure and the peak drift of the SDOF system can be compared directly. The SDOF estimations are compared by plotting the MDOF response against the SDOF estimation. A linear trend line is fitted through the drift estimates using least squares regression and the coefficient of determination (R^2) of the trend is calculated to provide an indication of the dispersion of the data. If the SDOF system gives a perfect estimation of the MDOF response, the trend line will have a gradient and correlation coefficient of unity. A typical example of the correlation between the displacement from the MDOF structures and SDOF equivalent systems is shown in Figure 7.9. The full results for all analyses are given in Table 7.7.

The results show the importance of the initial period of the SDOF representation, even if this is for a small part of the hysteretic behaviour as is the case for the tri-linear hysteretic rules. SDOF models with an initial period based on the uncracked initial period of the structure can consistently underestimate the MDOF response by up to a factor of 1.6 while SDOF models with an initial period based on a cracked stiffness generally overestimate the MDOF response (Table 7.7). The use of the initial period of the MDOF system for the SDOF representation is recommended by several authors (e.g. Seneviratna and Krawinkler 1995) presumably because of the relative ease by which this can be calculated. However, this study shows that SDOF representations constructed using this philosophy have consistently poorer correlations to the MDOF response than SDOF representations constructed to obtain a good general fit to the inelastic response (Table 7.7). This finding is logical as the initial stiffness of the concrete structures is rapidly lost with the onset of the ground motion (e.g. Aschheim and Black 1999).

The difference caused by using a different lateral force distribution in the pushover analysis has less influence on the ability to make accurate drift predictions than other factors such as the hysteretic rule and initial stiffness of the SDOF model. The SDOF models developed using the uniform force distribution generally provide more

reliable estimates of peak drift than those developed using a triangular force distribution; however, differences are only of the order of 10%.

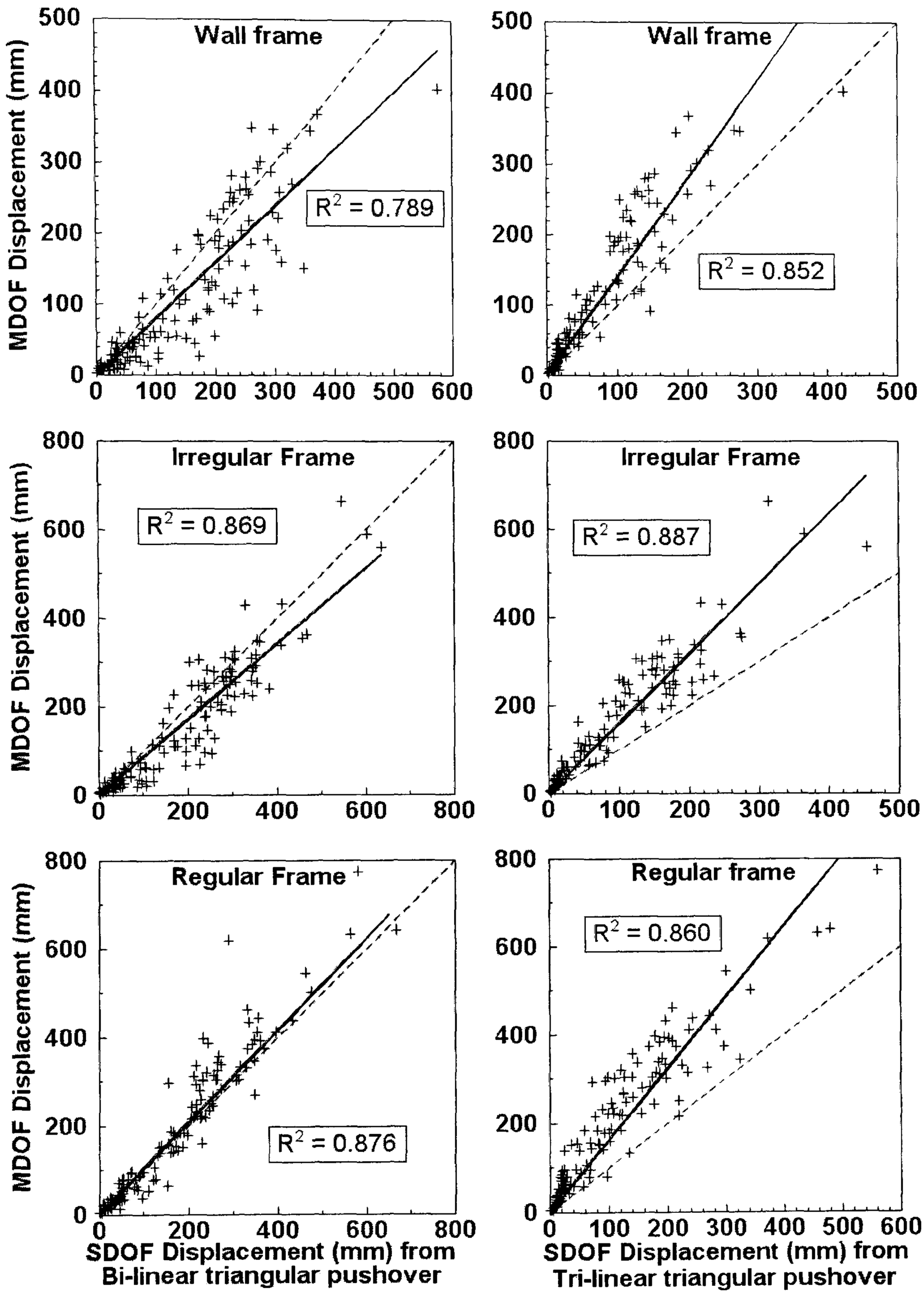


Figure 7.9. – Ability of different bi-linear and tri-linear equivalent SDOF models to predict MDOF displacement at the effective height of the structure. Trend line shown by solid line; ideal 1:1 target shown by dashed line. Crosses show the response from each ground motion.

Table 7.7. – Ability of different SDOF models to predict MDOF displacement at the effective height of the structure. Best values given in bold.

Structure	SDOF Hys. model	Initial Period based on:	Gradient of trend line	Coeff. of det. (R^2)
Wall-frame	Bi-linear	Initial Stiffness	1.588	0.748
Wall-frame	Bi-linear	Triangular pushover	0.793	0.789
Wall-frame	Bi-linear	Uniform pushover	**0.839**	0.877
Wall-frame	Takeda	Initial Stiffness	1.404	0.834
Wall-frame	Takeda	Triangular pushover	0.715	0.806
Wall-frame	Takeda	Uniform pushover	0.775	**0.933**
Wall-frame	Tri-linear	Triangular pushover	1.393	0.852
Wall-frame	Tri-linear	Uniform pushover	1.207	0.869
Irregular-frame	Bi-linear	Initial Stiffness	1.642	0.700
Irregular-frame	Bi-linear	Triangular pushover	0.855	0.869
Irregular-frame	Bi-linear	Uniform pushover	**0.925**	0.881
Irregular-frame	Takeda	Initial Stiffness	1.423	0.780
Irregular-frame	Takeda	Triangular pushover	0.771	0.862
Irregular-frame	Takeda	Uniform pushover	0.821	**0.936**
Irregular-frame	Tri-linear	Triangular pushover	1.583	0.887
Irregular-frame	Tri-linear	Uniform pushover	1.497	0.854
Regular-frame	Bi-linear	Initial Stiffness	1.665	0.764
Regular-frame	Bi-linear	Triangular pushover	**0.965**	0.876
Regular-frame	Bi-linear	Uniform pushover	0.869	0.886
Regular-frame	Takeda	Initial Stiffness	1.471	0.778
Regular-frame	Takeda	Triangular pushover	0.900	0.857
Regular-frame	Takeda	Uniform pushover	0.812	**0.949**
Regular-frame	Tri-linear	Triangular pushover	1.613	0.860
Regular-frame	Tri-linear	Uniform pushover	1.345	0.817

The tri-linear hysteretic rule provides the best correlations with the MDOF displacement at low response amplitudes because of the improved refinement of this model at small displacements. However, this model consistently under-estimates the MDOF response so a correction factor would be required for accurate predictions. At larger amplitudes the ability of the bi-linear and Takeda SDOF models to predict the MDOF response is broadly comparable with that of the SDOF systems with tri-linear hysteretic rules.

7.6.2 Peak inter-storey drift

In order to predict inter-storey drift from a SDOF model a transfer function is required that links the SDOF displacement to the required inter-storey drift. The transfer functions used in this analysis are taken directly from the pushover analysis

and are simply the relationship between the inter-storey drift and the displacement at the effective height of the structure during the pushover (Figure 7.10). The relationship is not linear as reported by Ghobarah (2004), but varies with the type of structure and the level of the loading. The ability of pushover analysis with uniform and triangular lateral force profiles to predict the inter-storey drift from drift at the effective height is quantified by calculating the mean and standard deviation of the difference (residual) between the predicted inter-storey drift from the time-history analysis and that predicted by the pushover analysis when given the drift at the effective height from the time-history analysis (Table 7.8). This shows that the transfer functions obtained from a pushover analysis using a triangular lateral force distribution are generally more reliable than those obtained from a pushover using a uniform force distribution. The notable exception to this is the first storey of the irregular frame, which is predicted more reliably with the uniform pushover. This is logical as the uniform force profile provides a better estimate of the non-linear displaced shape of this structure which has a soft first storey. The mean difference between the time-history results and the transfer function predictions is within 0.1% drift for all cases except the 9^{th}, 10^{th} and 11^{th} storey of the regular frame structure, which are within 0.15% drift. However, these results only show the validity of the transfer functions to relate drift at the effective height of the MDOF structure to inter-storey drift. To develop predictions of the MDOF inter-storey drift from SDOF systems the transfer functions must be used in conjunction with the drift predictions of the equivalent SDOF systems.

The ability to predict the inter-storey drift using the SDOF representation and transfer functions from pushover analysis rather than a MDOF time-history analysis is investigated by comparing the peak drift predictions from the two methods (Figure 7.11). As with the estimates of the peak drift at the effective height of the structure, the accuracy of the estimates are quantified by fitting a linear trend line through the estimations and calculating the coefficient of determination of the trend line (Tables 7.9 to 7.11). The drift predictions of the equivalent SDOF systems based on the initial period of the structure are generally less accurate than the estimates of the other SDOF representations as they under-predict the inter-storey drift and have a greater dispersion in the estimation. The Takeda hysteretic rule is more complex than the more commonly used bi-linear approximation and the increased complexity slightly

improves the accuracy of the prediction. Although the tri-linear hysteretic rule improves drift estimates for small displacements, the results of this study suggest that the additional complexity does not provide significant improvements over the other two SDOF representations for a full range of ground-motion amplitudes.

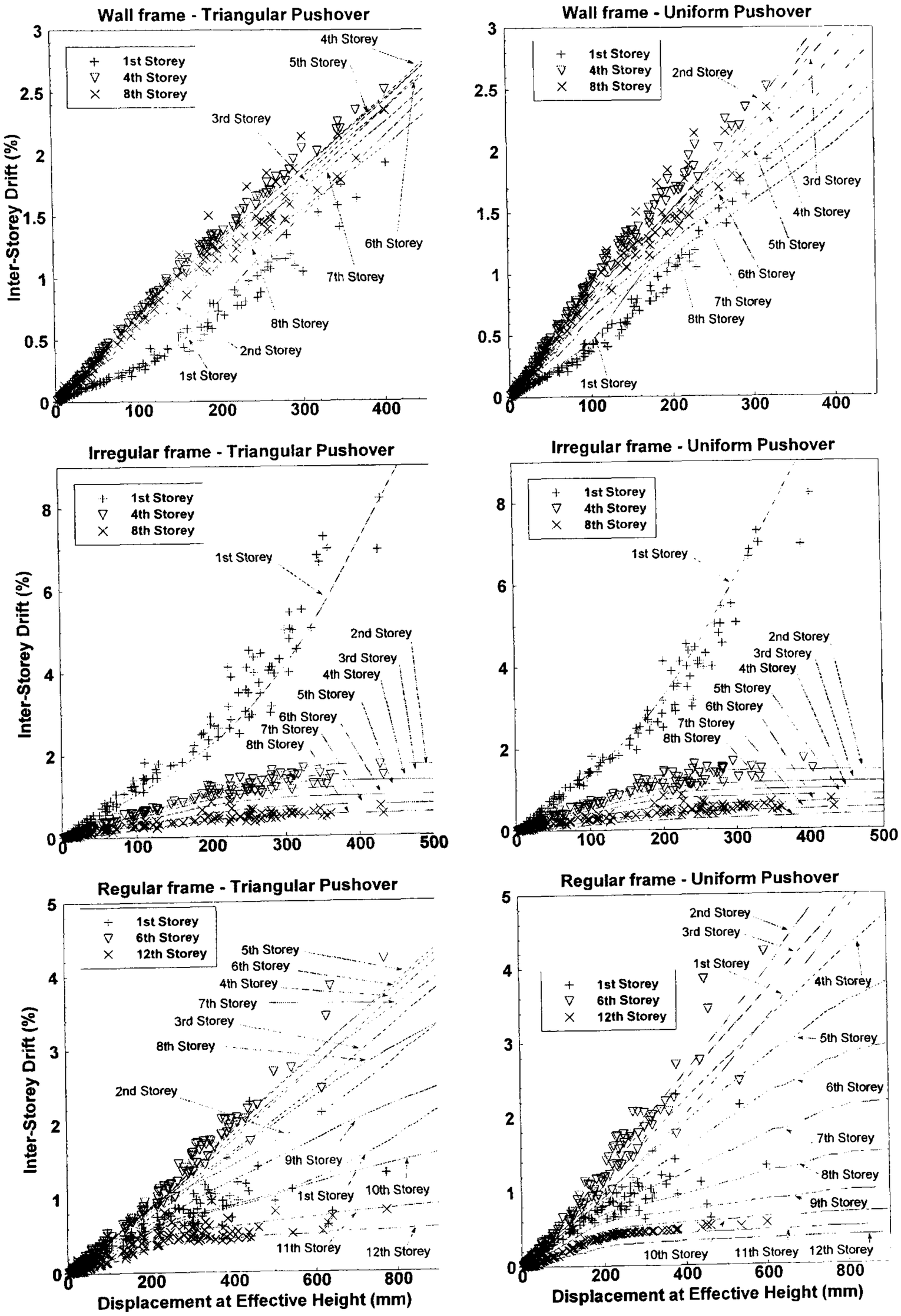


Figure 7.10. – Transfer functions relating drift at the effective height with inter-storey drift from pushover with triangular force distribution (*left*) and uniform force distribution (*right*). Solid lines show transfer functions from pushover analysis. Data points show results from time-history analysis.

Table 7.8. – Mean and standard deviation of the difference between actual inter-storey drift from MDOF time-history analysis and the transfer function relating inter-storey drift and displacement at the effective height obtained from pushover analysis. Best values given in bold.

Structure	Wall frame				Irregular frame				Regular frame			
Pushover profile:	Triangular		Uniform		Triangular		Uniform		Triangular		Uniform	
	Mean	StDev	Mean	StDev	Mean	StDev	Mean	StDev	Mean	StDev	Mean	StDev
1st Storey	**-0.035**	**0.098**	-0.095	0.137	0.253	0.408	**-0.145**	**0.391**	**0.059**	**0.191**	-0.176	0.327
2nd Storey	0.019	0.056	**-0.007**	**0.037**	**0.056**	**0.134**	0.092	0.199	**0.056**	**0.227**	-0.164	0.314
3rd Storey	**0.020**	**0.036**	0.032	0.039	**0.024**	**0.089**	0.126	0.160	**0.051**	0.152	-0.057	**0.143**
4th Storey	**0.026**	**0.035**	0.070	0.078	**0.051**	**0.104**	0.189	0.190	**0.060**	**0.099**	0.082	0.101
5th Storey	**0.045**	**0.068**	0.118	0.125	**0.069**	**0.110**	0.221	0.190	**0.056**	**0.094**	0.198	0.256
6th Storey	**0.064**	**0.090**	0.160	0.159	**0.084**	**0.110**	0.233	0.181	**0.057**	**0.124**	0.289	0.367
7th Storey	**0.079**	**0.107**	0.182	0.179	**0.083**	**0.107**	0.213	0.162	**0.076**	**0.178**	0.354	0.432
8th Storey	**0.091**	**0.112**	0.186	0.179	**0.061**	**0.080**	0.166	0.113	**0.093**	**0.219**	0.365	0.420
9th Storey	-	-	-	-	-	-	-	-	**0.133**	**0.225**	0.353	0.375
10th Storey	-	-	-	-	-	-	-	-	**0.145**	**0.194**	0.302	0.291
11th Storey	-	-	-	-	-	-	-	-	**0.125**	**0.147**	0.236	0.204
12th Storey	-	-	-	-	-	-	-	-	**0.079**	**0.094**	0.163	0.131

Table 7.9. – Gradient (Grad) and coefficient (R^2) of determination of linear trend line between SDOF predictions of inter-storey drift and drift obtained from MDOF time-history analysis for wall frame structure. Best values given in bold.

SDOF Hys. model	Initial Period based on:	1st Storey		2nd Storey		3rd Storey		4th Storey		5th Storey		6th Storey		7th Storey		8th Storey	
		Grad	R^2	Grad	R^2	Grad	R^2	Grad	R^2	Grad	R^2	Grad	R^2	Grad	R^2	Grad	R^2
Bi-linear	Initial	1.700	0.565	2.512	0.532	1.590	0.747	2.909	0.527	1.605	0.800	1.648	0.808	2.888	0.554	2.691	0.570
Bi-linear	Triangular	0.668	0.751	**0.991**	0.758	0.824	0.789	1.144	0.766	0.855	0.798	0.874	0.798	1.124	0.755	1.044	0.757
Bi-linear	Uniform	0.643	0.841	0.954	0.868	**0.889**	0.879	1.103	0.889	1.010	0.898	1.079	0.904	1.089	0.904	**1.013**	0.909
Takeda	Initial	1.416	0.702	2.071	0.653	1.417	0.832	2.372	0.619	1.433	0.867	1.467	0.872	2.341	0.626	2.184	0.648
Takeda	Triangular	0.577	0.780	0.849	0.763	0.746	0.807	0.975	0.746	0.780	0.803	0.796	0.795	0.950	0.706	0.883	0.710
Takeda	Uniform	0.577	**0.912**	0.851	**0.926**	0.826	**0.931**	**0.978**	**0.930**	**0.949**	**0.935**	**1.012**	**0.934**	**0.960**	**0.919**	0.893	**0.922**
Tri-linear	Triangular	1.361	0.712	1.962	0.615	1.415	0.856	2.236	0.559	1.426	0.872	1.455	0.868	2.194	0.545	2.044	0.561
Tri-linear	Uniform	**0.981**	0.765	1.433	0.722	1.256	0.883	1.645	0.702	1.406	0.927	1.499	0.930	1.625	0.715	1.514	0.729

Table 7.10. – Gradient (Grad) and coefficient (R^2) of determination of linear trend line between SDOF predictions of inter-storey drift and drift obtained from MDOF time-history analysis for irregular frame structure. Best values given in bold.

SDOF Hys. model	Initial Period based on:	1st Storey		2nd Storey		3rd Storey		4th Storey		5th Storey		6th Storey		7th Storey		8th Storey	
		Grad	R^2	Grad	R^2	Grad	R^2	Grad	R^2	Grad	R^2	Grad	R^2	Grad	R^2	Grad	R^2
Bi-linear	Initial	2.182	0.520	1.633	0.762	1.495	0.806	1.536	0.836	1.568	0.843	1.629	0.824	1.693	0.783	1.706	0.716
Bi-linear	Triangular	**0.927**	0.873	0.925	0.819	0.895	0.833	**0.934**	0.824	**0.962**	0.820	**1.000**	0.817	1.028	0.795	**1.003**	0.772
Bi-linear	Uniform	0.884	0.842	1.023	0.805	**1.097**	0.826	1.234	0.821	1.351	0.832	1.499	0.840	1.666	0.818	1.807	0.791
Takeda	Initial	1.830	0.679	1.422	0.783	1.321	0.809	1.364	0.832	1.394	0.834	1.447	0.819	1.496	0.774	1.486	0.697
Takeda	Triangular	0.739	0.829	0.895	0.799	0.877	0.823	0.919	0.814	0.948	0.811	0.986	0.811	**1.011**	0.793	0.983	0.773
Takeda	Uniform	0.723	**0.933**	**1.006**	0.798	1.085	0.826	1.223	0.821	1.337	0.833	1.477	**0.844**	1.629	**0.823**	1.739	**0.792**
Tri-linear	Triangular	2.105	0.817	1.563	0.860	1.431	0.855	1.465	0.843	1.486	0.815	1.531	0.764	1.576	0.693	1.558	0.576
Tri-linear	Uniform	1.588	0.737	1.492	**0.891**	1.539	**0.910**	1.716	**0.905**	1.880	**0.877**	2.099	0.827	2.332	0.767	2.523	0.669

Table 7.11. – Gradient (Grad) and coefficient (R^2) of determination of linear trend line between SDOF predictions of inter-storey drift and drift obtained from MDOF time-history analysis for regular frame structure. Best values given in bold.

SDOF Hys. model	Initial Period based on:	1st Storey		2nd Storey		3rd Storey		4th Storey		5th Storey		6th Storey		7th Storey		8th Storey	
		Grad	R^2	Grad	R^2	Grad	R^2	Grad	R^2	Grad	R^2	Grad	R^2	Grad	R^2	Grad	R^2
Bi-linear	Initial	1.618	0.600	1.596	0.629	1.763	0.711	1.919	0.752	1.846	0.746	1.884	0.765	1.832	0.778	1.923	0.784
Bi-linear	Triangular	1.060	0.736	**1.016**	0.782	1.117	0.840	1.206	0.839	**1.029**	0.860	**1.028**	0.859	0.994	0.853	1.064	0.826
Bi-linear	Uniform	0.570	0.559	0.664	0.696	0.741	0.821	0.810	0.878	1.154	0.895	1.355	0.893	1.314	0.896	1.698	0.819
Takeda	Initial	1.461	0.530	1.430	0.573	1.597	0.703	1.752	0.777	1.610	0.773	1.639	0.806	1.596	0.826	1.693	0.826
Takeda	Triangular	**1.018**	**0.761**	0.967	**0.799**	**1.062**	0.852	**1.145**	0.845	0.951	0.835	0.948	0.825	**0.915**	0.810	**0.986**	0.778
Takeda	Uniform	0.519	0.602	0.616	0.754	0.688	**0.886**	0.752	**0.938**	1.083	**0.946**	1.280	**0.929**	1.237	**0.920**	1.647	0.838
Tri-linear	Triangular	1.609	0.624	1.576	0.678	1.764	0.819	1.933	0.882	1.770	0.862	1.784	0.857	1.720	0.834	1.798	0.776
Tri-linear	Uniform	0.886	0.375	1.016	0.519	1.149	0.702	1.271	0.810	1.784	0.887	2.047	0.914	1.985	0.916	2.407	**0.862**

SDOF Hys. model	Initial Period based on:	9th Storey		10th Storey		11th Storey		12th Storey	
		Grad	R^2	Grad	R^2	Grad	R^2	Grad	R^2
Bi-linear	Initial	1.543	0.809	1.245	0.808	**0.925**	**0.779**	**0.647**	0.739
Bi-linear	Triangular	0.948	0.798	0.763	0.786	0.569	0.775	0.399	**0.750**
Bi-linear	Uniform	0.641	**0.869**	0.513	0.829	0.379	0.774	0.264	0.712
Takeda	Initial	1.415	0.854	**1.136**	**0.833**	0.837	0.765	0.581	0.685
Takeda	Triangular	0.892	0.763	0.718	0.751	0.536	0.738	0.375	0.709
Takeda	Uniform	0.586	0.856	0.467	0.807	0.345	0.741	0.240	0.668
Tri-linear	Triangular	1.497	0.776	1.194	0.720	0.882	0.659	0.613	0.584
Tri-linear	Uniform	**1.004**	0.792	0.798	0.722	0.585	0.618	0.403	0.511

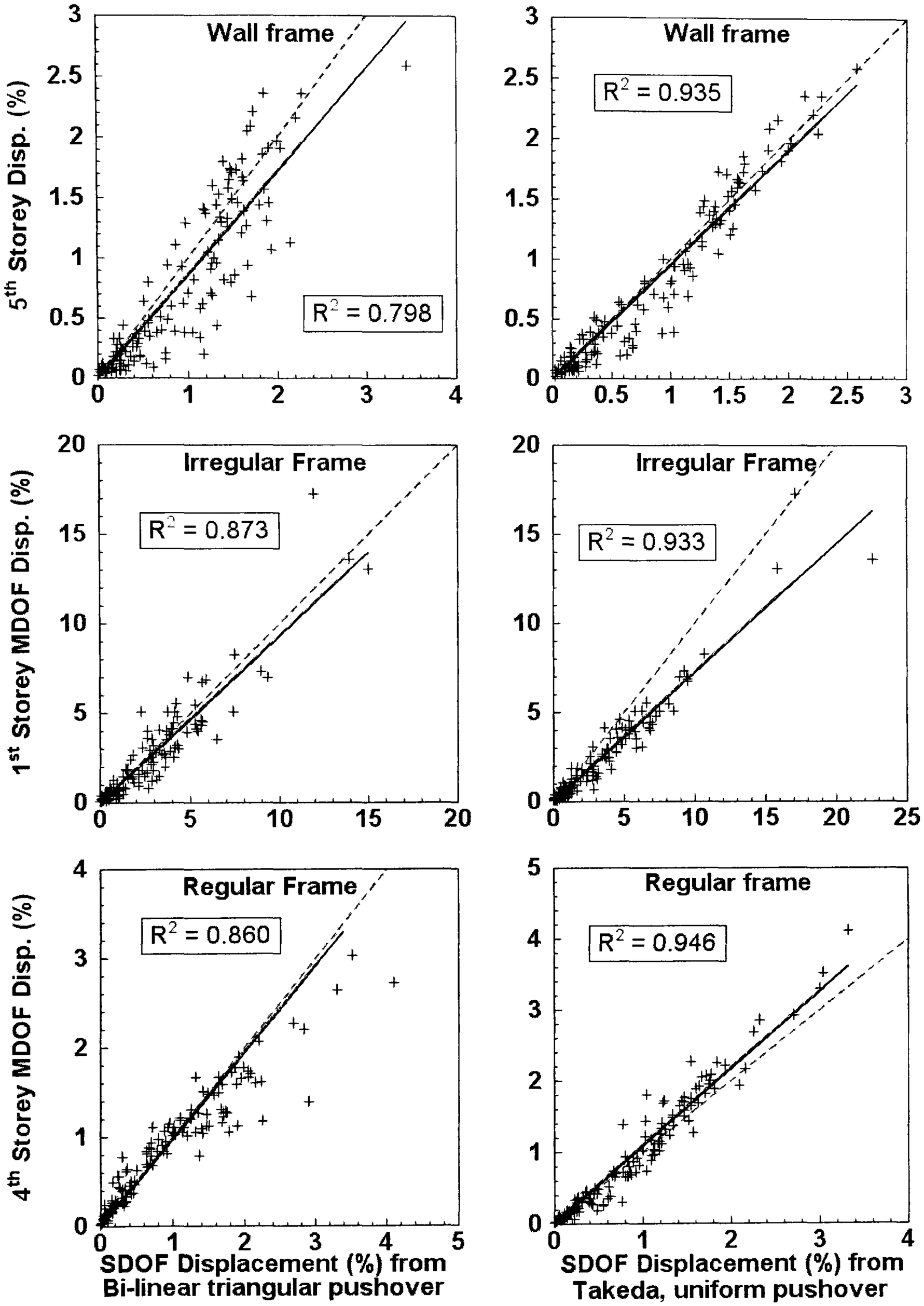


Figure 7.11. – Ability of different bi-linear and Takeda equivalent SDOF models to predict MDOF inter-storey drift for critical storeys of different frame structures. Trend line shown by solid line; ideal 1:1 target shown by dashed line.

Equivalent SDOF systems developed from pushover analysis using a uniform and triangular lateral force profile have generally similar ability to predict MDOF response. However, the 8-storey wall frame and irregular frame appear to be slightly better approximated with the equivalent SDOF systems developed using a uniform lateral force pushover and the 12-storey regular frame is slightly better correlated by the SDOF systems developed using a tri-angular pushover. All SDOF estimations overestimate the inter-storey drift of the upper storeys of the 12-storey regular frame.

7.6.3 Displacement time-series

A number of ground motions and structural responses are used to investigate the ability of SDOF systems to represent the displacement time-series of a MDOF structure. The SDOF-MDOF pair with the smallest bias (as measured by the gradient of the trend line) is the bi-linear SDOF model with back-bone curve developed using triangular pushover. This is capable of estimating the response of the 12-storey regular frame with less than 5% difference in the average peak displacement (Table 7.7). Further investigation of the displacement time-series from this structure and SDOF reveals that the ground motions with a good match in the SDOF-MDOF peak response are in one of the following groups:

1. Impulsive with peak responses that influence a wide range of periods over a relatively short time.
2. Have a peak response early in the time-series.
3. "Fortuitous" in that the peak response of the SDOF and MDOF occur at different times in the ground-motion but have similar amplitude by chance.

Examples of the first two types are shown in Figure 7.12. Although there is a logical explanation as to why the SDOF and MDOF have similar responses, chance still plays an important role as it is not possible to predict in advance that these ground motions would have a similar MDOF and SDOF response. An example of a ground motion that has a SDOF and MDOF response with similar amplitudes largely by chance is shown in Figure 7.13; although the amplitude of the peak response of the SDOF is within half a percent of the MDOF displacement the time of the peak response of the SDOF is 5 seconds earlier than the peak response of the MDOF system.

The displacement time-series for the SDOF models using the Takeda and tri-linear hysteretic behaviours are also shown on the Figures 7.12 and 7.13. The tri-linear hysteretic model gives consistently smaller response than the other models, while the Takeda and bi-linear models are not consistently larger or smaller than each other. While a good estimation of the largest displacement cycle is achieved, the amplitude of the secondary cycles is less well predicted, particularly for the ground-motions with longer durations, which are strongly influenced by the way in which energy is dissipated by hysteresis.

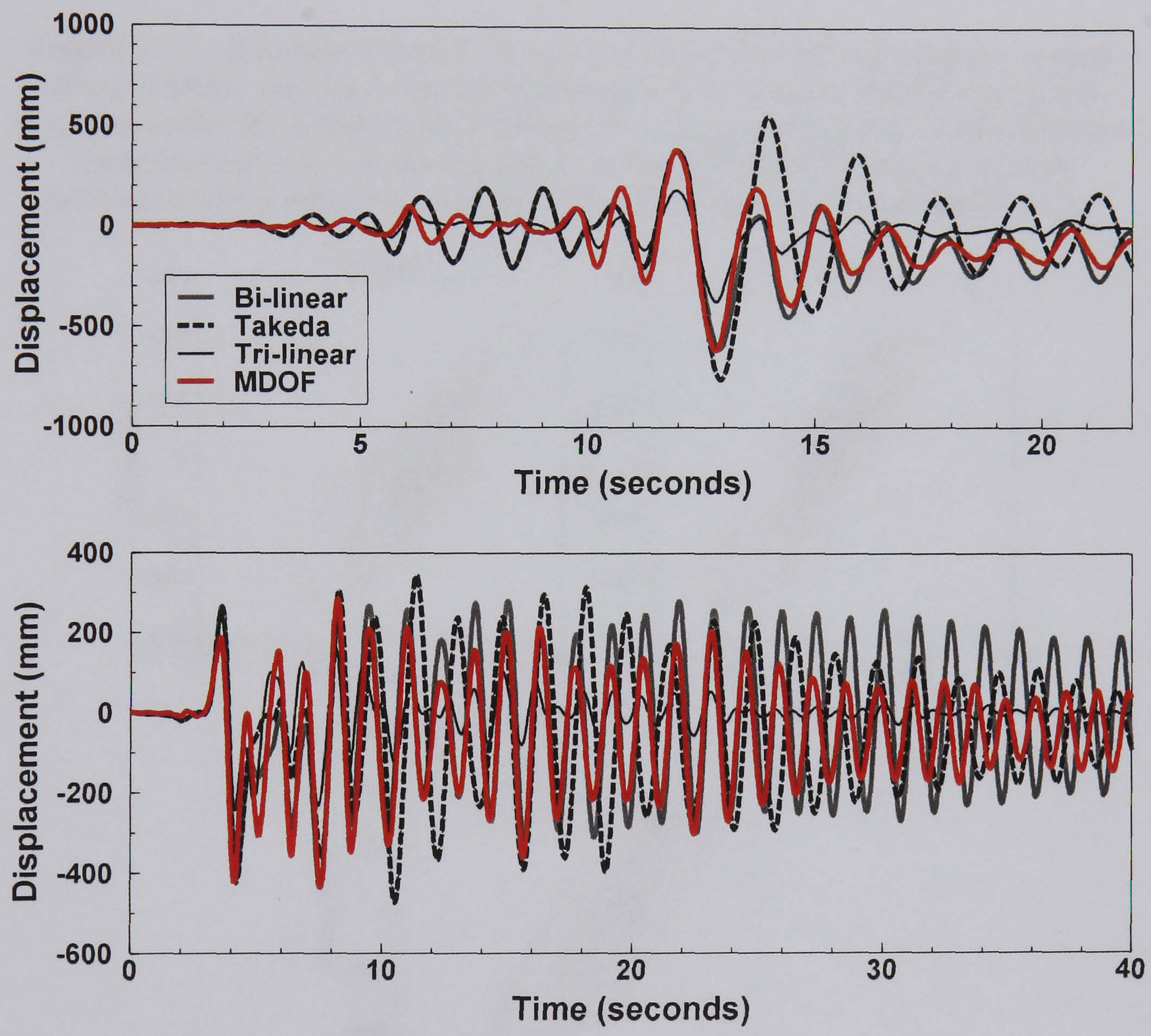


Figure 7.12. – Examples of cases where the bi-linear SDOF response has a good match with the regular frame MDOF response at the effective height of the structure. MODF and SDOF response under the action of the 1987 M_W 6.5 Superstition Hills earthquake recorded 1km from the fault rupture on stiff soil at parachute test site (*upper*) and the 1994 M_W 6.7 Northridge earthquake recorded 5.3km from the fault rupture on stiff soil at Sylmar Converter Station (*lower*). All SDOF hysteretic models developed using pushover analysis with triangular lateral load distribution.

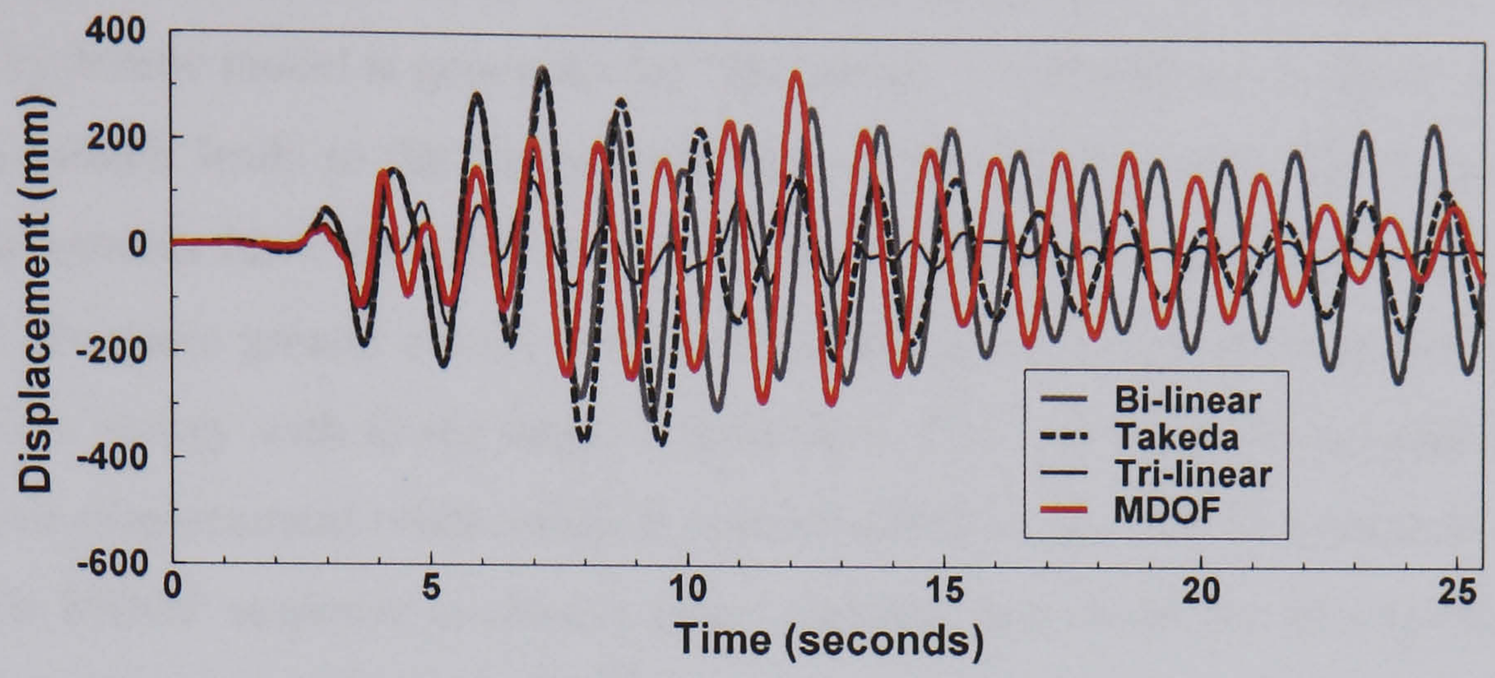


Figure 7.13. - Example of cases where the bi-linear SDOF response has a good match with the regular frame MDOF response by chance. MODF and SDOF response under the action of the 1999 M_W 7.1 Duzce earthquake recorded 6.5km from the fault rupture on stiff soil at Duzce. All SDOF hysteretic models developed using pushover analysis with triangular lateral load distribution.

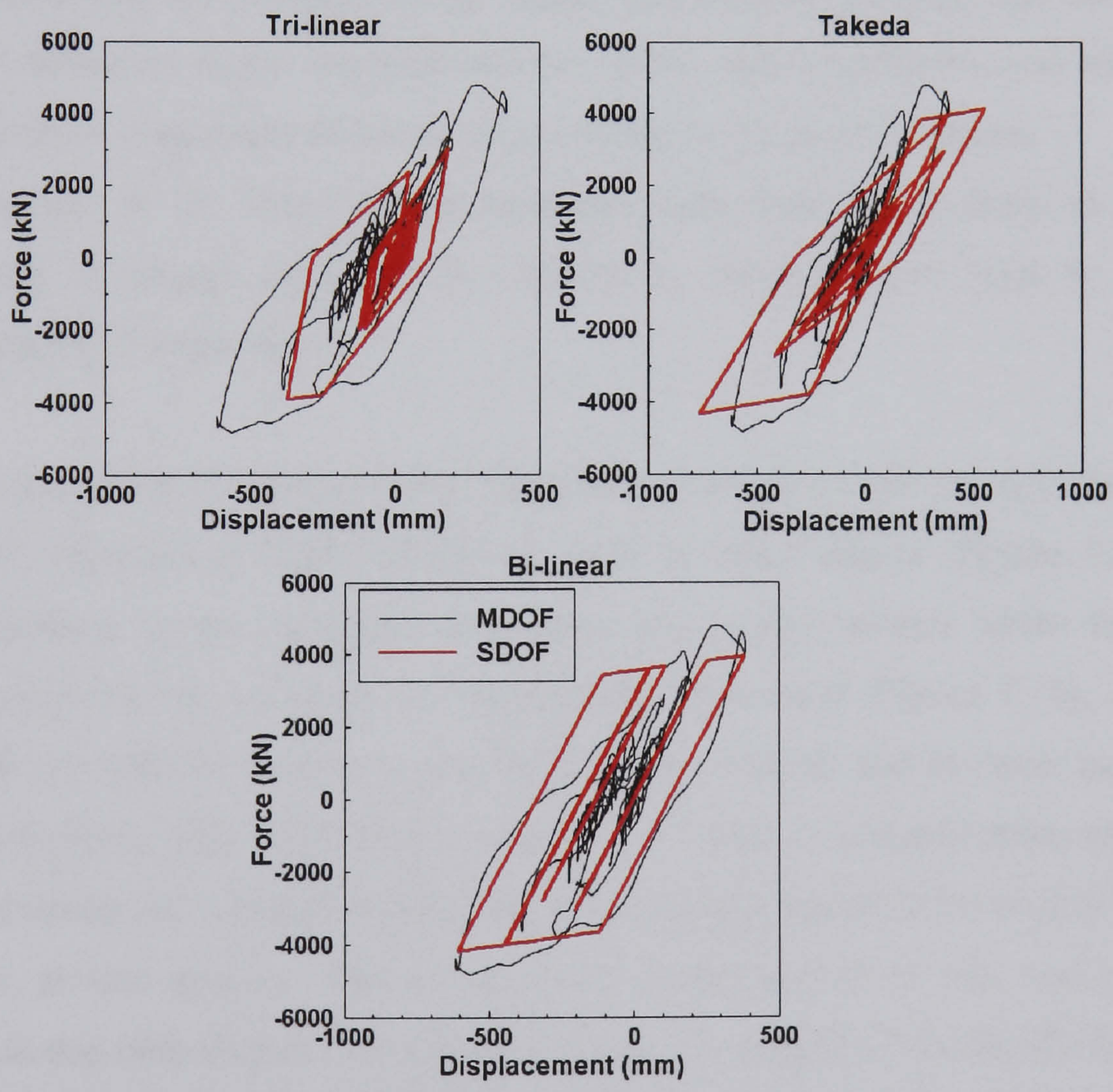


Figure 7.14. – Force-displacement characteristics of Takeda, bi-linear and tri-linear hysteretic models compared to the regular frame MDOF response at the effective height of the structure under the action of the 1987 M_W 6.5 Superstition Hills earthquake recorded 1km from the fault rupture on stiff soil at Parachute Test Site.

The shape of the hysteretic model plays an important role in the response. The tri-linear hysteretic model is generally too "fat" at low amplitudes so dissipates too much energy, which leads to the under-prediction of the displacement. The bi-linear and Takeda models have the same behaviour up to first yield, after which the Takeda model dissipates greater energy with lower amplitude cycles and the bi-linear model dissipates energy with fewer larger amplitude cycles. Although the general shape of the force-displacement relationship is approximated by the SDOF hysteretic models, the true MDOF response is always more complex and could not be expected to be described by a simple hysteretic model.

Examination of the MDOF responses which are poorly estimated by the SDOF approximation reveals that the poor estimation is from to two main factors:

1. Differences in the stiffness of the SDOF and MDOF systems; this can cause a phase difference in the response and the SDOF, and in addition cause the MDOF structures to respond to different period waves in the ground motion.
2. Differences in the shape of the hysteretic behaviour, which leads to different amounts of energy dissipated by hysteresis, which in turn leads to different amplitudes of response.

The response of the 12-storey regular frame structure to the 1989 M_W 6.9 Loma Prieta earthquake recorded at LGPC illustrates both of these effects (Figure 7.15). The MDOF stiffness varies constantly throughout the ground motion whilst the SDOF systems prescribe the set shape of the hysteretic behaviour (Figure 7.16). Although the SDOF and MDOF responses start in phase the Takeda and bi-linear models are 180° out of phase, with the MDOF response by 17 and 21 seconds respectively. The MDOF structure has a peak displacement at 10 seconds, probably because of the large amplitude ground motions that occur at the initial period of the structure (0.77 seconds) at this time (Figure 7.17). However, the bi-linear and Takeda SDOF systems have initial periods based on the cracked stiffness (1.35s) and have a peak response of opposite sign to the MDOF response at the slightly later time of 11 seconds. The tri-linear system has the same initial period as the uncracked MDOF but has too fat hysteresis loops at low amplitudes, which increase hysteretic damping and lead to an under-estimation of the response. The importance of the hysteretic shape and the appropriate dissipation of hysteretic energy are further demonstrated by the bi-linear

model, which does not dissipate sufficient energy after 12 seconds and as a consequence has secondary displacement cycles that are too large.

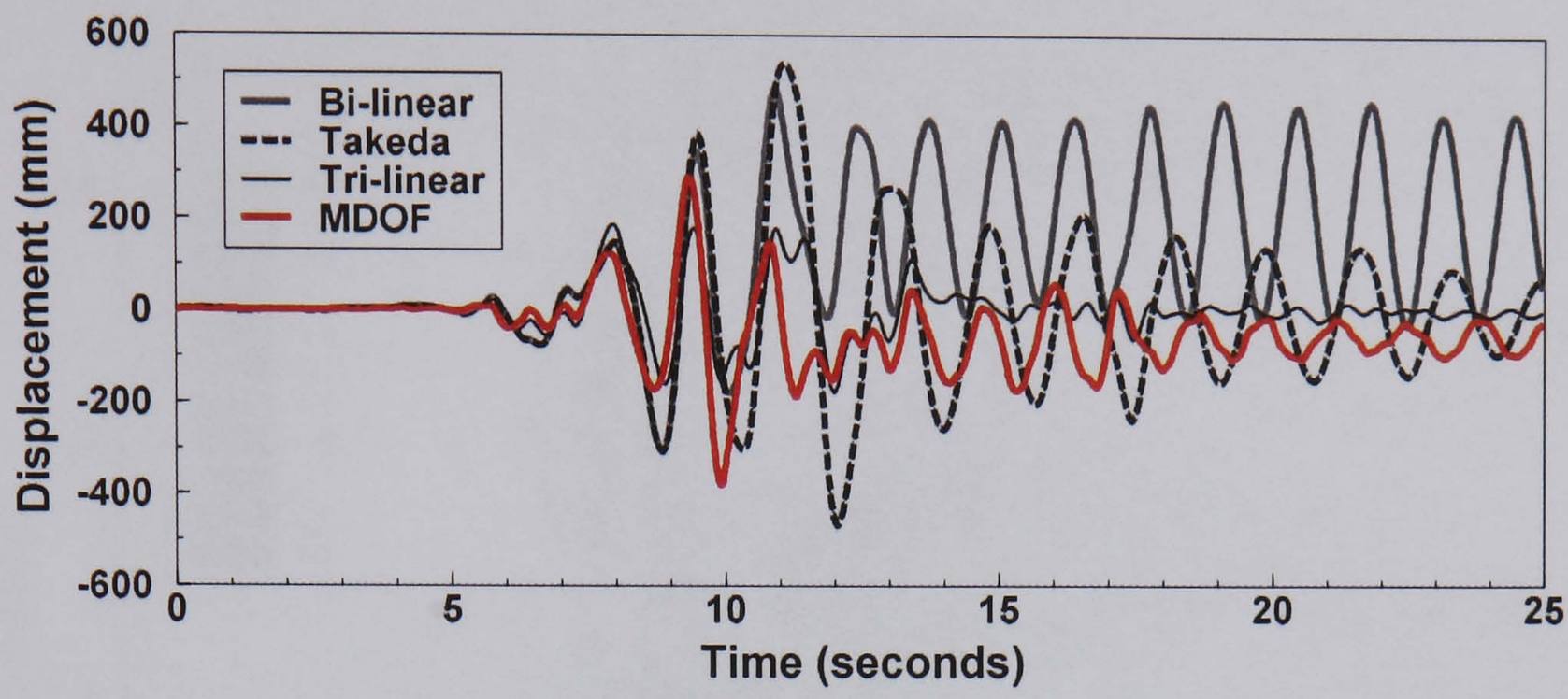


Figure 7.15. – MODF and SDOF response under the action of the 1989 M_W 6.9 Loma Prieta earthquake recorded 3.8km from the fault rupture on stiff soil at LGPC. MDOF response at the effective height of the 12-storey regular frame. SDOF hysteretic curves derived using triangular pushover.

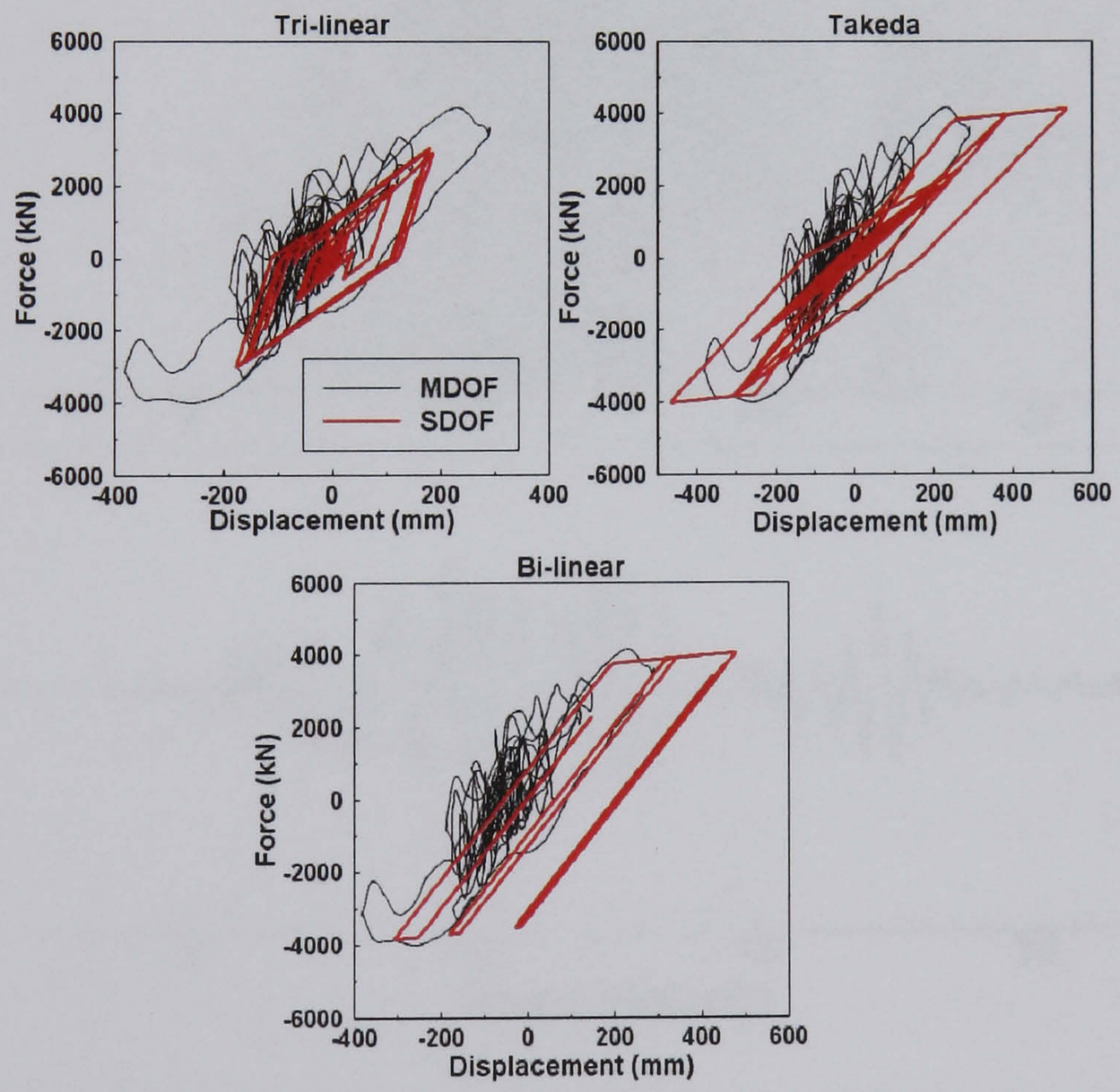


Figure 7.16. – Force-displacement characteristics of Takeda, bi-linear and tri-linear hysteretic models compared to the regular frame MDOF response at the effective height of the structure under the action of the 1989 M_W 6.9 Loma Prieta earthquake recorded 3.8km from the fault rupture on stiff soil at LGPC.

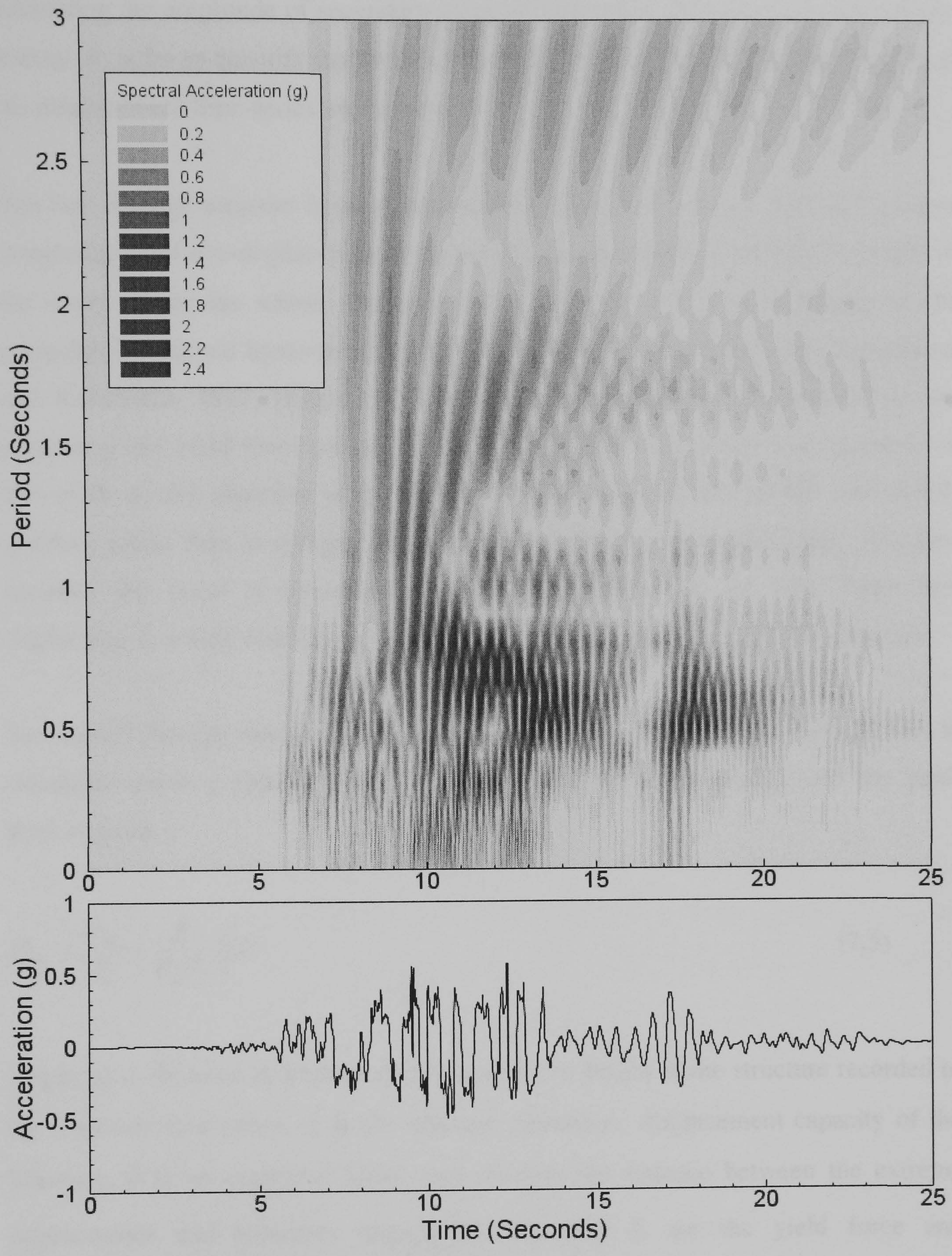


Figure 7.17. – 3D elastic response spectra of the 1989 M_W 6.9 Loma Prieta earthquake recorded 3.8km from the fault rupture on stiff soil at LGPC.

7.6.4 Global damage measures dependent on time-series

The previous section demonstrated that although SDOF systems may be able to estimate the peak displacement of the MDOF structure they are less well suited to

estimating the amplitude of secondary displacement peaks or the absorbed hysteretic energy. In order to quantify this further, three global damage measures that depend on the displacement time-series are employed.

The first damage measure is the global absorbed hysteretic energy. This is found by integrating the force-displacement hysteresis loop described at the effective height of the structure for the whole time-series (e.g. Figure 7.16). This is similar to the normalized absorbed hysteretic energy used by several researchers (e.g. Seneviratna and Krawinkler 1997; Nassar and Krawinkler 1991) which is normalized by the product of the yield force and yield displacement. No normalization is required for this work as the objective is to compare the response of the MDOF and SDOF systems, rather than to compare the response of different structural types. This also removes the issue of determining appropriate values for the yield force and displacement, which would require a number of assumptions for a MDOF structure.

The second damage measure is the global Park and Ang damage index (D_{pa}). This is calculated from a combination of the absorbed hysteretic energy and the peak displacement:

$$D_{pa} = \frac{\delta_M}{\delta_u} + \frac{\beta}{F_y \delta_y} \int de \tag{7.5}$$

where δ_M is the peak displacement at the effective height of the structure recorded in the response time-series, δ_u is the ultimate monotonic displacement capacity of the structure, β is an empirical factor that changes the balance between the extreme displacement and hysteretic energy $\int de$; F_y and δ_y are the yield force and displacement respectively. As there is no clearly defined yield force or displacement for a MDOF, these values are taken from the properties derived for the SDOF systems (Table 7.3 to Table 7.6). The ultimate monotonic displacement is taken as the yield displacement of the SDOF system multiplied by the design ductility (2.625 for the wall-frame structure, 3.0 for the irregular frame and 3.75 for the regular frame structures). β is set to 0.15 as recommended as a median value by Cosenza and Manfredi (1998)

The third damage measure is the global displacement fatigue. This is calculated by counting the displacement cycles at the effective height of the structure using rainflow cycle counting (see section 2.4.3). The irregular amplitude cycles are converted into a damage measure using Miner's linear damage summation (Miner 1945):

$$Damage = \sum_{i=1}^{i=n} \frac{1}{a} S_i^k \tag{7.6}$$

where a and k are the fatigue constant and exponent respectively, S_i is the amplitude of the i^{th} cycle and n is the total number of displacement cycles. The fatigue damage is calculated for k=2.0 and k=3.86 to show the influence of different fatigue exponents. A fatigue exponent of 2.0 is a commonly used exponent in general studies (e.g. Krawinkler 1987; Jeong and Iwan 1988; Malhotra 2002). A fatigue exponent of 3.86 is derived from the experimental test results of Yamada (1992) for reinforced concrete columns with an axial load of 1/3 the ultimate axial strength. The fatigue constant a is set so that the damage parameter is equal to unity at the ultimate monotonic displacement, which is taken as the yield displacement of the SDOF system multiplied by the design ductility. As the fatigue constant a linearly scales the damage function by equal amounts for the SDOF and MDOF systems it has no influence on the correlation of the damage parameters of the two systems.

The ability of the SDOF systems to predict the MDOF response is again measured by plotting the SDOF response vs. the MDOF response and employing trend lines to highlight consistent differences in response. An example of this is shown for each of the damage measures in Figure 7.18. The scatter in the predictions is measured by the coefficient of determination of the trend lines (Tables 7.12 to 7.14). This shows that it is possible to predict the global absorbed hysteretic energy and Park and Ang damage index with comparable accuracy as the peak drift (Table 7.7). However, the global fatigue damage requires an accurate determination of the displacement time-series so it cannot be estimated with any reliability with SDOF systems.

Table 7.12. – Gradient (Grad) and coefficient (R^2) of determination of linear trend line between SDOF predictions of absorbed hysteretic energy, global Park and Ang damage, Global Fatigue with exponents 2.0 and 3.86 and values obtained from MDOF time-history analysis for wall frame structure. Best values given in bold.

		Hysteretic Energy		Park & Ang		Fatigue, Exponent 2.0		Fatigue, Exponent 3.86	
SDOF Hys. model	Initial Period based on:	Grad	R^2	Grad	R^2	Grad	R^2	Grad	R^2
Bi-linear	Initial	1.267	0.453	0.638	0.710	0.064	0.224	0.058	0.049
Bi-linear	Triangular	1.203	0.689	**0.990**	0.759	0.172	0.071	0.170	0.090
Bi-linear	Uniform	0.889	0.745	0.978	0.871	0.173	0.247	0.209	0.178
Takeda	Initial	1.229	0.750	0.562	0.834	0.084	0.291	0.078	0.395
Takeda	Triangular	0.900	0.672	0.870	0.795	0.224	0.171	0.193	**0.593**
Takeda	Uniform	0.876	**0.949**	0.904	**0.939**	0.147	0.166	0.185	0.358
Tri-linear	Triangular	1.312	0.874	1.581	0.884	4.362	**0.737**	5.276	0.458
Tri-linear	Uniform	**0.969**	0.711	1.312	0.856	**2.440**	0.650	**3.046**	0.339

Table 7.13. – Gradient (Grad) and coefficient (R^2) of determination of linear trend line between SDOF predictions of absorbed hysteretic energy, global Park and Ang damage, Global Fatigue with exponents 2.0 and 3.86 and values obtained from MDOF time-history analysis for irregular frame structure. Best values given in bold.

		Hysteric Energy		Park & Ang		Fatigue, Exponent 2.0		Fatigue, Exponent 3.86	
SDOF Hys. model	Initial Period based on:	Grad	R^2	Grad	R^2	Grad	R^2	Grad	R^2
Bi-linear	Initial	1.102	0.451	0.609	0.664	0.107	0.053	0.085	0.117
Bi-linear	Triangular	**1.031**	0.820	**1.019**	0.879	0.228	0.380	0.198	0.358
Bi-linear	Uniform	1.173	0.889	1.109	0.894	0.224	0.257	**0.245**	0.274
Takeda	Initial	1.063	0.747	0.533	0.790	0.149	0.036	0.054	0.648
Takeda	Triangular	0.866	0.735	0.907	0.861	0.184	0.240	0.080	0.508
Takeda	Uniform	0.919	0.875	0.963	**0.945**	**0.260**	0.349	0.168	**0.703**
Tri-linear	Triangular	1.294	**0.918**	1.713	0.916	5.058	0.570	5.858	0.643
Tri-linear	Uniform	1.230	0.826	1.625	0.871	4.438	**0.676**	4.721	0.344

Table 7.14. – Gradient (Grad) and coefficient (R^2) of determination of linear trend line between SDOF predictions of absorbed hysteretic energy, global Park and Ang damage, Global Fatigue with exponents 2.0 and 3.86 and values obtained from MDOF time-history analysis for regular frame structure. Best values given in bold.

		Hysteric Energy		Park & Ang		Fatigue, Exponent 2.0		Fatigue, Exponent 3.86	
SDOF Hys. model	Initial Period based on:	Grad	R^2	Grad	R^2	Grad	R^2	Grad	R^2
Bi-linear	Initial	1.482	0.534	0.621	0.755	0.203	0.302	0.198	0.450
Bi-linear	Triangular	1.578	0.823	1.224	0.865	0.376	0.319	**0.411**	0.327
Bi-linear	Uniform	**1.009**	0.772	**1.015**	0.889	0.306	0.384	0.281	0.377
Takeda	Initial	1.449	0.783	0.552	0.817	0.255	0.273	0.050	**0.695**
Takeda	Triangular	1.366	0.660	1.123	0.820	0.340	0.236	0.293	0.511
Takeda	Uniform	0.925	0.891	0.933	**0.939**	**0.385**	**0.624**	0.191	0.761
Tri-linear	Triangular	1.663	**0.917**	1.845	0.916	5.492	0.260	6.094	0.641
Tri-linear	Uniform	1.135	0.856	1.454	0.881	3.489	0.295	2.745	0.467

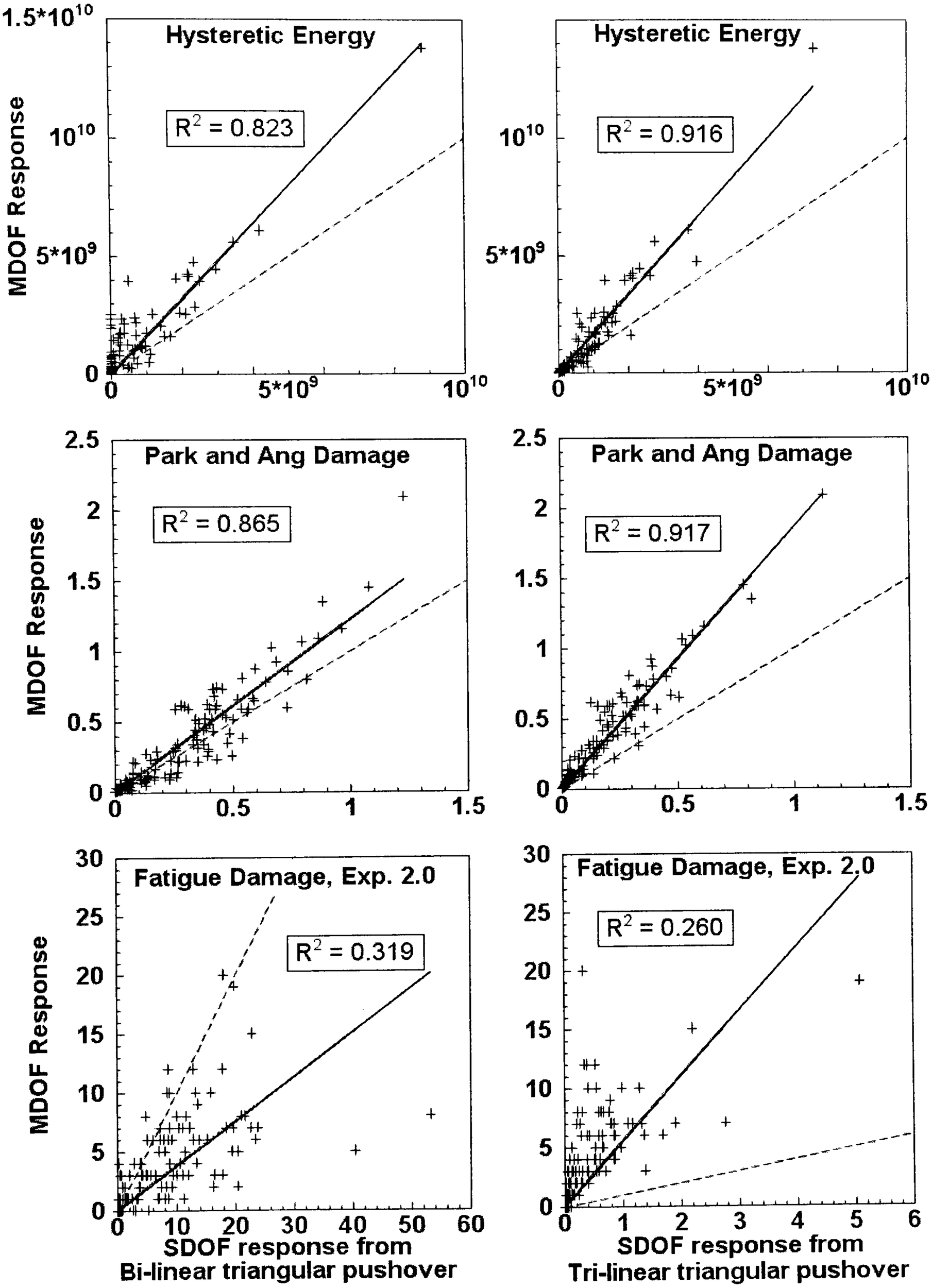


Figure 7.18. - Ability of bi-linear and tri-linear equivalent SDOF models to predict regular frame MDOF response at the effective height of the structure. Trend line shown by solid line; ideal 1:1 target shown by dashed line.

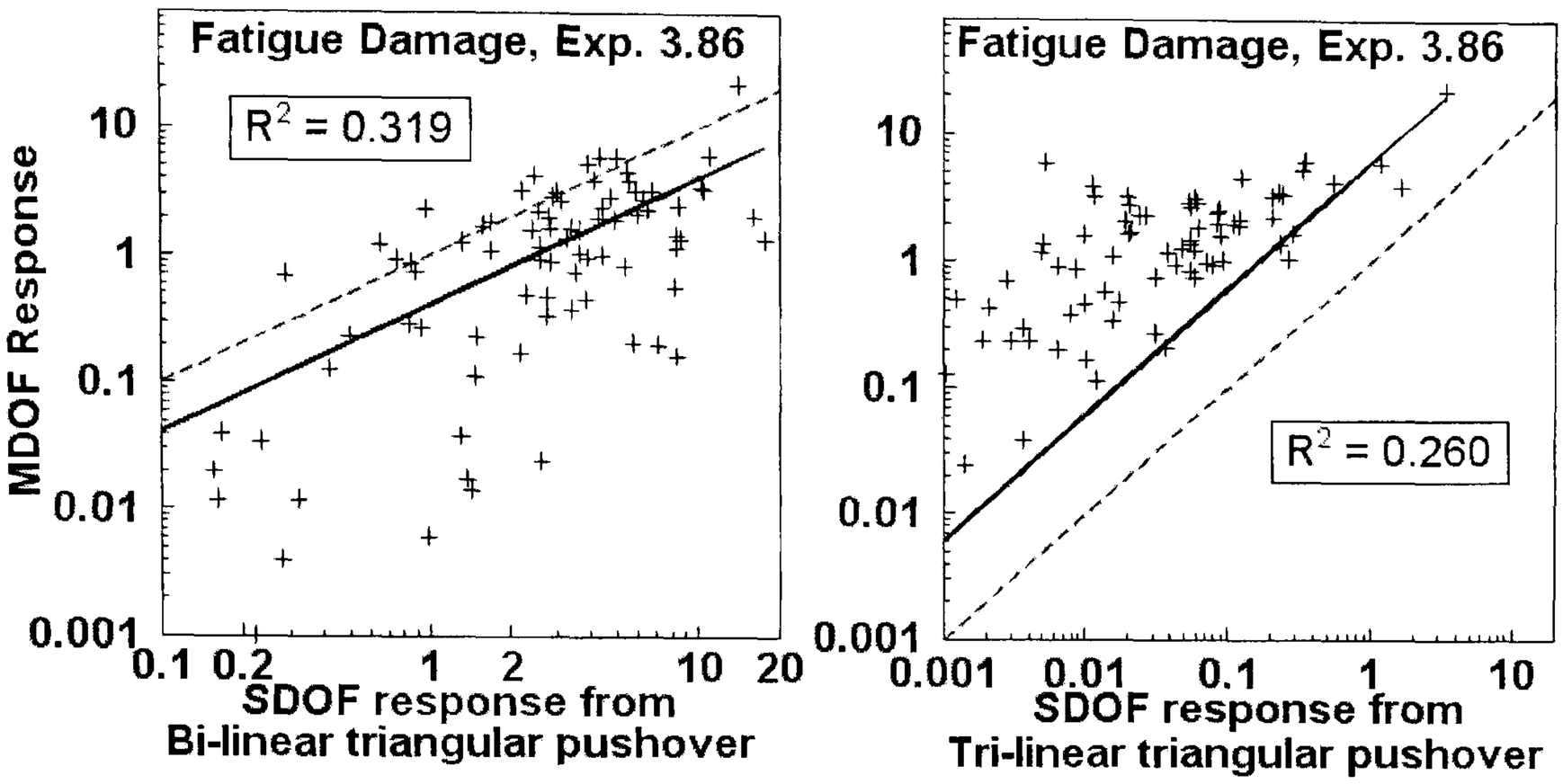


Figure 7.18 (continued) - Ability of bi-linear and tri-linear equivalent SDOF models to predict regular frame MDOF response at the effective height of the structure. Trend line shown by solid line; ideal 1:1 target shown by dashed line.

In contrast to damage measures based on the peak response, there is no consistent difference between the hysteretic energy estimated by SDOF systems based on the initial period of the structure and those based on a cracked period for the structure. This suggests that while the *total* SDOF hysteretic energy is fairly consistently predicted by SDOF systems, this energy can be accumulated in different ways. For example, the tri-linear hysteretic model accumulates energy in multiple "fat" hysteretic loops with small displacements, while the bi-linear model dissipates energy with fewer cycles of larger amplitude.

Another striking difference is that the bi-linear and Takeda models based on the initial period consistently under-predict the MDOF peak response, but consistently over-predict the MDOF global fatigue. The reason for this apparently contradictory finding is the influence of the secondary peaks on the fatigue damage. The SDOF systems based on the initial period may have lower peak response, but their shorter period leads to a greater number of secondary cycles (Figure 7.19).

Both the Takeda and bi-linear models developed with a pushover analysis with a lateral load profile consistently have good correlations (high R^2) and low bias (trend line gradient close to unity) with the MDOF response. Of the two, the Takeda model

is more accurate but the simplicity of the bi-linear model makes it more attractive for generic use and parameterization.

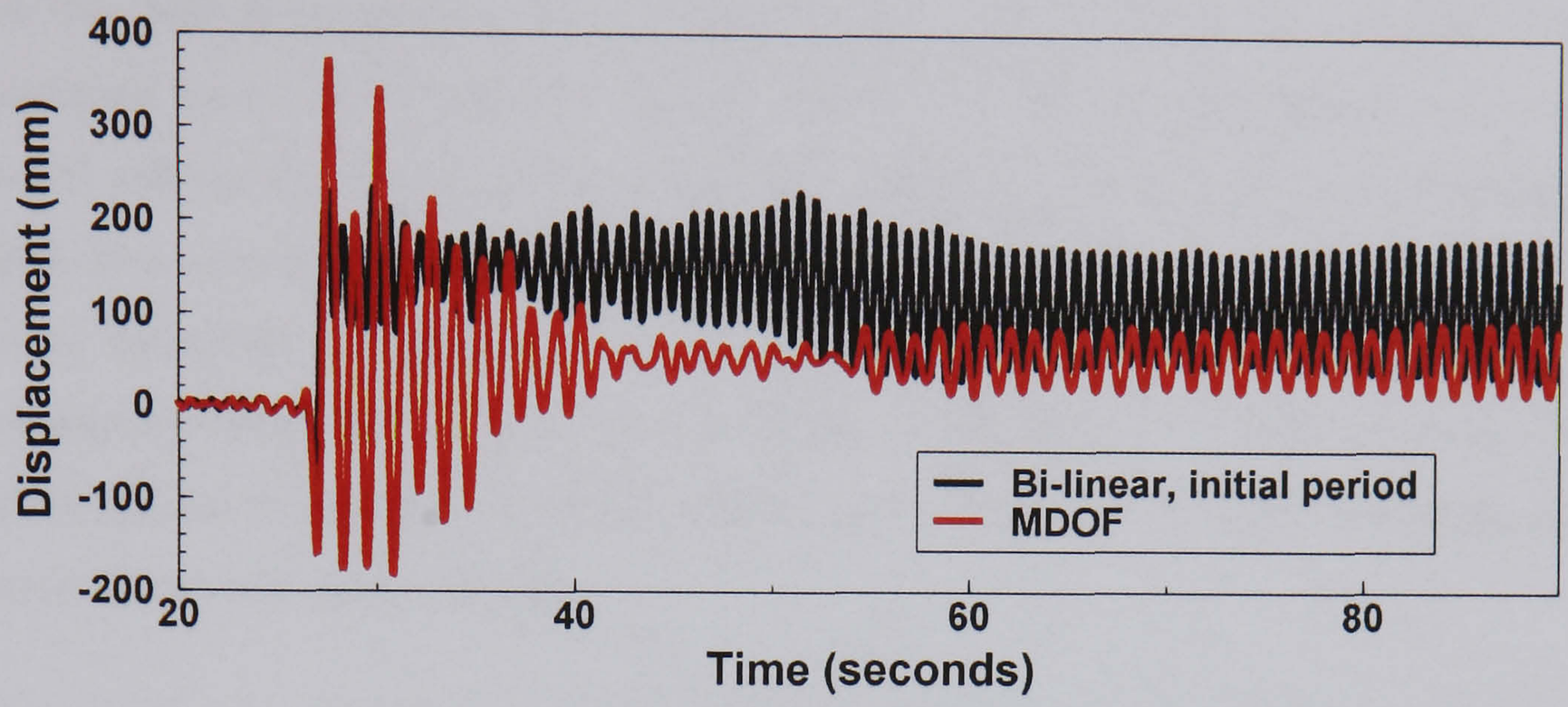


Figure 7.19. – Comparison of displacement time-series of regular frame MDOF and bi-linear SDOF representation based on the initial period of the structure, under the action of the 2002 M_W 7.9 Denali recorded on stiff soil 2.78km from the fault rupture at TAPS pump station #10.

7.7 Summary and Further Work

One of the most important factors that influence the ability of the SDOF system to estimate the MDOF structure is the initial period of the SDOF system. The use of an uncracked stiffness for the SDOF approximation, even as part of a tri-linear hysteretic model, causes the under-estimation of the peak response. However, the amplitude of the secondary peaks from these systems is consistently greater than those from the MDOF system which leads to an over-estimation of the global fatigue damage. The use of SDOF systems with initial periods that approximate the cracked period generally provides better predictions of MDOF response than those based on the initial period, although these predictions can over-estimate the peak MDOF response.

The shape of the hysteretic model plays an important role in the SDOF response. The tri-linear hysteretic model is generally too fat at low amplitudes and so dissipates too much energy, which leads to the under-prediction of the displacement. The bi-linear and Takeda models have the same behaviour up to first yield, after which the Takeda model dissipates greater energy with lower amplitude cycles, and the bi-linear model

dissipates energy with fewer larger amplitude cycles. Although the general shape of the force-displacement relationship is approximated by the SDOF hysteretic models, the true MDOF response is always more complex and could not be expected to be described by a simple hysteretic model. SDOF systems with the Takeda hysteretic model and cracked initial stiffness provide consistently reliable estimates of the peak drift, inter-storey drift, global Park and Ang index and global hysteretic energy. Bi-linear hysteretic models also provide reasonable estimations for these response parameters and remain an attractive option because of their conceptual simplicity. No SDOF model is capable of reliably predicting the amplitude of secondary peaks and hence the global fatigue damage.

The lateral force profile used in the pushover analysis to develop the backbone of the SDOF hysteretic rule and transfer function used to link the SDOF displacement to inter-storey drift should be based on the displaced shape of the MDOF system; however, the displaced shape of a true MDOF structure varies throughout the time-history analysis. However, the results of this study show that the shape of the lateral force profile has less importance than other factors such as the hysteretic model used.

SDOF systems are useful for estimating peak global response and also global energy absorption. However, local effects, such as inter-storey drift or the response of individual members, are more difficult to predict as they contain additional uncertainty from the derivation of the transfer functions that are required to link local effects to the SDOF response.

The hysteretic behaviour at the effective height of a MDOF is far more complex than the SDOF approximations available today. This means it is unrealistic to expect a SDOF system to be able to predict the displacement time-history, or fatigue damage, of a MDOF system. However, as SDOF systems can be analysed over 100 times faster than MDOF systems they still offer a useful tool to approximate the peak displacements of MDOF, particularly when a large number of analyses need to be completed. Work is currently underway at UC Berkeley to study the influence of different ground motion parameters on the response of bi-linear SDOF systems. This will be used to identify the damaging characteristics of the ground motion for structures with a wide range of periods and ductilities, which in turn will be used to

develop a method of selecting and scaling accelerograms using multiple ground-motion parameters in a similar way to earlier work using Newmark sliding blocks (Watson-Lamprey and Abrahamson 2006a).

8. SELECTION AND SCALING OF ACCELEROGRAMS

The issue of selecting and scaling accelerograms is of critical importance for both engineering design and assessment as it enables structural response to be determined with greater confidence, but using fewer analyses than if unscaled accelerograms are employed. The objective of selecting and scaling accelerograms is to provide ground motions that cause the same damage level as the either the mean damage level, or another target percentile damage level, that would be found if the structure had been analysed with a large suite of ground motions corresponding to the design magnitude, source-to-site distance and site classification. There are many ways in which recorded accelerograms can be selected and scaled to meet this objective, but as yet only limited efforts have been made to demonstrate the relative strengths and weaknesses of each method. This chapter determines the expected response of a seismically designed 8-storey MDOF reinforced concrete wall frame structure by conducting non-linear time domain analysis of the structure under the action of 1656 unscaled accelerograms. Three different methods of selecting and scaling accelerograms are investigated and the response of the structure compared with the expected response. An abridged description of this work is provided in Hancock and Bommer (2006b).

8.1 Design Code Provisions

The first reference to the use of time-history analysis in US design codes was in the 1990 SEAOC "blue book" (SEAOC 1990), which was drafted by Charles Kircher, Gary Hart and Karl Romstad. At the 2005 COSMOS workshop on the selection and scaling of accelerograms, Charles Kircher made a presentation on the origins of the code requirements and stated that the SEAOC code committee specified the use of time-history when they were unsure of the seismic response of the structure. Unfortunately the SEAOC code committee did not fully appreciate what time-history analysis really involved either, which is why there was little guidance provided on its use. Bommer and Ruggeri (2002) review over 30 seismic design codes and show that there is still little guidance in most current seismic design codes. The guidance that is available is usually related to ensuring that the spectral acceleration from the recorded acceleration time-series do not fall below a certain level related to the design response spectrum. For example, Eurocode 8 (CEN 2004) states that "*No value of the mean 5%*

damping elastic spectrum – calculated from all time histories – is less than 90% of the corresponding value of the 5% damping elastic response spectrum". US codes and standards (IBC 2000, FEMA 2000) require that the square-root-sum-of-the-squares (SRSS) of the spectra from the two horizontal components of each accelerogram are constructed. The records are then scaled such that average of the SRSS spectra of all records does not fall below 1.4 times the 5% spectrum for periods between $0.2T_0$ and $1.5T_0$ seconds, where T_0 is the fundamental period of the structure.

Guidance on the duration of the ground motion is particularly lacking, probably because of the controversy surrounding the significance of duration for inelastic demands and the methods for determining and measuring this parameter. The North American design codes (IBC 2000; UBC 1994) imply that where site specific procedures are used a seismic hazard study should be conducted. Although not explicitly stated in the code, a seismic hazard study should provide an indication of the characteristics of the earthquake or earthquakes controlling the local seismic hazard and an estimation of the duration of the ground motion (e.g. Malhotra 2003) or expected earthquake magnitude. Eurocode 8 explicitly states that the duration of the "*stationary part of the accelerograms*" should be 10 seconds for artificial accelerograms if no site-specific information is available. Recorded accelerograms are required to be "*adequately qualified with regard to the seismogenetic features of the sources and to the soil conditions appropriate to the site*", which also requires some form of a seismic hazard assessment as the earthquakes underlying seismic hazard is not defined in the design code (Bommer and Pinho 2006).

The minimum number of records required to be used in the analysis also varies between design codes although is frequently based (e.g. IBC 2000; CEN 2004) on the guidance of the 1994 Uniform Building Code (UBC 1994). This states that the maximum response should be used if three records are used, while the average response may be used if seven or more records are used. However, this recommendation was chosen arbitrarily by the code drafting committee and has no scientific basis (Kircher 2005). Shome *et al.* (1998) point out that the number of records required to obtain an estimate of the median response to within a defined confidence level depends on the standard deviation of the response. Therefore the number of records to be used should depend on both the procedure used to select and

scale the accelerograms and the nature of the structural response being investigated. Shome *et al.* (1998) also found that scaling accelerograms to the initial period of the structure could reduce the number of runs required to estimate the median response by a factor of about 4, compared to using unscaled records from a magnitude and distance bin created on the design scenario. These findings are further investigated in this study.

8.2 Assessment of "True" MDOF Response

When accelerograms are selected and scaled using an elastic spectral response parameter, such as the elastic response spectrum, the implicit assumption made is that the response of the non-linear MDOF structure to be analysed is proportional to the response of the elastic SDOF system used to construct the response spectra. In order to determine the "true" response of a MDOF structure without making this assumption, a MDOF reinforced concrete wall frame structure is analysed under the action of a suite of 1656 unscaled accelerograms. The wall frame structure used in this study is described in greater detail in Chapter 7, although this work employs an earlier SeismoStruct model of the structure that does not include the non-linear shear springs described in the previous chapter. The relationship between a range of damage measures and earthquake magnitude, source-to-site distance and site classification is determined by regression analysis of the responses obtained from the time-history analysis. This provides the best estimate of the "true" response of the structure that should be observed if analysis is conducted with a much smaller set of accelerograms that have been appropriately selected and scaled.

8.3 Ground Motions

The accelerograms used in this study are subset 1 from the NGA database (Appendix A1) excluding records where either component has a high-pass filter frequency greater than 0.33Hz (less than 3s period). The magnitude – distance distribution of the dataset is given in Table 8.1 and Figure 8.1. The site soil classification is based on the average shear wave velocity in the upper 30m (V_{s30}). For this work V_{s30} is converted into the widely used four category system (Boore and Joyner 1993; Ambraseys *et al.* 1996). Sites with V_{s30} > 760m/s are classed as rock; sites with V_{s30} between 360m/s

and 760m/s are classed as stiff soil; sites with V_{s30} 360m/s to 180m/s are classified as soft soil and sites with V_{s30} < 180m/s are classified as very soft. The style of faulting used for the NGA dataset is determined using the rake angle (Table 8.2). Residuals from predictive equations developed in this work show that earthquakes with reverse-oblique mechanism have similar trends as those from earthquakes with reverse mechanism, so records from reverse-oblique events are combined with the reverse records.

Table 8.1. – Distribution of the dataset for earthquake style of faulting and site soil classification.

	V. Soft**	Soft	Stiff	Rock	Total	(%)
Normal	0	7	8	17	32	4
Strike-slip	11	272	130	6	419	50
Reverse*	6	171	182	24	383	46
Total	17	450	320	47	834	100
(%)	2	54	38	6	100	

*Reverse-Oblique events are included as reverse

** Due to the small number of records V. Soft sites are included with the soft soil sites

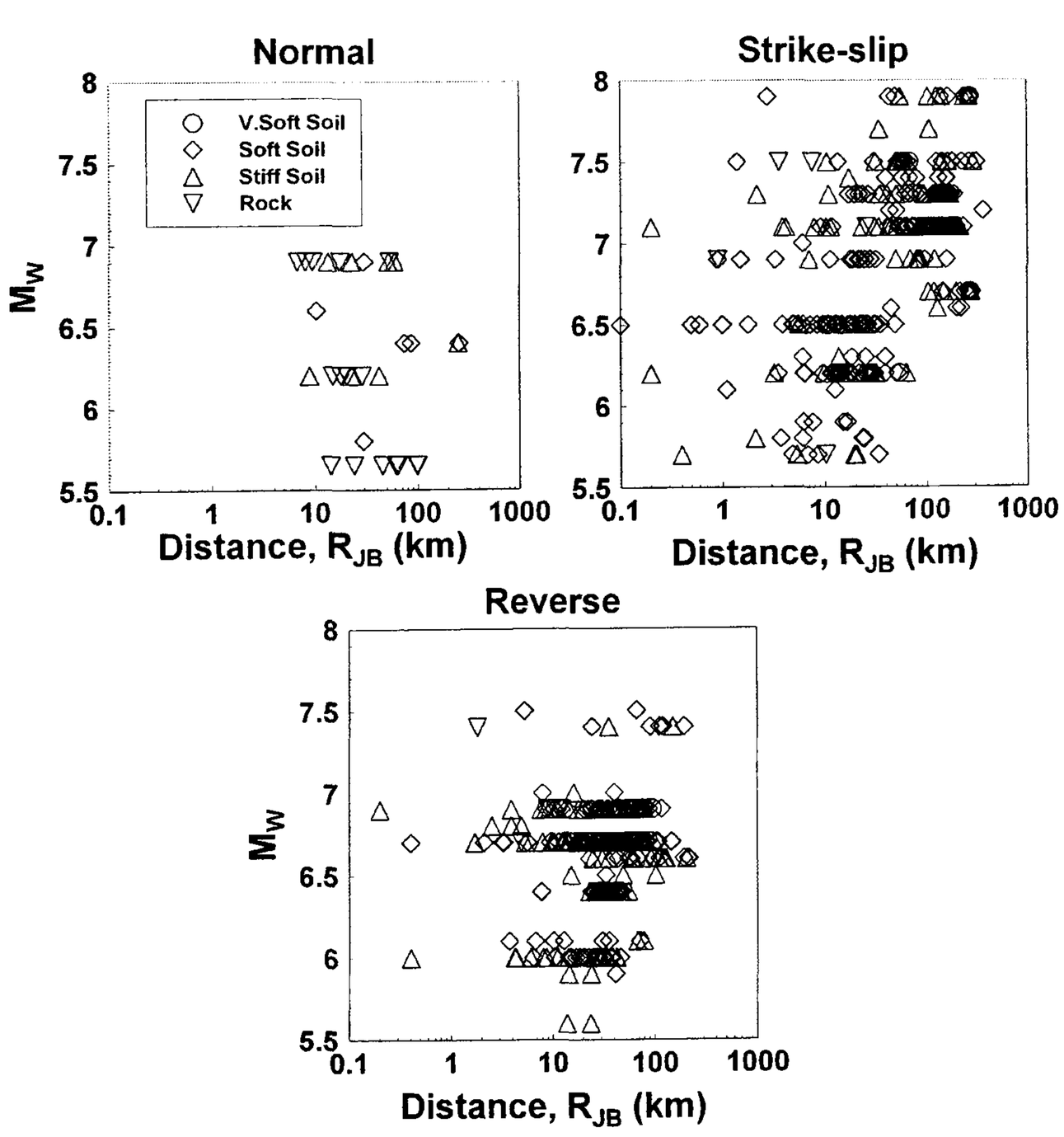


Figure 8.1. – Magnitude –Distance distribution of the dataset for earthquake style of faulting and site classification.

Table 8.2. – Earthquake mechanism classification used for NGA database

Mechanism Class	Rake Angles
Strike-Slip	-180 < Rake < -150 -30 < Rake < 30 150 < Rake < 180
Normal	-120 < Rake < -60
Reverse	60 < Rake < 120
Reverse-Oblique	30 < Rake < 60 120 < Rake < 150
Normal – Oblique	-150 < Rake < -120 -60 < Rake < -30

8.4 Damage Measures

Chapter 3 shows that there is a wide range of damage measures proposed in the literature. These can be divided into four main categories

1. Measures of maximum response (force or displacement)
2. Cyclic fatigue measures
3. Energy measures
4. Measures using a combination of the above

Whilst it is not possible to use all of the proposed damage measures at least one from each generic category is used. The damage measures employed are:

- Peak roof drift (peak response)
- Peak inter-storey drift, for all storeys (peak response)
- Peak member end rotation, local member damage measure (peak response)
- Member rotational fatigue, local member damage measure (fatigue measure)
- Absorbed hysteretic energy, local member damage measure (energy measure)
- Park and Ang damage index, local member damage measure (combo measure)

More detailed definitions of the damage measures are given in the following sections.

8.5 Regression Method and Functional Form

A one-stage maximum likelihood regression method is used (Joyner and Boore 1993) to prevent bias from any non-uniform distribution of ground motions with magnitude and distance. All of the damage indices are related to the amplitude of the motion so the functional form used in the regression model should be similar to those commonly

used to predict other amplitude-dependent parameters. An initial investigation was conducted to find the optimal functional form which provided the lowest standard deviation for estimating building drift, which yielded the following functional form:

$$\log(y) = r_1 + r_2 M_w + r_3 M_w^2 + r_4 \log\left(\sqrt{R_{jb}^2 + r_6^2}\right) + r_5 \sqrt{R_{jb}^2 + r_6^2} + r_7 S_1 + r_8 S_2 + r_9 F_1 + r_{10} F_2 \pm \sigma_t P \quad (8.1)$$

where log(y) is the base-10 log of the parameter to be regressed; $r_1, r_2, r_3, r_4, r_5, r_6, r_7, r_8, r_9$ and r_{10} are coefficients to be determined by regression; M_w is moment magnitude (Hanks and Kanamori 1979); R_{jb} is the closest distance to the surface projection of the fault rupture, as proposed by Joyner and Boore (1981); S_1 and S_2 are dummy variables for site classification that have a default value of zero, S_1 equals one for soft soil sites and S_2 equals one for stiff soil sites; F_1 and F_2 are dummy variables for style-of-faulting that have a default of zero; F_1 equals one for normal and F_2 equals one for reverse events; to reduce the number of coefficients required to describe the style-of-faulting reverse-oblique events are included as reverse faults. P equals 0 for the median response and 1 for the 84-percentile level assuming a log normal distribution of the residuals with standard deviation σ_t. The standard deviation is comprised of two components, the standard deviation from the site-to-site variability σ_s and the standard deviation from the earthquake-to-earthquake variability σ_e:

$$\sigma_t = \sqrt{\sigma_s^2 + \sigma_e^2} \quad (8.2)$$

All the terms of the chosen functional form are related to physical characteristics. Magnitude scaling is achieved using the second term and magnitude saturation with the third. The attenuation with distance due to geometric spreading and anelastic attenuation is modelled with the fourth and fifth terms respectively, in which r_6 is an empirical depth term. The sixth and seventh terms represent the amplification by stiff and soft soil respectively. The eighth and ninth terms enable a distinction between normal, strike-slip and reverse faulting mechanisms to be established.

The use of a magnitude dependent distance term was tried initially; however, this did not reduce the standard deviation of the residuals so was dropped from the functional form. Several researchers have reported that variability decreases with magnitude (e.g. Youngs *et al.* 1995; Ambraseys *et al.* 2005) however initial investigation of the residuals for the predictive equation for roof drift indicates this is not the case for this dataset (Figure 8.2). Additional terms have not been included to account for effects such as rupture directivity as this would not be straight forward to implement and this level of complexity is not warranted for this study. Ground motions with particular features such as forward directivity or fling have not been removed from the data set as this would artificially reduce the variability of the ground motion. As there is no physical interpretation for positive values of coefficients r_3 and r_5 they are fixed to be equal or less than zero.

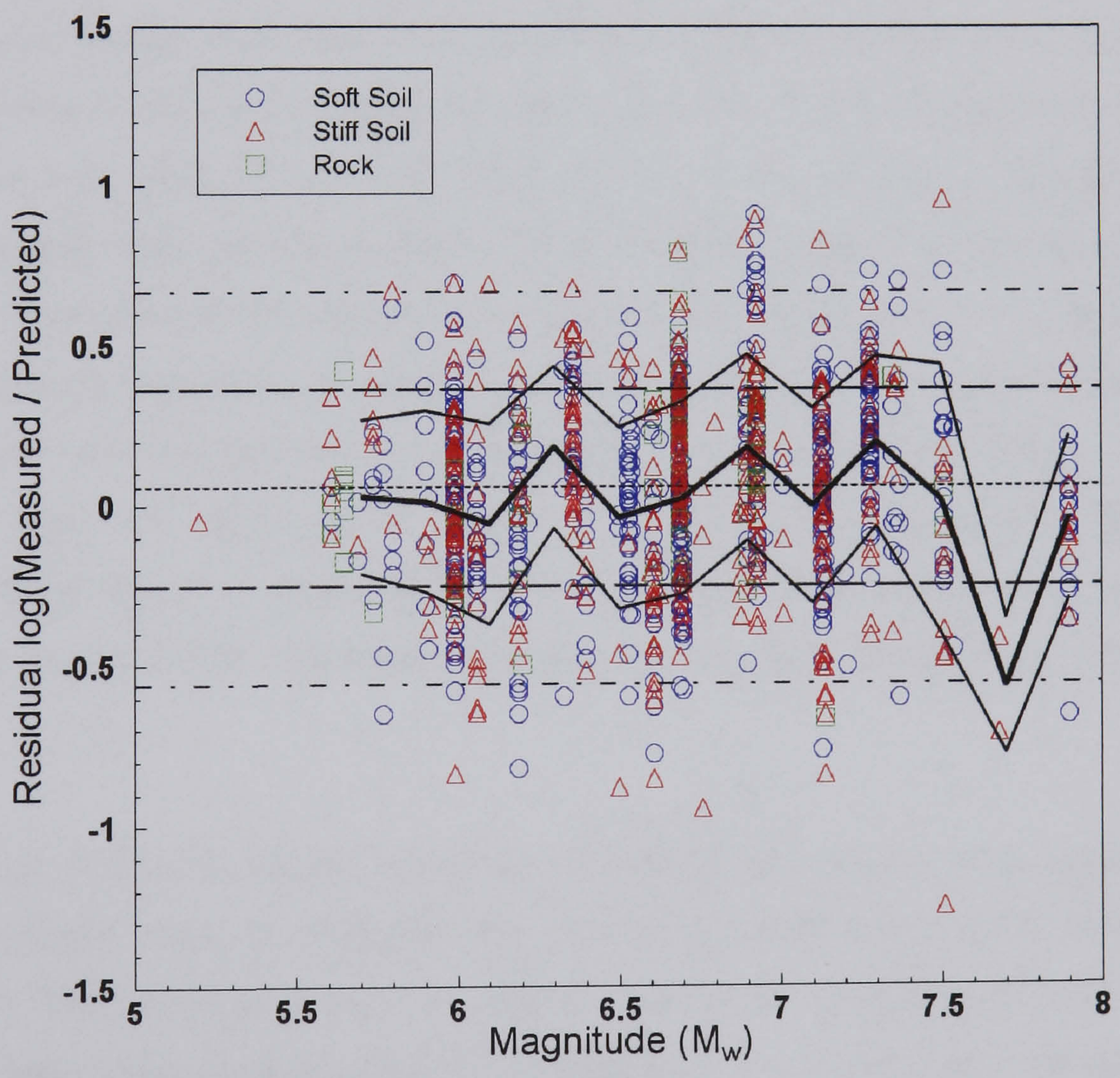


Figure 8.2. – Residuals of roof drift vs. Magnitude. Thin dashed lines indicate median, ±1 and 2 standard deviations of the whole dataset. Solid lines indicate median and ±1 standard deviation of the data binned in 0.2M units

As discussed in section 2 and by Beyer and Bommer (2006) there are different ways of treating the horizontal components of the motion. In this study predictive equations are derived using the larger of the two horizontal components. The geometric mean is not used as the weaker component artificially reduces the amplitude and dispersion of the response with this definition; real structures are loaded with both components of the motion, not the geometric mean.

8.6 Predictive Equations for Damage

8.6.1 Peak roof drift and inter-storey drift

Regression analysis is conducted to produce predictive equations for inter-storey drift and peak roof drift. The derived regression coefficients are given in Table 8.1. The coefficients for the site class indicate that peak drift is greater for structures on sites with stiff soil and soft soil by factors of approximately 1.5 and 2.0 compared with structures on sites classified as rock. The coefficients for the source mechanism indicate that peak drift is lower by about 5% for structures exposed to motions from earthquakes with normal faulting and approximately 8% greater for reverse faulting than for structures subjected to motions from earthquakes with strike-slip mechanism. The predicted relationships between peak drift and source-to-site distance and earthquake magnitude are shown in Figure 8.3 and Figure 8.4 respectively. When examining these figures it should be borne in mind that large drifts would not be expected as this is a stiff wall-frame structure that has been designed for seismic resistance.

The observed displacements are binned by magnitude and distance and compared with the predicted values to check that the equations provide a good fit to the data (Figure 8.5). The observed values are only plotted if the magnitude-distance bin contains at least five ground motions. To account for the site and source effects the observed points are normalized to a strike-slip earthquake and stiff soil site class using the coefficients of the predictive equation. The appropriateness of the use of the exponential magnitude term is confirmed as the observed drift does not increase linearly with magnitude; indeed some of the drifts for the M_W 6.5-6.9 bins are greater than those observed for the M_W 7.0-7.9 bin. The residuals from the equations have

been checked to ensure that they are approximately normally distributed and have approximately zero mean (Figure 8.6). The mean is not expected to be exactly zero as the weights from the maximum likelihood regression are not applied to the residuals.

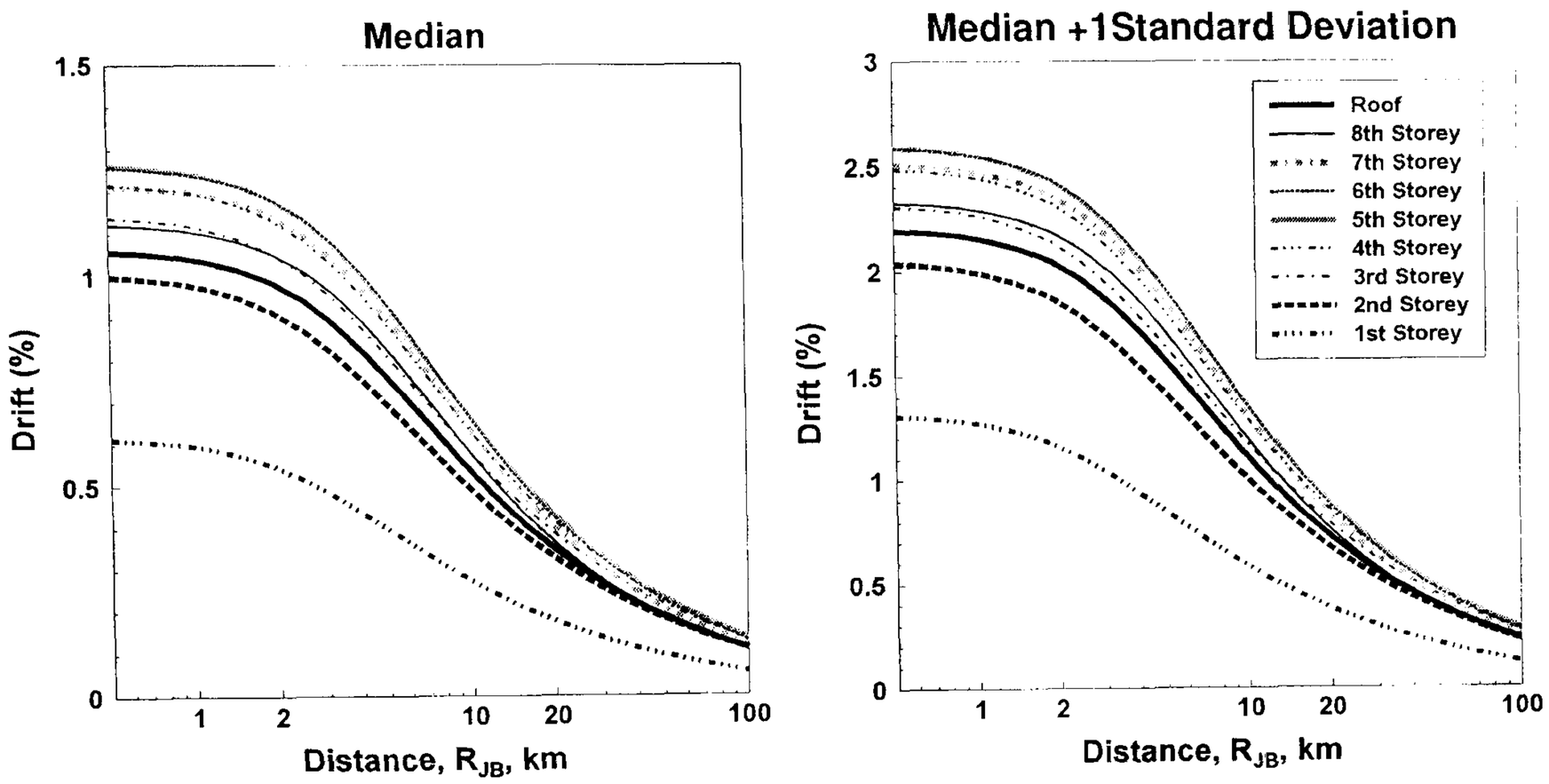


Figure 8.3. - Predicted median and median-plus-one-standard-deviation peak drift vs. Source-to-site distance for Magnitude M_w7.0, soft soil site and strike-slip rupture mechanism.

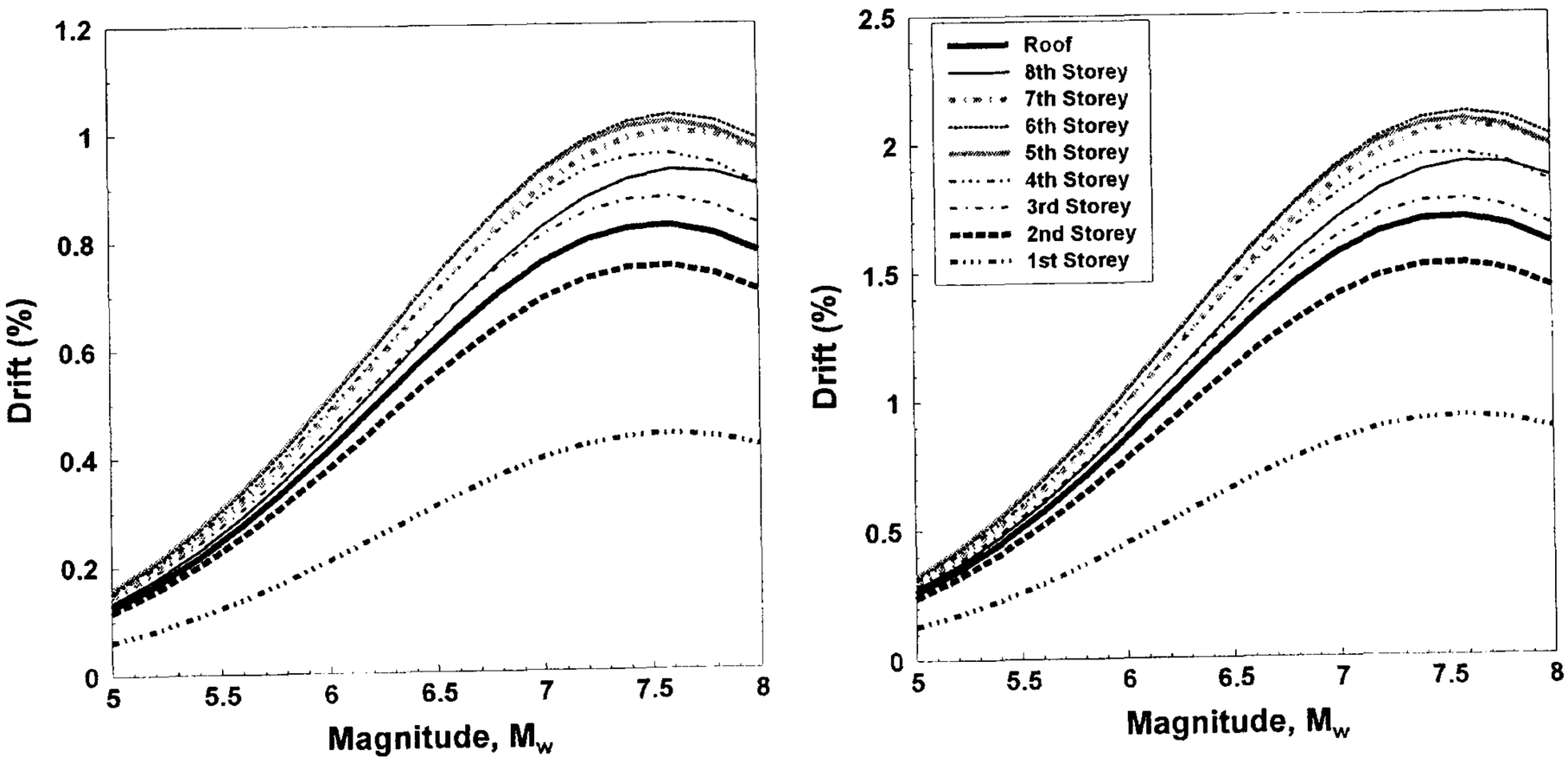


Figure 8.4. – Predicted median and median-plus-one-standard-deviation peak drift vs. Magnitude for a source-to site distance of 5km; soft soil site and strike-slip rupture mechanism.

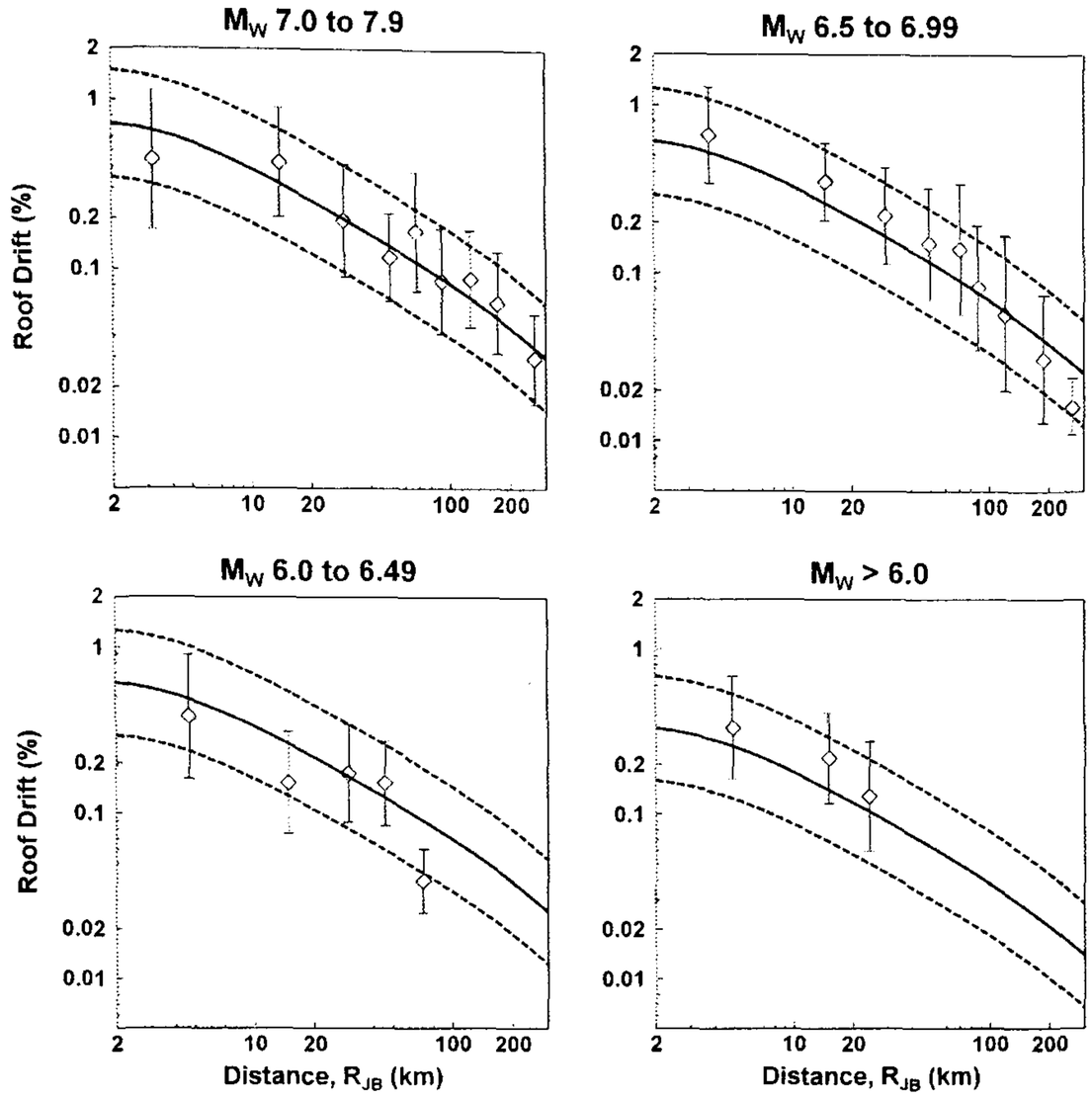


Figure 8.5. - Comparison of peak roof drift predicted by the predictive equations (solid line-median; plus and minus one standard deviation-dashed) and those of the measured data binned by magnitude and distance, adjusted to strike-slip and stiff soil using the coefficients of predictive equation (diamonds median, error bars plus minus one standard deviation).

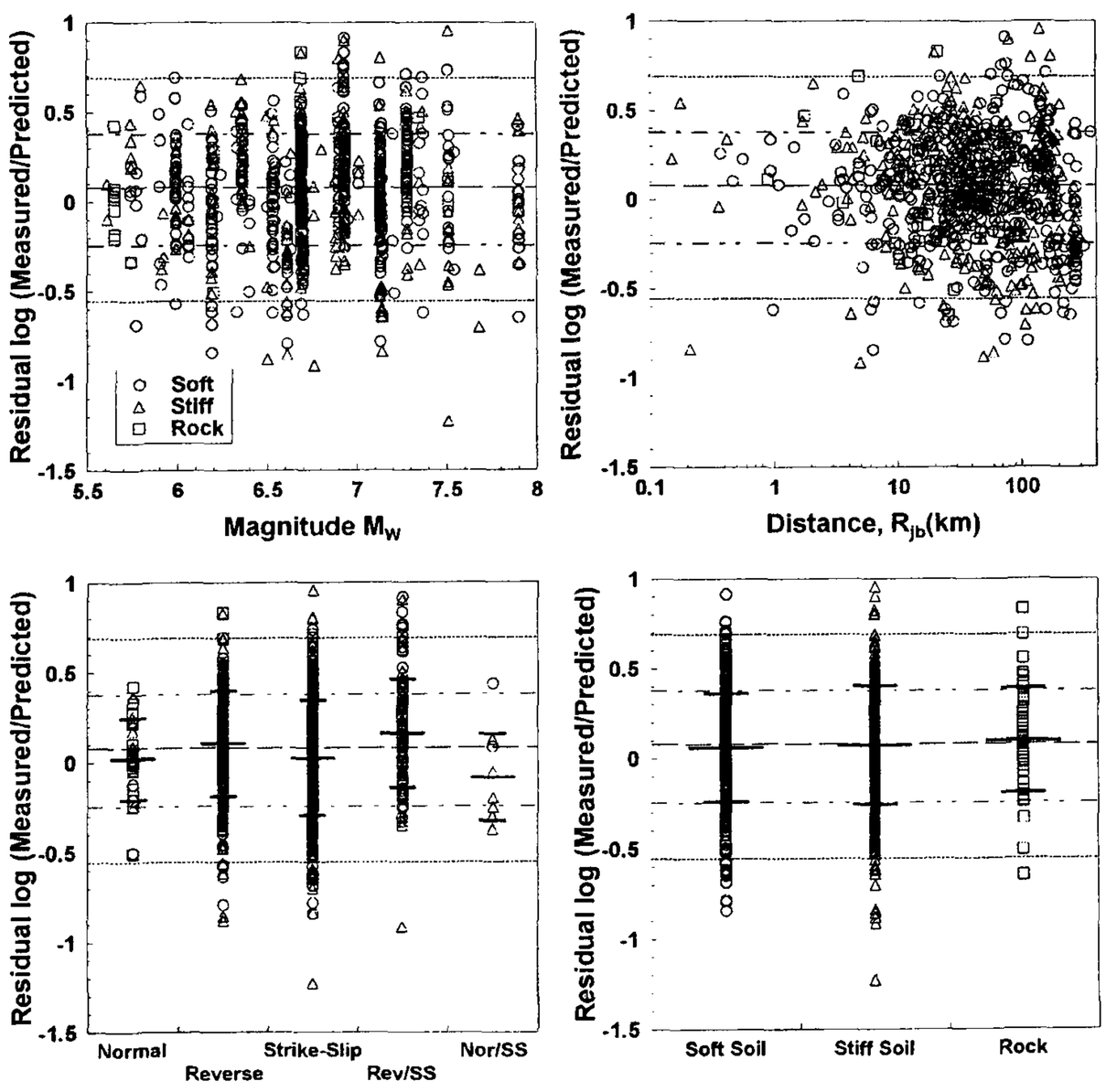


Figure 8.6. – Residuals for roof drift in terms of earthquake magnitude (*top left*), source-to-site distance (*top right*), site classification (*lower right*) and rupture mechanism (*lower left*).

Table 8.3. – Regression coefficients and standard deviations for inter-storey drift and roof drift

	Derived coefficients										Standard Deviations		
	r_1	r_2	r_3	r_4	r_5	r_6	r_7	r_8	r_9	r_{10}	σ_e	σ_s	σ_t
1st Storey drift (%)	-7.155	1.902	-0.126	-0.581	-0.001	3.121	0.320	0.170	-0.027	0.030	0.165	0.262	0.309
2nd Storey drift (%)	-6.907	1.852	-0.123	-0.587	-0.001	3.348	0.333	0.181	-0.022	0.032	0.162	0.260	0.307
3rd Storey drift (%)	-6.967	1.882	-0.125	-0.617	-0.001	3.679	0.348	0.191	-0.020	0.036	0.161	0.265	0.310
4th storey drift (%)	-6.837	1.852	-0.122	-0.645	-0.001	3.947	0.351	0.193	-0.017	0.037	0.159	0.268	0.312
5th storey drift (%)	-6.816	1.850	-0.122	-0.670	-0.001	4.131	0.344	0.186	-0.014	0.037	0.158	0.270	0.313
6th storey drift (%)	-6.837	1.854	-0.122	-0.691	-0.001	4.216	0.338	0.180	-0.014	0.037	0.157	0.272	0.315
7th storey drift (%)	-6.794	1.828	-0.119	-0.696	-0.001	4.176	0.335	0.177	-0.016	0.038	0.158	0.274	0.316
8th storey drift (%)	-7.156	1.918	-0.127	-0.637	-0.001	3.655	0.354	0.194	-0.020	0.034	0.164	0.271	0.316
Roof drift (%)	-7.589	1.94	-0.128	-0.603	-0.001	2.746	0.331	0.175	-0.031	0.027	0.176	0.278	0.329

8.6.2 Local element damage measures

Predictive equations for a number of local element damage measures including the absorbed hysteretic energy and Park and Ang damage parameter have been calculated. However, while the two dimensional wall frame model used in this study can accurately model global parameters, such as inter-storey drift, local effects are less accurately modelled. For example, greater deformations, damage and inelasticity would be expected in the beams of the outer frames of the structure than is indicated from the single frame model (Mwafy 2001). For this reason, the absolute values of the local damage measures have little meaning. However, as the MDOF model is consistent in all of the analyses, these measures can still be used to provide an estimate of the ability of different methods of selecting and scaling accelerograms to estimate different types of local damage measures.

Peak member end rotation

Peak member end rotation is defined as the peak rotational displacement over the end of the member (θ_{max}) induced by the earthquake ground motion. Peak member end rotation is measured in local element co-ordinates so is the rotational displacement over the end of the member relative to the rotation of the joint at the end of the member. Predictive equations are derived for the member end rotation for the ends of all members. Regression coefficients for the predictive equations are provided in Appendix A3. The influence of earthquake magnitude and source-to-site distance on the end rotation of the base of the outer ground floor column and 1st floor beam is shown in Figures 8.7 and 8.8 respectively. These figures also show that there is fair agreement between the observed and predicted rotations; this is also demonstrated by the residuals, which are approximately normally distributed with almost zero mean (Figures 8.9 and 8.10).

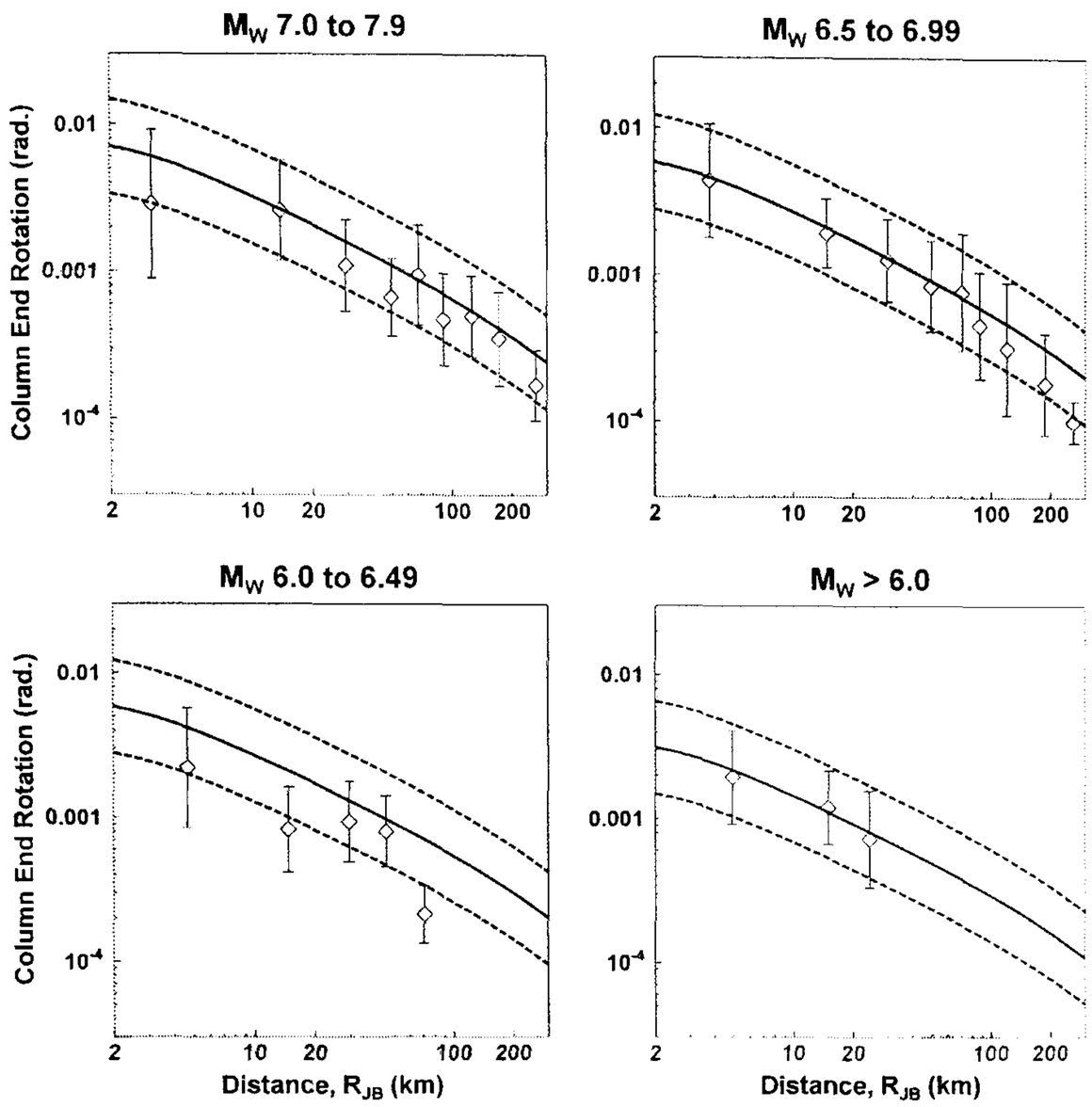


Figure 8.7. - Comparison of peak end rotation of the base of the outer ground floor column predicted by the predictive equations (solid line-median; plus and minus one standard deviation-dashed) and those of the measured data binned by magnitude and distance, adjusted to strike-slip and stiff soil using the coefficients of the predictive equation (diamonds median, error bars plus minus one standard deviation).

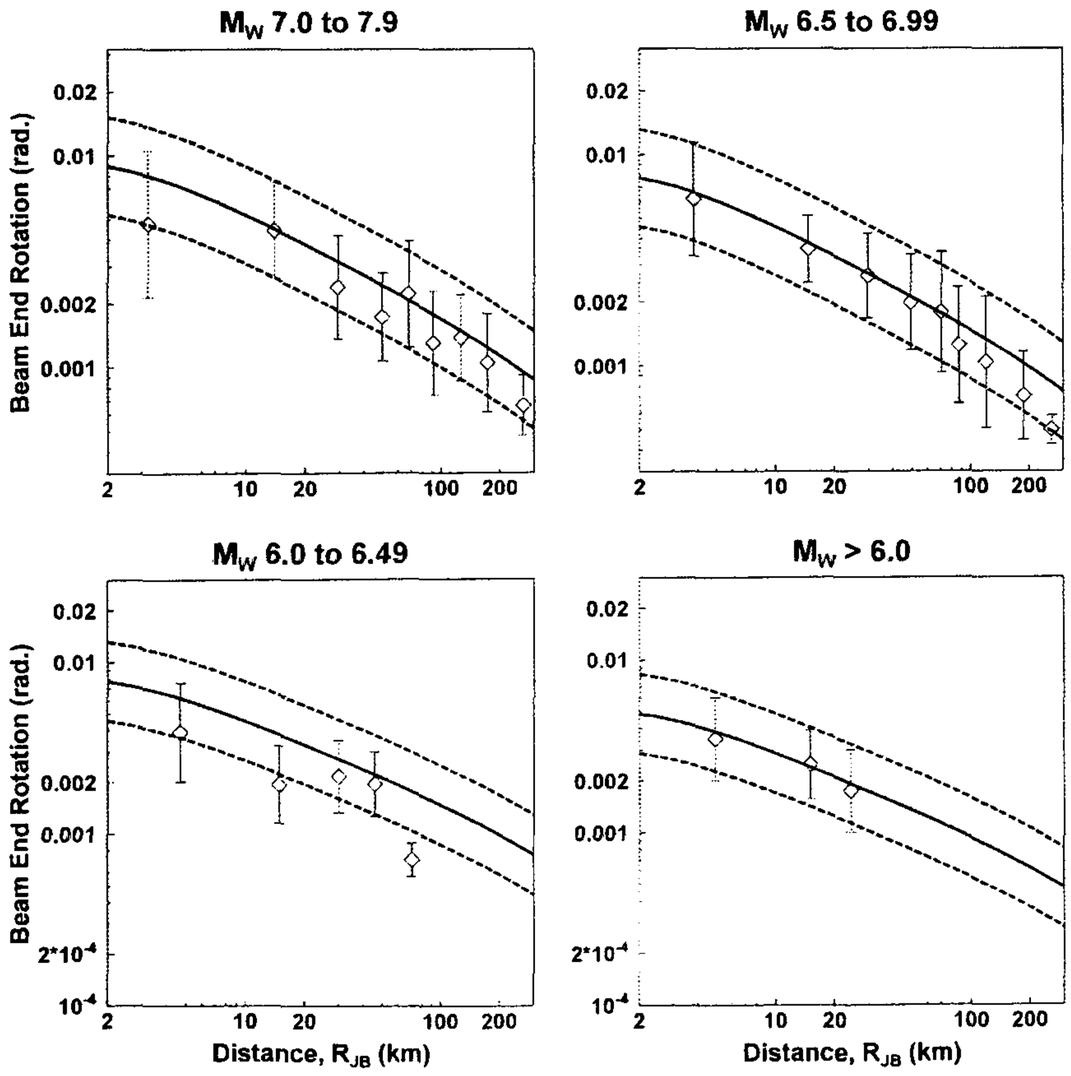


Figure 8.8. – As Figure 8.7 but for the outer end of the 1st floor beam at the edge of the structure.

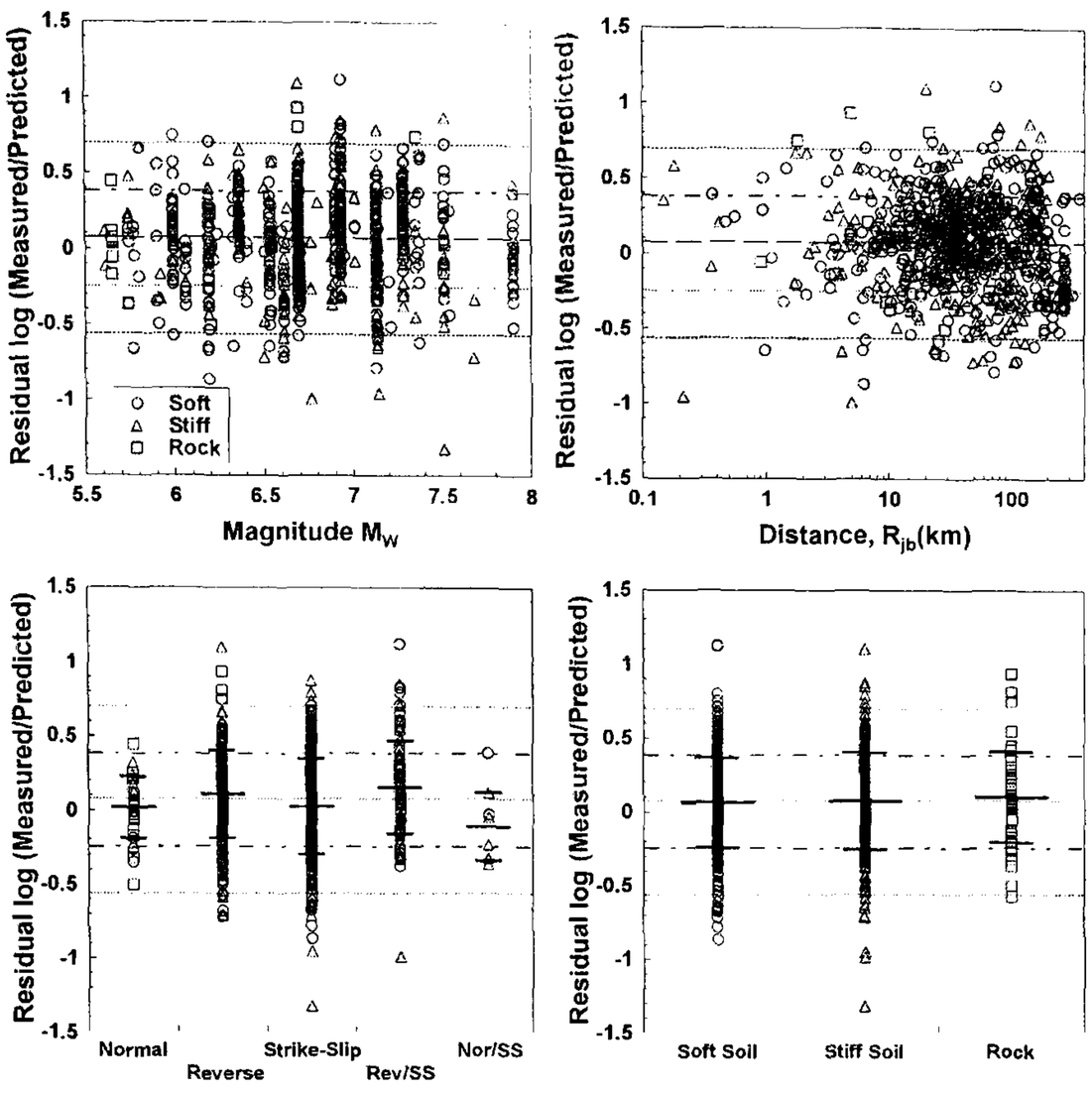


Figure 8.9. – Residuals for peak end rotation of the base of the outer ground floor column in terms of earthquake magnitude (*top left*), source-to-site distance (*top right*), site classification (*lower right*) and rupture mechanism (*lower left*).

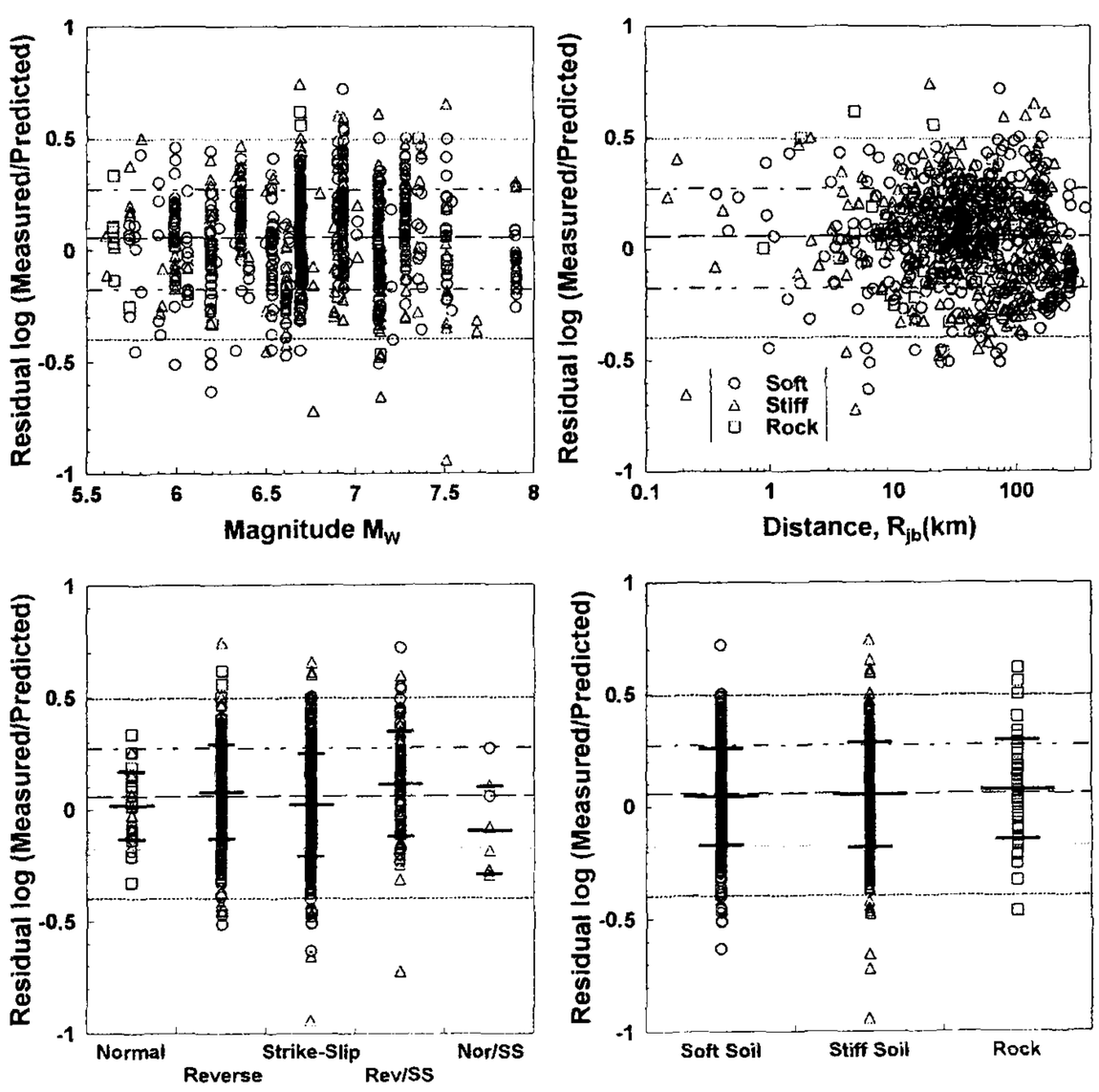


Figure 8.10. – Residuals for peak end rotation the outer end of the 1st floor beam at the edge of the structure in terms of earthquake magnitude (*top left*), source-to-site distance (*top right*), site classification (*lower right*) and rupture mechanism (*lower left*).

Member absorbed hysteretic energy

The member absorbed hysteretic energy is calculated for the end of each member by integrating the area enclosed by the moment-rotation hysteresis envelope. Predictive equations are derived for the ends of all members and the coefficients of the equations are provided in Appendix A3. The influence of earthquake magnitude and source-to-site distance on the absorbed hysteretic energy of the base of the outer ground floor column and the outer end of the 1st floor beam is shown in Figures 8.11 and 8.12. These figures show that there is fair agreement between the observed and predicted absorbed energy. This is also demonstrated by the residuals, which are approximately normally distributed with close to zero mean (Figures 8.13 and 8.14). The dispersion of the residuals shows that there is greater variability in the hysteretic energy than the peak member end rotation. For example, the one standard deviation level of rotation at the base of the ground floor external column is a factor of 2 greater than the median, while the one standard deviation hysteretic energy is a factor of 11 above the median. The greater variability is probably because the hysteretic energy is related to both the duration and the amplitude of the motion.

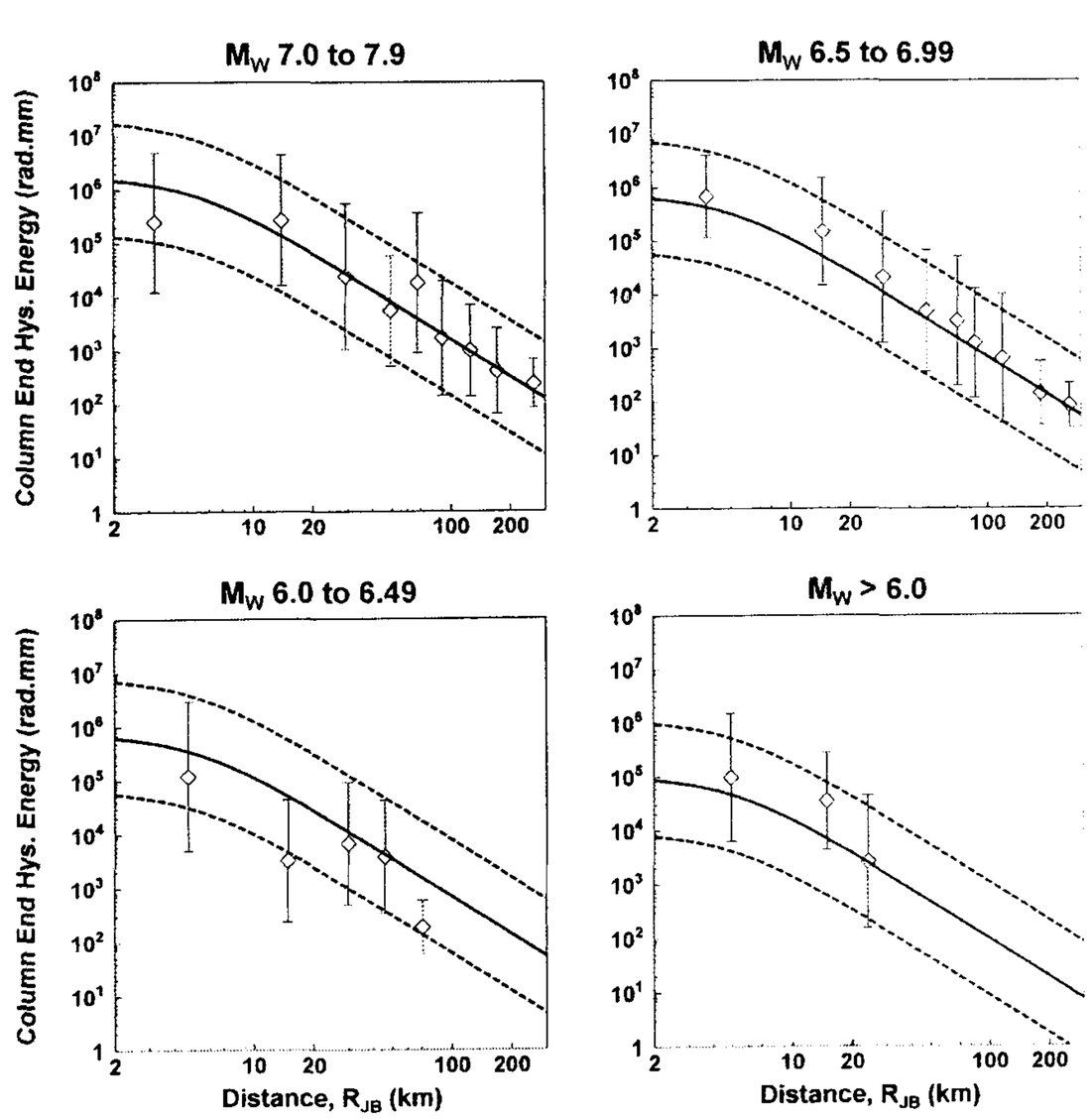


Figure 8.11. - Comparison of the absorbed hysteretic energy of the base of the outer ground floor column predicted by the predictive equations (solid line-median; plus and minus one standard deviation-dashed) and those of the measured data binned by magnitude and distance, adjusted to strike-slip and stiff soil using the coefficients of the predictive equation (diamonds median, error bars plus minus one standard deviation).

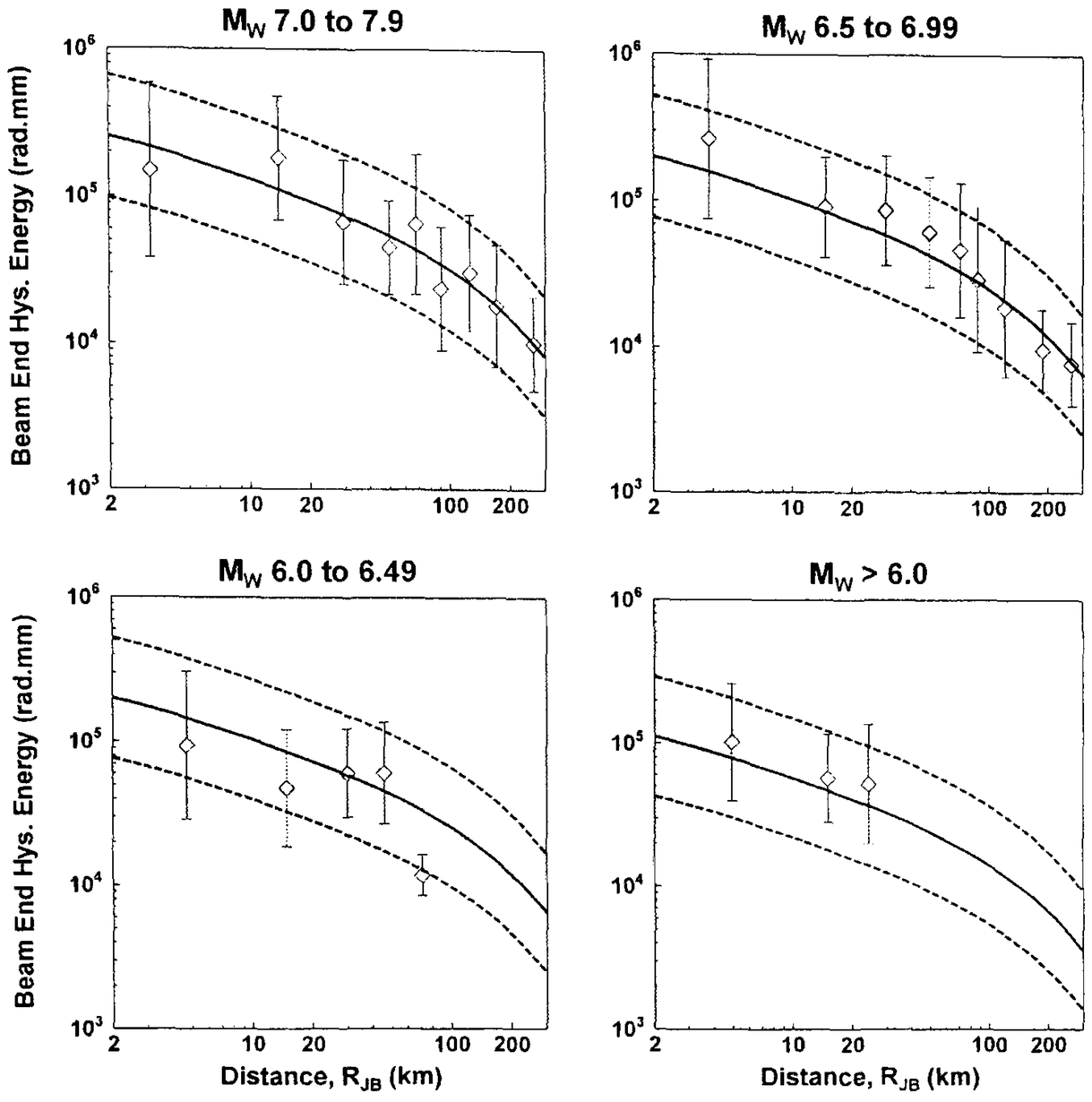


Figure 8.12. – As Figure 8.11 but for the outer end of the 1st floor beam at the edge of the structure.

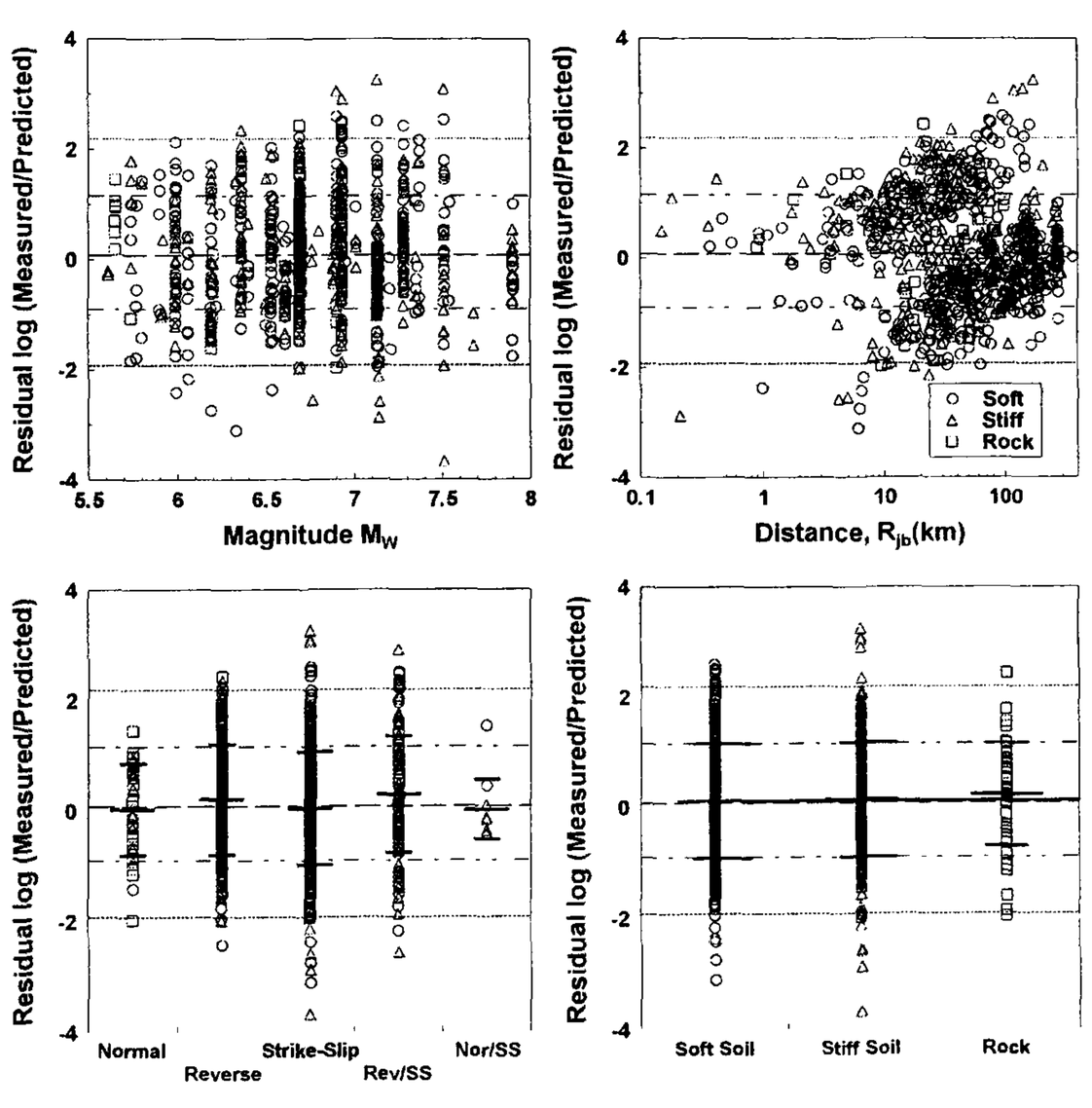


Figure 8.13. – Residuals for absorbed hysteretic energy of the base of the outer ground floor column in terms of earthquake magnitude (*top left*), source-to-site distance (*top right*), site classification (*lower right*) and rupture mechanism (*lower left*).

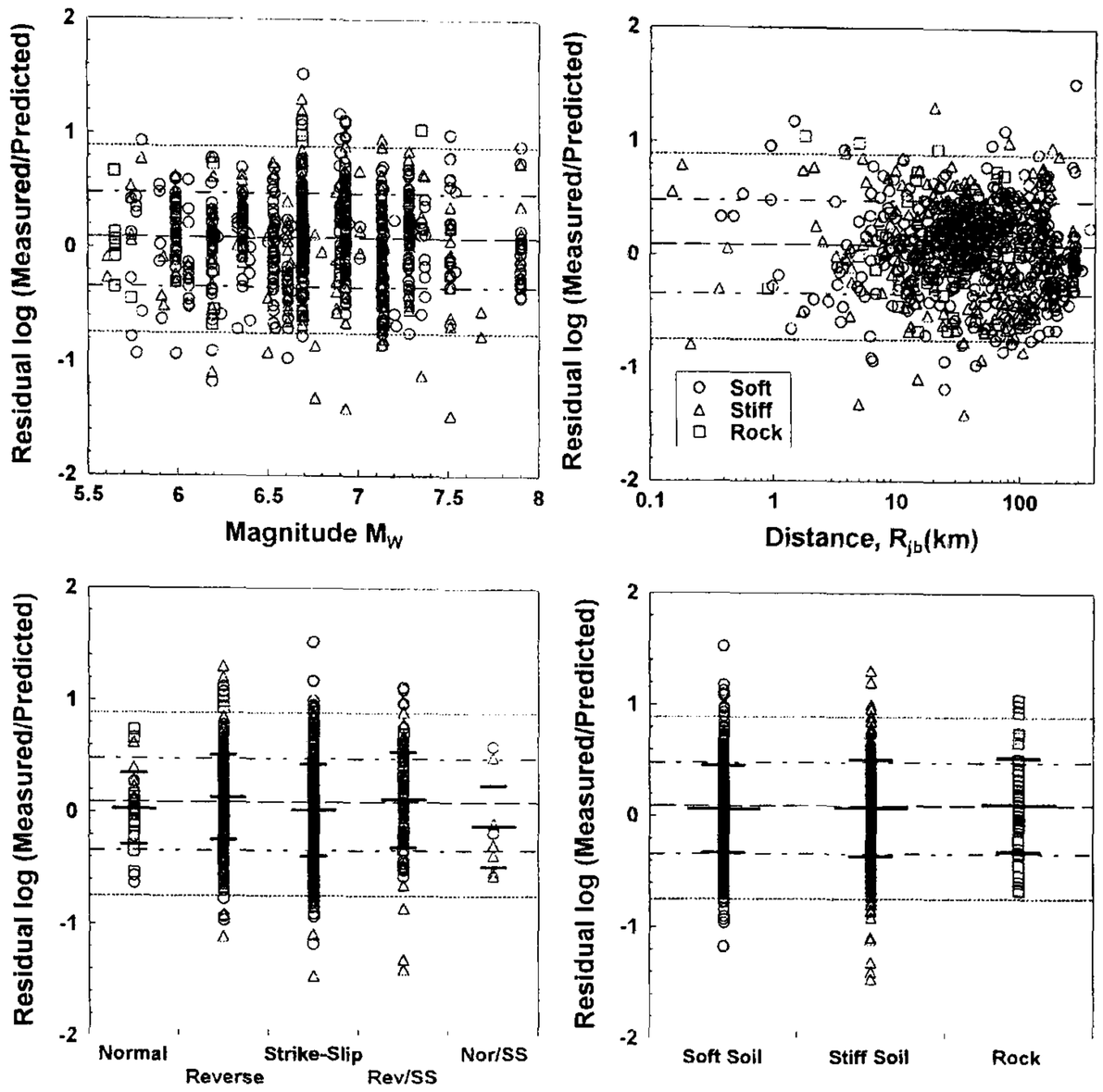


Figure 8.14. – Residuals for absorbed hysteretic energy of the outer end of the 1st floor beam at the edge of the structure in terms of earthquake magnitude (*top left*), source-to-site distance (*top right*), site classification (*lower right*) and rupture mechanism (*lower left*).

Park and Ang damage index

The Park and Ang damage index is calculated for the member end rotation ($D_{pa\theta}$). This is calculated from a combination of the absorbed hysteretic energy and the peak rotation:

$$D_{pa\theta} = \frac{\theta_M}{\theta_u} + \frac{\beta}{M_y \theta_y} \int d\theta \qquad (8.3)$$

where θ_M is the peak rotation of the member recorded in the response time-series, θ_u is the ultimate monotonic rotation capacity of the member, β is an empirical factor that changes the balance between the extreme displacement and hysteretic energy $\int d\theta$. β is set to 0.15 as recommended as a median value by Cosenza and Manfredi (1998). M_y and θ_y are the yield moment and rotation respectively. The ultimate rotation, yield rotation and yield moment are calculated from first principles

using section analysis as described by Park and Paulay (1975) and Paulay and Priestley (1992). The yield moment is provided directly by section analysis. However, assumptions on the curvature distribution along the member length are required to calculate the yield and ultimate rotations. The yield rotation is calculated by integrating the curvature along the member starting with the yield curvature at one end and assuming zero curvature at mid-span. The ultimate rotation is calculated assuming linear elastic curvature distribution along the member length plus a region of constant ultimate curvature in the plastic hinge at each end of the member (Paulay and Priestley 1992). The plastic hinge length is taken as half the section depth as suggested by Paulay and Priestley (1992). The effects of static gravity loads are considered in the section analysis. However, axial load fluctuations during the analysis are not considered as this would lead to different element capacities at different times in the analysis. The influence of ignoring the axial load fluctuations can be seen by comparing the calculated and measured moment-rotation characteristics of the outer columns of the first storey when the structure is subjected to a lateral pushover with a triangular load distribution (Figure 8.15)

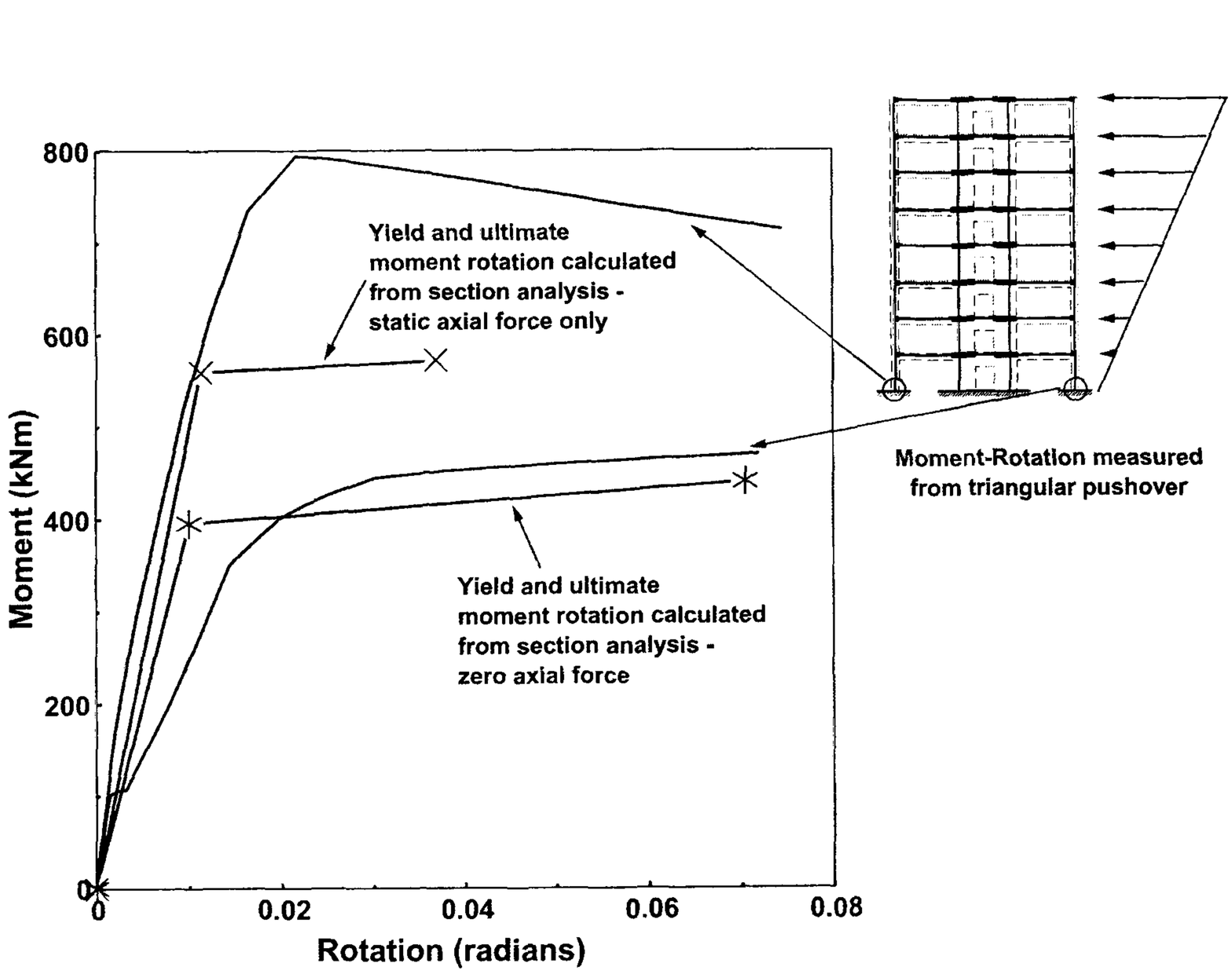


Figure 8.15. – Comparison of member end moment-rotation relations from triangular pushover analysis and that calculated from section analysis with different axial loads. Pushover forces decrease the axial load in the right-hand ground floor column to zero at approximately 0.08 radians rotation.

Predictive equations are derived for the ends of all members and the coefficients for the predictive equations are provided in Appendix A3. The influence of earthquake magnitude and source-to-site distance on the Park and Ang damage of the base of the outer ground floor column and end of the 1st floor beam is shown in Figures 8.16 and 8.17 respectively. The residuals for these members are shown in Figures 8.18 and 8.19.

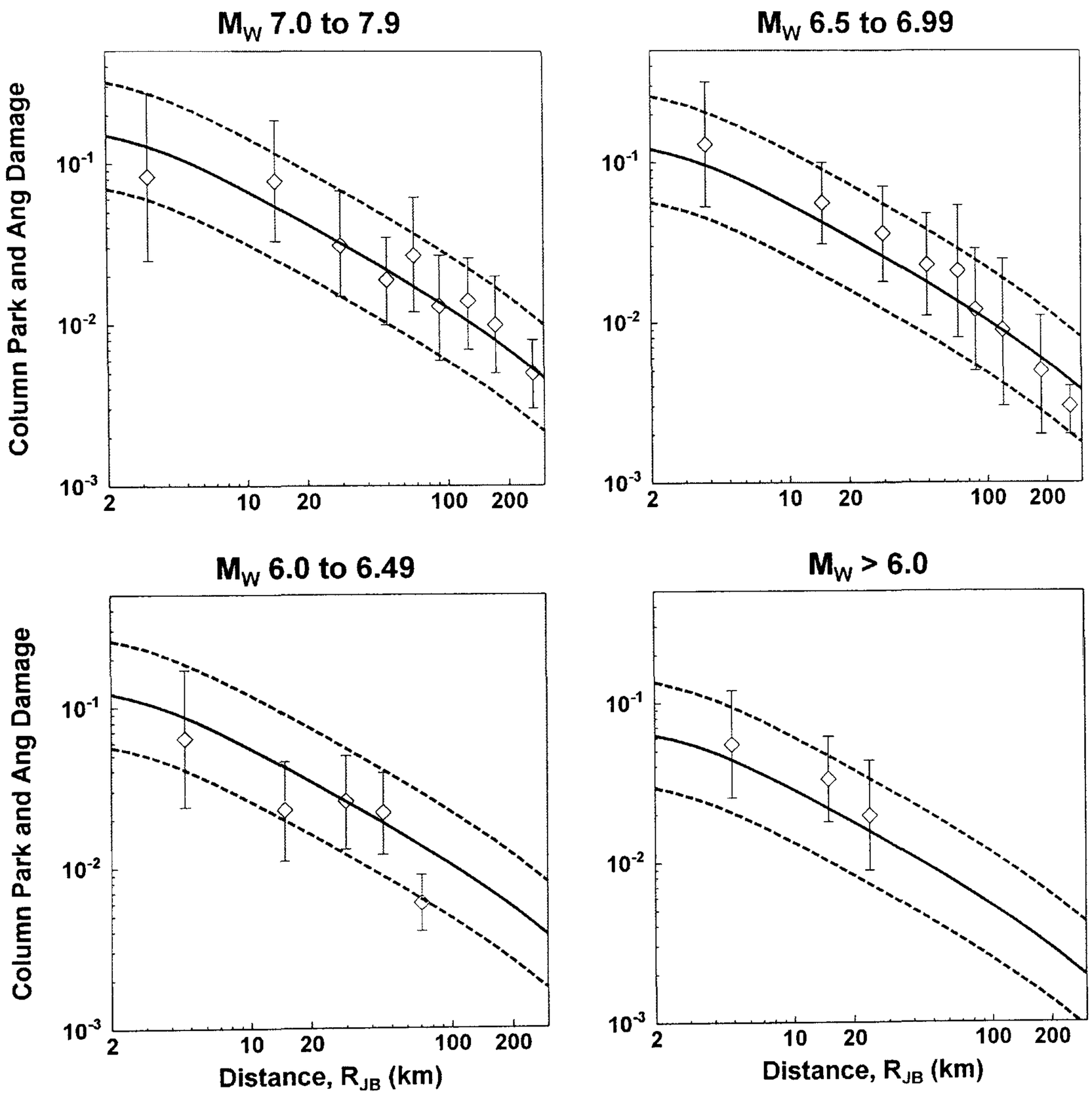


Figure 8.16. - Comparison of the Park and Ang damage of the base of the outer ground floor column predicted by the predictive equations (solid line-median; plus and minus one standard deviation-dashed) and those of the measured data binned by magnitude and distance, adjusted to strike-slip and stiff soil using the coefficients of predictive equation (diamonds median, error bars plus minus one standard deviation).

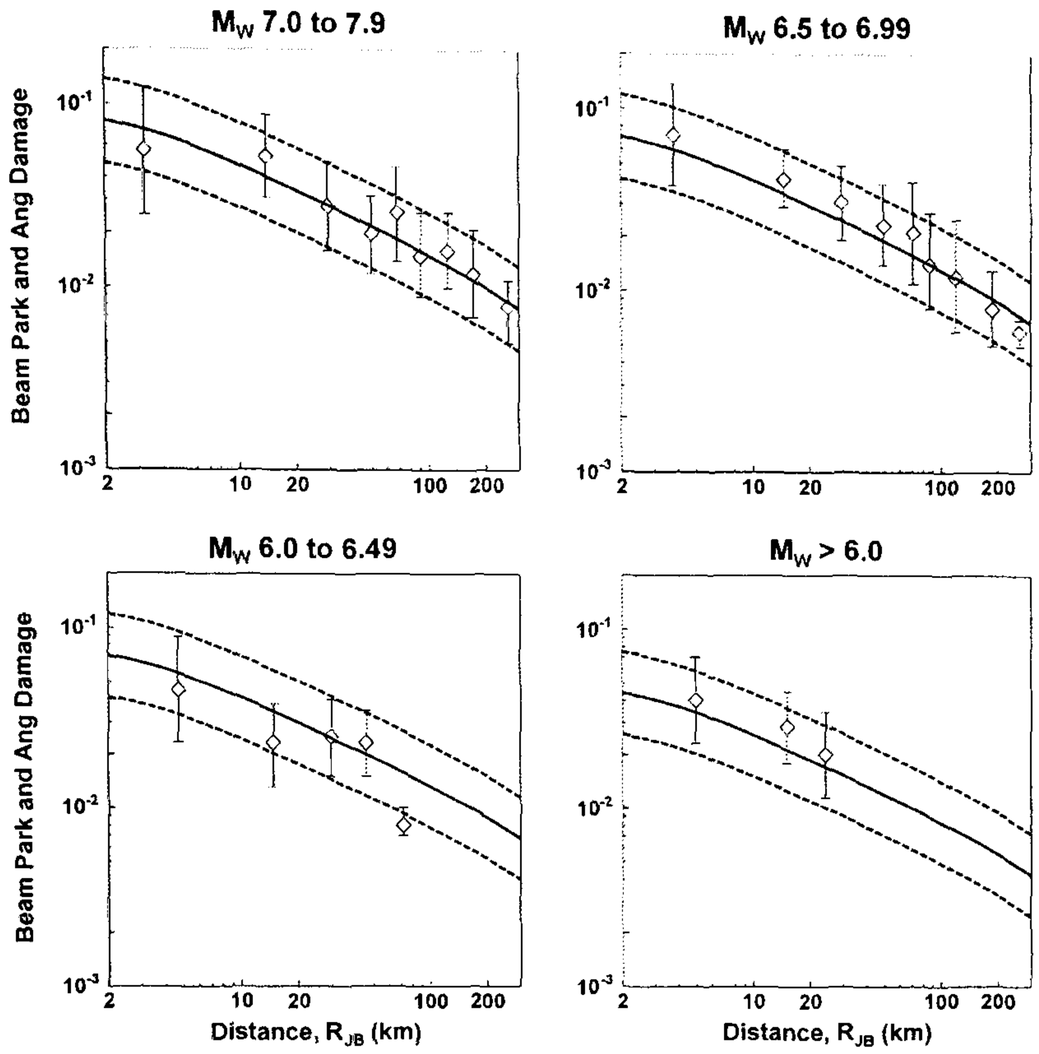


Figure 8.17. – As Figure 8.16 but for the outer end of the 1st floor beam at the edge of the structure.

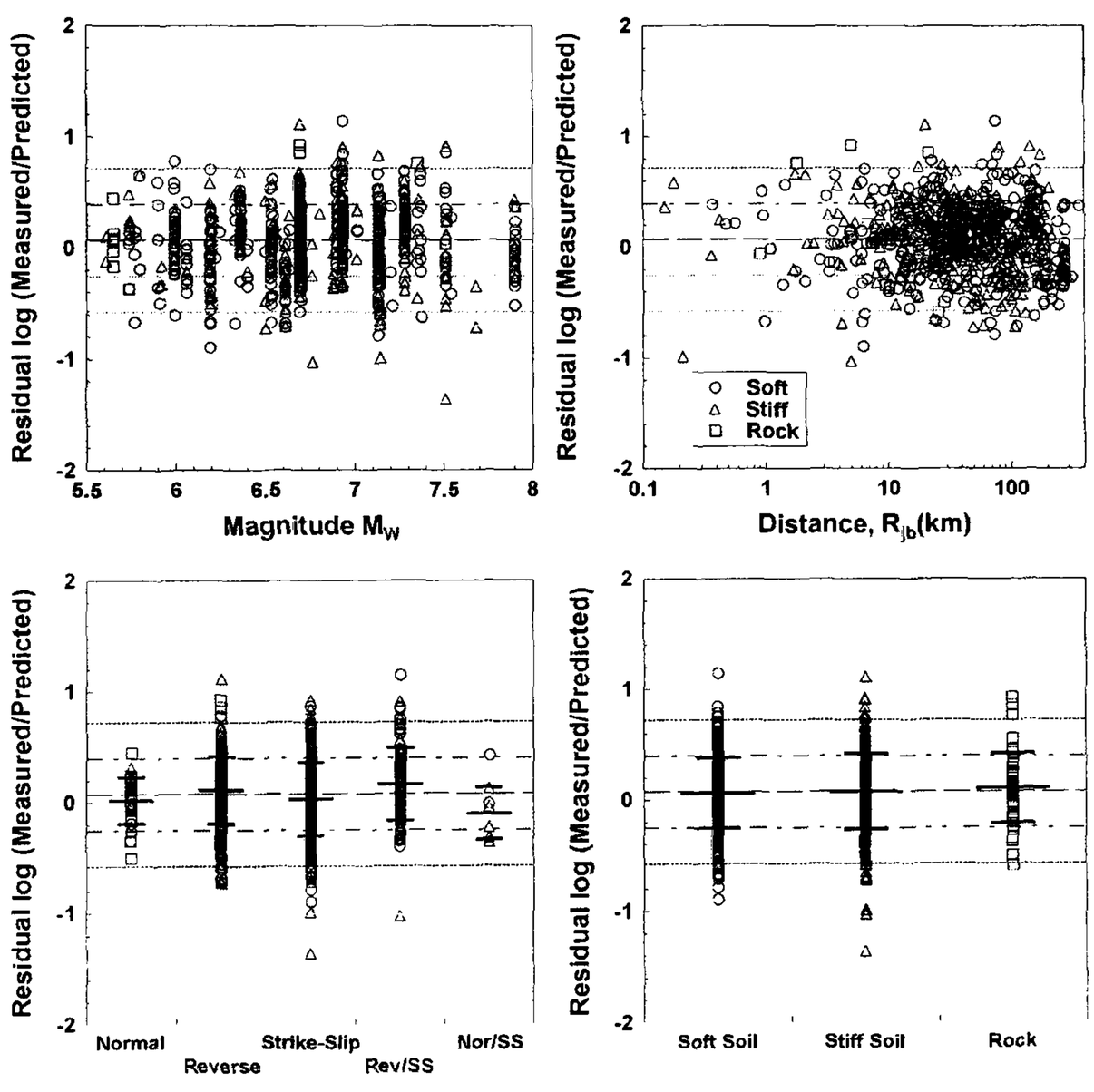


Figure 8.18. – Residuals for Park and Ang damage index of the base of the outer ground floor column in terms of earthquake magnitude (*top left*), source-to-site distance (*top right*), site classification (*lower right*) and rupture mechanism (*lower left*).

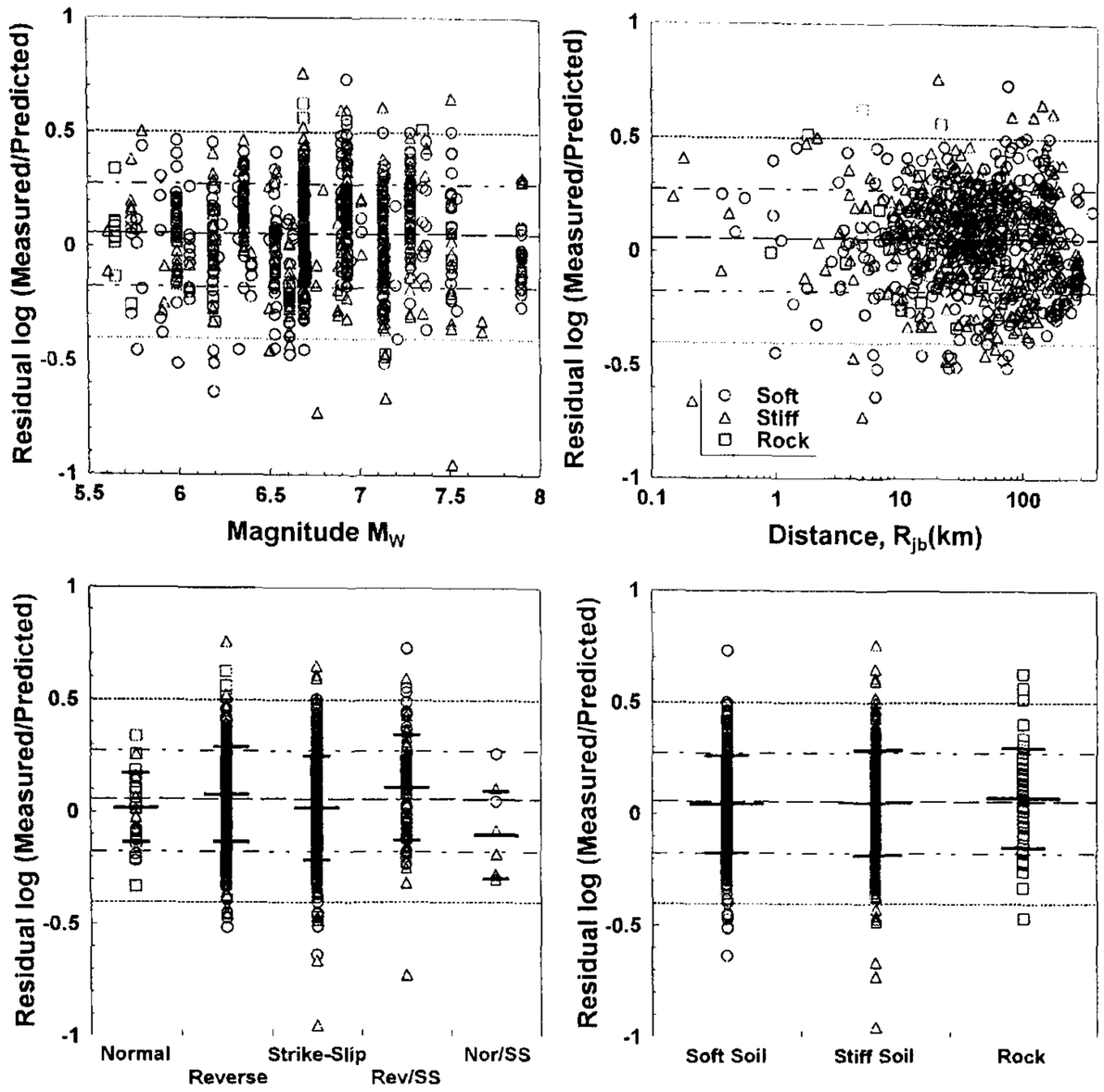


Figure 8.19. – Residuals for Park and Ang damage index of the outer end of the 1st floor beam at the edge of the structure in terms of earthquake magnitude (*top left*), source-to-site distance (*top right*), site classification (*lower right*) and rupture mechanism (*lower left*).

Member rotational fatigue

Member rotational fatigue damage is calculated by counting the member end-rotations using rainflow cycle counting (see section 2.4). The total damage is calculated by summing each cycle using Miner's linear damage accumulation:

$$Damage = \sum_{i=1}^{i=n} \frac{1}{a} \theta_i^k \tag{8.4}$$

where a and k are the fatigue constant and exponent respectively, θ_i is the amplitude of the i^{th} rotation cycle and n is the total number of cycles. A fatigue exponent k of 3.86 is used, which is derived from the experimental test results of Yamada (1992) for reinforced concrete columns with an axial load of 1/3 the ultimate axial strength. The fatigue constant a is set so that the damage parameter is equal to unity at the ultimate monotonic rotation, which is calculated from section analysis and is described in the previous subsection.

Predictive equations are derived for the ends of all members and the coefficients for the predictive equations are provided in Appendix A3. The member rotational fatigue has the greatest scatter of all of the damage measures and is the most difficult to approximate with predictive equations. The best estimate fatigue damage at the base of the ground floor column and end of the 1st floor beam is shown in Figure 8.20 and Figure 8.21 respectively. These figures indicate that the predictive equations may over-estimate the damage in the members for earthquakes with magnitude over M_w 6.0 and source-to-site distances less than 30km. The residuals have approximately zero mean and are normally distributed (Figure 8.22 and Figure 8.23). The dispersion in the residuals appears to reduce with distance, although this could be due to a lack of data at shorter distances.

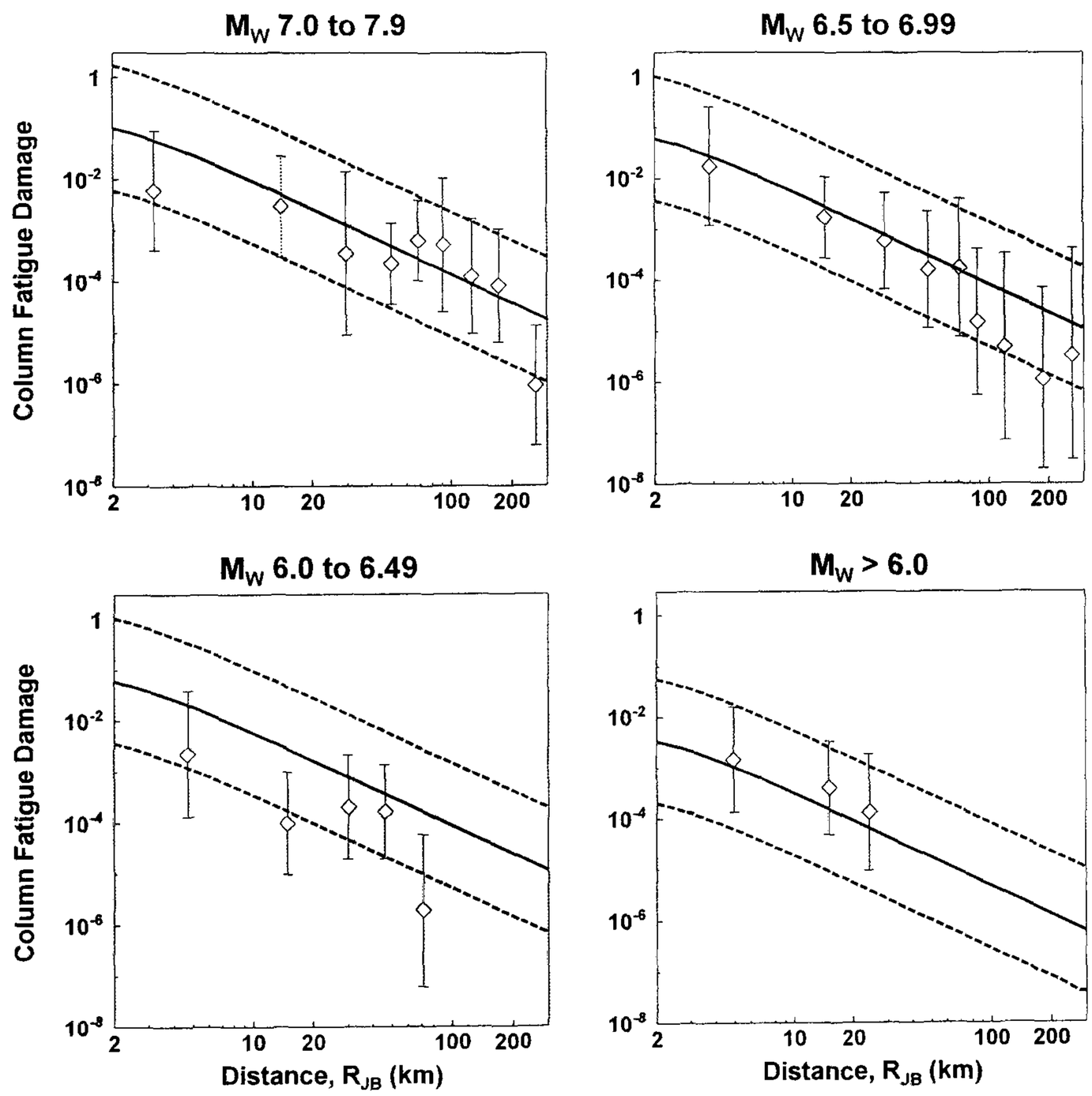


Figure 8.20. - Comparison of the fatigue damage of the base of the outer ground floor column predicted by the predictive equations (solid line-median; plus and minus one standard deviation-dashed) and those of the measured data binned by magnitude and distance, adjusted to strike-slip and stiff soil using the coefficients of predictive equation (diamonds median, error bars plus minus one standard deviation).

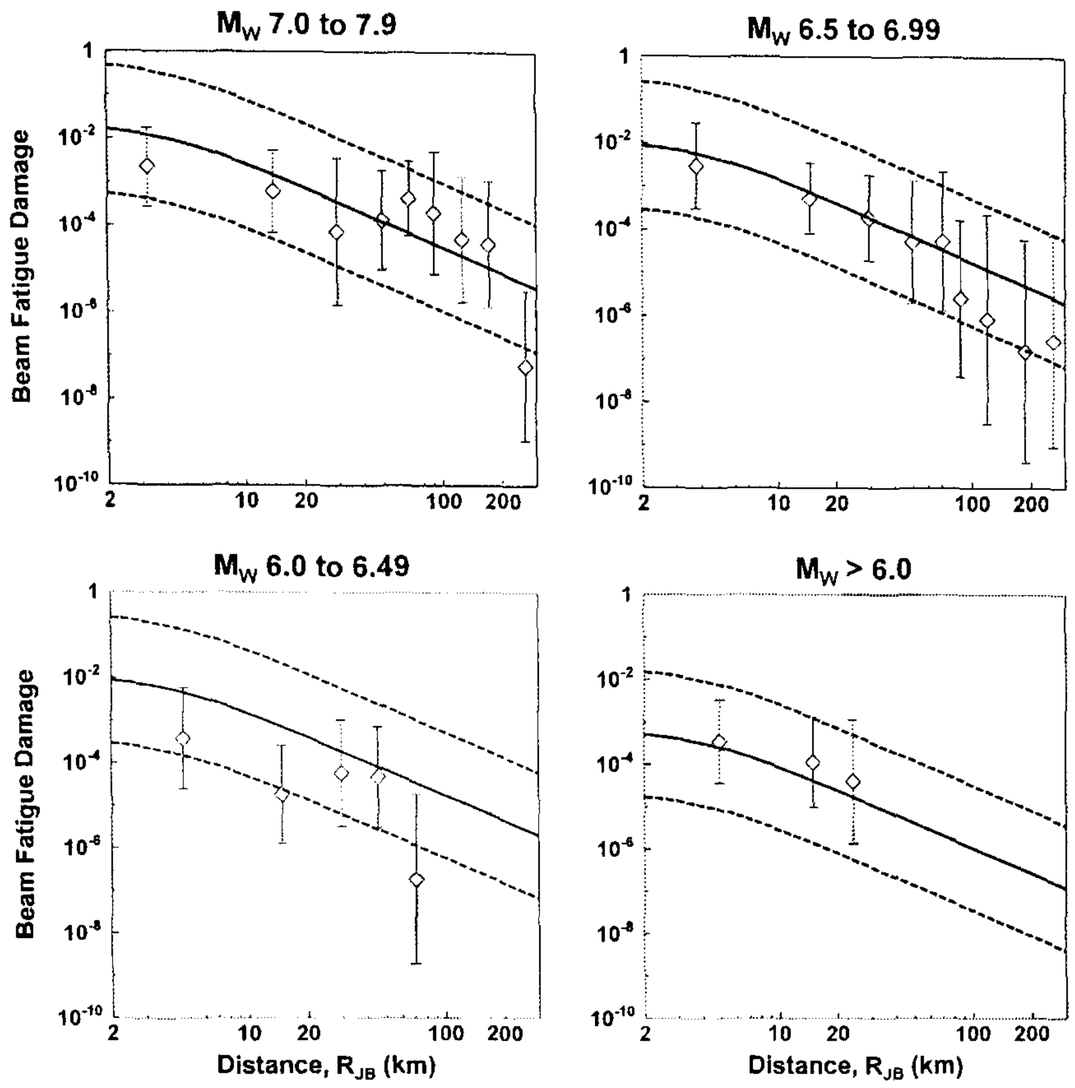


Figure 8.21. – As Figure 8.20 but for the outer end of the 1st floor beam at the edge of the structure.

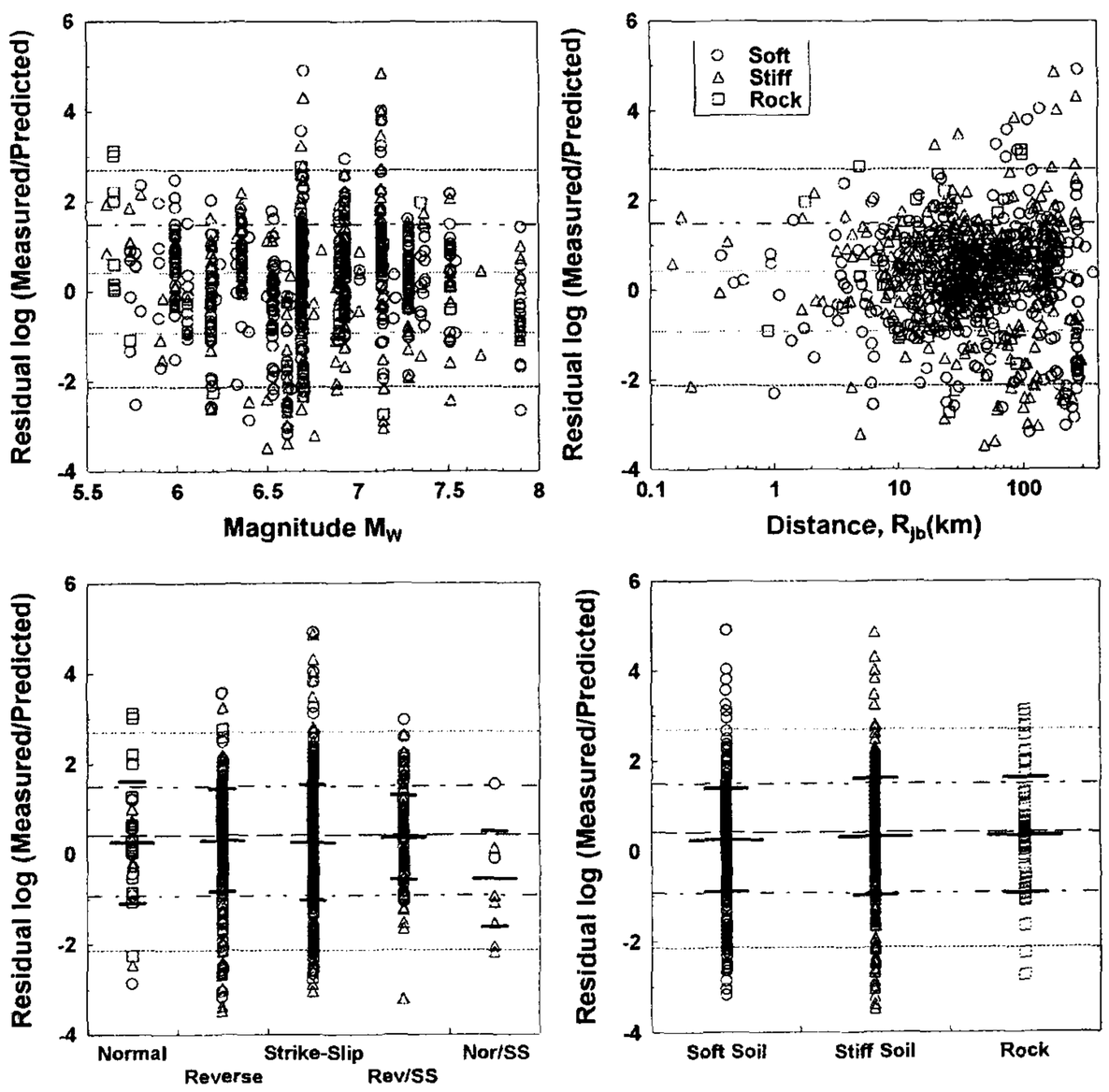


Figure 8.22. – Residuals for fatigue damage index of the base of the outer ground floor column in terms of earthquake magnitude (*top left*), source-to-site distance (*top right*), site classification (*lower right*) and rupture mechanism (*lower left*).

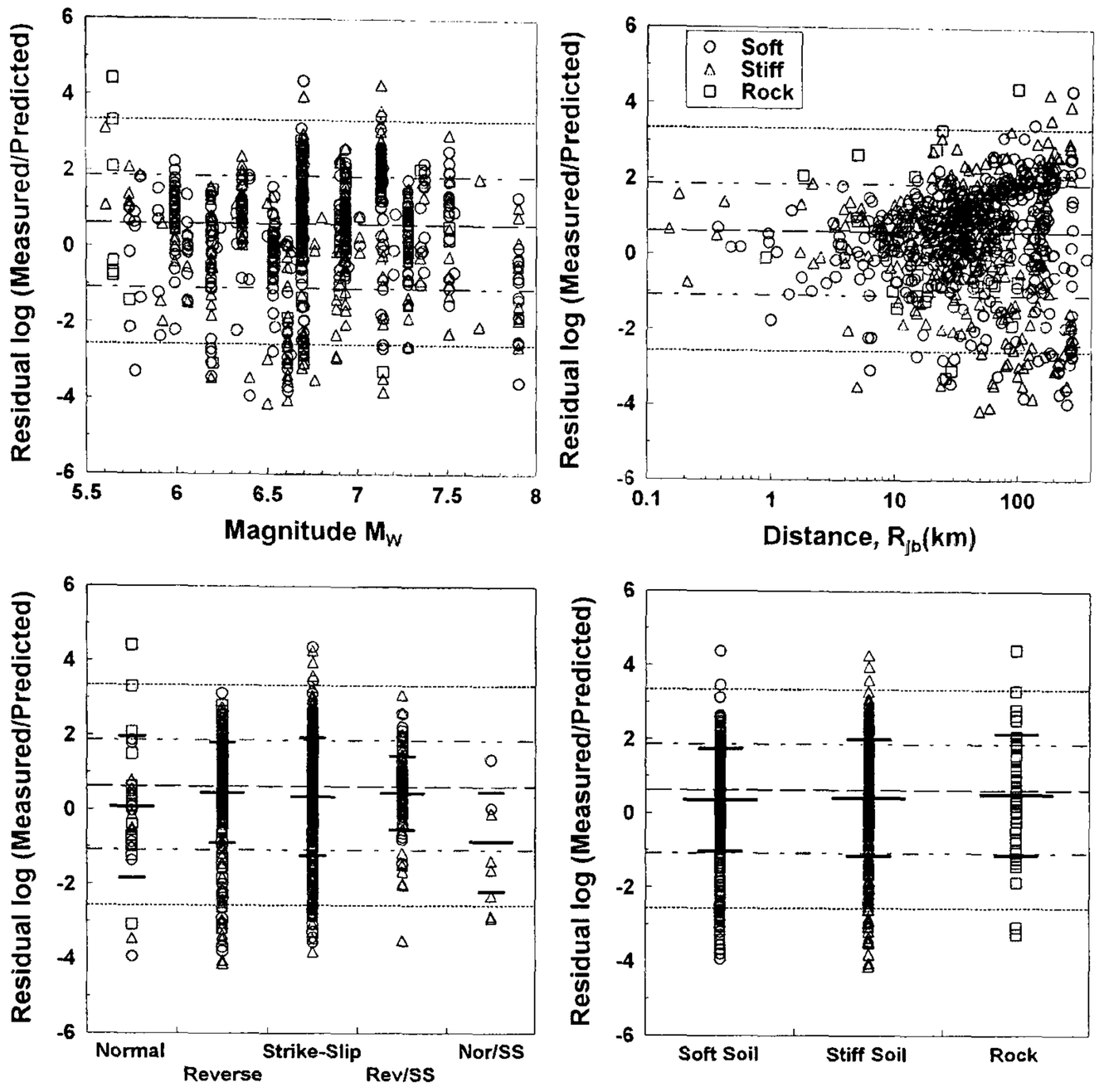


Figure 8.23 – Residuals for fatigue damage index of the outer end of the 1st floor beam at the edge of the structure in terms of earthquake magnitude (*top left*), source-to-site distance (*top right*), site classification (*lower right*) and rupture mechanism (*lower left*).

8.6.3 Spectral acceleration

Although not a robust damage measure, several scaling methods require estimates of the elastic spectral acceleration so this is predicted using the same data set used to derive predictive equations for the response of the wall frame structure (Figure 8.24 and Figure 8.25). The pseudo spectral acceleration is used as this is directly linked to the spectral displacement. As discussed in previous chapters, the pseudo spectral acceleration is essentially equal to the absolute spectral acceleration for damping levels less than about 20%.

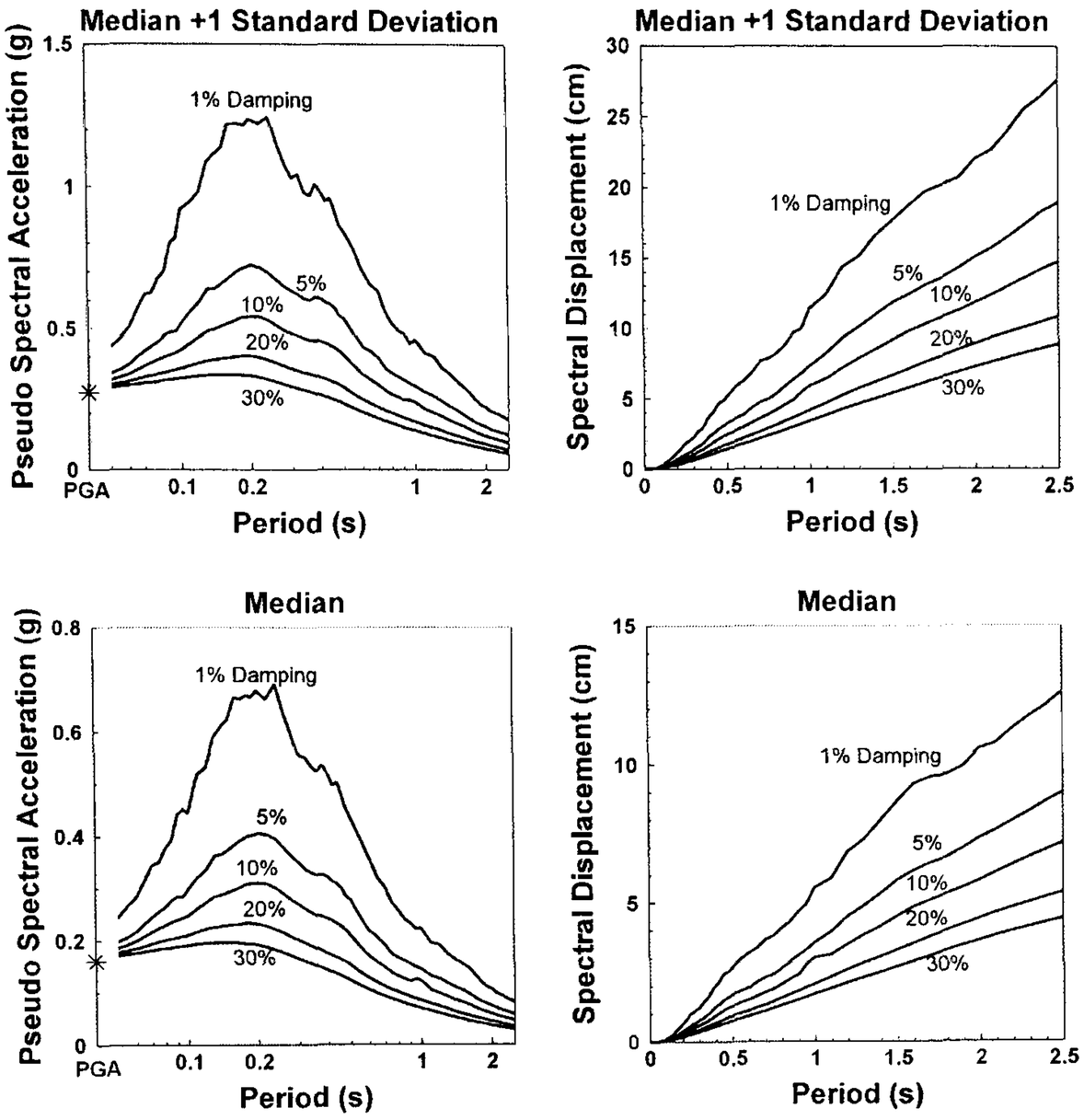


Figure 8.24. – Pseudo spectral acceleration and spectral displacement spectra predicted by the new equations for a M_W 7.0 strike-slip earthquake at 20km R_{jb} for a site with stiff soil.

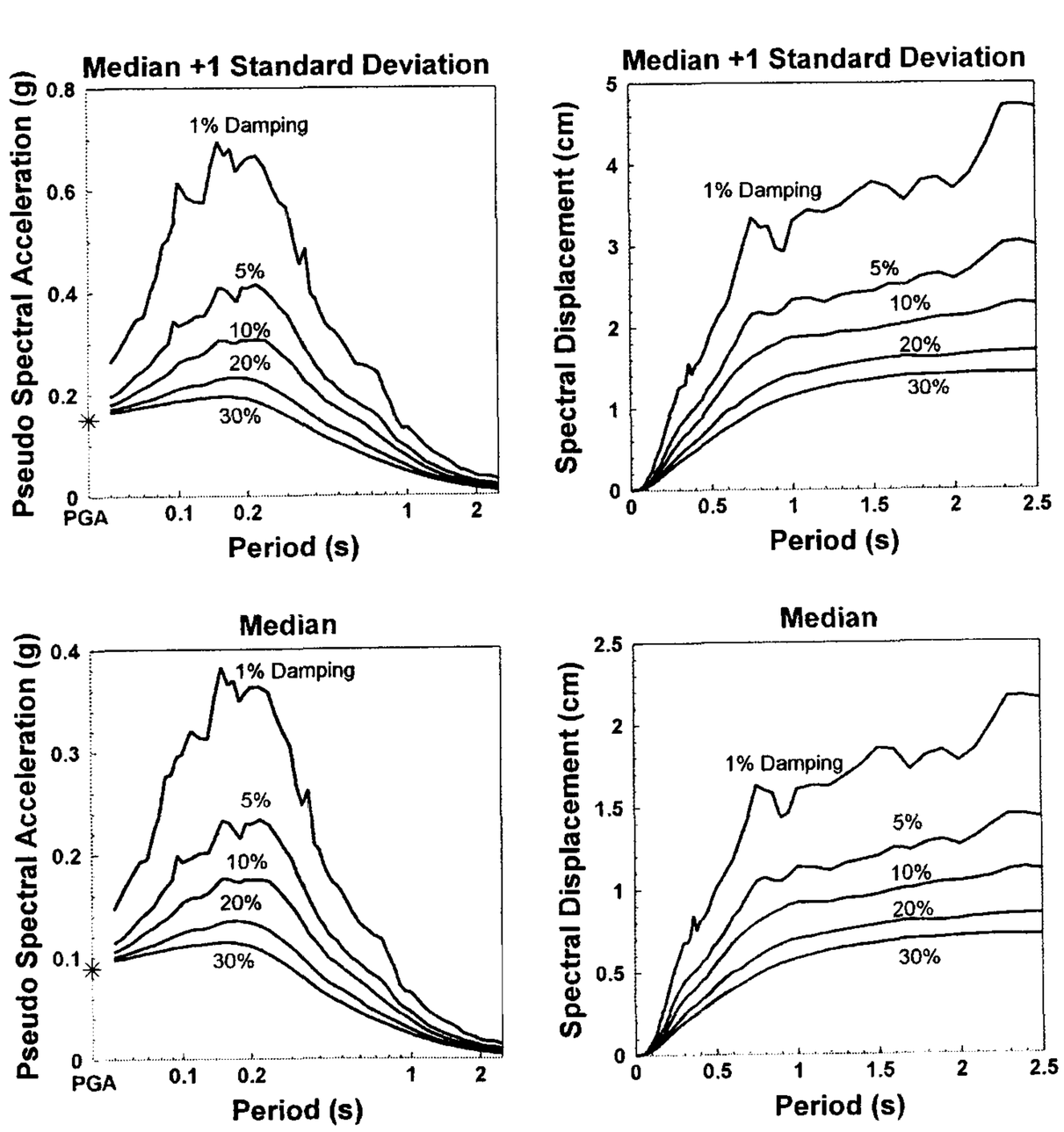


Figure 8.25. – Pseudo spectral acceleration and spectral displacement spectra predicted by the new equations for a M_W 5.5 strike-slip earthquake at 20km R_{jb} for a site with stiff soil.

The pseudo spectral accelerations predicted by the new predictive equations are compared with the predictions of equations derived by other researchers (Figure 8.26). The M_s used in the predictive equations derived by Bommer *et al.* (1998) have been converted to M_w using the equations of Ambraseys and Free (1997). Although the new equations generally have the same trends as the other equations there are significant differences in the predictions, which highlight the range of predictions possible with different datasets, functional forms and regression methods. This demonstrates the importance of deriving new predictions for this work where the dataset, functional form and regression method are fixed so that the only difference between the equations is the parameter to be predicted. A further check that the new equation makes reasonable predictions of the observed data is conducted by comparing the prediction against the observations binned by magnitude and distance (Figure 8.27 to Figure 8.29). The differences between the observed and predicted motions are essentially caused by the variability in the underlying ground motion; notice that the median amplitude of several of the bins are lower for larger magnitude earthquakes or greater distances. This level of variability also confirms the applicability of the methodology used in this work, which is able to determine the trends in the response by using a large number of ground motions.

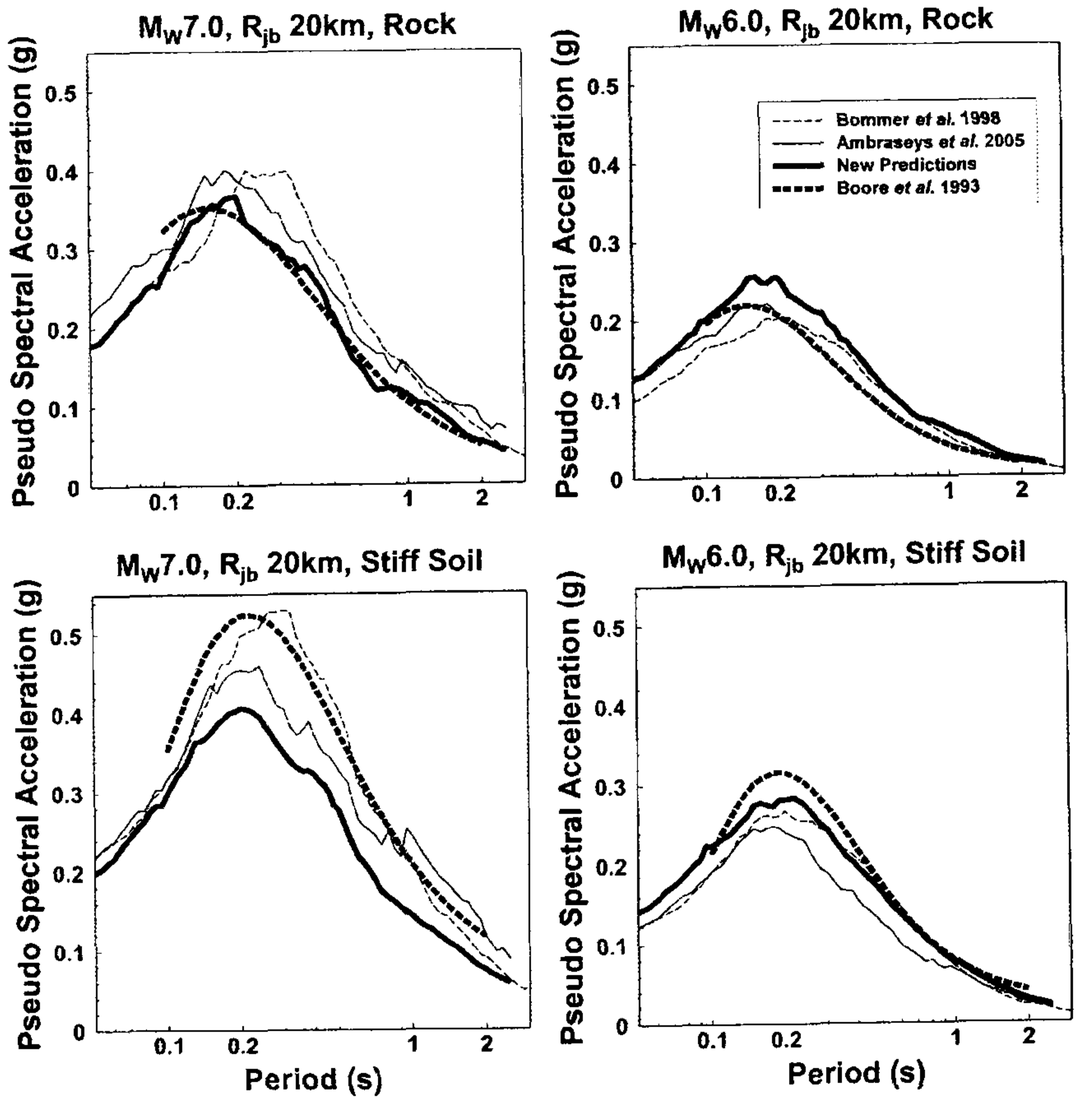


Figure 8.26. – Comparison of the prediction of pseudo spectral acceleration for the 5% damped spectrum from this work with the predictive equations of other researchers.

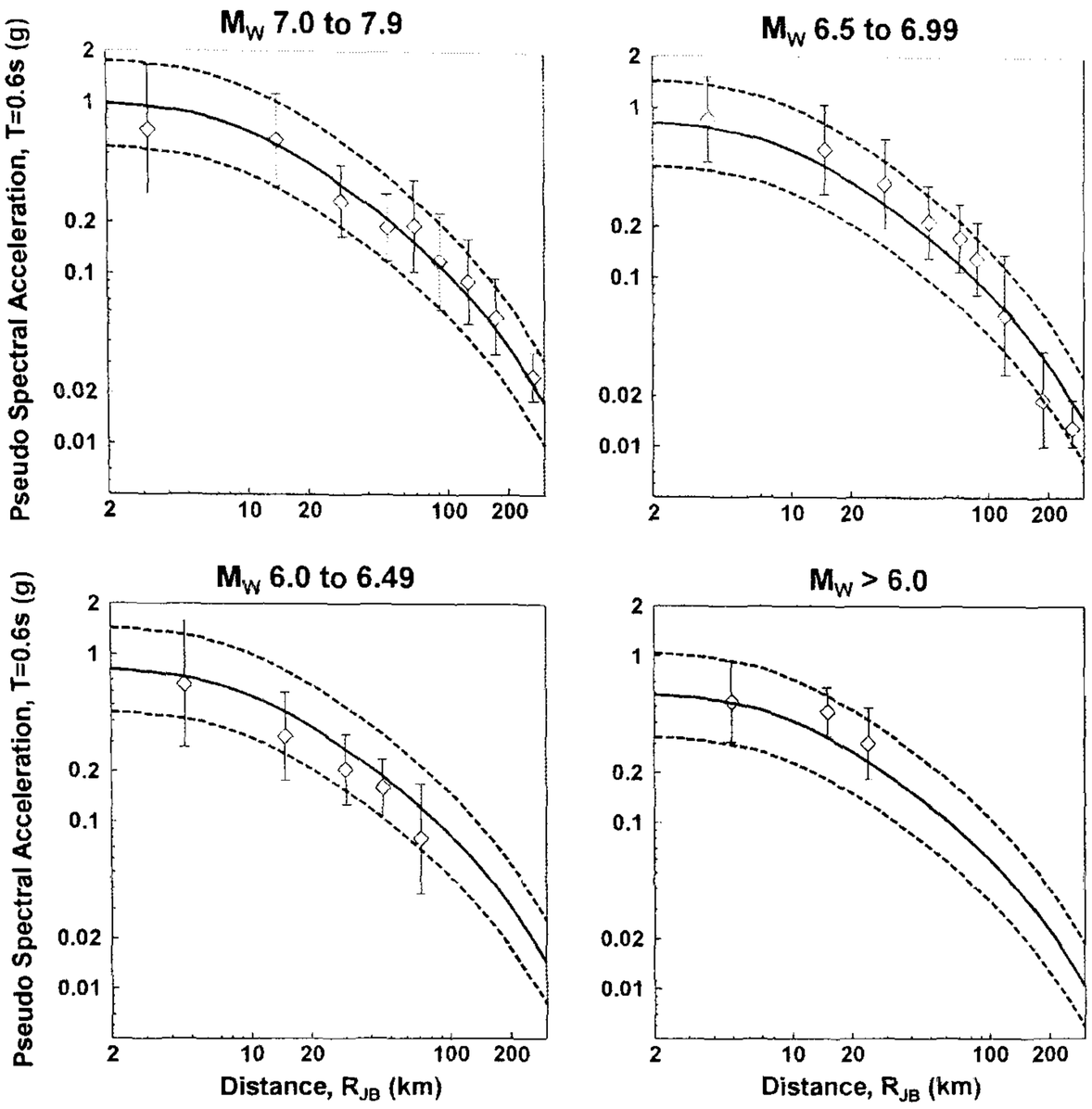


Figure 8.27. - Comparison of pseudo spectral acceleration for 5% damping at 0.2s period predicted by new predictive equations (smooth lines, solid line median, plus and minus one standard deviation dashed) and those of the observed data binned by magnitude and distance adjusted to strike-slip and stiff soil using the coefficients of predictive equation (diamonds median, error bars plus minus one standard deviation).

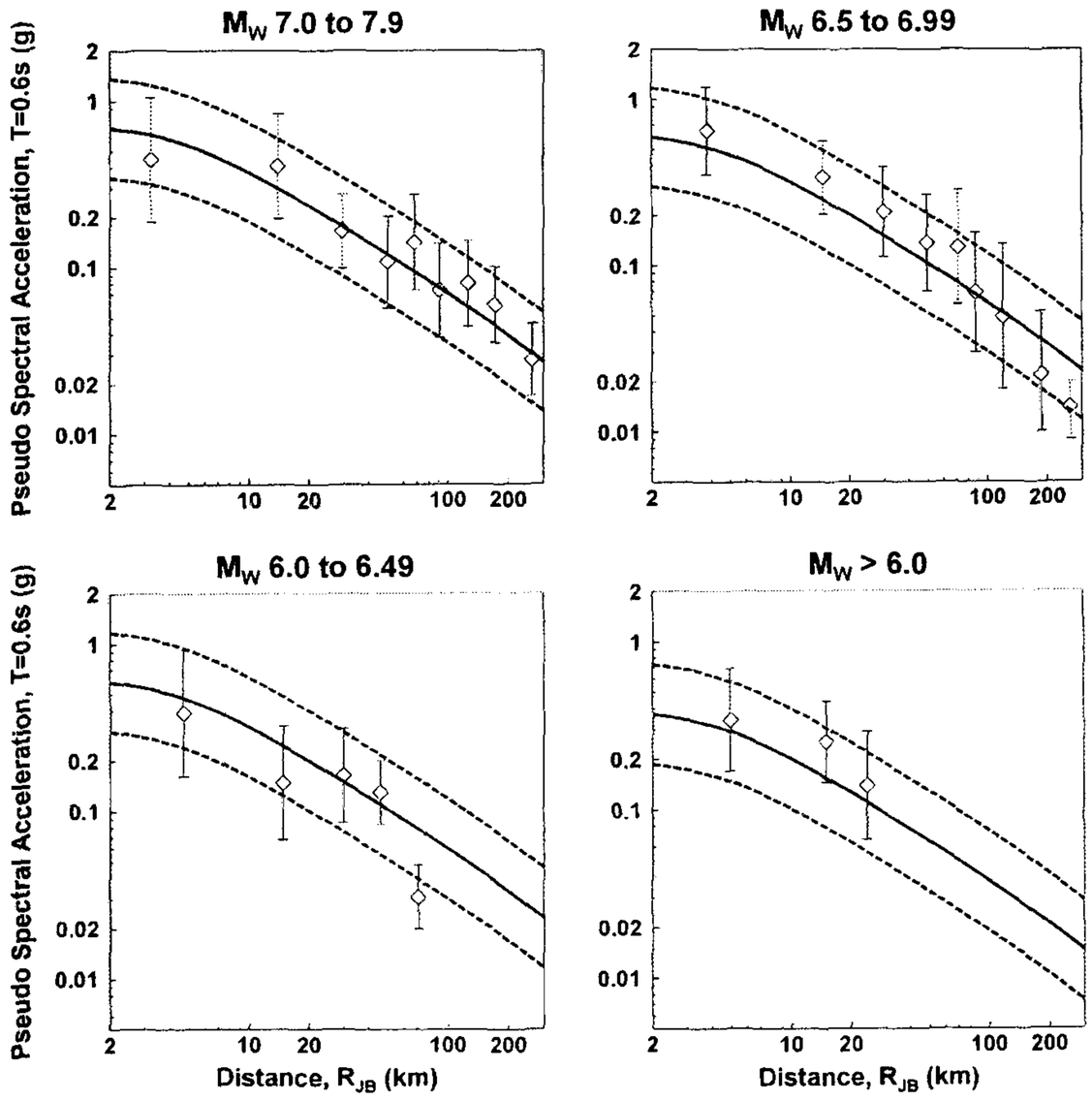


Figure 8.28. – As Figure 8.27 but for a pseudo spectral acceleration for 5% damping at 0.6s period.

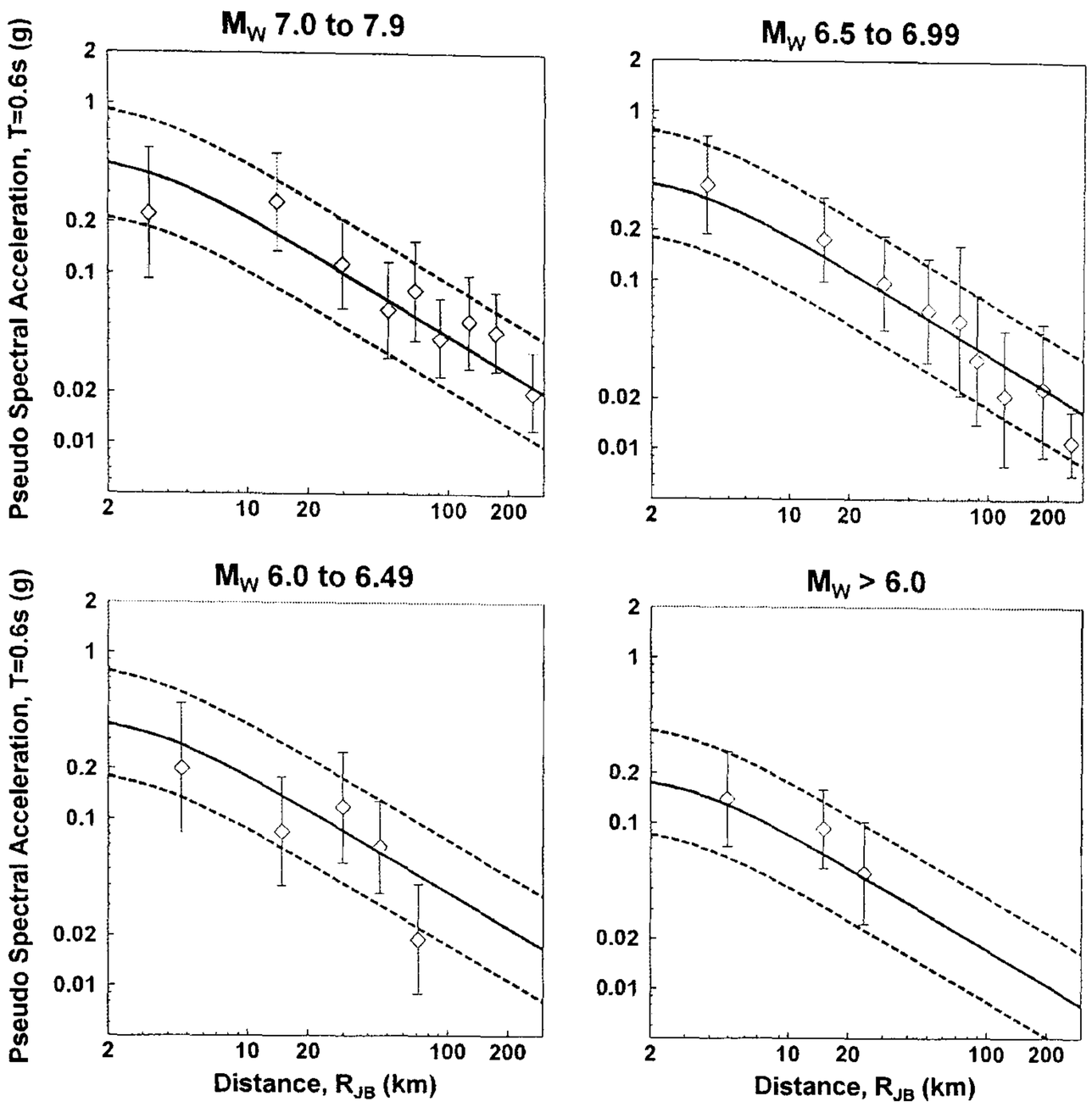


Figure 8.29. – As Figure 8.27 but for a pseudo spectral acceleration for 5% damping at 1.2s period.

8.7 Selecting and Scaling Accelerograms

8.7.1 Target Scenario

The structure used in this investigation has been designed to resist seismic actions in accordance with a modern design code and so genuinely strong ground-motions are required to generate non-linear response. The target scenario used for this work is an M_w 7.0 strike-slip earthquake at 5km distance from a site with soft soil conditions. Both the median and median-plus-one-standard-deviation target spectra are used to investigate the response of the structure with two different levels of loading. In practice the design scenario can be derived from either de-aggregating a probabilistic seismic hazard assessment or by conducting a deterministic seismic hazard assessment (e.g. McGuire 1995; Reiter 1990). The vertical component of the ground motion is not used in this study to ensure that the characteristics of the observed response are only caused by the horizontal component of the ground motion.

Abrahamson *et al.* (2003) point out that the standard deviation of the predictive equation for the target spectral acceleration should be reduced if records are to be used to derive fragility curves and are matched by linear scaling to the average spectral acceleration over a range of periods. This reduction is required to counteract the effect of double-counting the "peak-to-trough" variability in the acceleration spectra. The double counting arises because the peak-to-trough variability is present, firstly in the standard deviation of the response spectral ordinates of the target spectrum and, secondly, in the linearly scaled records used to match the target spectrum. However, as the aim of this study is not to develop fragility curves only the median response is considered, so no reduction factor is applied to the standard deviation as the peak-to-trough variability is counted once in the target response spectra.

8.7.2 Selection based on seismological characteristics

The first set of records consists of 25 accelerograms chosen to match the seismological characteristics of the scenario event. The number of available records from the NGA database is shown in Table 8.4. The 25 selected records are chosen from those recorded from earthquakes within ±0.2 magnitude units of the scenario event with soft or stiff soil site classification. The records are from within 10.35 km from the surface projection of the fault rupture and only the larger component, selected by the elastic spectral acceleration at the initial period of the structure, is used from each record. The selected records are given in Table 8.5. The spectral characteristics of the records are shown in Figure 8.30, which also confirms that these records have a good match to the median and median-plus-one-standard-deviation elastic spectral response in the period range of interest to this structure.

Table 8.4. – Number of records (each with two horizontal components) from the full NGA database within ±0.2 magnitude units of the scenario event

Site Class	R_{JB}<10km	R_{JB}<20km
Soft	9 (4)	17 (7)
Stiff	14 (6)	24 (12)
Rock	5 (3)	8 (4)

(Number in brackets is largest number of records from a single earthquake)

Table 8.5. – Records selected based on seismological characteristics

Year	Mw	Earthquake	Mechanism	Distance, R_{jb}, (km)	Station	Site Class	Record
1940	6.95	Imperial Valley-02	Strike-slip	6.09	El Centro Array #9	Soft	00006L
1976	6.80	Gazli, USSR	Reverse	3.92	Karakyr	Stiff	00126T
1989	6.93	Loma Prieta	Rev-Oblique	0.00	LGPC	Stiff	00779L
1989	6.93	Loma Prieta	Rev-Oblique	0.15	Corralitos	Stiff	00753T
1989	6.93	Loma Prieta	Rev-Oblique	3.85	BRAN	Stiff	00741L
1989	6.93	Loma Prieta	Rev-Oblique	7.58	Saratoga - Aloha Ave	Stiff	00802L
1989	6.93	Loma Prieta	Rev-Oblique	8.48	Saratoga - W Valley Coll.	Stiff	00803T
1989	6.93	Loma Prieta	Rev-Oblique	9.19	Gilroy - Gavilan Coll.	Stiff	00763T
1989	6.93	Loma Prieta	Rev-Oblique	8.65	Capitola	Soft	00752L
1989	6.93	Loma Prieta	Rev-Oblique	10.27	Gilroy - Historic Bldg.	Soft	00764T
1992	7.01	Cape Mendocino	Reverse	0.00	Cape Mendocino	Stiff	00825L
1992	7.01	Cape Mendocino	Reverse	0.00	Petrolia	Stiff	00828T
1992	7.01	Cape Mendocino	Reverse	7.88	Rio Dell Overpass - FF	Soft	00829T
1995	6.90	Kobe, Japan	Strike-slip	7.08	Nishi-Akashi	Stiff	01111L
1995	6.90	Kobe, Japan	Strike-slip	0.00	Takarazuka	Soft	01119L
1995	6.90	Kobe, Japan	Strike-slip	0.94	KJMA	Soft	01106L
1995	6.90	Kobe, Japan	Strike-slip	1.46	Takatori	Soft	01120L
1995	6.90	Kobe, Japan	Strike-slip	3.31	Port Island (0 m)	Soft	01114L
1999	7.14	Duzce, Turkey	Strike-slip	0.21	Lamont 1058	Stiff	01611T
1999	7.14	Duzce, Turkey	Strike-slip	3.93	Lamont 375	Stiff	01617L
1999	7.14	Duzce, Turkey	Strike-slip	4.17	Lamont 1059	Stiff	01612L
1999	7.14	Duzce, Turkey	Strike-slip	8.03	Lamont 531	Stiff	01618T
1999	7.13	Hector Mine	Strike-slip	10.35	Hector	Stiff	01787T
1999	7.14	Duzce, Turkey	Strike-slip	0.00	Duzce	Soft	01605L
1999	7.14	Duzce, Turkey	Strike-slip	9.15	Lamont 1062	Soft	01615T

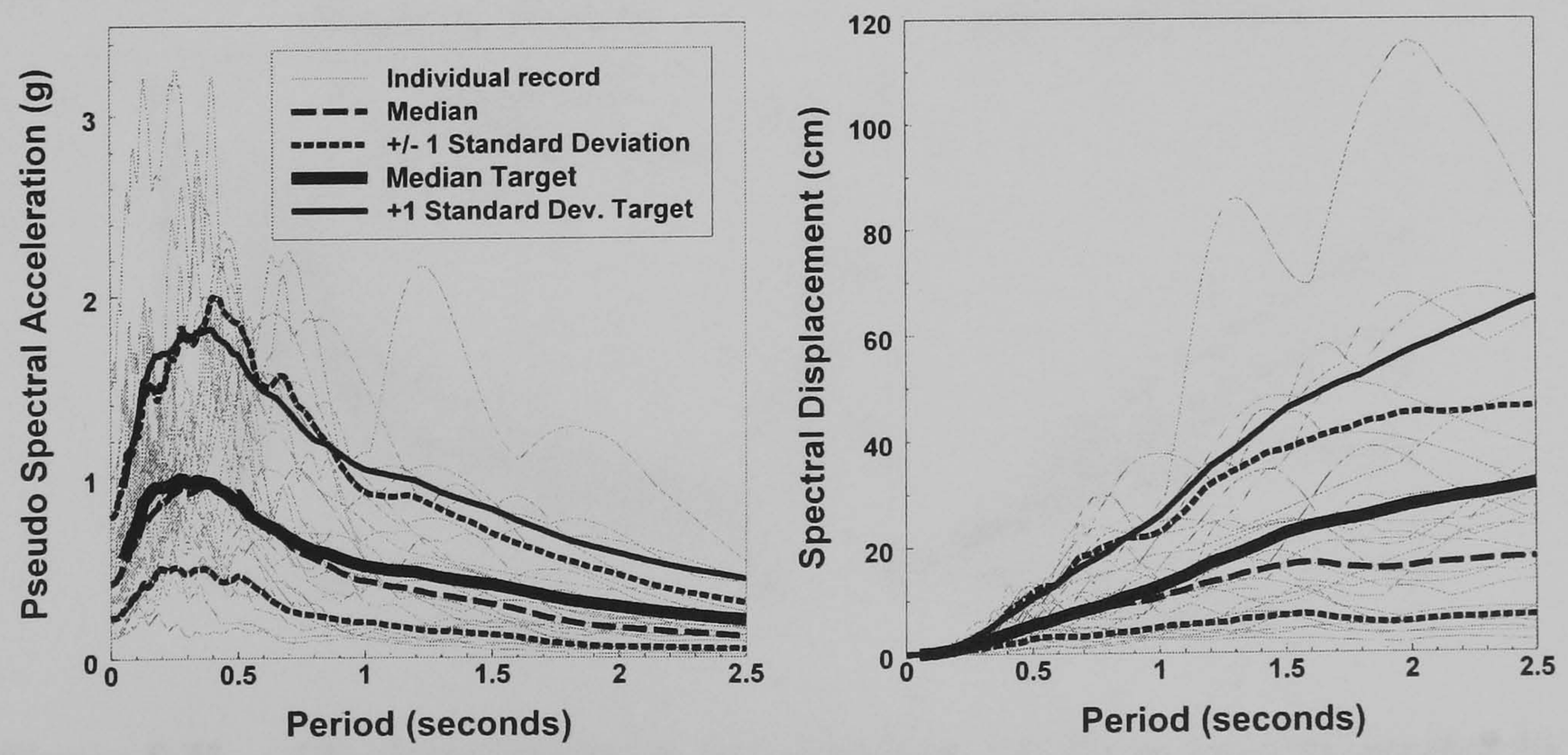


Figure 8.30. – 5% Damped response spectra for records selected on the basis of seismological characteristics

8.7.3 Linearly scaled to SA at the initial period of the structure

The second set of records is selected from earthquakes within 0.2 magnitude units of the scenario event. The records chosen have the lowest RMS difference in the normalized spectral acceleration (ΔSAn_{RMS}, see equation 6.10) to the 5% damped target spectrum between 0.05 to 2.5s periods (Table 8.6). Initial selection of the records based on spectral shape is conducted to avoid the bias that can be encountered if records are selected that consistently have a peak or a trough at the initial period of the structure (e.g. Watson-Lamprey and Abrahamson 2006b).

For this scaling definition the records are linearly scaled so that they match the median and median-plus-one-standard-deviation 5% damped target spectra at the initial period of the structure (0.56s). As the records have been chosen based on spectral shape, the average spectra also have a reasonable match with the target spectra (Figure 8.31).

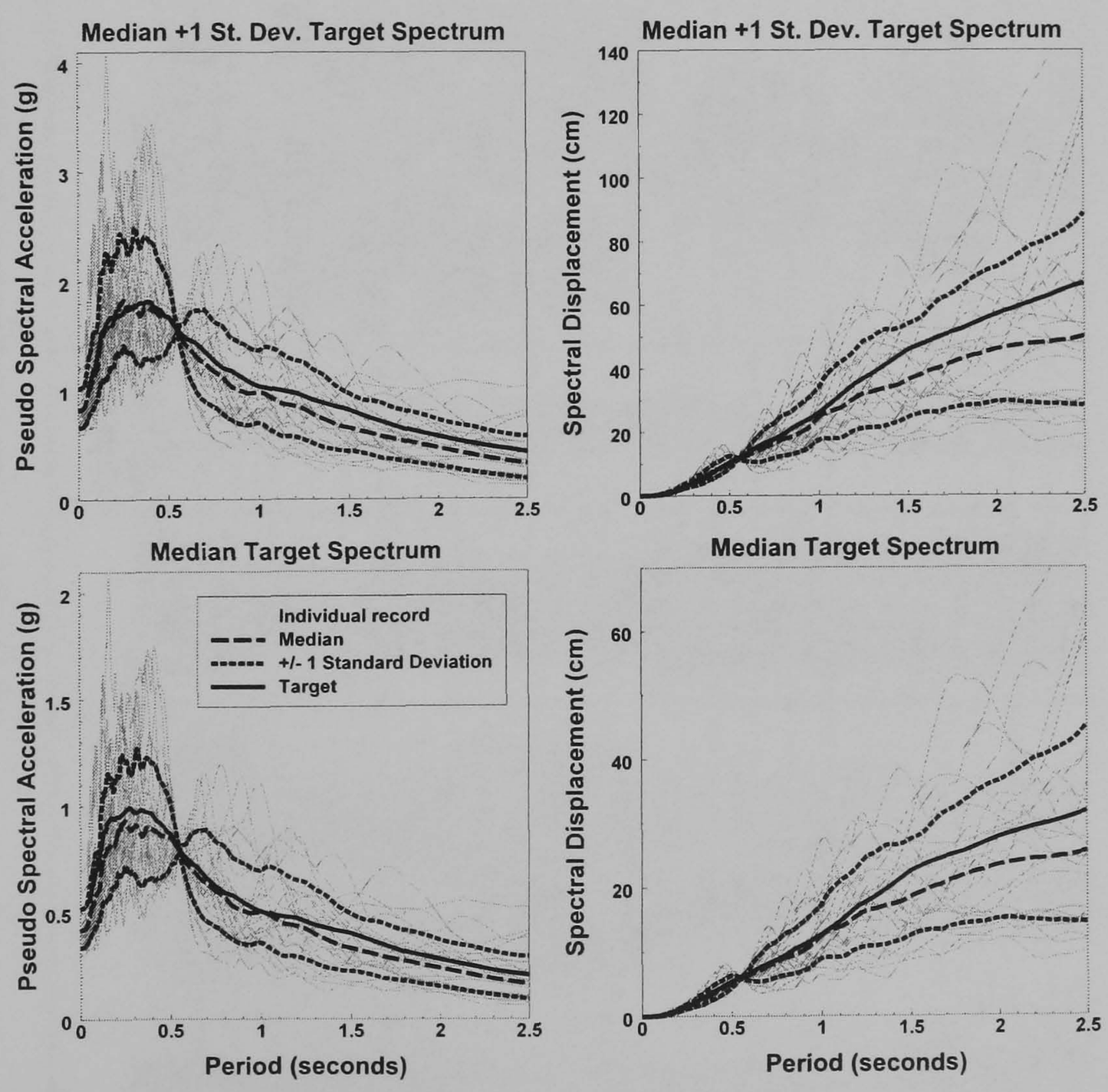


Figure 8.31. – 5% damped-elastic spectral response from records selected by spectral shape and magnitude, scaled to the 5% damped target spectral acceleration at the initial period of the structure. Median target spectra (*lower*) and median-plus-one-standard-deviation (*upper*)

Table 8.6. – Records selected by spectral shape and magnitude

Year	Mw	Earthquake	Mechanism	Distance, Rjb, (km)	Station	Site Class	Accelerogram	Scale Factor Initial SA		Scale Factor Average SA	
								Median	+1SD	Median	+1SD
1940	6.95	Imperial Valley-02	Strike-Slip	6.1	El Centro Array #9	Soft	00006L	1.040	2.044	1.329	2.612
1940	6.95	Imperial Valley-02	Strike-Slip	6.1	El Centro Array #9	Soft	00006T	1.423	2.795	1.857	3.652
1980	6.9	Irpinia, Italy-01	Normal	6.8	Sturno	Rock	00292L	1.295	2.545	1.571	3.067
1989	6.93	Loma Prieta	Rev/SS	19.9	Anderson Dam (L Abut)	Stiff	00740T	4.696	9.228	5.749	11.34
1989	6.93	Loma Prieta	Rev/SS	10.3	Gilroy - Historic Bldg.	Soft	00764T	1.464	2.877	1.924	3.762
1989	6.93	Loma Prieta	Rev/SS	30.6	Palo Alto - 1900 Embarc.	Soft	00786L	2.422	4.758	2.484	4.856
1989	6.93	Loma Prieta	Rev/SS	72.9	Piedmont Jr High	Rock	00788L	4.580	9.000	6.485	12.64
1989	6.93	Loma Prieta	Rev/SS	23.9	Sunnyvale - Colton Ave.	Soft	00806L	1.793	3.524	2.310	4.551
1992	7.01	Cape Mendocino	Reverse	40.2	Eureka - Myrtle & West	Soft	00826L	2.915	5.727	3.004	5.851
1992	7.01	Cape Mendocino	Reverse	40.2	Eureka - Myrtle & West	Soft	00826T	1.829	3.593	2.892	5.657
1992	7.01	Cape Mendocino	Reverse	16.0	Fortuna - Fortuna Blvd	Stiff	00827T	3.408	6.697	3.585	7.065
1992	7.01	Cape Mendocino	Reverse	16.0	Fortuna - Fortuna Blvd	Stiff	00827L	3.690	7.250	3.487	6.884
1992	7.01	Cape Mendocino	Reverse	7.9	Rio Dell Overpass - FF	Soft	00829L	1.069	2.100	1.156	2.271
1995	6.9	Kobe, Japan	Strike-Slip	24.9	Abeno	Soft	01100L	3.098	6.088	2.406	4.715
1995	6.9	Kobe, Japan	Strike-Slip	22.5	Kakogawa	Soft	01107T	1.741	3.421	1.486	2.890
1995	6.9	Kobe, Japan	Strike-Slip	0.9	Kobe University	Rock	01108T	1.972	3.876	1.488	2.919
1995	6.9	Kobe, Japan	Strike-Slip	7.1	Nishi-Akashi	Stiff	01111T	1.030	2.024	0.909	1.781
1995	6.9	Kobe, Japan	Strike-Slip	0.0	Takarazuka	Soft	01119L	0.558	1.096	0.627	1.240
1999	7.14	Duzce, Turkey	Strike-Slip	12.0	Bolu	Soft	01602L	0.481	0.945	0.603	1.175
1999	7.14	Duzce, Turkey	Strike-Slip	9.2	Lamont 1062	Soft	01615L	4.298	8.446	4.635	9.013
1999	7.13	Hector Mine	Strike-Slip	64.1	Baker Fire Station	Soft	01766T	4.868	9.565	4.557	8.877
1999	7.13	Hector Mine	Strike-Slip	64.1	Baker Fire Station	Soft	01766L	2.523	4.957	2.897	5.688
1999	7.13	Hector Mine	Strike-Slip	65.0	Fort Irwin	Soft	01783T	3.067	6.027	3.024	5.988
1999	7.13	Hector Mine	Strike-Slip	10.4	Hector	Stiff	01787L	1.932	3.797	2.133	4.183
1999	7.13	Hector Mine	Strike-Slip	31.1	Joshua Tree	Stiff	01794L	2.709	5.323	2.972	5.859

8.7.4 Linearly scaled average SA

The third set of records are selected and scaled so that the median spectral acceleration matches the target spectral acceleration in the period range of interest to this structure. The same seed records are used as those scaled to the initial period of the structure (Table 8.6). Linear scaling of the records was conducted using the solver function in Excel to minimize the RMS of the SA for spectral points at periods between 0.25s and 1.2s for all records, whilst ensuring the median spectral acceleration of the records at any point in this period range did not fall below 5% of the target spectrum.

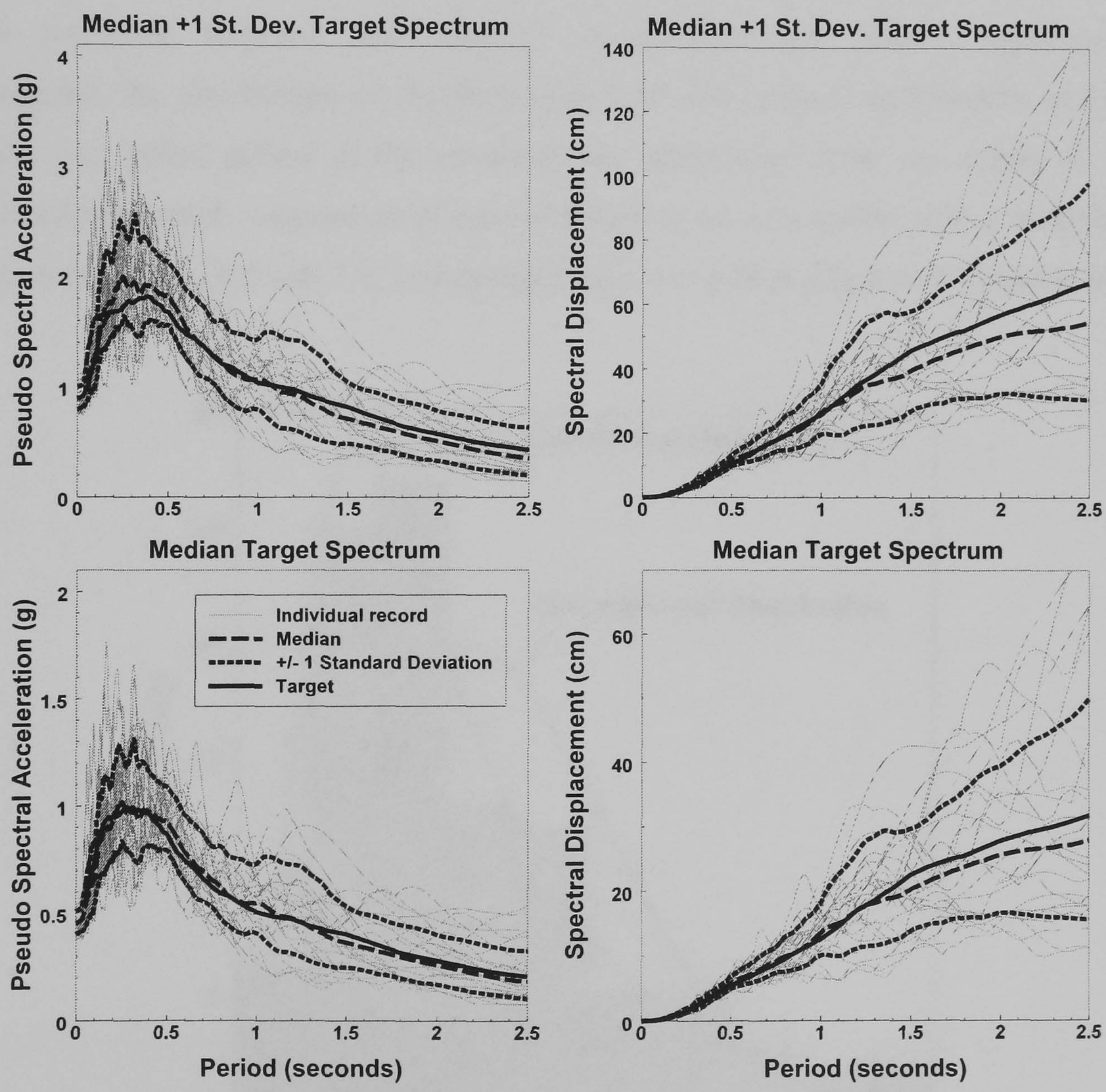


Figure 8.32. – 5% damped elastic spectral response from records linearly scaled to match to the 5% damped target spectral acceleration between 0.5 and 1.2s. Median target spectra (*lower*) and median-plus-one-standard-deviation (*upper*)

8.8 Mean vs. Median

Most design codes require that accelerograms are scaled so that the average of their response spectra matches or exceeds the target spectrum. Many codes also permit the average structural response to be taken. However, there are many different ways to measure the average response and in many cases the engineer must decide which measure of average should be used. From presentations by and discussions with the US code drafters (e.g. Kircher, 2005), it is clear that they intended the arithmetic mean to be used; the mean is also specified by Eurocode 8 (CEN 2004). However, most predictive equations used to derive the target spectra assume a log-normal distribution, so the use of the median (log average) is appropriate. To illustrate that both structural response and spectral accelerations are indeed log-normally distributed, the distribution of the peak roof drift and spectral acceleration at 0.56s period (the initial period of the structure) are determined from the action of 100 unscaled horizontal components of accelerograms from earthquakes with a magnitude range between M_w 6.5 and 7.0, and distance R_{jb} 0 to 15.5km (Figures 8.33 and 8.34).

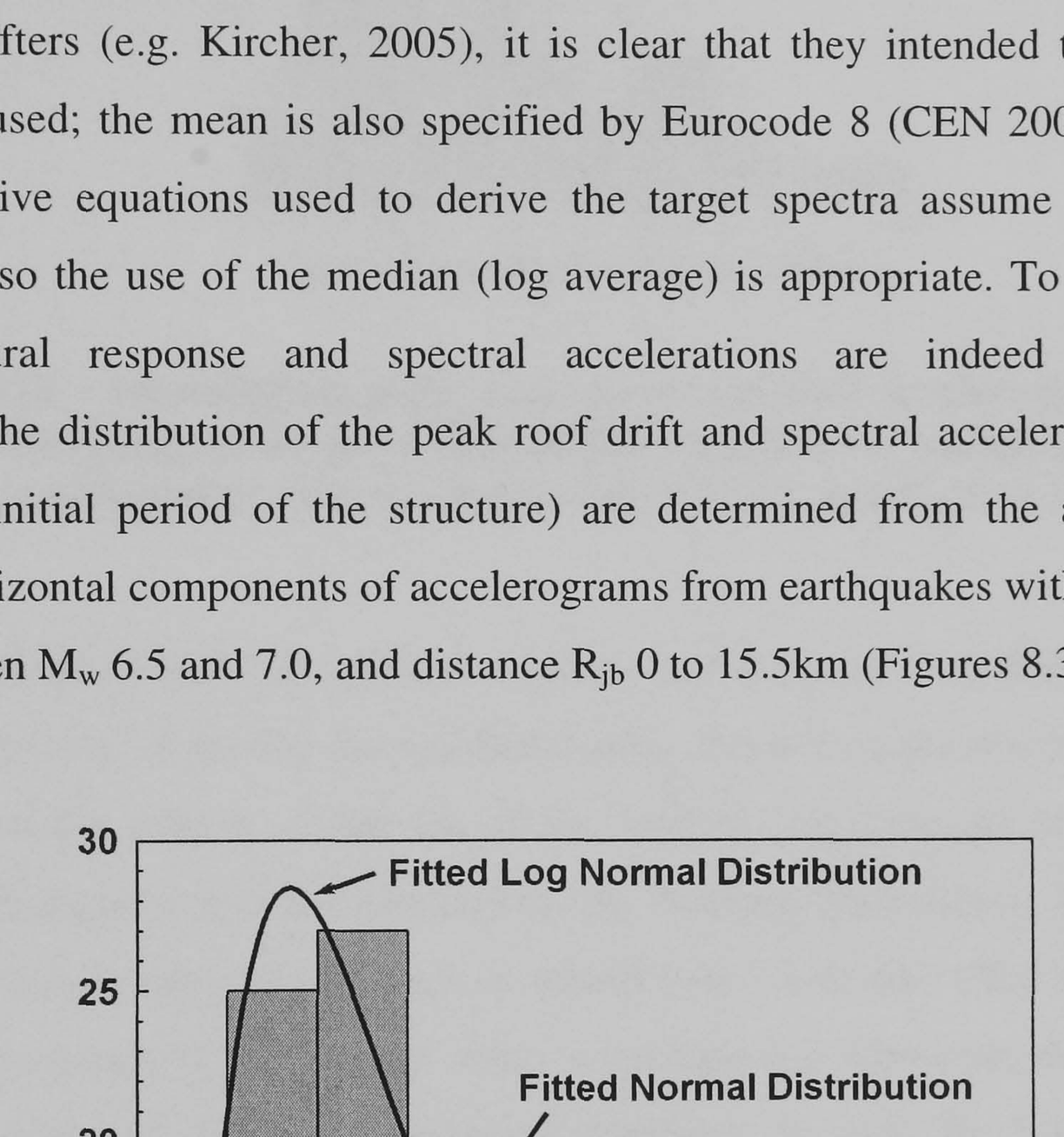


Figure 8.33. – Distribution of peak roof drift of 8-storey regular wall-frame structure under the action of 100 unscaled horizontal accelerograms from earthquakes with magnitude M_w 6.5 -7.0 and R_{jb} 0 to 15.5km.

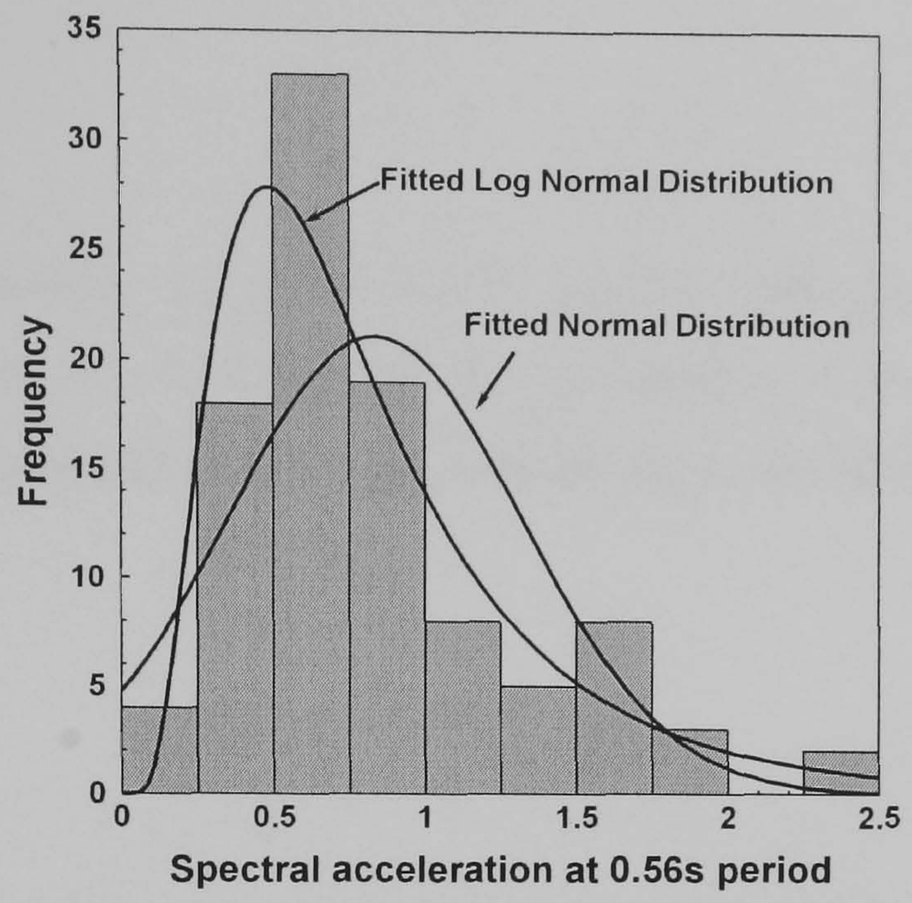


Figure 8.34. – Distribution of the peak elastic spectral acceleration at 0.56s period (5% damping) under the action of 100 unscaled horizontal accelerograms from earthquakes with magnitude M_w 6.5 -7.0 and R_{jb} 0 to 15.5km

The distributions of both the spectral response and the peak roof drift have a shape more characteristic of the log-normal distribution rather than the normal distribution. This confirms the validity of the use of the median (log average) in this work for scaling accelerograms and for interpreting the response parameters. The use of the arithmetic mean in engineering practice would only be strictly valid if the response parameters are normally distributed, which is not the case. However, the consequence of this issue is reduced as a consistent definition is used for both scaling the accelerograms and for measuring the response. Essentially using the mean rather than the median decreases the applied loading but increases the estimate of the observed response.

8.9 Response from Scaled Records

Different response measures are used to compare the response of the wall-frame structure under the action of records selected and scaled using different methods.

The standard error of the estimate (SEE) is used to measure the level of confidence that can be attributed to a result obtained from a sample of data:

$$SEE = \frac{\sigma}{\sqrt{N_{obs}}} \tag{8.5}$$

where σ is the standard deviation of the sample and N_{obs} is the number of observations. This can be re-arranged to find the number of observations required to give the required standard error given the standard deviation of the sample:

$$N_{obs} = \left(\frac{\sigma}{SEE}\right)^2 \tag{8.6}$$

This equation can be used to determine the number of records required to predict a given measure of structural response to a required accuracy, SEE, given the standard deviation of the response, σ. However, this equation cannot determine if the median value of the sample is biased. A biased estimate is defined as an estimate that does not predict the median (or other target percentile) response of the structure under the action of a large number of unscaled accelerograms consistent with the target scenario (M, D, site class). The bias of the estimate is determined in this work by comparing the response predicted by equations derived from regression of the response of the structure under the action of 1656 unscaled accelerograms with the response of the structure from the selected and scaled accelerograms.

8.9.1 Peak drift

The peak roof drift and inter-storey drift of the structure is measured under the action of the accelerograms selected and linearly scaled using the different methods described in the previous sub-sections. These are then compared with the estimates obtained from the predictive equations derived earlier in this chapter (Figures 8.35 and 8.37, Tables 8.37 to 8.10). All scaling methods can be used to estimate the expected median target drift given by the predictive equations (Figures 8.35 and 8.37). As the structure remains essentially linear for the median design scenario, the good agreement between the different methods could be expected. However, the peak roof drift and inter-storey drift of the upper floors is consistently under-estimated by the analysis using records selected and scaled to the elastic response spectrum for the median-plus-one-standard-deviation target scenario (Figures 8.35 and 8.37). This

shows that it can be unconservative to use the elastic response spectra to select and scale ground motions for use in an inelastic analysis of this type of MDOF structure. The difference in response could have several different causes including:

- differences between inelastic and elastic response at higher load levels
- higher mode or travelling wave effects in the upper storeys
- the lower standard deviation of the elastic spectral acceleration than the peak response of the MDOF structure

This study confirms the findings of earlier researchers (e.g. Shome *et al.* 1998) that the standard deviation of the response, and hence the number of records required to predict the response to a given level of confidence, is reduced by scaling the ground motions to the elastic spectral acceleration at the initial period of the structure. However, this study also shows that further reduction can be achieved by matching the spectral acceleration on average over a range of periods. The number of records to obtain an estimate of peak drift to ±5% (measured on a log scale) accuracy at 1 standard deviation confidence reduces by a factor of about 4 when records are scaled to the initial period of the structure. This reduces by a further factor of about 3 when records are selected and scaled to the average spectral acceleration over a range of periods. This is particularly useful as it reduces the number of records required to estimate the response to this confidence level from 50 unscaled records to 5 records scaled to the average spectral acceleration.

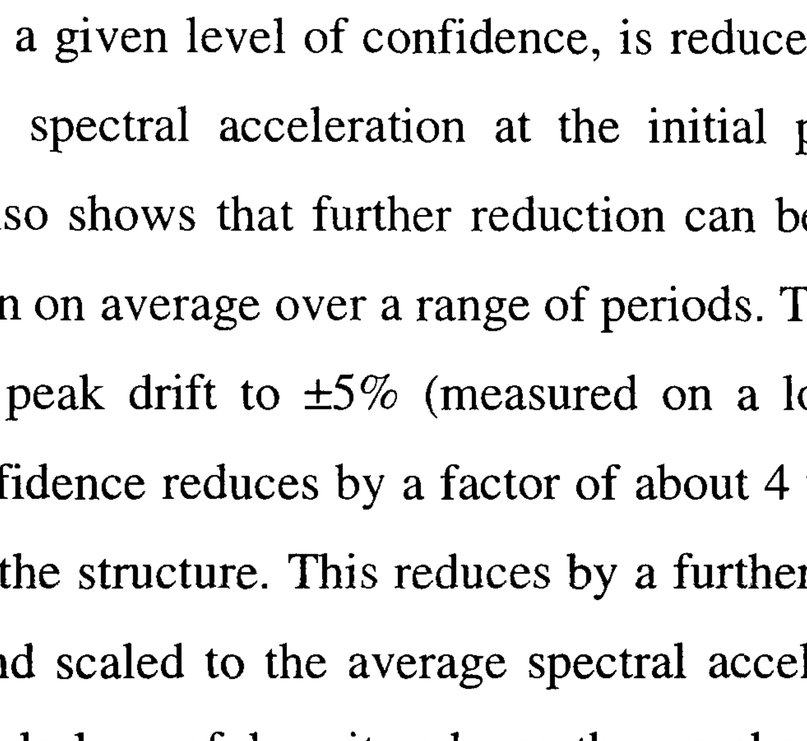


Figure 8.35. – Peak roof drift from records selected and scaled based on seismological characteristics, SA at the initial period, SA over a range of periods. Error bars show median and ±1 standard deviation. Dashed lines show drift predicted by regression of 1656 unscaled MDOF time-history analyses.

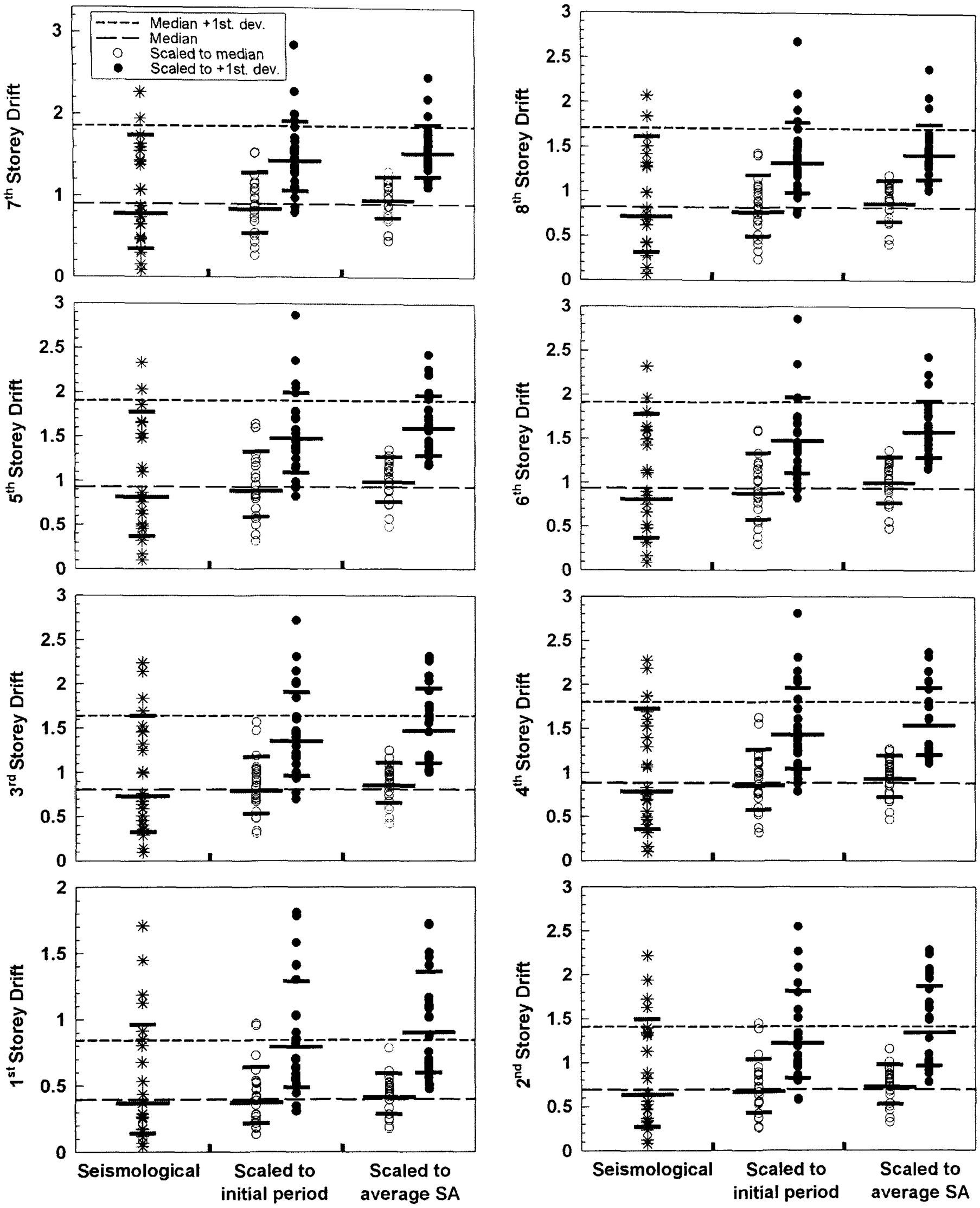


Figure 8.36. – Peak inter-storey drift from records selected and scaled based on seismological characteristics, SA at the initial period, SA over a range of periods. Error bars show median and ±1 standard deviation. Dashed lines show drift predicted by regression of 1656 unscaled MDOF time-history analyses.

Table 8.7. – Statistics of peak roof drift predicted from suites of records selected and linearly scaled using different criteria.

Scale Method	Regression (Unscaled)	Seismological (Unscaled)	Initial SA (5%) Median	Initial SA (5%) Median +1St. Dev.	Average SA (5%) Median	Average SA (5%) Median +1St. Dev.
Median	0.758	0.673	0.723	1.272	0.803	1.376
1St Dev. (log)	0.316	0.354	0.182	0.146	0.113	0.109
Median +1St.Dev.	1.572	1.522	1.099	1.780	1.043	1.769
No. Records	834	25	25	25	25	25
SEE at 1St.Dev.	1.1%	7.1%	3.6%	2.9%	2.3%	2.2%
No. Records for +/-10% (log) at 1St.Dev. confidence	10	13	3	2	1	1
No. Records for +/-5% (log) at 1St.Dev. confidence	40	50	13	8	5	5

Table 8.8. – Statistics of peak inter-storey drift at the 8th storey, predicted from suites of records selected and linearly scaled using different criteria.

Scale Method	Regression (Unscaled)	Seismological (Unscaled)	Initial SA (5%) Median	Initial SA (5%) Median +1St. Dev.	Average SA (5%) Median	Average SA (5%) Median +1St. Dev.
Median	0.825	0.715	0.769	1.324	0.869	1.419
1St Dev. (log)	0.316	0.354	0.188	0.129	0.115	0.095
Median +1St.Dev.	1.709	1.616	1.187	1.780	1.131	1.764
No. Records	834	25	25	25	25	25
SEE at 1St.Dev.	1.1%	7.1%	3.8%	2.6%	2.3%	1.9%
No. Records for +/-10% (log) at 1St.Dev. confidence	10	13	4	2	1	1
No. Records for +/-5% (log) at 1St.Dev. confidence	40	50	14	7	5	4

Table 8.9. – Statistics of peak inter-storey drift at the 6th storey, predicted from suites of records selected and linearly scaled using different criteria.

Scale Method	Regression (Unscaled)	Seismological (Unscaled)	Initial SA(5%) Median	Initial SA(5%) Median +1St. Dev.	Average SA(5%) Median	Average SA(5%) Median +1St. Dev.
Median	0.931	0.806	0.876	1.472	0.994	1.576
1St Dev. (log)	0.313	0.343	0.183	0.126	0.113	0.088
Median +1St.Dev.	1.914	1.777	1.334	1.968	1.288	1.931
No. Records	834	25	25	25	25	25
SEE at 1St.Dev.	1.1%	6.9%	3.7%	2.5%	2.3%	1.8%
No. Records for +/-10% (log) at 1St.Dev. confidence	10	12	3	2	1	1
No. Records for +/-5% (log) at 1St.Dev. confidence	39	47	13	6	5	3

Table 8.10. – Statistics of peak inter-storey drift at the 1st storey, predicted from suites of records selected and linearly scaled using different criteria.

Scale Method	Regression (Unscaled)	Seismological (Unscaled)	Initial SA (5%) Median	Initial SA (5%) Median +1St. Dev.	Average SA (5%) Median	Average SA (5%) Median +1St. Dev.
Median	0.395	0.369	0.372	0.791	0.410	0.900
1St Dev. (log)	0.329	0.416	0.237	0.211	0.157	0.179
Median +1St.Dev.	0.843	0.963	0.641	1.286	0.590	1.359
No. Records	834	25	25	25	25	25
SEE at 1St.Dev.	1.1%	8.3%	4.7%	4.2%	3.1%	3.6%
No. Records for +/-10% (log) at 1St.Dev. confidence	11	17	6	4	2	3
No. Records for +/-5% (log) at 1St.Dev. confidence	43	69	22	18	10	13

8.9.2 Local element damage measures

Peak member end rotations

The rotational deformations at the ends of the beams of this wall frame structure govern the inter-storey and global drift. For this reason they follow the same trends as the inter-storey drifts with good estimations of the median response and a consistent under-estimation of the response of the upper storeys at the median-plus-one-standard-deviation level from the accelerograms scaled to the elastic response spectrum (Figure 8.37).

The peak deformations at the median-plus-one-standard-deviation level at the base of the outer columns of the 2nd, 3rd and 4th storeys is greater in the scaled accelerograms than is predicted by regression (Figure 8.38). However, these rotations are smaller than the rotations in the beams and do not govern the global response.

The dispersion in the estimates of the member end rotations from the different scaling methods is broadly comparable with those from the estimates for inter-storey drift (Tables 8.11 to 8.17). This means that the number of accelerograms required to estimate the member end rotation is reduced by a factor of about 4 when records are scaled to the initial period of the structure. A further reduction of a factor of about 3 can be achieved by scaling records to the average spectral acceleration.

Absorbed hysteretic energy

Although the absolute member end rotation is greater in the ends of the beams than the columns, the columns have a lower yield rotation and dissipate broadly comparable amounts of hysteretic energy as the beams. There is considerable uncertainty in the prediction of the absorbed hysteretic energy with, for example, a difference of four orders of magnitude between the absorbed hysteretic energy dissipated at the base of the ground floor columns under the action of different accelerograms selected on seismological characteristics (Figure 8.40). Selecting and scaling accelerograms to the elastic response spectra can reduce the dispersion of the response so, for example, the number of accelerograms required to predict the median absorbed hysteretic energy at the base of the outer ground floor column response within +/-10% to one standard deviation confidence reduces from 138 for records

selected on seismological characteristics to 54 and 15 for those scaled to the spectral acceleration at the initial period of the structure and on average over a period range respectively (Table 8.17 to Table 8.22)

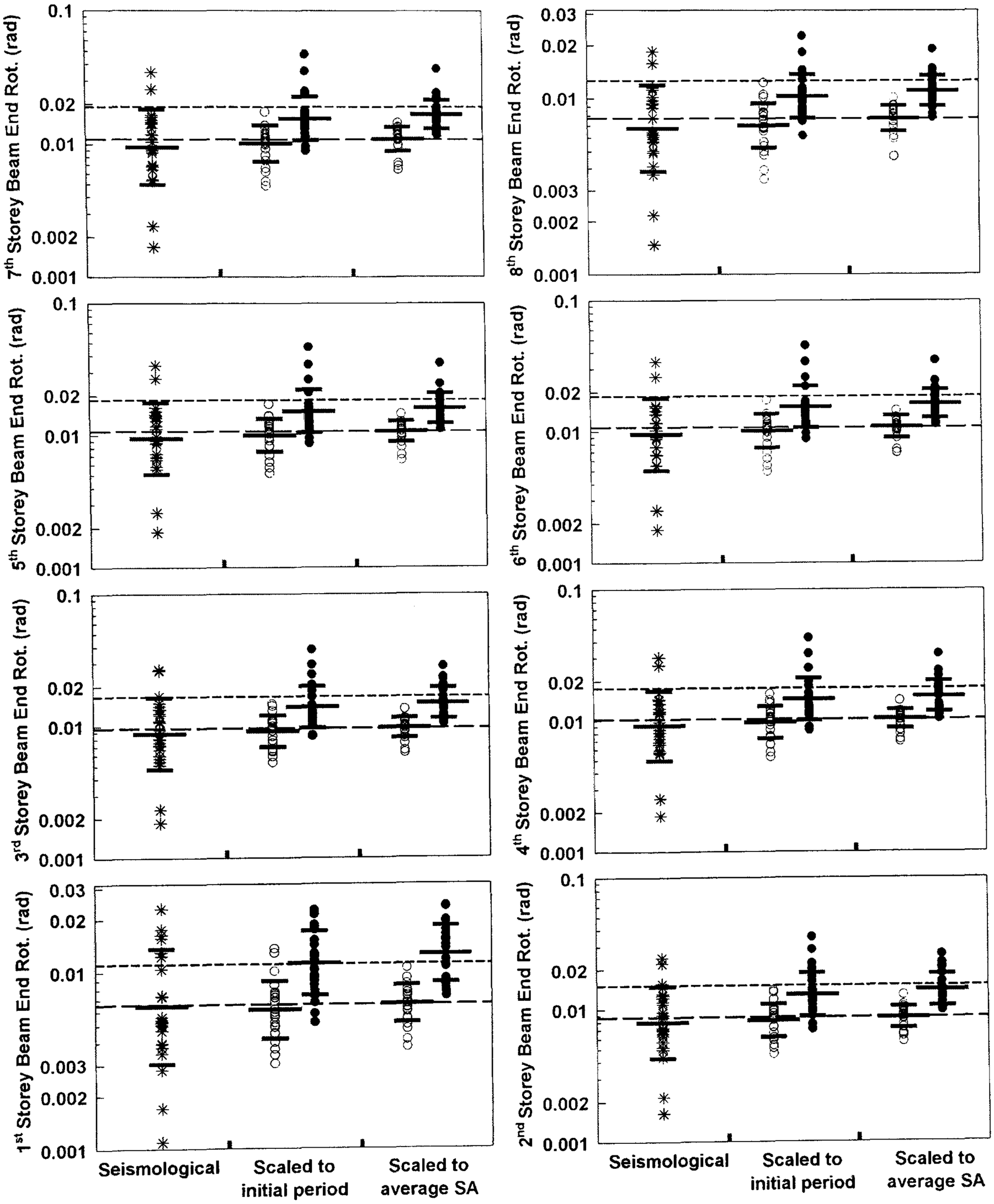


Figure 8.37. – Peak end rotation of beams at the edge of the structure from records selected and scaled based on seismological characteristics, SA at the initial period, SA over a range of periods. Error bars show median and ±1 standard deviation. Dashed lines show drift predicted by regression of 1656 unscaled MDOF time-history analyses.

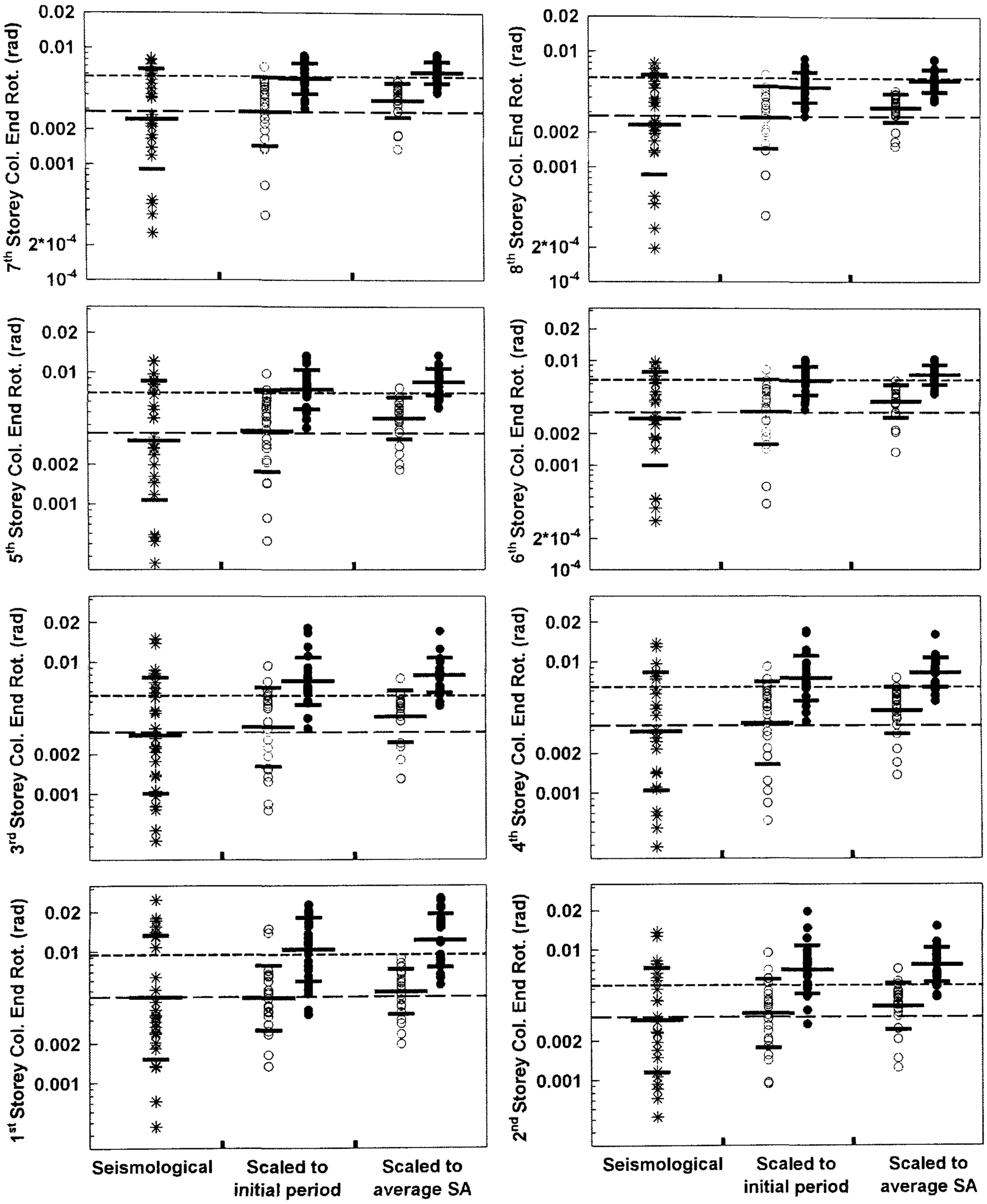


Figure 8.38. – Peak end rotation of the base of the columns at the edge of the structure from records selected and scaled based on seismological characteristics, SA at the initial period, SA over a range of periods. Error bars show median and ±1 standard deviation. Dashed lines show drift predicted by regression of 1656 unscaled MDOF time-history analyses.

Table 8.11. – Statistics of peak end rotation of the beam on the 8th storey at the edge of the structure, predicted from suites of records selected and linearly scaled using different criteria.

Scale Method	Regression (Unscaled)	Seismological (Unscaled)	Initial SA (5%) Median	Initial SA (5%) Median +1St. Dev.	Average SA (5%) Median	Average SA (5%) Median +1St. Dev.
Median	0.008	0.007	0.0070	0.010	0.0077	0.011
1St Dev. (log)	0.215	0.246	0.127	0.123	0.071	0.086
Median +1St.Dev.	0.013	0.012	0.0094	0.014	0.0091	0.014
No. Records	834	25	25	25	25	25
SEE at 1St.Dev.	0.7%	4.9%	2.5%	2.5%	1.4%	1.7%
No. Records for +/-10% (log) at 1St.Dev. confidence	5	6	2	2	1	1
No. Records for +/-5% (log) at 1St.Dev. confidence	18	24	6	6	2	3

Table 8.12. – Statistics of peak end rotation of the beam on the 6th storey at the edge of the structure, predicted from suites of records selected and linearly scaled using different criteria.

Scale Method	Regression (Unscaled)	Seismological (Unscaled)	Initial SA(5%) Median	Initial SA(5%) Median +1St. Dev.	Average SA(5%) Median	Average SA(5%) Median +1St. Dev.
Median	0.011	0.010	0.0101	0.015	0.0109	0.016
1St Dev. (log)	0.238	0.275	0.129	0.159	0.084	0.108
Median +1St.Dev.	0.019	0.018	0.0136	0.022	0.0132	0.021
No. Records	834	25	25	25	25	25
SEE at 1St.Dev.	0.8%	5.5%	2.6%	3.2%	1.7%	2.2%
No. Records for +/-10% (log) at 1St.Dev. confidence	6	8	2	3	1	1
No. Records for +/-5% (log) at 1St.Dev. confidence	23	30	7	10	3	5

Table 8.13. – Statistics of peak end rotation of the beam on the 1st storey at the edge of the structure, predicted from suites of records selected and linearly scaled using different criteria.

Scale Method	Regression (Unscaled)	Seismological (Unscaled)	Initial SA (5%) Median	Initial SA (5%) Median +1St. Dev.	Average SA (5%) Median	Average SA (5%) Median +1St. Dev.
Median	0.007	0.006	0.0061	0.011	0.0066	0.013
1St Dev. (log)	0.229	0.326	0.163	0.182	0.105	0.161
Median +1St.Dev.	0.011	0.014	0.0089	0.017	0.0084	0.018
No. Records	834	25	25	25	25	25
SEE at 1St.Dev.	0.8%	6.5%	3.3%	3.6%	2.1%	3.2%
No. Records for +/-10% (log) at 1St.Dev. confidence	5	11	3	3	1	3
No. Records for +/-5% (log) at 1St.Dev. confidence	21	43	11	13	4	10

Table 8.14. – Statistics of peak end rotation of the base of the column on the 8th storey at the edge of the structure, predicted from suites of records selected and linearly scaled using different criteria.

Scale Method	Regression (Unscaled)	Seismological (Unscaled)	Initial SA (5%) Median	Initial SA (5%) Median +1St. Dev.	Average SA (5%) Median	Average SA (5%) Median +1St. Dev.
Median	0.003	0.002	0.0027	0.005	0.0033	0.006
1St Dev. (log)	0.329	0.431	0.268	0.131	0.122	0.097
Median +1St.Dev.	0.006	0.006	0.0050	0.007	0.0044	0.007
No. Records	834	25	25	25	25	25
SEE at 1St.Dev.	1.1%	8.6%	5.4%	2.6%	2.4%	1.9%
No. Records for +/-10% (log) at 1St.Dev. confidence	11	19	7	2	1	1
No. Records for +/-5% (log) at 1St.Dev. confidence	43	74	29	7	6	4

Table 8.15. – Statistics of peak end rotation of the base of the column on the 6th storey at the edge of the structure, predicted from suites of records selected and linearly scaled using different criteria.

Scale Method	Regression (Unscaled)	Seismological (Unscaled)	Initial SA(5%) Median	Initial SA(5%) Median +1St. Dev.	Average SA(5%) Median	Average SA(5%) Median +1St. Dev.
Median	0.003	0.003	0.0032	0.006	0.0041	0.007
1St Dev. (log)	0.311	0.446	0.309	0.136	0.156	0.092
Median +1St.Dev.	0.007	0.008	0.0066	0.009	0.0058	0.009
No. Records	834	25	25	25	25	25
SEE at 1St.Dev.	1.1%	8.9%	6.2%	2.7%	3.1%	1.8%
No. Records for +/-10% (log) at 1St.Dev. confidence	10	20	10	2	2	1
No. Records for +/-5% (log) at 1St.Dev. confidence	39	80	38	7	10	3

Table 8.16. – Statistics of peak end rotation of the base of the column on the 1st storey at the edge of the structure, predicted from suites of records selected and linearly scaled using different criteria.

Scale Method	Regression (Unscaled)	Seismological (Unscaled)	Initial SA (5%) Median	Initial SA (5%) Median +1St. Dev.	Average SA (5%) Median	Average SA (5%) Median +1St. Dev.
Median	0.005	0.004	0.0044	0.010	0.0049	0.012
1St Dev. (log)	0.321	0.470	0.247	0.243	0.171	0.202
Median +1St.Dev.	0.009	0.013	0.0078	0.018	0.0073	0.019
No. Records	834	25	25	25	25	25
SEE at 1St.Dev.	1.1%	9.4%	4.9%	4.9%	3.4%	4.0%
No. Records for +/-10% (log) at 1St.Dev. confidence	10	22	6	6	3	4
No. Records for +/-5% (log) at 1St.Dev. confidence	41	89	24	24	12	16

As with the peak member end rotation the absorbed hysteretic energy is under-predicted in the upper storeys at the median-plus-one-standard-deviation level. This appears to be more acute than with member end rotation. This could because of the greater uncertainty in the prediction, or because the absorbed hysteretic energy is also related to the duration of the motion and the main focus of the scaling procedure is to match the amplitude of the accelerograms (Figures 8.39 and 8.40).

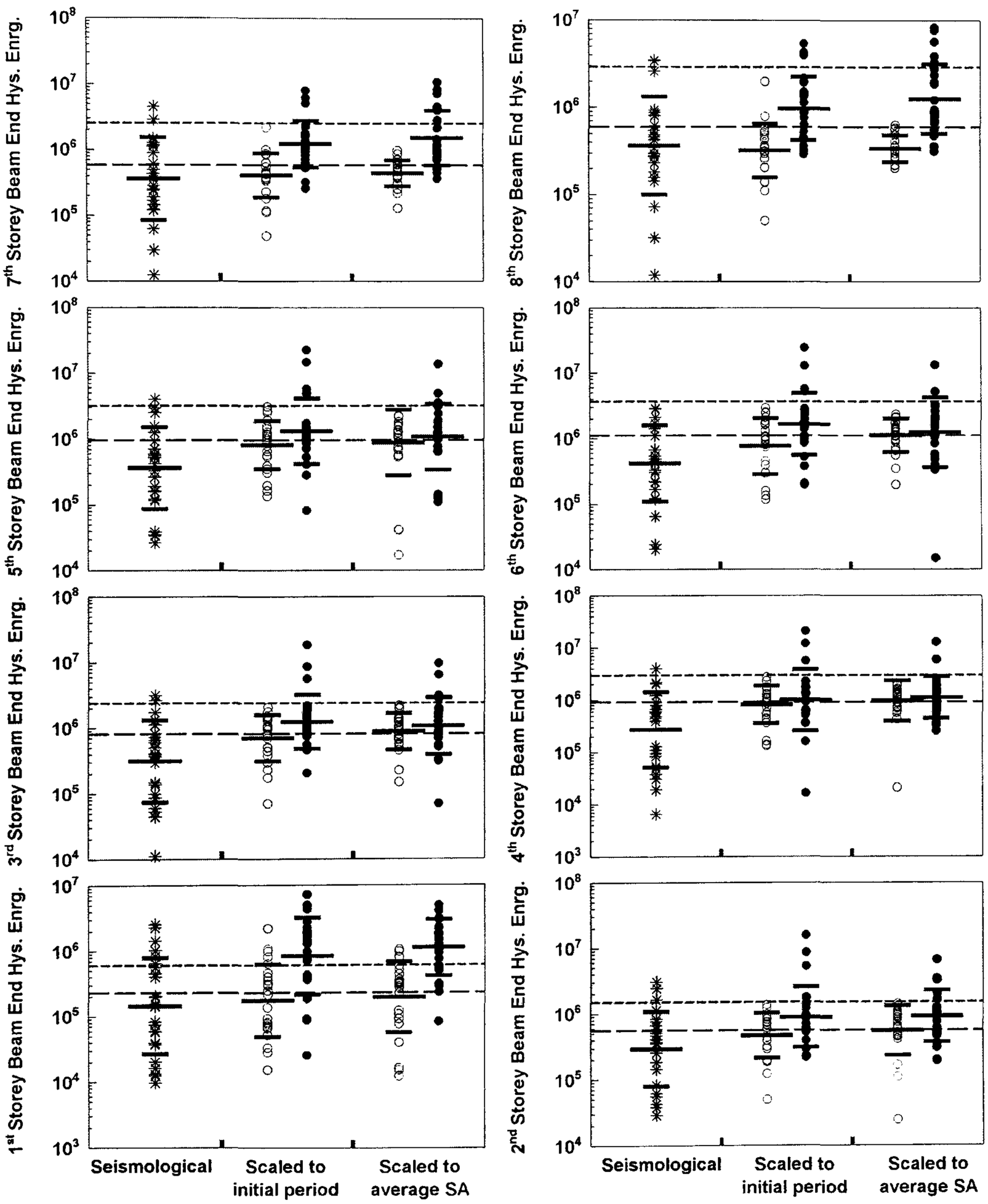


Figure 8.39. – Absorbed hysteretic energy at the end of the beams at the edge of the structure from records selected and scaled based on seismological characteristics, SA at the initial period, SA over a range of periods. Error bars show median and ±1 standard deviation. Dashed lines show drift predicted by regression of 1656 unscaled MDOF time-history analyses.

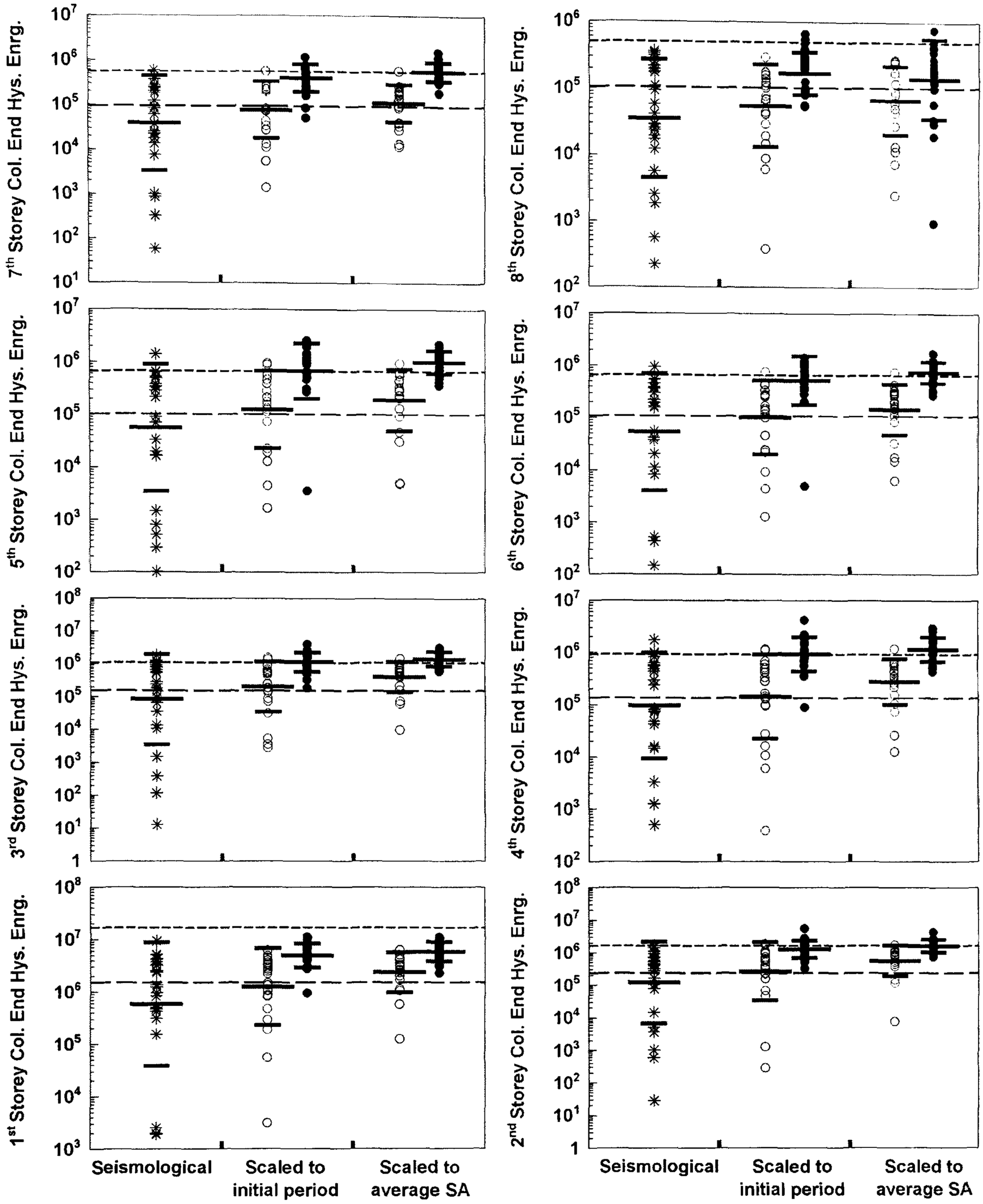


Figure 8.40. – Absorbed hysteretic energy at the base of the columns at the edge of the structure from records selected and scaled based on seismological characteristics, SA at the initial period, SA over a range of periods. Error bars show median and ±1 standard deviation. Dashed lines show drift predicted by regression of 1656 unscaled MDOF time-history analyses.

Table 8.17. – Statistics of the absorbed hysteretic energy at the end of the beam on the 8th storey at the edge of the structure, predicted from suites of records selected and linearly scaled using different criteria.

Scale Method	Regression (Unscaled)	Seismological (Unscaled)	Initial SA (5%) Median	Initial SA (5%) Median +1St. Dev.	Average SA (5%) Median	Average SA (5%) Median +1St. Dev.
Median	553139	655339	351727	640167	445408	1196972
1St Dev. (log)	0.559	0.746	0.544	0.484	0.517	0.418
Median +1St.Dev.	2005079	3652587	1230833	1951824	1464913	3134265
No. Records	834	25	25	25	25	25
SEE at 1St.Dev.	1.9%	14.9%	10.9%	9.7%	10.3%	8.4%
No. Records for +/-10% (log) at 1St.Dev. confidence	31	56	30	23	27	17
No. Records for +/-5% (log) at 1St.Dev. confidence	125	223	118	94	107	70

Table 8.18. – Statistics of the absorbed hysteretic energy at the end of the beam on the 6th storey at the edge of the structure, predicted from suites of records selected and linearly scaled using different criteria.

Scale Method	Regression (Unscaled)	Seismological (Unscaled)	Initial SA(5%) Median	Initial SA(5%) Median +1St. Dev.	Average SA(5%) Median	Average SA(5%) Median +1St. Dev.
Median	1108933	704517	765589	1668110	1130241	1247641
1St Dev. (log)	0.525	0.710	0.429	0.473	0.255	0.535
Median +1St.Dev.	3718550	3609786	2057342	4958493	2032398	4272370
No. Records	834	25	25	25	25	25
SEE at 1St.Dev.	1.8%	14.2%	8.6%	9.5%	5.1%	10.7%
No. Records for +/-10% (log) at 1St.Dev. confidence	28	50	18	22	6	29
No. Records for +/-5% (log) at 1St.Dev. confidence	110	201	74	90	26	114

Table 8.19. – Statistics of the absorbed hysteretic energy at the end of the beam on the 1st storey at the edge of the structure, predicted from suites of records selected and linearly scaled using different criteria.

Scale Method	Regression (Unscaled)	Seismological (Unscaled)	Initial SA (5%) Median	Initial SA (5%) Median +1St. Dev.	Average SA (5%) Median	Average SA (5%) Median +1St. Dev.
Median	231511	177314	175133	831201	196430	1112838
1St Dev. (log)	0.416	0.655	0.555	0.584	0.541	0.430
Median +1St.Dev.	603572	800495	627887	3191563	682396	2992467
No. Records	834	25	25	25	25	25
SEE at 1St.Dev.	1.4%	13.1%	11.1%	11.7%	10.8%	8.6%
No. Records for +/-10% (log) at 1St.Dev. confidence	17	43	31	34	29	18
No. Records for +/-5% (log) at 1St.Dev. confidence	69	171	123	137	117	74

Table 8.20. – Statistics of the absorbed hysteretic energy at the base of the column on the 8th storey at the edge of the structure, predicted from suites of records selected and linearly scaled using different criteria.

Scale Method	Regression (Unscaled)	Seismological (Unscaled)	Initial SA (5%) Median	Initial SA (5%) Median +1St. Dev.	Average SA (5%) Median	Average SA (5%) Median +1St. Dev.
Median	103462	34993	55349	171481	67541	143547
1St Dev. (log)	0.685	0.887	0.621	0.319	0.515	0.600
Median +1St.Dev.	500543	269592	231139	357126	221270	571943
No. Records	834	25	25	25	25	25
SEE at 1St.Dev.	2.4%	17.7%	12.4%	6.4%	10.3%	12.0%
No. Records for +/-10% (log) at 1St.Dev. confidence	47	79	39	10	27	36
No. Records for +/-5% (log) at 1St.Dev. confidence	188	315	154	41	106	144

Table 8.21. – Statistics of the absorbed hysteretic energy at the base of the column on the 6th storey at the edge of the structure, predicted from suites of records selected and linearly scaled using different criteria.

Scale Method	Regression (Unscaled)	Seismological (Unscaled)	Initial SA(5%) Median	Initial SA(5%) Median +1St. Dev.	Average SA(5%) Median	Average SA(5%) Median +1St. Dev.
Median	110034	53671	103065	527922	147028	754894
1St Dev. (log)	0.781	1.121	0.709	0.467	0.489	0.204
Median +1St.Dev.	665112	708756	526960	1546608	453205	1208314
No. Records	834	25	25	25	25	25
SEE at 1St.Dev.	2.7%	22.4%	14.2%	9.3%	9.8%	4.1%
No. Records for +/-10% (log) at 1St.Dev. confidence	61	126	50	22	24	4
No. Records for +/-5% (log) at 1St.Dev. confidence	244	502	201	87	96	17

Table 8.22. – Statistics of the absorbed hysteretic energy at the base of the column on the 1st storey at the edge of the structure, predicted from suites of records selected and linearly scaled using different criteria.

Scale Method	Regression (Unscaled)	Seismological (Unscaled)	Initial SA (5%) Median	Initial SA (5%) Median +1St. Dev.	Average SA (5%) Median	Average SA (5%) Median +1St. Dev.
Median	1523654	585150	1247856	4950206	2350569	5845033
1St Dev. (log)	1.047	1.176	0.737	0.227	0.383	0.183
Median +1St.Dev.	16996892	8785026	6815094	8354959	5678629	8904915
No. Records	834	25	25	25	25	25
SEE at 1St.Dev.	3.6%	23.5%	14.7%	4.5%	7.7%	3.7%
No. Records for +/-10% (log) at 1St.Dev. confidence	110	138	54	5	15	3
No. Records for +/-5% (log) at 1St.Dev. confidence	439	554	217	21	59	13

Park and Ang damage index

The Park and Ang damage index is a combination of the peak end rotation and the absorbed hysteretic energy. As the trends of both of these measures are similar, the Park and Ang damage index also follows the same trends. In fact exactly the same conclusions can be drawn for the Park and Ang damage measure as have already been described for peak member end rotation (Tables 8.25 to 8.28, Figures 8.41 and 8.42)

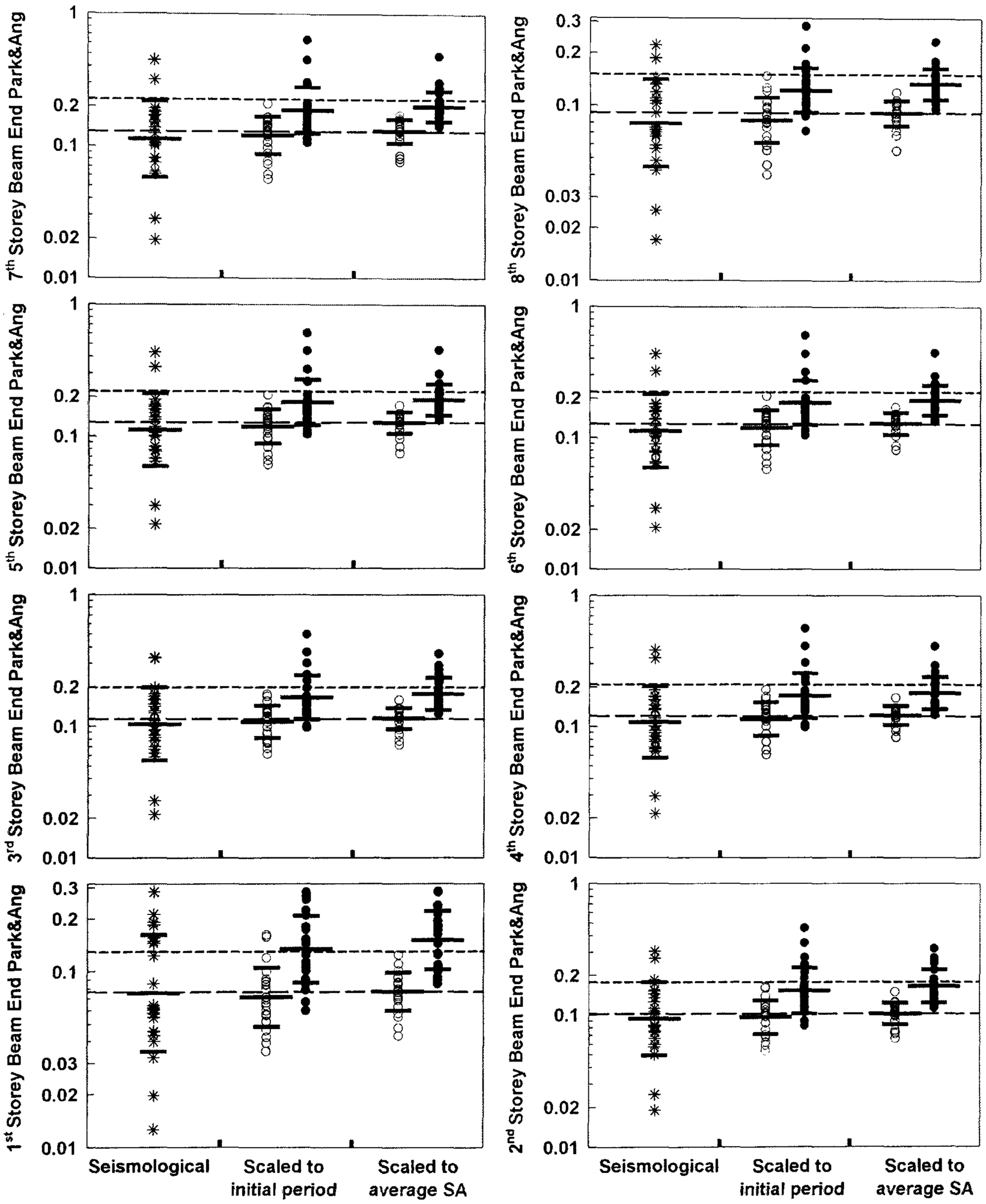


Figure 8.41. – Park and Ang damage index at the end of the beams at the edge of the structure from records selected and scaled based on seismological characteristics, SA at the initial period, SA over a range of periods. Error bars show median and ±1 standard deviation. Dashed lines show drift predicted by regression of 1656 unscaled MDOF time-history analyses.

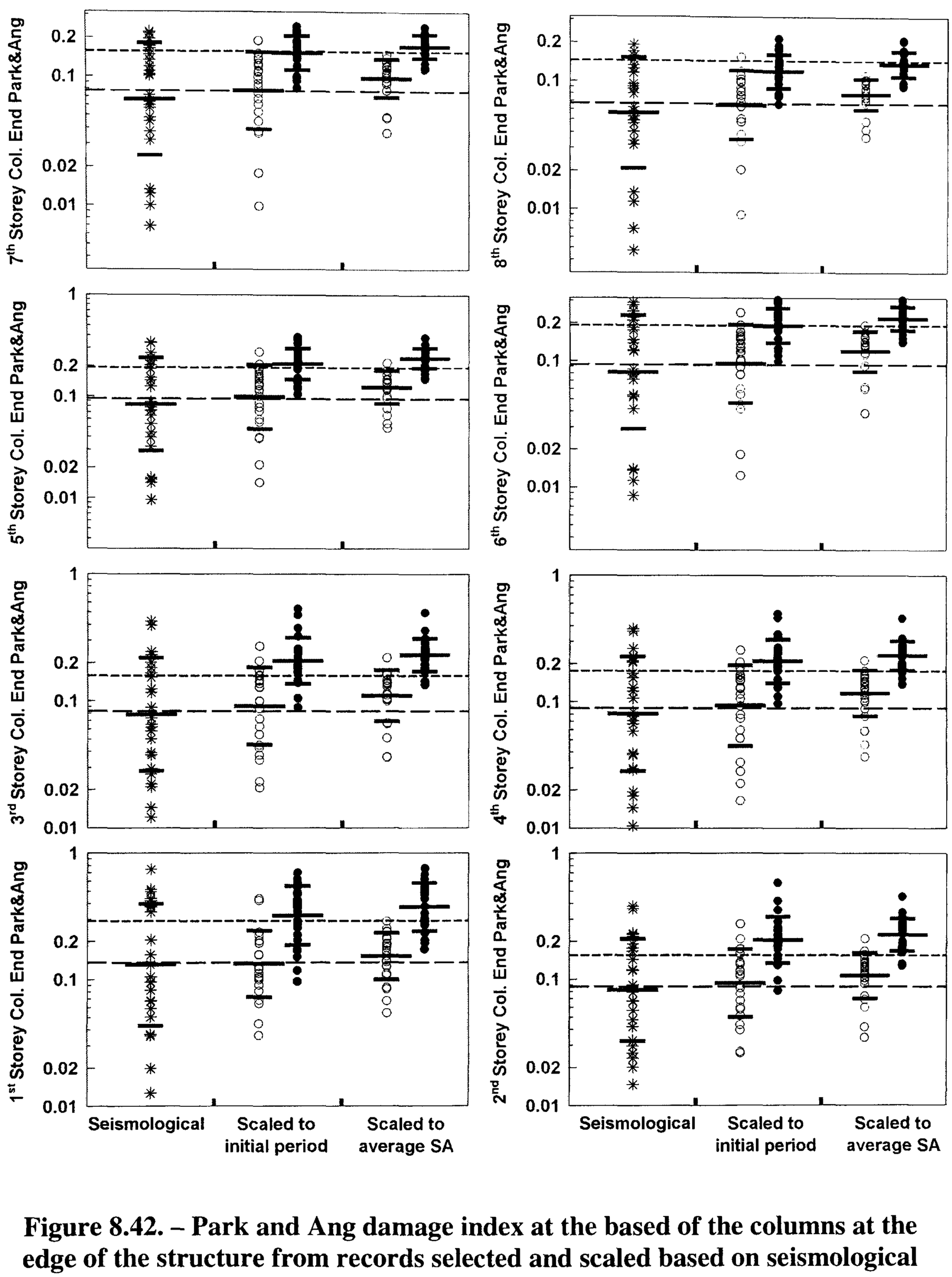


Figure 8.42. – Park and Ang damage index at the based of the columns at the edge of the structure from records selected and scaled based on seismological characteristics, SA at the initial period, SA over a range of periods. Error bars show median and ±1 standard deviation. Dashed lines show drift predicted by regression of 1656 unscaled MDOF time-history analyses.

Table 8.23. – Statistics of Park and Ang damage index at the end of the beam on the 8th storey at the edge of the structure, predicted from suites of records selected and linearly scaled using different criteria.

Scale Method	Regression (Unscaled)	Seismological (Unscaled)	Initial SA (5%) Median	Initial SA (5%) Median +1St. Dev.	Average SA (5%) Median	Average SA (5%) Median +1St. Dev.
Median	0.091	0.079	0.0829	0.123	0.0912	0.134
1St Dev. (log)	0.218	0.250	0.130	0.127	0.071	0.089
Median +1St.Dev.	0.151	0.141	0.1117	0.165	0.1073	0.164
No. Records	834	25	25	25	25	25
SEE at 1St.Dev.	0.8%	5.0%	2.6%	2.5%	1.4%	1.8%
No. Records for +/-10% (log) at 1St.Dev. confidence	5	6	2	2	0	1
No. Records for +/-5% (log) at 1St.Dev. confidence	19	25	7	6	2	3

Table 8.24. – Statistics of Park and Ang damage index at the end of the beam on the 6th storey at the edge of the structure, predicted from suites of records selected and linearly scaled using different criteria.

Scale Method	Regression (Unscaled)	Seismological (Unscaled)	Initial SA(5%) Median	Initial SA(5%) Median +1St. Dev.	Average SA(5%) Median	Average SA(5%) Median +1St. Dev.
Median	0.127	0.113	0.1198	0.186	0.1291	0.193
1St Dev. (log)	0.241	0.281	0.134	0.169	0.085	0.114
Median +1St.Dev.	0.222	0.215	0.1631	0.274	0.1570	0.252
No. Records	834	25	25	25	25	25
SEE at 1St.Dev.	0.8%	5.6%	2.7%	3.4%	1.7%	2.3%
No. Records for +/-10% (log) at 1St.Dev. confidence	6	8	2	3	1	1
No. Records for +/-5% (log) at 1St.Dev. confidence	23	32	7	11	3	5

Table 8.25. – Statistics of the Park and Ang damage index at the end of the beam on the 1st storey at the edge of the structure, predicted from suites of records selected and linearly scaled using different criteria.

Scale Method	Regression (Unscaled)	Seismological (Unscaled)	Initial SA (5%) Median	Initial SA (5%) Median +1St. Dev.	Average SA (5%) Median	Average SA (5%) Median +1St. Dev.
Median	0.076	0.075	0.0715	0.134	0.0769	0.151
1St Dev. (log)	0.231	0.333	0.168	0.190	0.108	0.166
Median +1St.Dev.	0.130	0.162	0.1053	0.208	0.0986	0.221
No. Records	834	25	25	25	25	25
SEE at 1St.Dev.	0.8%	6.7%	3.4%	3.8%	2.2%	3.3%
No. Records for +/-10% (log) at 1St.Dev. confidence	5	11	3	4	1	3
No. Records for +/-5% (log) at 1St.Dev. confidence	21	44	11	14	5	11

Table 8.26. – Statistics of the Park and Ang damage index at the base of the column on the 8th storey at the edge of the structure, predicted from suites of records selected and linearly scaled using different criteria.

Scale Method	Regression (Unscaled)	Seismological (Unscaled)	Initial SA (5%) Median	Initial SA (5%) Median +1St. Dev.	Average SA (5%) Median	Average SA (5%) Median +1St. Dev.
Median	0.067	0.056	0.0651	0.120	0.0796	0.137
1St Dev. (log)	0.330	0.432	0.268	0.132	0.120	0.097
Median +1St.Dev.	0.144	0.152	0.1209	0.162	0.1050	0.171
No. Records	834	25	25	25	25	25
SEE at 1St.Dev.	1.1%	8.6%	5.4%	2.6%	2.4%	1.9%
No. Records for +/-10% (log) at 1St.Dev. confidence	11	19	7	2	1	1
No. Records for +/-5% (log) at 1St.Dev. confidence	44	75	29	7	6	4

Table 8.27. – Statistics of the Park and Ang damage index at the base of the column on the 6th storey at the edge of the structure, predicted from suites of records selected and linearly scaled using different criteria.

Scale Method	Regression (Unscaled)	Seismological (Unscaled)	Initial SA(5%) Median	Initial SA(5%) Median +1St. Dev.	Average SA(5%) Median	Average SA(5%) Median +1St. Dev.
Median	0.093	0.081	0.0952	0.191	0.1197	0.218
1St Dev. (log)	0.312	0.449	0.311	0.138	0.158	0.093
Median +1St.Dev.	0.192	0.229	0.1949	0.262	0.1723	0.270
No. Records	834	25	25	25	25	25
SEE at 1St.Dev.	1.1%	9.0%	6.2%	2.8%	3.2%	1.9%
No. Records for +/-10% (log) at 1St.Dev. confidence	10	20	10	2	2	1
No. Records for +/-5% (log) at 1St.Dev. confidence	39	81	39	8	10	3

Table 8.28. – Statistics of the Park and Ang damage index at the base of the column on the 1st storey at the edge of the structure, predicted from suites of records selected and linearly scaled using different criteria.

Scale Method	Regression (Unscaled)	Seismological (Unscaled)	Initial SA (5%) Median	Initial SA (5%) Median +1St. Dev.	Average SA (5%) Median	Average SA (5%) Median +1St. Dev.
Median	0.136	0.131	0.1330	0.321	0.1527	0.375
1St Dev. (log)	0.330	0.482	0.263	0.234	0.185	0.191
Median +1St.Dev.	0.292	0.397	0.2437	0.549	0.2338	0.582
No. Records	834	25	25	25	25	25
SEE at 1St.Dev.	1.1%	9.6%	5.3%	4.7%	3.7%	3.8%
No. Records for +/-10% (log) at 1St.Dev. confidence	11	23	7	5	3	4
No. Records for +/-5% (log) at 1St.Dev. confidence	44	93	28	22	14	15

Member rotational fatigue

The member rotational fatigue has the greatest scatter of all of the damage measures with, for example, over five orders of magnitude between the fatigue damage at the base of the ground floor columns under the action of different accelerograms selected on seismological characteristics (Figure 8.44). As described in earlier subsections, the scatter leads to difficulties in predicting the fatigue damage using predictive equations. However, the estimates of the fatigue damage from the structure under the action of the accelerograms selected and scaled to the spectral acceleration give reasonable agreement with that observed from the analyses conducted with the accelerograms selected by seismological characteristics (Figures 8.44 and 8.45).

The scatter in the response also means that more accelerograms are required to predict the fatigue damage to a given confidence level than any other damage measures (Tables 8.29 to 8.34). As with the other damage measures, selecting and scaling accelerograms to the spectral acceleration reduces the scatter and the number of accelerograms required to predict the response to a given confidence level. For example, 167 analyses are required to predict the median level of fatigue damage at the base of the outer column to within ±10% accuracy to one standard deviation confidence, which reduces to 82 and 44 for accelerograms scaled to the spectral acceleration at the initial period of the structure and over an average period range respectively.

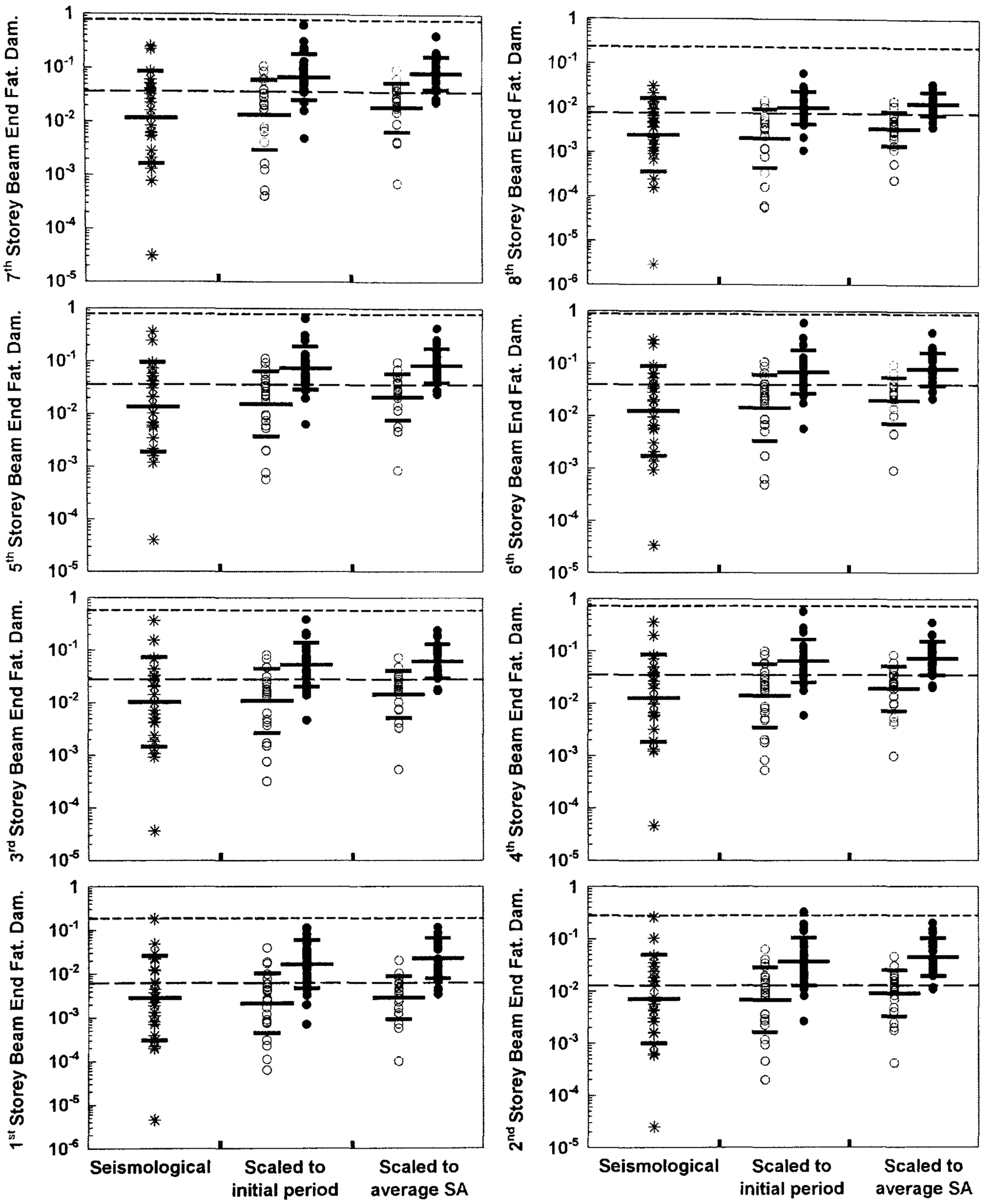


Figure 8.43. – Fatigue damage index at the end of the beams at the edge of the structure from records selected and scaled based on seismological characteristics, SA at the initial period, SA over a range of periods. Error bars show median and ±1 standard deviation. Dashed lines show drift predicted by regression of 1656 unscaled MDOF time-history analyses.

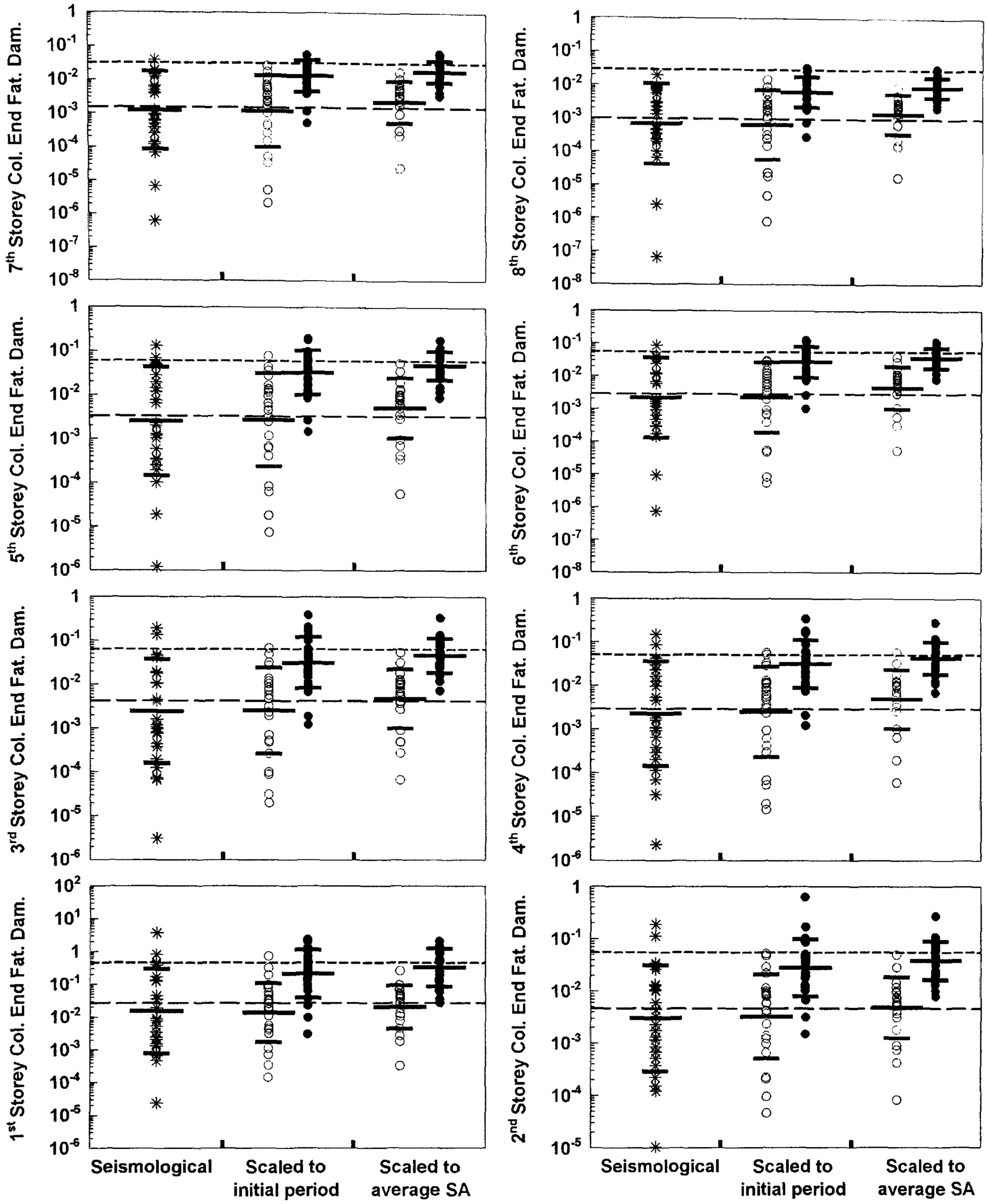


Figure 8.44. – Fatigue damage index at the base of the columns at the edge of the structure from records selected and scaled based on seismological characteristics, SA at the initial period, SA over a range of periods. Error bars show median and ±1 standard deviation. Dashed lines show drift predicted by regression of 1656 unscaled MDOF time-history analyses.

Table 8.29. – Statistics of fatigue damage at the end of the beam on the 8th storey at the edge of the structure, predicted from suites of records selected and linearly scaled using different criteria.

Scale Method	Regression (Unscaled)	Seismological (Unscaled)	Initial SA (5%) Median	Initial SA (5%) Median +1St. Dev.	Average SA (5%) Median	Average SA (5%) Median +1St. Dev.
Median	0.008	0.002	0.0021	0.010	0.0035	0.013
1St Dev. (log)	1.481	0.827	0.658	0.371	0.385	0.263
Median +1St.Dev.	0.236	0.016	0.0094	0.024	0.0085	0.024
No. Records	834	25	25	25	25	25
SEE at 1St.Dev.	5.1%	16.5%	13.2%	7.4%	7.7%	5.3%
No. Records for +/-10% (log) at 1St.Dev. confidence	219	68	43	14	15	7
No. Records for +/-5% (log) at 1St.Dev. confidence	878	273	173	55	59	28

Table 8.30. – Statistics of fatigue damage at the end of the beam on the 6th storey at the edge of the structure, predicted from suites of records selected and linearly scaled using different criteria.

Scale Method	Regression (Unscaled)	Seismological (Unscaled)	Initial SA(5%) Median	Initial SA(5%) Median +1St. Dev.	Average SA(5%) Median	Average SA(5%) Median +1St. Dev.
Median	0.784	0.215	0.4754	1.271	0.5758	1.370
1St Dev. (log)	0.959	0.927	0.436	0.251	0.328	0.216
Median +1St.Dev.	7.127	1.814	1.2966	2.265	1.2252	2.254
No. Records	834	25	25	25	25	25
SEE at 1St.Dev.	3.3%	18.5%	8.7%	5.0%	6.6%	4.3%
No. Records for +/-10% (log) at 1St.Dev. confidence	92	86	19	6	11	5
No. Records for +/-5% (log) at 1St.Dev. confidence	368	344	76	25	43	19

Table 8.31. – Statistics of the fatigue damage at the end of the beam on the 1st storey at the edge of the structure, predicted from suites of records selected and linearly scaled using different criteria.

Scale Method	Regression (Unscaled)	Seismological (Unscaled)	Initial SA (5%) Median	Initial SA (5%) Median +1St. Dev.	Average SA (5%) Median	Average SA (5%) Median +1St. Dev.
Median	2.615	0.812	1.6618	8.156	2.1627	10.404
1St Dev. (log)	1.152	1.270	0.602	0.388	0.442	0.309
Median +1St.Dev.	37.122	15.110	6.6458	19.932	5.9816	21.212
No. Records	834	25	25	25	25	25
SEE at 1St.Dev.	4.0%	25.4%	12.0%	7.8%	8.8%	6.2%
No. Records for +/-10% (log) at 1St.Dev. confidence	133	161	36	15	20	10
No. Records for +/-5% (log) at 1St.Dev. confidence	531	645	145	60	78	38

Table 8.32. – Statistics of the fatigue damage at the base of the column on the 8th storey at the edge of the structure, predicted from suites of records selected and linearly scaled using different criteria.

Scale Method	Regression (Unscaled)	Seismological (Unscaled)	Initial SA (5%) Median	Initial SA (5%) Median +1St. Dev.	Average SA (5%) Median	Average SA (5%) Median +1St. Dev.
Median	0.001	0.001	0.0007	0.006	0.0014	0.009
1St Dev. (log)	1.473	1.207	1.046	0.452	0.598	0.298
Median +1St.Dev.	0.029	0.011	0.0074	0.018	0.0055	0.018
No. Records	834	25	25	25	25	25
SEE at 1St.Dev.	5.1%	24.1%	20.9%	9.0%	12.0%	6.0%
No. Records for +/-10% (log) at 1St.Dev. confidence	217	146	109	20	36	9
No. Records for +/-5% (log) at 1St.Dev. confidence	868	583	438	82	143	35

Table 8.33. – Statistics of the fatigue damage at the base of the column on the 6th storey at the edge of the structure, predicted from suites of records selected and linearly scaled using different criteria.

Scale Method	Regression (Unscaled)	Seismological (Unscaled)	Initial SA(5%) Median	Initial SA(5%) Median +1St. Dev.	Average SA(5%) Median	Average SA(5%) Median +1St. Dev.
Median	0.003	0.002	0.0023	0.028	0.0045	0.037
1St Dev. (log)	1.279	1.225	1.078	0.473	0.649	0.309
Median +1St.Dev.	0.056	0.037	0.0276	0.083	0.0200	0.075
No. Records	834	25	25	25	25	25
SEE at 1St.Dev.	4.4%	24.5%	21.6%	9.5%	13.0%	6.2%
No. Records for +/-10% (log) at 1St.Dev. confidence	164	150	116	22	42	10
No. Records for +/-5% (log) at 1St.Dev. confidence	655	601	464	89	168	38

Table 8.34. – Statistics of the fatigue damage at the base of the column on the 1st storey at the edge of the structure, predicted from suites of records selected and linearly scaled using different criteria.

Scale Method	Regression (Unscaled)	Seismological (Unscaled)	Initial SA (5%) Median	Initial SA (5%) Median +1St. Dev.	Average SA (5%) Median	Average SA (5%) Median +1St. Dev.
Median	0.027	0.015	0.0137	0.213	0.0203	0.326
1St Dev. (log)	1.232	1.292	0.903	0.734	0.663	0.583
Median +1St.Dev.	0.461	0.300	0.1097	1.153	0.0933	1.248
No. Records	834	25	25	25	25	25
SEE at 1St.Dev.	4.3%	25.8%	18.1%	14.7%	13.3%	11.7%
No. Records for +/-10% (log) at 1St.Dev. confidence	152	167	82	54	44	34
No. Records for +/-5% (log) at 1St.Dev. confidence	607	668	326	216	176	136

8.9.3 Scale Factor bias

The ability to linearly scale accelerograms without introducing bias – consistently over- or under-predicting with increasing scale factor – is checked by plotting different damage measures vs the scale factor used to scale the accelerogram (Figure 8.45). Linear trend lines are fitted through the data and show that there is no consistent increase or decrease of the response with scale factor; indeed the coefficients of determination of the trend lines are all less than 0.05. This shows that accelerograms can be scaled by factors of 10 without causing a bias if they are initially selected to match the earthquake magnitude and spectral shape. A bias might have been found if the records had not been initially selected to have a good match to the target spectrum. This prevents the records consistently having a spectral peak at the initial period of the structure, which is known to cause a bias as these records require lower scaling, but will cause less damage than records with a "trough" at the initial period of the structure (e.g. Baker and Cornell 2005; Watson-Lamprey and Abrahamson 2006). The fatigue and absorbed hysteretic energy damage measures are known to be dependent on ground-motion duration (see section 9.5). The lack of bias in these damage measures demonstrates that selecting records to match the earthquake magnitude is sufficient to prevent scale bias from different ground-motion durations. As the scale factor is strongly correlated with source-to-site distance, the lack of bias also confirms the validity of selecting and scaling records from a range of source-to-site distances (Table 8.6).

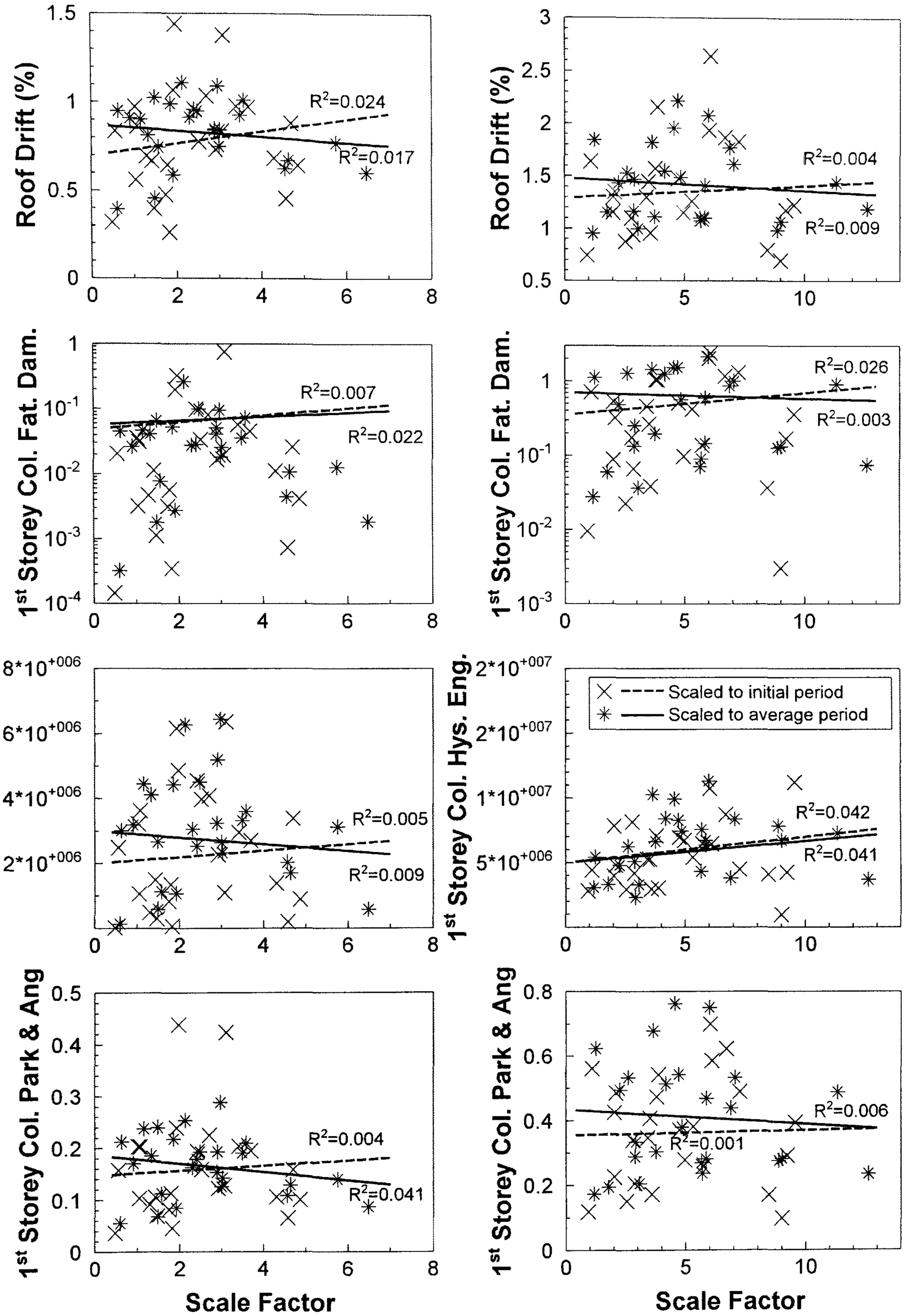


Figure 8.45. – Scale factor vs different response measures, demonstrating that there is no consistent increase or decrease (bias) introduced with scale factor. Median level motions (*left*), median-plus-one-standard-deviation motion (*right*). Straight lines show linear trend lines fitted through the data by least squares regression.

8.10 Summary and Further Work

Selecting and scaling accelerograms enables structural response to be determined with greater confidence, but using fewer analyses than if unscaled accelerograms are employed. This study uses regression of the response of an 8-storey wall frame structure under the action of 1656 unscaled accelerograms to determine the expected response for any given target scenario. Accelerograms are selected and scaled to the spectral acceleration at the initial period of the structure and to the average acceleration over the period range 0.25 and 1.2s. Scaling the accelerograms to the initial period of the structure reduces the number of analyses required to predict the response to a given confidence level by a factor of approximately 4, but scaling the accelerograms to the average spectral acceleration reduces the number of accelerograms required by a further factor of about 2 or 3. As the accelerograms are initially selected on spectral shape, linear scale factors of up to 10 can be used without causing a bias in the predicted response.

The number of accelerograms required to predict the response to a given level of accuracy also depends on the damage metric to be predicted as well as the method used to select and scale the accelerograms. The fatigue damage and absorbed hysteretic energy have considerably greater dispersion than measures of peak response and so require a greater number of analyses for a given confidence level in the inelastic response (e.g. Table 8.35).

Table 8.35. – Statistics of the numbers of analyses required to predict the median of different damage measures to +/-10% accuracy (log) at one standard deviation confidence, predicted from suites of records selected and linearly scaled using different criteria.

Scale Method	Seismological (Unscaled)	Scaled to Initial SA (5%)	Scaled to Average SA (5%)
1st Floor drift	17	6	2
1st Floor column rotation	22	6	3
1st Floor column hysteretic energy.	138	54	15
1st Floor column Park and Ang damage index	23	7	3
1st Floor column fatigue	668	326	176

Selecting and scaling accelerograms to the elastic spectral acceleration does not bias the response for low-amplitude motions for this structure. However, the inter-storey drift and member end rotation in the upper storeys is consistently under-predicted by the analysis using scaled records for the higher amplitude median-plus-one-standard-deviation motions. The difference in response could have several different causes including:

- differences between inelastic and elastic response at higher load levels
- higher mode or travelling wave effects in the upper storeys
- the lower standard deviation of the elastic spectral acceleration than the peak response of the MDOF structure

As one of the possible causes of the differences of response is that the accelerograms are scaled to the elastic response, a more accurate response may be obtained if accelerograms are scaled to the inelastic response. A further study could be undertaken to develop predictive equations for a representative inelastic SDOF system. Accelerograms could then be scaled so that the inelastic response of this simplified system matches that expected for the target scenario as determined by the regression analysis.

The results of this study are only strictly valid for the wall frame structure used in this analysis. Further studies using different structural forms, materials and number of storeys are required to prove that the conclusions drawn here are more generally applicable. However, the findings of this study are consistent with the work of other researchers, so the general conclusions are expected to be applicable for a broad range of structural configurations.

It is important to have an appreciation for the approximate equivalent damping of the structure to be analysed so that the response spectrum can be matched at an appropriate damping level. The structure used in this study is modelled using fibre elements so inelastic material damping is accurately modelled by the elements, this avoids possible problems that can be encountered when using Rayleigh damping in a non-linear analysis (e.g. Hall 2005; Priestley and Grant 2005). The possible contribution of non-structural elements and the foundation to the damping is

conservatively ignored, however further studies on this subject (in particular studies calibrated with experimental test results) would be useful.

9. LINEARLY SCALED vs. SPECTRAL MATCHED ACCELEROGRAMS

This chapter explores the differences between linearly scaled accelerograms (Chapter 8) with those adjusted with the new version of RSPMatch (Chapter 7) to match the target response spectra. The primary objective of this study is to quantify the advantages and possible limitations of spectral matched accelerograms vs. linearly scaled accelerograms. A secondary objective of this work is to identify the influence of ground-motion duration on structural response using a suite of accelerograms, which have a wide range of durations but have been adjusted with RSPMatch to have the same spectral acceleration. An abridged describtion of the work for the primary and secondary objectives are provided in Hancock and Bommer (2006*c* and *d*) respectively

To make full use of the analysis already conducted for Chapter 8 of this thesis, the same 8-storey wall frame reinforced concrete structure is used for this study. The same target scenario as the previous chapter (a strike-slip, magnitude M_w 7.0 earthquake at a soft soil site 5km R_{jb} distance from the fault rupture at median and median-plus-one-standard-deviation level of shaking) is also used in this work.

Previous studies by other authors using accelerograms adjusted to match a target response spectrum produce conflicting conclusions. The study of Naeim and Lew (1995) uses a frequency domain adjustment to create spectral matched accelerograms. They find that the maximum building displacement under the matched accelerograms is approximately twice than that under the action of accelerograms linearly scaled to exceed the target spectrum. This is probably because the procedure used to adjust these accelerograms creates a base-line drift in the displacement time-series of the ground motion and also introduces high levels of energy into the accelerograms. Carballo-Arevalo (2000) found that using spectrum matched accelerograms caused a biased response and underestimated the response. They also found that matching accelerograms to the target spectrum reduced the number of accelerograms required to achieve an estimate of the median response to a given confidence level by a factor of about four compared to using unscaled accelerograms. The work described in this chapter investigates if either of these apparently contradictory findings is applicable to accelerograms adjusted using the latest version of RSPMatch developed in this thesis.

9.1 Spectral Matched Accelerograms – 5% Damping

A set of 25 spectrally matched accelerograms are developed to match the 5% damped elastic response spectrum derived in the previous chapter using 1656 unscaled accelerograms from the NGA database. 25 accelerograms from the NGA database with the lowest RMS difference in normalized spectral acceleration (ΔSAn_{RMS}, see equation 6.10) from earthquakes with magnitude within 0.2 M_w of the target scenario are used as seeds for the matching process. These are the same accelerograms selected for linear scaling described in the previous chapter (see Table 8.6). The seed accelerograms are linearly scaled individually to have a good initial match to the target spectrum. They are then adjusted using RSPMatch2005 so that they match the 5% damped target spectrum over the period range 0.05s to 2.5s. The scaling and matching exercise is repeated to produce two suites of records: the first set to match the median spectral acceleration and the second matching the median-plus-one-standard-deviation spectral acceleration (Figure 9.1). Pseudo spectral acceleration is used in this work because it is directly related to spectral displacement, which thus ensures that the accelerograms match both the acceleration and displacement spectra.

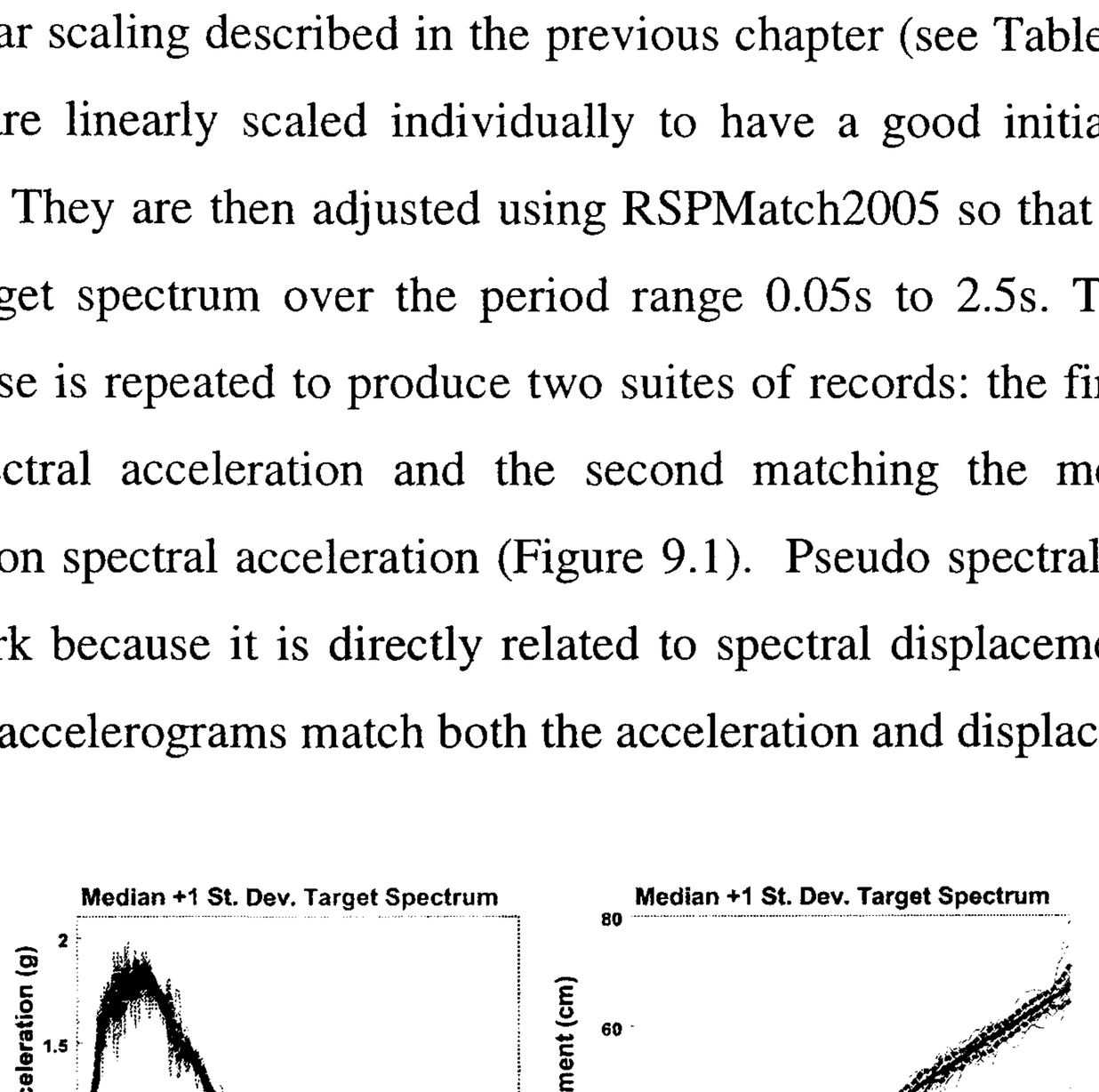


Figure 9.1. – 5% damped elastic spectral response from records matched to the 5% damped target spectral acceleration using RSPMatch2005. Median target spectrum (*lower*) and median-plus-one-standard-deviation target spectrum (*upper*)

9.2 Spectral Matched Accelerograms – Multiple Damping

The second set of matched accelerograms also uses the seed accelerograms chosen to match the target magnitude and spectral shape (Table 8.6). These records are adjusted using RSPMatch2005 to match the 1%, 5%, 10% and 20% damped response spectra (Figure 9.2). The median response of the accelerograms shows a good match to the target spectra. However, it is difficult to match the response at the 1% damping level and the standard deviation of the responses at this damping level is ±20% at 0.5s period, which compares with a standard deviation of between +/-2% to +/-10% for the other damping levels. The scaling and matching exercise is repeated to produce two suites of records: the first set to match the median spectral acceleration and the second matching the median-plus-one-standard-deviation spectral acceleration (Figure 9.2).

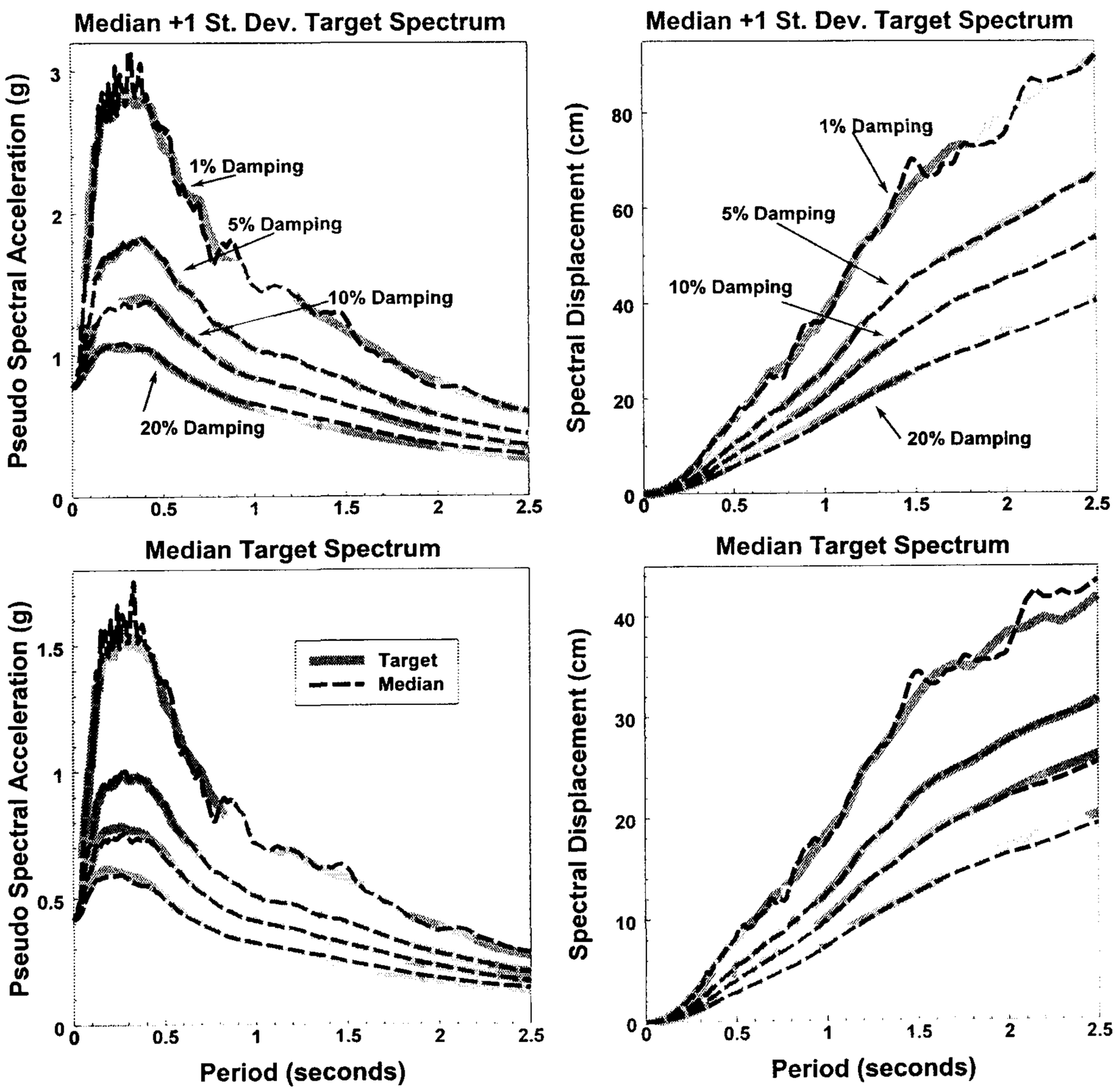


Figure 9.2. – 1, 5, 10 and 20% damped elastic spectral response from records matched to the 1% and 5% damped target spectral acceleration using RSPMatch2005. Median target spectra (*lower*) and median-plus-one-standard-deviation target spectra (*upper*)

9.3 Spectral Matched Records with Different Durations

In order to identify the influence of ground-motion duration on structural response, 30 accelerograms with 5-95% significant durations ranging from 6 to 113 seconds are selected for further analysis (Table 9.1). To remove the influence of spectral amplitude from the results, the accelerograms are scaled and matched to the median-plus-one-standard-deviation target spectra at multiple damping levels using RSPMatch (Figure 9.3). The accelerograms not only have a good match on average to the target spectrum, but also have a close individual match to the 5% damped spectrum (Figure 9.4); this ensures that the main difference between the records is the ground-motion duration. Although there is not an exact correlation between the different definitions of duration and number of cycles definitions, there is an approximate correlation for the records used in this study (Figure 9.5). This is because the records have been selected to have a broad distribution of durations and have been matched to similar amplitudes; this reduces the significant differences usually experienced between relative and absolute definitions.

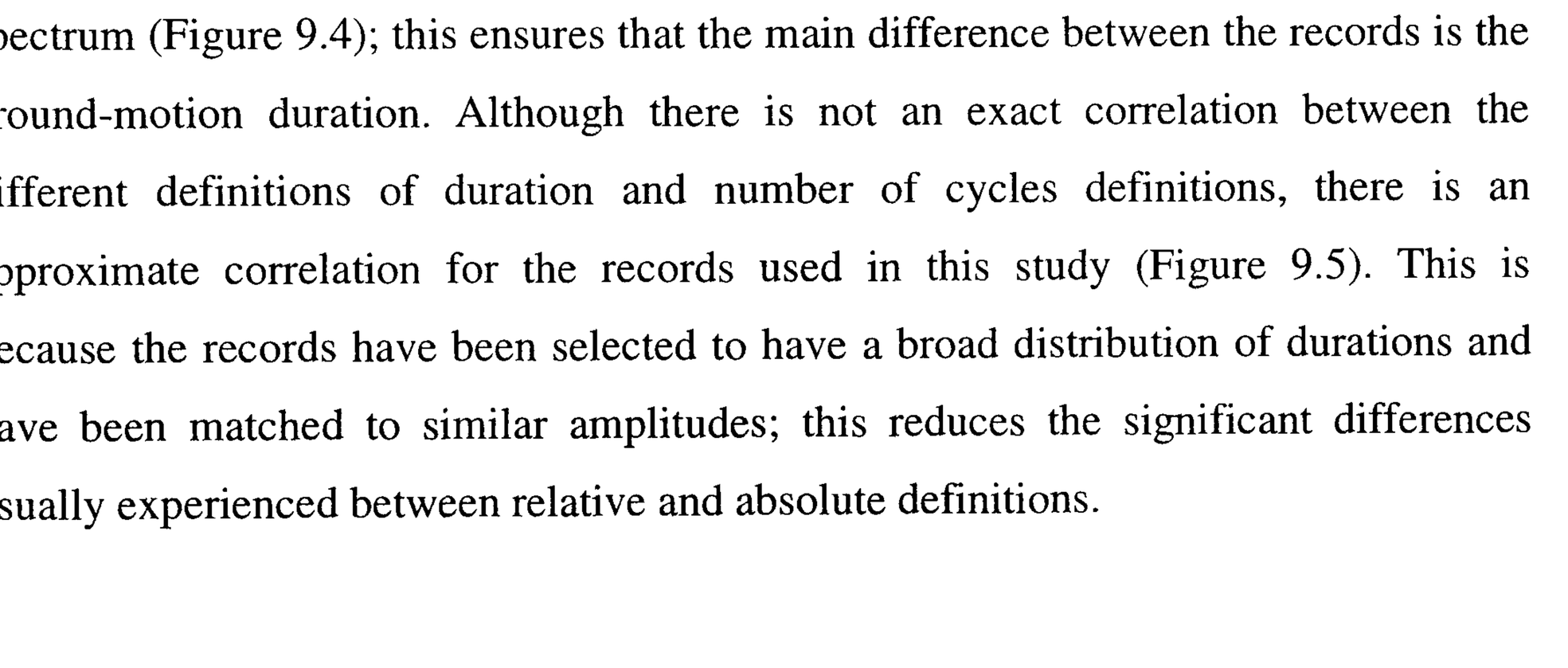


Figure 9.3. – Comparison of target spectra and median spectra from selected records with different durations which have been matched to fit the target using RSPMatch.

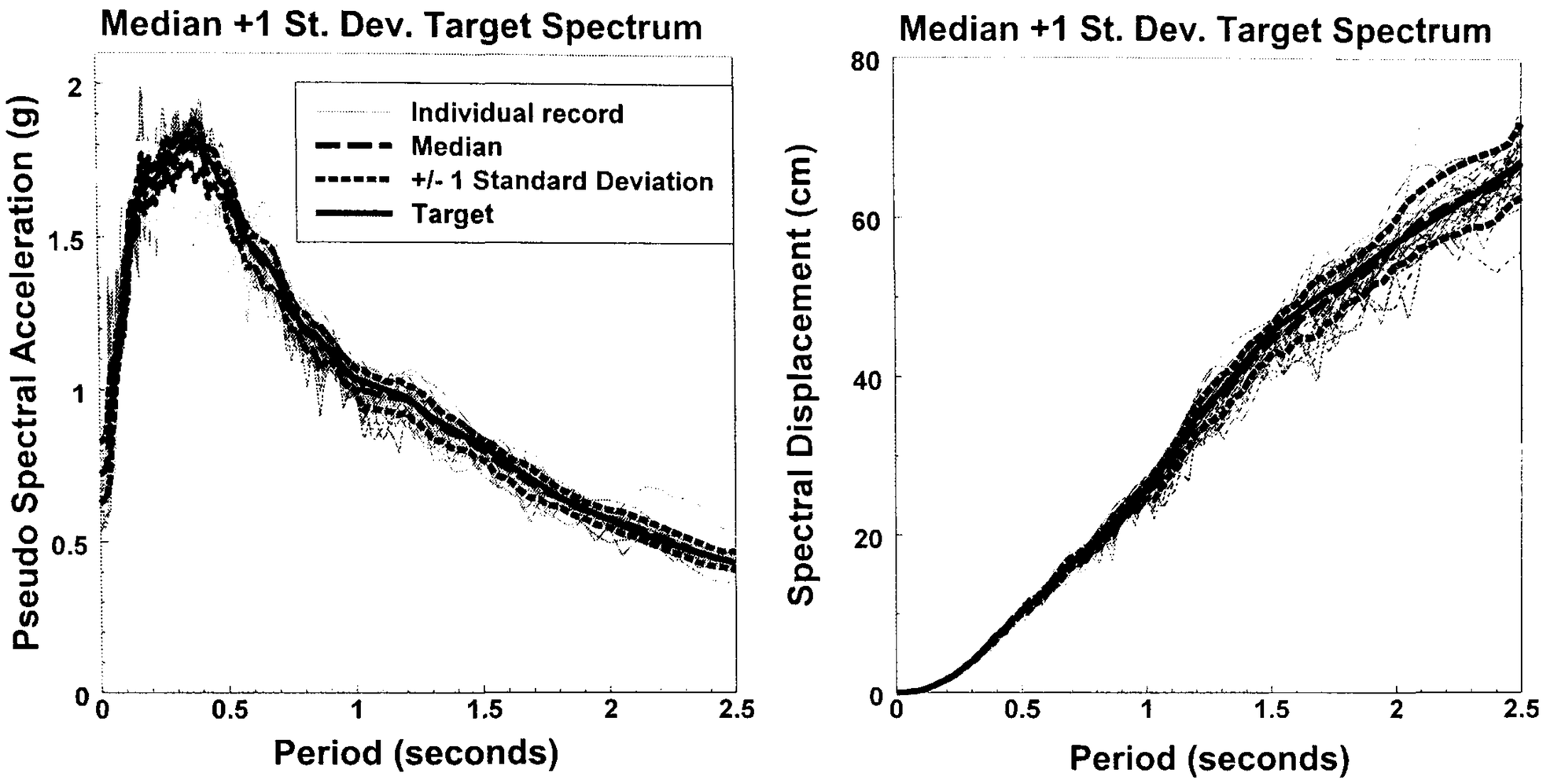


Figure 9.4. – Comparison of 5% damped target spectrum and the spectra from selected records with different durations, which have been matched to fit the target using RSPMatch.

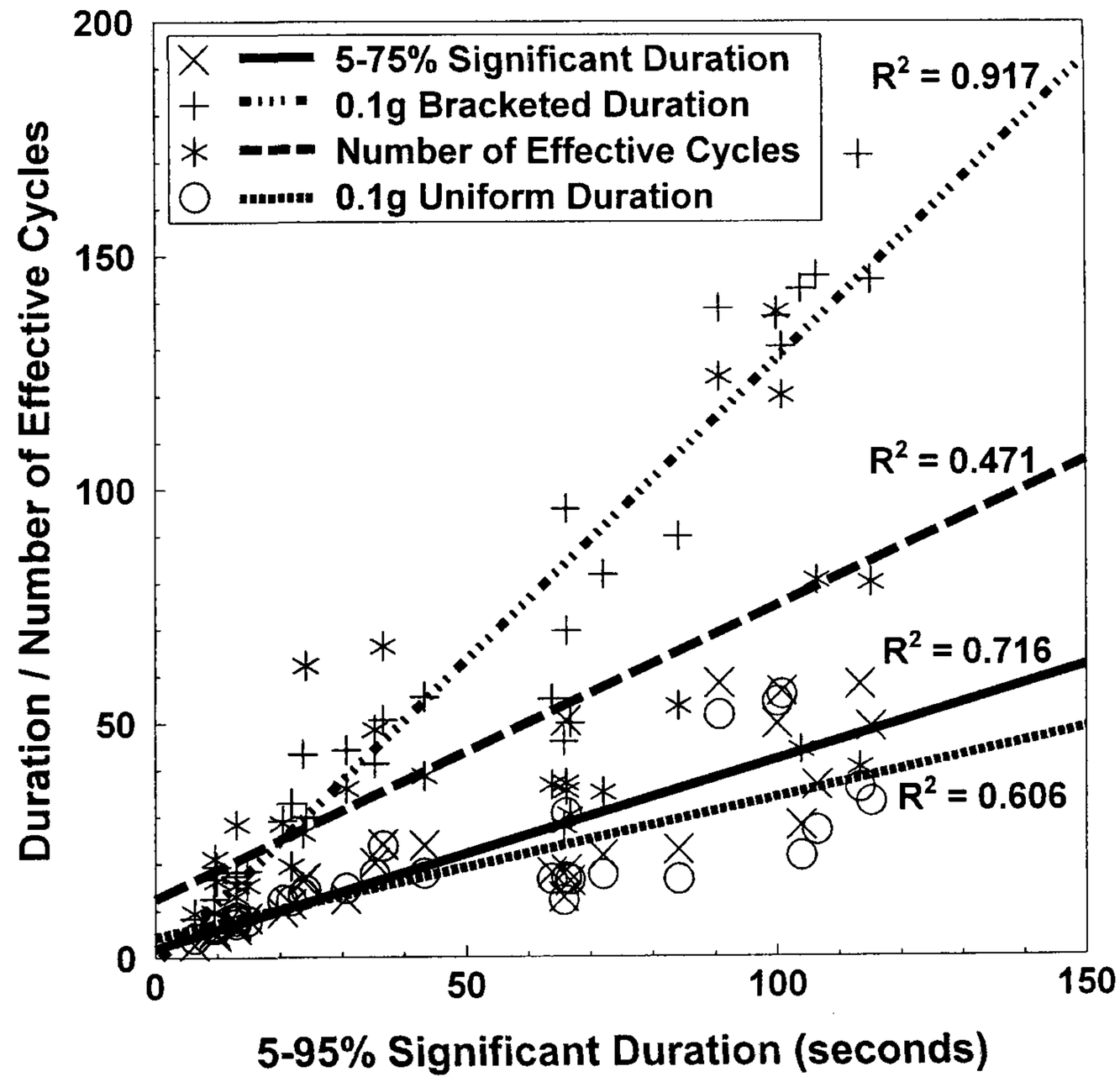


Figure 9.5. – Correlation between different definitions of duration and numbers of effective cycles. Number of cycles measured using rainflow counting and converted to an equivalent number of cycles using exponent 2.0 (see 2.4.6).

Table 9.1. – Accelerograms selected to have different durations

Year	Mw	Earthquake	Mechanism	Distance, Rjb (km)	Station	Soil Class	Accelerogram	Significant Dur	
								5-75%	5-95%
1979	5.74	Coyote Lake	Strike-Slip	8.5	Gilroy Array #2	Soft	00147T	2.64	6.35
1994	6.69	Northridge-01	Reverse	0	Sylmar - Converter Sta East	Stiff	01085L	5.07	9.43
1995	6.9	Kobe, Japan	Strike-Slip	0.9	Kobe University	Rock	01108T	5.64	9.55
1994	6.69	Northridge-01	Reverse	20.1	Castaic - Old Ridge Route	Stiff	00963L	4.64	9.84
1989	6.93	Loma Prieta	Rev/SS	72.9	Piedmont Jr High	Rock	00788L	6.87	12.97
1989	6.93	Loma Prieta	Rev/SS	19.9	Anderson Dam (L Abut)	Stiff	00740T	7.5	13.07
1979	5.74	Coyote Lake	Strike-Slip	4.8	Gilroy Array #4	Soft	00149T	6.09	13.08
1987	6.54	Superstition Hills-02	Strike-Slip	18.2	El Centro Imp. Co. Cent	Soft	00721L	8.39	14.79
1994	6.69	Northridge-01	Reverse	27.8	LA - Pico & Sentous	Soft	01000L	9.65	20.43
1994	6.69	Northridge-01	Reverse	25.6	LA - W 15th St	Stiff	01008T	11.22	21.82
1999	7.13	Hector Mine	Strike-Slip	172.1	Leona Valley - Fire Station #1	Soft	01806T	16.41	23.7
1940	6.95	Imperial Valley-02	Strike-Slip	6.1	El Centro Array #9	Soft	00006T	16.77	24.14
1952	7.36	Kern County	Rev/SS	35.1	Taft Lincoln School	Stiff	00015T	12.38	30.63
1987	6.54	Superstition Hills-02	Strike-Slip	23.9	Wildlife Liquef. Array	Soft	00729L	19.97	35.28
1992	7.28	Landers	Strike-Slip	26.8	North Palm Springs	Soft	00882L	23.9	36.57
1999	7.51	Kocaeli, Turkey	Strike-Slip	52	Zeytinburnu	Soft	01177L	23.62	43.24
1995	6.9	Kobe, Japan	Strike-Slip	24.9	Abeno	Soft	01100L	17.79	63.73
1995	6.9	Kobe, Japan	Strike-Slip	28.1	Sakai	Soft	01115L	12.64	65.68
2002	7.9	Denali, Alaska	Strike-Slip	164.7	TAPS Pump Station #12	Soft	02116T	50.1	66.04
1995	6.9	Kobe, Japan	Strike-Slip	24.9	Abeno	Soft	01100T	18.29	66.07
1995	6.9	Kobe, Japan	Strike-Slip	31.7	Tadoka	Soft	01118T	16.01	66.69
1995	6.9	Kobe, Japan	Strike-Slip	21.4	OSAJ	Soft	01113T	21.52	71.96
2002	7.9	Denali, Alaska	Strike-Slip	140.7	Fairbanks - Geophysic. Obs, CIGO	Stiff	02110L	22.67	84.14
2002	7.9	Denali, Alaska	Strike-Slip	126.4	TAPS Pump Station #11	Stiff	02115L	58.13	90.71
2002	7.9	Denali, Alaska	Strike-Slip	55.6	TAPS Pump Station #09	Stiff	02113T	49.5	100.02
2002	7.9	Denali, Alaska	Strike-Slip	55.6	TAPS Pump Station #09	Stiff	02113L	56.41	100.79
2002	7.9	Denali, Alaska	Strike-Slip	140.7	Fairbanks - Geophysic. Obs, CIGO	Stiff	02110T	27.82	103.9
2002	7.9	Denali, Alaska	Strike-Slip	139.3	Fairbanks - Ester Fire Station	Soft	02109T	35.79	106.43
2002	7.9	Denali, Alaska	Strike-Slip	275.9	Anchorage - New Fire Station #7	Soft	02104T	57.92	113.39
2002	7.9	Denali, Alaska	Strike-Slip	139.3	Fairbanks - Ester Fire Station	Soft	02109L	48.85	115.2

9.4 Response from Scaled and Matched Records

Different damage measures are used to compare the response of the structure under the action of linearly scaled and spectrum matched accelerograms. As discussed in the previous chapter, the number of analyses required to predict the response to a given confidence level depends on the standard deviation of the response (see equation 8.6). Knowledge of the standard deviation of the response does not prove that the estimation is not biased, i.e. consistently over- or under-estimated for the hazard level. In this study bias is determined by comparing the response predicted by equations derived from regression of the response of the structure under the action of 1656 unscaled accelerograms (described in detail in the previous chapter) with the response of the structure from the accelerograms that have been selected, scaled and matched to the target spectra.

9.4.1 Peak drift

The peak roof drift and inter-storey drift of the structure is measured under the action of accelerograms selected, scaled and matched to the elastic spectral acceleration at 5% damping and multiple damping levels (Figures 9.5 and 9.6; Tables 9.2 to 9.5). These are compared to the response of the structure under the action of the unscaled accelerograms and under the action of accelerograms linearly scaled to match the average acceleration over a range of periods (as described in Chapter 8). This shows that the median drift from the matched accelerograms is comparable to the median drift from the accelerograms linearly scaled to the average acceleration over a range of periods. However, the standard deviation of the response has reduced by a factor of approximately two, which reduces the number of accelerograms required to estimate the response to a given confidence level by a factor of about 4. The response of the structure to accelerograms matched to multiple damping levels also have consistently lower standard deviation than under the action of the accelerograms matched only to the 5% damping level (Tables 9.2 to 9.5).

The improved confidence of the response prediction further highlights the conclusion of the previous chapter that peak roof drift and inter-storey drift in the upper floors is consistently under-estimated by the analyses using the accelerograms scaled to match

the elastic response spectrum. The differences in response could have several different causes including:

- differences between inelastic and elastic response at higher load levels
- higher mode or travelling wave effects in the upper storeys
- the lower standard deviation of the elastic spectral acceleration than the peak response of the MDOF structure

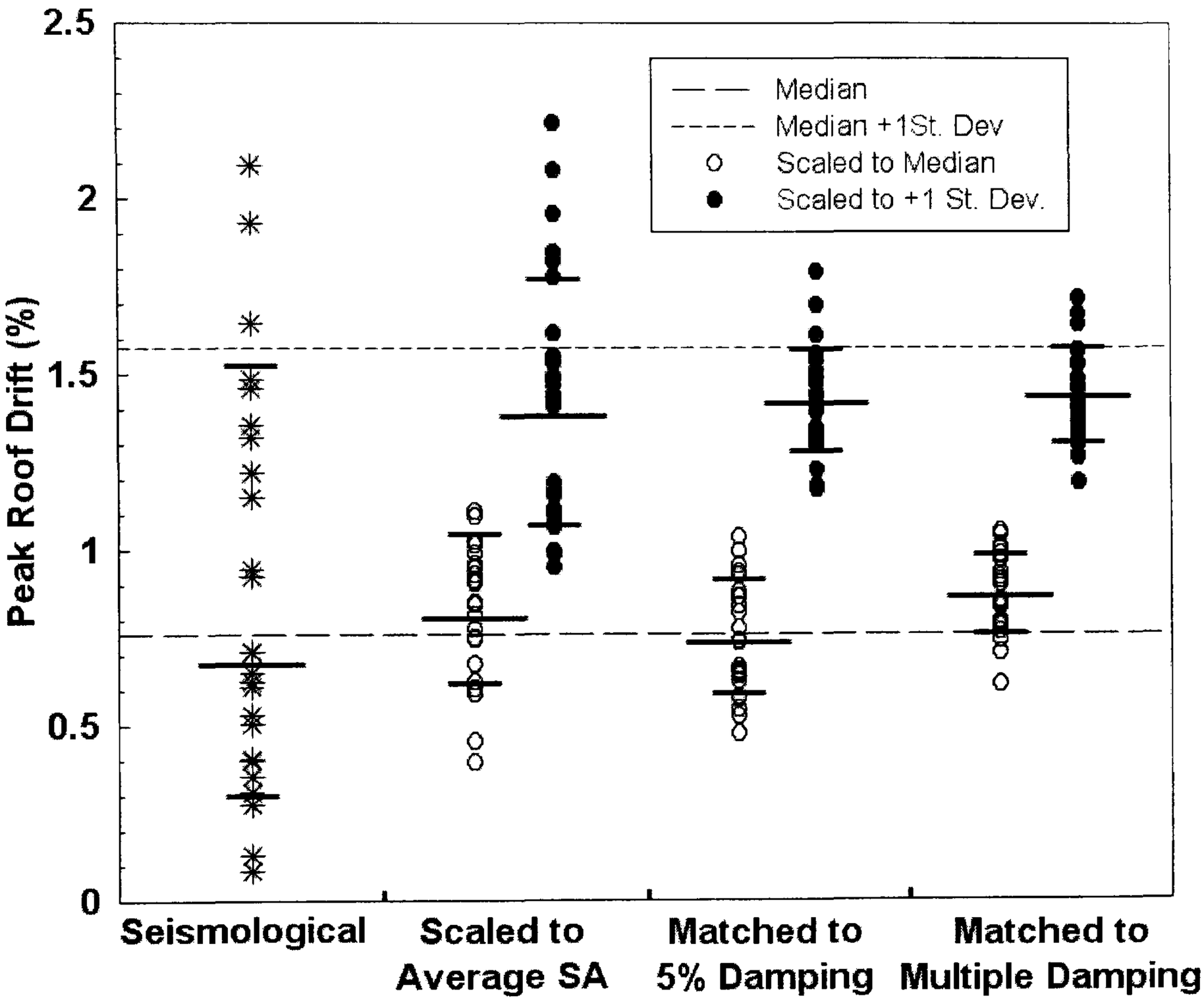


Figure 9.6. – Peak roof drift from records selected on seismological characteristics and those selected and matched to the target spectra at different damping levels. Error bars show median and +/-1 standard deviation. Dashed lines show drift predicted by regression of 1656 unscaled MDOF time-history analyses.

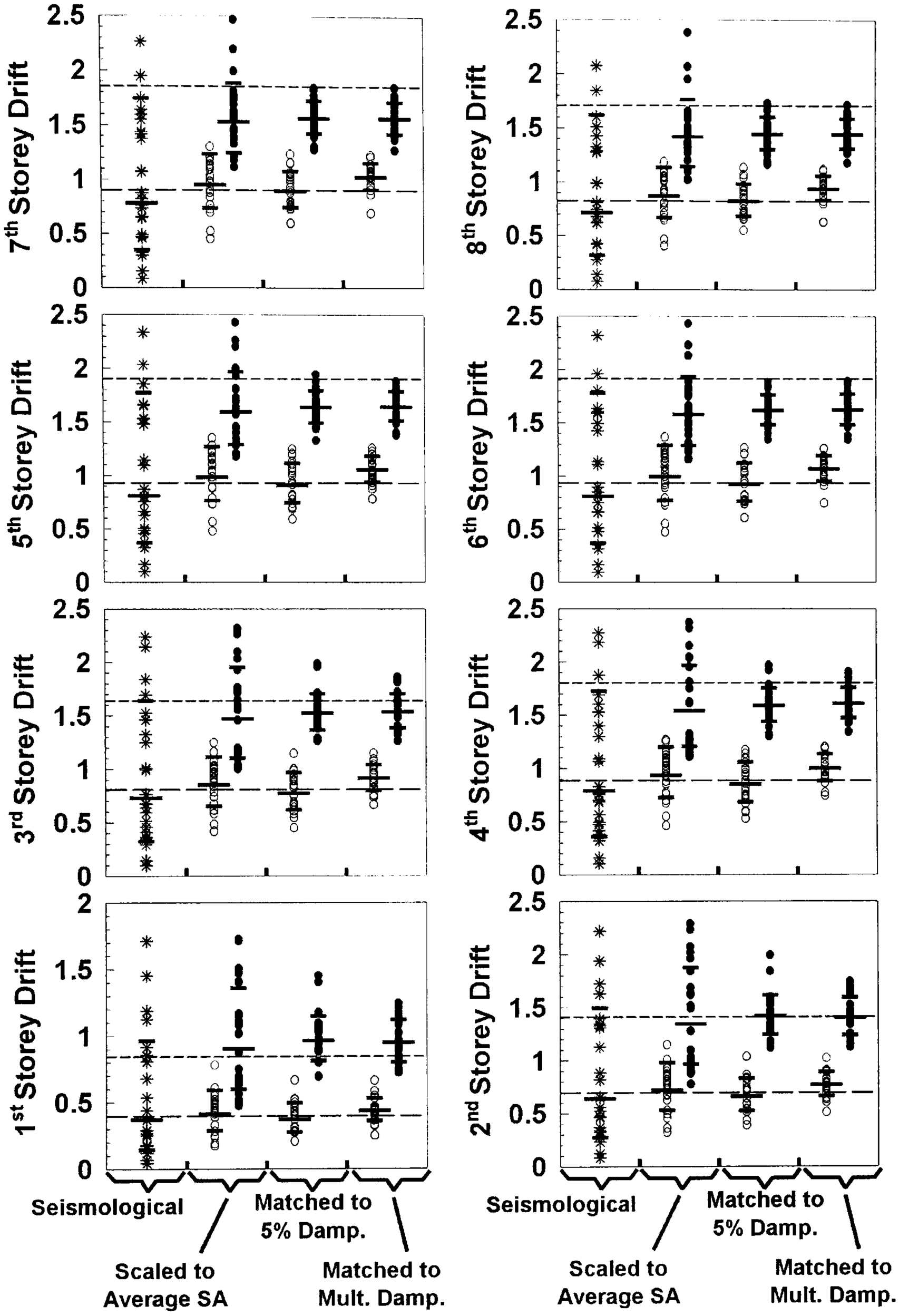


Figure 9.7. – Inter-storey drift from records selected on seismological characteristics and those selected and matched to the target spectra at different damping levels. Error bars show median and +/-1 standard deviation. Dashed lines show drift predicted by regression of 1656 unscaled MDOF time-history analyses.

Table 9.2. – Statistics of roof drift predicted from suites of records selected and matched to the target spectrum using different criteria.

Scale/Match Method	Regression	Linear, Ave SA Median	Linear, Ave SA Median +1St. Dev.	Matched 5% Median	Matched 5% Median +1St. Dev.	Matched 1 & 5% Median	Matched 1 & 5% Median +1St. Dev.
Median	0.758	0.803	1.376	0.734	1.415	0.862	1.431
1St Dev. (log)	0.316	0.113	0.109	0.095	0.045	0.056	0.041
Median +1SD	1.572	1.043	1.769	0.913	1.569	0.982	1.572
No. Records	834	25	25	25	25	25	25
SEE at 1SD	1.1%	2.3%	2.2%	1.9%	0.9%	1.1%	0.8%
No. Records for +/-10% confidence(log) at 1SD	10	1	1	1	1	1	1
No. Records for +/-5% confidence(log) at 1SD	40	5	5	4	1	1	1

Table 9.3. – Statistics of 8th storey drift predicted from suites of records selected and matched to the target spectrum using different criteria.

Scale/Match Method	Regression	Linear, Ave SA Median	Linear, Ave SA Median +1St. Dev.	Matched 5% Median	Matched 5% Median +1St. Dev.	Matched 1 & 5% Median	Matched 1 & 5% Median +1St. Dev.
Median	0.825	0.869	1.419	0.821	1.444	0.939	1.445
1St Dev. (log)	0.316	0.115	0.095	0.079	0.045	0.052	0.041
Median +1SD	1.709	1.131	1.764	0.985	1.603	1.059	1.589
No. Records	834	25	25	25	25	25	25
SEE at 1SD	1.1%	2.3%	1.9%	1.6%	0.9%	1.0%	0.8%
No. Records for +/-10% confidence(log) at 1SD	10	1	1	1	1	1	1
No. Records for +/-5% confidence(log) at 1SD	40	5	4	2	1	1	1

Table 9.4. – Statistics of 6th storey drift predicted from suites of records selected and matched to the target spectrum using different criteria.

Scale/Match Method	Regression	Linear, Ave SA Median	Linear, Ave SA Median +1St. Dev.	Matched 5% Median	Matched 5% Median +1St. Dev.	Matched 1 & 5% Median	Matched 1 & 5% Median +1St. Dev.
Median	0.931	0.994	1.576	0.924	1.618	1.066	1.621
1St Dev. (log)	0.313	0.113	0.088	0.084	0.037	0.049	0.038
Median +1SD	1.914	1.288	1.931	1.121	1.763	1.193	1.770
No. Records	834	25	25	25	25	25	25
SEE at 1SD	1.1%	2.3%	1.8%	1.7%	0.7%	1.0%	0.8%
No. Records for +/-10% confidence(log) at 1SD	10	1	1	1	1	1	1
No. Records for +/-5% confidence(log) at 1SD	39	5	3	3	1	1	1

Table 9.5. – Statistics of 1st storey drift predicted from suites of records selected and matched to the target spectrum using different criteria.

Scale/Match Method	Regression	Linear, Ave SA Median	Linear, Ave SA Median +1St. Dev.	Matched 5% Median	Matched 5% Median +1St. Dev.	Matched 1 & 5% Median	Matched 1 & 5% Median +1St. Dev.
Median	0.395	0.410	0.900	0.369	0.963	0.434	0.945
1St Dev. (log)	0.329	0.157	0.179	0.126	0.075	0.085	0.073
Median +1SD	0.843	0.590	1.359	0.493	1.146	0.528	1.118
No. Records	834	25	25	25	25	25	25
SEE at 1SD	1.1%	3.1%	3.6%	2.5%	1.5%	1.7%	1.5%
No. Records for +/-10% confidence(log) at 1SD	11	2	3	2	1	1	1
No. Records for +/-5% confidence(log) at 1SD	43	10	13	6	2	3	2

9.4.2 Local element damage measures

Local element damage measures are calculated for each element of the structure under the action of the unscaled, linearly scaled and matched accelerograms. The local element damage measures used in this study are:

- Peak member end rotation
- Normalised absorbed hysteretic energy
- Park and Ang damage index
- Member rotational fatigue

These measures have been described in detail in the previous chapter so a description of each is not repeated here. As was also noted in the previous chapter, the two-dimensional frame model used in this study is able to accurately model global parameters, such as inter-storey drift; however, local effects are less accurately modelled and the absolute values of the local damage measures have little meaning. This is because the two-dimensional frame model does not accurately model the outer frame, which will have greater deformations, damage and inelasticity than is indicated by the single-frame model used in this study (Mwafy 2001).

The peak rotations at the ends of the beams govern the inter-storey and global drift and so follow the same trends as the inter-storey drifts. Estimations of the median response are consistent with those predicted by regression equations. However, the rotations at the end of the beams of the upper storeys at the median-plus-one-standard-deviation level from accelerograms either scaled or matched to the elastic response spectrum consistently under-estimate the response (Figure 9.8). This study shows that the median response is essentially the same under the action of suites of accelerograms either linearly scaled or spectrally matched to the elastic response spectrum for both the beams and columns (Figures 9.7 and 9.8, Tables 9.6 to 9.11). The standard deviation of the peak end rotation also decreases when accelerograms are matched to the elastic response spectrum (Tables 9.6 to 9.11). For example, the number of accelerograms required to estimate the median peak rotation at the base of the outer ground floor column to within +/-5% at one standard deviation confidence level requires 12 analyses with accelerograms linearly scaled to the average spectral acceleration, but only 5 and 4 with accelerograms matched to the 5% damped

acceleration spectrum and multiple damping levels respectively. The Park and Ang damage measure depends on the member end rotation and absorbed hysteretic energy. This damage measure follows essentially the same trends as the peak member end rotation (Figures 9.9 and 9.10, Tables 9.12 to 9.17)

The absorbed hysteretic energy under the action of different accelerograms has considerable dispersion and is particularly difficult to estimate reliably. Indeed the median hysteretic energy of some members under the action of accelerograms scaled and matched to the median-plus-one-standard-deviation elastic spectral acceleration is greater than the median hysteretic energy from accelerograms matched to the median elastic spectral acceleration. (Figures 9.11 and 9.12). Using accelerograms matched to the elastic response spectrum generally has lower dispersion of the response compared with linearly scaled accelerograms (Table 9.18 to 9.23). For example, the number of accelerograms required to estimate the median hysteretic energy at the base of the outer ground floor column to within +/-5% at one standard deviation confidence level requires 59 analysis with accelerograms linearly scaled to the average spectral acceleration, but only 41 and 17 with accelerograms matched to the 5% damped acceleration spectrum and multiple damping levels respectively.

The member rotational fatigue has the greatest scatter of all of the damage measures. However, the median fatigue damage estimated using the spectrally matched accelerograms is comparable with that estimated by linearly scaled accelerograms (Figures 9.13 and 9.14). The matched accelerograms have the additional advantage of reducing the number of analyses required to predict the fatigue damage to a given confidence level (Tables 9.24 to 9.29). For example, the number of accelerograms required to estimate the median fatigue damage at the base of the outer ground floor column to within +/-5% at one standard deviation confidence level requires 176 analysis with accelerograms linearly scaled to the average spectral acceleration, but only 111 and 52 with accelerograms matched to the 5% damped acceleration spectrum and multiple damping levels respectively.

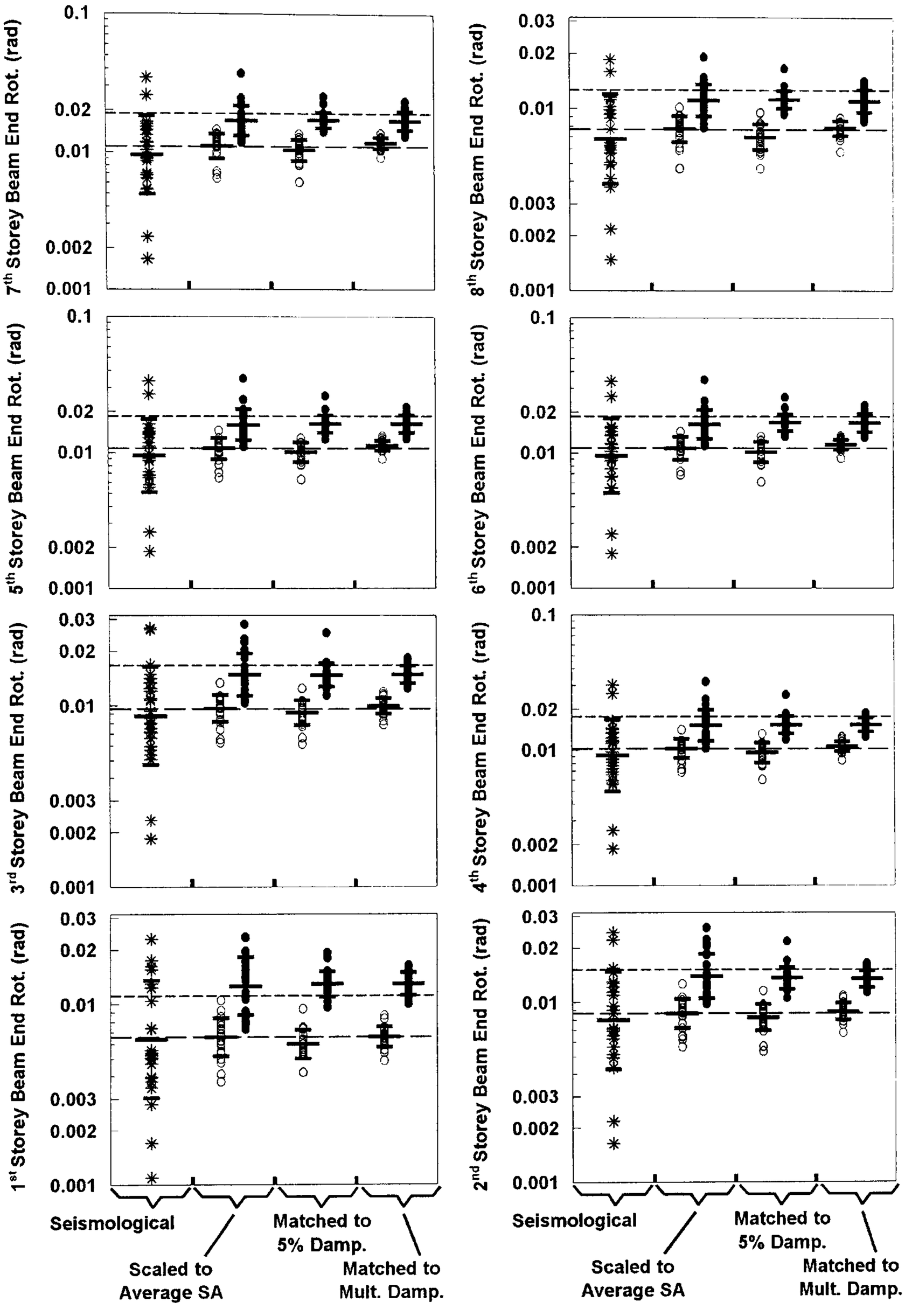


Figure 9.8. – Peak end rotation of beams at the edge of the structure from records scaled and matched using different criteria. Error bars show median and ±1 standard deviation. Dashed lines show drift predicted by regression of 1656 unscaled MDOF time-history analyses.

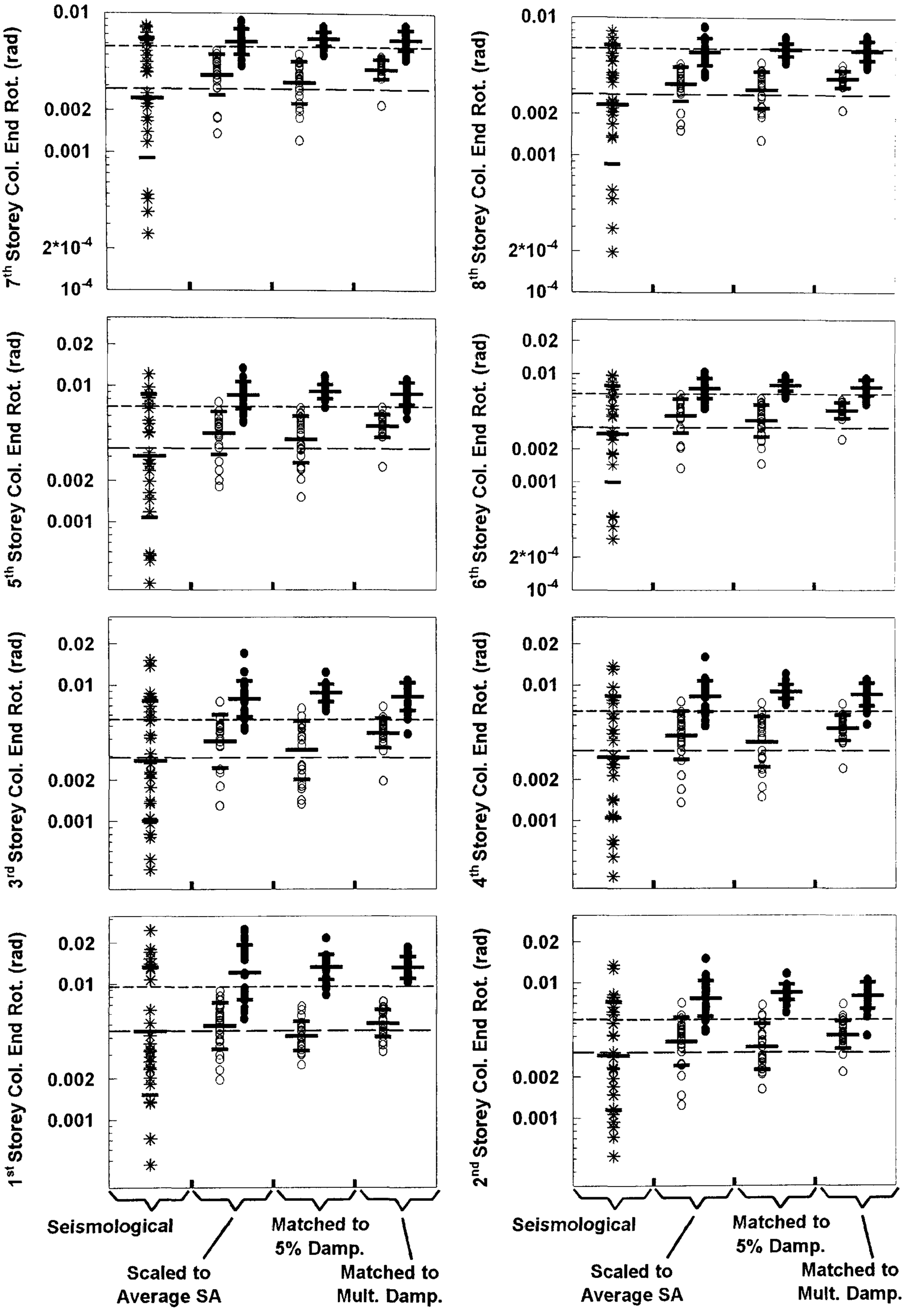


Figure 9.9. – Peak end rotation of the base of the columns at the edge of the structure from records scaled and matched using different criteria. Error bars show median and ±1 standard deviation. Dashed lines show drift predicted by regression of 1656 unscaled MDOF time-history analyses.

Table 9.6. – Statistics of peak end rotation of the beam on the 8th storey at the edge of the structure, predicted from suites of records selected, linearly scaled and matched using different criteria.

Scale/Match Method	Regression	Linear, Ave SA Median	Linear, Ave SA Median +1St. Dev.	Matched 5% Median	Matched 5% Median +1St. Dev.	Matched 1 & 5% Median	Matched 1 & 5% Median +1St. Dev.
Median	0.008	0.0077	0.011	0.0070	0.011	0.0079	0.011
1St Dev. (log)	0.215	0.071	0.086	0.071	0.049	0.041	0.061
Median +1SD	0.013	0.0091	0.014	0.008	0.013	0.0086	0.013
No. Records	834	25	25	25	25	25	25
SEE at 1SD	0.7%	1.4%	1.7%	1.4%	1.0%	0.8%	1.2%
No. Records for +/-10% confidence(log) at 1SD	5	1	1	0.5	0.2	0.2	0.4
No. Records for +/-5% confidence(log) at 1SD	18	2	3	2	1.0	1	1.5

Table 9.7. – Statistics of peak end rotation of the beam on the 6th storey at the edge of the structure, predicted from suites of records selected, linearly scaled and matched using different criteria.

Scale/Match Method	Regression	Linear, Ave SA Median	Linear, Ave SA Median +1St. Dev.	Matched 5% Median	Matched 5% Median +1St. Dev.	Matched 1 & 5% Median	Matched 1 & 5% Median +1St. Dev.
Median	0.011	0.0109	0.016	0.0102	0.017	0.0116	0.017
1St Dev. (log)	0.238	0.084	0.108	0.075	0.060	0.036	0.068
Median +1SD	0.019	0.0132	0.021	0.012	0.019	0.0126	0.019
No. Records	834	25	25	25	25	25	25
SEE at 1SD	0.8%	1.7%	2.2%	1.5%	1.2%	0.7%	1.4%
No. Records for +/-10% confidence(log) at 1SD	6	1	1	0.6	0.4	0.1	0.5
No. Records for +/-5% confidence(log) at 1SD	23	3	5	2	1.5	1	1.9

Table 9.8. – Statistics of peak end rotation of the beam on the 1st storey at the edge of the structure, predicted from suites of records selected, linearly scaled and matched using different criteria.

Scale/Match Method	Regression	Linear, Ave SA Median	Linear, Ave SA Median +1St. Dev.	Matched 5% Median	Matched 5% Median +1St. Dev.	Matched 1 & 5% Median	Matched 1 & 5% Median +1St. Dev.
Median	0.007	0.0066	0.013	0.0060	0.013	0.0066	0.013
1St Dev. (log)	0.229	0.105	0.161	0.080	0.071	0.057	0.064
Median +1SD	0.011	0.0084	0.018	0.007	0.015	0.0075	0.015
No. Records	834	25	25	25	25	25	25
SEE at 1SD	0.8%	2.1%	3.2%	1.6%	1.4%	1.1%	1.3%
No. Records for +/-10% confidence(log) at 1SD	5	1	3	0.6	0.5	0.3	0.4
No. Records for +/-5% confidence(log) at 1SD	21	4	10	3	2.0	1	1.6

Table 9.9. – Statistics of peak end rotation of the base of the column on the 8th storey at the edge of the structure, predicted from suites of records selected, linearly scaled and matched using different criteria.

Scale/Match Method	Regression	Linear, Ave SA Median	Linear, Ave SA Median +1St. Dev.	Matched 5% Median	Matched 5% Median +1St. Dev.	Matched 1 & 5% Median	Matched 1 & 5% Median +1St. Dev.
Median	0.007	0.0033	0.006	0.0030	0.006	0.0036	0.006
1St Dev. (log)	0.229	0.122	0.097	0.133	0.047	0.063	0.071
Median +1SD	0.011	0.0044	0.007	0.004	0.007	0.0042	0.007
No. Records	834	25	25	25	25	25	25
SEE at 1SD	0.8%	2.4%	1.9%	2.7%	0.9%	1.3%	1.4%
No. Records for +/-10% confidence(log) at 1SD	5	1	1	1.8	0.2	0.4	0.5
No. Records for +/-5% confidence(log) at 1SD	21	6	4	7	0.9	2	2.0

Table 9.10. – Statistics of peak end rotation of the base of the column on the 6th storey at the edge of the structure, predicted from suites of records selected, linearly scaled and matched using different criteria.

Scale/Match Method	Regression	Linear, Ave SA Median	Linear, Ave SA Median +1St. Dev.	Matched 5% Median	Matched 5% Median +1St. Dev.	Matched 1 & 5% Median	Matched 1 & 5% Median +1St. Dev.
Median	0.003	0.0041	0.007	0.0037	0.008	0.0046	0.008
1St Dev. (log)	0.311	0.156	0.092	0.149	0.049	0.072	0.071
Median +1SD	0.007	0.0058	0.009	0.005	0.009	0.0055	0.009
No. Records	834	25	25	25	25	25	25
SEE at 1SD	1.1%	3.1%	1.8%	3.0%	1.0%	1.4%	1.4%
No. Records for +/-10% confidence(log) at 1SD	10	2	1	2.2	0.2	0.5	0.5
No. Records for +/-5% confidence(log) at 1SD	39	10	3	9	0.9	2	2.0

Table 9.11. – Statistics of peak end rotation of the base of the column on the 1st storey at the edge of the structure, predicted from suites of records selected, linearly scaled and matched using different criteria.

Scale/Match Method	Regression	Linear, Ave SA Median	Linear, Ave SA Median +1St. Dev.	Matched 5% Median	Matched 5% Median +1St. Dev.	Matched 1 & 5% Median	Matched 1 & 5% Median +1St. Dev.
Median	0.005	0.0049	0.012	0.0041	0.013	0.0051	0.013
1St Dev. (log)	0.321	0.171	0.202	0.108	0.092	0.100	0.081
Median +1SD	0.009	0.0073	0.019	0.005	0.016	0.0064	0.016
No. Records	834	25	25	25	25	25	25
SEE at 1SD	1.1%	3.4%	4.0%	2.2%	1.8%	2.0%	1.6%
No. Records for +/-10% confidence(log) at 1SD	10	3	4	1.2	0.8	1.0	0.7
No. Records for +/-5% confidence(log) at 1SD	41	12	16	5	3.4	4	2.6

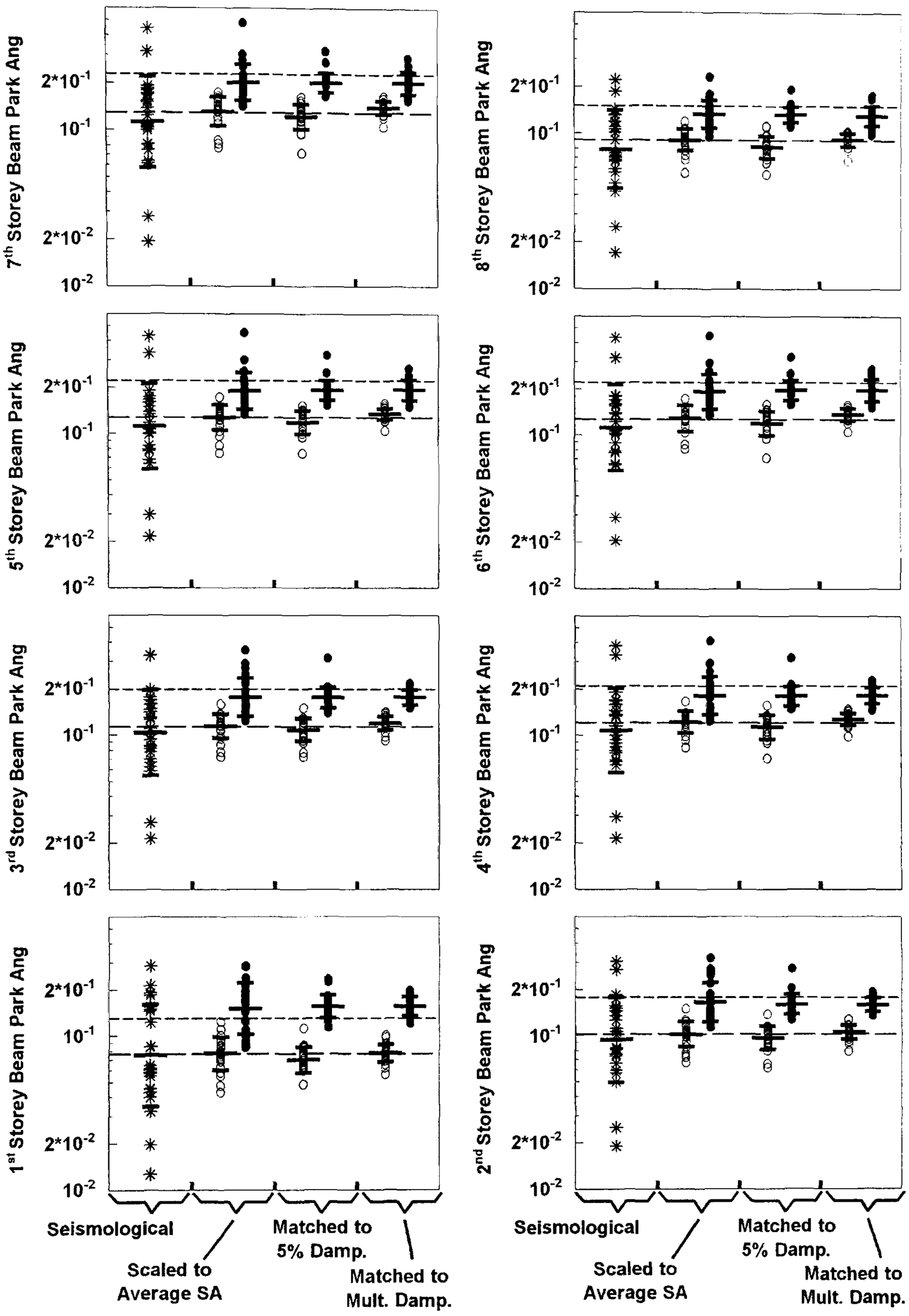


Figure 9.10. – Park and Ang damage index of beams at the edge of the structure from records scaled and matched using different criteria. Error bars show median and ±1 standard deviation. Dashed lines show drift predicted by regression of 1656 unscaled MDOF time-history analyses.

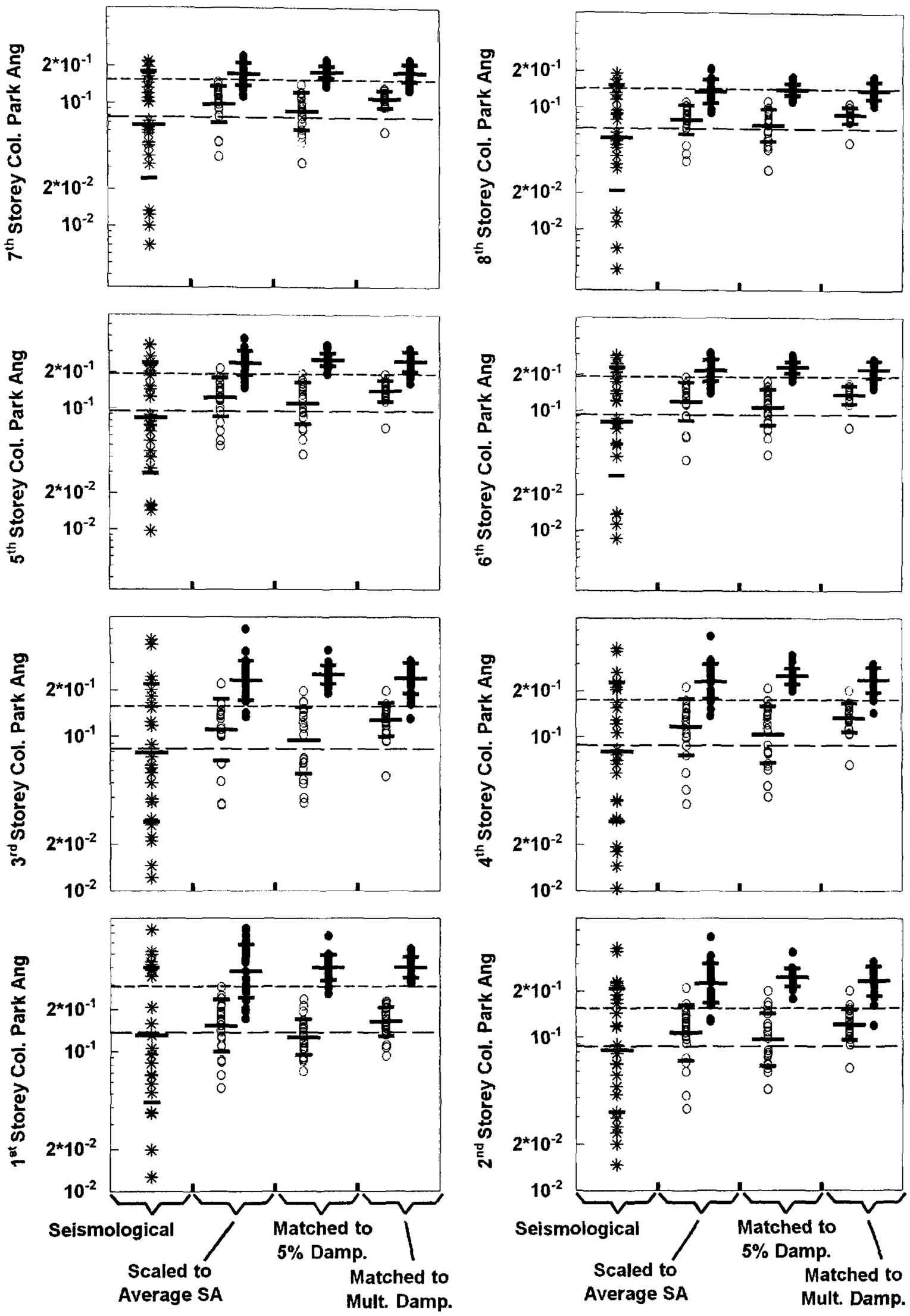


Figure 9.11. – Park and Ang damage index of the base of the columns at the edge of the structure from records scaled and matched using different criteria. Error bars show median and ±1 standard deviation. Dashed lines show drift predicted by regression of 1656 unscaled MDOF time-history analyses.

Table 9.12. – Statistics of the Park and Ang damage index of the beam on the 8th storey at the edge of the structure, predicted from suites of records selected, linearly scaled and matched using different criteria.

Scale/Match Method	Regression	Linear, Ave SA Median	Linear, Ave SA Median +1St. Dev.	Matched 5% Median	Matched 5% Median +1St. Dev.	Matched 1 & 5% Median	Matched 1 & 5% Median +1St. Dev.
Median	0.091	0.0912	0.134	0.0826	0.134	0.0925	0.131
1St Dev. (log)	0.218	0.071	0.089	0.072	0.050	0.043	0.065
Median +1SD	0.151	0.1073	0.164	0.097	0.150	0.1021	0.152
No. Records	834	25	25	25	25	25	25
SEE at 1SD	0.8%	1.4%	1.8%	1.4%	1.0%	0.9%	1.3%
No. Records for +/-10% confidence(log) at 1SD	5	0	1	0.5	0.2	0.2	0.4
No. Records for +/-5% confidence(log) at 1SD	19	2	3	2	1.0	1	1.7

Table 9.13. – Statistics of the Park and Ang damage index of the beam on the 6th storey at the edge of the structure, predicted from suites of records selected, linearly scaled and matched using different criteria.

Scale/Match Method	Regression	Linear, Ave SA Median	Linear, Ave SA Median +1St. Dev.	Matched 5% Median	Matched 5% Median +1St. Dev.	Matched 1 & 5% Median	Matched 1 & 5% Median +1St. Dev.
Median	0.127	0.1291	0.193	0.1203	0.198	0.1379	0.198
1St Dev. (log)	0.241	0.085	0.114	0.078	0.064	0.038	0.072
Median +1SD	0.222	0.1570	0.252	0.144	0.229	0.1505	0.233
No. Records	834	25	25	25	25	25	25
SEE at 1SD	0.8%	1.7%	2.3%	1.6%	1.3%	0.8%	1.4%
No. Records for +/-10% confidence(log) at 1SD	6	1	1	0.6	0.4	0.1	0.5
No. Records for +/-5% confidence(log) at 1SD	23	3	5	2	1.6	1	2.1

Table 9.14. – Statistics of the Park and Ang damage index of the beam on the 1st storey at the edge of the structure, predicted from suites of records selected, linearly scaled and matched using different criteria.

Scale/Match Method	Regression	Linear, Ave SA Median	Linear, Ave SA Median +1St. Dev.	Matched 5% Median	Matched 5% Median +1St. Dev.	Matched 1 & 5% Median	Matched 1 & 5% Median +1St. Dev.
Median	0.076	0.0769	0.151	0.0697	0.156	0.0773	0.156
1St Dev. (log)	0.231	0.108	0.166	0.082	0.074	0.057	0.063
Median +1SD	0.130	0.0986	0.221	0.084	0.185	0.0881	0.181
No. Records	834	25	25	25	25	25	25
SEE at 1SD	0.8%	2.2%	3.3%	1.6%	1.5%	1.1%	1.3%
No. Records for +/-10% confidence(log) at 1SD	5	1	3	0.7	0.5	0.3	0.4
No. Records for +/-5% confidence(log) at 1SD	21	5	11	3	2.2	1	1.6

Table 9.15. – Statistics of the Park and Ang damage index of the base of the column on the 8th storey at the edge of the structure, predicted from suites of records selected, linearly scaled and matched using different criteria.

Scale/Match Method	Regression	Linear, Ave SA Median	Linear, Ave SA Median +1St. Dev.	Matched 5% Median	Matched 5% Median +1St. Dev.	Matched 1 & 5% Median	Matched 1 & 5% Median +1St. Dev.
Median	0.067	0.0796	0.137	0.0724	0.142	0.0881	0.141
1St Dev. (log)	0.330	0.120	0.097	0.132	0.049	0.066	0.071
Median +1SD	0.144	0.1050	0.171	0.098	0.159	0.1026	0.166
No. Records	834	25	25	25	25	25	25
SEE at 1SD	1.1%	2.4%	1.9%	2.6%	1.0%	1.3%	1.4%
No. Records for +/-10% confidence(log) at 1SD	11	1	1	1.7	0.2	0.4	0.5
No. Records for +/-5% confidence(log) at 1SD	44	6	4	7	0.9	2	2.0

Table 9.16. – Statistics of the Park and Ang damage index of the base of the column on the 6th storey at the edge of the structure, predicted from suites of records selected, linearly scaled and matched using different criteria.

Scale/Match Method	Regression	Linear, Ave SA Median	Linear, Ave SA Median +1St. Dev.	Matched 5% Median	Matched 5% Median +1St. Dev.	Matched 1 & 5% Median	Matched 1 & 5% Median +1St. Dev.
Median	0.093	0.1197	0.218	0.1080	0.232	0.1370	0.224
1St Dev. (log)	0.312	0.158	0.093	0.151	0.049	0.074	0.071
Median +1SD	0.192	0.1723	0.270	0.153	0.259	0.1625	0.263
No. Records	834	25	25	25	25	25	25
SEE at 1SD	1.1%	3.2%	1.9%	3.0%	1.0%	1.5%	1.4%
No. Records for +/-10% confidence(log) at 1SD	10	2	1	2.3	0.2	0.5	0.5
No. Records for +/-5% confidence(log) at 1SD	39	10	3	9	1.0	2	2.0

Table 9.17. – Statistics of the Park and Ang damage index of the base of the column on the 1st storey at the edge of the structure, predicted from suites of records selected, linearly scaled and matched using different criteria.

Scale/Match Method	Regression	Linear, Ave SA Median	Linear, Ave SA Median +1St. Dev.	Matched 5% Median	Matched 5% Median +1St. Dev.	Matched 1 & 5% Median	Matched 1 & 5% Median +1St. Dev.
Median	0.136	0.1527	0.375	0.1265	0.400	0.1634	0.399
1St Dev. (log)	0.330	0.185	0.191	0.128	0.090	0.104	0.076
Median +1SD	0.292	0.2338	0.582	0.170	0.492	0.2074	0.474
No. Records	834	25	25	25	25	25	25
SEE at 1SD	1.1%	3.7%	3.8%	2.6%	1.8%	2.1%	1.5%
No. Records for +/-10% confidence(log) at 1SD	11	3	4	1.6	0.8	1.1	0.6
No. Records for +/-5% confidence(log) at 1SD	44	14	15	7	3.2	4	2.3

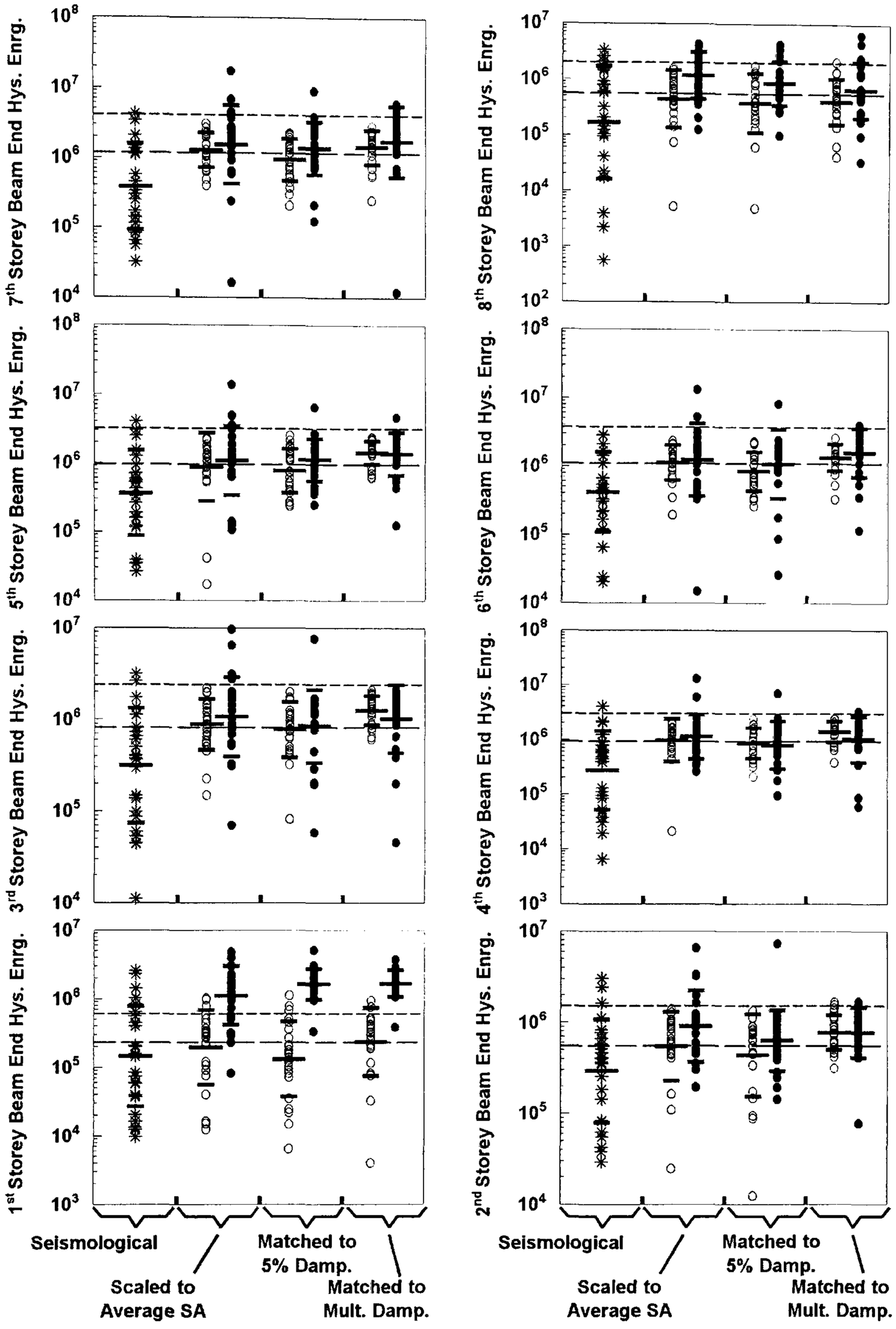


Figure 9.12. – Absorbed hysteretic energy (rad.mm) of beams at the edge of the structure from records scaled and matched using different criteria. Error bars show median and ±1 standard deviation. Dashed lines show drift predicted by regression of 1656 unscaled MDOF time-history analyses.

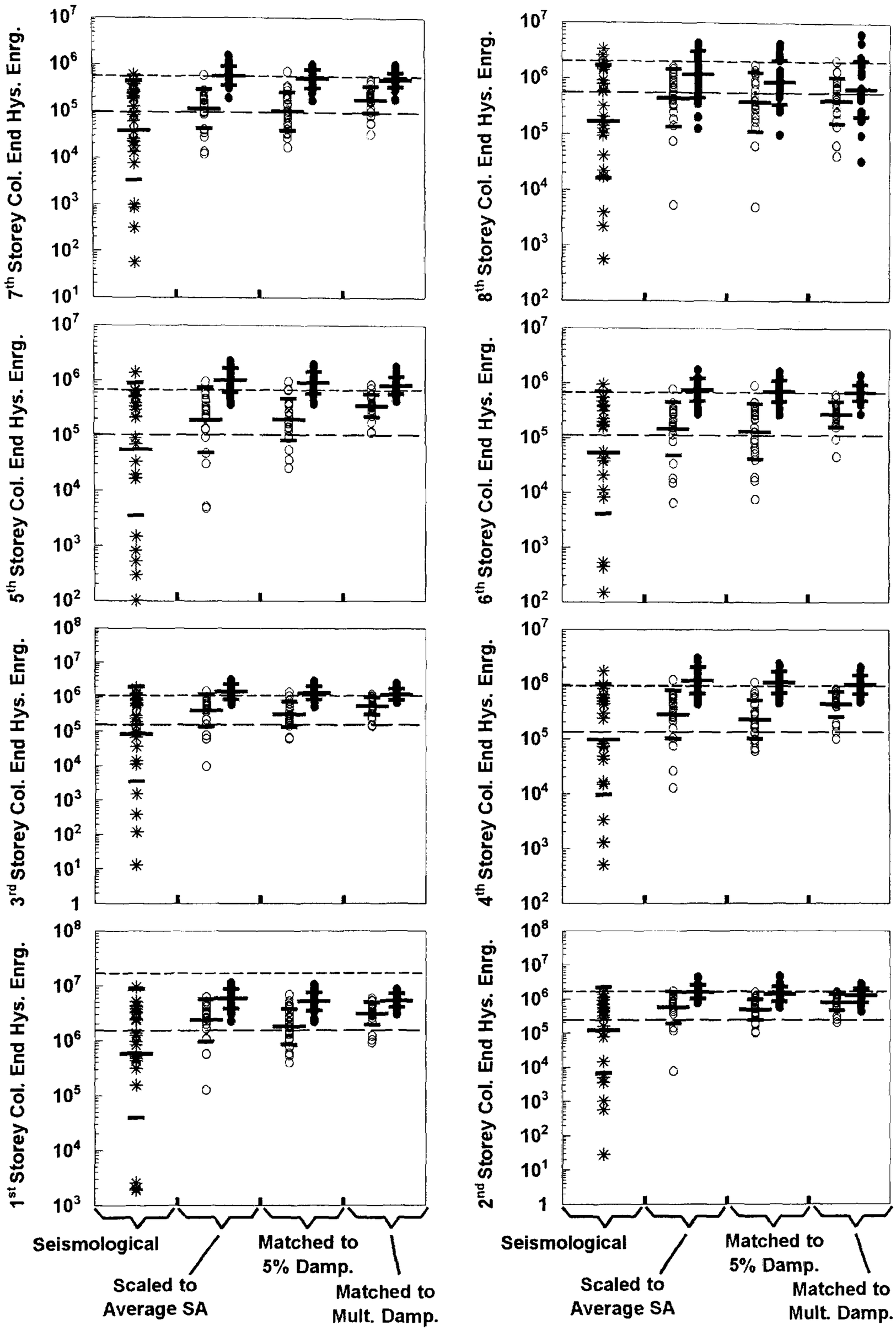


Figure 9.13. – Absorbed hysteretic energy (rad.mm) of the base of the columns at the edge of the structure from records scaled and matched using different criteria. Error bars show median and ±1 standard deviation. Dashed lines show drift predicted by regression of 1656 unscaled MDOF time-history analyses.

Table 9.18. – Statistics of absorbed hysteretic energy (rad.mm) of the beam on the 8th storey at the edge of the structure, predicted from suites of records selected, linearly scaled and matched using different criteria.

Scale/Match Method	Regression	Linear, Ave SA Median	Linear, Ave SA Median +1St. Dev.	Matched 5% Median	Matched 5% Median +1St. Dev.	Matched 1 & 5% Median	Matched 1 & 5% Median +1St. Dev.
Median	553139	445408	1196972	385936	874520	411897	672441
1St Dev. (log)	0.559	0.517	0.418	0.531	0.396	0.407	0.504
Median +1SD	2005079	1464913	3134265	1311963	2175543	1050847	2148539
No. Records	834	25	25	25	25	25	25
SEE at 1SD	1.9%	10.3%	8.4%	10.6%	7.9%	8.1%	10.1%
No. Records for +/-10% confidence(log) at 1SD	31	27	17	28.2	15.7	16.5	25.5
No. Records for +/-5% confidence(log) at 1SD	125	107	70	113	62.7	66	101.8

Table 9.19. – Statistics of absorbed hysteretic energy (rad.mm) of the beam on the 6th storey at the edge of the structure, predicted from suites of records selected, linearly scaled and matched using different criteria.

Scale/Match Method	Regression	Linear, Ave SA Median	Linear, Ave SA Median +1St. Dev.	Matched 5% Median	Matched 5% Median +1St. Dev.	Matched 1 & 5% Median	Matched 1 & 5% Median +1St. Dev.
Median	1108933	1130241	1247641	848387	1084118	1367550	1604531
1St Dev. (log)	0.525	0.255	0.535	0.283	0.506	0.199	0.357
Median +1SD	3718550	2032398	4272370	1627911	3474128	2164340	3647615
No. Records	834	25	25	25	25	25	25
SEE at 1SD	1.8%	5.1%	10.7%	5.7%	10.1%	4.0%	7.1%
No. Records for +/-10% confidence(log) at 1SD	28	6	29	8.0	25.6	4.0	12.7
No. Records for +/-5% confidence(log) at 1SD	110	26	114	32	102.3	16	50.9

Table 9.20. – Statistics of absorbed hysteretic energy (rad.mm) of the beam on the 1st storey at the edge of the structure, predicted from suites of records selected, linearly scaled and matched using different criteria.

Scale/Match Method	Regression	Linear, Ave SA Median	Linear, Ave SA Median +1St. Dev.	Matched 5% Median	Matched 5% Median +1St. Dev.	Matched 1 & 5% Median	Matched 1 & 5% Median +1St. Dev.
Median	231511	196430	1112838	131463	1633359	236820	1672415
1St Dev. (log)	0.416	0.541	0.430	0.550	0.221	0.494	0.194
Median +1SD	603572	682396	2992467	466158	2716188	739276	2614149
No. Records	834	25	25	25	25	25	25
SEE at 1SD	1.4%	10.8%	8.6%	11.0%	4.4%	9.9%	3.9%
No. Records for +/-10% confidence(log) at 1SD	17	29	18	30.2	4.9	24.4	3.8
No. Records for +/-5% confidence(log) at 1SD	69	117	74	121	19.5	98	15.1

Table 9.21. – Statistics of absorbed hysteretic energy (rad.mm) of the base of the column on the 8th storey at the edge of the structure, predicted from suites of records selected, linearly scaled and matched using different criteria.

Scale/Match Method	Regression	Linear, Ave SA Median	Linear, Ave SA Median +1St. Dev.	Matched 5% Median	Matched 5% Median +1St. Dev.	Matched 1 & 5% Median	Matched 1 & 5% Median +1St. Dev.
Median	103462	67541	143547	58671	237645	66458	246290
1St Dev. (log)	0.685	0.515	0.600	0.391	0.376	0.373	0.339
Median +1SD	500543	221270	571943	144380	564697	156711	537818
No. Records	834	25	25	25	25	25	25
SEE at 1SD	2.4%	10.3%	12.0%	7.8%	7.5%	7.5%	6.8%
No. Records for +/-10% confidence(log) at 1SD	47	27	36	15.3	14.1	13.9	11.5
No. Records for +/-5% confidence(log) at 1SD	188	106	144	61	56.5	56	46.0

Table 9.22. – Statistics of absorbed hysteretic energy (rad.mm) of the base of the column on the 6th storey at the edge of the structure, predicted from suites of records selected, linearly scaled and matched using different criteria.

Scale/Match Method	Regression	Linear, Ave SA Median	Linear, Ave SA Median +1St. Dev.	Matched 5% Median	Matched 5% Median +1St. Dev.	Matched 1 & 5% Median	Matched 1 & 5% Median +1St. Dev.
Median	110034	147028	754894	130894	723051	273490	679735
1St Dev. (log)	0.781	0.489	0.204	0.505	0.194	0.231	0.144
Median +1SD	665112	453205	1208314	418875	1130180	465716	946465
No. Records	834	25	25	25	25	25	25
SEE at 1SD	2.7%	9.8%	4.1%	10.1%	3.9%	4.6%	2.9%
No. Records for +/-10% confidence(log) at 1SD	61	24	4	25.5	3.8	5.3	2.1
No. Records for +/-5% confidence(log) at 1SD	244	96	17	102	15.1	21	8.3

Table 9.23. – Statistics of absorbed hysteretic energy (rad.mm) of the base of the column on the 1st storey at the edge of the structure, predicted from suites of records selected, linearly scaled and matched using different criteria.

Scale/Match Method	Regression	Linear, Ave SA Median	Linear, Ave SA Median +1St. Dev.	Matched 5% Median	Matched 5% Median +1St. Dev.	Matched 1 & 5% Median	Matched 1 & 5% Median +1St. Dev.
Median	1523654	2350569	5845033	1783447	5156610	3094726	5348206
1St Dev. (log)	1.047	0.383	0.183	0.321	0.163	0.205	0.126
Median +1SD	16996892	5678629	8904915	3732008	7502054	4957352	7141993
No. Records	834	25	25	25	25	25	25
SEE at 1SD	3.6%	7.7%	3.7%	6.4%	3.3%	4.1%	2.5%
No. Records for +/-10% confidence(log) at 1SD	110	15	3	10.3	2.7	4.2	1.6
No. Records for +/-5% confidence(log) at 1SD	439	59	13	41	10.6	17	6.3

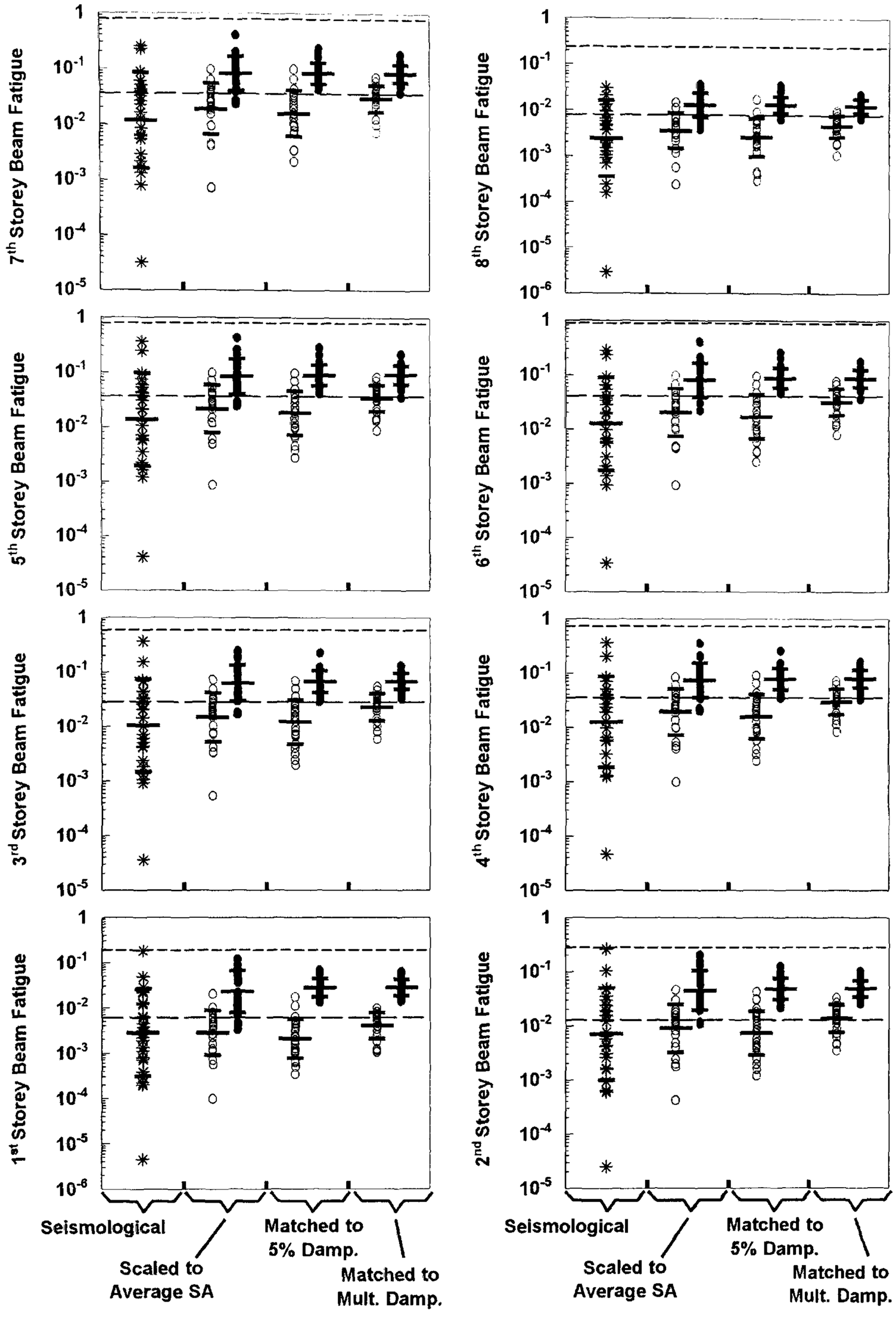


Figure 9.14. – Fatigue damage index of beams at the edge of the structure from records scaled and matched using different criteria. Error bars show median and ±1 standard deviation. Dashed lines show drift predicted by regression of 1656 unscaled MDOF time-history analyses.

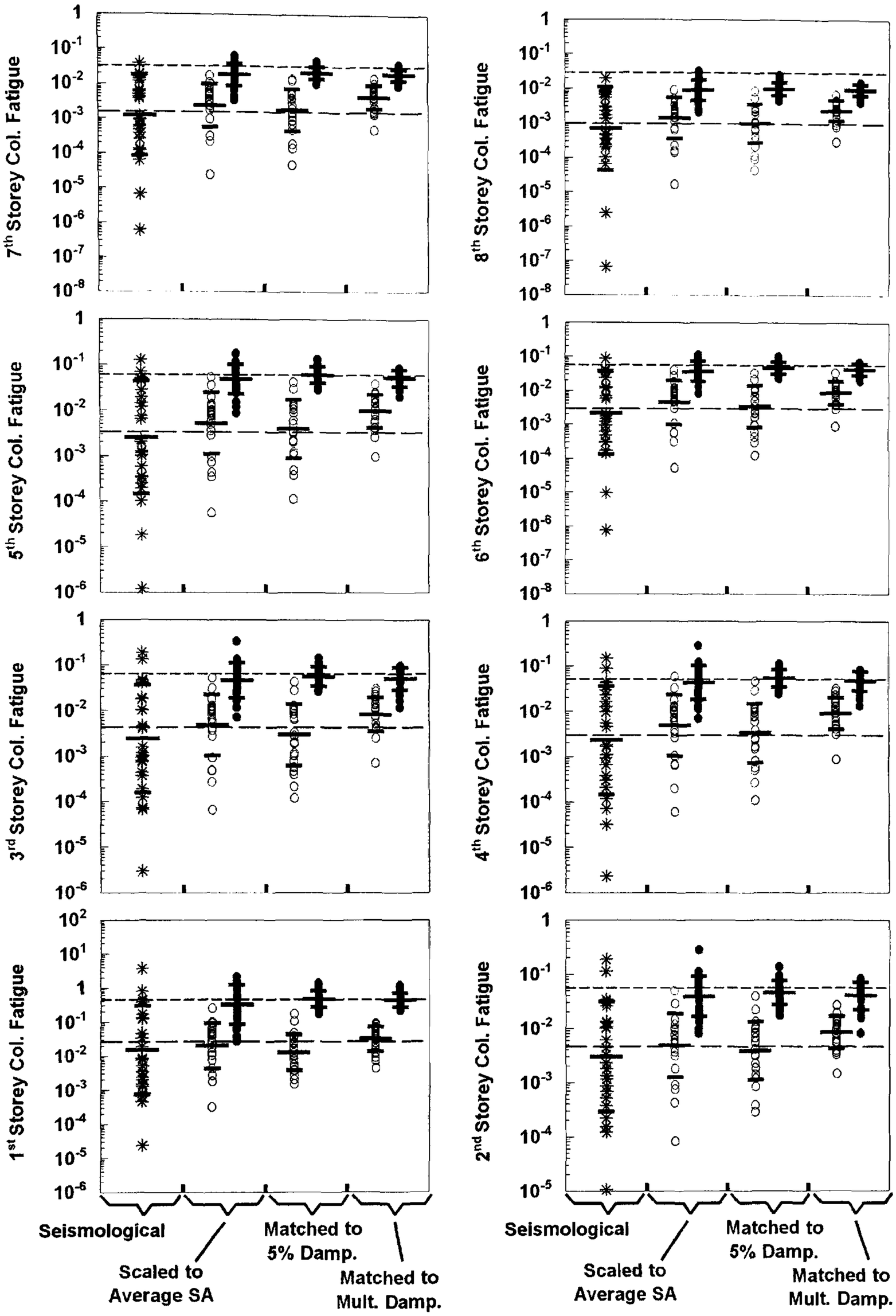


Figure 9.15. – Fatigue damage index of the base of the columns at the edge of the structure from records scaled and matched using different criteria. Error bars show median and ±1 standard deviation. Dashed lines show drift predicted by regression of 1656 unscaled MDOF time-history analyses.

Table 9.24. – Statistics of the fatigue damage index of the beam on the 8th storey at the edge of the structure, predicted from suites of records selected, linearly scaled and matched using different criteria.

Scale/Match Method	Regression	Linear, Ave SA Median	Linear, Ave SA Median +1St. Dev.	Matched 5% Median	Matched 5% Median +1St. Dev.	Matched 1 & 5% Median	Matched 1 & 5% Median +1St. Dev.
Median	0.008	0.0035	0.013	0.0026	0.013	0.0046	0.013
1St Dev. (log)	1.481	0.385	0.263	0.416	0.178	0.236	0.148
Median +1SD	0.236	0.0085	0.024	0.007	0.020	0.0079	0.018
No. Records	834	25	25	25	25	25	25
SEE at 1SD	5.1%	7.7%	5.3%	8.3%	3.6%	4.7%	3.0%
No. Records for +/-10% confidence(log) at 1SD	219	15	7	17.3	3.2	5.6	2.2
No. Records for +/-5% confidence(log) at 1SD	878	59	28	69	12.6	22	8.7

Table 9.25. – Statistics of the fatigue damage index of the beam on the 6th storey at the edge of the structure, predicted from suites of records selected, linearly scaled and matched using different criteria.

Scale/Match Method	Regression	Linear, Ave SA Median	Linear, Ave SA Median +1St. Dev.	Matched 5% Median	Matched 5% Median +1St. Dev.	Matched 1 & 5% Median	Matched 1 & 5% Median +1St. Dev.
Median	0.784	0.5758	1.370	0.0169	0.087	0.0313	0.086
1St Dev. (log)	0.959	0.328	0.216	0.407	0.184	0.245	0.156
Median +1SD	7.127	1.2252	2.254	0.043	0.133	0.0550	0.124
No. Records	834	25	25	25	25	25	25
SEE at 1SD	3.3%	6.6%	4.3%	8.1%	3.7%	4.9%	3.1%
No. Records for +/-10% confidence(log) at 1SD	92	11	5	16.6	3.4	6.0	2.4
No. Records for +/-5% confidence(log) at 1SD	368	43	19	66	13.6	24	9.7

Table 9.26. – Statistics of the fatigue damage index of the beam on the 1st storey at the edge of the structure, predicted from suites of records selected, linearly scaled and matched using different criteria.

Scale/Match Method	Regression	Linear, Ave SA Median	Linear, Ave SA Median +1St. Dev.	Matched 5% Median	Matched 5% Median +1St. Dev.	Matched 1 & 5% Median	Matched 1 & 5% Median +1St. Dev.
Median	2.615	2.1627	10.404	0.0021	0.028	0.0040	0.028
1St Dev. (log)	1.152	0.442	0.309	0.430	0.203	0.287	0.177
Median +1SD	37.122	5.9816	21.212	0.006	0.045	0.0078	0.042
No. Records	834	25	25	25	25	25	25
SEE at 1SD	4.0%	8.8%	6.2%	8.6%	4.1%	5.7%	3.5%
No. Records for +/-10% confidence(log) at 1SD	133	20	10	18.5	4.1	8.2	3.1
No. Records for +/-5% confidence(log) at 1SD	531	78	38	74	16.6	33	12.5

Table 9.27. – Statistics of the fatigue damage index of the base of the column on the 8th storey at the edge of the structure, predicted from suites of records selected, linearly scaled and matched using different criteria.

Scale/Match Method	Regression	Linear, Ave SA Median	Linear, Ave SA Median +1St. Dev.	Matched 5% Median	Matched 5% Median +1St. Dev.	Matched 1 & 5% Median	Matched 1 & 5% Median +1St. Dev.
Median	0.001	0.0014	0.009	0.0010	0.010	0.0023	0.009
1St Dev. (log)	1.473	0.598	0.298	0.563	0.189	0.297	0.156
Median +1SD	0.029	0.0055	0.018	0.004	0.015	0.0046	0.013
No. Records	834	25	25	25	25	25	25
SEE at 1SD	5.1%	12.0%	6.0%	11.3%	3.8%	5.9%	3.1%
No. Records for +/-10% confidence(log) at 1SD	217	36	9	31.6	3.6	8.8	2.4
No. Records for +/-5% confidence(log) at 1SD	868	143	35	127	14.3	35	9.7

Table 9.28. – Statistics of the fatigue damage index of the base of the column on the 6th storey at the edge of the structure, predicted from suites of records selected, linearly scaled and matched using different criteria.

Scale/Match Method	Regression	Linear, Ave SA Median	Linear, Ave SA Median +1St. Dev.	Matched 5% Median	Matched 5% Median +1St. Dev.	Matched 1 & 5% Median	Matched 1 & 5% Median +1St. Dev.
Median	0.003	0.0045	0.037	0.0035	0.046	0.0087	0.042
1St Dev. (log)	1.279	0.649	0.309	0.616	0.180	0.347	0.167
Median +1SD	0.056	0.0200	0.075	0.014	0.070	0.0194	0.061
No. Records	834	25	25	25	25	25	25
SEE at 1SD	4.4%	13.0%	6.2%	12.3%	3.6%	6.9%	3.3%
No. Records for +/-10% confidence(log) at 1SD	164	42	10	38.0	3.3	12.0	2.8
No. Records for +/-5% confidence(log) at 1SD	655	168	38	152	13.0	48	11.1

Table 9.29. – Statistics of the fatigue damage index of the base of the column on the 1st storey at the edge of the structure, predicted from suites of records selected, linearly scaled and matched using different criteria.

Scale/Match Method	Regression	Linear, Ave SA Median	Linear, Ave SA Median +1St. Dev.	Matched 5% Median	Matched 5% Median +1St. Dev.	Matched 1 & 5% Median	Matched 1 & 5% Median +1St. Dev.
Median	0.027	0.0203	0.326	0.0130	0.464	0.0315	0.437
1St Dev. (log)	1.232	0.663	0.583	0.527	0.241	0.361	0.204
Median +1SD	0.461	0.0933	1.248	0.044	0.809	0.0723	0.700
No. Records	834	25	25	25	25	25	25
SEE at 1SD	4.3%	13.3%	11.7%	10.5%	4.8%	7.2%	4.1%
No. Records for +/-10% confidence(log) at 1SD	152	44	34	27.8	5.8	13.1	4.2
No. Records for +/-5% confidence(log) at 1SD	607	176	136	111	23.3	52	16.7

9.5 Influence of Duration on Structural Response

The influence of duration on different structural response is investigated using 30 accelerograms with a range of different durations that have been matched to the median-plus-one-standard-deviation target spectra at 1, 5, 10 and 20% damping levels using RSPMatch (see section 9.3). Both a relative (5-95% significant duration) and absolute (0.1g uniform duration) definition are used to determine the influence of ground-motion duration on different damage measures. This study broadly confirms the conclusions found by the literature review presented in Chapter 3 that damage measures based on the peak response (such as peak roof drift, inter-storey drift and peak member rotation) do not depend significantly on the duration of the ground motion (Figures 9.16 to 9.18). However, damage measures such as the absorbed hysteretic energy and fatigue measure are consistently greater for ground motions with longer duration (Figure 9.18). The correlation between duration and damage is far from exact, although this would not be expected as these damage measures are also influenced by the amplitude of the structural response, which has not been completely normalized by matching the accelerograms to the elastic spectral acceleration.

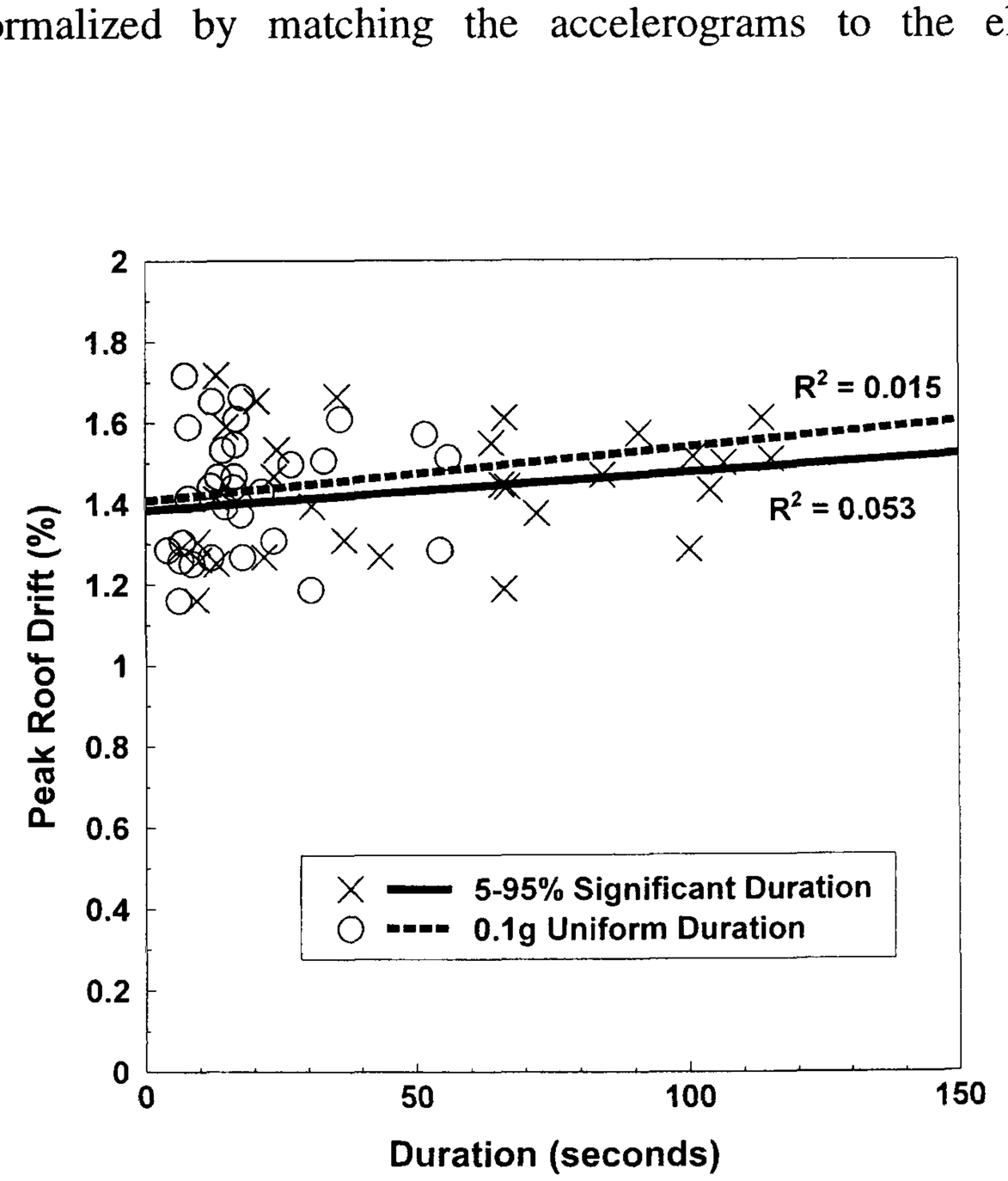


Figure 9.16. – Influence of duration on peak roof drift for accelerograms matched to the elastic spectral acceleration at multiple damping levels.

The Park and Ang damage index also shows some duration dependence for the base of the ground floor column but little or no dependence for the end of the 1st floor beams (Figure 9.18). This is logical because the lower yield rotation of the column results in a greater amount of hysteretic energy dissipation for a given level of end rotation. Stronger duration dependence might be found for larger loading levels, which would cause greater deformation and hysteretic energy dissipation in both the beams and columns.

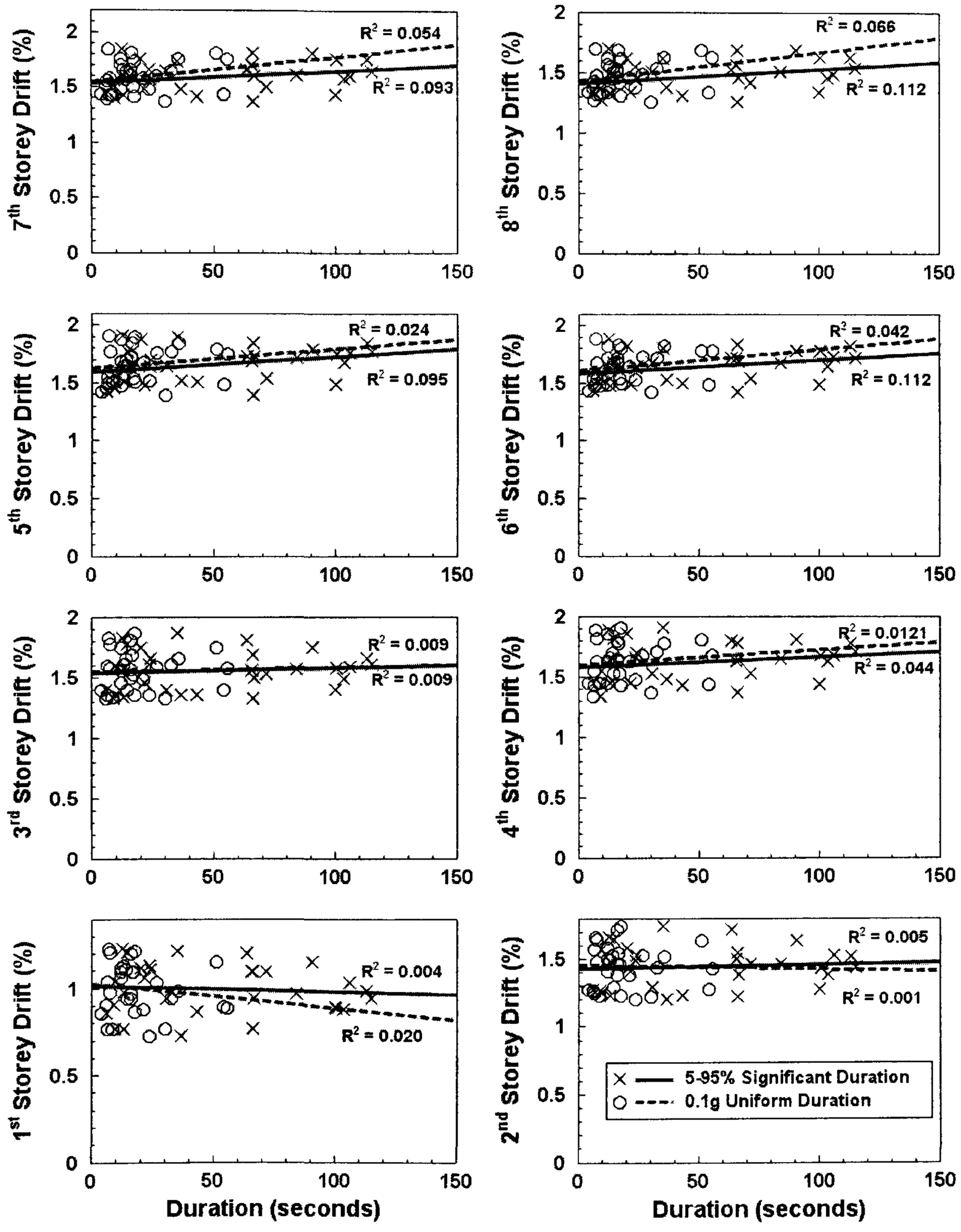


Figure 9.17. – Influence of duration on peak inter-storey drift for accelerograms matched to the elastic spectral acceleration at multiple damping levels.

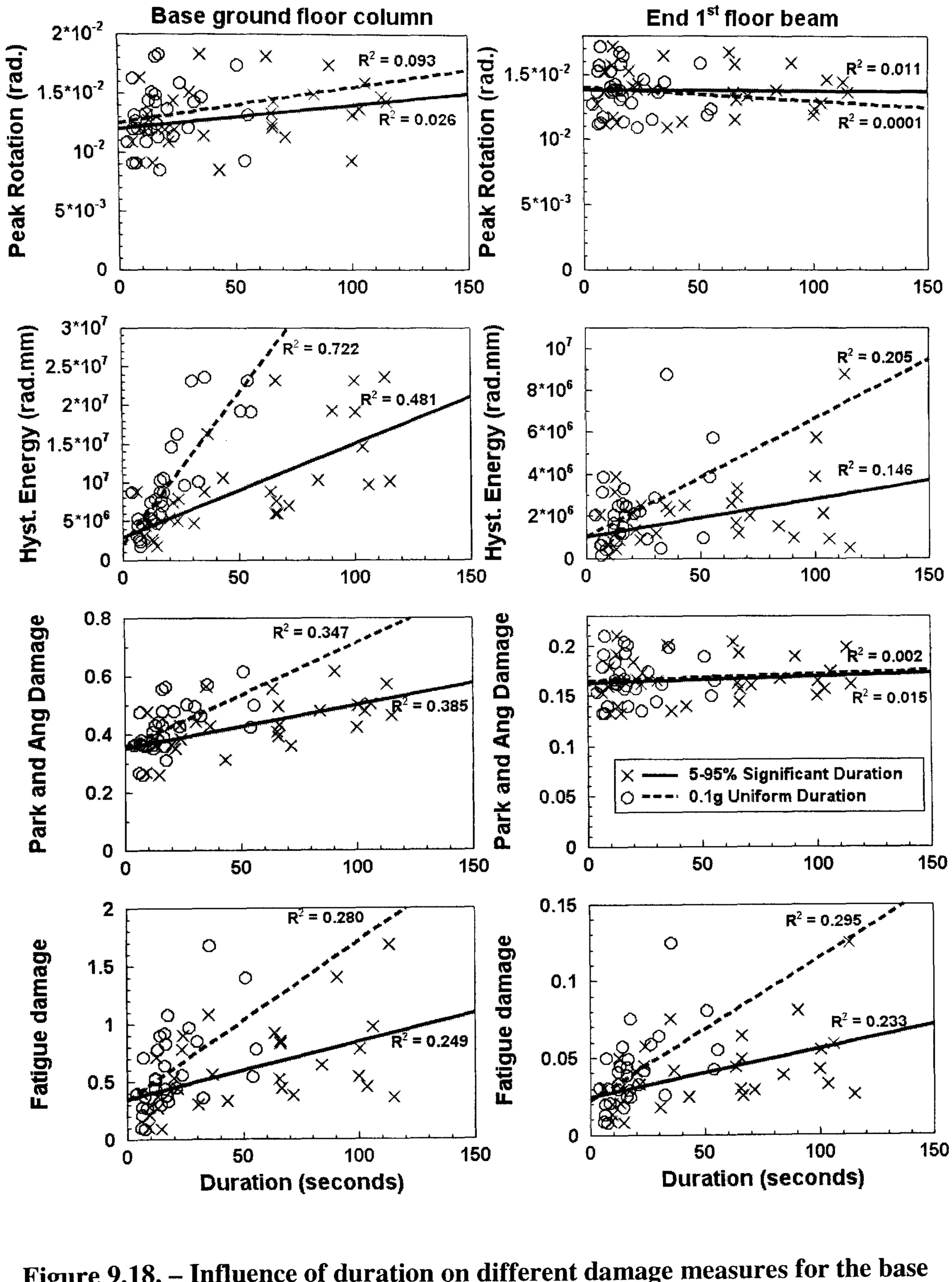


Figure 9.18. – Influence of duration on different damage measures for the base of the outer ground floor column (*left*) and the outer end of the first floor beam (*right*). Analysis using accelerograms matched to the elastic spectral acceleration at multiple damping levels.

9.6 Summary

A comparison is made between the response of an 8-storey reinforced concrete wall frame structure under the action of accelerograms selected and linearly scaled to the elastic response spectrum and accelerograms adjusted using the new version of RSPMatch to have a more exact match to the elastic response spectrum. The median response of the structure under the action of both sets of accelerograms is broadly comparable for a wide range of damage metrics. This shows that no bias has been introduced by adjusting the accelerograms to match the target spectra.

The standard deviation of the response reduces for the accelerograms adjusted to match the elastic response spectrum. This means that fewer accelerograms are required to predict the response to a given confidence level if they have been spectrally matched with RSPMatch (e.g. Table 9.30)

Table 9.30. – Statistics of the numbers of analyses required to predict the median of different damage measures to +/-5% accuracy (log) at one standard deviation confidence, predicted from suites of records selected, linearly scaled and spectrally matched using different criteria.

Scale Method	Seismological (Unscaled)	Linear scaled to average SA (5%)	Matched to SA (5%)	Matched to SA (multiple damping)
1st Floor drift	69	10	6	3
1st Floor column end rotation	89	12	5	4
1st Floor column hysteretic energy.	554	59	41	17
1st Floor column Park and Ang damage	93	14	7	4
1st Floor column fatigue	668	176	111	52

30 accelerograms with different durations, adjusted with RSPMatch to match the elastic response spectra at multiple damping levels, are used to investigate the influence of ground-motion duration on different damage measures. This shows that damage measures based on the peak response do not depend on the duration of the ground motion; while damage measures such as the absorbed hysteretic energy and fatigue damage are consistently greater for ground motions with longer duration.

10. CONCLUSIONS AND RECOMMENDATIONS

10.1 General Overview and Summary

There are different causes of structural failure under seismic loading which are measured using different damage indices. Damage measures using peak response require the engineer to know the allowable peak response of the structure. However, tests of structural members under the action of cyclic loading demonstrate that the amplitude of the peak deformation to cause failure is usually dependent on the number of cycles of loading (e.g. Miner 1945; Krawinkler and Zohrei 1983; Krawinkler 1987, 1997). This is explicitly recognised by cyclic fatigue damage measures, which were also found to be applicable for the analysis of the liquefaction of soils by Seed and co-workers (e.g. Seed and Idriss 1971). While the importance of the number of cycles and the duration of the ground motion is acknowledged as being important by the geotechnical engineering community, it remains a matter of considerable debate by researchers working in the structural engineering field (e.g. Shome *et al.* 1998). This thesis shows that studies measuring damage with the peak response generally do not find a correlation with duration or number of cycles, whilst those using energy or fatigue-based measures generally find a positive correlation. One of difficulties of employing damage measures that account for the number of cycles is that they are more variable than measures just based on the peak response. A method of reducing the variability of the structural response is developed in this thesis by adjusting recorded accelerograms to match the elastic response spectrum. This enables the response of the structure to be determined with greater confidence but with fewer analyses than using accelerograms either selected based on seismological characteristics and/or linearly scaled to match the elastic response spectrum.

10.2 Summary of Conclusions

This section provides a summary of the most significant observations from each chapter.

Measures of the seismic action

- Most of the knowledge of the characteristics of the ground motion is derived from accelerograms recorded from previous earthquakes.
- The elastic response spectrum is one of the more useful measures of the peak amplitude of earthquake ground motion. It is particularly valuable as it provides a measure of the frequency content and is unaffected by the non-stationary character of the ground-motion.
- There are many different definitions of ground-motion duration and number of effective cycles in the technical literature. One of the most important differences between the definitions is if they are measured relative to an absolute or relative threshold.
- In general, definitions of the strong-motion duration cannot be used to estimate the number of effective cycles, although some correlation does exist between the uniform duration at 0.1g and absolute measures of the number of effective cycles of the ground motion.

Review of the influence of duration on structural damage

- There are several hundred papers in the literature that make conflicting conclusions on the influence of ground-motion duration on structural damage.
- The primary reason for the different conclusions is the different definition of structural damage used. Studies employing damage metrics based on peak response generally do not find a link between duration and damage, whereas studies using damage metrics based on absorbed energy or cumulative fatigue generally find a positive link between duration and damage.
- Experimental studies of the low-cycle behaviour of a wide range of components including both steel and reinforced concrete members indicate that cumulative damage measures have the potential to provide a more accurate estimate of the likelihood of failure. However, cumulative damage measures are, by definition, more complex than those using maximum response and so are more difficult to calibrate and reliably estimate.

The influence of duration on masonry structures

- The strength degradation of masonry structures has the best correlation with the elastic spectral acceleration averaged between the initial period of the structure and a period three times this period.
- Although there is significant scatter in the results, duration is positively correlated to damage for ground motions with similar averaged spectral acceleration.
- The uniform duration – defined as the sum of time intervals for which the acceleration is above a specified threshold – provides a better insight into the damage potential of the ground motion, for a given average spectral acceleration, than other duration measures.
- Plotting the response spectrum in three dimensions with time as a third axis can be used to show the influence of time-domain ground-motion characteristics on damage.

Predicting duration and number of cycles

- Earthquake magnitude is universally acknowledged as the parameter that has the greatest influence on the number of cycles and ground-motion duration.
- The influence of the source-to-site distance depends on the definition. Ground-motion duration and number of cycles measured with relative thresholds of acceleration or arias intensity increase with distance, while those using absolute thresholds decrease.
- Some studies indicate that rupture directivity also plays an important role in the duration and number of cycles in the near-source region. However, further studies are required to determine the quantitive influence that this has on the number of ground-motion cycles.
- Several authors report that sites with soft soil classification have longer duration and greater number of cycles; however, the influence is usually small; with the possible exception of basin effects.
- New predictive equations for relative bracketed duration have been derived. The equations are derived for a range of cut-off levels but the duration measured at the 25% PGA level is recommended as this captures the majority

of the ground motion of importance for liquefaction potential and has good correlation with the predictive parameters.

Wavelet adjustment of recorded ground motions

- A stable method is presented for the wavelet adjustment of recorded ground motions. The method enables records to be adjusted so that they match smooth response spectra at multiple damping levels with closer period spacing than previously possible.
- New wavelets have been developed that have zero final velocity and displacement, ensuring that records do not require baseline correction after wavelet adjustment.
- The procedure can be applied with either absolute spectral acceleration or with pseudo-spectral accelerations if spectral displacements need to be matched.

Equivalent SDOF systems

- One of the most important factors that influence the ability of single-degree-of-freedom (SDOF) systems to estimate multi-degree-of-freedom (MDOF) structural response is the initial period of the SDOF system.
- The use of an uncracked stiffness for the SDOF approximation, even as part of a tri-linear hysteretic model, causes the under-estimation of the peak response. However, the amplitude of the secondary peaks from these systems is consistently greater than those from the MDOF system, which leads to an over-estimation of the global fatigue damage.
- The use of SDOF systems with initial periods that approximate the cracked period generally provide better predictions of MDOF response than those based on the initial period, although these predictions can over-estimate the peak MDOF response.
- The shape of the hysteretic model plays an important role in the SDOF response:
    - The tri-linear hysteretic model is generally too fat at low amplitudes so dissipates too much energy, which leads to the under-prediction of the peak displacement.

- The bi-linear and Takeda models have the same behaviour up to first yield, after which the Takeda model dissipates greater energy with lower amplitude cycles and the bi-linear model dissipates energy with fewer larger amplitude cycles.

- Although the general shape of the force-displacement relationship is approximated by SDOF hysteretic models, the true MDOF response is always more complex and could not be expected to be described by a simple hysteretic model.
- SDOF systems with the Takeda hysteretic model and cracked initial period are able to provide consistently reliable estimates of the peak drift, inter-storey drift, global Park and Ang damage index and global hysteretic energy. Bi-linear hysteretic models also provide reasonable estimations for these response parameters and remain an attractive option because of their conceptual simplicity.
- No SDOF model is capable of reliably predicting the amplitude of secondary peaks and hence the global fatigue damage.
- The shape of the lateral force profile used to derive the backbone curve of the SDOF model has less importance than other factors such as the hysteretic model used.
- As SDOF systems can be analysed over 100 times faster than MDOF systems they offer a useful tool to approximate the peak displacements of MDOF, particularly when a large number of analyses need to be completed.

Selection and scaling accelerograms

- Scaling accelerograms to the initial period of the 8-storey reinforced concrete wall-frame structure used in this study reduces the number of analyses required to predict the response to a given confidence level by a factor of approximately 4 from accelerograms selected purely with seismological criteria. Scaling the accelerograms to the average spectral acceleration reduces the number of accelerograms required by a further factor of about 2 or 3.
- Accelerograms used in this study are initially selected on spectral shape, which enables linear scale factors of up to 10 to be used without causing a bias in the predicted roof drift.

- The number of accelerograms required to predict the response to a given level of confidence also depends on the damage metric to be predicted as well as the method used to select and scale the accelerograms. The fatigue damage and absorbed hysteretic energy have considerably greater dispersion than measures of peak response so require a greater number of analyses to predict for a given confidence level.
- Selecting and scaling accelerograms to the elastic spectral acceleration does not bias the response for low-amplitude motions for this structure. However, the inter-storey drift and member end rotation in the upper storeys is consistently under-predicted by the analysis using scaled records for the higher amplitude median-plus-one-standard-deviation motions.

Linearly scaled vs spectral matched accelerograms

- The median response of the 8-storey reinforced concrete wall frame structure used in this study under the action of accelerograms both linearly scaled and spectrally matched to the elastic response spectrum is broadly comparable for a wide range of damage metrics. This shows that no bias has been introduced by adjusting the accelerograms to match smooth target spectra.
- The standard deviation of the inelastic response reduces for the accelerograms adjusted to match the smooth elastic response spectrum. This means that fewer accelerograms are required to predict the response to a given confidence level if they have been spectrally matched.
- The standard deviation of the response, and hence number of accelerograms required, reduces further if accelerograms are matched to the spectra at multiple damping levels.
- A study using accelerograms with different durations, but matched to the elastic response spectra at multiple damping levels confirms that damage measures based on the peak response do not depend on the duration of the ground motion, while damage measures such as the absorbed hysteretic energy and fatigue damage are consistently greater for ground motions with longer duration.

10.3 Summary of recommendations for further work

The main areas of work that would benefit from further development are summarized by the points below.

- New predictive equations for a much wider range of definitions of duration and number of cycles could be developed. These new predictions could also address the important issue of cross-correlation between the duration and amplitude of the ground motion.
- The new predictive equations derived in this thesis for relative bracketed duration could be used for developing duration scale factors for use in liquefaction assessment. This would require further work to derive duration scale factors using empirical observations of liquefied and non-liquefied sites from the field.
- The work described in this thesis has significantly improved the program implementing the wavelet method for adjusting accelerograms to match the smooth target elastic response spectra. However, further improvements to the program can still be made, these include:
    1. Windows interface
    2. Checks for holes in the Fourier Amplitude Spectrum
    3. Checks for baseline drift caused by rounding errors
- Further research is required to determine the amount of modification to the adjusted accelerogram that is acceptable for different applications.
- The influence of different ground-motion parameters on the response of SDOF systems could be conducted to identify the damaging characteristics of the ground motion for structures with a wide range of periods and ductilities. This in turn could be used to develop a method of selecting and scaling accelerograms using multiple ground-motion parameters.
- Further investigation of the differences between the expected response of the reinforced concrete wall frame structure and the response under the action of accelerograms scaled to the elastic response spectrum is required. A better understanding of the differences could lead to an improved method of selecting and scaling accelerograms.

- The possibility of using the response of non-linear SDOF systems as an improved method of selecting and scaling accelerograms is well worth further investigation.
- Although the findings of this study are consistent with the work of other researchers, the results are only strictly valid for the structures used in this analysis. Further studies using different structural forms, materials and number of storeys are required to prove that the conclusions drawn here are more generally applicable.
- The possible contribution of non-structural elements to damping is conservatively ignored in the analysis of the reinforced concrete structures; however further studies on this subject, particularly those employing experimental test results, would be welcome and would be a good topic for future research.

REFERENCES

Abed, A., Plumier, A, and Tiliouine, B. (1998) Resistance of partially encased beams to low cycle fatigue. *11th European Conference on Earthquake Engineering*.

Abrahamson, N.A. and Litehiser, J.J. (1989) Attenuation of vertical peak acceleration. *Bulletin of the Society of America* **79**(3), 549-580.

Abrahamson, N.A. (1992) Non-Stationary Spectral Matching. *Seismological Research Letters* **63**(1), 30.

Abrahamson, N. A. and Silva, W. J. (1997). Empirical response spectral attenuation relations for shallow crustal earthquakes. *Seismological Research Letters* **68**(1) 94-127.

Abrahamson, N.A., Krammerer, A. and Gregor, N. (2003) Summary of scaling relations for spectral damping, peak velocity and spectral acceleration. *PEGASOS Project Report,* NAGRA (Swiss cooperative for disposal of Nuclear Waste).

Akkar, S. and Ozen, O. (2005) Effect of peak ground velocity on deformation demands for SDOF systems. *Earthquake Engineering and Structural Dynamics* **34**(13), 1551-1571.

Alavi, B. and Krawinkler, H. (2004) Behaviour of moment-resisting frame structures subjected to near-fault ground motions. *Earthquake Engineering and Structural Dynamics* **33**, 687-706.

Ambraseys, N.N. and Sarma, S.K. (1967) Response of earth dams to strong earthquakes. *Geotechnique* **17**, 181-213.

Ambraseys, N.N., Simpson, K.A. and Bommer, J.J. (1996) Prediction of horizontal response spectra in Europe. *Earthquake Engineering and Structural Dynamics* **25**, 371-400.

Ambraseys, N.N. and Free, M.W. (1997) Surface-wave magnitude calibration for European region earthquakes. *Journal of Earthquake Engineering* **1**(1), 1-22.

Ambraseys, N.N. and Douglas, J. (2003) Near-field horizontal and vertical earthquake ground motions *Soil Dynamics and Earthquake Engineering* **23**(1), 1-18.

Ambraseys, N.N, Douglas, J., Rinaldis, D., Berge-Thierry, C., Suhadolc, P., Costa, G., Sigbjörnsson, R. and Smit, P. (2004) Dissemination of European strong-

motion data, Vol. 2. *CD-ROM Collection*, Engineering and Physical Sciences Research Council, United Kingdom.

Ambraseys, N.N., Douglas, J., Sarma, S.K. and Smit, P.M. (2005) Equations for the estimation of strong ground motions from shallow crustal earthquakes using data from Europe and the Middle East: Horizontal Peak Ground Acceleration and Spectral Acceleration. *Bulletin of Earthquake Engineering* **3**(1), 1-53.

Amini, A. and Trifunac, M.D. (1981) Distribution of peaks in linear earthquake response. *Journal of the Engineering Division* **107**(EM1) 207-227.

Anastasiadis, A., Gioncu, V. and Mazzolani, F.M. (2000) New trends in the evaluation of available ductility of steel members. *Behaviour of Steel Structures in Seismic Areas,* Mazzolani and Tremblay (eds) Balkema, Rotterdam ISBN 9058091309, 3-10.

Anderson, J.C. and Bertero, V.V. (1988) Uncertainties in establishing design earthquakes. *Journal of Structural Engineering* **113**(8), 1709-1724.

Annaki, M. and Lee, L.K. (1977) Equivalent uniform cycle concept for soil dynamics. *Journal of the Geotechnical Engineering Division ASCE* **103**(GT3), 549-564.

Antoniou, S. and Pinho, R. (2004) Advantages and limitations of adaptive and non-adaptive force-based pushover procedures. *Journal of Earthquake Engineering* **8**(4), 497-522.

Aptikaev, F.F. (1977) The correlation between MM-intensity, relative duration of shaking and peak acceleration. *EERI Newsletter* **3**, Earthquake Engineering Research Institute.

Aptikaev, F.F. (1982) On the correlations of MM Intensity with parameters of ground shaking. *Proceedings of the 7th European Conference on Earthquake Engineering,* Athens Greece, Vol. **2**, 95-97.

Arango I. Magnitude scaling factors for soil liquefaction evaluations. *Journal of Geotechnical Engineering* 1996; **122**(11): 929-936.

Araya, R., and Saragoni, G.R. (1980) Capacity of the strong ground-motion to cause structural damage. *Proceedings of the Seventh World Conference on Earthquake Engineering*, Istanbul, 483-490.

Arias, A. (1970) A measure of earthquake intensity. in *Seismic design for nuclear power plants,* (ed. Hansen, R.J.) MIT Press, Cambridge, Massachusetts, 438-489.

Aschheim, M. and Black, E. (1999) Effects of prior earthquake damage on response of simple stiffness-degrading structures. *Earthquake Spectra* **15**(1), 1-24.

Assimaki, D. and Gazetas, G. (2004) Soil and topographic amplification on canyon banks and the 1999 Athens earthquake. *Journal of Earthquake Engineering* **8**(1), 1-43.

ASTM (1985) Cycle counting in fatigue analysis. *Annual Book of ASTM Standards* **03.01** issue E1049-85, 836-848.

ATC (1978) Tentative provisions for the development of seismic regulations for buildings, *ATC Publication* ATC 3-06, report number NBS SP-510.

Baker, J.W. and Cornell, A.C. (2005) A vector-valued ground motion intensity measure consisting of spectral acceleration and epsilon. *Earthquake Engineering and Structural Dynamics* **34**, 1193-1217.

Ballio, G. and Castiglioni, C.A. (1995) A unified approach for the design of steel structures under low and/or high cycle fatigue. *Journal of Construction Steel Research*, **34**, 75-101.

Barltrop, N. and Adams, A. (1991) Dynamics of fixed marine structures. *Marine Technology Directorate Ltd and Butterworth-Heinemann.*

Basu, B. and Gupta, V.K. (1997) Non-stationary response of MDOF systems by wavelet transform. *Earthquake Engineering and Structural Dynamics* **26**, 1243-1258.

Basu, B. and Gupta, V. K. (1998) A damage-based definition of effective peak acceleration. *Earthquake Engineering and Structural Dynamics* **27**, 503-512.

Basu, B. and Gupta, V.K. (1999) Wavelet-based analysis of the non-stationary response of a slipping foundation. *Journal of Sound and Vibration* **222**(4), 547-563.

Basu, B. and Gupta, V.K. (2000a) Wavelet-based non-stationary response analysis of a friction base-isolated structure. *Earthquake Engineering and Structural Dynamics* **29**, 1659-1676.

Basu, B. and Gupta, V.K. (2000b) Stochastic seismic response of single-degree-of-freedom systems through wavelets. *Engineering Structures* **22**, 1714-1722.

Bazzurro, P. and Cornell, A.C. (1992) Seismic risk: non-linear MDOF structures. *10^{th} World Conference on Earthquake Engineering* **1**, 563-568.

Bazzurro, P. and Cornell, A.C. (1994a) Seismic hazard analysis of nonlinear structures. I: Methodology. *Journal of Structural Engineering* **120**(11), 3320-3344.

Bazzurro, P. and Cornell, A.C. (1994b) Seismic hazard analysis of nonlinear structures. II: Applications. *Journal of Structural Engineering* **120**(11), 3345-3365.

Bazzurro, P. and Cornell, A.C. (1999) Disaggregation of Seismic Hazard. *Bulletin of the Seismological Society of America* **89**(2), 501-520.

Bazzurro, P. and Cornell, A.C. (2002) Vector-valued probabilistic seismic hazard analysis (VPSHA). *Proceedings, 7th U.S. National Conference on Earthquake Engineering* Boston MA.

Benioff, H. (1934) The physical evaluation of seismic destructiveness. *Bulletin of the Seismological Society of America* **31**, 398-403.

Bertero, V.V., Mahin, S.A. and Herrera, R.A. (1978) Aseismic design implications of near-fault San Fernando earthquake records. *Earthquake Engineering and Structural Dynamics* **6**, 31-42.

Bernuzzi, C., Calado, L. and Castiglioni, C.A. (1997) Ductility and load carrying capacity prediction of steel beam-to-column connections under seismic reversal loading. *Journal of Earthquake Engineering* **1**(1), 401-432.

Beyer, K. and Bommer, J.J. (2006) Relationships between median values and aleatory variabilities for different definitions of the horizontal component of motion. *Bulletin of the Seismological Society of America* **96**, submitted for publication.

Biot, M.A. (1941) A mechanical analyzer for the prediction of earthquake stresses. *Bulletin of the Seismological Society of America* **31**, 151-171.

Bolt, B.A. (1973) Duration of strong ground motions *Proceedings of the Fifth World Conference on Earthquake Engineering,* Vol. 1, Rome, pp. 1304-1313.

Bolt, B.A. and Abrahamson, N.A. (1982) New attenuation relations for peak and expected accelerations of strong ground motion. *Bulletin of the Seismological Society of America* **72**(6), 2307-2321.

Bommer, J.J., Udias, A., Cepeda, J.M., Hasbun, J.C., Salazar, W.M., Suarez, A., Ambraseys, N. N., Buforn, E., Cortina, J., Madariaga, R., Mendez, P., Menzcua, J. and Papstamatiou, D. (1997) A new digital accelerograph network for El Salvador. *Seismological Research Letters* **68**(3) 426-436.

Bommer, J.J., Elnashai, A.S., Climintzas, G.O. and Lee, D. (1998) Review and development of response spectra for displacement-based design. *ESEE Research Report No. 98-3,* Imperial College London, 1998.

Bommer, J.J. and Martínez-Pereira, A. (1999) The effective duration of earthquake strong motion. *Journal of Earthquake Engineering* **3**(2), 127-172.

Bommer, J.J. and Elnashai, A.S. (1999) Displacement spectra for seismic design. *Journal of Earthquake Engineering* **3**(1), 1-32.

Bommer, J.J., Elnashai, A.S. and Weir, A. G. (2000a) Compatible acceleration and displacement spectra for seismic design codes. *12th World Conference on Earthquake Engineering, Auckland,* paper 207.

Bommer, J.J., Scott, S.G. and Sarma, S.K. (2000b) Hazard-consistent earthquake scenarios. *Soil Dynamics and Earthquake Engineering* **19**, 219-231.

Bommer, J.J. and Martinez-Pereira, A. (2000) Strong motion parameters: definition, usefulness and predictability. *12th World Conference on Earthquake Engineering, Auckland* **3**(2), 127-172.

Bommer, J.J., Georgallides, G. and Tromans, I.J. (2001) Is there a near-field for small-to-moderate magnitude earthquakes? *Journal of Earthquake Engineering* **5**(3), 395-423.

Bommer, J.J. and Ruggeri, C. (2002) The specification of acceleration time-histories in seismic design codes. *European Earthquake Engineering* **XVI** (1), 3-17.

Bommer, J.J. (2002) Deterministic vs. probabilistic seismic hazard assessment: an exaggerated and obstructive dichotomy. *Journal of Earthquake Engineering* **6**(1), 43-73.

Bommer, J.J. (2003) Engineering Seismology. *Master of Science Course,* Imperial College London.

Bommer, J.J., Douglas, J. and Strasser, F. O. (2003) Style-of-faulting in ground motion prediction equations. *Bulletin of Earthquake Engineering* **1**(2), 171 - 203.

Bommer, J.J. and Acevedo, A.B. (2004) The use of real earthquake accelerograms as input to dynamic analysis. *Journal of Earthquake Engineering* **8**(Special Issue1), 43-91.

Bommer, J.J. and Alarcon, J.E. (2005) The prediction and use of peak ground velocity. *Journal of Earthquake Engineering* **10**(1), 1-31.

Bommer, J.J. and Mendis, R. (2005) Scaling of displacement spectral ordinates with damping ratios. *Earthquake Engineering and Structural Dynamics* **34**, 145-165.

Bommer, J.J., Magenes, G., Hancock, J. and Penazzo, P. (2004) The influence of strong-motion duration on the seismic response of masonry structures. *Bulletin of Earthquake Engineering* **2**(1), 1-26.

Bommer, J.J., Hancock, J. and Alarcon, J. (2006) Correlations between duration and number of effective cycles of earthquake ground motion. *Soil Dynamics and Earthquake Engineering* **26**(1), 1-13.

Bommer, J.J. and Pinho, R. (2006) Adapting earthquake actions in Eurocode 8 for performance-based seismic design. *Earthquake Engineering and Structural Dynamics* **35**(1), 39-55.

Bonelli, P. (1998a) Long seismic velocity pulse effect and damage. *Structural Engineering World Wide,* Paper T227-3.

Bonelli, P. (1998b) An evaluation of the effects of long acceleration pulses on the seismic response of structures. *Proceedings of the 11th European Conference on Earthquake Engineering*.

Boore, D. (1983) Stochastic simulation of high-frequency ground motions based on Seismological models of the radiated spectra. *Bulletin of the Seismological Society of America* **73**, 1865-1894.

Boore, D.M. and Joyner, W.B. (1993). Empirical prediction of strong ground motion. *Structural Engineering in Natural Hazards Mitigation: Proceedings of Papers Presented at the Structures Congress '93,* ASCE, New York **1**, 241-246.

Boore, D.M., Joyner, W.B. and Fumal, T.E. (1993) Estimation of response spectra and peak accelerations from Western North America: an interim report. *US Geological Survey Open-File Report 93-509.*

Boore, D. (2003) Simulation of ground motions using the stochastic method. *Pure and Applied Geophysics* **160**, 635-676.

Boore, D. and Bommer, J.J. (2005) Processing of strong-motion accelerograms: needs, options and consequences. *Soil Dynamics and Earthquake Engineering* **25**(2), 93-115.

Boore, D., Watson-Lamprey, J. and Abrahamson, N. (2006) GMRotD and GMRotI: Orientation-independent measures of ground motion. *Bulletin of the Seismological Society* **96**, (submitted for publication).

Bozorgnia, Y. and Campbell, K. (2004) The vertical-to-horizontal response spectral ratio and the tentative procedures for developing simplified V/H and vertical design spectra. *Journal of Earthquake Engineering* **8**(2), 172-207.

Brune, J., N. (1970) Tectonic stress and the spectra of seismic shear waves from earthquakes. *Journal of Geophysical Research* **75**(26), 4997-5009.

Bruneau, M., Wilson, J.C. and Tremblay, R. (1996) Performance of steel bridges during the 1995 Hyogo-ken Nanbu (Kobe, Japan) earthquake. *Canadian Journal of Civil Engineering* **23**, 678-713.

Bursi, O. and Caldara, R. (2000) Composite substructures with partial shear connection: Low cycle fatigue behaviour and analysis issues. *12th World Conference on Earthquake Engineering, Auckland,* paper 0498.

Calado, L., Azevedo, J. and Lamas, A. (1995) Assessment of q factors for seismic design of low-rise steel buildings. *Journal of Construction Steel Research* **35**, 1-17.

Calado, L., Castiglioni, C.A., Barbaglia, P. and Bernuzzi, C. (1998) Seismic design criteria based on cumulative damage concepts. *11th European Conference on Earthquake Engineering.*

Calado, L., Castiglioni, C.A. and Carydis, P. (2002) Shaking table tests for seismic performance evaluation of steel frames. *12th European Conference on Earthquake Engineering,* Paper 685.

Calado, L. (2003) Non-linear cyclic model of top and seat with web angle for steel beam-to-column connections *Engineering Structures* **25**, 1189-1197.

Calvi, G.M. and Macchi, G. (1990) Dynamic parametric simulation of masonry structures. *Volume dedicated to the 60th Anniversary of Prof. T.P. Tassios,* National Technical University of Athens, 461-485.

Campbell, K.W. (1985) Strong motion attenuation relations: a ten-year perspective. *Earthquake Spectra* **1**(4), 759-804.

Campbell, K.W. (1997). Empirical near-source attenuation relationships for horizontal and vertical components of peak ground acceleration, peak ground velocity, and pseudo-absolute acceleration response spectra. *Seismological Research Letters* **68**(1), 154-179.

Carballo-Arevalo, J.E. (2000) Probabilistic seismic demand analysis spectrum matching and design. *PhD Thesis,* Stanford University, CA.

Cartwright, D.E. and Longuet-Higgins, M.S. (1956) The statistical distribution of the maxima of a random function. *Proceedings of the Royal Society*, London **237** (Series A), 212-232.

Castiglioni, C.A. and Calado, L. (1996) Comparisons of two cumulative damage approaches for the assessment of behaviour factors for low-rise steel buildings. *Journal of Steel Research* **40**(1), 39-61.

Castiglioni, C.A., Bernuzzi, C. and Calado, L. (2000) Cyclic behaviour of steel beam-to-column joints with a concrete slab. *Behaviour of Steel Structures in Seismic Areas, Mazzolani and Tremblay (eds),* Balkema, Rotterdam, 147-154.

CEN (2004) Eurocode 8: Design of structures for Earthquake resistance-Part 1: General rules, seismic actions and rule for buildings. *EN 1998-1: 2004.* Comité Européen de Normalisation, Brussels.

Chai, T.H., Romstad, K.M. and Bird, S.M. (1995) Energy-based linear damage model for high-intensity seismic loading. *Journal Of Structural Engineering* **121** (5), 857-864.

Chai, Y.H. and Romstad, K.M. (1996) Characterization of structural damage under high-intensity seismic loading. *11th World Conference on Earthquake Engineering,* paper number 681.

Chai, Y.H., Fajfar, P. and Romstad, K.M. (1998) Formulation of duration-dependent inelastic seismic design spectrum. *Journal of Structural Engineering* **124**(8), 913-921.

Chai, Y.H. and Fajfar, P. (2000) A procedure for estimating input spectra for seismic design. *Journal of Earthquake Engineering* **4**(4), 539-561.

Chai, Y.H. (2005) Incorporating low-cycle fatigue model into duration-dependent inelastic design spectra. *Earthquake Engineering and Structural Dynamics* **34**, 83-06.

Chiu, H.-C. (1997) Stable baseline correction of digital strong-motion data. *Bulletin of the Seismological Society of America,* **87**(4), 932–944.

Chopra, A.K. (1980) Dynamics of Structures, a Primer. *Earthquake Engineering Research Institute,* Engineering Monographs on Earthquake Criteria, Structural Design and Strong Motion Records. Library of Congress Catalog card number 81-65052.

Chopra, A.K. and Goel, R.K. (1999a) Capacity-Demand-Diagram methods for estimating seismic deformations of inelastic structures: SDF systems. *PEER Report,* **PEER-1999/02** University of California, Berkeley.

Chopra, A.K. and Goel, R.K. (1999b) Capacity-Demand-Diagram methods based on inelastic design spectrum. *Earthquake Spectra* **15**(4), 637-656.

Chopra, A.K. and Goel, R.K. (2002) A modal pushover analysis procedure for estimating seismic demands for buildings. *Earthquake Engineering and Structural Dynamics* **31**, 561-582.

Chopra, A.K. and Goel, R.K. (2003) Statistics of Single-Degree-of-Freedom Estimate of Displacement for Pushover Analysis of Buildings. *Journal of Structural Engineering* **129**(4), 459-469.

Chou, C-C. and Uang, C-M. (2002) Evaluation of site-specific energy demand for building structures. *7th US National Conference on Earthquake Engineering, Boston, Massachusetts,* Paper 144.

Chung. Y.S., Meyer, C. and Shinozuka, M. (1988) A new damage model for reinforced concrete structures. *Proceedings of 9th World Conference on Earthquake Engineering, Tokyo* **8**, 205-210.

Chung, Y.S., Meyer, C. and Shinozuka, M. (1989) Modelling of concrete damage. *ACI Structural Journal* **86**(3), 259-271.

Clough, R.W. and Penzien, J. (1975) Dynamics of Structures. *McGraw-Hill.*

Cornell, A.C. (1997) Does duration really matter? *Proceedings of the FHWA/NCEER Workshop on the National Representation of Seismic Ground Motion for New and Existing Highway Facilities,* Burlingame, California, Organized by NCEER (project 106-F-5.4.1) and ATC (project ATC-18-1), pp 125-133.

Cosenza, E., Manfredi, G., Ramasco, R. (1990) An evaluation of the use of damage functions in earthquake-resistant design. *9th European Conference on Earthquake Engineering,* Moscow **9**, 303-312.

Cosenza, E., Manfredi, G. and Ramasco, R. (1993) The use of damage functionals in earthquake engineering: a comparison between different methods. *Earthquake Engineering and Structural Dynamics* **22**, 855-868.

Cosenza, E. and Manfredi, G. (1997) The improvement of the seismic resistant design

Methodologies for the Next Generation of Codes Balkema, Fajfar and Krawinkler Eds, 119-130.

Cosenza E. and Manfredi, G. (1998) A seismic design method including damage effect. *11th European Conference on Earthquake Engineering*, Paris.

Cosenza, E. and Manfredi, G. (2000) Damage indices and damage measures. *Progress in Structural Engineering and Materials* **2**(1), 50-59.

Cosenza, E., Iervolino, I. and Manfredi, G. (2004) On ground motion duration and engineering demand parameters. *International Workshop on Performance-Based Seismic Design, Concepts and Implementation,* Bled, Slovenia.

Cruz, A. and Lopez, O.A. (2000) Plastic energy during an earthquake as a function of structural properties and ground-motion characteristics. *Engineering Structures* **22**(7), 784-792.

DeAlba, P., H. B. Seed, and Chan, C. K. (1976). Sand Liquefaction in Large Scale Simple Shear Tests, *Journal of the Geotechnical Engineering Division ASCE* **102**(GT9), 909-927.

De Matteis, G., Landolfo, R. and Calado, L. (2000) Cyclic behaviour of semi-rigid angle connections: A comparative study of tests and modelling. *Behaviour of Steel Structures in Seismic Areas,* Mazzolani and Tremblay (eds) Balkema, Rotterdam ISBN 9058091309, 165-174.

Dutta, A. and Mander, J.B. (2001) Energy based methodology for ductile design of concrete columns. *Journal of Structural Engineering* **127**(12), 1374-1381.

Dobry, R., Idriss, I. M. and Ng, E. (1978). Duration characteristics of horizontal components of strong-motion earthquake records, *Bulletin of the Seismological Society of America* **68** (5), 1487-1520.

Donovan, N.C. (1972). Earthquake hazard for buildings in building practices for disaster mitigation. *Building Science Series,* **46**, 1-32.

Douglas, J. (2001) A critical reappraisal of some problems in engineering seismology. *PhD Thesis,* Imperial College, University of London.

Douglas, J. (2003a) What is a poor quality strong-motion record? *Bulletin of Earthquake Engineering* **1**, 141-156.

Douglas, J. (2003b) Earthquake ground motion estimation using strong-motion records: a review of equations for the estimation of peak ground acceleration and response spectral ordinates. *Earth-Science Reviews* **61**(1-2), 43-104

Dowling, N.E. (1972) Fatigue failure predictions for complicated stress-strain histories. *Journal of Materials, ASTM* **7**(1), 71-87.

Eibl, J., Keintzel, E. and Vratsanou, V. (1996) Determination of earthquake duration dependent behaviour factors for unreinforced brick masonry panels by non-linear time-history calculations. *11th World Conference on Earthquake Engineering,* paper no 6.

El-Bahy, A., Kunnath, S.K., Stone, W.C., and Taylor, A.W. (1999a) Cumulative seismic damage of circular bridge columns: Benchmark and low-cycle fatigue tests. *ACI Structural Journal* **96**(4), 633-641.

El-Bahy, A., Kunnath, S.K., Stone, W.C., and Taylor, A.W. (1999b) Cumulative seismic damage of circular bridge columns: Variable amplitude tests. *ACI Structural Journal* **96**(5), 711-719.

Elenas, A. (2000) Correlation between seismic acceleration parameters and overall structural damage indices of buildings. *Soil Dynamics and Earthquake Engineering* **20,** 93-100.

Elenas, A. and Meskouris, K. (2001) Correlation study between seismic acceleration parameters and damage indices of structures. *Engineering Structures* **23**, 698-704.

Elghadamsi, F.E., Mohraz, B. and Lee, C.T. (1998) Time-dependent power spectral density of earthquake ground motion *Soil Dynamics and Earthquake Engineering* **7**(1), 15-21.

Ellis, G.W., Srinivasan, M. and Cakmak, A.S. (1990) A program to generate site dependent time histories: EQGEN. *Technical Report NCEER-90-0009,* National Center for Earthquake Engineering Research.

Emori, K. and Schnobrich, W.C. (1978) Analysis of reinforced concrete wall-frame structures for strong-motion earthquakes, *Structural Research Series No. 434,* Civil Engineering Studies, University of Illinois at Urbana-Champaign. *Not seen referenced in SeismoSoft (2005b).*

Erberik, M.A. and Sucuoglu, H. (2002) Energy-based low-cycle fatigue characteristics of degrading structures. *12th European Conference on Earthquake Engineering*, paper 118.

Esteva, L. and Rosenblueth, E. (1964). Spectra of earthquakes at moderate and large distances. *Boletín Sociedad Mexicana De Ingeniería Sismica,* **2**(1), 1-18.

Esteva, L. (1988) The Mexico Earthquake of September 19, 1985 – Consequences, Lessons, and Impact on research and practice. *Earthquake Spectra* **4**(3), 413-426.

Fajfar, P., Vidic, T. and Fischinger, J. (1989) Seismic demand in medium and long period structures. *Earthquake Engineering and Structural Dynamics* **18**, 1133-1144.

Fajfar, P., and Fischinger, J. (1990a) A seismic design procedure including energy concept. *9th European Conference on Earthquake Engineering,* Moscow **2**, 312-321.

Fajfar, P., and Fischinger, J. (1990b) Earthquake design spectra considering duration of ground-motion. *Proceedings 2nd U.S. National Conference on Earthquake Engineering,* Stanford **2**, 15-24.

Fajfar, P., Vidic, T. and Fischinger, J. (1990) A measure of earthquake motion capacity to damage medium-period structures. *Soil Dynamics and Earthquake Engineering* **9**(5), 236-242.

Fajfar, P. (1992) Equivalent ductility factors, taking into account low-cycle fatigue. *Earthquake Engineering and Structural Dynamics* **21**, 837-848.

Fajfar, P., and Vidic, T. (1994) Consistent inelastic design spectra: Hysteretic and input energy. *Earthquake Engineering and Structural Dynamics* **23**, 523-537.

Fajfar, P. (2000) A nonlinear analysis method for performance-based seismic design. *Earthquake Spectra* **16**(3), 573-592.

Fardis, M.N. (1994) Analysis and design of reinforced concrete buildings according to Eurocodes 2 and 8, Configurations 3, 5 and 6. *Reports on Prenormative Research in Support of Eurocode 8.* (not seen, reported in Mwafy 2001).

FEMA (1999) HAZUS99 Earthquake loss estimation methodology: user's manual. Federal Emergency Management Agency, Washington DC.

FEMA (2000) FEMA 365 – Prestandard and commentary for the seismic rehabilitation of buildings. Federal Emergency Management Agency, Washington DC.

FEMA (2003) HAZUS-MH Technical Manuals. Federal Emergency Management Agency, Washington DC.

Filippou, F.C., Popov, E.P. and Bertero, V.V. (1983) Modelling of R/C joints under cyclic excitations *Journal of Structural Engineering* **109**(11), 2666-2684. (not seen, referenced in SeismoStruct, SeismoSoft 2005b)

Fragiadakis, M. Pinho, R. and Antoniou, S. (2004) Modelling of reinforcing steel bars under transient loading and subjected to buckling. (not seen, referenced in SeismoStruct, SeismoSoft 2005b)

Freeman, S.A. (1998) Development and use of capacity spectrum method. *Proceedings of the 6th U.S. National Conference on Earthquake Engineering* CD ROM.

Friedland, I.M., Power, M.S. and Mayes, R.L. (1997) Introduction and Overall Objectives of the Workshop *Proceedings of the FHWA/NCEER Workshop on the National Representation of Seismic Ground Motion for New and Existing Highway Facilities,* Burlingame, California, Organized by NCEER (project 106-F-5.4.1) and ATC (project ATC-18-1).

Galiana-Merino, J.J., Rosa-Herranz, J., Giner, J., Molina, S. and Botella, F. (2003) De-Noising of short period seismograms by wavelet packet transform. *Bulletin of the Seismological Society of America* **93**(6), 2554-2562.

Gasparini, D.A. and Vanmarcke, E.H. (1976) Simulated Earthquake Motions Compatible with Prescribed Response Spectra. *Department of Civil Engineering,* Research Report R76-4, Massachusetts Institute of Technology, Cambridge, Massachusetts.

Gazetas, G., Kallou, P.V. and Psarropoulos, P.N. (2002) Topography and soil effects in the Ms 5.9 Parnitha (Athens) earthquake: The case of Adames. *Natural Hazards* **27**, 133-169.

Ghobarah, A. (2004) On drift limits associated with different damage levels. *International Workshop on Performance-Based Seismic Design, Concepts and Implementation,* Bled, Slovenia. – downloaded from conference web site.

Gupta, I.D. (1991) A note on the response spectra of peak amplitudes to be expected for a given number of cycles. *Soil Dynamics and Earthquake Engineering* **10**(1), 5-9

Gupta, I.D. and Joshi, R.G. (1993) On synthesizing response spectrum compatible accelerograms. *European Earthquake Engineering* **7**(2), 25-33.

Gupta, I.D. (1994) Defining effective peak acceleration via order statistics of acceleration peaks. *European Earthquake Engineering* **2**, 3-11.

Gupta, I.D. and Trifunac, M.D. (1994) A note on the statistics of ordered peaks in stationary processes. *Soil Dynamics and Earthquake Engineering* **17**(3), 317-328.

Gupta, I.D. and Trifunac, M.D. (1996) Investigation of the non stationary in stochastic response of structures. *University of Southern California,* Report CE96-01.

Gupta, I.D. and Trifunac, M.D. (1998a) A note on statistics of level crossings and peak amplitude in stationary stochastic processes. *European Earthquake Engineering* **3**, 52-59.

Gupta, I.D. and Trifunac, M.D. (1998b) A note on the statistics of ordered peaks in stationary processes. *Soil Dynamics and Earthquake Engineering* **17**(3), 317-328.

Gupta, I.D. and Trifunac, M.D. (2000) A note on the nonstationary of seismic response of structures. *Engineering Structures* **23**, 1567-1577.

Gupta, V.K., Nielsen, S.R.K. and Kirkegaard, P.H. (2001) A preliminary prediction of seismic damage-based degradation in RC structures. *Earthquake Engineering and Structural Dynamics* **30**, 298-993.

Green RA. Energy-based evaluation and remediation of liquefiable soils. *PhD. dissertation,* Faculty of the Virginia Polytechnic Institute and State University, Blacksburg Virginia, 2001.

Green, R.A., Terri, G.A. and Nouri, Y. (2004) The number of equivalent cycles concept for liquefaction evaluations – revisited. *Department of Civil Engineering and Environmental Engineering Report UMCEE 04-07 rev1,* University of Michigan.

Green, R.A. and Lee, J. (2005) Computation of number of equivalent strain cycles a theoretical framework. *Proceedings of the 2nd Japan-US Workshop, Geomechanics II: Testing, Modelling and Simulation,* Kyoto, Japan.

Green, R.A. and Terri, G.A. (2005) Number of equivalent cycles concept for liquefaction – revisited. *Journal of Geotechnical Engineering* **131**(4), 477-488.

Hachem, M.M. (2004) Bispec version 1.5.3 Program downloadable from the internet from *http://www.ce.berkeley.edu/~hachem/bispec.*

Haigh, S.K., Teymur, B., Madabhushi, S.P.G. and Newland, D.E. (2002) Applications of Wavelet Analysis to the Investigation of the dynamic behaviour of geotechnical structures. *Soil Dynamics and Earthquake Engineering* **22**(9-12), 995-1005.

Haldar A, Tang WH. (1981) Statistical study of uniform cycles in earthquakes. *Journal of the Geotechnical Engineering Division ASCE* **107**(GT5), 577-589.

Hall, J.F. (2005) Problems encountered from the use (or misuse) of Rayleigh damping. *Earthquake Engineering and Structural Dynamics* in press.

Hancock, J. and Bommer, J.J. (2005) The effective number of cycles of earthquake ground motion. *Earthquake Engineering and Structural Dynamics* **34**, 637-664.

Hancock, J., Watson-Lamprey, J., Abrahamson, N.A., Bommer, J.J., Markatis, A., McCoy, E. and Mendis, R. (2006) An improved method of matching response spectra of recorded earthquake ground motion using wavelets. *Journal of Earthquake Engineering* **10**(Special Issue 1), 1-23.

Hancock, J. and Bommer, J.J. (2006a) The influence of strong-motion duration on structural damage. *Earthquake Spectra,* submitted for publication.

Hancock, J. and Bommer, J.J. (2006b) Accelerograms for estimating inelastic structural response. Par 1: Linear scaling. *Earthquake Engineering and Structural Dynamics,* submitted for publication.

Hancock, J. and Bommer, J.J. (2006c) Accelerograms for estimating inelastic structural response. Part 2: Linear scaled vs spectral matched. *Earthquake Engineering and Structural Dynamics,* submitted for publication.

Hancock, J. and Bommer, J.J. (2006d) Using spectral matched records to explore the influence of strong-motion duration on inelastic structural response. *Soil Dynamics and Earthquake Engineering,* submitted for publication.

Hanks, T.C. (1979) b Values and $\omega^{-\gamma}$ seismic source models: Implications for tectonic stress variations along active crustal fault zones and the estimation of high-frequency strong motion. *Journal of Geophysical Research* **84**(B4), 2235-2242.

Hanks, T.C. and Kanamori, H. (1979). A moment magnitude scale, *Journal of Geophysical Research* **84** (B5), 2348-2350.

Hanks, T.C. and McGuire, R.K. (1981) The character of high-frequency strong ground motion. *Bulletin of the Seismological Society of America* **71**(6), 2071-7095.

Harp, E.L. and Wilson, R.C. (1995). Shaking intensity thresholds for rock falls and slides: evidence from Whittier Narrows and Superstition Hills earthquake strong-motion records. *Bulletin of the Seismological Society of America* **85**, 1739-1757.

Harvard Seismology (2003). CMT Catalog search. On Internet at http://www.seismology.harvard.edu/CMTsearch.html. Department of Earth and Planetary Sciences and Department of Engineering and Applied Science, Harvard University.

Heredia-Zavoni, E., Zeballos, A. and Esteva, L. (2000) Theoretical models and recorded response in the estimation of cumulative seismic damage on non-linear structures. *Earthquake Engineering and Structural Dynamics* **29**, 1779-1796.

Hilber, H.M., Hughes, T.J.R. and Taylor, R.L. (1977) Improved numerical dissipation for the time-integration algorithms in structural dynamics, *Earthquake Engineering and Structural Dynamics* **5**, 283-292.

Hisada, T. and Ando, H. (1976) Relation between duration of earthquake and ground motion and magnitude, *Kajima ICT,* Japan, June Issue

Housner, G.W. (1952) Spectrum Intensity of Strong Motion Earthquakes. *Proceedings of Symposium on Earthquake and Blast Effects on Structures* pp20-36.

Housner, G.W. (1956) Limit design of structures to resist earthquakes. *Proceedings of the World Conference on Earthquake Engineering* Berkeley, 5.1-5.13.

Housner, G.W. (1965) Intensity of ground shaking near the causative fault. *Proceedings of the 3rd World Conference on Earthquake Engineering* **1**, 81-91.

Housner, G.W. (1975) Intensity of ground shaking near the causative fault *Proceedings of the Third World Conference on Earthquake Engineering,*Vol 1, Auckland, New Zealand, pp 81 -94.

Hsu, H-L. and Liang, L-L. (2003) Performance of hollow composite members subjected to cyclic loading. *Earthquake Engineering and Structural Dynamics* **32**, 443-461.

Hu, Y., Tao, X.X. and Zhang, M. (1985) Joint evaluation of spectrum and duration for sites of critical structures. *Transactions of the 8th International Conference on Structural Mechanics in Reactor Technology* volume M, 315-320.

Hudson, D.E. (1979) Reading and interpreting strong motion accelerograms. *Earthquake Engineering Research Institute,* Engineering Monographs on Earthquake Criteria, Structural Design and Strong Motion Records. Library of Congress Catalog card number 79-53973.

Huh, J., Haldar, A. and Seo, S-G. (2000) Seismic risk analysis of buildings using SFEM. *Proceedings of the 12th World Conference on Earthquake Engineering*, Auckland paper 1196.

Hughes, T.J.R. (1983) Analysis of transient algorithms with particular reference to stability behaviour, in *Computer Methods for Transient Analysis* (eds Belytschko T. and Hughes, T.J.R.), Amsterdam, 67-155.

Husid, L.R. (1969) Caracteristicas de terremotos – Analisis general. *Revista del IDIEM, Santiago de Chile,* **8**, 21-42.

IBC (2000) International Building Code 2000 *International Code Council* ISBN 1892395258.

Iervolino, I., Manfredi, G. and Cosenza, E. (2005) Ground motion duration effects on nonlinear seismic response. *Earthquake Engineering and Structural Dynamics* (in press).

Iyama, J. and Kuwamura, H. (1999) Application of wavelets to analysis and simulation of earthquake motions. *Earthquake Engineering and Structural Dynamics* **28**, 255-272.

Iyengar, R.N. and Rao, P.N. (1979) Generation of spectrum compatible accelerograms. *Earthquake Engineering and Structural Dynamics* **7**, 253-263.

Izzuddin, B.A. (2001) Conceptual issues in geometrically nonlinear analysis of 3D framed structures. *Computer Methods in Applied Mechanics and Engineering* **191**(9), 1029-1053.

Jenkins, P.A.M. (2004) Displacement capacity of reinforced concrete columns with limited shear resistance. *MSc Dissertation ROSE School,* Pavia Italy.

Jennings, P.C. and Husid, R. (1968) Collapse of yielding structures. *Journal of Engineering Mechanics Division Proceedings of the ASCE* **94**(EM5), 1045-1065.

Jeong, G.D. and Iwan, W.D. (1988) The effect of earthquake duration on the damage of structures. *Earthquake Engineering and Structural Dynamics* **16**, 1201-1211.

Ji, C., Wald, D.V. and Helmberger, D.V. (2002) Source description of the 1999 Hector Mine, California, earthquake, Part 1: Wavelet domain inversion theory and resolution analysis. *Bulletin of the Seismological Society of America* **92**(4), 1192-1207.

Joannon, J.G., Arias, A. and Saragoni, R.G. (1977) The time variation of the predominant frequency of earthquake motions. *Proceedings of the 6th World Conference on Earthquake Engineering* **1**, 560-568.

Jones, N. (1989) Structural Impact. *Cambridge University Press,* Cambridge, ISBN 0-521-30180-7

Joyner, W.B. and Boore, D.M. (1981) Peak horizontal acceleration and velocity from strong-motion records including records from the 1979 Imperial Valley, California, earthquake. *Bulletin of the Seismological Society of America* **71**(6), 2011-2038.

Joyner, W.B. and Boore, D.M. (1988) Measurement, characterization and prediction of strong ground motion. *Proceedings of Speciality Conference on Earthquake Engineering and Soil Dynamics II*, ASCE Geotechnical Engineering Division, 43-102.

Joyner, W.B. and Boore, D.M. (1993) Methods for regression analysis of strong-motion data. *Bulletin of the Seismological Society of America*, **83**(2) 469-487.

Joyner, W.B. and Boore, D.M. (1994) Errata. *Bulletin of the Seismological Society of America* **84**(3), 955-956.

Joyner W.B. (2000) Strong motion from surface waves in deep sedimentary basins. *Bulletin of the Seismological Society of America* **90**(6B), S95-S112.

Kanamori, H. (1977). The energy release in great earthquakes, *Journal of Geophysical Research* **82**(10), 2981 – 2987.

Kaul, M.K. (1978) Spectrum-consistent time-history generation. *Journal of the Engineering Mechanics Division, ASCE* **104** (EM4), 781-788.

Kavazanjian, E., Echezuria, H. and McCann, M.W. (1985) RMS acceleration hazard for San Francisco. *Soil Dynamics and Earthquake Engineering* **4**(3), 106-123.

Kawashima, K., Aizawa, K. (1986) Earthquake response spectra taking account of number of response cycles. *Earthquake Engineering and Structural Dynamics* **14**, 185-197.

Kawashima, K. and Aizawa, K. (1989). Bracketed and normalised durations of earthquake ground acceleration. *Earthquake Engineering and Structural Dynamics* **18,** 1041 – 1051.

Kijewski-Correa, T. and Kareem, A. (2004) Time-frequency perspectives in the analysis and interpretation of ground motions and structural response. *Proceedings of the 13th World Conference on Earthquake Engineering,* Vancouver, B.C., Canada. Paper 2569.

Kinemetrics (2004) Products, systems and solutions for earthquake and seismic monitoring *http://www.kinemetrics.com*

Kircher, C.A., Nassar, A.A., Kustu, O. and Holmes, W.T. (1997) Development of building damage functions for earthquake loss estimation. *Earthquake Spectra* **13**(4), 663-682.

Kircher, C.A. (2005) Code requirements for the selection and scaling of ground motion records. *Presentation made to the 2005 COSMOS Annual Meeting,* San Francisco, California.

Kitada, Y. (1998) Identification of nonlinear structural dynamic systems using wavelets. *Journal of Engineering Mechanics (ASCE)* **124**(10), 1059-1066.

Kobayashi, Y. (1971) Effects of earthquakes on ground (II) *Journal of Physics of the Earth* **19,** 231-241.

Koliopoulos, P.K. and Margaris, B.N. (2001) The 1999 Athens (Greece) earthquake: energy and duration-related response spectral characteristics of different site conditions. *Proceedings: Fourth International Conference on Recent Advances in Geotechnical Earthquake Engineering and Soil Dynamics,* paper 10.31.

Kunnath, S.K. and Chai, Y.H. (2004) Cumulative damage-based inelastic cyclic demand spectrum. *Earthquake Engineering and Structural Dynamics* **33**, 499-520.

Krawinkler, H. and Zohrei, M. (1983) Cumulative damage in steel structures subjected to earthquake ground motions. *Computers and Structures* **16**(1-4), 531-541.

Krawinkler, H. (1987) Performance assessment of steel components. *Earthquake Spectra* **3**(1), 27-41.

Krawinkler, H. (1997) Impact of duration/energy in design. *Proceedings of the FHWA/NCEER Workshop on the National Representation of Seismic Ground*

Motion for New and Existing Highway Facilities, Burlingame, California, Organized by NCEER (project 106-F-5.4.1) and ATC (project ATC-18-1) pp. 115-123.

Lam, N., Wilson, J. and Hutchinson, G. (2000) Generation of synthetic earthquake accelerograms using seismological modelling: a review. *Journal of Earthquake Engineering* **4**(3), 321-354.

Lee, K.L. and Chan, K. (1972). Number of equivalent significant cycles in strong motion earthquake, *Proceedings of the International Conference on Microzonation for Safer Construction Research and Application*, Seattle **2,** 609-627.

Levy, S., Wilkinson, J.P.D. (1976) Generation of artificial time-histories, rich in all frequencies, from given response spectra. *Nuclear Engineering and Design* **38**, 241-251.

Lilhanand, K. and Tseng, W.S. (1987) Generation of synthetic time histories compatible with multiple-damping design response spectra. *Transactions of the 9th International Conference on Structural Mechanics in Reactor Technology,* Lausanne, **Vol K1**, 105-110.

Lilhanand, K. and Tseng, W.S. (1988) Development and application of realistic earthquake time histories compatible with multiple-damping design spectra. *Proceedings of the 9th World Conference on Earthquake Engineering,* Tokyo Japan, **Vol II**, 819-824.

Liu, A., Stewart, J. P., Abrahamson, N. A. and Moriwaki, Y. (2001) Equivalent number of uniform stress cycles for soil liquefaction analysis. *Journal of Geotechnical and Environmental Engineering* **127**(12) 1017-1026.

López-Menjivar, M. A. (2004) Verification of a displacement-based adaptive pushover method for assessment of 2-D Reinforced Concrete Buildings. *PhD Thesis, Rose School, European School for Advanced Studies in Reduction of Seismic Risk,* Pavia, Italy.

Lu, L., Annaka, T., Tanabe, S. and Kawamura, N. (1998) Estimation of velocity range distribution of earthquake ground motion for fatigue assessment. *Proceedings of the 11th European Conference on Earthquake Engineering, Paris.*

Lynch, R.D. (1967) A statistical relationship between band-pass filter and pseudo-relative velocity spectra. *Atomic Energy Commission Report NVO-1163-188.*

McCann, M.W. and Shah, H. (1979) Determining strong-motion duration of earthquakes. *Bulletin of the Seismological Society of America* **69**(4), 1253-1565.

McCann, M.W. and Boore, D.M. (1983) Variability in ground motions: Root mean square acceleration and peak acceleration for the 1971 San Fernando, California, Earthquake. *Bulletin of the Seismological*

McGuire, R.K. (1977) Seismic design spectra and mapping procedures using hazard analysis based directly on oscillator response. *Earthquake Engineering and Structural Dynamics* **5,** 211-234.

McGuire, R.K. (1995) Probabilistic seismic hazard analysis and design earthquakes: Closing the loop. *Bulletin of the Seismological Society of America* **85**(5), 1275-1284.

McGuire, R. K. and Barnhard, T.P. (1979). The usefulness of ground motion duration in predicting the severity of shaking. *Proceedings of the 2nd U.S. National Conference on Earthquake Engineering,* Stanford. 713-722

Magenes, G., Calvi, G.M. and Kingsley, G.R. (1995) Seismic testing of a full-scale, two-storey masonry building: test procedure and measured experimental response. In *Experimental and Numerical Investigation on a Brick Masonry Building Prototype – Numerical Prediction of the Ecperiment* Report 3.0 – G.N.D.T., January.

Magenes, G., Calvi, G.M. and Gaia, F. (1996) Seismic testing on reinforced masonry walls. *Sceintific Report RS-03/96,* Dipartimento di Meccanica Strutturale dell'Universita di Pavia, Italy. (not seen, figure supplied by Prof Magenes)

Magenes, G. and Calvi, G.M. (1997) In-plane seismic response of brick masonry walls. *Earthquake Engineering and Structural Dynamics* **26**(11) 1091-1112.

Magenes, G. and Baietta, S. (1998) Cyclic modelling of reinforced masonry shear walls for dynamic analysis: indications coming from experiments. *in Computer Methods in Structural Masonry* E and FN Spon, London, 136-143.

Mahin, S.A. (1980) Effects of duration and aftershocks on inelastic design earthquakes. *Proceedings of the 7th World Conference on Earthquake Engineering* **5**, 677-680.

Mahin, S.A. and Lin, J. (1983) Construction of inelastic response spectra for single-degree-of-freedom systems. *Earthquake Engineering Research Center,* Berkeley, Report UCB/EERC-83/17.

Malhotra, P.K. (2002) Cyclic-demand spectrum. *Earthquake Engineering and Structural Dynamics* **31**, 1441-1457.

Malhotra, P.K. (2003) Strong motions records for site specific analysis. *Earthquake Spectra* **19**(3), 557-578.

Mander, J.B., Priestley, M.J.N. and Park (1989) Theoretical stress-strain model for confined concrete. *Journal of Structural Engineering* **114**(8) 1804-1826.

Mander, J.B., Chen, S. and Peckan, G. (1994a) Low cycle fatigue behaviour of semi-rigid top-and-seat angle connections. *Engineering Journal AISC* **31**(3), 111-122.

Mander, J.B., Panthanki, F.D. and Kasalanati, A. (1994b) Low-cycle fatigue behaviour of reinforcing steel. *Journal of Materials in Civil Engineering* **6**(4), 453-468.

Mander, J.B., Peckan, G. and Chen, S.S. (1995) Low-cycle variable amplitude fatigue modelling of top-and-seat connections. *Engineering Journal AISC* **32**(2), 54-63.

Mander, J.B., Dutta, A. (1996) A practical energy-based design methodology for performance based seismic engineering. *Proceedings 65th Annual Convention, Structural Engineers Association of California*, 319-338.

Mander, J.B., Dutta, A. (1997) How can energy be accommodated in seismic mapping. *NCEER Workshop on the National Representation of Seismic Ground-motion for New and Existing Highway Facilities,* 95-114.

Manfredi, G. and Pecce, M. (1997) Low cycle fatigue of RC beams in NSC and HSC. *Engineering Structures* **19**(3), 217-223.

Manfredi, G. (2001) Evaluation of seismic energy demand. *Earthquake Engineering and Structural Dynamics* **30,** 485-499.

Manfredi, G., Polese, M. and Cosenza E. (2002) Cyclic demand in the near fault area. *Proceedings of the 7th US National Conference on Earthquake Engineering,* Boston, Massachusetts, paper 00075.

Manfredi, G., Polese, M. and Cosenza, E. (2003) Cumulative demand of the earthquake ground-motions in the near source. *Earthquake Engineering and Structural Dynamics* **32**, 1853-1865.

Manzocchi, G.M.E., Chryssanthopoulos, M., Elnashai, A.S. (1994) An analytical solution for the probabilistic response of SDOF non-linear random systems subjected to variable amplitude cyclic loading. *Earthquake Engineering and Structural Dynamics* **23**, 489-506.

Martinez-Rueda, J.E. and Elnashai, A.S. (1997) Confined concrete model under cyclic load. *Materials and Structures* **30**(197), 139-147.

Martinez-Rueda, J.E. (1998) Scaling procedure for natural accelerograms based on a system of spectrum intensity scales. *Earthquake Spectra* **14**(1), 135-152.

Matsumoto, Y., Yamada, S. and Akiyama, H. (2000) Fracture of beam-to-column connection simulated by means of the shaking table test using the inertial loading equipment. *Behaviour of Steel Structures in Seismic Areas, Mazzolani and Tremblay (eds),* Balkema, Rotterdam, 215-222.

Matsumura, K. (1992) On the intensity of strong motions related to structural failures. *Proceedings of the 10th World Conference on Earthquake Engineering,* Madrid Spain, Vol. 1, pp375-380.

Matteis, G.D., Landolfo, R. and Calado, L. (2000) Cyclic behaviour of semi-rigid angle connections: A comparative study of tests and modelling. *Behaviour of Steel Structures in Seismic Areas, Mazzolani and Tremblay (eds),* Balkema, Rotterdam, 165-174.

Mavroeidis, G.P. and Papageorgiou, A.S. (2003) A mathematical representation of near-fault ground motions. *Bulletin of the Seismological Society of America* **93**(3), 1099-1131.

Mendis, R. and Bommer, J.J. (2006) Constructing over-damped displacement spectra for seismic design codes. *100th Anniversary Earthquake Conference Commemorating the 1906 San Francisco Earthquake,* EERI, San Francisco, paper 1743.

Menegotto, M. and Pinto, P.E. (1973) Method of analysis for cyclically loaded R.C. plane frames including changes in geometry and non-elastic behaviour of elements under combined normal force and bending. *Symposium on the resistance and ultimate deformability of structures acted on by well defined repeated loads,* Zurich Switzerland, International association for bridge and structural engineering pp. 15-22.

Meskouris, K. (1983) Influence of earthquake strong motion duration on nonlinear structural response. *Transactions of the 7th International Conference on Structural Mechanics in Reactor Technology* **K**, 267-275.

Miner, M.A. (1945) Cumulative damage in fatigue. *Transactions of the ASME, Journal of Applied Mechanics* **12**(3), 159-164.

Miranda, E. and Ruiz-Garcia, J. (2002) Evaluation of approximate methods to estimate maximum inelastic displacement demands. *Earthquake Engineering and Structural Dynamics* **31**, 539-560.

Mohammadioun, B. (1997) Nonlinear response of soils to horizontal and vertical bedrock earthquake motion. *Journal of Earthquake Engineering* **1**(1), 93-119.

Mohraz, B. and Peng, M.H. (1989) The use of low-pass filter in determining the duration of strong ground-motion. *ASCE Journal of Pressure Vessels and Piping Division* **182**, 197-200.

Mork, K.J. (1994) Response analysis of reinforced concrete structures under seismic excitation. *Earthquake Engineering and Structural Dynamics* **23**, 33-48.

Mortgat, C.P. (1979) – A probabilistic definition of effective acceleration. *Proceedings of the 2nd U.S. National Conference on Earthquake Engineering, Stanford,* 743-751.

Mukherjee, S. and Gupta, V.K. (2002a) Wavelet-based characterisation of design ground motions. *Earthquake Engineering and Structural Dynamics* **31**, 1173-1190.

Mukherjee, S. and Gupta, V.K. (2002b) Wavelet-based generation of spectrum-compatible time-histories. *Soil Dynamics and Earthquake Engineering* **22**, 799-804.

Mwafy, A-A. M. (2001) Seismic performance of code-designed RC buildings. *PhD Thesis,* Imperial College London, United Kingdom.

Naeim, F., Anderson, J.C. and Jain, S. (1994) A database of earthquake records for design. *Proceedings of the 5th U.S. National Conference on Earthquake Engineering* **2**, 263-272.

Naeim, F. (1995) On seismic design implications of the 1994 Northridge earthquake records. *Earthquake Spectra* **11**(1), 91-109.

Naeim, F. and Lew, M. (1995) On the use of design spectrum compatible time histories. *Earthquake Spectra* **11**(1), 111-127.

Naeim, F., Alimoradi, A. and Pezeshk, S. (2004) Selection and scaling of ground motion time histories for structural design using genetic algorithms. *Earthquake Spectra* **20**(2), 413-426.

Nassar, A.A. and Krawinkler, H. (1991) Seismic demands for SDOF and MDOF systems. *John Blume Earthquake Engineering Centre Report,* Stanford University, report number 95.

Newmark, N.M. (1959) A method for computation for structural dynamics. *Proceedings of the ASCE* **85**(EM3), 67-94.

Newmark, N.M. and Hall, W.J. (1982) Earthquake spectra and design. *Engineering monographs on earthquake criteria, structural design and strong motion records,* Earthquake Engineering Institute, Berkeley.

Newmark, N.W. and Hall, W.K. (1969) Seismic design criteria for nuclear reactor facilities. *Proceedings of the 4th World Conference on Earthquake Engineering, Santiago Chile,* **Vol II,** B4, pp 37-50.

Nigam, N.C. and Jennings, P.C. (1969) Calculation of response spectra from strong-motion earthquake records. *Bulletin of the Seismological Society of America* **59**(2), 909-922.

Novikova, E. I. and Trifunac, M.D. (1995). Frequency dependent duration of strong earthquake ground motion update empirical equations. *Department of Civil Engineering Report* CE 95-01, University of Southern California, Los Angeles, California.

O'Brien, J. L., Murphy, J.R. and Lahoud, J.A. (1977) Correlation of peak ground acceleration amplitude with seismic intensity and other physical parameters. *Report NUREG-0143,* US Nuclear Regulatory Commission.

Ohsaki, Y., Watabe, M. and Tohdo, M. (1980) Analysis on seismic ground motion parameters including vertical components. *Proceedings of the 7th World Conference on Earthquake Engineering*, Istanbul, Turkey **2**, 97-104.

Osinov, V.A. (2003) Cyclic shearing and liquefaction of soil under irregular loading: an incremental model for the dynamic earthquake-induced deformation. *Soil Dynamics and Earthquake Engineering* **23**, 535-548.

Osteraas, J. and Krawinkler, H. (1989) The Mexico earthquake of September 19, 1985 – behaviour of steel buildings. *Earthquake Spectra* **5**(1), 51-87.

Otani, S. (1978) SAKE, A computer program for inelastic response of R/C frames to earthquakes. *Report UILU-Eng-74-2029,* Civil Engineering Studies, University of Illinois at Urbana-Champaign, USA, *not seen referenced in SesimoSoft (2005b).*

Page, R.A., Boore, D.M., Joyner, W.B. and Coulter, H.W. (1972) Ground motion values fo use in seismic design of the trans-Alaska pipeline system, *US Geological Survey Circular 672.*

Pagratis, D. (1995) Prediction of earthquake strong ground motion duration for engineering use. *Imperial College, University of London*, MSc thesis.

Papazachos, B.C., Papainnou, C.A., Margaris, V.N. and Theodulidis, N.P. (1992) Seismic hazard assessment in Greece based on strong motion duration. *Proceedings of the Tenth World Conference on Earthquake Engineering,* Vol 2., Madrid, pp. 425-430.

Park, R. and Paulay, T. (1975) Reinforced concrete structures. *John Wiley and Sons,* New York, ISBN 0-471-65917-7.

Park, Y., Ang, A.H. and Wen, Y.K. (1984) Stochastic model for seismic damage assessment. *Engineering Mechanics in Civil Engineering: Proceedings of the Fifth Engineering Mechanics Division Speciality Conference,* ASCE, New York, 1168-1171.

Park, Y., Ang, A.H. and Wen, Y.K. (1985) Seismic damage analysis of reinforced concrete buildings. *Journal of Structural Engineering* **111**(4), 740-757.

Park, Y. and Ang, A.H. (1985) Mechanistic seismic damage model for reinforced concrete. *Journal of Structural Engineering* **111**(4), 722-739.

Park, Y., Ang, A. H., Wen, Y.K. (1987) Damage-limited aseismic design of buildings. *Earthquake Spectra* **3**(1), 1-26.

Park, Y., Reinhorn, A.M. and Sashi, K.K. (1988) Seismic damage analysis of reinforced concrete buildings. *Proceedings of the 9th World Conference on Earthquake Engineering,* Tokyo, Japan **8** 211-216.

Paciello, A., Rinaldis, D. and Romeo, R. (2000) Incorporating ground motion parameters related to earthquake damage into seismic hazard analysis. *Proceedings of the 6th International Conference on Seismic Zonation* **1**, 321-326.

Paulay, T. and Priestley, M.J.N. (1992) Seismic design of reinforced concrete and masonry buildings. *John Wiley and Sons,* New York, ISBN 0-471-54915-0.

Pauschke, J.M. and Krishnamurty, S. (1984) Peak vs root-mean-square (RMS) acceleration as a response parameter. *Proceedings of the 8th World Conference on Earthquake Engineering*, San Francisco **IV**, 45-52.

Pauschke, J.M. (1985) Peak vs. root-mean-square acceleration to characterize strong ground motion. *Proceedings of the 2nd International Conference on Soil Dynamics and Earthquake Engineering,* QE2, New York to Southampton, 1-29 – 1-38.

Paz, M. (1997) Structural Dynamics Theory and Computation. *Chapman and Hall, New York,* ISBN 0-412-07461-3.

Penazzo, P., Bommer, J.J., Magenes, G. (2002) The influence of strong-motion duration on inelastic structural demand. *12th European Conference on Earthquake Engineering*, paper 694.

Penazzo, P. (2001) Influence of strong-motion characteristics on inelastic structural demand in masonry structures *MSc Thesis Imperial College London.*

Peng, M-H, Elghadamsi, F. and Mohraz, B. (1988) A stochastic procedure for nonlinear response spectra. *Proceedings of the 9th World Conference on Earthquake Engineering*. Tokyo **V**, 1069-1073.

Peng, M-H, Elghadamsi, F. and Mohraz, B. (1989) A simplified procedure for constructing probabilistic response spectra. *Earthquake Spectra* **5**(2), 393-408.

Perera, R., Alarcon, E. and Carnicero, A. (2000) Modelization of low cycle fatigue damage in frames. *12th World Conference on Earthquake Engineering*, paper 0714.

Perez, V. (1980) Spectra of amplitudes sustained for a given number of cycles: an interpretation of response duration for strong-motion earthquake records. *Bulletin of the Seismological Society of America* **70**(5) 1943-1954.

Preumont, A. (1984) The generation of spectrum compatible accelerograms for the design of nuclear power plants. *Earthquake Engineering and Structural Dynamics* **12**, 481-497.

Priestley, M.J.N. and Kowalsky, M. (2000) Direct displacement-based seismic design of concrete buildings. Bulletin of the New Zealand Society for Earthquake Engineering **33**(4), 421-444.

Priestley, M.J.N. (2003) Myths and fallacies in earthquake engineering, revisited. *Ninth Mallet Milne Lecture,* IUSS Press Istituto Universitario di Studi Superiori di Pavia, Italy.

Priestley, M.J.N. and Grant, D. (2005) Viscous damping in seismic design and analysis. *Journal of Earthquake Engineering* **9**(Special Issue 2), 229-255.

Plumier, A., Agatino, M.R., Castellani, A., Castiglioni, C.A. and Chesi, C. (1998) Resistance of steel connections to low-cycle fatigue. *11th European Conference on Earthquake Engineering*.

Powell, G. H. and Allahabadi, R. (1988) Seismic damage prediction by deterministic methods: concepts and procedures. *Earthquake Engineering and Structural Dynamics* **16**, 719-734.

Rahnama, M. and Manuel, L. (1996) The effect of strong motion duration on seismic demands. *11th World Conference on Earthquake Engineering*, paper 924.

Reinoso, E., Ordaz, M. and Guerrero, R. (2000) Influence of strong ground-motion duration in seismic design of structures. *12th World Conference on Earthquake Engineering,* Auckland, paper 1151.

Reiter, L. (1990) Earthquake hazard analysis – Issues and insights. *Columbia University Press, New York.* ISBN 0-231-06534-5.

Rice, S.O. (1945) Mathematical analysis of random noise. *Bell System Technical Journal* **XXIV**

Rizzo, P.C., Shaw, D.E. and Jarecki, S.J. (1975) Development of real/synthetic time histories to match smooth design spectra. *Nuclear Engineering and Design* **32**, 148-155.

Rodriguez, M. (1994) A measure of the capacity of earthquake ground-motions to damage structures. *Earthquake Engineering and Structural Dynamics* **23**, 627-643.

Rosenblueth, E. and Bustamante, J.I. (1962) Distribution of structural response to earthquakes. *Journal of the Engineernig Mechanics Division, Proceedings of the ASCE* **EM3**, 75-106

Rossetto, T. (2002) Prediction of deformation capacity of non-seismically designed reinforced concrete members. *Proceedings of the 7th US National Conference on Earthquake Engineering*, Boston Massachusetts, paper 00280.

Rovithakis, A. (2001) Verification of adaptive pushover analysis procedures *MSc. Dissertation*, Department of Civil and Environmental Engineering, Imperial College London, United Kingdom.

Sabetta, F. and Bommer, J.J. (2002) Modification of the spectral shapes and subsoil conditions in Eurocode 8. *Proceedings of the 12th European Conference on Earthquake Engineering,* London, paper 518.

Şafak, E. (1998) 3D Response spectra: a method to include duration in response spectra. *11th European Conference on Earthquake Engineering.*

Salajegheh, E. and Heidari, A. (2005) Time-history dynamic analysis of structures using filter banks and wavelet transforms. *Computers and Structures* **83**, 53-68.

Santa-Ana, P.R. and Miranda, E. (2000) Strength reduction factors for multi-degree-of-freedom systems. *Proceedings of the 12th World Conference on Earthquake Engineering,* Auckland, paper 1446.

Saragoni, G.R. (1977) The αβγ method for the characterization of earthquake accelerograms. *Proceedings of the Sixth World Conference on Earthquake Engnieering,* Vol 1, New Dehli, 357-362.

Saragoni, G.R. (1985) Azimuthal effects on earthquake destructiveness. *Transactions of the 8th International Conference on Structural Mechanics in Reactor Technology* volume M, 303-308.

Saragoni, G.R. (1990) Response spectra and earthquake destructiveness. *Proceedings of 4th U.S. National Conference on Earthquake Engineering.* Palm Springs, California **2**, 35-43.

Sarma, S.K. (1971) Energy flux of strong earthquakes. *Techtonophysics* **11**, 159-173.

Sarma, S.K. and Yang, K.S. (1987) An evaluation of strong motion records and a new parameter A_{95}. *Earthquake Engineering and Structural Dynamics* **15**, 119-132.

Sarma, S.K. and Casey, B.J. (1990) Duration of strong motion earthquakes. *Proceedings of the 9th European Conference on Earthquake Engineering* **10-A**, 174-179.

Sarma, S.K. and Srbulov, M. (1998) A uniform estimation of some basic ground motion parameters. *Journal of Earthquake Engineering* **2**(2), 267-287.

Scanlan, R.H. and Sachs, K. (1974) Earthquake time histories and response spectra. *Journal of the Engineering Mechanics Division,* ASCE **100**(4), 635-655.

Schreiber, J., Ingham, J.M. and Davidson, B. J. (2002) Using damage indices to describe the influence of loading history on reinforced concrete structures. *12th European Conference on Earthquake Engineering,* paper 624.

Schwarz, J. (1996) Evaluation of effective design spectra for Eurocode 8. *Seismology in Europe, XXV General Assembly of the European Seismological Commission,* Reykjavik, Iceland, 648-654.

Schwarz, J. (1998) Evaluation of effective design spectra. *Seismic Design Practice into the Next Century: Research and Application, Proceedings of the 6th SECED Conference.* 467-475.

Scott, B.D., Park, R. and Priestley, M.J.N. (1982) Stress-strain behaviour of concrete confined by overlapping hoops at low and high strain rates. *ACI Journal* **79**(1), 13-27.

Scott, R.F. (1994). Lessons learned from VELACS project *Verifications of numerical procedures for the analysis of soil liquefaction problems* **2**, 1773-1784

Seed H.B. and Idriss I.M. (1967) Analysis of soil liquefaction: Niigata earthquake. *Journal of the Soil Mechanics and Foundations Division ASCE* **93**(SM3), 83-108.

Seed H.B. and Idriss I.M. (1971) Simplified procedure for evaluating soil liquefaction potential. *Journal of the Soil Mechanics and Foundations Division ASCE* **97**(SM9), 1249-1273.

Seed, H.B., Idriss, I.M., Makdisi, F., Banerjee, N. (1975) Representation of irregular stress time histories by equivalent uniform stress series in liquefaction analysis. *Earthquake Engineering Research Centre Report EERC 75-29,* University of California Berkeley, 1975.

SeismoSoft (2005a) SeismoSignal - A computer program for signal processing of strong-motion data *Online. Available from URL* http://www.seismosoft.com.

SeismoSoft (2005b) SeismoStruct - A computer program for static and dynamic nonlinear analysis of framed structures. *Online. Available from URL* http://www.seismosoft.com.

Seneviratna, G.D.P.K. and Krawinkler, H. (1997) Evaluation of inelastic MDOF effects for seismic design. *John A Blume Earthquake Engineering Centre,* Stanford University, report number 120.

SEAOC (1990) Recommended Lateral Force Requirements and Commentary (SEAOC Blue Book). *Structural Engineers Association of California.*

Shahabi, M. and Mostaghel, N. (1984) Strong ground motion duration and effective cyclic acceleration. *Proceedings of the Eighth World Conference on Earthquake Engineering,* Vol. 2, San Francisco, pp 843-850.

Shome, N., Cornell, A.C., Bazzurro, P., Carballo, J.E. (1998) Earthquakes, records and nonlinear responses. *Earthquake Spectra* **14**(3), 469-500.

Shrikhande, M. and Gupta, V.K. (1996) On Generating ensemble of design spectrum compatible accelerograms. *European Earthquake Engineering* **10**(3), 49-56.

Siddharthan, R. and Norris, G.M. (1990) Residual porewater pressure and structural response. *Soil Dynamics and Earthquake Engineering* **9**(5), 265-271.

Somerville, P.G., Smith, N.F., Graves, R.W. and Abrahamson, N.A. (1997) Modification of empirical strong ground motion attenuation relations to include the amplitude and duration effects of rupture directivity. *Seismological Research Letters* **68**(1), 199-222.

Somerville, P. (2000) New developments in seismic hazard estimation. *Proceedings of the Sixth International Conference on Seismic Zonation*, Palm Springs, California.

Sorace, S. (1998) Seismic damage assessment of steel frames. *Journal of Structural Engineering* **124**(5), 531-540.

Suarez, L.E. and Montejo, L.A. (2003) Generacion de registros artificiales compatibles con un espectro de respuesta mediante la transformada "wavelet". *Proceedings of II Congreso Nacional de Ingenieria Sismica,* Medellin.

Suarez, L.E. and Montejo, L.A. (2005) Generation of artificial earthquakes via the wavelet transform. *International Journal of Solids and Structures* in press.

Sucuoglu, H. and Nurtug, A. (1995) Earthquake ground-motion characteristics and seismic energy dissipation. *Earthquake Engineering and Structural Dynamics* **24** 1195-1213.

Stephens, J.E., and Yao, J.T. (1986) Damage assessment using response measurements. *Journal of Structural Engineering* **113**(4), 787-801.

Stewart, J.P., Chiou, S.J., Bray, J.D., Graves, R.W. Somerville, P.G. and Abrahamson, N.A. (2001) Ground motion evaluation procedures for performance-based design. *PEER Report* 2001/09, 57-85.

Takeda, T. Sozen, M.A. and Nielsen, N.N. (1970) Reinforced concrete response to simulated earthquakes. *Journal of the Structural Division, ASCE,* **96**(ST12), 2557-2573.

Takemiya, H. and Fujiwara, A. (1994) SH-wave scattering and propagation analyses at irregular sites by time domain BEM. *Bulletin of the Seismological Society of America* **84**(5), 1443-1455.

Takizawa, H. and Jennings, P.C. (1980) Collapse of a model for ductile reinforced concrete frames under extreme earthquake motions, *Earthquake Engineering and Structural Dynamics* **8**, 117-144.

Tan, T. Y. and Chao, Y.T. (1992) Construction of a design response spectrum from evolutionary spectra of seismogram. *10th World Conference in Earthquake Engineering* **10**, 5853-5858.

Tang, J. and Yao, T.P. (1972) Expected fatigue damage of seismic structures. *Journal of Engineering Mechanics Division ASCE* **98**(EM3), 695-709.

Taucer, F., Negro, P. and Colombo, A. (2000) Low cycle fatigue cyclic and PSD testing of a two-storey moment resisting steel frame with beam-to-column welded connections. *Journal of Earthquake Engineering* **4**(4) 437-477.

Teran-Gilmore, A., Avila, E. and Rangel, G. (2003) On the use of plastic energy to establish strength requirements in ductile structures. *Engineering Structures* **23**, 965-980.

Teymur, B., Madabhushi, S.P.G. and Newland, D.E. (2003) Application of wavelet theory in the analysis of earthquake motions recorded during the Kocaeli earthquake Turkey 1999. *Proceedings of the Fourth International Conference on Recent Advances in Geotechnical Earthquake Engineering and Soil Dynamics,* San Diego, California, paper 10.41.

Theofanopoulos, N. and Drakopoulos, J. (1986) A study of stong ground-motion duration of earthquakes in Greece. *Proceedings of the 8th European Conferenc on Earthquake Engineering,* Lisbon, Vol. 1, pp. 3.2/65 - 3.2/72

Theofanopoulos, N. and Watabe, M. (1989) A new definition for strong motion duration and comparisons with other durations. *Structural Engineering and Earthquake Engineering* **6**(1), 111-122.

Tiwari, A.K. and Gupta, V.K. (2000) Scaling of ductility and damage-based strength reduction factors for horizontal motions. *Earthquake Engineering and Structural Dynamics* **29**, 969-987.

Todorovska, M.I. (2004) Estimation of instantaneous frequency of signals using the continuous wavelet transform. *University of Southern California Report* No. CE-01-07. (revised Jan 2004).

Tremblay, R., Timler, P., Bruneau, M. and Filiatrault, A. (1995) Performance of steel structures during the 1994 Northridge earthquake. *Canadian Journal of Civil Engineering* **22**, 338-360.

Tremblay, R., Bruneau, M., Nakashima, M., Prion, G.L., Filiatrault, A. and DeVall, R. (1996) Seismic design of steel buildings: lessons from the 1995 Hyogo-ken Nanbu earthquake. *Canadian Journal of Civil Engineering* **23**, 727-756.

Tremblay, R. and Bouatay, N. (2002) Loading protocols for the seismic testing of ductile bracing members in concentrically braced steel frames. *Proceedings of the 12th European Conference on Earthquake Engineering, London,* paper 480.

Tremblay, R. (1998) Development of design spectra for long-duration ground-motions from Cascadia subduction earthquakes. *Canadian Journal of Civil Engineering* **25**, 1078-1090.

Tremblay, R. (2003) Achieving a stable inelastic seismic response for multi-story concentrically braced steel frames. *Engineering Journal* **40**(2), 111-129.

Trifunac, M.D. (1971a) Response envelope spectrum and interpretation of strong earthquake ground motion. *Bulletin of the Seismological Society of America* **61**(2), 343-356.

Trifunac, M.D. (1971b) A method for synthesizing realistic strong ground motion. *Bulletin of the Seismological Society of America* **61**(6), 1739-1753.

Trifunac, M.D. and Brady, A.G. (1975a) A study on the duration of strong earthquake ground-motion. *Bulletin of the Seismological Society of America* **65**(3), 581-626.

Trifunac, M.D. and Brady, A.G. (1975b) On the correlation of seismic intensity scales with peaks of recorded strong ground motion. *Bulletin of the Seismological Society of America* **65**(1), 139-162.

Trifunac, M.D. and Westermo, B.D. (1976) Dependence of the duration of strong earthquake ground motion on magnitude, epicentral distance, geologic

conditions at the recording station and frequency of motion. *Department of Civil Engineering University of Southern California, LA,* Report No 76-02.

Trifunac, M.D. and Westermo, B.D. (1977) A note of the correlation of frequency dependent duration of strong earthquake ground motion with the Modified Mercalli intensity and the geologic conditions at th recording site. *Bulletin of the Seismological Society of America* **67**(3), 917-927.

Trifunac, M.D. and Westermo, B.D. (1982) Duration of strong earthquake shaking. *Soil Dynamics and Earthquake Engineering* **1**(3), 117-121.

Trifunac, M.D. and Novikova, E.I. (1995) Duration of earthquake fault motion in California. *Earthquake Engineering and Structural Dynamics* **24** 781-799.

Trifunac, M.D., Lee, V.W. and Todorovska, M.I. (1999) Common problems in automatic digitisation of strong motion accelerograms. *Soil Dynamics and Earthquake Engineering* **18**, 519-530.

Tromans, I. and Bommer, J. J. (2002) The attenuation of strong-motion peaks in Europe. *Proceedings of the 12th European Conference on Earthquake Engineering,* Paper 394.

Tromans, I. (2004) Behaviour of buried water supply pipelines in earthquake zones. *PhD Thesis,* University of London.

Uang, C.M. and Bertero, V.V. (1988) Use of energy as a design criterion in earthquake-resistant design. *Earthquake Engineering Research Center, Berkeley,* Report UCB/EERC-88/18.

Uang, C.M. and Bertero, V.V. (1990) Evaluation of seismic energy in structures. *Earthquake Engineering and Structural Dynamics* **19** 77-90.

UBC (1994) Uniform building code 1994. *International Conference of Building Officials.* ISBN 1884590438.

UBC (2000) Uniform building code 2000. *International Conference of Building Officials.* ISBN 188459087X.

Valera JE, Donovan N. (1977) Soil liquefaction procedures – A review. *Journal of the Geotechnical Engineering Division ASCE* **103**(GT6), 607-625.

Vanmarcke, E.H. (1985) The effect of spatial averaging of earthquake ground-motion on the response of structures and equipment. *Transactions of the 8th International Conference on Structure Mechanics in Reactor Technology* volume M, 293-296.

Vanmarcke, E.H. and Lai, S.P. (1980) Strong-motion duration and RMS amplitude of earthquake records. *Bulletin of the Seismological Society of America* **70**(4), 1293-1307.

Vidic, T., Fajfar, P. and Fischinger, J. (1994) Consistent inelastic design spectra: strength and displacement. *Earthquake Engineering and Structural Dynamics* **23,** 507-521.

Vidic, T. and Fajfar, P. (1995) Behaviour factors taking into account cumulative damage. *10th European Conference on Earthquake Engineering* **2**, 959-964.

Walker, J. S. (1999) Wavelets and their scientific application. *Chapman and Hall*, London.

Watson-Lamprey, J. A. and Abrahamson, N.A. (2006a) Selection of ground motion time-series and limits on scaling. *Soil Dynamics and Earthquake Engineering* **26**, 477-482.

Watson-Lamprey, J. A. and Abrahamson, N.A. (2006b) Bias caused by use of spectrum compatible motions. *100th Anniversary Earthquake Conference Commemorating the 1906 San Francisco Earthquake,* San Francisco, paper 0909.

Weitzmann, R., Ohsaki, H. and Nakashima, M. (2006) Simplified methods for design of base-isolated structures in the long-period high-damping range. *Earthquake Engineering and Structural Dynamics,* in press.

Wembo, Z. and Kehong (1997) Estimation of the duration of strong ground motion. *In: Mitigating the Impact of Impending Earthquakes,* eds. Vogel and Brandes, Balkema, pp. 149-156.

Westermo, B.D. (1980) The duration of strong motion and its dependence on the recording site geology. *Proceedings 7th World Conference on Earthquake Engineering,* Istanbul **2,** 263-266.

Whitman, R.V., Anagnos, T., Kircher, C., Lagorio, H.J., Lawson, R.S. and Schneider, P. (1997) Development of a national earthquake loss estimation methodology. *Earthquake Spectra* **13**(4), 643-661.

Xie, L. and Zhang, X. (1988) Engineering duration of strong motion and its effects on seismic damage. *Proceedings of the 9th World Conference On Earthquake Engineering,* Tokyo, Japan **2**, 307-312.

Yamada, M., Tsuji, B., Nakanishi, S. (1977) Elasto-plastic behaviour of braced frames under cyclic horizontal loading. *Proceedings of the 6th World Conference on Earthquake Engineering,* New Delhi, India **3**, 2778-2784.

Yamada, M., Kawamura, H., Tani, A., Katsunobu, I., Sakai, Y., Nishikawa, H., Masui, A and Yamada, M. (1988a) Fracture ductility of structural elements and of structures. *Proceedings of the 9th World Conference on Earthquake Engineering,* Tokyo Japan **IV**, 219-224.

Yamada, M., Kasahara and Kotoda, K. (1988b) Seismic pulses repeated in coda part of strong seismic waves. *Proceedings of the 9th World Conference on Earthquake Engineering,* Tokyo Japan **II**, 313-318.

Yamada, M. (1969) Low cycle fatigue fracture limits of various kinds of structural members subjected to alternatively repeated plastic bending under axial compression as an evaluation basis or design criteria for aseismic capacity. *Proceedings of the 4th World Conference on Earthquake Engineering,* Santiago, Chile **1**(B-2), 137-151

Yamada, M. (1992) Practical ductility assurance of structures for aseismic design. *Proceedings of the 10th World Conference on Earthquake Engineering,* Madrid, Spain **6**, 3409-3414.

Yayong, W. and Minxian, C. (1990) Dependence of structural damage on the parameters of earthquake strong motion. *European Earthquake Engineering* **1**, 13-23.

Yokoyama, H. (1996) Predominant period of sedimentary surface wave and analysis of earthquake in the Osaka Plain. *Proceedings of the 11th World Conference in Earthquake Engineering*, Acapulco, paper 87.

Yoshimi, Y., Tokimatsu, K. and Kaneko, O. (1984). Undrained cyclic shear strength of a dense Niigata sand. *Soils and Foundations* **24**(4), 131-145.

Youd, T. L. and Idriss, I. M. (2001). Liquefaction resistance of soils: Summary report from the 1996 NCEER and 1998 NCEER/NSF workshops on evaluation of liquefaction resistance of soils. *Journal of Geotechnical and Geoenvironmental Engineering* **127**, 297-313.

Youngs, R.R., Abrahamson, N.A., Makdisi, F.I. and Sadigh, K. (1995) Magnitude-dependent variance of peak ground acceleration. *Bulletin of the Seismological Society of America* **85**(4), 1161-1176.

Zahrah, T.F. and Hall, W.J. (1984) Earthquake energy absorption in SDOF structures. *Journal Structural Engineering Division ASCE* **110**(ST8), 1757-1772.

Zhou, Y. and Xie, L. (1984) A new definition of duration of strong ground motion. *Proceedings of the Chinese National Conference on Earthquake Engineering*, Shanghai, (in Chinese).

APPENDIX 1. ACCELEROGRAMS USED FOR RC FRAME ANALYSIS

Records used for the analysis of the reinforced concrete frames are taken from the NGA database (Version3.2, 19th November 2004). Records are only used if the moment magnitude, site classification and source-to-site distance, defined by both the distance to the rupture (R_{rup}) and the distance from the surface projection of the fault rupture (R_{jb}), are known. Records are selected to form two smaller subsets of single component horizontal accelerograms. The first subset of 2035 accelerograms is derived by excluding all records from Taiwan. This reduces the size of the database and prevents the 1852 accelerograms from the ChiChi earthquake dominating the results. The magnitude-distance distribution of this sub-set is shown in Figure A1.1.

The second subset aims to capture the pertinent features of the first subset but with far fewer records. This is achieved by selecting records to fulfil three criteria:-

1. Records with a similar magnitude – distance distribution as the full dataset
2. Records with unusual characteristics (velocity and displacement pulses, long and short durations, recorded on very soft soil) to highlight the influence of the variability of the ground motion.
3. Records with genuinely strong ground-motion that is likely to induce significant non-linear response

As these criteria can be mutually exclusive, records are selected to fulfil each criterion separately, essentially dividing the second subset into three sub-subsets. As site soil conditions have an important influence on the ground motions the records recorded on sites classified as rock and those classified as soil are treated separately in the first criteria. The NGA database uses the average shear wave velocity in the upper 30m (V_{s30}) to classify site soil conditions. For this work V_{s30} is converted into the widely used four category system (Boore and Joyner 1993; Ambraseys *et al.* 1996). Sites with $V_{s30} > 760$m/s are classed as rock; sites with V_{s30} from 360m/s to 760m/s are classed as stiff soil; sites with V_{s30} 360m/s to 180m/s are classified as soft soil, and sites with $V_{s30} < 180$m/s are classified as very soft.

The records selected to meet the first criteria are chosen by dividing the database into 20 magnitude and distance bins and selecting four accelerograms from each bin, two

from sites classified as rock, and the other two from sites classified as stiff or soft soil. Further details of the binning system is given in Figure A1.1 and Table A1.1. Accelerograms are selected to represent each bin if they have the closest match to the average spectral acceleration of all the accelerograms in the bin, over the period range of interest to this study, i.e. 0.6 to 1.2 seconds. Accelerograms with strong velocity pulses, characteristic of forward directivity, are excluded from this sub-subset, as were the 26 accelerograms from sites classified as very soft soil. Details of the 70 accelerograms in this dataset are given in Table A1.2.

The second sub-subset consists of 23 accelerograms with unusual characteristics, such as those with large velocity and displacement pulses, long and short durations. This includes the record from Northridge, Rinaldi Receiving Station, which was noted by Alavi and Krawinkler (2004) to have forward directivity pulse. Further details of these records are given in Table A1.3.

The third sub-subset consists of 43 accelerograms with an average spectral acceleration greater than 0.7g, over the period range of interest to this study, 0.6 to 1.2 seconds. Further details of these records are given in Table A1.4.

Table A1.1: Details of Magnitude – Distance Bins for NGA Data Set

Bin	Magnitude Range (M_w)	Distance Range, R_{rup} (km)	Number of Soil Records[1]	Number of Rock Records[1]	Soil Mean SA (0.6to1.2s)	Rock Mean SA (0.6to1.2s)
1	<6.0	<13	16	2	0.346	0.081
2	<6.0	13 to 30	82	6	0.168	0.046
3	<6.0	30 to 50	44	2	0.064	0.013
4	<6.0	50 to 100	16	6	0.042	0.010
5	6.0 – 6.49	<15	29	1	0.348	0.160
6	6.0 – 6.49	15 to 30	42	2	0.177	0.056
7	6.0 – 6.49	30 to 50	59	2	0.118	0.028
8	6.0 – 6.49	50 to 100	24	0	0.056	-
9	6.5-6.99	<13	62	8	0.635	0.485
10	6.5-6.99	13 to 30	88	9	0.311	0.173
11	6.5-6.99	30 to 50	79	5	0.148	0.093
12	6.5-6.99	50 to 100	162	10	0.120	0.084
13	7.0-7.49	<13	13	1	0.443	1.061
14	7.0-7.49	13 to 30	13	1	0.272	0.044
15	7.0-7.49	30 to 50	12	0	0.151	-
16	7.0-7.49	50 to 100	42	0	0.114	-
17	>7.5	<8	4	1	0.487	0.271
18	>7.5	8 to 30	2	1	0.341	0.211
19	>7.5	30 to 50	4	0	0.130	-
20	>7.5	50 to 100	13	0	0.132	-
		Total	806	57	(863 total)	

[1]Each record has typically two horizontal components (accelerograms)

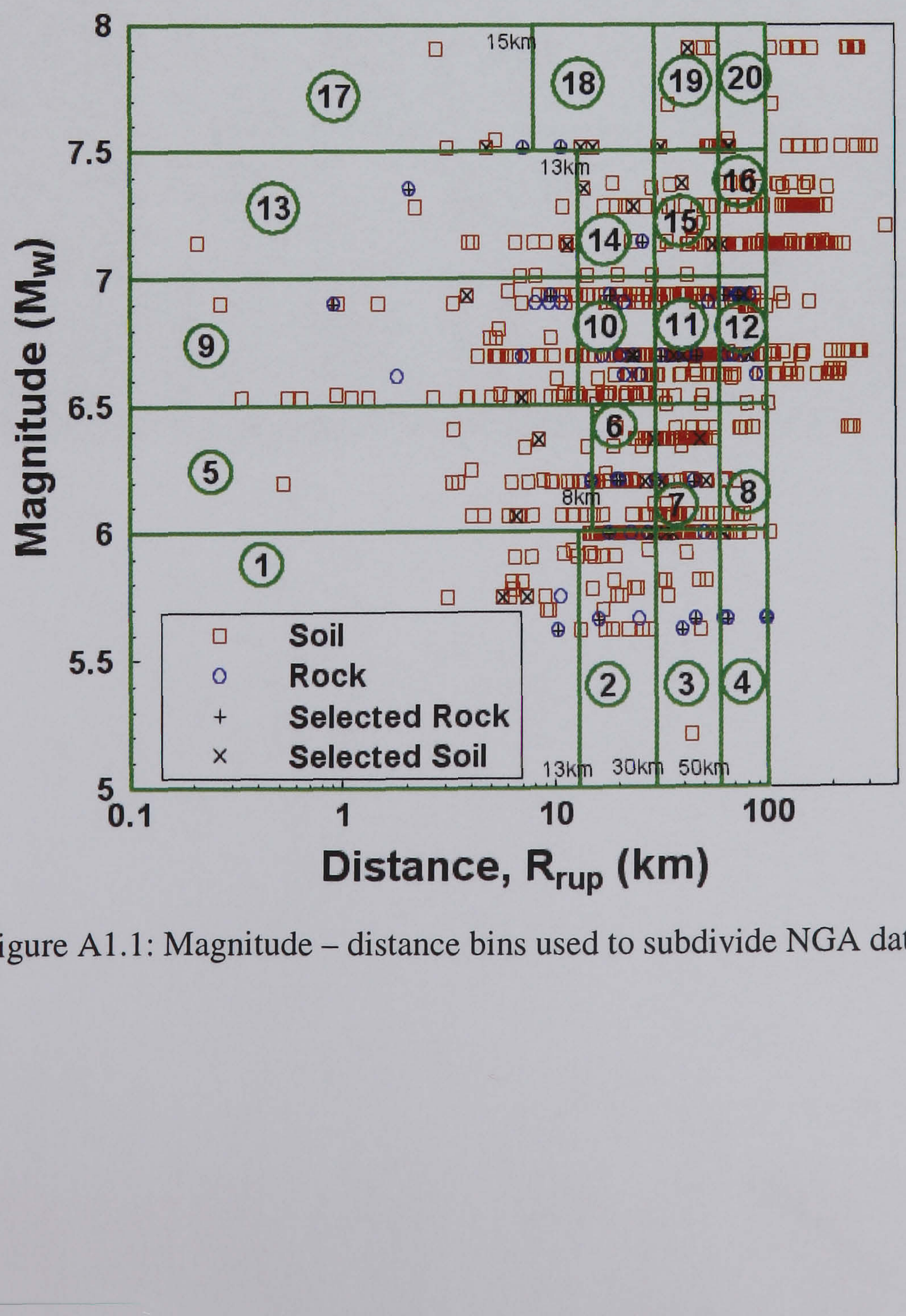


Figure A1.1: Magnitude – distance bins used to subdivide NGA data set

Table A1.2: Details of Selected Records – Rock

Bin*	Ref	Date	Mw	Earthquake	R_{rup} (km)	Station Name	Average SA (0.6 to 1.2s)	Cmpnnt
1	1645	28/06/1991	5.61	Sierra Madre	10.4	Mt Wilson – CIT Seis Sta	0.061	T
1	1645	28/06/1991	5.61	Sierra Madre	10.4	Mt Wilson – CIT Seis Sta	0.113	L
2	1740	29/06/1994	5.65	Little Skull Mtn,NV	16.1	Station#1 Lathrop Wells	0.037	L
2	680	01/10/1987	5.99	Whittier Narrows	18.1	Pasadena-CIT Kresge Lab	0.037	T
3	1649	28/06/1991	5.61	Sierra Madre	39.8	Vasquez Rocks Park	0.017	L
3	1742	29/06/1994	5.65	Little Skull Mtn,NV	45.6	Station #3-Beaty	0.009	T
4	1744	29/06/1994	5.65	Little Skull Mtn,NV	64.9	Station #5-Pahrump 1	0.011	T
4	1746	29/06/1994	5.65	Little Skull Mtn,NV	99.6	Station 7 – Las Vegas Ann Road	0.006	L
5	297	23/11/1980	6.2	Irpinia, Italy-02	14.7	Bisaccia	0.152	L
5	297	23/11/1980	6.2	Irpinia, Italy-02	14.7	Bisaccia	0.169	T
6	296	23/11/1980	6.2	Irpinia, Italy-02	19.6	Bagnoli Irpinio	0.062	T
6	303	23/11/1980	6.2	Irpinia, Italy-02	20.4	Sturno	0.058	T
7	295	23/11/1980	6.2	Irpinia, Italy-02	29.9	Auletta	0.022	T
7	476	24/04/1984	6.19	Morgan Hill	45.5	UCSC Lick Observatory	0.026	L
9	1108	16/01/1995	6.9	Kobe	0.9	Kobe University	0.439	T
9	765	18/10/1989	6.93	Loma Prieta	9.6	Gilroy Array #1	0.311	T
10	809	18/10/1989	6.93	Loma Prieta	18.5	UCSC	0.102	L
10	1091	17/01/1994	6.69	Northridge-01	23.6	Vasquez Rocks Park	0.18	L
11	1021	17/01/1994	6.69	Northridge-01	31.7	Lake Hughes #4 Camp Mend	0.094	L
11	1033	17/01/1994	6.69	Northridge-01	46.6	Littlerock – Brainard Can	0.093	T
12	804	18/10/1989	6.93	Loma Prieta	63.2	So. San Franciso, Sierra Pt.	0.088	L
12	788	18/10/1989	6.93	Loma Prieta	73.0	Piedmont Jr High	0.086	L
13	143	16/09/1978	7.35	Tabas	2.1	Tabas	1.094	L
13	143	16/09/1978	7.35	Tabas	2.1	Tabas	1.029	T
14	1613	12/11/1999	7.14	Duzce	25.9	Lamont	0.045	L
14	1613	12/11/1999	7.14	Duzce	25.9	Lamont	0.043	T
15		No records						
15		No records						
16		No records						
16		No records						
17	1165	17/08/1999	7.51	Kocaeli	7.2	Izmit	0.256	L
17	1165	17/08/1999	7.51	Kocaeli	7.2	Izmit	0.286	T
18	1161	06/08/1999	7.51	Kocaeli	10.9	Gebze	0.249	L
18	1161	06/08/1999	7.51	Kocaeli	10.9	Gebze	0.172	T

*Note the NGA database does not contain Rock records for bins 15, 16, 19 or 20.

Table A1.3: Details of Selected Records – Soil

Bin	Ref	Date	Mw	Earthquake	R_{rup} (km)	Station Name	Average SA (0.6 to 1.2s)	Component
1	149	06/08/1979	5.74	Coyote Lake	5.7	Gilroy Array #4	0.347	L
1	148	06/08/1979	5.74	Coyote Lake	7.4	Gilroy Array #3	0.354	L
2	598	01/10/1987	5.99	Whittier Narrows-01	28.5	Big Tujunga, Angeles Nat F	0.0452	L
2	685	01/10/1987	5.99	Whittier Narrows-01	29.7	Pomona – 4th Locust FF	0.0395	L
3	647	01/01/1987	5.99	Whittier Narrows-01	33.7	LB – recreation park	0.0627	L
3	693	01/01/1987	5.99	Whittier Narrows-01	35.9	Santa Monica – Second St	0.063	T
4	659	01/01/1987	5.99	Whittier Narrows-01	62.1	Malibu – W Pacific Cst Hwy	0.04	L
4	658	01/01/1987	5.99	Whittier Narrows-01	63.2	Malibu – Point Dume Sch	0.044	L
5	230	25/05/1980	6.06	Mammoth Lakes-01	6.6	Convict Creek	0.360	L
5	367	02/05/1983	6.36	Coalinga-01	8.4	Pleasant Vally P.P. – bldg	0.344	T
6	463	24/04/1984	6.19	Morgan Hill	26.4	Hollister Diff Array #1	0.176	T
6	360	02/05/1983	6.36	Coalinga-01	29.1	Parkfield – Vineyard Cany 1W	0.176	L
7	472	24/04/1984	6.19	Morgan Hill	31.9	San Justo Dam (R Abut)	0.116	L
7	355	02/05/1983	6.36	Coalinga-01	47.9	Parkfield – Gold Hill 6W	0.117	T
8	446	24/04/1984	6.19	Morgan Hill	51.7	APEEL 1E – Hayward	0.055	L
8	446	24/04/1984	6.19	Morgan Hill	51.7	APEEL 1E – Hayward	0.048	T
9	753	18/10/1989	6.93	Loma Prieta	3.9	Corralitos	0.619	L
9	179	15/10/1979	6.53	Imperial Valley-06	7.1	El Centro Array #4	0.623	L
10	988	17/01/1994	6.69	Northridge-01	23.4	LA Century City CC North	0.313	L
10	1009	17/01/1994	6.69	Northridge-01	23.6	LA Wandsworth VA hospital	0.307	T
11	990	17/01/1994	6.69	Northridge-01	36.6	LA – City Terrace	0.148	L
11	1026	17/01/1994	6.69	Northridge-01	39.9	Lawndale – Osage Ave	0.147	T
12	749	18/10/1989	6.93	Loma Prieta	78.4	Berkeley – Strawberry Canyon	0.116	L
12	972	17/01/1994	6.69	Northridge-01	82.3	Featherly Park – Maint	0.116	L
13	1787	16/10/1999	7.13	Hector	11.7	Hector	0.356	L
13	1787	16/10/1999	7.13	Hector	11.7	Hector	0.409	T
14	139	16/09/1978	7.35	Tabas	13.9	Dayhook	0.286	L
14	900	28/06/1992	7.28	Landers	23.6	Yermo Fire Station	0.287	T
15	1636	20/06/1990	7.37	Manjil, Iran	40.1	Qazvin	0.149	L
15	1636	20/06/1990	7.37	Manjil, Iran	40.1	Qazvin	0.134	T
16	1776	16/10/1999	7.13	Hector Mine	56.4	Desert Hot Springs	0.116	T
16	1816	16/10/1999	7.13	Hector Mine	61.8	North Palm Springs Fire Sta#3	0.114	T
17	1176	17/08/1999	7.51	Kocaeli, Turkey	4.8	Yarimca	0.502	L
17	1176	17/08/1999	7.51	Kocaeli, Turkey	4.8	Yarimca	0.496	T
18	1148	17/08/1999	7.51	Kocaeli, Turkey	13.5	Arcelik	0.137	L
18	1158	17/08/1999	7.51	Kocaeli, Turkey	15.4	Duzce	0.470	T
19	1162	17/08/1999	7.51	Kocaeli, Turkey	31.7	Goynuk	0.137	T
19	2111	03/11/2002	7.9	Denali, Alaska	43	R109(temp)	0.133	T
20	1157	17/08/1999	7.51	Kocaeli, Turkey	66.7	Cekmece	0.142	T
20	1154	17/08/1999	7.51	Kocaeli, Turkey	65.5	Bursa Sivil	0.136	T

Table A1.4 - Details of Selected Records – Unusual Accelerograms

Ref	Date	Mw	Earthquake	Rrup (km)	Station Name	Average SA (0.6 to 1.2s)	Component	Site Class	Notes
146	06/08/1979	5.74	Coyote Lake	10.7	Gilroy Array #1	0.103	T	Rock	Velocity pulse
568	10/10/1986	5.8	San Salvador	6.3	Geotech Investig Center	0.903	L	Stiff Soil	Large PGA, Small Magnitude
182	15/10/1979	6.53	Imperial Valley-06	0.6	El Centro Array #7	0.940	T	Soft Soil	Large PGV, low duration
1051	17/01/1994	6.69	Northridge-01	7.0	Pacoima Dam (upper left)	1.393	T	Rock	Large SA, short uniform duration
1063	17/01/1994	6.69	Northridge-01	6.5	Rinaldi Receiving Sta	1.872	L	Soft Soil	Largest SA and velocity pulse
982	17/01/1994	6.69	Northridge-01	5.4	Jensen Filter Plant	1.631	T	Stiff Soil	Large SA (peak 1.1seconds)
1121	16/01/1995	6.9	Kobe, Japan	27.8	Yae	0.500	L	Soft Soil	Long relative uniform and significant duration and high SA
1104	16/01/1995	6.9	Kobe, Japan	17.9	Fukushima	0.711	L	Soft Soil	Largest bracketed duration
732	18/10/1989	6.93	Loma Prieta	43.2	APEEL 2 - Redwood City	0.888	L	V. Soft Soil	V soft soil and peak SA at about 1.0s.
808	18/10/1989	6.93	Loma Prieta	77.4	Treasure Island	0.379	T	V. Soft Soil	V soft soil and peak SA at about 0.6s.
779	18/10/1989	6.93	Loma Prieta	3.9	LGPC	1.487	L	Stiff Soil	Large SA
1171	17/08/1999	7.51	Kocaeli, Turkey	3.1	Sakarya	0.375	T	Stiff Soil	Large Mag and Velocity pulse
1148	17/08/1999	7.51	Kocaeli, Turkey	13.5	Arcelik	0.148	T	Stiff Soil	Large Magnitude
1158	17/08/1999	7.51	Kocaeli, Turkey	15.4	Duzce	0.470	L	Soft Soil	Large Magnitude
1166	17/08/1999	7.51	Kocaeli, Turkey	30.7	Iznik	0.319	T	Soft Soil	Large Magnitude
1162	17/08/1999	7.51	Kocaeli, Turkey	31.7	Goynuk	0.137	L	Stiff Soil	Large Magnitude
1160	17/08/1999	7.51	Kocaeli, Turkey	55.5	Fatih	0.129	T	Soft Soil	Odd displacement pulse
1160	17/08/1999	7.51	Kocaeli, Turkey	55.5	Fatih	0.239	L	Soft Soil	Odd displacement pulse
1147	17/08/1999	7.51	Kocaeli, Turkey	69.6	Ambarli	0.582	T	V. Soft Soil	V soft soil (and displacement pulse)
1628	28/02/1979	7.54	St Elias, Alaska	5.3	Icy Bay	0.319	T	Soft Soil	Large Mag and long-period motion
1626	30/07/1972	7.68	Sitka, Alaska	34.6	Sitka Observatory	0.063	T	Stiff Soil	Large Mag and Velocity pulse
2114	03/11/2002	7.9	Denali, Alaska	2.8	TAPS Pump Station #10	0.917	L	Soft Soil	Large Magnitude
2111	03/11/2002	7.9	Denali, Alaska	43	R109 (temp)	0.064	L	Soft Soil	Large Magnitude

Table A1.5: Details of Selected Records – Particularly Strong Motions

Ref	Date	Mw	Earthquake	Rrup	Station Name	SA (0.6 to 1.2s)	Cmpnt	Site Class
1106	16/01/1995	6.90	Kobe, Japan	0.96	KJMA	1.596	T	Soft Soil
1120	16/01/1995	6.90	Kobe, Japan	1.47	Takatori	1.488	T	Soft Soil
1084	17/01/1994	6.69	Northridge-01	5.35	Sylmar – Conv. Sta	1.479	T	Soft Soil
1044	17/01/1994	6.69	Northridge-01	5.92	Newhall - Fire Sta	1.469	T	Soft Soil
1054	17/01/1994	6.69	Northridge-01	7.46	Pardee – SCE	1.460	T	Soft Soil
1087	17/01/1994	6.69	Northridge-01	15.6	Tarzana-Cedar HillA	1.338	T	Soft Soil
1004	17/01/1994	6.69	Northridge-01	8.44	LA - Sepulveda VA Hospital	1.337	T	Stiff Soil
451	24/04/1984	6.19	Morgan Hill	0.53	Coyote Lake Dam (SW Abut)	1.312	T	Stiff Soil
828	25/04/1992	7.01	Cape Mendocino	8.18	Petrolia	1.265	T	Stiff Soil
1602	12/11/1999	7.14	Duzce, Turkey	12.04	Bolu	1.169	T	Soft Soil
983	17/01/1994	6.69	Northridge-01	5.43	Jensen Filter Plant Generator	1.146	T	Stiff Soil
569	10/10/1986	5.80	San Salvador	6.99	National Geografical Inst	1.144	T	Soft Soil
1119	16/01/1995	6.90	Kobe, Japan	0.27	Takarazuka	1.100	T	Soft Soil
1085	17/01/1994	6.69	Northridge-01	5.19	Sylmar - Converter Sta East	1.099	T	Stiff Soil
77	09/02/1971	6.61	San Fernando	1.81	Pacoima Dam (upper left abut)	1.040	T	Rock
1086	17/01/1994	6.69	Northridge-01	5.3	Sylmar - Olive View Med FF	1.035	T	Stiff Soil
953	17/01/1994	6.69	Northridge-01	17.15	Beverly Hills - 14145 Mulhol	1.018	T	Soft Soil
723	24/11/1987	6.54	Superstition Hills-02	0.95	Parachute Test Site	0.985	T	Soft Soil
776	18/10/1989	6.93	Loma Prieta	27.93	Hollister - South and Pine	0.948	T	Stiff Soil
963	17/01/1994	6.69	Northridge-01	20.72	Castaic - Old Ridge Route	0.947	T	Stiff Soil
368	02/05/1983	6.36	Coalinga-01	8.41	Pleasant Valley P.P. – yard	0.942	T	Soft Soil
1080	17/01/1994	6.69	Northridge-01	13.42	Simi Valley - Katherine Rd	0.920	T	Stiff Soil
1605	12/11/1999	7.14	Duzce, Turkey	6.58	Duzce	0.914	T	Soft Soil
126	17/05/1976	6.80	Gazli, USSR	5.46	Karakyr	0.906	T	Stiff Soil
1048	17/01/1994	6.69	Northridge-01	12.09	Northridge - 17645 Saticoy St	0.899	T	Soft Soil
741	18/10/1989	6.93	Loma Prieta	10.72	BRAN	0.893	T	Stiff Soil
558	21/07/1986	6.19	Chalfant Valley-02	7.58	Zack Brothers Ranch	0.881	T	Soft Soil
825	25/04/1992	7.01	Cape Mendocino	6.96	Cape Mendocino	0.878	T	Stiff Soil
1045	17/01/1994	6.69	Northridge-01	5.48	Newhall - W Pico Canyon Rd.	0.831	T	Soft Soil
727	24/11/1987	6.54	Superstition Hills-02	5.61	Superstition Mtn Camera	0.812	T	Stiff Soil
160	15/10/1979	6.53	Imperial Valley-06	2.68	Bonds Corner	0.808	T	Soft Soil
529	08/07/1986	6.06	N. Palm Springs	4.04	North Palm Springs	0.804	T	Soft Soil
29	28/06/1966	6.19	Parkfield	6.28	Cholame - Shandon Array #2	0.795	T	Soft Soil
821	13/03/1992	6.69	Erzican, Turkey	4.38	Erzincan	0.794	T	Soft Soil

Table A1.5 (continued): Details of Selected Records – Particularly Strong Motions

Ref	Date	Mw	Earthquake	Rrup	Station Name	SA (0.6 to 1.2s)	Cmpnt	Site Class
1101	16/01/1995	6.90	Kobe, Japan	11.34	Amagasaki	0.784	T	Soft Soil
1013	17/01/1994	6.69	Northridge-01	5.92	LA Dam	0.773	T	Stiff Soil
338	02/05/1983	6.36	Coalinga-01	29.48	Parkfield - Fault Zone 14	0.771	T	Soft Soil
1114	16/01/1995	6.90	Kobe, Japan	3.31	Port Island (0 m)	0.766	T	Soft Soil
319	26/04/1981	5.90	Westmorland	6.5	Westmorland Fire Sta	0.743	T	Soft Soil
960	17/01/1994	6.69	Northridge-01	12.44	Canyon Country - W Lost Cany	0.737	T	Soft Soil
759	18/10/1989	6.93	Loma Prieta	43.94	Foster City - APEEL 1	0.731	T	V. Soft Soil
1052	17/01/1994	6.69	Northridge-01	7.26	Pacoima Kagel Canyon	0.709	T	Stiff Soil
1082	17/01/1994	6.69	Northridge-01	10.05	Sun Valley - Roscoe Blvd	0.707	T	Soft Soil

APPENDIX 2. SELECTION OF NUMERICAL INTEGRATION SCHEME

Initial analysis is conducted to investigate the optimum numerical integration scheme to be used in the analysis of the 2D reinforced concrete frames. Two options are available for use in the SesimoStruct FEA package:

- Hilber-Hughes-Taylor (HHT) integration method, Hilber *et al.* (1977) and Hughes (1983)
- Newmark integration method, Newmark (1959)

The 8-storey three-bay dual wall frame building, described in Chapter 7, is analysed under the action of the longitudinal component of the ground motion from the 1978 (M_w 7.35) Tabas earthquake recorded 1.79km from the surface projection of the fault rupture at Tabas. Both numerical integration schemes are employed and the default integration coefficients for each method are used (Table A2.1). The lateral displacement at the roof of the structure and the response of the non-linear spring used to represent the shear deformation of the beam-wall connection at the top of the structure are used to compare the suitability of each methods (Figures A2.1 and A2.2).

Table A2.1 – Coefficients used for Numerical integration schemes

Integration Scheme	Alpha	Beta	Gamma
Newmark	N.A.	0.25	0.5
HHT	-0.1	0.3025	0.6

Although the maximum predicted lateral deformation of the structure is within 4% for both integration schemes, significant differences exist between the predicted joint hysteretic responses. Further investigation of the joint response shows that the HHT integration provides numerical damping to the solution preventing spurious higher modes from dominating the response later in the time-series (Figures A2.3 and A2.4). This finding is consistent with that of Broderick *et al.* (1994), who conducted a more detailed investigation of the two numerical integration schemes. The HHT integration scheme is employed for the analysis of multi-degree-of-freedom (MDOF) systems presented in this thesis.

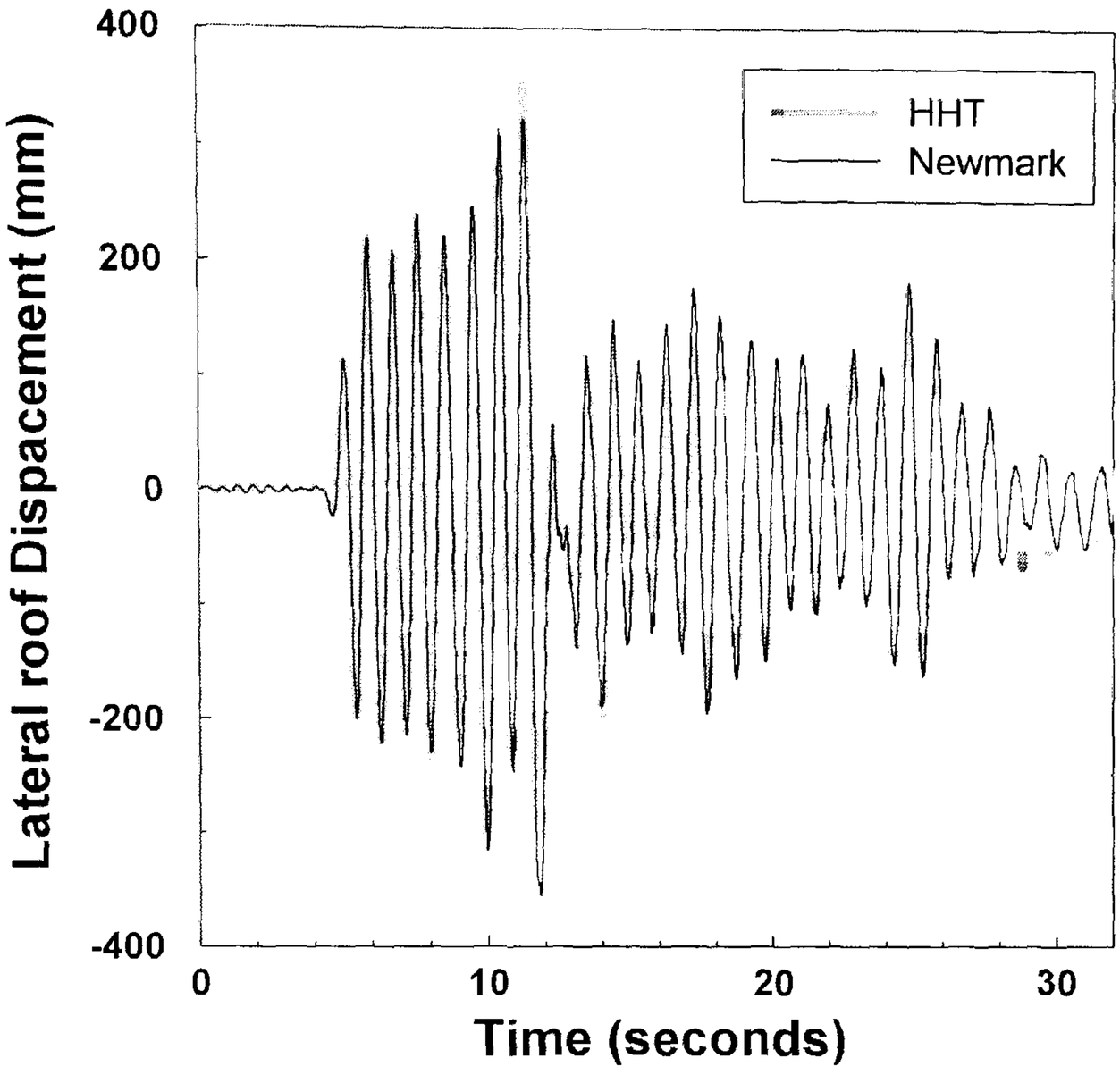


Figure A2.1 – Lateral roof drift estimated using Newmark and HHT numerical integration schemes.

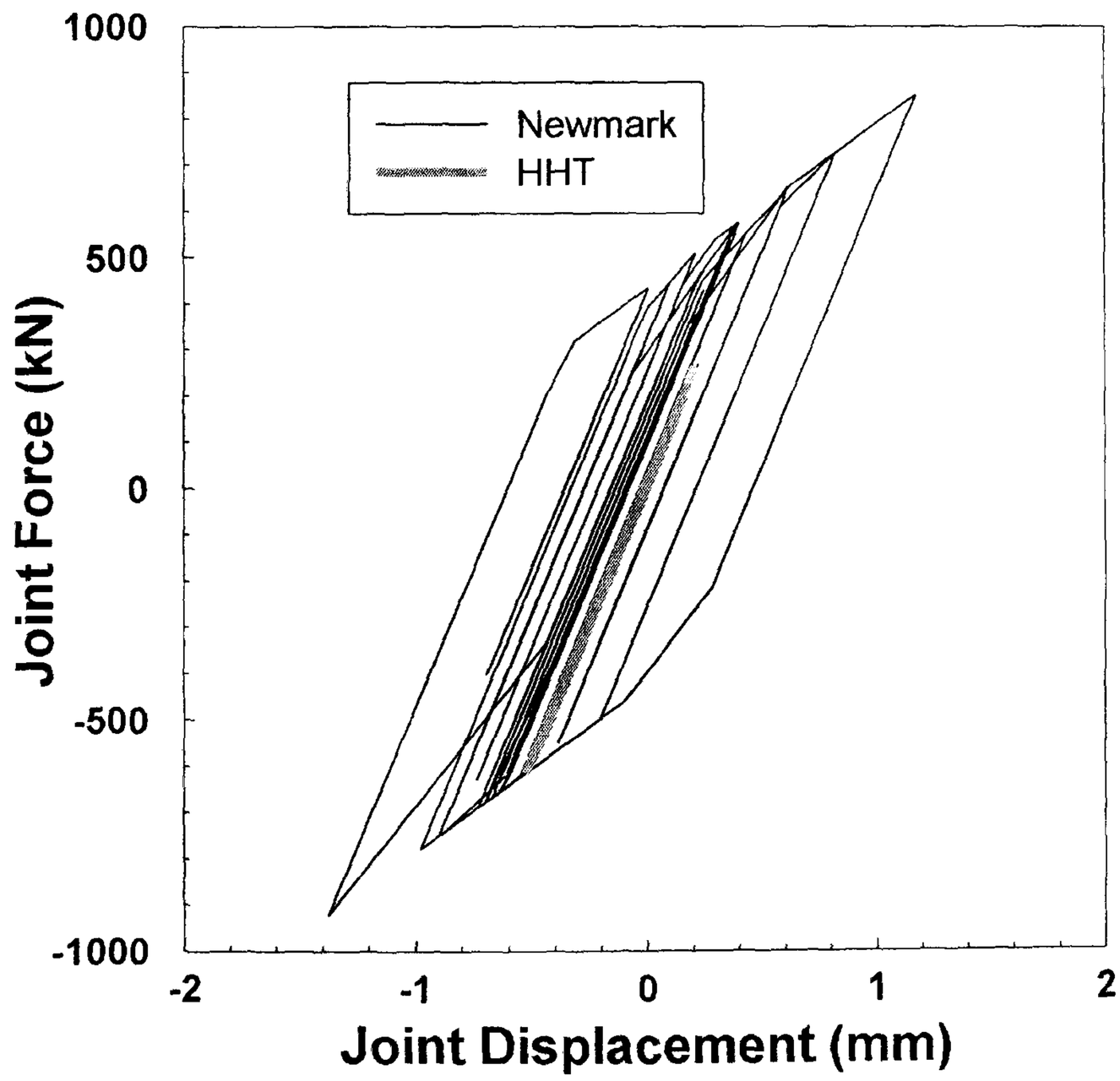


Figure A2.2 – Joint shear response estimated using Newmark and HHT numerical integration schemes.

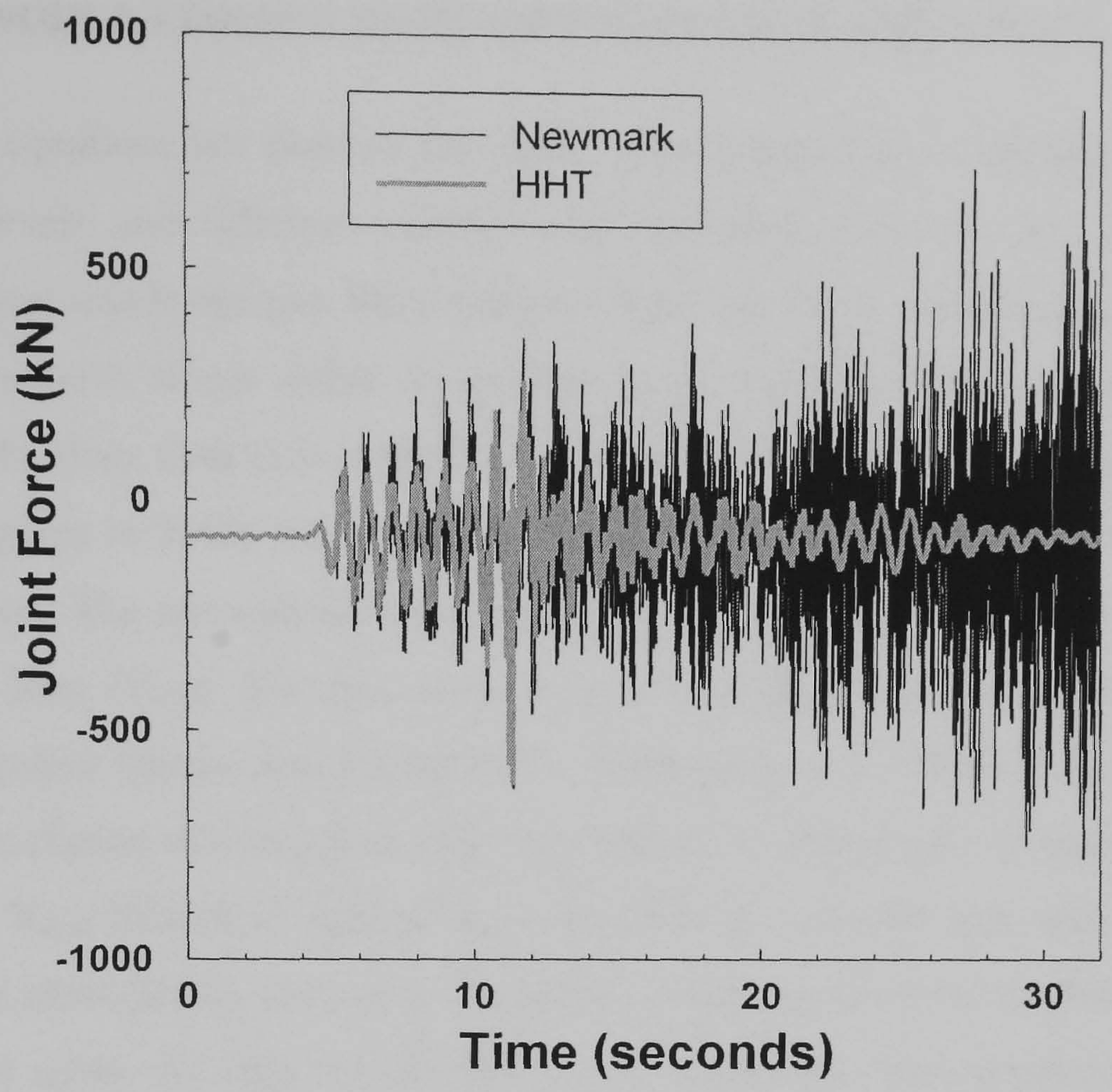


Figure A2.3 - Joint shear force predicted using Newmark and HHT numerical integration schemes.

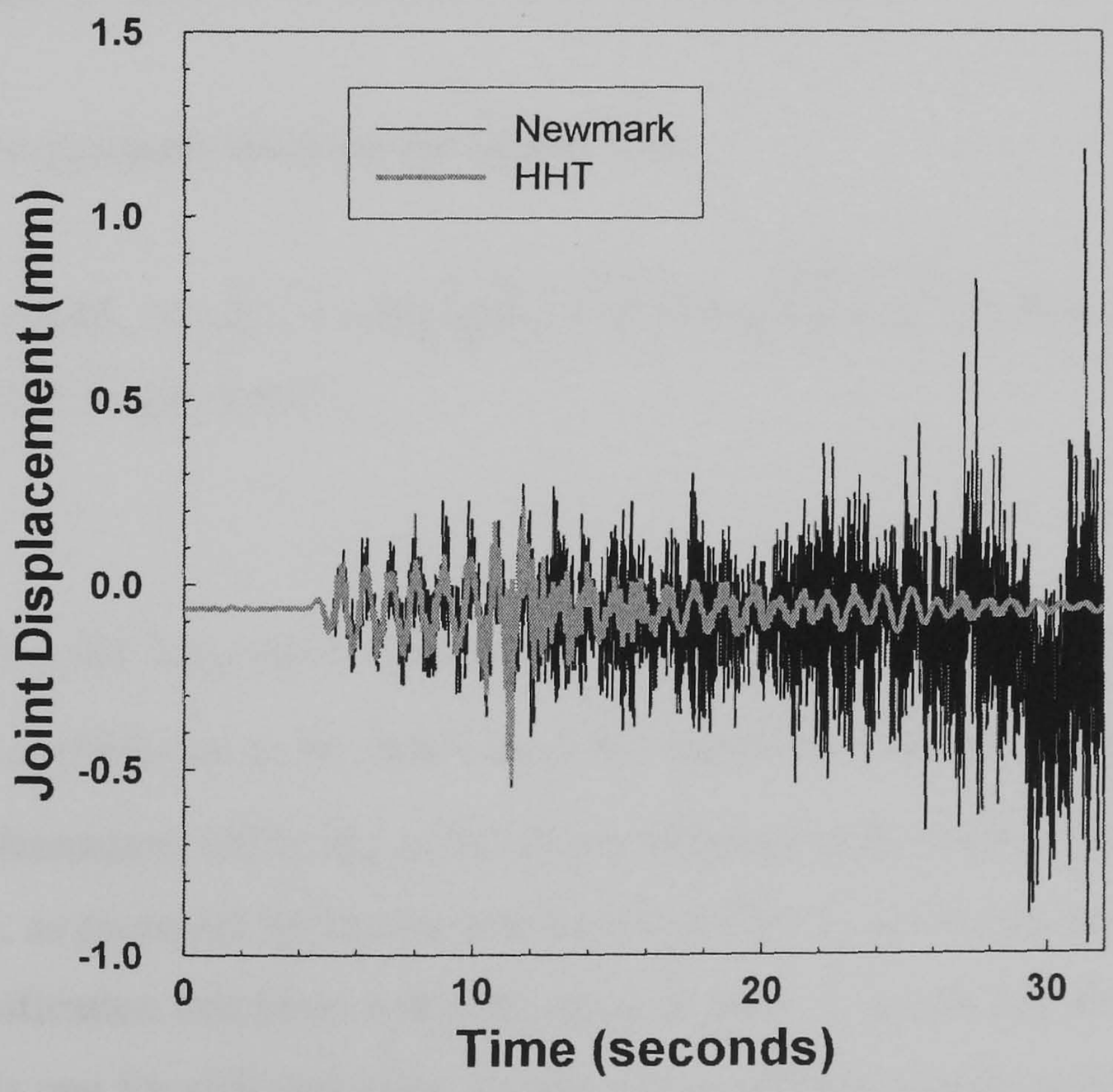


Figure A2.4 - Joint shear deformation predicted using Newmark and HHT numerical integration schemes.

APPENDIX 3, COEFFICIENTS OF PREDICTIVE EQUATIONS

Predictive equations are derived for elastic pseudo-spectral acceleration at multiple damping levels and different measures of structural response. All equations are derived using accelerograms from subset 1 from the NGA database (Appendix A1) excluding records where either component has a high-pass filter frequency greater than 0.33Hz (less than 0.3s period). The magnitude – distance distribution of the dataset is given in Table 8.1 and Figure 8.1 for earthquake style-of-faulting and site classification. The site classification is based on the average shear wave velocity in the upper 30m (V_{s30}). For this work V_{s30} is converted into the widely used four category system (Boore and Joyner 1993; Ambraseys *et al.* 1996). Sites with V_{s30} > 760m/s are classed as rock; sites with V_{s30} 360m/s to 760m/s are classed as stiff soil; sites with V_{s30} 360m/s to 180m/s are classified as soft soil and sites with V_{s30} < 180m/s are classified as very soft. The style-of-faulting used for the NGA dataset is determined using the rake angle (Table 8.2). Residuals from predictive equations developed in this work show that earthquakes with reverse-oblique mechanism have similar trends as those from earthquakes with reverse mechanism, so records from reverse-oblique events are included with the reverse records.

All predictive equations have the functional form:

$$\log(y) = r_1 + r_2 M_w + r_3 M_w^2 + r_4 \log\left(\sqrt{R_{jb}^2 + r_6^2}\right) + r_5 \sqrt{R_{jb}^2 + r_6^2} + r_7 S_1 + r_8 S_2 + r_9 F_1 + r_{10} F_2 \pm \sigma_t P \qquad \text{(A3.1)}$$

where *log(y)* is the $\log_{10}$ of the parameter to be regressed; $r_1, r_2, r_3, r_4, r_5, r_6, r_7, r_8, r_9$ and r_{10} are coefficients to be determined by regression; M_w is moment magnitude (Hanks and Kanamori 1979); R_{jb} is the closest distance to the surface projection of the fault rupture, as proposed by Joyner and Boore (1981); S_1 and S_2 are dummy variables for site classification that have a default value of zero; S_1 equals one for soft soil sites and S_2 equals one for stiff soil sites; F_1 and F_2 are dummy variables that for style-of-faulting that have a default of zero; F_1 equals one for normal (rake between -120 and -60 degrees) and F_2 equals one for reverse events (rake between 120 and 60 degrees);

to reduce the number of coefficients required to describe the style-of-faulting, reverse-oblique events (rake between 30 and 60 or 120 and 150 degrees) are included as reverse faults. P equals 0 for median and 1 for 84-percentile levels considering log normal distribution of the residuals with standard deviation σ_t. The standard deviation is comprised of two components, the standard deviation from the site-to-site variability σ_s and the standard deviation from the earthquake-to-earthquake variability σ_e:

$$\sigma_t = \sqrt{\sigma_s^2 + \sigma_e^2} \tag{A3.2}$$

A range of different damage measures are calculated based on the member end rotation. The members are identified by storey and column and beam reference numbers (Figure A3.1). The top and bottom of each column is deliminated with the subscript "*t*" and "*b*" respectively. The right and left ends of the beams are identified with the subscript "*r*" and "*l*" respectively.

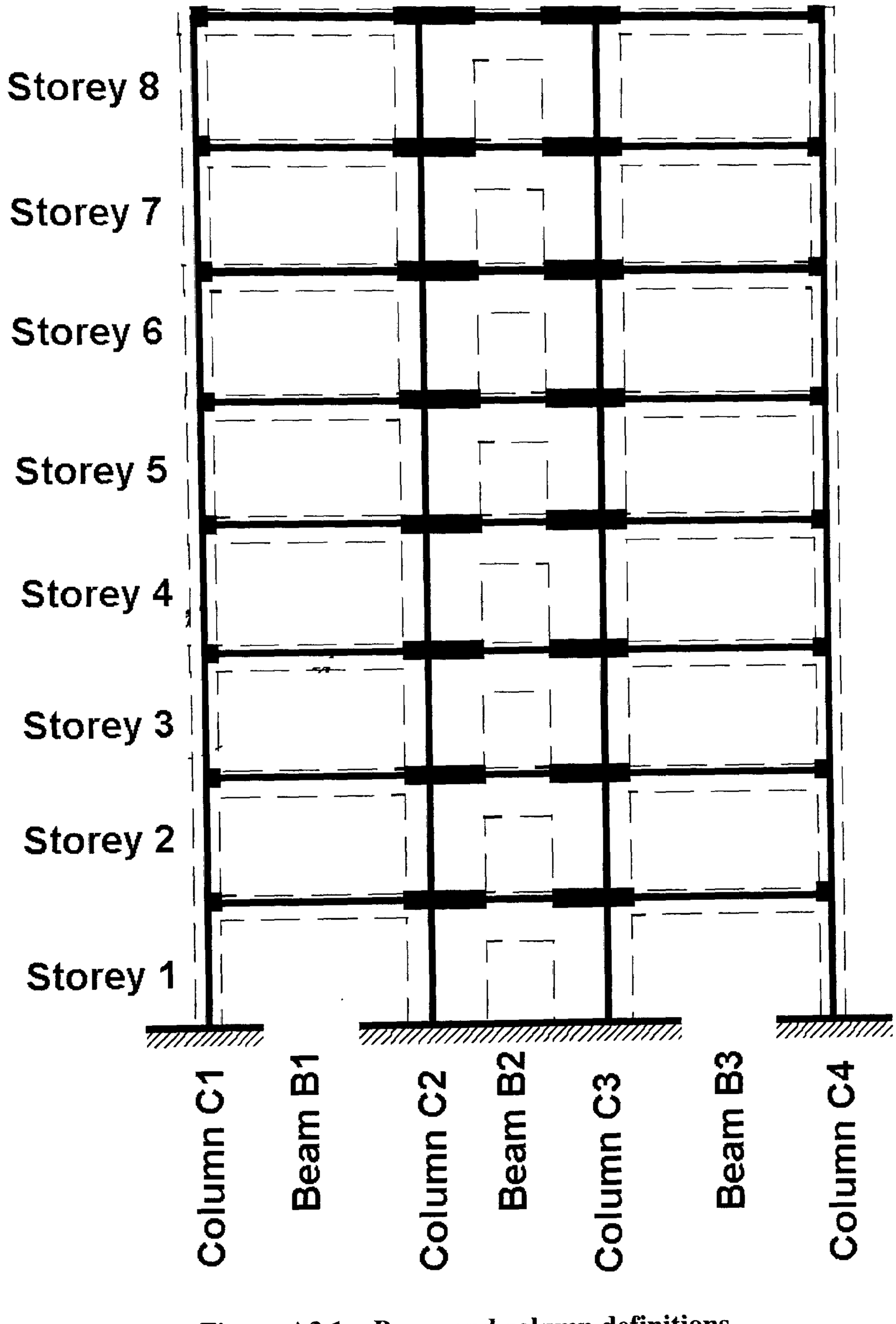


Figure A3.1 – Beam and column definitions

Table A3.1 - Coefficients of the equation derived to predict pseudo spectral acceleration at 1% damping

	Predictive Equation Coefficients										Standard Deviations	
Period (s)	r1	r2	r3	r4	r5	r6	r7	r8	r9	r10	σ_e	σ_s
0	-0.945	0.156	0.000	-0.749	-0.001	5.466	0.164	0.066	-0.157	0.058	0.087	0.207
0.05	-1.702	0.513	-0.029	-0.823	-0.001	6.008	0.110	0.046	-0.217	0.035	0.126	0.219
0.055	-0.397	0.139	0.000	-0.866	-0.002	6.774	0.091	0.029	-0.232	0.028	0.099	0.223
0.06	-0.312	0.133	0.000	-0.865	-0.002	6.972	0.074	0.017	-0.248	0.041	0.110	0.225
0.065	-0.915	0.313	-0.014	-0.814	-0.002	6.684	0.060	0.012	-0.271	0.019	0.125	0.222
0.07	-1.681	0.536	-0.030	-0.784	-0.002	6.738	0.058	0.011	-0.276	0.020	0.125	0.223
0.075	-0.405	0.129	0.000	-0.699	-0.003	5.376	0.073	0.023	-0.257	0.010	0.114	0.225
0.08	-0.413	0.131	0.000	-0.665	-0.003	5.666	0.062	0.012	-0.253	0.007	0.117	0.225
0.085	-0.139	0.102	0.000	-0.697	-0.003	5.720	0.039	-0.001	-0.291	0.025	0.113	0.225
0.09	-0.243	0.135	0.000	-0.772	-0.003	7.482	0.069	0.031	-0.258	0.007	0.125	0.227
0.095	-0.206	0.123	0.000	-0.736	-0.003	7.378	0.073	0.036	-0.230	0.019	0.123	0.227
0.1	-0.273	0.118	0.000	-0.663	-0.003	5.647	0.078	0.040	-0.231	0.037	0.221	0.225
0.11	-0.266	0.140	0.000	-0.725	-0.003	7.661	0.073	0.032	-0.235	0.008	0.119	0.232
0.12	-0.412	0.154	0.000	-0.678	-0.003	7.094	0.082	0.028	-0.217	0.015	0.130	0.231
0.13	-1.621	0.554	-0.030	-0.751	-0.003	8.468	0.097	0.030	-0.231	0.013	0.131	0.230
0.14	-0.348	0.157	0.000	-0.707	-0.003	8.605	0.106	0.045	-0.202	0.011	0.126	0.230
0.15	-0.251	0.142	0.000	-0.668	-0.003	7.405	0.067	0.007	-0.251	-0.010	0.123	0.228
0.16	-0.857	0.302	-0.010	-0.693	-0.003	8.168	0.111	0.052	-0.225	0.004	0.122	0.231
0.17	-0.427	0.169	0.000	-0.693	-0.003	8.358	0.117	0.050	-0.225	0.031	0.121	0.236
0.18	-1.398	0.462	-0.022	-0.689	-0.003	8.613	0.118	0.044	-0.212	0.025	0.111	0.235
0.19	-0.495	0.181	0.000	-0.698	-0.003	8.550	0.109	0.038	-0.188	0.042	0.103	0.239
0.2	-0.498	0.182	0.000	-0.690	-0.002	8.164	0.094	0.032	-0.200	0.032	0.105	0.239
0.22	-0.777	0.246	-0.006	-0.656	-0.002	7.731	0.151	0.082	-0.187	0.022	0.110	0.241
0.24	-0.452	0.191	0.000	-0.798	-0.002	9.371	0.144	0.068	-0.183	0.011	0.104	0.233
0.26	-0.657	0.188	0.000	-0.678	-0.002	6.828	0.176	0.089	-0.163	0.038	0.106	0.234
0.28	-0.749	0.183	0.000	-0.609	-0.002	5.382	0.207	0.095	-0.140	0.047	0.097	0.239
0.3	-1.376	0.372	-0.016	-0.560	-0.002	4.338	0.199	0.074	-0.168	0.040	0.111	0.244
0.32	-2.796	0.791	-0.046	-0.595	-0.002	4.813	0.220	0.091	-0.175	0.042	0.125	0.247
0.34	-2.922	0.849	-0.050	-0.670	-0.001	5.180	0.206	0.071	-0.139	0.042	0.108	0.240
0.36	-0.806	0.200	0.000	-0.724	-0.001	6.112	0.235	0.104	-0.108	0.039	0.115	0.240
0.38	-3.771	1.064	-0.063	-0.678	-0.001	5.703	0.207	0.078	-0.118	0.030	0.119	0.248
0.4	-3.810	1.051	-0.062	-0.625	-0.002	4.656	0.212	0.077	-0.117	0.009	0.133	0.242
0.42	-4.815	1.370	-0.087	-0.662	-0.001	5.200	0.227	0.081	-0.148	0.004	0.145	0.240
0.44	-5.138	1.466	-0.093	-0.697	-0.001	5.630	0.222	0.084	-0.154	0.014	0.141	0.241
0.46	-4.869	1.354	-0.085	-0.662	-0.001	4.978	0.251	0.109	-0.113	0.003	0.145	0.240
0.48	-4.658	1.302	-0.081	-0.695	-0.001	5.341	0.264	0.115	-0.105	0.010	0.144	0.243
0.5	-4.735	1.335	-0.084	-0.735	-0.001	5.960	0.268	0.125	-0.095	0.042	0.141	0.250
0.55	-5.269	1.464	-0.094	-0.687	-0.001	4.986	0.291	0.131	-0.061	0.031	0.151	0.255
0.6	-6.067	1.685	-0.112	-0.654	-0.001	4.440	0.320	0.158	-0.096	0.030	0.161	0.244
0.65	-5.294	1.457	-0.095	-0.681	0.000	3.938	0.302	0.138	-0.096	0.037	0.175	0.255
0.7	-5.007	1.346	-0.086	-0.687	0.000	3.564	0.345	0.181	-0.104	0.061	0.180	0.265
0.75	-4.218	1.088	-0.067	-0.677	0.000	3.061	0.376	0.217	-0.086	0.058	0.175	0.260
0.8	-4.492	1.143	-0.070	-0.654	0.000	2.969	0.338	0.170	-0.045	0.058	0.164	0.256
0.85	-5.008	1.287	-0.080	-0.651	0.000	2.813	0.305	0.133	-0.049	0.055	0.164	0.264

Table A3.1 (Continued) - Coefficients of the equation derived to predict pseudo spectral acceleration at 1% damping

	Predictive Equation Coefficients										Standard Deviations	
Period (s)	r1	r2	r3	r4	r5	r6	r7	r8	r9	r10	σ_e	σ_s
0.9	-6.243	1.629	-0.103	-0.667	0.000	3.166	0.297	0.120	-0.040	0.071	0.167	0.268
0.95	-6.892	1.823	-0.117	-0.657	0.000	3.212	0.278	0.091	-0.038	0.064	0.133	0.271
1	-6.724	1.764	-0.112	-0.670	0.000	3.857	0.294	0.111	-0.032	0.048	0.161	0.268
1.1	-8.935	2.428	-0.165	-0.650	0.000	3.529	0.341	0.140	-0.064	0.044	0.184	0.267
1.2	-9.750	2.645	-0.178	-0.668	0.000	3.219	0.326	0.125	-0.056	0.026	0.170	0.274
1.3	-9.981	2.698	-0.182	-0.658	0.000	3.054	0.313	0.105	-0.061	0.022	0.172	0.265
1.4	-9.768	2.601	-0.173	-0.660	0.000	3.051	0.321	0.113	-0.052	0.016	0.181	0.262
1.5	-9.236	2.416	-0.158	-0.689	0.000	3.481	0.344	0.136	-0.046	0.005	0.166	0.261
1.6	-9.593	2.494	-0.162	-0.692	0.000	3.685	0.352	0.144	-0.022	0.001	0.152	0.264
1.7	-10.744	2.800	-0.184	-0.665	0.000	3.207	0.378	0.167	0.003	-0.010	0.157	0.274
1.8	-10.443	2.686	-0.176	-0.628	0.000	2.595	0.378	0.167	-0.001	-0.011	0.166	0.276
1.9	-10.873	2.808	-0.186	-0.625	0.000	2.281	0.385	0.169	-0.011	-0.014	0.160	0.276
2	-11.422	2.940	-0.194	-0.613	0.000	2.053	0.375	0.165	-0.027	-0.032	0.159	0.277
2.1	-11.060	2.822	-0.185	-0.602	0.000	1.987	0.354	0.142	-0.053	-0.029	0.159	0.281
2.2	-10.662	2.696	-0.176	-0.598	0.000	2.017	0.346	0.141	-0.041	-0.030	0.167	0.282
2.3	-10.250	2.561	-0.166	-0.581	0.000	1.960	0.346	0.153	-0.049	-0.037	0.187	0.282
2.4	-10.979	2.775	-0.182	-0.586	0.000	1.992	0.359	0.171	-0.052	-0.032	0.187	0.283
2.5	-11.117	2.795	-0.183	-0.592	0.000	2.100	0.364	0.180	-0.067	-0.028	0.188	0.283

Table A3.2 – Coefficients of the equation derived to predict pseudo spectral acceleration at 5% damping

	Predictive Equation Coefficients										Standard Deviations	
Period (s)	r1	r2	r3	r4	r5	r6	r7	r8	r9	r10	σ_e	σ_s
0	-2.097	0.510	-0.027	-0.744	-0.001	5.496	0.164	0.067	-0.162	0.046	0.105	0.206
0.05	-2.146	0.588	-0.034	-0.777	-0.001	5.493	0.127	0.047	-0.192	0.046	0.109	0.210
0.055	-1.749	0.474	-0.025	-0.792	-0.001	5.784	0.132	0.056	-0.194	0.044	0.107	0.211
0.06	-1.509	0.412	-0.021	-0.783	-0.001	5.754	0.118	0.045	-0.211	0.047	0.105	0.213
0.065	-1.548	0.430	-0.022	-0.772	-0.002	5.834	0.112	0.045	-0.219	0.039	0.108	0.212
0.07	-1.417	0.392	-0.019	-0.771	-0.002	6.001	0.113	0.048	-0.211	0.033	0.105	0.211
0.075	-1.243	0.349	-0.016	-0.780	-0.002	6.391	0.105	0.042	-0.205	0.033	0.101	0.212
0.08	-0.898	0.245	-0.008	-0.762	-0.002	6.305	0.108	0.044	-0.212	0.031	0.100	0.213
0.085	-0.798	0.227	-0.007	-0.777	-0.002	6.568	0.103	0.045	-0.217	0.030	0.098	0.213
0.09	-0.683	0.193	-0.004	-0.769	-0.002	6.616	0.108	0.048	-0.209	0.029	0.101	0.213
0.095	-0.276	0.103	0.000	-0.757	-0.002	6.531	0.111	0.053	-0.203	0.028	0.105	0.213
0.1	-0.444	0.127	0.000	-0.733	-0.002	6.302	0.105	0.046	-0.196	0.025	0.102	0.216
0.11	-0.482	0.142	0.000	-0.755	-0.002	7.113	0.102	0.040	-0.199	0.027	0.101	0.219
0.12	-0.510	0.149	0.000	-0.749	-0.002	7.127	0.106	0.034	-0.204	0.031	0.106	0.221
0.13	-1.305	0.399	-0.018	-0.769	-0.002	7.701	0.112	0.038	-0.202	0.029	0.109	0.219
0.14	-0.689	0.231	-0.006	-0.779	-0.002	8.053	0.113	0.035	-0.199	0.034	0.108	0.217
0.15	-0.474	0.171	-0.003	-0.756	-0.002	7.500	0.109	0.033	-0.222	0.025	0.110	0.218
0.16	-0.810	0.258	-0.009	-0.730	-0.002	7.351	0.110	0.035	-0.219	0.026	0.106	0.220
0.17	-1.217	0.368	-0.016	-0.724	-0.002	7.486	0.125	0.046	-0.204	0.036	0.106	0.223

Table A3.2 (Continued) – Coefficients of the equation derived to predict pseudo spectral acceleration at 5% damping

	Predictive Equation Coefficients										Standard Deviations	
Period (s)	r1	r2	r3	r4	r5	r6	r7	r8	r9	r10	σ_e	σ_s
0.18	-1.631	0.490	-0.025	-0.731	-0.002	7.752	0.122	0.042	-0.194	0.040	0.104	0.225
0.19	-0.875	0.265	-0.008	-0.725	-0.002	7.890	0.119	0.042	-0.194	0.037	0.106	0.227
0.2	-0.989	0.297	-0.011	-0.728	-0.002	7.764	0.121	0.045	-0.190	0.026	0.107	0.227
0.22	-0.889	0.262	-0.008	-0.734	-0.002	7.838	0.168	0.086	-0.178	0.025	0.106	0.225
0.24	-0.763	0.222	-0.005	-0.748	-0.002	7.485	0.176	0.088	-0.170	0.028	0.106	0.222
0.26	-0.900	0.236	-0.006	-0.699	-0.002	6.216	0.184	0.084	-0.159	0.043	0.106	0.225
0.28	-0.953	0.223	-0.005	-0.647	-0.002	5.071	0.188	0.074	-0.164	0.048	0.104	0.230
0.3	-1.485	0.381	-0.017	-0.630	-0.002	4.737	0.184	0.066	-0.171	0.043	0.109	0.234
0.32	-1.990	0.523	-0.027	-0.640	-0.002	4.662	0.199	0.071	-0.178	0.048	0.116	0.237
0.34	-2.248	0.598	-0.032	-0.665	-0.002	4.839	0.203	0.064	-0.162	0.042	0.117	0.236
0.36	-2.642	0.704	-0.039	-0.685	-0.001	5.061	0.216	0.077	-0.127	0.039	0.121	0.237
0.38	-3.408	0.932	-0.056	-0.693	-0.001	5.138	0.207	0.071	-0.140	0.021	0.130	0.240
0.4	-3.859	1.053	-0.064	-0.694	-0.001	5.021	0.217	0.080	-0.143	0.018	0.136	0.238
0.42	-4.364	1.199	-0.075	-0.685	-0.001	4.866	0.222	0.084	-0.151	0.018	0.141	0.237
0.44	-4.837	1.336	-0.085	-0.702	-0.001	5.056	0.229	0.092	-0.145	0.019	0.144	0.238
0.46	-4.782	1.319	-0.084	-0.720	-0.001	5.154	0.240	0.100	-0.133	0.019	0.147	0.239
0.48	-4.783	1.322	-0.085	-0.733	-0.001	5.175	0.256	0.111	-0.128	0.026	0.148	0.240
0.5	-5.029	1.397	-0.090	-0.762	-0.001	5.443	0.261	0.114	-0.124	0.035	0.150	0.243
0.55	-4.961	1.347	-0.087	-0.724	-0.001	4.887	0.286	0.125	-0.088	0.047	0.160	0.246
0.6	-4.958	1.343	-0.088	-0.722	0.000	4.208	0.309	0.139	-0.095	0.049	0.165	0.247
0.65	-4.949	1.321	-0.085	-0.729	0.000	3.990	0.310	0.142	-0.105	0.055	0.176	0.251
0.7	-4.437	1.141	-0.071	-0.724	0.000	3.531	0.326	0.164	-0.097	0.061	0.180	0.256
0.75	-3.990	0.991	-0.060	-0.718	0.000	3.239	0.336	0.165	-0.093	0.064	0.176	0.257
0.8	-4.643	1.172	-0.073	-0.703	0.000	3.077	0.314	0.143	-0.082	0.062	0.173	0.257
0.85	-5.414	1.387	-0.088	-0.702	0.000	3.002	0.292	0.117	-0.076	0.058	0.171	0.259
0.9	-6.170	1.603	-0.103	-0.703	0.000	3.177	0.282	0.107	-0.079	0.063	0.174	0.260
0.95	-6.419	1.666	-0.107	-0.699	0.000	3.294	0.276	0.099	-0.076	0.064	0.175	0.259
1	-6.766	1.765	-0.115	-0.704	0.000	3.493	0.285	0.108	-0.072	0.057	0.175	0.260
1.1	-8.762	2.359	-0.160	-0.703	0.000	3.414	0.305	0.110	-0.088	0.048	0.183	0.262
1.2	-9.785	2.636	-0.178	-0.708	0.000	3.172	0.293	0.098	-0.092	0.037	0.176	0.263
1.3	-9.982	2.666	-0.180	-0.693	0.000	2.917	0.301	0.102	-0.084	0.029	0.180	0.260
1.4	-10.002	2.638	-0.176	-0.699	0.000	2.933	0.312	0.111	-0.062	0.021	0.179	0.258
1.5	-10.110	2.642	-0.175	-0.713	0.000	3.112	0.332	0.128	-0.035	0.013	0.171	0.257
1.6	-10.208	2.651	-0.175	-0.713	0.000	3.186	0.354	0.149	-0.021	0.009	0.166	0.257
1.7	-10.877	2.822	-0.187	-0.692	0.000	2.909	0.373	0.165	-0.013	0.002	0.169	0.260
1.8	-10.822	2.785	-0.185	-0.668	0.000	2.496	0.370	0.160	-0.021	-0.005	0.169	0.261
1.9	-10.991	2.816	-0.186	-0.660	0.000	2.280	0.363	0.154	-0.038	-0.014	0.166	0.264
2	-11.406	2.915	-0.192	-0.651	0.000	2.132	0.351	0.144	-0.047	-0.018	0.163	0.266
2.1	-11.239	2.853	-0.187	-0.644	0.000	2.059	0.341	0.136	-0.067	-0.020	0.162	0.269
2.2	-11.001	2.771	-0.181	-0.640	0.000	2.041	0.335	0.135	-0.078	-0.024	0.166	0.269
2.3	-10.992	2.758	-0.180	-0.635	0.000	2.036	0.336	0.142	-0.068	-0.024	0.176	0.268
2.4	-11.384	2.860	-0.187	-0.635	0.000	2.058	0.339	0.151	-0.062	-0.025	0.182	0.269
2.5	-11.513	2.875	-0.187	-0.638	0.000	2.103	0.346	0.163	-0.062	-0.027	0.179	0.270

Table A3.3 – Coefficients of the equation derived to predict pseudo spectral acceleration at 10% damping

Period (s)	Predictive Equation Coefficients										Standard Deviations	
	r1	**R2**	**r3**	**r4**	**r5**	**r6**	**r7**	**r8**	**r9**	**r10**	σ_e	σ_s
0	-2.097	0.510	-0.027	-0.744	-0.001	5.496	0.164	0.067	-0.162	0.046	0.105	0.206
0.05	-2.121	0.558	-0.031	-0.765	-0.001	5.385	0.139	0.055	-0.182	0.047	0.104	0.208
0.055	-1.968	0.518	-0.028	-0.776	-0.001	5.630	0.141	0.059	-0.184	0.046	0.104	0.208
0.06	-1.803	0.472	-0.025	-0.769	-0.001	5.572	0.136	0.058	-0.190	0.047	0.102	0.209
0.065	-1.681	0.441	-0.022	-0.767	-0.001	5.668	0.130	0.055	-0.193	0.044	0.101	0.208
0.07	-1.541	0.402	-0.019	-0.765	-0.002	5.865	0.127	0.055	-0.192	0.040	0.100	0.208
0.075	-1.496	0.393	-0.019	-0.765	-0.002	6.022	0.123	0.052	-0.192	0.036	0.097	0.209
0.08	-1.423	0.374	-0.017	-0.757	-0.002	5.991	0.122	0.051	-0.194	0.035	0.096	0.209
0.085	-1.379	0.365	-0.017	-0.760	-0.002	6.110	0.121	0.051	-0.192	0.034	0.096	0.209
0.09	-1.196	0.312	-0.013	-0.751	-0.002	6.124	0.120	0.049	-0.187	0.032	0.097	0.209
0.095	-1.112	0.292	-0.012	-0.744	-0.002	6.060	0.120	0.048	-0.184	0.031	0.098	0.210
0.10	-0.917	0.240	-0.008	-0.744	-0.002	6.171	0.120	0.047	-0.183	0.028	0.098	0.212
0.11	-0.922	0.249	-0.008	-0.761	-0.002	6.635	0.116	0.040	-0.190	0.030	0.098	0.214
0.12	-1.118	0.305	-0.012	-0.756	-0.002	6.722	0.114	0.035	-0.197	0.033	0.098	0.215
0.13	-1.252	0.354	-0.015	-0.771	-0.002	7.074	0.121	0.040	-0.189	0.037	0.101	0.215
0.14	-1.072	0.311	-0.013	-0.779	-0.002	7.251	0.122	0.041	-0.191	0.038	0.103	0.215
0.15	-0.991	0.289	-0.011	-0.768	-0.002	7.055	0.127	0.045	-0.201	0.033	0.105	0.215
0.16	-1.166	0.333	-0.014	-0.749	-0.002	6.867	0.132	0.048	-0.203	0.035	0.104	0.216
0.17	-1.454	0.416	-0.020	-0.746	-0.002	6.958	0.132	0.048	-0.202	0.038	0.103	0.216
0.18	-1.583	0.452	-0.023	-0.750	-0.002	7.147	0.137	0.052	-0.192	0.036	0.104	0.217
0.19	-1.401	0.394	-0.018	-0.743	-0.002	7.145	0.141	0.058	-0.187	0.034	0.104	0.218
0.20	-1.478	0.413	-0.020	-0.740	-0.002	7.050	0.148	0.063	-0.181	0.029	0.105	0.218
0.22	-1.436	0.400	-0.019	-0.752	-0.002	7.124	0.169	0.079	-0.170	0.025	0.108	0.219
0.24	-1.162	0.310	-0.012	-0.747	-0.002	6.855	0.186	0.088	-0.159	0.031	0.109	0.219
0.26	-1.306	0.339	-0.014	-0.722	-0.002	6.133	0.189	0.082	-0.153	0.041	0.108	0.220
0.28	-1.528	0.389	-0.018	-0.684	-0.002	5.367	0.185	0.068	-0.162	0.043	0.108	0.223
0.30	-1.766	0.445	-0.022	-0.662	-0.002	4.900	0.187	0.064	-0.164	0.044	0.111	0.227
0.32	-1.912	0.478	-0.024	-0.664	-0.002	4.780	0.195	0.064	-0.171	0.043	0.116	0.231
0.34	-2.198	0.555	-0.029	-0.678	-0.001	4.790	0.207	0.067	-0.156	0.040	0.119	0.232
0.36	-2.691	0.692	-0.039	-0.693	-0.001	4.823	0.220	0.077	-0.134	0.038	0.124	0.234
0.38	-3.132	0.821	-0.048	-0.705	-0.001	4.865	0.226	0.085	-0.136	0.027	0.132	0.235
0.40	-3.438	0.905	-0.054	-0.704	-0.001	4.827	0.233	0.091	-0.142	0.021	0.138	0.235
0.42	-3.992	1.064	-0.066	-0.703	-0.001	4.766	0.237	0.094	-0.144	0.020	0.142	0.235
0.44	-4.316	1.154	-0.072	-0.704	-0.001	4.745	0.240	0.095	-0.139	0.020	0.145	0.236
0.46	-4.342	1.162	-0.073	-0.720	-0.001	4.846	0.247	0.101	-0.138	0.023	0.148	0.236
0.48	-4.460	1.201	-0.076	-0.740	-0.001	4.987	0.255	0.107	-0.136	0.027	0.150	0.237
0.50	-4.471	1.203	-0.076	-0.750	-0.001	5.032	0.266	0.113	-0.128	0.034	0.152	0.238
0.55	-4.455	1.184	-0.075	-0.747	0.000	4.769	0.284	0.123	-0.110	0.045	0.161	0.241
0.60	-4.428	1.163	-0.074	-0.745	0.000	4.285	0.301	0.135	-0.099	0.052	0.166	0.245
0.65	-4.449	1.153	-0.073	-0.752	0.000	4.038	0.307	0.140	-0.099	0.057	0.174	0.248
0.70	-4.404	1.113	-0.069	-0.747	0.000	3.701	0.317	0.149	-0.095	0.062	0.176	0.251
0.75	-4.355	1.078	-0.066	-0.739	0.000	3.441	0.320	0.147	-0.086	0.064	0.175	0.254
0.80	-5.010	1.267	-0.080	-0.726	0.000	3.246	0.304	0.129	-0.091	0.058	0.174	0.254
0.85	-5.458	1.390	-0.089	-0.720	0.000	3.195	0.292	0.118	-0.091	0.057	0.172	0.255
0.90	-5.834	1.491	-0.096	-0.720	0.000	3.265	0.285	0.110	-0.089	0.060	0.173	0.255

Table A3.3 (Continued) – Coefficients of the equation derived to predict pseudo spectral acceleration at 10% damping

	Predictive Equation Coefficients										Standard Deviations	
Period (s)	r1	r2	r3	r4	r5	r6	r7	r8	r9	r10	σ_e	σ_s
0.95	-6.182	1.587	-0.102	-0.723	0.000	3.430	0.281	0.105	-0.086	0.059	0.175	0.255
1.00	-6.808	1.767	-0.116	-0.728	0.000	3.504	0.284	0.104	-0.086	0.056	0.176	0.256
1.10	-8.263	2.189	-0.147	-0.728	0.000	3.407	0.282	0.093	-0.103	0.049	0.177	0.258
1.20	-9.137	2.422	-0.163	-0.721	0.000	3.137	0.279	0.089	-0.113	0.039	0.178	0.258
1.30	-9.546	2.514	-0.168	-0.711	0.000	2.975	0.289	0.096	-0.102	0.032	0.181	0.257
1.40	-9.824	2.566	-0.171	-0.712	0.000	2.927	0.301	0.103	-0.067	0.027	0.181	0.255
1.50	-10.112	2.624	-0.174	-0.716	0.000	2.962	0.319	0.119	-0.045	0.019	0.176	0.254
1.60	-10.480	2.714	-0.180	-0.715	0.000	2.980	0.337	0.136	-0.044	0.010	0.172	0.254
1.70	-10.913	2.820	-0.188	-0.702	0.000	2.833	0.349	0.146	-0.044	0.005	0.171	0.255
1.80	-11.012	2.826	-0.188	-0.685	0.000	2.547	0.348	0.144	-0.050	0.001	0.170	0.256
1.90	-10.994	2.801	-0.185	-0.676	0.000	2.338	0.343	0.137	-0.061	-0.004	0.169	0.258
2.00	-11.222	2.849	-0.188	-0.669	0.000	2.232	0.339	0.133	-0.066	-0.010	0.166	0.260
2.10	-11.308	2.856	-0.188	-0.664	0.000	2.161	0.335	0.132	-0.070	-0.013	0.163	0.261
2.20	-11.350	2.851	-0.187	-0.663	0.000	2.133	0.331	0.131	-0.070	-0.016	0.164	0.262
2.30	-11.279	2.816	-0.184	-0.662	0.000	2.132	0.331	0.136	-0.067	-0.018	0.168	0.261
2.40	-11.271	2.796	-0.182	-0.660	0.000	2.143	0.331	0.140	-0.064	-0.020	0.171	0.261
2.50	-11.433	2.821	-0.182	-0.659	0.000	2.138	0.335	0.147	-0.062	-0.021	0.170	0.263

Table A3.4 - Coefficients of the equation derived to predict pseudo spectral acceleration at 20% damping

	Predictive Equation Coefficients										Standard Deviations	
Period (s)	r1	r2	r3	r4	r5	r6	r7	r8	r9	r10	σ_e	σ_s
0	-2.097	0.510	-0.027	-0.744	-0.001	5.496	0.164	0.067	-0.162	0.046	0.105	0.206
0.05	-2.058	0.522	-0.028	-0.755	-0.001	5.415	0.151	0.064	-0.171	0.047	0.103	0.207
0.055	-1.980	0.502	-0.027	-0.758	-0.001	5.487	0.149	0.064	-0.174	0.046	0.102	0.206
0.06	-1.884	0.477	-0.025	-0.759	-0.001	5.561	0.147	0.063	-0.175	0.046	0.101	0.206
0.065	-1.801	0.454	-0.023	-0.757	-0.001	5.617	0.143	0.061	-0.177	0.044	0.100	0.206
0.07	-1.781	0.451	-0.023	-0.756	-0.001	5.705	0.139	0.059	-0.178	0.041	0.099	0.206
0.075	-1.744	0.441	-0.022	-0.752	-0.001	5.763	0.137	0.058	-0.180	0.038	0.097	0.206
0.08	-1.694	0.429	-0.021	-0.750	-0.001	5.811	0.136	0.057	-0.179	0.036	0.097	0.207
0.085	-1.625	0.412	-0.020	-0.748	-0.002	5.856	0.134	0.055	-0.178	0.034	0.097	0.207
0.09	-1.585	0.404	-0.020	-0.747	-0.002	5.914	0.132	0.053	-0.178	0.032	0.097	0.208
0.095	-1.544	0.396	-0.019	-0.749	-0.002	5.997	0.131	0.051	-0.178	0.032	0.098	0.209
0.10	-1.504	0.388	-0.019	-0.753	-0.002	6.103	0.131	0.049	-0.178	0.033	0.098	0.210
0.11	-1.443	0.375	-0.017	-0.761	-0.002	6.342	0.131	0.047	-0.181	0.035	0.097	0.210
0.12	-1.526	0.402	-0.019	-0.766	-0.002	6.494	0.134	0.047	-0.183	0.037	0.097	0.211
0.13	-1.645	0.439	-0.022	-0.765	-0.002	6.541	0.136	0.048	-0.182	0.038	0.098	0.211
0.14	-1.585	0.423	-0.021	-0.764	-0.002	6.548	0.142	0.053	-0.183	0.037	0.100	0.211
0.15	-1.505	0.400	-0.019	-0.763	-0.002	6.502	0.148	0.058	-0.186	0.035	0.102	0.211
0.16	-1.529	0.407	-0.020	-0.758	-0.002	6.429	0.150	0.059	-0.190	0.035	0.103	0.210
0.17	-1.560	0.416	-0.021	-0.755	-0.002	6.414	0.152	0.062	-0.193	0.034	0.105	0.210
0.18	-1.669	0.445	-0.023	-0.751	-0.002	6.391	0.156	0.065	-0.193	0.032	0.106	0.211

Table A3.4 (Continued) - Coefficients of the equation derived to predict pseudo spectral acceleration at 20% damping

	Predictive Equation Coefficients										Standard Deviations	
Period (s)	r1	r2	r3	r4	r5	r6	r7	r8	r9	r10	σ_e	σ_s
0.19	-1.703	0.451	-0.023	-0.746	-0.001	6.336	0.163	0.070	-0.187	0.031	0.107	0.212
0.20	-1.712	0.450	-0.023	-0.744	-0.001	6.297	0.170	0.077	-0.179	0.030	0.109	0.212
0.22	-1.705	0.437	-0.022	-0.738	-0.001	6.154	0.183	0.084	-0.164	0.029	0.110	0.213
0.24	-1.686	0.421	-0.021	-0.731	-0.001	5.941	0.191	0.086	-0.153	0.034	0.112	0.214
0.26	-1.845	0.458	-0.023	-0.721	-0.001	5.655	0.194	0.081	-0.148	0.038	0.113	0.216
0.28	-1.878	0.457	-0.023	-0.709	-0.001	5.364	0.196	0.075	-0.147	0.041	0.114	0.218
0.30	-2.022	0.490	-0.025	-0.701	-0.001	5.142	0.200	0.072	-0.151	0.042	0.116	0.220
0.32	-2.171	0.524	-0.027	-0.700	-0.001	4.973	0.209	0.075	-0.154	0.041	0.119	0.223
0.34	-2.457	0.602	-0.033	-0.707	-0.001	4.880	0.221	0.081	-0.147	0.040	0.123	0.225
0.36	-2.804	0.697	-0.039	-0.715	-0.001	4.834	0.232	0.087	-0.139	0.037	0.128	0.228
0.38	-3.089	0.776	-0.045	-0.722	-0.001	4.815	0.238	0.091	-0.137	0.033	0.134	0.229
0.40	-3.356	0.849	-0.050	-0.724	-0.001	4.746	0.243	0.093	-0.136	0.030	0.139	0.230
0.42	-3.663	0.934	-0.056	-0.726	-0.001	4.673	0.242	0.092	-0.138	0.027	0.143	0.231
0.44	-3.875	0.991	-0.060	-0.726	-0.001	4.619	0.243	0.091	-0.137	0.028	0.146	0.231
0.46	-4.029	1.032	-0.063	-0.728	-0.001	4.587	0.248	0.095	-0.135	0.030	0.148	0.232
0.48	-4.149	1.066	-0.066	-0.733	-0.001	4.602	0.255	0.100	-0.131	0.033	0.150	0.232
0.50	-4.190	1.075	-0.067	-0.737	-0.001	4.581	0.262	0.105	-0.127	0.036	0.153	0.233
0.55	-4.128	1.046	-0.065	-0.748	0.000	4.411	0.277	0.116	-0.115	0.045	0.159	0.237
0.60	-4.327	1.097	-0.069	-0.767	0.000	4.324	0.290	0.126	-0.106	0.049	0.165	0.240
0.65	-4.623	1.169	-0.073	-0.781	0.000	4.464	0.300	0.126	-0.103	0.056	0.164	0.243
0.70	-4.849	1.223	-0.077	-0.764	0.000	3.890	0.301	0.127	-0.102	0.053	0.170	0.245
0.75	-5.059	1.270	-0.080	-0.758	0.000	3.729	0.299	0.123	-0.100	0.053	0.170	0.247
0.80	-5.320	1.336	-0.085	-0.752	0.000	3.608	0.293	0.118	-0.098	0.054	0.170	0.248
0.85	-5.624	1.417	-0.091	-0.748	0.000	3.531	0.287	0.111	-0.096	0.053	0.170	0.248
0.90	-5.927	1.497	-0.096	-0.747	0.000	3.509	0.280	0.104	-0.095	0.052	0.170	0.248
0.95	-6.301	1.600	-0.104	-0.745	0.000	3.474	0.279	0.100	-0.095	0.050	0.171	0.249
1.00	-6.762	1.729	-0.113	-0.744	0.000	3.429	0.275	0.094	-0.098	0.047	0.173	0.250
1.10	-7.697	1.987	-0.131	-0.738	0.000	3.273	0.268	0.085	-0.106	0.044	0.171	0.249
1.20	-8.338	2.153	-0.143	-0.733	0.000	3.168	0.273	0.088	-0.107	0.036	0.175	0.251
1.30	-8.737	2.245	-0.149	-0.727	0.000	3.064	0.278	0.092	-0.097	0.034	0.178	0.251
1.40	-9.019	2.303	-0.152	-0.722	0.000	2.961	0.284	0.093	-0.087	0.031	0.181	0.250
1.50	-9.284	2.356	-0.155	-0.718	0.000	2.898	0.296	0.103	-0.080	0.026	0.178	0.250
1.60	-9.705	2.460	-0.162	-0.712	0.000	2.830	0.307	0.112	-0.083	0.020	0.176	0.251
1.70	-10.124	2.563	-0.169	-0.706	0.000	2.735	0.315	0.118	-0.083	0.014	0.174	0.252
1.80	-10.557	2.669	-0.176	-0.701	0.000	2.632	0.320	0.121	-0.082	0.011	0.172	0.252
1.90	-10.848	2.734	-0.180	-0.695	0.000	2.520	0.322	0.122	-0.083	0.007	0.171	0.253
2.00	-10.955	2.745	-0.180	-0.689	0.000	2.441	0.322	0.123	-0.079	0.003	0.169	0.253
2.10	-10.953	2.725	-0.178	-0.686	0.000	2.380	0.320	0.122	-0.079	-0.001	0.167	0.254
2.20	-10.996	2.718	-0.177	-0.683	0.000	2.328	0.320	0.123	-0.077	-0.003	0.165	0.254
2.30	-11.047	2.715	-0.176	-0.682	0.000	2.304	0.319	0.124	-0.074	-0.005	0.164	0.255
2.40	-11.061	2.701	-0.174	-0.682	0.000	2.294	0.319	0.125	-0.073	-0.006	0.163	0.256
2.50	-11.150	2.710	-0.174	-0.681	0.000	2.283	0.319	0.128	-0.072	-0.008	0.163	0.257

Table A3.5 - Coefficients of the equation derived to predict pseudo spectral acceleration at 30% damping

Period	Predictive Equation Coefficients										Standard Deviations	
(s)	r1	r2	r3	r4	r5	r6	r7	r8	r9	r10	σ_e	σ_s
0	-2.097	0.510	-0.027	-0.744	-0.001	5.496	0.164	0.067	-0.162	0.046	0.105	0.206
0.05	-1.959	0.484	-0.025	-0.749	-0.001	5.479	0.156	0.065	-0.166	0.046	0.103	0.206
0.055	-1.918	0.474	-0.025	-0.750	-0.001	5.522	0.154	0.065	-0.168	0.044	0.102	0.206
0.06	-1.860	0.459	-0.024	-0.751	-0.001	5.579	0.152	0.064	-0.169	0.044	0.101	0.206
0.065	-1.794	0.442	-0.022	-0.750	-0.001	5.636	0.150	0.063	-0.171	0.042	0.101	0.205
0.07	-1.761	0.433	-0.022	-0.751	-0.001	5.698	0.148	0.062	-0.172	0.040	0.100	0.206
0.075	-1.709	0.420	-0.021	-0.750	-0.001	5.763	0.147	0.061	-0.173	0.039	0.099	0.206
0.08	-1.678	0.412	-0.020	-0.751	-0.001	5.815	0.147	0.060	-0.173	0.037	0.099	0.206
0.085	-1.683	0.415	-0.020	-0.751	-0.001	5.875	0.146	0.060	-0.173	0.037	0.099	0.206
0.09	-1.671	0.414	-0.020	-0.752	-0.001	5.942	0.146	0.059	-0.173	0.036	0.099	0.207
0.095	-1.686	0.422	-0.021	-0.754	-0.001	6.010	0.147	0.059	-0.173	0.036	0.099	0.207
0.10	-1.685	0.423	-0.021	-0.756	-0.001	6.084	0.147	0.059	-0.174	0.037	0.099	0.207
0.11	-1.685	0.425	-0.021	-0.757	-0.001	6.168	0.149	0.059	-0.176	0.037	0.100	0.208
0.12	-1.683	0.426	-0.021	-0.758	-0.001	6.216	0.150	0.059	-0.177	0.038	0.100	0.208
0.13	-1.659	0.419	-0.021	-0.758	-0.001	6.226	0.153	0.061	-0.177	0.038	0.102	0.208
0.14	-1.648	0.416	-0.021	-0.755	-0.001	6.189	0.159	0.065	-0.177	0.038	0.103	0.209
0.15	-1.699	0.430	-0.022	-0.750	-0.001	6.107	0.163	0.068	-0.179	0.036	0.105	0.209
0.16	-1.710	0.432	-0.022	-0.748	-0.001	6.064	0.166	0.070	-0.180	0.035	0.107	0.209
0.17	-1.735	0.437	-0.022	-0.745	-0.001	5.998	0.169	0.071	-0.181	0.035	0.108	0.209
0.18	-1.781	0.448	-0.023	-0.741	-0.001	5.928	0.173	0.073	-0.179	0.034	0.109	0.209
0.19	-1.808	0.452	-0.023	-0.739	-0.001	5.877	0.177	0.076	-0.175	0.033	0.110	0.210
0.20	-1.809	0.449	-0.023	-0.736	-0.001	5.811	0.182	0.080	-0.170	0.032	0.111	0.210
0.22	-1.857	0.454	-0.023	-0.732	-0.001	5.732	0.192	0.084	-0.158	0.032	0.114	0.212
0.24	-1.899	0.456	-0.023	-0.730	-0.001	5.622	0.199	0.087	-0.149	0.035	0.115	0.213
0.26	-2.014	0.480	-0.025	-0.727	-0.001	5.482	0.205	0.086	-0.144	0.037	0.117	0.214
0.28	-2.102	0.499	-0.026	-0.725	-0.001	5.323	0.209	0.084	-0.143	0.040	0.119	0.216
0.30	-2.293	0.548	-0.029	-0.721	-0.001	5.132	0.214	0.083	-0.144	0.040	0.121	0.218
0.32	-2.514	0.605	-0.033	-0.722	-0.001	4.989	0.220	0.084	-0.145	0.040	0.125	0.220
0.34	-2.746	0.668	-0.038	-0.727	-0.001	4.923	0.225	0.084	-0.145	0.039	0.128	0.222
0.36	-2.992	0.734	-0.042	-0.732	-0.001	4.873	0.231	0.086	-0.141	0.037	0.132	0.224
0.38	-3.208	0.791	-0.046	-0.736	-0.001	4.810	0.238	0.089	-0.137	0.035	0.136	0.226
0.40	-3.418	0.845	-0.050	-0.737	-0.001	4.744	0.244	0.093	-0.133	0.035	0.140	0.227
0.42	-3.634	0.902	-0.054	-0.738	-0.001	4.670	0.247	0.094	-0.130	0.034	0.144	0.228
0.44	-3.840	0.958	-0.058	-0.736	-0.001	4.602	0.248	0.094	-0.129	0.035	0.146	0.229
0.46	-3.980	0.994	-0.061	-0.737	-0.001	4.547	0.251	0.096	-0.127	0.035	0.148	0.230
0.48	-4.110	1.027	-0.063	-0.738	-0.001	4.486	0.256	0.099	-0.125	0.037	0.150	0.230
0.50	-4.149	1.035	-0.064	-0.742	-0.001	4.444	0.259	0.101	-0.122	0.038	0.152	0.231
0.55	-4.317	1.076	-0.067	-0.759	0.000	4.417	0.271	0.108	-0.113	0.042	0.158	0.233
0.60	-4.622	1.160	-0.073	-0.776	0.000	4.361	0.279	0.113	-0.109	0.044	0.163	0.236
0.65	-4.936	1.243	-0.079	-0.778	0.000	4.198	0.283	0.113	-0.108	0.047	0.165	0.238
0.70	-5.079	1.270	-0.081	-0.772	0.000	3.998	0.285	0.112	-0.106	0.050	0.165	0.240
0.75	-5.208	1.296	-0.082	-0.767	0.000	3.866	0.284	0.110	-0.104	0.050	0.166	0.241
0.80	-5.403	1.341	-0.085	-0.761	0.000	3.746	0.281	0.106	-0.103	0.049	0.167	0.242
0.85	-5.635	1.398	-0.089	-0.757	0.000	3.647	0.276	0.100	-0.101	0.050	0.168	0.243
0.90	-5.897	1.464	-0.094	-0.755	0.000	3.578	0.275	0.098	-0.099	0.048	0.168	0.244
0.95	-6.218	1.549	-0.100	-0.752	0.000	3.495	0.273	0.095	-0.098	0.046	0.169	0.245

Table A3.5 (Continued) - Coefficients of the equation derived to predict pseudo spectral acceleration at 30% damping

Period (s)	Predictive Equation Coefficients										Standard Deviations	
	r1	r2	r3	r4	r5	r6	r7	r8	r9	r10	σ_e	σ_s
1.00	-6.575	1.646	-0.106	-0.749	0.000	3.404	0.271	0.092	-0.097	0.043	0.170	0.246
1.10	-7.274	1.834	-0.120	-0.741	0.000	3.253	0.267	0.086	-0.100	0.039	0.172	0.247
1.20	-7.757	1.956	-0.128	-0.737	0.000	3.182	0.268	0.087	-0.101	0.034	0.173	0.247
1.30	-8.095	2.030	-0.133	-0.732	0.000	3.075	0.272	0.089	-0.096	0.034	0.176	0.247
1.40	-8.460	2.115	-0.138	-0.727	0.000	3.011	0.277	0.090	-0.092	0.032	0.176	0.247
1.50	-8.795	2.192	-0.143	-0.722	0.000	2.935	0.282	0.093	-0.094	0.030	0.175	0.248
1.60	-9.052	2.245	-0.146	-0.718	0.000	2.884	0.288	0.098	-0.095	0.027	0.174	0.249
1.70	-9.366	2.317	-0.151	-0.713	0.000	2.816	0.294	0.103	-0.095	0.023	0.173	0.249
1.80	-9.698	2.394	-0.156	-0.710	0.000	2.749	0.301	0.108	-0.092	0.021	0.171	0.249
1.90	-9.971	2.453	-0.159	-0.707	0.000	2.691	0.307	0.113	-0.089	0.018	0.169	0.249
2.00	-10.179	2.494	-0.161	-0.702	0.000	2.621	0.311	0.117	-0.086	0.014	0.167	0.250
2.10	-10.281	2.505	-0.162	-0.698	0.000	2.558	0.312	0.118	-0.084	0.011	0.166	0.250
2.20	-10.426	2.530	-0.163	-0.695	0.000	2.498	0.310	0.117	-0.083	0.007	0.164	0.251
2.30	-10.602	2.564	-0.165	-0.693	0.000	2.447	0.311	0.117	-0.082	0.004	0.163	0.252
2.40	-10.770	2.597	-0.166	-0.692	0.000	2.416	0.311	0.118	-0.080	0.001	0.162	0.253
2.50	-10.911	2.624	-0.168	-0.690	0.000	2.400	0.311	0.119	-0.079	-0.003	0.161	0.253

Table A3.6 - Coefficients of the equation derived to predict member end rotation

Beam/ Col.	Predictive Equation Coefficients										Standard Deviations	
	r1	r2	r3	r4	r5	r6	r7	r8	r9	r10	σ_e	σ_s
C1t	-9.149	1.834	-0.120	-0.649	-0.001	2.476	0.336	0.183	-0.017	0.037	0.165	0.276
C1b	-6.453	0.928	-0.058	-0.445	0.000	2.453	0.207	0.096	-0.009	0.038	0.110	0.204
C2t	-9.229	1.846	-0.121	-0.613	-0.001	2.272	0.327	0.176	-0.033	0.024	0.173	0.276
C2b	-8.321	1.482	-0.098	-0.497	-0.001	2.632	0.293	0.151	-0.045	0.018	0.162	0.245
C3t	-9.527	1.929	-0.127	-0.600	-0.001	2.145	0.325	0.174	-0.034	0.025	0.177	0.282
C3b	-9.116	1.716	-0.114	-0.568	-0.001	3.540	0.305	0.161	-0.014	0.030	0.144	0.241
C4t	-9.137	1.835	-0.121	-0.598	-0.001	2.493	0.314	0.168	-0.020	0.026	0.164	0.267
C4b	-6.375	0.906	-0.055	-0.493	0.000	1.715	0.231	0.119	-0.015	0.040	0.120	0.224
C1t	-7.427	1.344	-0.089	-0.520	0.000	1.977	0.231	0.119	-0.024	0.010	0.109	0.219
C1b	-6.696	1.010	-0.062	-0.508	0.000	0.909	0.150	0.061	-0.049	-0.003	0.094	0.269
C2t	-10.41	2.125	-0.141	-0.644	-0.001	3.171	0.374	0.201	-0.016	0.030	0.192	0.300
C2b	-9.130	1.632	-0.107	-0.591	-0.001	3.648	0.328	0.171	-0.025	0.039	0.155	0.257
C3t	-10.01	1.985	-0.134	-0.479	-0.002	4.638	0.377	0.208	-0.073	0.031	0.184	0.292
C3b	-8.596	1.454	-0.094	-0.551	0.000	4.135	0.252	0.124	-0.025	0.039	0.123	0.215
C4t	-7.949	1.492	-0.098	-0.556	0.000	1.777	0.253	0.139	-0.001	0.018	0.109	0.237
C4b	-7.572	1.291	-0.082	-0.548	0.000	1.033	0.167	0.076	-0.042	-0.002	0.096	0.276
C1t	-7.967	1.471	-0.096	-0.597	0.000	2.035	0.268	0.140	-0.012	0.019	0.115	0.252
C1b	-8.077	1.477	-0.096	-0.599	0.000	1.606	0.219	0.102	-0.034	0.000	0.104	0.269
C2t	-10.51	2.130	-0.140	-0.817	-0.001	5.834	0.401	0.212	-0.014	0.060	0.176	0.317
C2b	-8.921	1.626	-0.098	-1.066	0.000	6.994	0.353	0.179	0.012	0.081	0.161	0.344
C3t	-10.50	2.117	-0.138	-0.818	-0.001	7.328	0.400	0.204	0.034	0.079	0.165	0.330
C3b	-8.218	1.361	-0.081	-0.848	-0.001	6.959	0.284	0.132	0.001	0.066	0.132	0.302
C4t	-8.545	1.646	-0.108	-0.621	0.000	1.936	0.275	0.149	0.007	0.019	0.112	0.265
C4b	-8.329	1.567	-0.102	-0.613	0.000	1.644	0.235	0.116	-0.009	0.011	0.107	0.269

Table A3.6 (Contuinued) - Coefficients of the equation derived to predict member end rotation

Beam/ Col.	Predictive Equation Coefficients										Standard Deviations	
	r1	r2	r3	r4	r5	r6	r7	r8	r9	r10	σ_e	σ_s
C1t	-8.318	1.584	-0.103	-0.657	0.000	2.183	0.266	0.133	-0.017	0.014	0.112	0.269
C1b	-8.267	1.558	-0.101	-0.653	0.000	2.080	0.251	0.119	-0.023	0.018	0.109	0.274
C2t	-9.664	1.929	-0.122	-1.097	0.000	7.512	0.369	0.186	-0.003	0.061	0.160	0.348
C2b	-8.851	1.642	-0.101	-1.028	0.000	6.518	0.318	0.151	-0.017	0.049	0.150	0.341
C3t	-11.10	2.329	-0.151	-1.068	0.000	7.764	0.377	0.200	0.018	0.059	0.158	0.368
C3b	-8.488	1.486	-0.090	-0.919	0.000	6.309	0.304	0.150	-0.017	0.062	0.144	0.306
C4t	-8.598	1.664	-0.107	-0.692	0.000	2.214	0.287	0.148	0.004	0.022	0.112	0.288
C4b	-8.538	1.631	-0.105	-0.676	0.000	2.146	0.276	0.140	0.011	0.029	0.112	0.283
C1t	-7.913	1.464	-0.092	-0.711	0.000	2.414	0.254	0.116	-0.011	0.023	0.111	0.286
C1b	-8.266	1.562	-0.100	-0.687	0.000	2.597	0.271	0.129	-0.011	0.026	0.116	0.276
C2t	-7.206	1.197	-0.064	-1.271	0.000	7.484	0.377	0.187	-0.011	0.062	0.154	0.405
C2b	-9.117	1.696	-0.106	-0.895	0.000	6.436	0.315	0.153	-0.007	0.048	0.149	0.314
C3t	-6.971	1.098	-0.058	-1.157	0.000	6.183	0.310	0.132	-0.058	0.041	0.156	0.389
C3b	-8.604	1.549	-0.097	-0.826	0.000	6.164	0.282	0.132	-0.069	0.017	0.147	0.280
C4t	-8.223	1.562	-0.099	-0.747	0.000	2.499	0.278	0.136	-0.002	0.020	0.113	0.305
C4b	-8.858	1.733	-0.112	-0.702	0.000	2.420	0.282	0.135	0.001	0.027	0.119	0.289
C1t	-8.209	1.541	-0.098	-0.725	0.000	2.570	0.257	0.116	-0.007	0.020	0.109	0.291
C1b	-8.435	1.616	-0.104	-0.690	0.000	2.806	0.283	0.139	-0.004	0.029	0.116	0.275
C2t	-8.673	1.589	-0.095	-1.098	0.000	5.758	0.270	0.113	-0.061	-0.010	0.155	0.369
C2b	-10.03	1.940	-0.125	-0.858	0.000	5.380	0.369	0.195	0.025	0.041	0.148	0.308
C3t	-8.847	1.592	-0.098	-0.954	0.000	4.548	0.216	0.086	-0.074	0.002	0.137	0.320
C3b	-9.002	1.592	-0.101	-0.658	-0.001	4.602	0.337	0.173	-0.040	0.032	0.159	0.270
C4t	-8.401	1.596	-0.101	-0.751	0.000	2.610	0.265	0.122	-0.011	0.024	0.114	0.306
C4b	-8.555	1.644	-0.105	-0.703	0.000	2.730	0.290	0.144	0.004	0.034	0.120	0.285
C1t	-7.859	1.426	-0.089	-0.721	0.000	2.689	0.250	0.112	-0.020	0.024	0.112	0.283
C1b	-8.139	1.508	-0.095	-0.742	0.000	3.048	0.284	0.132	-0.011	0.033	0.124	0.290
C2t	-9.384	1.678	-0.108	-0.765	0.000	3.066	0.220	0.098	-0.082	0.014	0.133	0.281
C2b	-11.85	2.459	-0.164	-0.842	0.000	5.363	0.382	0.199	0.028	0.077	0.133	0.313
C3t	-8.501	1.321	-0.083	-0.516	-0.001	2.717	0.144	0.056	-0.037	0.049	0.103	0.215
C3b	-10.54	2.050	-0.135	-0.746	-0.001	5.625	0.398	0.220	0.026	0.075	0.164	0.306
C4t	-8.192	1.519	-0.095	-0.739	0.000	2.773	0.268	0.130	-0.006	0.025	0.117	0.293
C4b	-8.882	1.724	-0.110	-0.757	0.000	3.105	0.306	0.151	0.007	0.041	0.127	0.302
C1t	-7.945	1.436	-0.089	-0.773	0.000	3.058	0.282	0.130	-0.013	0.031	0.125	0.305
C1b	-8.075	1.582	-0.102	-0.627	-0.001	3.656	0.285	0.141	-0.022	0.033	0.141	0.253
C2t	-8.435	1.205	-0.077	-0.362	-0.001	1.227	0.159	0.071	-0.064	0.035	0.125	0.208
C2b	-9.334	1.641	-0.109	-0.626	0.000	2.321	0.257	0.141	-0.035	0.009	0.125	0.260
C3t	-9.349	1.502	-0.098	-0.442	-0.001	3.077	0.215	0.106	-0.031	0.038	0.124	0.206
C3b	-9.519	1.731	-0.110	-0.830	0.000	4.565	0.308	0.146	-0.004	0.034	0.129	0.306
C4t	-8.404	1.556	-0.097	-0.762	0.000	2.818	0.293	0.143	-0.003	0.031	0.123	0.307
C4b	-8.317	1.664	-0.108	-0.663	0.000	3.801	0.290	0.148	-0.016	0.037	0.138	0.255
B1l	-7.278	1.380	-0.091	-0.469	0.000	2.712	0.233	0.124	0.005	0.031	0.115	0.199
B1r	-7.621	1.408	-0.093	-0.457	0.000	2.793	0.233	0.124	0.002	0.028	0.116	0.196
B2l	-8.593	1.721	-0.113	-0.505	-0.001	3.213	0.282	0.147	-0.036	0.024	0.155	0.242
B2r	-8.651	1.747	-0.115	-0.520	-0.001	3.370	0.292	0.152	-0.031	0.025	0.160	0.247
B3l	-8.095	1.612	-0.106	-0.570	0.000	2.865	0.295	0.161	0.008	0.036	0.144	0.238
B3r	-7.030	1.300	-0.084	-0.481	0.000	2.702	0.248	0.132	0.007	0.037	0.120	0.204
B1l	-7.504	1.474	-0.097	-0.453	-0.001	3.487	0.255	0.137	0.007	0.031	0.126	0.205
B1r	-7.339	1.369	-0.090	-0.462	0.000	3.161	0.247	0.130	-0.002	0.026	0.123	0.201

Table A3.6 (Contuinued) - Coefficients of the equation derived to predict member end rotation

Beam/ Col.	Predictive Equation Coefficients										Standard Deviations	
	r1	r2	r3	r4	r5	r6	r7	r8	r9	r10	σ_e	σ_s
B2l	-8.331	1.680	-0.112	-0.474	-0.001	3.730	0.276	0.146	-0.033	0.022	0.149	0.228
B2r	-8.326	1.687	-0.112	-0.492	-0.001	4.042	0.283	0.150	-0.032	0.024	0.152	0.232
B3l	-8.023	1.624	-0.107	-0.502	-0.001	2.878	0.296	0.162	-0.008	0.033	0.144	0.234
B3r	-7.469	1.457	-0.096	-0.458	-0.001	3.056	0.264	0.140	0.001	0.037	0.128	0.212
B1l	-7.189	1.405	-0.093	-0.468	0.000	3.780	0.265	0.143	0.005	0.033	0.124	0.204
B1r	-7.351	1.397	-0.093	-0.481	0.000	3.484	0.258	0.136	-0.008	0.028	0.119	0.201
B2l	-8.100	1.609	-0.107	-0.436	-0.001	3.773	0.277	0.148	-0.039	0.019	0.144	0.222
B2r	-8.158	1.635	-0.109	-0.459	-0.001	4.188	0.280	0.150	-0.038	0.021	0.146	0.226
B3l	-7.975	1.633	-0.108	-0.514	-0.001	3.128	0.305	0.170	0.008	0.036	0.141	0.232
B3r	-7.282	1.422	-0.093	-0.460	-0.001	3.240	0.272	0.150	0.012	0.036	0.127	0.209
B1l	-7.122	1.400	-0.093	-0.488	0.000	4.088	0.265	0.143	0.004	0.032	0.121	0.203
B1r	-7.185	1.358	-0.089	-0.505	0.000	3.735	0.257	0.134	-0.003	0.036	0.092	0.204
B2l	-8.109	1.600	-0.107	-0.419	-0.001	3.964	0.277	0.151	-0.042	0.021	0.143	0.220
B2r	-8.137	1.618	-0.108	-0.438	-0.001	4.171	0.281	0.151	-0.045	0.021	0.143	0.224
B3l	-7.943	1.637	-0.108	-0.536	-0.001	3.401	0.310	0.174	0.012	0.038	0.137	0.232
B3r	-7.286	1.432	-0.094	-0.478	-0.001	3.479	0.277	0.154	0.015	0.040	0.122	0.210
B1l	-7.066	1.397	-0.092	-0.518	0.000	4.276	0.260	0.137	0.002	0.034	0.119	0.204
B1r	-7.143	1.358	-0.089	-0.536	0.000	3.932	0.254	0.130	0.001	0.041	0.085	0.207
B2l	-7.828	1.508	-0.100	-0.419	-0.001	4.230	0.261	0.141	-0.039	0.021	0.136	0.213
B2r	-7.899	1.538	-0.102	-0.438	-0.001	4.200	0.265	0.142	-0.040	0.019	0.136	0.215
B3l	-7.921	1.646	-0.109	-0.564	0.000	3.652	0.303	0.168	0.011	0.039	0.135	0.232
B3r	-7.335	1.464	-0.096	-0.505	0.000	3.703	0.273	0.151	0.012	0.037	0.122	0.210
B1l	-7.088	1.409	-0.093	-0.540	0.000	4.377	0.253	0.130	0.004	0.035	0.118	0.207
B1r	-7.160	1.376	-0.091	-0.561	0.000	4.120	0.251	0.129	-0.002	0.033	0.114	0.206
B2l	-7.467	1.384	-0.091	-0.413	-0.001	4.378	0.238	0.125	-0.045	0.021	0.131	0.208
B2r	-7.456	1.385	-0.091	-0.423	-0.001	4.153	0.241	0.124	-0.048	0.019	0.131	0.209
B3l	-7.841	1.630	-0.108	-0.587	0.000	3.830	0.295	0.161	0.014	0.042	0.136	0.232
B3r	-7.268	1.447	-0.095	-0.521	0.000	3.757	0.267	0.146	0.015	0.040	0.124	0.211
B1l	-6.967	1.372	-0.090	-0.564	0.000	4.390	0.260	0.135	0.000	0.036	0.119	0.211
B1r	-7.174	1.375	-0.090	-0.572	0.000	4.074	0.254	0.131	0.000	0.033	0.114	0.209
B2l	-7.197	1.281	-0.082	-0.405	-0.001	4.502	0.212	0.104	-0.059	0.024	0.128	0.207
B2r	-7.198	1.283	-0.082	-0.417	-0.001	4.418	0.217	0.105	-0.056	0.024	0.129	0.209
B3l	-7.752	1.600	-0.105	-0.594	0.000	3.900	0.289	0.158	0.014	0.041	0.134	0.233
B3r	-7.163	1.417	-0.093	-0.537	0.000	3.873	0.266	0.144	0.018	0.042	0.122	0.215
B1l	-6.272	1.121	-0.072	-0.472	0.000	4.429	0.212	0.103	-0.009	0.034	0.103	0.188
B1r	-7.005	1.314	-0.086	-0.557	0.000	4.176	0.247	0.125	0.000	0.034	0.109	0.204
B2l	-7.252	1.281	-0.081	-0.428	-0.002	5.347	0.216	0.102	-0.062	0.027	0.128	0.215
B2r	-7.325	1.308	-0.083	-0.449	-0.001	4.904	0.222	0.106	-0.058	0.025	0.129	0.218
B3l	-7.840	1.612	-0.106	-0.570	0.000	3.942	0.280	0.152	0.009	0.035	0.131	0.226
B3r	-6.666	1.235	-0.080	-0.456	0.000	3.986	0.221	0.117	-0.003	0.027	0.108	0.187

Table A3.7 - Coefficients of the equation derived to predict absorbed hysteretic energy at the member ends (rad.mm)

Beam/ Col.	Predictive Equation Coefficients										Standard Deviations	
	r1	r2	r3	r4	r5	r6	r7	r8	r9	r10	σ_e	σ_s
C1t	-9.359	4.047	-0.241	-2.323	0.000	4.914	0.978	0.508	0.035	0.200	0.392	0.971
C1b	-3.421	2.155	-0.132	-1.084	0.000	1.967	0.481	0.270	-0.069	0.065	0.242	0.577
C2t	-10.50	4.732	-0.304	-0.999	-0.007	3.059	0.901	0.500	-0.102	0.043	0.543	0.848
C2b	-10.64	4.768	-0.306	-1.626	-0.004	7.989	1.111	0.602	-0.108	0.158	0.483	0.889
C3t	-6.302	3.524	-0.210	-1.753	-0.002	4.096	0.851	0.460	-0.055	0.092	0.448	0.786
C3b	-6.881	3.528	-0.207	-2.012	0.000	4.394	0.829	0.463	0.055	0.092	0.338	0.796
C4t	-11.38	4.825	-0.308	-2.390	0.000	6.197	1.037	0.484	0.091	0.185	0.411	0.923
C4b	-7.030	3.215	-0.205	-1.235	0.000	2.637	0.484	0.212	0.117	0.035	0.208	0.593
C1t	-5.261	2.723	-0.161	-1.522	0.000	2.158	0.568	0.240	0.155	0.043	0.264	0.788
C1b	-4.027	2.259	-0.134	-1.056	0.000	1.241	0.244	0.054	-0.107	-0.027	0.218	0.546
C2t	-13.16	5.525	-0.359	-1.914	-0.002	5.905	1.069	0.574	0.146	0.155	0.463	0.851
C2b	-7.825	3.935	-0.243	-2.200	0.000	6.633	0.866	0.440	0.044	0.123	0.349	0.809
C3t	-12.74	5.312	-0.355	-1.450	-0.002	4.310	0.839	0.440	-0.240	0.028	0.430	0.764
C3b	-5.016	2.885	-0.173	-1.529	-0.001	4.708	0.540	0.243	0.021	0.119	0.280	0.645
C4t	-6.478	3.158	-0.196	-1.552	0.000	2.304	0.536	0.209	0.049	-0.010	0.252	0.813
C4b	-2.859	1.963	-0.114	-1.115	0.000	1.488	0.256	0.060	-0.086	-0.002	0.201	0.569
C1t	-8.723	3.694	-0.230	-1.636	0.000	2.408	0.533	0.219	0.026	0.047	0.274	0.807
C1b	-5.525	2.731	-0.166	-1.275	0.000	1.801	0.354	0.124	-0.035	0.044	0.203	0.616
C2t	-8.980	4.306	-0.269	-2.245	0.000	6.042	0.789	0.353	0.028	0.136	0.327	0.831
C2b	-8.043	3.984	-0.255	-1.956	0.000	6.436	0.733	0.410	0.139	0.143	0.329	0.709
C3t	-5.914	3.254	-0.197	-1.894	0.000	6.249	0.697	0.310	-0.065	0.170	0.300	0.723
C3b	-3.529	2.484	-0.146	-1.515	0.000	6.661	0.416	0.177	-0.024	0.133	0.274	0.526
C4t	-5.013	2.592	-0.149	-1.569	0.000	2.742	0.528	0.206	-0.040	0.100	0.283	0.726
C4b	-3.474	2.108	-0.118	-1.265	0.000	1.723	0.300	0.058	-0.093	0.042	0.227	0.619
C1t	-6.320	2.921	-0.168	-1.690	0.000	2.403	0.497	0.182	-0.022	0.030	0.288	0.782
C1b	-4.717	2.519	-0.146	-1.477	0.000	2.505	0.360	0.111	-0.108	0.003	0.231	0.678
C2t	-6.180	3.436	-0.209	-2.105	0.000	6.114	0.694	0.339	-0.131	0.064	0.314	0.738
C2b	-7.491	3.781	-0.240	-1.766	0.000	5.957	0.525	0.185	-0.024	0.068	0.284	0.663
C3t	-5.775	3.259	-0.199	-1.870	0.000	7.019	0.508	0.182	-0.099	0.114	0.281	0.661
C3b	-9.336	4.202	-0.270	-1.632	0.000	6.772	0.486	0.241	-0.026	0.040	0.299	0.576
C4t	-6.880	3.127	-0.189	-1.523	0.000	2.369	0.444	0.140	0.018	0.050	0.275	0.705
C4b	-4.222	2.338	-0.135	-1.388	0.000	2.076	0.424	0.169	-0.010	0.065	0.209	0.666
C1t	-8.170	3.473	-0.214	-1.587	0.000	2.494	0.543	0.222	-0.005	0.014	0.259	0.771
C1b	-3.380	2.157	-0.121	-1.618	0.000	2.921	0.537	0.237	-0.049	-0.032	0.260	0.722
C2t	-6.422	3.526	-0.223	-1.887	0.000	6.822	0.545	0.279	-0.208	0.072	0.262	0.620
C2b	-4.765	2.952	-0.177	-1.889	0.000	6.737	0.587	0.218	-0.132	0.089	0.257	0.680
C3t	-7.890	3.895	-0.244	-1.935	0.000	6.772	0.508	0.208	-0.028	0.065	0.271	0.635
C3b	-2.816	2.254	-0.125	-1.533	-0.001	7.641	0.426	0.164	-0.069	0.057	0.276	0.586
C4t	-6.074	2.904	-0.173	-1.589	0.000	2.504	0.473	0.168	-0.013	0.033	0.251	0.734
C4b	-6.506	3.025	-0.182	-1.546	0.000	2.525	0.457	0.153	0.009	-0.003	0.222	0.697
C1t	-9.042	3.827	-0.241	-1.677	0.000	3.174	0.420	0.106	-0.123	0.022	0.233	0.746
C1b	-3.125	2.121	-0.114	-1.788	0.000	3.652	0.461	0.110	-0.124	-0.021	0.306	0.735
C2t	-3.530	2.597	-0.156	-1.749	0.000	7.374	0.419	0.191	-0.080	0.051	0.255	0.605
C2b	-5.561	3.129	-0.188	-1.927	0.000	6.940	0.578	0.260	0.026	0.037	0.271	0.670
C3t	-5.169	3.010	-0.184	-1.705	0.000	4.837	0.397	0.133	-0.134	0.023	0.275	0.599
C3b	-4.195	2.562	-0.150	-1.443	-0.001	6.484	0.561	0.248	-0.056	0.103	0.288	0.599

Table A3.7 (Continued) - Coefficients of the equation derived to predict absorbed hysteretic energy at the member ends (rad.mm)

Beam/ Col.	Predictive Equation Coefficients										Standard Deviations	
	r1	r2	r3	r4	r5	r6	r7	r8	r9	r10	σ_e	σ_s
C4t	-6.101	2.905	-0.172	-1.604	0.000	2.892	0.406	0.128	0.081	0.049	0.272	0.723
C4b	-3.729	2.205	-0.118	-1.633	0.000	2.860	0.423	0.119	-0.078	-0.007	0.255	0.747
C1t	-4.107	2.300	-0.125	-1.663	0.000	3.476	0.401	0.130	-0.180	0.016	0.266	0.728
C1b	-3.671	2.219	-0.116	-1.865	0.000	4.808	0.488	0.127	-0.195	0.048	0.269	0.753
C2t	-1.973	1.908	-0.107	-1.496	0.000	5.139	0.459	0.245	-0.004	0.093	0.265	0.543
C2b	-3.621	2.471	-0.141	-1.831	-0.001	7.593	0.684	0.334	-0.127	0.108	0.308	0.647
C3t	-3.359	2.204	-0.128	-1.227	-0.001	5.679	0.376	0.219	-0.026	0.110	0.217	0.536
C3b	-5.262	2.934	-0.181	-1.510	-0.001	7.898	0.561	0.228	-0.197	0.136	0.329	0.634
C4t	-4.840	2.459	-0.137	-1.525	0.000	2.906	0.382	0.083	-0.071	0.054	0.276	0.700
C4b	-4.836	2.494	-0.133	-1.778	0.000	4.627	0.445	0.078	-0.019	0.094	0.298	0.731
C1t	-1.434	1.499	-0.066	-1.444	-0.001	4.865	0.401	0.080	-0.123	0.081	0.285	0.623
C1b	-7.805	3.623	-0.226	-1.592	-0.001	4.667	0.603	0.268	-0.058	0.105	0.322	0.657
C2t	0.178	0.851	-0.028	-0.737	-0.003	3.171	0.319	0.111	-0.165	0.111	0.255	0.527
C2b	-4.334	2.430	-0.150	-1.150	0.000	2.403	0.385	0.199	-0.059	0.149	0.257	0.576
C3t	-0.834	1.510	-0.089	-1.124	-0.001	12.59	0.280	0.108	-0.211	0.048	0.241	0.486
C3b	-3.734	2.433	-0.145	-1.571	0.000	6.400	0.434	0.177	-0.061	0.079	0.237	0.620
C4t	-5.067	2.633	-0.150	-1.583	0.000	6.701	0.432	0.140	-0.058	0.066	0.298	0.602
C4b	-8.178	3.802	-0.243	-1.688	0.000	5.073	0.609	0.298	-0.027	0.082	0.309	0.627
B1l	0.209	1.311	-0.080	-0.439	-0.002	1.321	0.230	0.070	-0.114	0.000	0.153	0.387
B1r	-4.994	2.882	-0.196	-0.796	0.000	2.053	0.331	0.172	0.016	0.010	0.171	0.411
B2l	-9.019	3.897	-0.242	-1.291	-0.003	6.077	0.804	0.446	0.083	-0.015	0.408	0.686
B2r	-8.643	3.813	-0.236	-1.384	-0.002	5.214	0.808	0.437	0.125	0.008	0.400	0.686
B3l	-5.214	2.989	-0.196	-0.959	0.000	2.600	0.405	0.204	0.047	0.047	0.213	0.443
B3r	-3.933	2.485	-0.166	-0.428	-0.002	1.264	0.349	0.187	-0.051	0.077	0.187	0.422
B1l	-4.608	2.832	-0.190	-0.668	-0.001	4.665	0.391	0.196	-0.040	-0.040	0.204	0.386
B1r	-7.240	3.577	-0.240	-1.025	0.000	2.909	0.455	0.243	0.100	0.054	0.204	0.490
B2l	-6.465	3.361	-0.204	-1.675	-0.001	7.948	0.886	0.502	0.119	0.048	0.397	0.661
B2r	-5.976	3.189	-0.192	-1.596	-0.002	7.495	0.898	0.508	0.094	0.061	0.405	0.676
B3l	-5.554	3.163	-0.206	-1.096	0.000	3.204	0.444	0.230	0.070	0.045	0.237	0.493
B3r	-1.949	2.012	-0.124	-0.779	-0.001	4.169	0.404	0.198	0.094	0.062	0.205	0.420
B1l	-1.883	2.026	-0.124	-0.968	0.000	6.355	0.551	0.313	0.000	-0.006	0.220	0.412
B1r	-3.724	2.580	-0.164	-1.148	0.000	3.542	0.494	0.248	0.127	0.099	0.212	0.518
B2l	-7.013	3.504	-0.215	-1.668	-0.001	7.390	0.903	0.514	0.115	0.074	0.378	0.667
B2r	-5.927	3.236	-0.197	-1.709	-0.001	7.875	0.883	0.497	0.097	0.047	0.391	0.671
B3l	-7.965	3.918	-0.261	-1.181	0.000	3.923	0.525	0.270	0.096	0.068	0.234	0.511
B3r	-0.547	1.661	-0.099	-0.942	0.000	4.789	0.488	0.228	0.052	0.094	0.197	0.466
B1l	-2.712	2.343	-0.147	-1.109	0.000	6.889	0.521	0.249	0.005	0.005	0.215	0.461
B1r	-4.031	2.685	-0.171	-1.202	0.000	3.876	0.549	0.284	0.127	0.110	0.216	0.524
B2l	-4.485	2.712	-0.161	-1.441	-0.001	6.483	0.851	0.494	0.060	0.064	0.364	0.635
B2r	-5.032	2.888	-0.172	-1.516	-0.002	6.941	0.857	0.479	0.088	0.051	0.384	0.680
B3l	-7.789	3.855	-0.254	-1.202	0.000	4.052	0.552	0.263	0.059	0.114	0.248	0.514
B3r	-4.926	2.990	-0.195	-1.087	0.000	6.198	0.485	0.274	0.114	0.100	0.234	0.459
B1l	-2.352	2.307	-0.148	-1.096	0.000	6.369	0.453	0.194	-0.103	0.020	0.213	0.475
B1r	-3.735	2.593	-0.162	-1.266	0.000	4.089	0.586	0.333	0.089	0.097	0.222	0.535
B2l	-7.487	3.619	-0.231	-1.456	-0.001	6.455	0.780	0.467	0.072	0.009	0.361	0.617
B2r	-6.534	3.356	-0.210	-1.535	-0.001	6.962	0.770	0.453	0.110	0.024	0.352	0.610
B3l	-6.619	3.552	-0.234	-1.227	0.000	4.179	0.556	0.279	0.085	0.103	0.238	0.522
B3r	-4.044	2.741	-0.176	-1.092	0.000	4.970	0.484	0.201	0.046	0.048	0.228	0.474

Table A3.7 (Continued) - Coefficients of the equation derived to predict absorbed hysteretic energy at the member ends (rad.mm)

Beam/ Col.	Predictive Equation Coefficients										Standard Deviations	
	r1	r2	r3	r4	r5	r6	r7	r8	r9	r10	σ_e	σ_s
B1l	-2.636	2.372	-0.148	-1.183	0.000	6.683	0.436	0.160	-0.005	0.044	0.192	0.489
B1r	-4.146	2.750	-0.173	-1.294	0.000	4.208	0.519	0.262	0.098	0.066	0.217	0.547
B2l	-4.496	2.656	-0.159	-1.260	-0.002	6.660	0.668	0.388	0.016	0.003	0.319	0.548
B2r	-3.827	2.498	-0.145	-1.479	-0.001	7.388	0.693	0.373	0.131	-0.002	0.341	0.578
B3l	-4.993	3.066	-0.197	-1.241	0.000	3.986	0.495	0.236	0.059	0.125	0.226	0.525
B3r	-2.449	2.259	-0.139	-1.117	0.000	4.967	0.494	0.229	-0.025	0.071	0.242	0.495
B1l	1.705	1.022	-0.046	-1.193	0.000	5.654	0.496	0.209	-0.003	0.027	0.209	0.504
B1r	-4.767	2.924	-0.186	-1.305	0.000	3.971	0.522	0.254	0.054	0.078	0.219	0.566
B2l	-1.038	1.627	-0.077	-1.326	-0.002	7.915	0.515	0.269	0.051	-0.012	0.317	0.556
B2r	1.307	0.961	-0.026	-1.447	-0.001	8.423	0.485	0.242	0.098	-0.007	0.338	0.573
B3l	-5.843	3.311	-0.214	-1.228	0.000	3.822	0.448	0.205	0.024	0.112	0.220	0.550
B3r	-4.805	2.962	-0.190	-1.204	0.000	5.853	0.546	0.284	0.054	0.070	0.222	0.503
B1l	-2.295	2.105	-0.122	-1.106	0.000	6.394	0.299	0.137	-0.034	0.059	0.219	0.514
B1r	-3.691	2.607	-0.160	-1.344	0.000	3.746	0.451	0.181	0.059	0.064	0.227	0.599
B2l	-1.634	1.823	-0.089	-1.393	-0.002	9.732	0.486	0.220	0.060	-0.003	0.327	0.605
B2r	-3.762	2.423	-0.133	-1.401	-0.002	8.883	0.552	0.309	0.096	-0.048	0.351	0.621
B3l	-5.422	3.214	-0.206	-1.272	0.000	4.616	0.416	0.165	0.006	0.060	0.221	0.510
B3r	1.012	1.157	-0.053	-1.140	0.000	5.519	0.383	0.195	0.025	0.060	0.172	0.523

Table A3.8 - Coefficients of the equation derived to predict Park and Ang damage at the member ends (rad.mm)

Beam/ Col.	Predictive Equation Coefficients										Standard Deviations	
	r1	r2	r3	r4	r5	r6	r7	r8	r9	r10	σ_e	σ_s
C1t	-7.878	1.889	-0.123	-0.692	-0.001	2.695	0.349	0.191	-0.014	0.040	0.167	0.285
C1b	-5.108	0.958	-0.060	-0.462	0.000	2.408	0.212	0.100	-0.009	0.038	0.112	0.208
C2t	-7.315	1.861	-0.121	-0.640	-0.001	2.370	0.343	0.183	-0.037	0.022	0.185	0.299
C2b	-7.121	1.696	-0.113	-0.553	-0.001	5.438	0.302	0.153	-0.048	0.032	0.151	0.260
C3t	-7.369	1.875	-0.123	-0.623	-0.001	2.741	0.329	0.173	-0.035	0.023	0.181	0.285
C3b	-7.415	1.797	-0.119	-0.603	0.000	3.617	0.313	0.168	-0.008	0.032	0.147	0.251
C4t	-7.867	1.893	-0.124	-0.639	-0.001	2.767	0.326	0.175	-0.018	0.028	0.167	0.275
C4b	-7.650	1.726	-0.116	-0.509	0.000	1.837	0.234	0.121	-0.025	0.037	0.119	0.227
C1t	-6.010	1.352	-0.089	-0.530	0.000	2.000	0.234	0.121	-0.022	0.012	0.109	0.223
C1b	-5.263	1.013	-0.062	-0.512	0.000	0.901	0.150	0.060	-0.049	-0.003	0.094	0.271
C2t	-8.652	2.185	-0.145	-0.686	-0.001	3.321	0.391	0.209	-0.007	0.036	0.197	0.314
C2b	-5.821	1.205	-0.075	-0.590	0.000	3.642	0.172	0.073	-0.051	0.017	0.082	0.204
C3t	-7.829	1.909	-0.127	-0.642	-0.001	5.057	0.348	0.189	-0.022	0.038	0.160	0.270
C3b	-6.591	1.480	-0.096	-0.573	-0.001	4.123	0.260	0.129	-0.034	0.041	0.125	0.221
C4t	-6.534	1.501	-0.099	-0.566	0.000	1.807	0.255	0.140	-0.001	0.018	0.110	0.241
C4b	-6.119	1.289	-0.082	-0.552	0.000	1.034	0.167	0.075	-0.043	-0.001	0.097	0.277
C1t	-6.569	1.484	-0.096	-0.603	0.000	2.029	0.270	0.141	-0.011	0.020	0.115	0.254
C1b	-6.644	1.479	-0.096	-0.602	0.000	1.594	0.219	0.102	-0.034	0.000	0.104	0.271
C2t	-8.597	2.187	-0.143	-0.853	-0.001	5.986	0.408	0.215	-0.021	0.062	0.179	0.324
C2b	-5.651	1.163	-0.070	-0.721	0.000	4.673	0.153	0.066	-0.056	0.019	0.097	0.219
C3t	-7.297	1.759	-0.114	-0.777	0.000	5.682	0.323	0.168	-0.032	0.041	0.145	0.269
C3b	-6.283	1.414	-0.085	-0.863	-0.001	6.900	0.295	0.141	0.006	0.068	0.132	0.307

Table A3.8 (Continued) - Coefficients of the equation derived to predict Park and Ang damage at the member ends (rad.mm)

Beam/ Col.	Predictive Equation Coefficients										Standard Deviations	
	r1	r2	r3	r4	r5	r6	r7	r8	r9	r10	σ_e	σ_s
C4t	-7.107	1.647	-0.108	-0.627	0.000	1.944	0.276	0.149	0.006	0.019	0.112	0.267
C4b	-6.890	1.568	-0.102	-0.616	0.000	1.639	0.235	0.115	-0.010	0.011	0.108	0.270
C1t	-6.905	1.589	-0.103	-0.661	0.000	2.168	0.267	0.132	-0.017	0.015	0.112	0.271
C1b	-6.855	1.563	-0.101	-0.656	0.000	2.065	0.251	0.119	-0.023	0.018	0.109	0.275
C2t	-7.493	1.909	-0.120	-1.114	0.000	7.473	0.377	0.190	-0.003	0.061	0.160	0.355
C2b	-6.269	1.441	-0.088	-0.869	0.000	5.655	0.162	0.058	-0.087	0.019	0.117	0.244
C3t	-7.852	1.946	-0.127	-0.918	0.000	6.236	0.267	0.127	-0.053	0.028	0.118	0.275
C3b	-5.863	1.364	-0.080	-1.022	0.000	6.827	0.318	0.152	-0.013	0.072	0.135	0.330
C4t	-7.185	1.670	-0.108	-0.696	0.000	2.207	0.288	0.148	0.004	0.022	0.112	0.289
C4b	-7.113	1.633	-0.105	-0.679	0.000	2.134	0.276	0.140	0.010	0.029	0.112	0.285
C1t	-6.496	1.469	-0.092	-0.714	0.000	2.398	0.255	0.116	-0.011	0.024	0.111	0.287
C1b	-6.855	1.570	-0.101	-0.691	0.000	2.576	0.272	0.129	-0.011	0.026	0.116	0.277
C2t	-5.137	1.217	-0.065	-1.276	0.000	7.406	0.373	0.185	-0.011	0.061	0.155	0.409
C2b	-6.319	1.460	-0.090	-0.803	0.000	5.589	0.241	0.107	-0.065	0.027	0.135	0.252
C3t	-4.716	1.025	-0.056	-1.060	0.000	6.658	0.207	0.088	-0.093	0.005	0.131	0.292
C3b	-6.409	1.545	-0.096	-0.845	0.000	6.282	0.285	0.134	-0.073	0.019	0.147	0.284
C4t	-6.802	1.566	-0.099	-0.750	0.000	2.489	0.278	0.136	-0.002	0.020	0.114	0.306
C4b	-7.446	1.740	-0.112	-0.705	0.000	2.409	0.283	0.135	0.000	0.027	0.119	0.291
C1t	-6.756	1.545	-0.098	-0.728	0.000	2.562	0.257	0.116	-0.008	0.020	0.109	0.293
C1b	-6.991	1.622	-0.105	-0.693	0.000	2.800	0.283	0.138	-0.004	0.029	0.116	0.276
C2t	-6.308	1.526	-0.090	-1.121	0.000	5.780	0.278	0.119	-0.062	-0.009	0.156	0.377
C2b	-6.975	1.580	-0.100	-0.690	-0.001	4.679	0.337	0.175	-0.020	0.046	0.155	0.272
C3t	-7.986	1.927	-0.123	-0.897	0.000	5.560	0.060	-0.011	-0.129	0.012	0.127	0.258
C3b	-6.981	1.611	-0.103	-0.662	-0.001	4.623	0.338	0.172	-0.041	0.032	0.159	0.271
C4t	-6.947	1.599	-0.101	-0.754	0.000	2.601	0.265	0.122	-0.011	0.024	0.115	0.307
C4b	-7.105	1.648	-0.106	-0.706	0.000	2.723	0.290	0.144	0.004	0.034	0.120	0.286
C1t	-6.438	1.429	-0.089	-0.724	0.000	2.681	0.250	0.112	-0.021	0.024	0.112	0.284
C1b	-6.713	1.510	-0.095	-0.745	0.000	3.049	0.284	0.131	-0.012	0.033	0.124	0.291
C2t	-7.440	1.710	-0.111	-0.754	0.000	2.776	0.199	0.082	-0.089	0.012	0.130	0.289
C2b	-8.838	2.138	-0.140	-0.778	-0.001	5.537	0.392	0.206	0.003	0.072	0.175	0.318
C3t	-5.947	1.124	-0.068	-0.468	-0.001	2.369	0.053	-0.001	-0.119	0.017	0.094	0.215
C3b	-8.555	2.073	-0.136	-0.769	0.000	5.899	0.402	0.224	0.036	0.082	0.162	0.310
C4t	-6.768	1.522	-0.095	-0.741	0.000	2.764	0.268	0.130	-0.006	0.026	0.117	0.294
C4b	-7.457	1.726	-0.110	-0.760	0.000	3.107	0.306	0.150	0.007	0.041	0.127	0.303
C1t	-6.565	1.435	-0.089	-0.776	0.000	3.076	0.282	0.129	-0.014	0.031	0.125	0.306
C1b	-6.735	1.595	-0.103	-0.637	0.000	3.647	0.286	0.142	-0.022	0.034	0.142	0.256
C2t	-6.451	1.215	-0.078	-0.352	-0.001	1.113	0.167	0.086	-0.061	0.031	0.125	0.209
C2b	-8.894	2.061	-0.138	-0.692	0.000	2.930	0.291	0.158	-0.051	0.012	0.161	0.307
C3t	-5.262	0.804	-0.047	-0.289	-0.001	1.104	0.101	0.038	-0.078	0.041	0.112	0.195
C3b	-7.416	1.707	-0.108	-0.833	0.000	4.546	0.309	0.146	-0.004	0.035	0.129	0.308
C4t	-7.012	1.553	-0.097	-0.765	0.000	2.836	0.292	0.142	-0.004	0.031	0.124	0.309
C4b	-7.007	1.687	-0.109	-0.675	0.000	3.823	0.292	0.149	-0.016	0.037	0.139	0.258
B1l	-6.193	1.374	-0.090	-0.469	0.000	2.637	0.233	0.123	0.004	0.031	0.116	0.200
B1r	-6.559	1.412	-0.093	-0.462	0.000	2.810	0.234	0.125	0.003	0.028	0.116	0.197
B2l	-5.327	1.088	-0.060	-0.575	-0.001	2.938	0.334	0.191	0.066	-0.008	0.186	0.272
B2r	-5.251	1.070	-0.058	-0.603	-0.001	2.926	0.351	0.199	0.070	-0.010	0.199	0.284
B3l	-7.074	1.627	-0.106	-0.576	0.000	2.814	0.296	0.161	0.008	0.036	0.144	0.240

Table A3.8 (Continued) - Coefficients of the equation derived to Park and Ang damage at the member ends (rad.mm)

Beam/ Col.	Predictive Equation Coefficients										Standard Deviations	
	r1	r2	r3	r4	r5	r6	r7	r8	r9	r10	σ_e	σ_s
B3r	-5.969	1.300	-0.084	-0.480	0.000	2.631	0.249	0.132	0.006	0.037	0.121	0.205
B1l	-6.490	1.489	-0.098	-0.456	-0.001	3.445	0.257	0.138	0.006	0.030	0.127	0.206
B1r	-6.326	1.388	-0.091	-0.474	0.000	3.147	0.249	0.131	-0.002	0.026	0.123	0.204
B2l	-4.681	0.940	-0.050	-0.548	0.000	3.786	0.335	0.199	0.072	-0.010	0.177	0.254
B2r	-4.413	0.919	-0.048	-0.685	0.000	5.995	0.335	0.191	0.034	0.003	0.188	0.264
B3l	-6.995	1.638	-0.108	-0.513	-0.001	2.819	0.297	0.162	-0.008	0.033	0.145	0.237
B3r	-6.402	1.455	-0.095	-0.463	-0.001	3.039	0.266	0.141	0.002	0.037	0.129	0.214
B1l	-6.154	1.414	-0.093	-0.475	0.000	3.790	0.269	0.145	0.006	0.033	0.125	0.206
B1r	-6.328	1.414	-0.094	-0.497	0.000	3.478	0.262	0.138	-0.007	0.029	0.120	0.206
B2l	-4.289	0.847	-0.044	-0.570	0.000	4.806	0.340	0.207	0.071	-0.007	0.175	0.249
B2r	-4.572	0.930	-0.050	-0.570	0.000	4.642	0.346	0.205	0.070	-0.014	0.180	0.258
B3l	-6.976	1.656	-0.110	-0.528	-0.001	3.073	0.308	0.171	0.008	0.037	0.143	0.236
B3r	-6.224	1.423	-0.093	-0.466	-0.001	3.226	0.276	0.152	0.014	0.036	0.128	0.212
B1l	-6.092	1.411	-0.093	-0.497	0.000	4.114	0.269	0.145	0.004	0.031	0.122	0.205
B1r	-6.139	1.361	-0.089	-0.514	0.000	3.615	0.260	0.133	0.001	0.045	0.079	0.211
B2l	-2.371	0.249	0.000	-0.524	0.000	4.912	0.332	0.201	0.056	0.001	0.172	0.249
B2r	-4.740	0.975	-0.055	-0.550	0.000	4.553	0.347	0.207	0.063	-0.009	0.174	0.257
B3l	-6.947	1.661	-0.110	-0.551	0.000	3.359	0.315	0.177	0.014	0.039	0.138	0.236
B3r	-6.263	1.445	-0.095	-0.486	0.000	3.490	0.281	0.156	0.017	0.040	0.123	0.213
B1l	-6.025	1.405	-0.093	-0.527	0.000	4.295	0.264	0.138	0.002	0.035	0.120	0.207
B1r	-5.978	1.341	-0.088	-0.563	0.000	4.024	0.262	0.138	-0.002	0.034	0.117	0.209
B2l	-2.293	0.242	0.000	-0.566	0.000	6.343	0.313	0.188	0.053	-0.011	0.148	0.241
B2r	-4.519	0.901	-0.049	-0.547	0.000	4.652	0.327	0.197	0.064	-0.014	0.168	0.246
B3l	-6.931	1.673	-0.111	-0.583	0.000	3.623	0.307	0.170	0.012	0.040	0.137	0.236
B3r	-6.303	1.474	-0.097	-0.514	0.000	3.699	0.276	0.152	0.014	0.038	0.123	0.213
B1l	-6.045	1.417	-0.093	-0.549	0.000	4.406	0.256	0.130	0.004	0.035	0.119	0.210
B1r	-6.148	1.394	-0.092	-0.575	0.000	4.070	0.255	0.130	-0.001	0.033	0.115	0.211
B2l	-4.595	0.881	-0.048	-0.483	-0.001	4.799	0.294	0.172	0.048	-0.010	0.164	0.236
B2r	-2.484	0.258	0.000	-0.547	-0.001	4.906	0.298	0.171	0.057	-0.002	0.146	0.240
B3l	-6.824	1.649	-0.109	-0.606	0.000	3.801	0.297	0.162	0.014	0.043	0.137	0.237
B3r	-6.264	1.466	-0.096	-0.531	0.000	3.769	0.269	0.146	0.016	0.041	0.125	0.214
B1l	-5.881	1.366	-0.089	-0.576	0.000	4.446	0.263	0.136	0.000	0.036	0.120	0.214
B1r	-6.170	1.396	-0.091	-0.587	0.000	4.034	0.258	0.132	0.000	0.033	0.115	0.215
B2l	-5.167	0.904	-0.048	-0.521	-0.001	4.899	0.272	0.153	0.034	-0.003	0.171	0.247
B2r	-5.240	0.924	-0.049	-0.536	-0.001	4.652	0.264	0.143	0.041	-0.002	0.169	0.250
B3l	-6.752	1.624	-0.107	-0.614	0.000	3.899	0.291	0.157	0.015	0.043	0.135	0.237
B3r	-6.144	1.430	-0.093	-0.547	0.000	3.888	0.270	0.146	0.019	0.043	0.122	0.218
B1l	-5.215	1.122	-0.071	-0.480	0.000	4.498	0.214	0.105	-0.008	0.035	0.105	0.191
B1r	-6.017	1.340	-0.087	-0.574	0.000	4.146	0.249	0.124	-0.002	0.035	0.111	0.211
B2l	-5.813	1.115	-0.062	-0.593	-0.001	5.849	0.274	0.146	0.027	0.004	0.178	0.268
B2r	-6.365	1.279	-0.074	-0.614	-0.001	4.985	0.288	0.159	0.033	-0.007	0.177	0.272
B3l	-6.859	1.643	-0.108	-0.592	0.000	3.998	0.281	0.151	0.008	0.036	0.133	0.230
B3r	-5.545	1.218	-0.079	-0.470	0.000	4.085	0.225	0.120	-0.003	0.029	0.109	0.190

Table A3.9 - Coefficients of the equation derived to predict fatigue damage at the member ends

Beam/ Col.	Predictive Equation Coefficients										Standard Deviations	
	r1	r2	r3	r4	r5	r6	r7	r8	r9	r10	σ_e	σ_s
C1t	-41.543	11.198	-0.778	-1.902	0.000	2.448	1.108	0.676	-0.007	-0.171	0.697	1.016
C1b	-14.517	2.062	-0.068	-2.288	-0.001	4.589	1.726	1.120	0.378	-0.206	1.131	1.507
C2t	-24.763	6.878	-0.458	-2.192	0.000	3.329	1.061	0.615	-0.262	-0.052	0.639	1.104
C2b	-31.827	8.568	-0.593	-1.702	0.000	4.933	0.903	0.505	-0.241	-0.050	0.557	0.871
C3t	-25.156	6.992	-0.467	-2.129	0.000	3.341	1.057	0.623	-0.266	-0.060	0.667	1.112
C3b	-18.289	4.484	-0.284	-1.901	0.000	4.670	0.979	0.549	-0.089	-0.053	0.508	0.912
C4t	-40.183	10.818	-0.751	-1.884	0.000	2.590	1.088	0.659	-0.023	-0.190	0.695	1.010
C4b	-54.344	14.061	-0.962	-2.398	0.000	3.790	1.709	1.111	0.315	-0.263	1.111	1.534
C1t	-13.097	2.540	-0.140	-1.535	0.000	2.262	0.983	0.603	-0.017	-0.177	0.606	0.892
C1b	-9.891	0.898	0.000	-1.476	0.000	0.539	0.692	0.391	-0.047	-0.456	0.763	1.151
C2t	-22.489	5.822	-0.381	-2.087	0.000	3.893	1.179	0.692	-0.134	-0.054	0.651	1.067
C2b	-33.170	8.574	-0.593	-1.523	0.000	2.661	0.803	0.432	-0.157	-0.076	0.489	0.792
C3t	-36.569	10.136	-0.709	-2.066	0.000	6.726	1.179	0.709	-0.213	-0.034	0.655	1.027
C3b	-29.260	7.363	-0.498	-1.448	0.000	3.863	0.621	0.312	-0.218	-0.069	0.475	0.718
C4t	-37.038	9.733	-0.674	-1.616	0.000	1.966	1.020	0.642	-0.020	-0.210	0.642	0.942
C4b	-9.975	0.950	-0.002	-1.587	0.000	0.665	0.789	0.476	0.034	-0.431	0.770	1.181
C1t	-39.475	10.336	-0.717	-1.640	0.000	1.664	1.049	0.643	0.059	-0.257	0.642	0.984
C1b	-11.681	1.750	-0.074	-1.532	0.000	1.056	0.918	0.549	0.022	-0.315	0.676	1.002
C2t	-23.964	6.205	-0.402	-2.422	0.000	5.401	1.252	0.719	-0.091	-0.026	0.654	1.109
C2b	-11.738	2.055	-0.075	-2.490	0.000	4.803	0.928	0.475	0.015	-0.070	0.647	1.054
C3t	-23.822	6.122	-0.394	-2.421	0.000	5.861	1.240	0.696	0.004	0.000	0.639	1.111
C3b	-9.391	1.336	-0.030	-2.168	0.000	5.103	0.720	0.371	-0.087	-0.150	0.587	0.881
C4t	-39.971	10.501	-0.728	-1.673	0.000	1.746	1.066	0.663	0.089	-0.239	0.647	0.996
C4b	-42.419	11.095	-0.771	-1.612	0.000	1.190	0.969	0.589	-0.023	-0.380	0.688	1.014
C1t	-42.415	11.065	-0.760	-1.583	0.000	1.620	0.808	0.449	-0.185	-0.185	0.683	1.037
C1b	-42.357	11.133	-0.775	-1.642	0.000	1.384	0.998	0.590	-0.046	-0.351	0.668	1.007
C2t	-20.336	5.020	-0.301	-2.802	0.000	5.432	1.151	0.634	-0.042	-0.110	0.671	1.165
C2b	-13.047	2.758	-0.133	-2.626	0.000	5.122	0.852	0.403	-0.130	-0.159	0.633	1.073
C3t	-19.499	4.726	-0.278	-2.768	0.000	5.624	1.174	0.666	-0.042	-0.133	0.661	1.189
C3b	-11.382	2.174	-0.091	-2.418	0.000	5.403	0.821	0.411	-0.104	-0.116	0.591	0.967
C4t	-15.649	3.143	-0.175	-1.845	0.000	1.839	1.127	0.704	0.077	-0.229	0.651	1.062
C4b	-42.676	11.213	-0.777	-1.740	0.000	1.642	1.038	0.634	0.093	-0.287	0.674	1.037
C1t	-15.289	3.003	-0.161	-1.899	0.000	1.770	1.051	0.619	0.055	-0.257	0.660	1.072
C1b	-41.561	10.933	-0.758	-1.754	0.000	1.881	1.048	0.633	0.025	-0.258	0.658	1.025
C2t	-8.495	1.440	-0.022	-3.193	0.000	5.631	1.012	0.491	-0.094	-0.148	0.727	1.309
C2b	-18.432	4.442	-0.264	-2.395	0.000	4.938	0.946	0.494	-0.123	-0.108	0.589	1.036
C3t	-7.649	1.147	0.000	-3.078	0.000	4.972	0.884	0.371	-0.203	-0.239	0.730	1.295
C3b	-16.302	3.860	-0.231	-2.202	0.000	5.378	0.813	0.428	-0.242	-0.170	0.549	0.897
C4t	-16.288	3.325	-0.183	-1.976	0.000	1.933	1.089	0.649	0.078	-0.255	0.671	1.098
C4b	-42.709	11.288	-0.782	-1.805	0.000	1.913	1.065	0.640	0.051	-0.272	0.671	1.053
C1t	-15.127	2.929	-0.153	-1.959	0.000	1.887	1.019	0.589	0.087	-0.295	0.671	1.089
C1b	-16.348	3.422	-0.197	-1.836	0.000	2.168	1.084	0.658	0.026	-0.211	0.625	1.032
C2t	-12.345	2.483	-0.106	-2.772	0.000	4.696	0.717	0.303	-0.222	-0.336	0.690	1.137
C2b	-22.473	5.500	-0.350	-2.225	0.000	3.911	1.178	0.696	0.012	-0.145	0.612	1.056
C3t	-10.342	1.736	-0.052	-2.550	0.000	3.778	0.582	0.222	-0.243	-0.326	0.679	1.063
C3b	-17.397	3.925	-0.238	-1.921	0.000	4.203	1.016	0.600	-0.098	-0.107	0.594	0.895
C4t	-15.388	3.016	-0.157	-2.005	0.000	1.972	1.039	0.601	0.069	-0.291	0.689	1.109

Table A3.9 (Continued) – Coefficients of the equation derived to predict fatigue damage at the member ends

Beam/ Col.	Predictive Equation Coefficients										Standard Deviations	
	R1	r2	r3	r4	r5	r6	r7	r8	r9	r10	σ_e	σ_s
C4b	-41.747	11.056	-0.766	-1.839	0.000	2.130	1.100	0.670	0.061	-0.249	0.657	1.042
C1t	-13.731	2.376	-0.109	-1.940	0.000	1.912	1.032	0.608	0.100	-0.304	0.707	1.107
C1b	-15.618	3.058	-0.163	-1.968	0.000	2.197	1.126	0.669	0.082	-0.236	0.680	1.098
C2t	-15.460	2.930	-0.158	-1.744	0.000	2.317	0.639	0.368	-0.194	-0.294	0.630	0.890
C2b	-23.232	5.614	-0.360	-2.154	0.000	3.503	1.270	0.751	-0.001	-0.088	0.644	1.088
C3t	-11.307	1.440	-0.045	-1.362	0.000	2.151	0.372	0.195	-0.072	-0.171	0.564	0.782
C3b	-21.432	5.051	-0.322	-2.021	0.000	4.119	1.259	0.765	0.035	-0.031	0.638	1.038
C4t	-45.740	12.029	-0.828	-2.005	0.000	2.094	1.056	0.618	0.096	-0.354	0.744	1.130
C4b	-45.706	12.120	-0.839	-1.965	0.000	2.180	1.161	0.690	-0.007	-0.327	0.716	1.104
C1t	-12.685	1.865	-0.061	-2.131	0.000	2.106	1.180	0.707	0.197	-0.301	0.790	1.244
C1b	-17.806	4.140	-0.245	-2.157	0.000	3.594	1.164	0.681	0.017	-0.113	0.674	1.053
C2t	-10.017	0.669	0.000	-0.697	-0.002	0.646	0.670	0.457	0.039	-0.159	0.640	0.871
C2b	-14.021	2.416	-0.130	-1.513	0.000	1.547	0.912	0.568	-0.034	-0.268	0.649	0.937
C3t	-9.898	0.668	0.000	-0.842	-0.001	-2.160	0.680	0.454	0.063	-0.201	0.616	0.842
C3b	-42.458	11.173	-0.775	-2.022	0.000	-3.978	1.009	0.553	-0.088	-0.269	0.675	1.011
C4t	-13.387	2.081	-0.078	-2.119	0.000	-2.012	1.220	0.732	0.174	-0.309	0.797	1.249
C4b	-17.880	4.184	-0.248	-2.190	0.000	-3.657	1.192	0.698	0.026	-0.129	0.677	1.057
B1l	-39.147	10.128	-0.689	-1.969	0.000	-3.819	1.362	0.862	0.159	-0.229	0.897	1.173
B1r	-45.420	11.713	-0.809	-1.628	0.000	-2.918	1.234	0.806	0.218	-0.291	0.890	1.117
B2l	-33.895	9.791	-0.676	-2.110	0.000	-6.728	0.866	0.485	-0.346	0.032	0.629	0.965
B2r	-35.149	10.175	-0.708	-2.085	0.000	-5.278	0.943	0.536	-0.251	-0.053	0.577	0.981
B3l	-44.940	11.949	-0.829	-1.867	0.000	-3.118	1.266	0.793	0.161	-0.159	0.842	1.095
B3r	-35.353	8.992	-0.603	-2.008	0.000	-4.131	1.381	0.879	0.161	-0.223	0.897	1.181
B1l	-15.650	3.268	-0.183	-1.748	-0.001	-3.940	1.243	0.769	0.029	-0.170	0.792	1.085
B1r	-12.469	2.042	-0.093	-1.579	0.000	3.207	1.205	0.757	0.099	-0.228	0.779	1.051
B2l	-21.935	6.385	-0.431	-1.923	0.000	6.690	0.905	0.516	-0.303	-0.019	0.544	0.956
B2r	-21.930	6.386	-0.431	-1.929	0.000	6.614	0.908	0.516	-0.308	-0.019	0.548	0.960
B3l	-15.663	3.381	-0.195	-1.754	0.000	3.526	1.182	0.742	0.000	-0.150	0.750	1.028
B3r	-16.388	3.501	-0.200	-1.791	-0.001	3.877	1.247	0.778	0.022	-0.152	0.797	1.091
B1l	-38.896	10.409	-0.718	-1.902	0.000	4.788	1.237	0.776	0.022	-0.192	0.767	1.070
B1r	-38.666	10.038	-0.693	-1.628	0.000	3.185	1.198	0.752	0.082	-0.218	0.754	1.033
B2l	-19.472	5.662	-0.382	-1.787	-0.001	6.796	0.895	0.520	-0.318	0.003	0.571	0.925
B2r	-28.688	8.504	-0.592	-1.959	0.000	8.145	0.889	0.512	-0.331	-0.008	0.540	0.932
B3l	-38.070	10.241	-0.708	-1.842	0.000	3.986	1.182	0.735	0.019	-0.157	0.706	1.032
B3r	-17.931	4.095	-0.245	-1.917	0.000	4.709	1.240	0.780	0.047	-0.142	0.763	1.074
B1l	-40.079	10.804	-0.748	-1.923	0.000	4.498	1.225	0.756	0.015	-0.183	0.771	1.073
B1r	-40.722	10.656	-0.738	-1.645	0.000	2.905	1.201	0.737	0.208	-0.157	0.773	1.041
B2l	-20.134	5.776	-0.391	-1.651	-0.001	6.577	0.883	0.513	-0.331	-0.001	0.525	0.925
B2r	-20.183	5.796	-0.392	-1.670	-0.001	6.560	0.889	0.518	-0.328	-0.002	0.526	0.927
B3l	-38.952	10.530	-0.730	-1.872	0.000	3.812	1.204	0.753	0.021	-0.159	0.726	1.041
B3r	-14.591	3.115	-0.173	-1.920	0.000	4.329	1.255	0.787	0.036	-0.125	0.755	1.080
B1l	-40.760	10.953	-0.756	-1.931	0.000	4.046	1.240	0.772	0.138	-0.070	0.815	1.060
B1r	-40.869	10.716	-0.741	-1.690	0.000	2.891	1.208	0.745	0.158	-0.236	0.774	1.033
B2l	-19.752	5.624	-0.379	-1.682	-0.001	7.002	0.848	0.493	-0.298	-0.018	0.515	0.877
B2r	-20.026	5.715	-0.385	-1.717	-0.001	7.197	0.856	0.494	-0.299	-0.023	0.515	0.887
B3l	-14.550	3.153	-0.178	-1.858	0.000	3.220	1.232	0.751	0.010	-0.058	0.686	1.038
B3r	-40.995	11.014	-0.759	-1.954	0.000	4.163	1.283	0.814	0.083	-0.057	0.798	1.068

Table A3.9 (Continued) - Coefficients of the equation derived to predict fatigue damage at the member ends

Beam/ Col.	Predictive Equation Coefficients										Standard Deviations	
	r1	r2	r3	r4	r5	r6	r7	r8	r9	r10	σ_e	σ_s
B1l	-43.111	11.571	-0.793	-1.925	0.000	3.086	1.076	0.598	-0.182	-0.177	0.811	1.068
B1r	-42.968	11.362	-0.788	-1.795	0.000	3.327	1.190	0.728	0.095	-0.273	0.791	1.036
B2l	-26.996	7.783	-0.536	-1.946	0.000	10.303	0.758	0.423	-0.291	-0.064	0.499	0.819
B2r	-27.125	7.796	-0.536	-1.946	0.000	9.867	0.759	0.421	-0.321	-0.067	0.536	0.823
B3l	-41.073	11.125	-0.771	-1.934	0.000	3.452	1.190	0.722	0.118	-0.114	0.728	1.039
B3r	-42.642	11.494	-0.794	-1.971	0.000	3.815	1.247	0.757	0.187	-0.117	0.802	1.073
B1l	-43.579	11.782	-0.814	-2.048	0.000	4.258	1.239	0.755	0.028	-0.217	0.806	1.070
B1r	-43.685	11.508	-0.800	-1.697	0.000	2.166	1.213	0.756	-0.019	-0.269	0.823	1.056
B2l	-11.123	2.081	-0.106	-1.415	-0.001	7.413	0.740	0.428	-0.084	-0.154	0.540	0.735
B2r	-11.328	2.150	-0.110	-1.444	-0.001	7.259	0.745	0.430	-0.082	-0.159	0.544	0.738
B3l	-42.705	11.488	-0.787	-1.950	0.000	3.094	1.083	0.558	-0.188	-0.144	0.709	1.054
B3r	-43.754	11.802	-0.815	-2.006	0.000	4.084	1.256	0.769	0.206	-0.135	0.807	1.078
B1l	-45.676	12.031	-0.822	-2.057	0.000	4.148	1.301	0.785	0.123	-0.275	0.921	1.161
B1r	-45.479	11.944	-0.824	-1.867	0.000	3.327	1.267	0.783	0.145	-0.287	0.851	1.093
B2l	-10.759	1.922	-0.091	-1.509	-0.001	9.120	0.750	0.432	-0.067	-0.172	0.561	0.763
B2r	-10.435	1.784	-0.081	-1.416	-0.001	8.227	0.741	0.430	-0.075	-0.177	0.563	0.757
B3l	-44.874	12.148	-0.845	-1.924	0.000	3.046	1.201	0.723	-0.123	-0.193	0.876	1.076
B3r	-46.599	12.297	-0.844	-1.967	0.000	3.588	1.330	0.809	0.191	-0.287	0.922	1.173